



# Effect of Dimensionality and Polymorphism on the properties of ZnO

Ilker Demiroglu

**ADVERTIMENT.** La consulta d'aquesta tesi queda condicionada a l'acceptació de les següents condicions d'ús: La difusió d'aquesta tesi per mitjà del servei TDX ([www.tdx.cat](http://www.tdx.cat)) i a través del Dipòsit Digital de la UB ([diposit.ub.edu](http://diposit.ub.edu)) ha estat autoritzada pels titulars dels drets de propietat intel·lectual únicament per a usos privats emmarcats en activitats d'investigació i docència. No s'autoritza la seva reproducció amb finalitats de lucre ni la seva difusió i posada a disposició des d'un lloc aliè al servei TDX ni al Dipòsit Digital de la UB. No s'autoritza la presentació del seu contingut en una finestra o marc aliè a TDX o al Dipòsit Digital de la UB (framing). Aquesta reserva de drets afecta tant al resum de presentació de la tesi com als seus continguts. En la utilització o cita de parts de la tesi és obligat indicar el nom de la persona autora.

**ADVERTENCIA.** La consulta de esta tesis queda condicionada a la aceptación de las siguientes condiciones de uso: La difusión de esta tesis por medio del servicio TDR ([www.tdx.cat](http://www.tdx.cat)) y a través del Repositorio Digital de la UB ([diposit.ub.edu](http://diposit.ub.edu)) ha sido autorizada por los titulares de los derechos de propiedad intelectual únicamente para usos privados enmarcados en actividades de investigación y docencia. No se autoriza su reproducción con finalidades de lucro ni su difusión y puesta a disposición desde un sitio ajeno al servicio TDR o al Repositorio Digital de la UB. No se autoriza la presentación de su contenido en una ventana o marco ajeno a TDR o al Repositorio Digital de la UB (framing). Esta reserva de derechos afecta tanto al resumen de presentación de la tesis como a sus contenidos. En la utilización o cita de partes de la tesis es obligado indicar el nombre de la persona autora.

**WARNING.** On having consulted this thesis you're accepting the following use conditions: Spreading this thesis by the TDX ([www.tdx.cat](http://www.tdx.cat)) service and by the UB Digital Repository ([diposit.ub.edu](http://diposit.ub.edu)) has been authorized by the titular of the intellectual property rights only for private uses placed in investigation and teaching activities. Reproduction with lucrative aims is not authorized nor its spreading and availability from a site foreign to the TDX service or to the UB Digital Repository. Introducing its content in a window or frame foreign to the TDX service or to the UB Digital Repository is not authorized (framing). Those rights affect to the presentation summary of the thesis as well as to its contents. In the using or citation of parts of the thesis it's obliged to indicate the name of the author.



Memòria presentada per

Ilker Demiroglu

per optar al grau de Doctor per la Universitat de Barcelona

Programa de doctorat en Química Teòrica i Computacional

**Effect of Dimensionality and Polymorphism  
on the properties of ZnO**

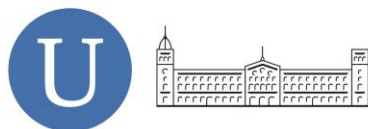
Dirigida per:

Dr. Stefan Thomas Bromley

Dr. Francesc Illas Riera

(Universitat de Barcelona i Institució  
Catalana de Recerca i Estudis Avançats)

(Universitat de Barcelona)



---

**B** Universitat de Barcelona

Barcelona, 2014

UNIVERSITAT DE BARCELONA  
FACULTAT DE QUÍMICA  
DEPARTAMENT DE QUÍMICA FÍSICA  
INSTITUT DE QUÍMICA TEÒRICA I COMPUTACIONAL

**Effect of Dimensionality and Polymorphism  
on the properties of ZnO**

Ilker Demiroglu

2014



Aileme

## Acknowledgments

First and foremost, I express my appreciation to Dr. Stefan Thomas Bromley for his mentoring, enormous support, motivation, patience, and for the opportunities he has provided throughout this study. I would like to thank Dr. Francesc Illas Riera for sharing his knowledge and experience, and also for his support and encouragement. This research would not have progressed as well without your expertise and support, so thank you all very much for your time and ideas.

I would like to express my gratitude to Dr. Konstantin Neyman for his support, which helped me a lot to finish up the study. I would like to also acknowledge Dr. Scott Woodley, Dr. Alexey Sokol and Dr. Martijn Zwijnenburg for their discussions, insight and guidance which have been very useful throughout the study.

I would like to thank to Oriol Lamiel Garcia, Sergey Kozlov, Albert Bruix Fuste, Dr. Francesc Viñes, Almudena Notario Estévez, Sergio Posada, and Alberto Figueroba for all of their help during my study and altogether with other members of our group for making me feel at home.

I would like to acknowledge the Center for Scientific and Academic Services of Catalonia (CESCA) and the Barcelona Supercomputer Center (BSC) for providing computer resources.

I also would like to acknowledge Thomas Young Centre (TYC) JRF and COST Action CM 1104 STSM schemes, which allowed me to do short time scientific visits to Materials Chemistry, London.

I also would like to express my thanks to my friends Ahmet Utku Yazgan, Ilker Demirkol, Bogachan Tahirbegi, Inci Gunler, Sivgin Dalkilic and Esra Yesilay for their moral support

Finally, I have to say an extra special thank to my family, Mehmet Demiroglu and Kadriye Demiroglu, for their continuous support and love.

“Every compound has different polymorphic forms, and that, in general, the number of forms known for a given compound is proportional to the time and money spent in research on that compound”

Walter Mc Crone

## **CONTENTS**

CHAPTER I: Introduction.....	1
1. Thesis Overview: .....	1
2. Structure .....	3
2.1. Crystal Structures: .....	4
2.2. Structural properties of ZnO .....	5
3. Semiconductivity .....	10
3.1. Semiconductivity and Band structure .....	10
3.2. ZnO as a wide bandgap semiconductor .....	12
3.3. Bandgap engineering of ZnO .....	16
3.4. Optical and Electronic properties of ZnO .....	16
4. Polymorphism.....	17
4.1. Introduction to Polymorphism .....	17
4.2. Polytypism .....	22
4.3. Hypothetical polymorphs .....	24
4.3.1. Structural Models by Analogy.....	24
4.3.2. Topological Modeling Methods .....	24
4.3.3. Directly Exploring Configurational Space (Global Optimization) .....	26
5. Scale and Dimensionality .....	29
5.1. Introduction.....	29
5.2. Synthesis of nano-ZnO .....	30
5.3. Nanostructured 3D materials.....	31
5.4. Nanofilms (2D) .....	32
5.5. Nanowires (1D).....	36
5.6. Nanoclusters (0D).....	38
6. Nanoporous systems.....	40
6.1. Introduction.....	40
6.2. Zeolites .....	41
6.3. Nanoporous ZnO .....	45
CHAPTER 3. METHODOLOGY .....	49
1. Energy Landscapes.....	49
2. Exploring the Configurational Space .....	51
2.1. Local Optimization Methods.....	52
2.1.1. Steepest Descent .....	53
2.1.2. Conjugate Gradient .....	53

2.1.3. Newton Raphson.....	54
2.2. Global Optimization Methods .....	54
2.2.1. Monte Carlo Basin-Hopping .....	55
3. Force Fields .....	58
3.1. Coulomb interaction .....	59
3.2. Electronic Polarizability .....	60
3.3. Interatomic Potential functions .....	61
3.3.1. Buckingham Potential .....	62
3.3.1. Lennard-Jones Potential .....	62
4. Electronic Structure Calculations.....	62
4.1. Many-Body Schrodinger Equation.....	62
4.2. Density Functional Theory.....	64
4.3. Exchange-Correlation Functional.....	65
4.4. Plane Waves.....	66
4.5. Projector Augmented Wave Method .....	67
4.6. Self Consistent Cycle.....	68
CHAPTER III Comparison of structures and stabilities of free space and surface-supported ZnO nanoclusters .....	69
1. Introduction.....	69
2. Methodology.....	71
3. Results and Discussion .....	76
3.1. Free Space Clusters .....	77
3.2. Interatomic Potential Based Global Optimization Results for ZnO Nanoclusters on the Ag(111) Surface.....	78
3.3. Effect of different surfaces; Ag(100) and Ag(110) .....	106
3.4. DFT results.....	117
5 Conclusions .....	127
CHAPTER IV: One monolayer ZnO A theoretical study of a ZnO graphene analogue: adsorption on Ag(111) and hydrogen transport.....	129
1. Introduction.....	129
2. Methodology.....	129
3. Results and discussion.....	132
3.1. Interaction of a 2D-ZnO single sheet with Ag(111).....	132
3.2. Transport of hydrogen through a 2D-ZnO single sheet .....	136
4. Conclusions.....	140
CHAPTER V: Effect of Finite Size on Epitaxial growth of ZnO on Ag(111) .....	141

1. Introduction.....	141
2. Methodology.....	143
3. Results and Discussion .....	144
3.1. ZnO coverages of 1 and 2 ML on Ag (111).....	144
3.2. ZnO coverages of 2.2, 2.3 and 2.75 ML on Ag (111).....	145
4. Conclusions.....	156
CHAPTER VI: Comparison of 3D-2D polymorphism of ZnO .....	157
1. Introduction.....	157
2. Methodology.....	158
3. Results and Discussion .....	159
4. Conclusions.....	167
CHAPTER VII: 3D polymorphism and effect of pore system (dimensionality): “Bandgap Engineering through Nanoporosity in ZnO” .....	168
1. Introduction .....	168
2. Methodology.....	169
3. Results and Discussion .....	171
4. Conclusions.....	182
Summary .....	183
Summary in Catalan.....	186
Publications: .....	208
Appendix .....	209
References .....	275

## List of Tables

Table 1. Unique unit cell Structures.....	5
Table 2. Experimentally determined principal phonon modes of wurtzite ZnO at 300 K. ....	8
Table 3. Basic physical properties of ZnO at 300 K. ....	12
Table 4. Ramsdell notations and layer stackings of simple SiC polytype structures. ....	22
Table 5. Some natural zeolites and date of discoveries.....	44
Table 6. Parameters for interatomic potentials used in this study. ....	74
Table 7. The average change of stabilization energy for 2D and 3D clusters from on Ag(111) surface to on Ag(100) and Ag(110) surfaces.....	116
Table 8. Energies and relevant distances for the 2D-ZnO-on-Ag(111) system. Column headings correspond to (i) level of theory: IP, DFT or DFT-D2, (ii) model: ratio of ZnO to Ag unit cells used, ((iii)–(iv)) $a_x$ :lattice parameter of isolated optimized subsystem (Å), (v) ratio of $a$ parameters of the individually optimized ZnO sheet and the Ag(111) slab,((vi)–(vii)) maximum and minimum distances in the 2D-ZnO-on-Ag(111) system (distances between ZnO and Ag(111) are in a direction normal to the surface and the ZnO sheet (Å)) and (viii) $BE_{ZnO-Ag}$ : binding energy between ZnO sheet and Ag(111) surface (eV/ZnO). The first values correspond to BEs calculated using the energy of a relaxed isolated 2D-ZnO sheet, whereas the second values use the energy of a 2D-ZnO sheet constrained to have the corresponding Ag(111) supercell lattice parameters. ....	133
Table 9 Relative energies (eV/ZnO) of considered free standing ZnO models and their corresponding corner and edge atom percentages. ....	152
Table 10. Comparison of structural data for calculated model systems with experimental results in terms of interlayer Zn-Zn distances ( $d_{Zn-Zn}$ ), interlayer Zn-O ( $d'_{Zn-O}$ ) distances and intralayer z-coordinate Zn-O spacings ( $u$ ). ....	153
Table 11. Energetic comparison of ZnO-Ag models. ....	155
Table 12. Comparison of differences in calculated structural data[interlayer Zn-Zn ( $d_{Zn-Zn}$ ) and Zn-O ( $d_{Zn-O}$ ) distances] for layered-ZnO and T1-ZnO 4 ML nanofilms and bulk wz-ZnO with experimental data for 3.5 and 4.5 ML. Best matches are underlined.....	163

## List of Figures

Figure 1. Article Count of “ZnO” word per year between years 1960 and 2013 (taken from web of science). ....	2
Figure 2. Illustrative example of crystalline and amorphous solid structures. ....	3
Figure 3. Lattice and basis forms crystal structure. ....	4
Figure 4. Phillips-van Vechten Plot for AB materials. $E_h$ and $C$ are homopolar and heteropolar parts of the complex energy gap, $E_g$ associated with the A-B bond in the crystal.....	6
Figure 5. Top view and side view of wurtzite (wz) ZnO structure. ....	7
Figure 6. Structure of zinc-blende. ....	9
Figure 7. Rocksalt Structure. ....	9
Figure 8. Electronic band structure in various types of materials.....	10
Figure 9. Bandstructures of Si and ZnO.....	11

Figure 10. Doping introduces new levels within the bandgap.....	12
Figure 11. Useful applications and properties of ZnO material.....	13
Figure 12. Coupling between the H 1s orbital and the Zn 4s dangling bonds (Zn dbs) to form the hydrogen multicenter bond in ZnO.....	15
Figure 13. Structures of Silica polymorphs, a) quartz b) tridymite c) cristobalite.....	20
Figure 14. Phase diagram of silica at various pressures and temperatures.....	21
Figure 15. Crystal structures of 3C (zinc blende), 2H (wurtzite) and 4H polytypes of SiC and high resolution images of their corresponding films fabricated at different laser pulse frequencies. ....	23
Figure 16. 3D nets of simple framework structures.....	25
Figure 17. An example of simulated annealing method used for prediction of crystal structure of BaMgAl <sub>4</sub> Si <sub>4</sub> O <sub>16</sub> . The different color lines corresponding the trajectories of ten runs starting from different starting points. Data points represents the local minima along each trajectory.....	27
Figure 18. An example of genetic algorithm method used for Pt <sub>12</sub> Pd <sub>12</sub> nanoclusters. ....	29
Figure 19. Schematical representations of (a) 0-dimensional (0D), (b) 1-dimensional (1D), (c) 2-dimensional (2D) and (d) 3-dimensional (3D) structures.....	30
Figure 20. Illustrative example of top-down and bottom-up approaches.....	31
Figure 21. Distrubition of charges <b>q</b> on planes for three stacking sequences parallel to surface.....	34
Figure 22. surfaces of wurtzite ZnO. ....	35
Figure 23. Illustrative model of (a) wz-ZnO and (b) layered-ZnO on Ag surface.....	36
Figure 24. Schematic diagram of common 1D ZnO morphologies. ....	37
Figure 25. SEM image of a ZnO tetrapod. ....	38
Figure 26. Global minimum structures of (ZnO) <sub>n</sub> nanoclusters.....	40
Figure 27. The building unit TO <sub>4</sub> where T denotes for framework atoms. ....	42
Figure 28. Examples of secondary building units (SBU) of zeolite frameworks. Each cyan ball represents one framework atom. ....	42
Figure 29. Examples of (a) composite building units (CBUs) and (b) chains for zeolite frameworks.....	43
Figure 30. Primary building unit of Silicates (left) and the two analog primary buildings of ZnO (right). ....	45
Figure 31. Structures of BCT and SOD zeolite frameworks. ....	46
Figure 32. Energy versus volume plots for ZnO phases. ....	47
Figure 33. Top and side views of $\left[ \text{K} \left[ \text{LiZn}_3\text{O}_4 \right] \right]$ structure in ATN zeolite framework. ....	48
Figure 34. Illustration of a multi-dimensional potential energy surface with important stationary points.....	50
Figure 35. Schematic picture of a multi-funnel potential energy surface.....	51
Figure 36. Schematic diagram of a one-dimensional PES, in which the original energy (solid line) is transformed onto the <i>E</i> (dashed line). The green arrow indicates a random move performed on a local minimum, which is followed by a local structural minimization (red arrows). ....	56
Figure 37. A schematic diagram of a Basin Hopping run. ....	57

Figure 38. Schematic representation of the core-shell model. Blue sphere represents the core while the grey circle represents for the shell. ....	60
Figure 39. The non-Coulombic interaction including the attractive and repulsive components of ion separation.....	61
Figure 40. Top view of Ag(111), Ag(100) and Ag(110) surfaces. The symmetry unique sites hollow (H), bridge (B) and on-top (T) sites are indicated with letters. ....	70
Figure 41. DFT calculated adsorption energy for (ZnO) <sub>6</sub> nanocluster on Ag(111) surface as a function of the adsorption height. Inset shows the graphical forms of the fitted Ag-O and Ag-Zn Buckingham potentials. ....	74
Figure 42. Nanocluster structures on the Ag(111) support for the sizes n = 1-3. ....	79
Figure 43. Energy ordering of (ZnO) <sub>4</sub> low-energy nanoclusters on the Ag(111) surface (red). Blue colored symbols are corresponding energies in free space. 2D planar structures are represented by sticks while 3D cluster structures are represented by filled circles. ....	81
Figure 44. Nanoluster structures of (ZnO) <sub>4</sub> both in free space (above) and on the Ag(111) support (below). ....	82
Figure 45. Energy ordering of (ZnO) <sub>5</sub> nanoclusters on the Ag(111) surface (red). Blue colored symbols are corresponding energies in free space. 2D planar structures are represented by barswhile 3D cluster structures represented by filled circles. ....	83
Figure 46. Structures of (ZnO) <sub>5</sub> clusters in free space and on support.....	84
Figure 47. Energy ordering of (ZnO) <sub>6</sub> nanoclusters on Ag(111) surface (red). Blue colored symbols are corresponding energies at free-space. 2D planar structures are represented by bars while 3D cluster structures represented by filled circles. ....	85
Figure 48. Structures of (ZnO) <sub>6</sub> in free space and on support. Side views of 2D clusters are also given beneath.....	86
Figure 49. Structures of (ZnO) <sub>7</sub> clusters in free space and on support. ....	88
Figure 50. Energy ordering of (ZnO) <sub>7</sub> and (ZnO) <sub>8</sub> nanoclusters on Ag(111) surface (red). Blue colored symbols are corresponding energies of clusters in freespace. 2D planar structures are represented by bars while 3D cluster structures represented by filled circles. Triangles represent the clusters having both 3D and 2D parts.....	89
Figure 51. Structures of (ZnO) <sub>8</sub> infree space and on support. ....	90
Figure 52 .Structures of (ZnO) <sub>9</sub> both free space and on support. ....	91
Figure 53. Energy ordering of (ZnO) <sub>9</sub> and(ZnO) <sub>10</sub> nanoclusters on Ag(111) surface (red). Blue colored symbols are corresponding energies in freespace. 2D planar structures are represented by bars whereas3D cluster structures are represented by filled circles. Triangles represent the clusters having both 3D and 2D parts. ....	92
Figure 54. structures of (ZnO) <sub>10</sub> in free space and on support.....	93
Figure 55. Energy ordering of (ZnO) <sub>11</sub> - (ZnO) <sub>16</sub> nanoclusters on Ag(111) surface (red). Blue colored symbols are corresponding energies infreespace. 2D planar structures are represented by bars whereas 3D cluster structures are represented by filled circles. Triangles represent the clusters having both 3D and 2D parts. ....	95
Figure 56. Structures of (ZnO) <sub>11-16</sub> in free space and on support. ....	96
Figure 57. Structures of (ZnO) <sub>20</sub> in free space and on support. ....	97
Figure 58. Energy ordering of (ZnO) <sub>20</sub> and (ZnO) <sub>24</sub> nanoclusters on Ag(111) surface (red). Blue colored symbols are corresponding energies in freespace. 2D planar structures are represented by bars whereas3D cluster structures are represented by filled circles. ....	99

Figure 59. Top views of $n = 20$ 2D ZnO structures on Ag(111) surface.....	100
Figure 60. $(\text{ZnO})_{24}$ structures: (a) 3D clusters in free space and on support, (b) 2D clusters on support.....	101
Figure 61. Average stabilization energies for 3D and planar structures on Ag support.....	102
Figure 62. Energies of best 2D and 3D structures in free space and on support with size.....	103
Figure 63. Relative stability and nucleation energy with respect to the cluster size.....	104
Figure 64. Energy difference of the best 2D and 3D clusters on support with respect to the cluster size. Positive values are where the 2D clusters are more stable than 3D clusters. ....	105
Figure 65. Top and side views of 6A, 6D and 6E clusters on Ag(111), Ag(100) and Ag(110) surfaces.....	107
Figure 66. Side views of 6B, 6I,6H, and 6U clusters on Ag(110) surface. ....	108
Figure 67. Top and side views of 7A, 7B and 7i clusters on Ag(111), Ag(100) and Ag(110) surfaces.....	109
Figure 68. Top and side views of 8A and 8p4 clusters on Ag(111), Ag(100) and Ag(110) surfaces.....	110
Figure 69. Side views of 8C and 8D clusters on Ag(110) surface. ....	111
Figure 70. Binding energies of low-energy clusters for the selected sizes both in free space and on different Ag surfaces. ....	112
Figure 71. Top and side views of 12A, 12B, 12D, and 12p1 clusters on Ag(111), Ag(100) and Ag(110) surfaces.....	113
Figure 72. Top and side views of 13A on Ag(111), 13F on Ag(100) and, 13B on Ag(110) surfaces.....	114
Figure 73. Top and side views of 16A cluster on Ag(111), Ag(100) and Ag(110) surfaces.....	115
Figure 74. Top and side views of 13p6 and 16p10 clusters on Ag(110) surface. ....	116
Figure 75. Side and top views of ring and stick structures of sizes $n = 1$ to 4 on Ag(111) surface. Numbers represent the heights from the surface plane for each of the individual Zn and O atoms. Black circles indicate the silver surface atoms, which displaced outwards from the surface plane. ....	119
Figure 76. Binding energies of low-energy clusters calculated with DFT for the selected sizes both in free space and on Ag(111) surface. ....	120
Figure 77. Structures and energetics of the lowest energy 2D and 3D $(\text{ZnO})_n$ nanoclusters on Ag(111) support. Relative energies are given under the structures and the stabilization energies due to support are given in paranthesis. ....	122
Figure 78. Energetical ordering of free space and supported nanoclusters with respect to cluster size .....	124
Figure 79. Energy difference of best 2D and 3D clusters with respect to the cluster size. Positive values are where the 2D clusters are more stable than the 3D clusters. ....	124
Figure 80. Relative stability and nucleation energy with respect to the cluster size.....	125
Figure 81. Global minima structures of $(\text{ZnO})_n$ clusters on Ag(111), Ag(100) and Ag(110) surfaces.....	127
Figure 82. Top (left) and side (right) views of the 2D-ZnO-on-Ag(111) 7:8 system after optimization using DFT. The solid bounded region highlights where the oxygen atoms (red/dark grey balls) are near to being directly above the Ag atoms (blue/grey balls) in the	

underlyingsurface slab. The dashed bounded region highlights where the zinc atoms (light green/light grey balls) are near to being directly above the Ag atoms. ....	134
Figure 83. Contour plots of the locally averaged z coordinates of Zn, O and Ag atoms in the 7:8 system shown in Figure 82. The fractional x–ycoordinates in the square plots correspond to those in the oblique angled 7:8 supercell. The ‘L’ and ‘H’ labels correspond to relatively lowerand higher regions (where the height is taken as the magnitude of the z coordinate measured from the bottom of the Ag slab). ....	136
Figure 84. PDOS for the hydrogen and 2D-ZnO sheet where (a) thehydrogen atom is far from the sheet and (b) H is in the centre of aZn <sub>3</sub> O <sub>3</sub> ring of the sheet (H@Zn <sub>3</sub> O <sub>3</sub> ). ....	137
Figure 85. Transport barrier for a single H atom to pass through aZn <sub>3</sub> O <sub>3</sub> ring of a 2D-ZnO sheet (GGA DFT calculation using a 4×4supercell). ....	138
Figure 86. Spin density of the H@Zn <sub>3</sub> O <sub>3</sub> system for the 3×3 supercell GGA DFT calculation (left) and the B3LYP cluster calculation (right). ....	139
Figure 87. The proposed Zn 4s–H 1s MCB orbital from the B3LYP cluster calculation (left) with the harge density difference of the periodicDFT calculations (right). Relative charge increase is found in the centre of the ring and to a lesser extent on the oxygen sites (lighter grey)whereas charge is depleted (dark grey) from the p-like lobes of the oxygen sites. ....	140
Figure 88. Main growth types in thin film formation; (a) Volmer-Weber, (b) Frank-van der Merwe, (c) Stranski-Krastanov. Here Θ stands for the coverage. ....	142
Figure 89. STM images of 2.2 ML ZnO on Ag(111)275 .....	143
Figure 90. Optimized structures of 1 ML ZnO on Ag(111) surface (a-side view, b-top view), 2 ML ZnO on Ag(111) surface (c-side view, d-top view). e and f shows side views of the optimized geometries of 3 layer thick BCT-ZnO and layered-ZnO. g and h illustrate the interlayer spacings in the BCT and WZ ZnO structures. The larger balls for Zn and O atoms are used to indicate where the interlayer separations occur, while the bigger balls for Ag atoms in b and d are used for indicating the surface rumpling, i.e. where the surface atoms move outwards. ....	145
Figure 91. Initial structures of ZnO coverage models. Red and Green stands for O and Zn atoms, respectively. The first two complete MLs are shown with thin sticks while the third layer is shown with a larger ball and stick model and the top layer is differentiated by the largest balls. ....	146
Figure 92. Optimized structures of both supported (a,b,c) and unsupported (d,e,f) 2.2 ML ZnO. Bigger balls are used to differentiate where the interlayer separations occur in top view figures (a and d). In c and f, cylindrical parts shown in a are separated from each other in side views. Red rectangular indicate the encircling BCT reconstructions which are not commensurate with each other. ....	148
Figure 93. Comparison of 2.2 ML island with the T1-ZnO cut: a) Top view of unsupported 2.2 ML ZnO, b) side view of supported 2.2 ML ZnO, c) top view of T1-ZnO, d) side view of T1-ZnO, and e) cylindrical cut of the islands perimeter. ....	150
Figure 94. Top and side view structures of 2.3 ML, 2.76 ML-A and 2.76 ML-B models. Red circles indicate BCT reconstructions while green circles indicate T1 reconstructions. ....	151
Figure 95. Top and side view structures of 2.70 ML free standing model. Black circle indicates the BCT reconstructed edge on Zn-excess island while Red circles indicates he BCT reconstructed edge on O-excess island. ....	152
Figure 96. Illustrative model for a truncated triangular ZnO island. ....	156

Figure 97. (a) Comparison of relative energies(eV/ZnO) of ZnO polymorphs as bulk and 4 ML nanofilms. Right and left energy y axes relate to bulk and nanofilm energies, respectively. (b) $\Delta E_{\text{bulk} \rightarrow \text{nano}}$ (eV/unit) for wz and BCT for ten wurtzite materials.....	160
Figure 98. Selected polymorphs. Top left: T1 with its trigonal basal plane, bottom left: BYL, right: BCT(upper) and BCT <sub>-o</sub> (lower) with respective <i>c</i> -aligned stacking sequences. ....	162
Figure 99. (a) Selected nanofilm energetic stability variation with thickness, (b) energy variation with in-plane strain for 4 ML layered-ZnO versus T1-ZnO, (c) energy variation with in-plane strain for 8 ML BCT-ZnO versus BYL-ZnO. Strains are relative to 1 ML layered-ZnO. Insets show polymorph energy differences. ....	166
Figure 100. $E_{\text{gap}}$ (GW) versus $E_{\text{gap}}$ (PBE) for 13 structures showing the linear fit. The open point relates to a structure with an indirect $E_{\text{gap}}$ . Structures and properties of the labelled polymorphs can be found in the full list also in the SI. ....	171
Figure 101. Variation relative to $V_{\text{pore}}$ of: a) $E_{\text{rel}}$ (grey line indicates $E_{\text{rel}}$ of rs-ZnO), b) .....	173
Figure 102. $\Delta E_{\text{gap}}$ versus strain for wz-ZnO calculated at various levels of theory. The linear fit to the GW data for porous non-strained structures has been applied to the DFT PBE data. ....	174
Figure 103. Comparison of a range of properties for three pairs of polymorphs having similar $V_{\text{pore}}$ values. Key: green-zinc, red-oxygen, grey line-unit cell. ....	175
Figure 104. VBM and CBM dependence on $V_{\text{pore}}$ for a selection of 4CN-based structures realised as CdSe (upper) and CdS (lower) polymorphs. ....	177
Figure 105. Plots of conduction band and valence band bandwidths versus: a) $\Delta E_{\text{gap}}$ (PBE <sub>GW-fit</sub> ) and b) $V_{\text{pore}}$ . ....	179
Figure 106. Dependence of $\Delta E_{\text{gap}}$ (PBE <sub>GW-fit</sub> ) on: a) $D_{\text{pore}}$ , where shaded bars show $\Delta E_{\text{gap}}$ (PBE <sub>GW-fit</sub> ) values ordered by increasing magnitude (dark to light) relative to $V_{\text{pore}}$ (right) and $E_{\text{rel}}$ (left) for each $D_{\text{pore}}$ (dashed line indicates average trend), b) $(\text{Pore}_{\text{max}}-1)/V_{\text{pore}}$ (inset shows $\Delta E_{\text{gap}}$ values of wz-ZnO-NP structures with similar $V_{\text{pore}}$ values but different labelled $\text{Pore}_{\text{max}}$ values – smaller pore sizes are in parentheses). ....	181

## **CHAPTER I: Introduction**

### **1. Thesis Overview:**

The metal elements can form a large diversity of oxide compounds which play a very important role in many areas of materials science, physics and chemistry<sup>1</sup>. Among the various inorganic materials of current technological interest, metal oxides have a pivotal position<sup>2</sup>. Due to their broad range of structures and properties metal oxides have wide range of applications. In industrial chemistry, a large proportion of the important catalysts and/or catalyst supports are oxides. In geology, some of the most important minerals are also oxides. For many of the important properties or phenomena in solid-state science such as: metallic ferromagnetism, high temperature ferroelectricity, fast-ion conductivity, and superconductivity<sup>3</sup>, one can find prototypical examples among metal oxides. The rich variety of electronic properties of metal oxides, ranging from insulating to metallic and even superconducting behavior, is continually opening up new perspectives for these materials in the electronics and optoelectronics industries.

The possibility for a single compound to exist in more than one distinct crystalline phase is a common phenomenon called polymorphism, which is of crucial importance in many branches of science and technology as polymorphs can and often do show significant differences in chemical and physical properties. With the continuing advances in the development of devices requiring low dimensional nanomaterials (e.g. 0-dimensional nanoparticles, 1-dimensional nanowires, 2-dimensional nanofilms) the importance of gaining a deeper and more general understanding of the relationship between the relative stability of competing crystalline phases (or polymorphs) and size and/or dimension is paramount. The polymorph exhibited by a material is remarkably sensitive to scale and/or dimensionality. This phenomenon is often particularly pronounced when comparing the polymorphism of a three-dimensional (3D) bulk material with that of the corresponding system at the nanoscale with reduced dimensions. Based upon the limited available experimental evidence, it has been reasonably suggested that bulk-nanoscale polymorphic stability crossovers could be due

a possible correlation between increasing metastability and decreasing surface energies, along with the higher surface area to bulk ratios found in nanosystems<sup>4</sup>. Titanium dioxide, for example, exhibits the rutile crystal structure in the bulk, but, in sufficiently small nanoparticles it displays the anatase phase, which is technologically highly valued for its photocatalytic properties.

In this thesis, the work has mainly focused on zinc oxide (ZnO), which is a group II-VI semiconductor compound having a wide range of technological applications. ZnO is a key element in many industrial manufacturing processes such as paints, cosmetics, pharmaceuticals, plastics, batteries, electrical equipment, rubber, soap, textiles, floor coverings and much more<sup>5</sup>. Apart from being widely used in a broad range of industries in our society, the development of technologies to grow high quality ZnO single crystals and epitaxial layers has also enhanced its scientific importance. Studies of such well-defined ZnO samples are promising to yield an even wider range of potential applications in further (nano)technologies such as energy harvesting and spintronics. In this sense ZnO can be regarded as a 'future material', which also explains the intense and increasing interest in ZnO in the scientific community (see Figure 1)

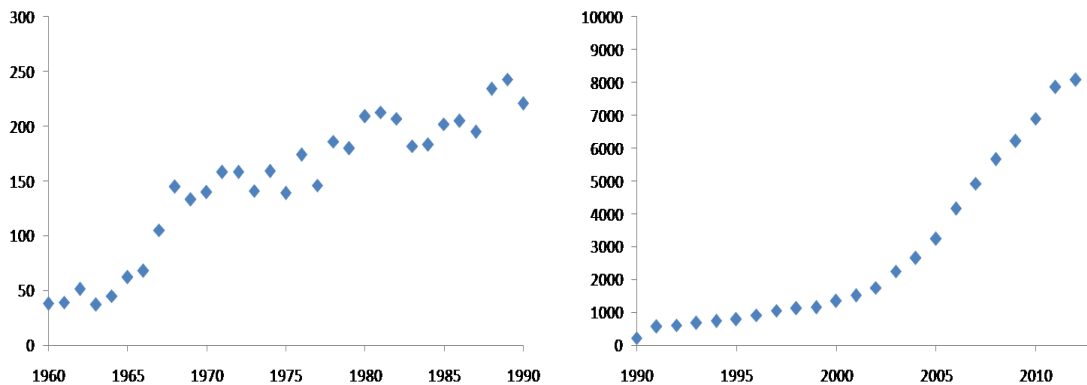


Figure 1. Article Count of “ZnO” word per year between years 1960 and 2013 (taken from web of science).

In Chapter 1, we give detailed introduction about important concepts related our work, such as crystal structure, semiconductivity, polymorphism, and nanoscale, and we

introduce related properties of ZnO material in detail. In chapter 2, we introduce the methodology used in this thesis together with related concepts. In chapter 3, we start to report our results with the case of 0-dimensional ZnO nanoclusters on Ag substrate and compare their properties with free space ZnO nanoclusters. In Chapter 4, we continue with a study of single 2D-ZnO sheet on Ag(111) surface and investigate also how H atoms interact with it. In chapter 5, we move on with the consideration of higher coverage models, including triangular islands prepared to model experimental systems. In chapter 6, we focus on 4ML nanofilms and compare bulk and nanofilm polymorphism of ZnO. Lastly, in chapter 7, we focus on bulk polymorphism and investigate the effect of nanoporosity

## **2. Structure**

Properties of materials are inherently linked to their structures. All substances, except helium, form a solid phase when they cooled sufficiently. The vast majority of these substances form one or more crystalline phases, where the atoms, molecules, or ions are packed in a regular way with long range order. If, however, there is only short range order the solid is said to be amorphous (see Figure 2).

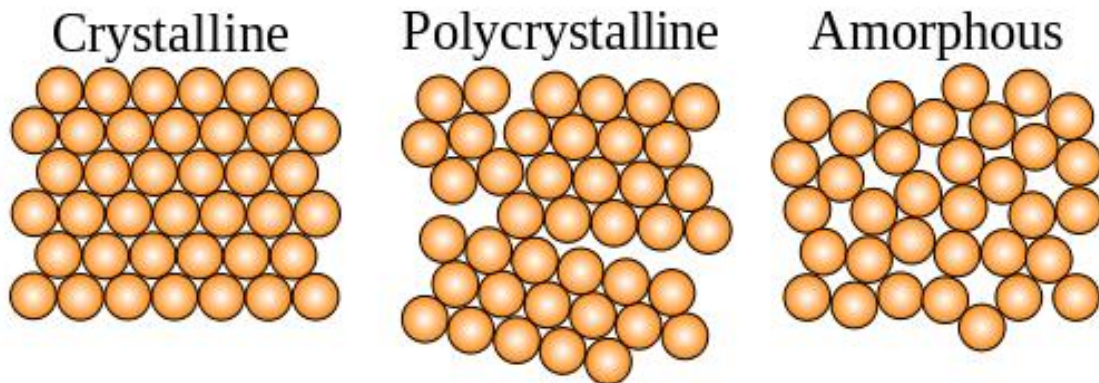


Figure 2. Illustrative example of crystalline and amorphous solid structures.

## 2.1. Crystal Structures:

Crystal structures consists of: (i) a lattice, which means a spatial periodicity or translation symmetry, and (ii) a basis, which is a repeating pattern of one or more atoms arranged in a particular way. All crystal structures can be obtained by repetition of the basis according to the lattice as seen in Figure 3.

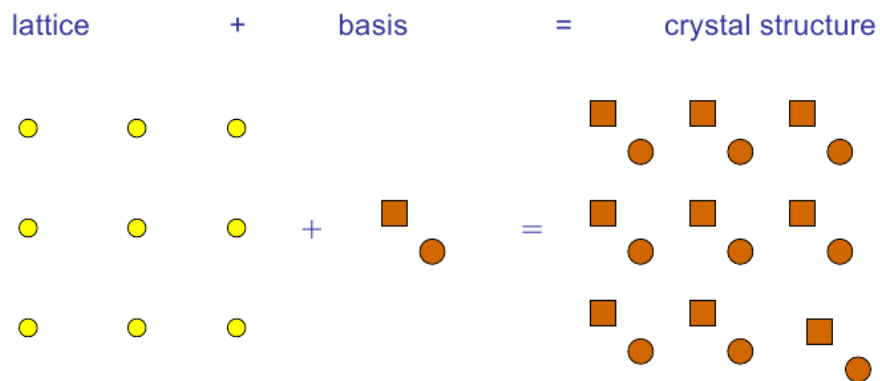


Figure 3. Lattice and basis forms crystal structure.

In 3-dimensional (3D) space we define three non-coplanar vectors;  $a_1$ ,  $a_2$ , and  $a_3$  that leave all the properties of the crystal unchanged after the shift as a whole by any of those vectors. As a result, any lattice point  $R_i$  can be obtained from another point  $R_0$  by

$$R_i = R_0 + m_1 a_1 + m_2 a_2 + m_3 a_3$$

where  $m_i$  are integers. Such a lattice of building blocks is called the Bravais lattice. The volume of the cell enclosed by the three vectors  $a_i$  is called unit cell. There is no unique way to choose  $a_i$ , which means for a given structure there is never one unique unit cell that is 'correct'. By convention  $a_1$  can be chosen as the shortest period of the lattice,  $a_2$  as the shortest period not parallel to  $a_1$ , and  $a_3$  as the shortest period not coplanar to  $a_1$  and  $a_2$ . Vectors  $a_i$  which are chosen in such a way are called primitive vectors and the volume cell enclosed by the primitive vectors is called the primitive unit cell. There are seven unique unit cell shapes that can be stacked together to fill 3D space as shown in Table 1.

Table 1. Unique unit cell Structures.

Lattice	Possible Variations	Axial Distances	Axial Angles	Examples
Cubic	Primitive, Body-centred, Face-centred	$a = b = c$	$\alpha = \beta = \gamma = 90^\circ$	NaCl, Zinc Blende, Cu
Tetragonal	Primitive, Body-centred	$a = b \neq c$	$\alpha = \beta = \gamma = 90^\circ$	White tin, SnO <sub>2</sub> , TiO <sub>2</sub> , CaSO <sub>4</sub>
Orthorhombic	Primitive, Body-centred, Face-centred, Base-centred	$a \neq b \neq c$	$\alpha = \beta = \gamma = 90^\circ$	Rhombic sulphur, KNO <sub>3</sub> , BaSO <sub>4</sub>
Hexagonal	Primitive	$a = b \neq c$	$\alpha = \beta = 90^\circ$ , $\gamma = 120^\circ$	Graphite, ZnO, CdS
Rhombohedral	Primitive	$a = b = c$	$\alpha = \beta = \gamma \neq 90^\circ$	Calcite(CaCO <sub>3</sub> ), Cinnabar(HgS)
Monoclinic	Primitive, Base-centred	$a \neq b \neq c$	$\alpha = \gamma = 90^\circ$ , $\beta \neq 90^\circ$	Monoclinic sulphur, Na <sub>2</sub> SO <sub>4</sub> .10H <sub>2</sub> O
Triclinic	Primitive	$a \neq b \neq c$	$\alpha \neq \beta \neq \gamma \neq 90^\circ$	K <sub>2</sub> Cr <sub>2</sub> O <sub>7</sub> , CuSO <sub>4</sub> .5H <sub>2</sub> O, H <sub>3</sub> BO <sub>3</sub>

In crystallography, to describe the crystal planes and directions, Miller indices are used, which are usually three integers  $h$ ,  $k$ , and  $\ell$ . A plane  $(hkl)$  intercepts the lattice at three points  $a_1/h$ ,  $a_2/k$ , and  $a_3/\ell$ . Negative indices are also allowed and, by convention, written with a bar, like in  $\bar{3}$  for  $-3$ . The direction normal to a  $(hkl)$  plane is shown as  $[hkl]$ . In a hexagonal crystal structure usually four indices are used instead of three, like  $(hkil)$ , where  $i = -h - k$ . This is not strictly necessary to define a plane, but it makes it easier to identify equivalent planes.

A real crystal is never perfect, which means it contains defects. These defects may be 0D (e.g. vacancies or interstitials), 1D (e.g. dislocations), 2D, (e.g. stacking faults), or 3D, (e.g. precipitates). For  $n > 0$ ,  $n$ -dimensional defects are usually undesirable, and can be avoided with proper care during sample fabrication and processing. However, 0D defects can develop for thermodynamic reasons. Defects of this nature are called intrinsic, as they cannot be avoided and are not caused by impurities. The equilibrium amount of defects depends on the material

## 2.2. Structural properties of ZnO

Most of the group-II-VI binary compounds have either cubic zinc-blende or hexagonal wurtzite structures. Both of these structures have tetrahedral coordination implying  $sp^3$  hybridised covalent bonding, but these materials also have a substantial ionic character.

The ionicity of ZnO resides at the borderline between covalent and ionic semiconductors, in the region where tetrahedral coordination is expected (see Figure 4).

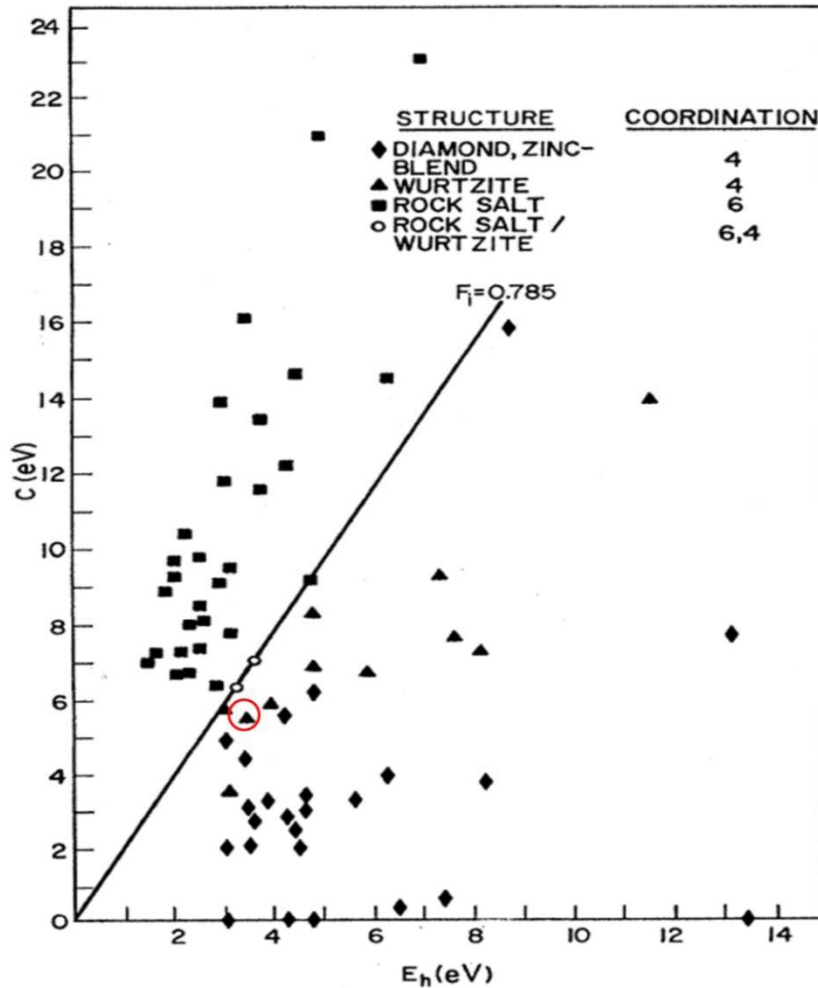


Figure 4. Phillips-van Vechten Plot for AB materials.  $E_h$  and  $C$  are homopolar and heteropolar parts of the complex energy gap,  $E_g$  associated with the A-B bond in the crystal.<sup>6</sup>

ZnO exhibits several crystal structures such as wurtzite, zinc blende and rocksalt phases. Of these, the wurtzite (wz) structure is thermodynamically most stable under ambient conditions, and is the most commonly observed phase<sup>7</sup>. As shown in Figure 5, wz-ZnO has a hexagonal lattice which is characterized by two interconnecting sublattices of  $Zn^{2+}$  and  $O^{2-}$ , such that each  $O^{2-}$  ion is surrounded by a tetrahedron of  $Zn^{2+}$  ions, and vice-versa. It belongs to the space group P63mc, which causes the wz structure to lack of center of inversion symmetry.

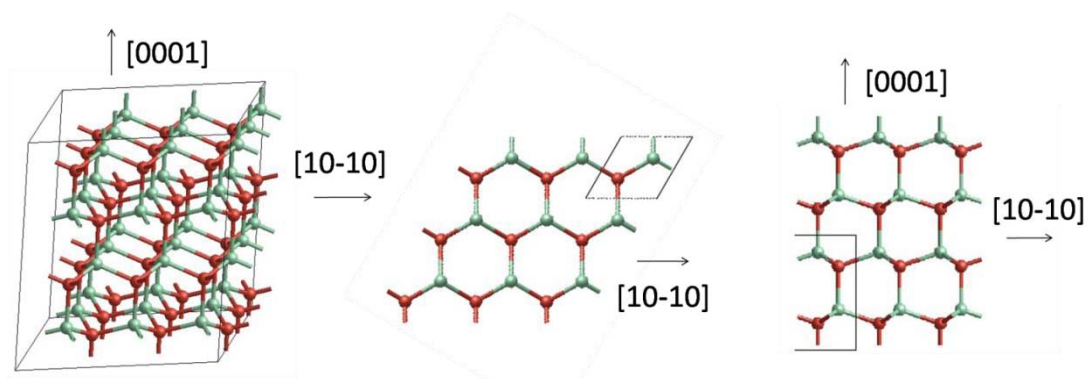


Figure 5. Top view and side view of wurtzite (wz) ZnO structure.

The primitive translation vectors  $a$  and  $b$  lay in the  $x$ - $y$  plane, are of equal length, and include an angle of  $120^\circ$ , while  $c$  is parallel to the  $z$ -axis. The primitive unit cell contains four ions, i.e. two formula units of ZnO, with the corresponding basis vectors:  $(1/3, 2/3, 0)$ ,  $(2/3, 1/3, 1/2)$  for the cations, and  $(2/3, 1/3, u)$ ,  $(1/3, 2/3, u+1/2)$  for the anions, where  $u$  is the separation between anions and cations in the  $z$ -direction. The values of the primitive translation vectors in wz-ZnO are  $a = b \approx 0.3249$  nm and  $c \approx 0.5206$  nm at room temperature. The deviation from the ideal lattice parameters are most likely due to the ionic nature of the ZnO bond, leading to a distortion of the bond angles<sup>8</sup>.

The wz structure can be also considered as an ABAB... stacking of one atom thick, charge neutral sheets, in which zinc and oxygen atoms form a hexagonal pattern like honeycomb, with three equivalent Zn-O bonds for each site (see top view in Figure 5). As can be clearly seen in the side view (Figure 5), these sheets are corrugated in the wz structure, with all zinc atoms occupying one side and oxygen atoms the other. Because of the ionic character of ZnO, each sheet thus possesses a dipole moment, which is normal to the surface.

There are 4 common surface terminations for the wz-ZnO crystal: Zn terminated  $(0001)$  and O terminated  $(000\bar{1})$  polar faces, and non-polar  $(11\bar{2}0)$  and  $(10\bar{1}0)$  faces containing equal numbers of Zn and O atoms. Of these surfaces, the non-polar  $(10\bar{1}0)$  surface has the lowest surface energy<sup>9</sup>.

In a wz-ZnO unit cell there are 4 atoms which gives 12 phonon modes, which are 1 longitudinal-acoustic (LA), 2 transverse-acoustic (TA), 3 longitudinal-optical (LO) and 6 transverse-optical (TO) modes. These modes are important to understand the electrical, optical and thermal properties of the crystal and therefore extensively studied<sup>10</sup>. The  $E_1$  and  $A_1$  branches are infrared and Raman active, while  $E_2$  branches are only Raman active and  $B_1$  branches are inactive. Experimental values of most common phonon modes visible at 300 K are given in Table 2.

Table 2. Experimentally determined principal phonon modes of wurtzite ZnO at 300 K.

Phonon mode	Value (cm <sup>-1</sup> )
$E_2^{low}$	101
$E_2^{low}$	437
TO ( $A_1$ )	380
LO ( $A_1$ )	574
TO ( $E_1$ )	591

When exposed to an electric field all materials undergo a change in dimensions, but the reverse effect, development of an electric polarization when an external stress or strain applied, does not occur for most of them. This latter property allows conversion of mechanical energy to electrical energy and is called piezoelectricity. Being a subclass of these materials, a pyroelectric material expands by heating and the net dipole moment changes with the temperature due to the compensating charges appearing on the opposite faces of the crystal. These materials are generally used as sensors, transducers and actuators. ZnO is a piezoelectric material because of the lack of inversion symmetry of the wurtzite crystal structure and a pyroelectric material due to the specific polar axis. Combined with its other advantageous properties, the piezoelectric<sup>11</sup> and pyroelectric<sup>12</sup> properties of ZnO make it a very promising material for applications such as energy harvesting<sup>13</sup>

Apart from wz, the zinc blende (ZB) ZnO structure can be also obtained. ZB-ZnO can be grown on cubic structures, such as ZnS<sup>14</sup>, GaAs/ZnS<sup>15</sup>, Pt/Ti/SiO<sub>2</sub>/Si<sup>16</sup>. ZB is a cubic structure, which belongs to the space group  $F\bar{4}3m$  (Figure 6). Like wz, all the ions in ZB are also tetrahedrally coordinated. Thus, although the wz and ZB structures belong to

different space groups, they have the same local tetrahedral environment and become different only in their third-nearest-neighbor atomic arrangement. In terms of a-b aligned hexagonal sheets, for the wz structure they are arranged in a ABABAB stacking in the c-direction, whereas ZB shows ABCABC stacking of the same sheets in the (111) direction.

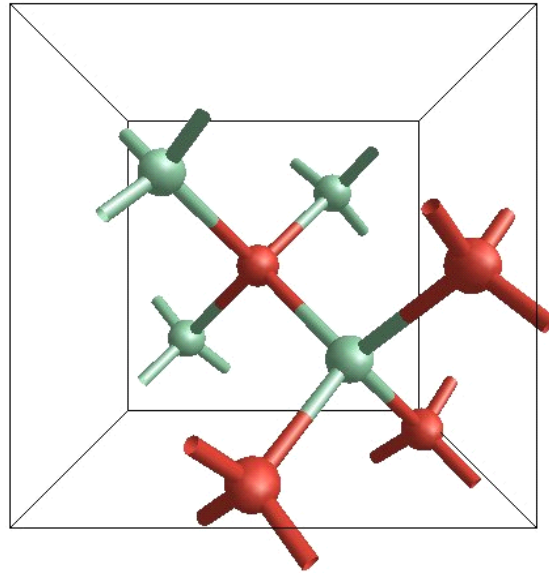


Figure 6. Structure of zinc-blende.

Like other group II-VI compounds, wz-ZnO can also be transformed into the rocksalt (RS) structure at high pressures ( $\sim 9$  Gpa<sup>17</sup>). The RS structure belongs to the space group Fm3m and the structure is sixfold coordinated as shown in the Figure 7. Recently the RS-ZnO structure has been stabilized at ambient conditions<sup>18</sup>.

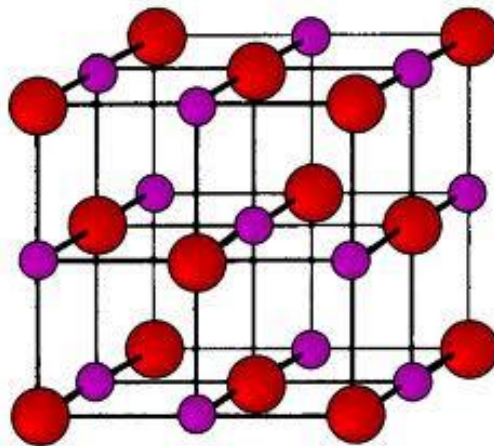


Figure 7. Rocksalt Structure.

### 3. Semiconductivity

#### 3.1. Semiconductivity and Band structure

Devices made from semiconductor materials are the foundation of modern electronics, including radio, computers, telephones, and many other devices. Semiconductors are a group of materials having electrical conductivities between those of metals and insulators, which can be easily controlled over a wide range of operating conditions.

Electrons in atoms or molecules occupy distinct atomic or molecular orbitals. Orbitals have discrete energy levels each with a different energy due to the Pauli exclusion principle. In solids, due to the large number of atoms brought together, the energy differences between orbitals become very small and they form continuous bands of energy instead of being discrete. The energetical variance of these continuous bands inside a periodic crystal with the wavevector is referred as band dispersion and the overall plot sketched for each band energy with respect to several crystal directions is called the band structure. The energy bands occupied by electrons are called valance bands while empty ones are called conduction bands. In metals these bands overlap and thus the electrons are free to move and electrical conduction can occur. Some intervals of energy between bands can remain forming energy gaps. For insulators and semiconductors the gap between valance and conduction bands is called the bandgap and electrons have to gain enough energy to overcome this gap.

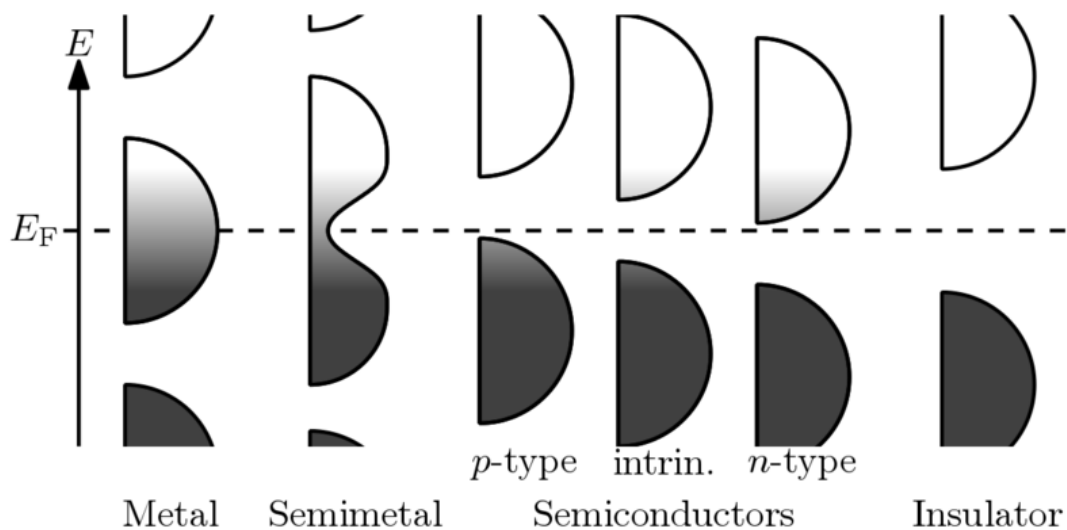


Figure 8. Electronic band structure in various types of materials.

Since the dispersion of the bands, two types of gaps emerge as direct and indirect gap. If the maximum of valance band and the minimum of the conduction band corresponds the same wavevector, the gap is called to be direct, or vice versa. In a direct gap, an electron transition between bands can occur without a change in electron momentum. However electron transition is less likely in indirect gaps since it requires a change in electron momentum. Examples of direct and indirect gaps are given in Figure 9 as bandstructures of Si and ZnO.

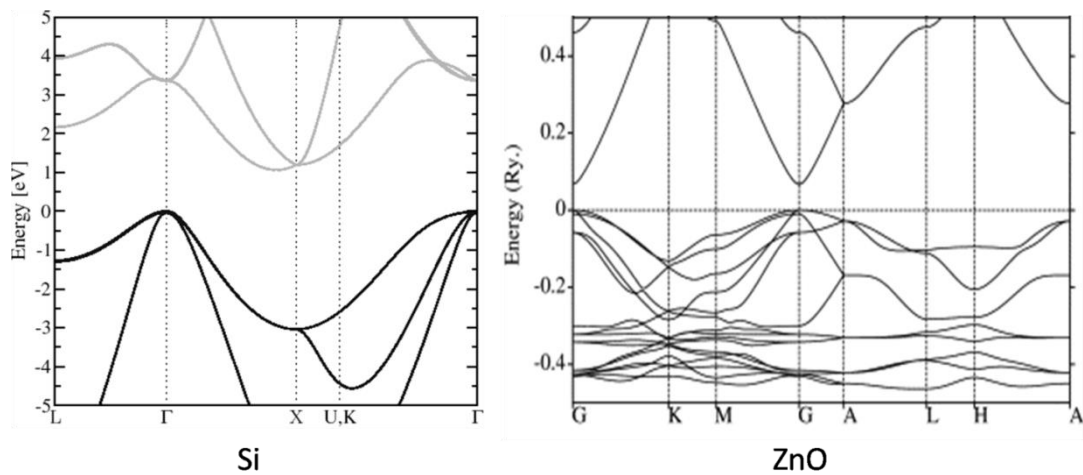


Figure 9. Bandstructures of Si and ZnO.

The difference between insulators and semiconductors is just the size of bandgap, which in semiconductors the electrons can thermally or optically excited from valance band to conduction band and thus transport current, whereas in insulators not.

In semiconductors, conductivity is controlled by two types of charge carriers; electrons in the conduction band and holes in the valence band. A hole refers to the situation where one electron is missing in the valence band. In order to control the conductivity, dopants can be introduced. To have an excess of negative charge carriers, the semiconductor can be doped with a donor impurity, which is called n-type doping. Vice-versa p-type doping (to introduce positive charge carriers) can be done by introducing an acceptor impurity.

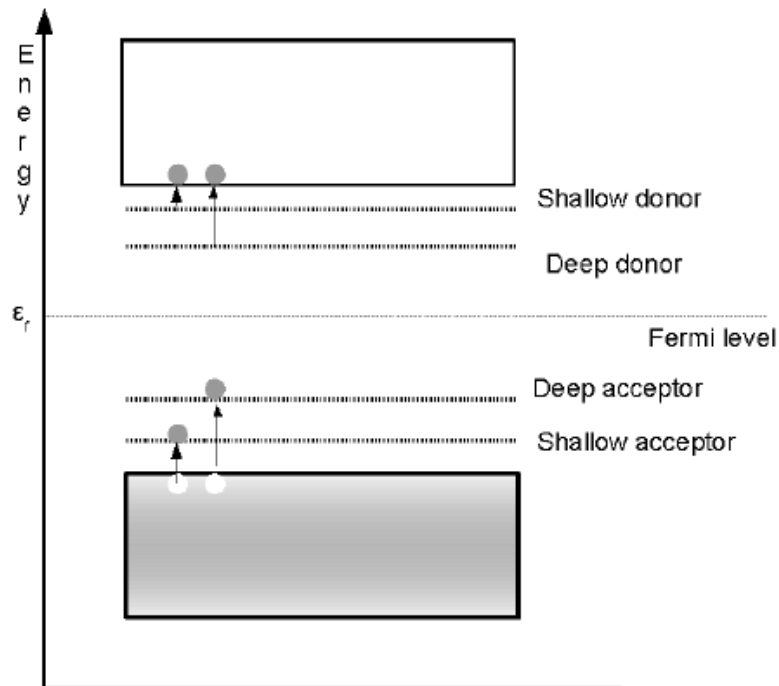


Figure 10. Doping introduces new levels within the bandgap.

### 3.2. ZnO as a wide bandgap semiconductor

Some of the useful applications and properties of ZnO are summarized in Figure 11 and some basic physical properties at 300 K<sup>19202122</sup> are given in Table 3. Large variation of thermal conductivity values are expected due to crystal defects<sup>23</sup>. Mobility and effective mass values are uncertain because of the problems to obtain reproducible and robust p-type ZnO, which will be discussed later in this chapter.

Table 3. Basic physical properties of ZnO at 300 K.

Parameters	Values
Lattice constant	a = 0.32495 nm, c = 0.52069 nm
Density	5.67526 g/cm <sup>3</sup>
Molecular mass	81.389 g/mol
Melting point	2250 K
Electron effective mass	0.28 m <sub>0</sub>
Hole effective mass	0.59 m <sub>0</sub>
Static dielectric constant	8.656

Refractive index	2.008, 2.029
Bandgap energy	3.37 eV
Exciton binding energy	60 meV
Thermal conductivity	0.6 –1.16 W/Km
Specific heat	0.125 cal/g°C
Thermal constant at 573	1200 mV/K
Electron mobility	~ 210 cm <sup>2</sup> /Vs

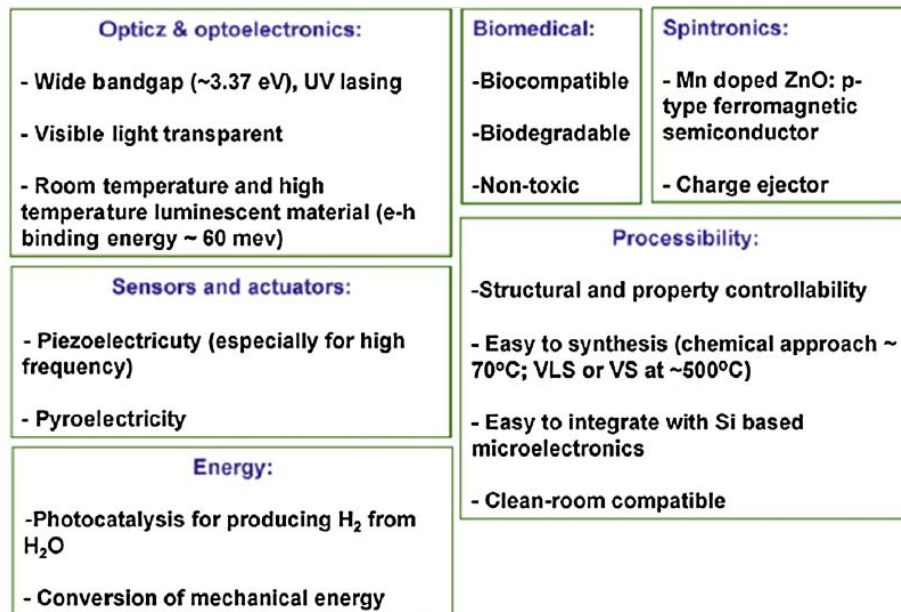


Figure 11. Useful applications and properties of ZnO material.

At present GaN is used in many opto-electronics devices as a semiconductor which has a direct bandgap of 3.44 eV<sup>24</sup>. Like ZnO, GaN also crystalizes in wz structure. ZnO is a very promising semiconductor material with its similar direct wide bandgap of 3.37 eV at room temperature<sup>25</sup>. However its use in electronic devices has been hindered by the lack of control over its electrical conductivity and, therefore, firstly, it has been considered as a substrate to GaN due to its close match<sup>26</sup>. ZnO is intrinsically n-type semiconductor without any intentional doping. However, to achieve p-type ZnO is a difficult task, which is essential for utilizing most of the semiconductor applications via junctions of p- and n- doped materials. Although p-type ZnO samples have been reported by several groups, mobility and the hole concentration are usually not high and the reproducibility of the results are under debate<sup>27</sup>. Still considerable efforts are

underway, both theoretically and experimentally<sup>28</sup>, to obtain p-type ZnO with various techniques and dopants. The availability of high-quality p-type ZnO would enable the use of ZnO itself directly in optoelectronic devices, which would heavily profit from the availability of large size high-quality single crystals<sup>29 30</sup> and compatibility with Si technology due to wet chemical processability<sup>31</sup>.

The reason for the n-type behavior of ZnO has been often attributed to the self-compensation from native donor defects and/or hydrogen incorporation<sup>32</sup> but the exact reason is not clear yet. Because all different growth techniques produce n-type ZnO, the first assumption was that there is only one responsible defect, which was thought to be a native zinc interstitial defect or oxygen vacancy<sup>33 34 35</sup>. However, theoretical calculations<sup>36</sup> have showed that the formation energies of these defects are relatively high, with, the most stable oxygen vacancy ( $V_O$ ) is seeming to induce a donor state which is too deep to account for the observed n-type behaviour. Although  $V_O$  cannot contribute to the n-type conductivity, it can be a relevant source of compensation in p-type ZnO. The Zn intersitial is a shallow donor (Figure 10) but considering its high formation energy one should not expect considerable amount to be present in the material to control the n-type conductivity.

Recently, attention has been drawn to the role of hydrogen<sup>37 38</sup> and other unintentional impurities<sup>39 40 41</sup> in affecting the electronic properties of ZnO. Hydrogen, in particular, is present in high concentrations in ZnO irrespective of the growth conditions. In most of the semiconductors studied, interstitial hydrogen has been observed to act as amphoteric impurity<sup>42 43 44</sup>, which means it always counteracts the conductivity by incorporating  $H_i^+$  in p-type samples, and  $H_i^-$  in n-type samples. This behavior prevents hydrogen from being the source of conductivity. However, in ZnO only the  $H_i^+$  is thermodynamically stable, thus interstitial hydrogen behaves as a shallow donor.

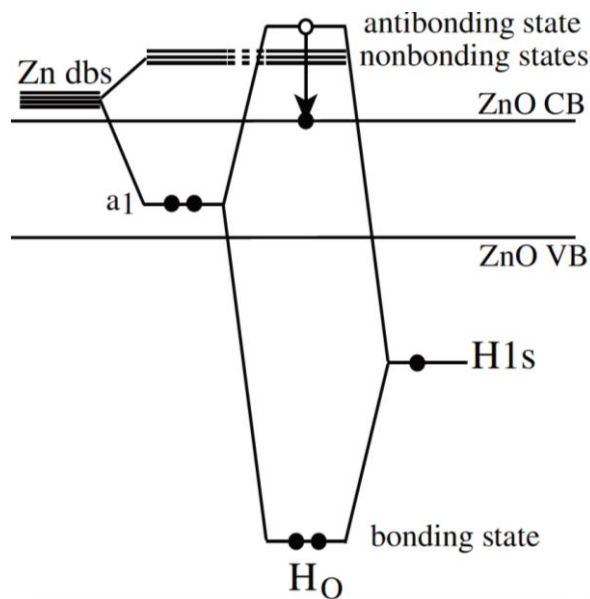


Figure 12. Coupling between the H 1s orbital and the Zn 4s dangling bonds (Zn dbs) to form the hydrogen multivalent bond in ZnO.

It was found that hydrogen can also replace oxygen in ZnO ( $H_O$ ) in addition to being in interstitial positions. When in a  $V_O$  position H forms a multivalent bond with four neighboring Zn centres equally. Exclusively occurring in the positive charge state  $H_O^+$ , such substitutional hydrogen is also a shallow donor in ZnO.

The hydrogen multivalent bond can be thought as a coupling between the H 1s orbital and the Zn 4s dangling bonds (Zn dbs) as in Figure 12. The H 1s orbital interacts with the a1 state and produces a fully symmetric bonding state in the valence band, and an antibonding state in the conduction band. The electron that would occupy this antibonding state is then transferred to the conduction-band minimum, making the substitutional hydrogen  $H_O$  a shallow donor<sup>45</sup>. Because of the formation energies of both interstitial and substitutional hydrogen are low, they can occur in significant concentrations making hydrogen a very attractive candidate for the reason of unintended n-type conductivity. There are also other possible donors, such as Al, Ga and Si, which have been suggested to explain the n-type behavior of ZnO, but the occurrence of these donors depends of the sample growth method.

### 3.3. Bandgap engineering of ZnO

The success of ZnO as a semiconductor depends also the possibilities of band gap engineering, ability to increase or decrease the band gap, as well as controllable n-type and p-type doping. Most semiconductor devices (e.g. high electron mobility transistors, lasers, LEDs, etc) use heterostructures to provide carrier and optical confinement. These heterostructures consist of layers of different materials or compositions and the important parameters are the bandgaps of each layer and the band offsets between the layers. Similar to GaN, which can be alloyed with AlN or InN, ZnO can be alloyed with MgO or CdO to increase the band gap. However, while GaN, AlN and InN all display the same wz structure, MgO and CdO exhibit the rocksalt structure, which is different from wz-ZnO. This becomes problematic when high proportions of MgO or CdO are used for alloying because a phase separation is expected to occur. However, the wz crystal structure can be preserved for moderate amounts of MgO and CdO, which still provides a range of band gaps and useful band offsets for practical device application<sup>46</sup>.  $Mg_xZn_{1-x}O$  films can be grown on various substrates such as sapphire, ZnO itself or  $ScAlMgO_4$  using different techniques<sup>47</sup>. It has been found that after ~33% incorporation of MgO in ZnO a phase transition to the cubic structure occurs, but a bandgap increase up to 3.99 eV can be achieved before this phase transition<sup>48</sup>. Like the inverse of MgO, alloying ZnO with CdO decreases the bandgap. For example, a 3.0 eV band gap has been observed for ZnO with 7% of Cd content grown on sapphire and  $ScAlMgO_4$  substrates by pulsed-laser deposition<sup>49</sup>.

### 3.4. Optical and Electronic properties of ZnO

Besides having a wide band gap, the optical properties of ZnO are very important because it has a high exciton binding energy of 60meV<sup>50,51</sup> which is much larger than the 25meV<sup>52</sup> of GaN. This high exciton binding energy allows efficient excitonic emission even at room temperature, which also makes ZnO a very promising material for optical devices based on excitonic effects.

ZnO has a strong luminescence in the green-white region, which makes it also suitable material for phosphor applications. It has an emission peak at 495nm and a broad half-

width of 0.4 eV<sup>53</sup>. It makes ZnO also appropriate material for applications in vacuum fluorescent displays and field emission displays combining with the n-type conductivity. Although the reason mechanism for the green luminescence is not really understood, Zn vacancies are suggested to be likely cause due to acceptor behavior in n-type ZnO<sup>54</sup>. Both in crystal and thin films, ZnO shows large second- and third-order non-linear optical behavior<sup>55</sup> depending on the crystallinity of the samples, which makes it suitable for non-linear optic devices.

ZnO exhibit exceptionally high radiation hardness, which makes it very suitable in applications where radiation damage is a factor, such as solar cells or space satellite applications<sup>56 57</sup>. Also ZnO Schottky rectifiers have been found to remain fully functional after high radiation exposure and showed little degradation in electrical performance even less than that of SiC and GaN devices<sup>58</sup>, which makes ZnO material very promising for aerospace and terrestrial applications.

A device which responds to specific chemical species or biological analyte in a selective way through a chemical reaction is called a chemical sensor. They can be used for a quantitative or qualitative determination of an analyte. Semiconductor materials are heavily used in this field because of their excellent properties<sup>59</sup>. Among them ZnO material is very important because it can be easily synthesized with a variety of nanostructures on different substrates<sup>60</sup>, and is also biocompatible and biodegradable<sup>61</sup>.

## **4. Polymorphism**

### **4.1. Introduction to Polymorphism**

The idea that a substance can exist in different physical states can be traced back to the speculations on the conceptions of matter in ancient Greek philosophy<sup>62</sup>. Aristotle (384-322 BC) developed a philosophical approach to explain natural phenomena like evaporation and the existence of different physical states. According to Aristotle, matter itself is something that is not a substance however it has the ability to receive forms. Thus, even drastical changes are possible, because one form can replace another and the

drastical changes happens when when it receives a new substantial form<sup>63</sup>. The connection from a philosophical to scientific interpretation of nature was done by mainly Aristotle's commentators in the following centuries. The philosophical theory, *minima naturalia*, which states that every kind of substance has its specific minimum sized particles was developed and had a big impact on the development of modern chemistry, since it can be regarded as predecessor of the atomistic theories<sup>64</sup>. The transition from philosophical to scientific atomistic theories took place between 17<sup>th</sup> and 19<sup>th</sup> centuries. At this period, M. H. Klaproth<sup>63 65</sup> addressed the question whether different solid matters should have different chemical compositions or not, and discovered that calcite and aragonite have the same chemical composition which is  $\text{CaCO}_3$ . His discovery had large effects on the development of the solid state theory. Later on the work on arsenates, phosphates and sulfur by E. Mitscherlich<sup>66 67</sup> gave additional evidence for the fact that a given substance can form different solids with different physical properties. He also realized that arsenates and phosphates crystallize in the same form and thus display enunciated isomorphism, which is the term to describe crystals of different composition generating the same form. From then on many other examples of solids that differ in physical properties while having same chemical composition have been found primarily for inorganic compounds followed by organic compounds. In 1839 the first transition between such so-called polymorphs was observed by Frankenheim<sup>63 68</sup>. He studied the crystallization of potassium nitrate from solution and demonstrated that the polymorphic transitions can be solvent mediated. Following decades, Lehmann<sup>69</sup> studied phase transitions and classified them into one direction only transitions and reversible transitions upon heating or cooling. With the discovery of X-Ray diffraction, the organization of atoms in the crystalline assembly become reachable and stimulated the field of polymorphism by giving a new impulse and a new direction from the structural point of view.

At first, polymorphism was called dimorphism because it is thought that a substance could crystallize into only two possible phases. Later it was named as polymorphism with the experimental evidence for substances that have more than two phases. Berzelius introduced a less general term allotropism<sup>70</sup>, for the chemical elements existing in two or more different forms. Most widely known cases of allotropism is

maybe that of the carbon which can have several solid structures such as graphite and diamond as well as more recent discovered nanotubes and fullerenes. For molecular crystals polymorphism has been defined by McCrone<sup>71</sup> as “A solid crystalline phase of a given compound resulting from the possibility of at least two different arrangements of the molecules of that compound in the solid state”. To eliminate the ambiguity with tautomerism, which is defined as the rapid interconversion of structural isomers in liquid or vapor state, the definition was strengthened by classifying two crystal structures as polymorphic if they lead to the same liquid or vapor phases<sup>72</sup>. A related term pseudopolymorphism is sometimes used for solvated forms, but the use is discouraged because there is a clear difference between a polymorphic transition and the process of desolvation<sup>73</sup>. Polymorphism is usually classified as packing polymorphism, in which the structures are different in the way that molecules are packed, and conformational polymorphism, in which there is a difference in molecular conformation for the structures. However this classification can be ambiguous because at the atomic level, there do not exist really frozen structures with exact bond lengths and bond angles but these entities are just averages over time of different vibrational modes happening on a very short time scale, which depend on different short and long range interactions. There can be also possible rotation flexibility around single bonds in some systems which adds additional degrees of freedom in the packing of molecules in a crystal lattice. Thus the classification of packing polymorphism and conformational polymorphism should be regarded as extremes on a floating scale. Polymorphism is an extremely widespread phenomenon within the chemistry branches of both inorganic and organic systems. A famous quote belonging to McCrone (1965) about the existence of polymorphism is as follows: “Every compound has different polymorphic forms and in general, the number of forms known for a given compound is proportional to the time and money spent on it.”

Silica (SiO<sub>2</sub>) can be regarded as an example of a material which shows a very high degree of polymorphism. It is one of the most common materials in nature and has many industrial applications. Thus, it is one of the most heavily and widely investigated materials. The five stable dense polymorphs: quartz, coesite, stishovite, cristobalite and tridymite, have been studied intensively for decades. There is also an increasing and

large number of other lower density polymorphs which have been synthesized (e.g. zeolites).

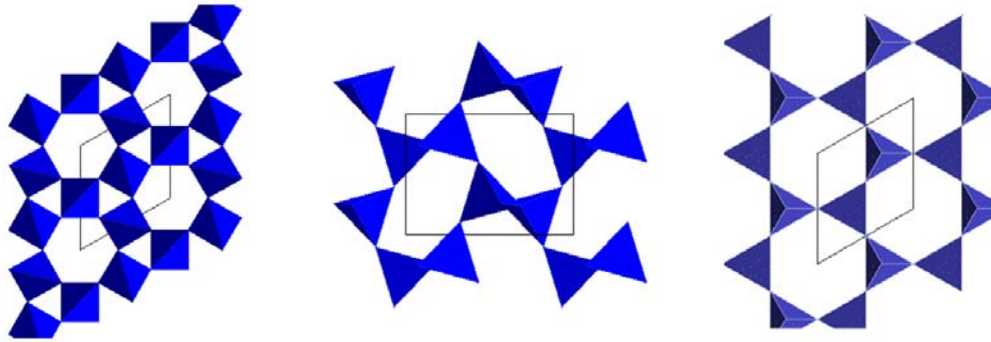
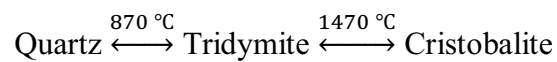


Figure 13. Structures of Silica polymorphs, a) quartz b) tridymite c) cristobalite.

At atmospheric pressure, silica has three distinct crystalline phases, which are quartz, cristobalite and tridymite. The stability ranges of these polymorphs have been subject to many studies, but one of the earliest and mostly quoted one is that of Fenner's<sup>74</sup>, who determined the stability relations among these phases as:



The low pressure phases are all built of corner-sharing SiO<sub>4</sub> tetrahedra. Also in the glass and the liquid phases, almost all Si atoms are tetrahedrally coordinated. However at higher pressures crystal structures six-fold coordination of Si atoms becomes more favorable so that octahedrally coordinated polymorphs occur (e.g. stishovite)..

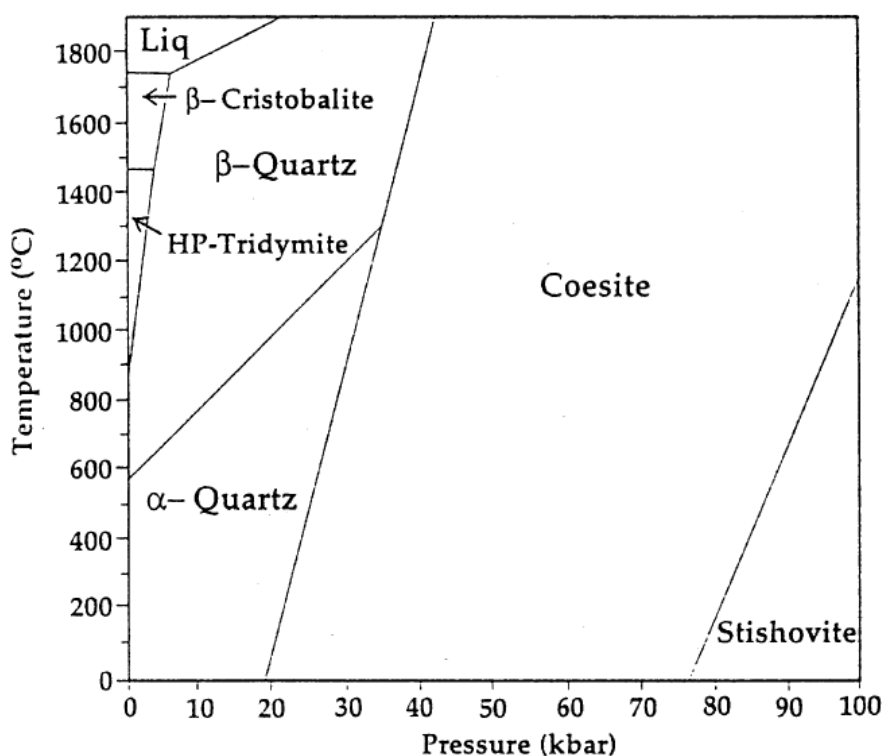


Figure 14. Phase diagram of silica at various pressures and temperatures.<sup>75</sup>

Depending on temperature, at pressures above 8-12 GPa, silica forms the stishovite phase, where oxygen atoms form a distorted hexagonal close packed structure and silicon atoms employ octahedral sites. At higher pressures above 45-50 GPa stishovite undergoes an orthorhombic distortion and transforms to a CaCl<sub>2</sub> phase<sup>76</sup>. In the same pressure range in a He pressure medium quartz was found to transform to a monoclinic post-quartz phase, which is built up of 3 x 2 kinked chains of edgesharing SiO<sub>6</sub> octahedra units<sup>77</sup>. Without a pressure medium, compression of quartz converts to a complex phase Quartz II or a mixture of phases<sup>78</sup>. At pressures around 35-40 GPa in a soft pressure medium cristobalite transforms to a PbO<sub>2</sub>-type structure<sup>79</sup>. Niccolite structure was reported in shock wave compression<sup>80</sup> and laser heated DAC experiments<sup>81</sup>. With several other methods, many other polymorphs of silica are continuing to be reported and the research to obtain new polymorphs and to characterize them is still going on.

For ZnO material, as previously mentioned, there are three experimentally known polymorphs, which are wurtzite, zinblende and rocksalt structure. However, will be

discussed throughout this thesis, ZnO has a very wide range of possible and promising polymorphs.

## 4.2. Polytypism

Polytypism is a special class of polymorphism. It is used for the polymorphism between two different crystal structures, which are composed of identical 2D layers but have differences only in stacking. Silicon carbide (SiC) is the most well-known example for this type of polymorphism, which can form such stable and long range modifications. More than 200 SiC polytypes have been determined so far<sup>82</sup>. The SiC polytypism occurs between two extreme polytype structures ZB, where cubic stacking of Si-C double layers occurs in the [111] direction and hexagonal wurtzite with hexagonal stacking in the [0001] direction. The other polytypes are hexagonal or rhombohedral combinations of these two stacking sequences with n Si-C double layers in the primitive cell (Figure 15). The most well known examples are 4H and 6H structures, which are named according to Ramsdell notation<sup>83</sup>. According to this notation the number of SiC double layers in the stacking direction in the primitive unit cell is combined with the letter representing the Bravais lattice type; ‘C’ for cubic, ‘H’ for hexagonal and ‘R’ for rhombohedral. With this notation cubic zinc blende is noted as 3C and hexagonal wurtzite as 2H as you can see also the corresponding ABC stackings of double layers in Table 4 for selected SiC polytypes.

Table 4. Ramsdell notations and layer stackings of simple SiC polytype structures.

Ramsdell notation	ABC stacking	% of hexagonality	No. of atoms per unit cell
3C	ABC	0	2
8H	ABACBABC	25	16
21R	ABCACBACABCBCACB	29	14
6H	ABCACB	33	12
15R	ABACBCACBABCACB	40	10
4H	ABAC	50	8
2H	ABAB	100	4

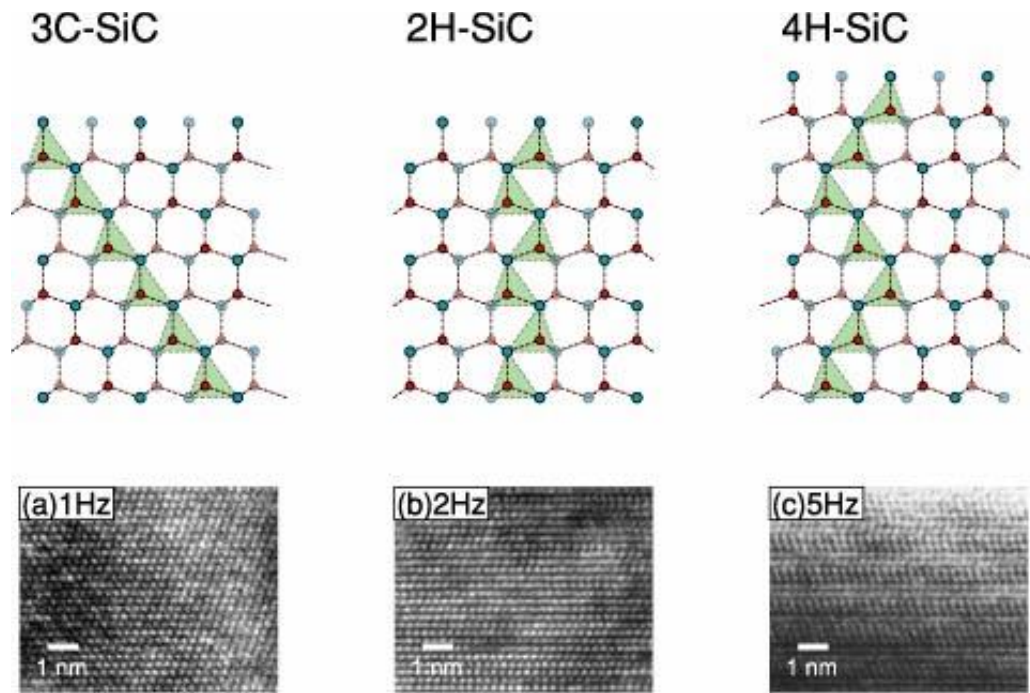


Figure 15. Crystal structures of 3C (zinc blende), 2H (wurtzite) and 4H polytypes of SiC and high resolution images of their corresponding films fabricated at different laser pulse frequencies.<sup>84</sup>

The driving forces for the occurrence of so many polytypes of SiC is not very clear yet despite many research in this field. There are roughly two categories of explanations of the polytypism of the SiC.<sup>85</sup> The first one focuses on the considerations of the thermodynamical stability of the common short-period polytypes, which are believed to act as basic structural elements for the generation of long-period polytypes. The second category deals with the growth mechanism for long-period polytypes around screw dislocations. However, there is no final conclusion so far, and a satisfactory explanation may contain both types of considerations to some degree depending on the actual growth conditions<sup>86</sup>. There also exist polymorphic transformations between SiC polytypes, among which the solid-solid phase transition of 3C to 6H structure at elevated temperatures is just one example<sup>87</sup>. The properties of various SiC polytypes differ also by the remarkable influence of different stacking of Si-C double layers. One common example is of their electronic structure, where the indirect bandgaps vary in a wide energy range from 2.4 eV to 3.3 eV going from one extreme cubic 3C polytype to the other extreme 2H with complete hexagonal stacking. Choyke et al.<sup>88</sup> determined a linear relationship between hexagonality of the polytype and the bandgap experimentally for a couple of polytypes. The position of the conduction band minimum

in  $k$ -space is also established by the polytype, which is important in microelectronic device applications as of certain polytypes<sup>89</sup>.

### **4.3. Hypothetical polymorphs**

If we are to believe the quote by McCrone at the start of this that new polymorphs can be found for most of the materials by investing more and more on research, a question arises whether we can predict new feasible structures before experimentally fabricating them. Similarly, can the theoretical study of potential new polymorphs help characterize experimentally found new structures. As well documented in a review of the current status of the field of material's prediction by Woodley and Catlow<sup>90</sup> the answer to both these questions is yes, up to some degree of accuracy. . Predicted structures are often called as hypothetical structures. There are several methods developed throughout several decades to generate reasonable hypothetical structures which can be roughly partitioned into three groups: (i) direct explorations of configurational space, (ii) topological modeling methods, and (iii) structural models by analogy.

#### **4.3.1. Structural Models by Analogy**

The simplest among all is the latter, which is generating approximate structural models by analogy with known structures of somehow related chemical composition and then refining their structures with usually quantum mechanical electronic structure methods<sup>91</sup>. This approach is not 'ab initio' in terms of generation because, so to speak, the structures are derived from "mining" in the literature for experimentally known or other predicted structures of similar systems and is thus usually called the 'data mining' approach. Although simple, data mining approaches can be very effective for some systems like alloys<sup>92,93</sup>, but intrinsically lack the ability to explore among the diversity of as-yet unknown structures.

#### **4.3.2. Topological Modeling Methods**

Topological principles have been also used for decades by enumerating and defining networks according to the bonding connectivity of considered materials. This approach

is particularly useful in analyzing real structures and for predicting hypothetical structures with directionally-bonded frameworks (e.g. zeolites). As an example, Smith<sup>94</sup> developed a systematic enumeration method for four connected three dimensional silicate materials (buildings on the earlier topological approach of Wells)<sup>95</sup> where he describes some 3D nets based on other 2D nets. For silicates, 2 dimensional simple hexagonal nets are used to describe the frameworks together with perpendicular upward or downward connections for each node to another 2 dimensional net. Thus, two adjacent nodes within a horizontal hexagonal net can have their internet linkages either pointing in the same (S) or in a changed (C) direction, which is how they are enumerated. Going around the six nodes of a single hexagonal ring in a single net, there are 8 ways, in which the internet connection sequences can occur: CCCCCC, SCCSCC, SCSCCC, SSCCCC, SSCSSC, SSSCSC, SSSSCC and SSSSSS (see Figure 16). Most of these sequences allow only one type of 3 dimensional nets, except for SSCCCC and SSSSCC, for which there exist two different choice of bringing hexagons together in adjacent nets. According to this enumeration there exist ten different simple framework structures, excluding the infinite number of possibilities due to polytypism in CCCCCC (which stands for wurtzite and zinblende polytypism) and SSSSCC. One should also note that there exist infinitely many possible structures by combining two or more of these simple framework enumerations. In principle, these type of enumeration methods may generate all the possible frameworks, however filtering the results in order to identify the more likely candidates can be sometimes problematic.

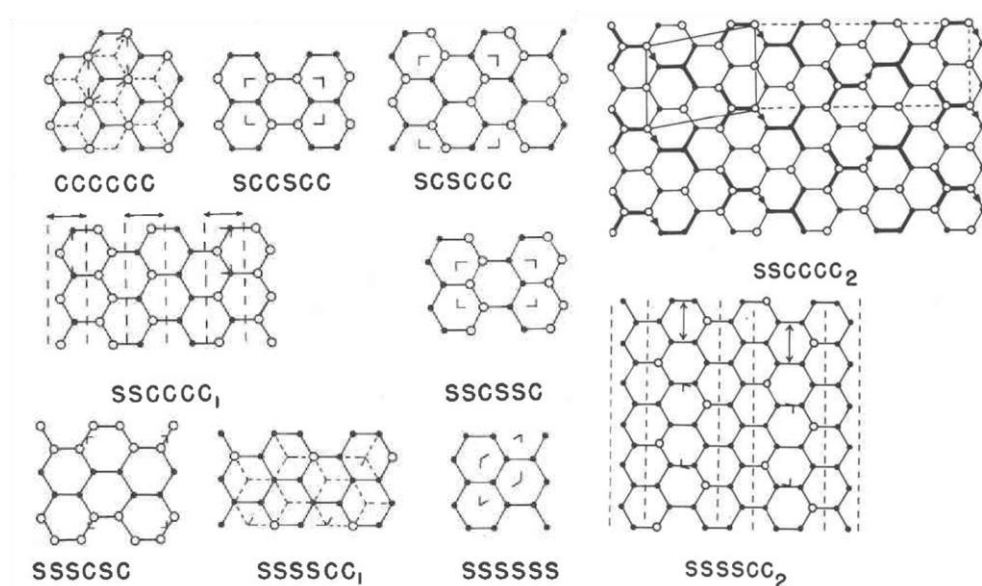


Figure 16. 3D nets of simple framework structures.

Another example would be tiling approach<sup>96</sup>, in which the four-connected 3D nets are divided into polyhedra and Euclidean space polyhedral tilings are used to enumerate the corresponding nets, and graph approach,<sup>97</sup> in which the atoms are treated as tetrahedral nodes and the frameworks are generated by permuting over all possible topological connections.

### **4.3.3. Directly Exploring Configurational Space (Global Optimization)**

Directly exploring the configurational space of structures has the potential to explore and selectively identify promising structures but can be computationally expensive. Such search methods are also called global optimization methods because they try to find the global minimum of the configurational space computationally. As such approaches (e.g. simulated annealing, evolutionary algorithms) require efficient procedures to explore the energy landscape of configurations, which is defined by the internal coordinates of the atoms in the unit cell and the corresponding energy. Usually energy functions at a classical or quantum level depending required accuracy and computational cost are used to evaluate the structures, however they sometimes also uses simpler cost functions or collective variables for some systems. Global optimization techniques evaluate the energy function many times in order to search the energy landscape of configurations. As examples, we outline two specific approaches to global optimization below. The Monte Carlo Basin hopping method, as used in my work, is discussed in more detailed in the methodology chapter.

#### **4.3.3.1. Simulated annealing**

The simulated annealing<sup>98</sup> is an approach based on simple concepts arising from physical annealing. The atoms are in a disordered manner when the substance is in melted state. While cooling slowly, the atoms may crystallize in an ordered manner, to reach the global minimum. However, if the cooling is rapid or if the starting temperature is not high enough, the system may be quenched into a local minimum or freeze into a crystalline system containing defects like vacancies and dislocations. In simulating annealing the positions of atoms are perturbed using molecular dynamics or a Monte Carlo scheme while decreasing the temperature gradually, so that the system can move around between local minima by overcoming the energy barriers depending on the temperature. After the continuation of this process slowly enough, the final structure is

likely to be the global minimum. However it is possible for complex energy landscapes that some low-energy regions may not be reachable for a specific starting point and thus the global minimum may be missed. To overcome this danger, usually multiple runs starting from different initial positions are being used. The simulated annealing approach has been used in a number of elegant, predictive studies of inorganic solids.<sup>99100</sup>

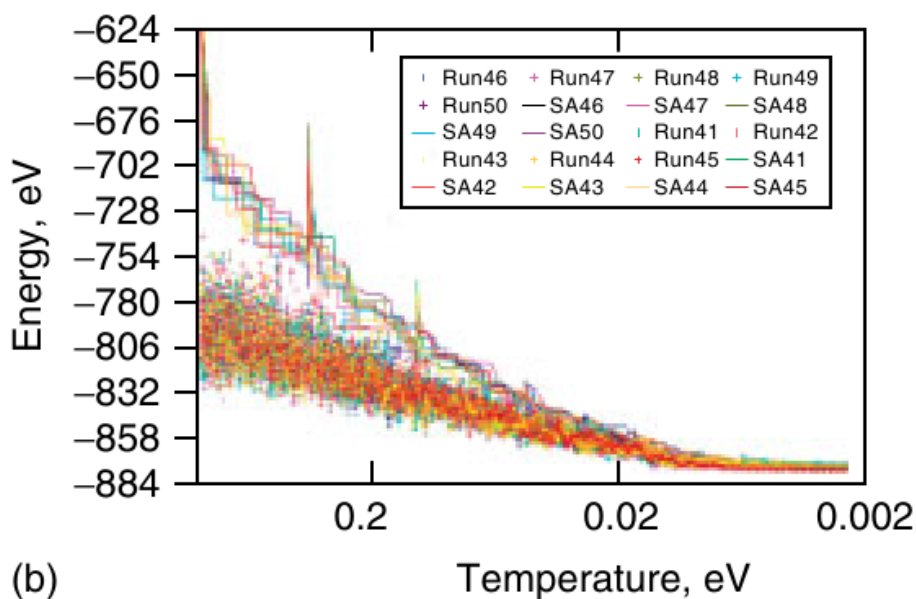


Figure 17. An example of simulated annealing method used for prediction of crystal structure of  $\text{BaMgAl}_4\text{Si}_4\text{O}_{16}$ <sup>101</sup>. The different color lines corresponding the trajectories of ten runs starting from different starting points. Data points represents the local minima along each trajectory.

#### 4.3.3.2. Genetic algorithm methods

Genetic algorithm<sup>102</sup> are another approach to explore the configurational landscape by mimicking biological evolution, which can also avoid the problems related with a single starting point, by introducing a population of structures. The initial population is usually produced by random configurations of atoms and than is being used to create new generations by mimicking evolutionary mechanisms like crossover, mutation and natural selection. According to natural selection, the organism that fits better to the environment continues to evolve. Thus, in genetic algorithms it is principal to define a fit function, which clearly becomes energy of a structure for physical sciences, so that

the lower the energy, higher the fitness. Crossover is described as taking two parent structures and combining them to obtain a new candidate structure for the new generation, whereas mutation is described as a random change on a single structure. However to optimize the efficiency of the algorithm there are several implementations of genetic algorithms varying how the crossover and mutation operators actually defined, how competition is simulated to become a parent structure and how the population is renewed or updated. Usually roulette wheel method is being used for the selection of parent structures. In this method, fitness value is taken for a random selected structure and compared with again a random number which is generated in a range covering all of fitness values in the population, and the procedure continues until two parent structure being selected for crossover. Thus, it is more likely that the low energy structures are being selected. After the selection, a crossover operation is used for mixing the parent structures, for which there is generally two types of approaches according to whether a genotype representation was used to define the phenotype of the structure or not. If there is not, crossover operators are defined as working directly on phenotypes, which are simply atomic positions for our case. By mixing structures it is likely to found better structures constituting from low-energy regions of the present structures, however no new low-energy regions are being introduced usually. Mutation operators serve better for this purpose as they operate on a single structure and the ability to introduce new low-energy regions by random changes like moving atoms, twisting the structure, swapping of atom types or even replacing with a random structure to keep the structural diversity. The selection of the new population includes always elitism, which is at least keeping the best structure from the last generation and usually taken more than one and merged with new generated structures with higher fitness. Duplicate structures are also eliminated to avoid a deadlock in a local minimum. The efficiency of genetic algorithm method has been shown in a series of studies, for metallic and alloy clusters<sup>103</sup>, for oxide structures<sup>104</sup> and for molecular crystals<sup>105</sup>

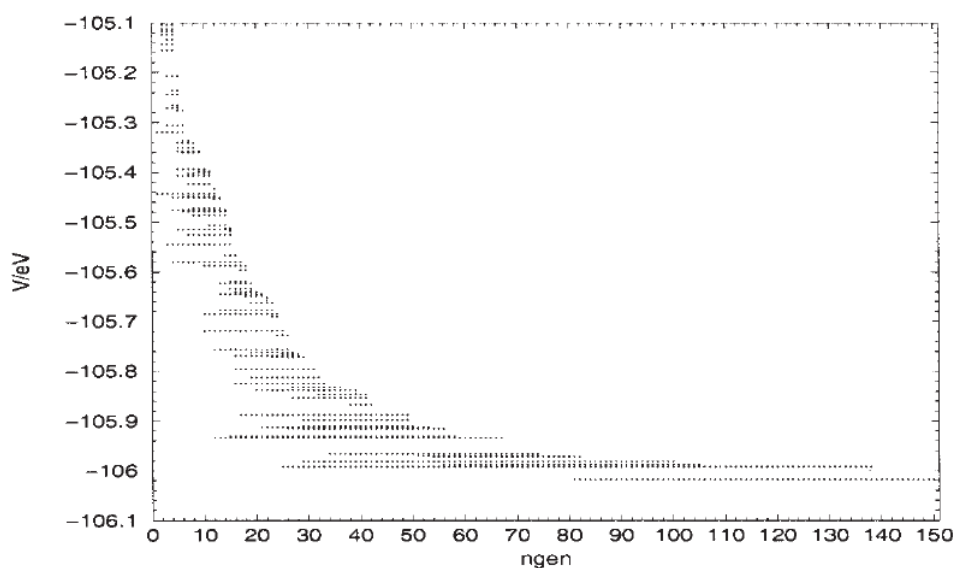


Figure 18. An example of genetic algorithm method used for Pt<sub>12</sub>Pd<sub>12</sub> nanoclusters.<sup>106</sup>

## **5. Scale and Dimensionality**

### **5.1. Introduction**

Going from the macroscopic scale to the atomic or molecular scale, one passes through the nanoscale where the properties of materials can change drastically because of both size and surface effects. The former is often termed the quantum size effect, which is the change in bulk electronic structure at the atomic scale due to influence of discrete electronic levels. The latter is surface or interface induced effect, which becomes important by the enormous increase of the surface to bulk ratio at reduced scales. Research into the properties of materials at the nanoscale (the term “nano” refers to 10<sup>-9</sup> m by definition and roughly corresponds to systems with 1-100 nm dimensions.) have had a great impact on the development of science and technology. The application performance of materials is determined by their properties which, in turn, strongly depend on their size and structure. The importance of the nanoscale is underlined by the way it opens up to opportunities to synthesize new (nano)materials with unique structure and properties. The research area concerned with the study of these new nanostructures and their properties is called nanoscience. The utilization of these new materials towards potential new applications found the basis of the field of nanotechnology.

Structures can be naively classified by their scale as 3-dimensional (3D), 2-dimensional (2D), 1-dimensional (1D) and 0-dimensional (0D) in terms of the size of that corresponding dimension as shown in Figure 19. Materials having a nanosized length scale at least in one dimension are called nanostructures.

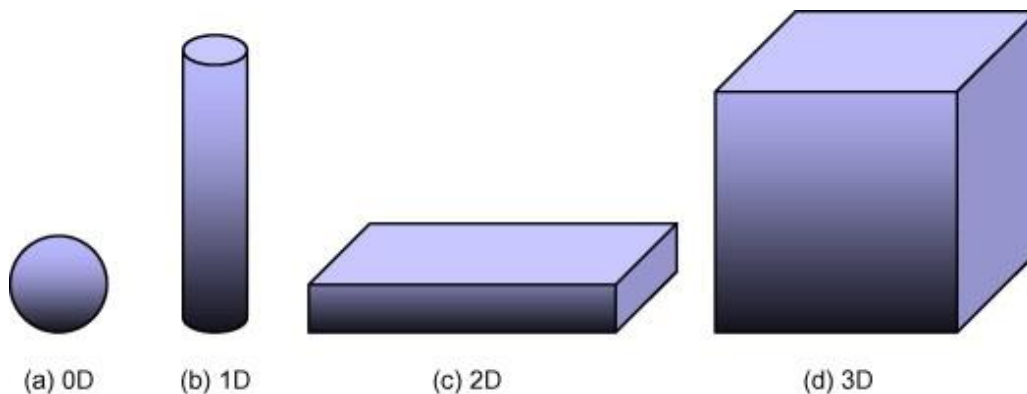


Figure 19. Schematic representations of (a) 0-dimensional (0D), (b) 1-dimensional (1D), (c) 2-dimensional (2D) and (d) 3-dimensional (3D) structures.

In general there are two approaches to produce nanostructures: top-down and bottom-up. The top-down approach obtains nanostructured materials from a parent bulk material by size-reduction via various techniques, while the bottom-up approach forms nanostructures by the assembling of atoms or particles.

## 5.2. Synthesis of nano-ZnO

To prepare ZnO nanostructures, both physical and chemical methods can be used within these two approaches. Wet chemical etching<sup>107</sup> is one example of a top-down approach. However high cost, high time-consumption, low controllability and repeatability of top-down approaches makes bottom-up approaches more promising and more researched. Molecular beam epitaxy<sup>108</sup>, metal-organic chemical vapor deposition<sup>109</sup>, pulsed laser deposition in a controlled atmosphere<sup>110</sup> or in liquids<sup>111</sup> are some examples of physical bottom-up approaches to obtain nanostructured ZnO thin films with high crystallinity, high homogeneity and adaptable chemical compositions. Chemical methods like sol-gel<sup>112</sup>, electrochemical<sup>113</sup> or hydrothermal pathways<sup>114</sup> are known to have the advantage of allowing one to obtain extremely small structures with tunable dimensions. However

the crystalline quality may be less because of the potential presence of impurities in the solution phase.

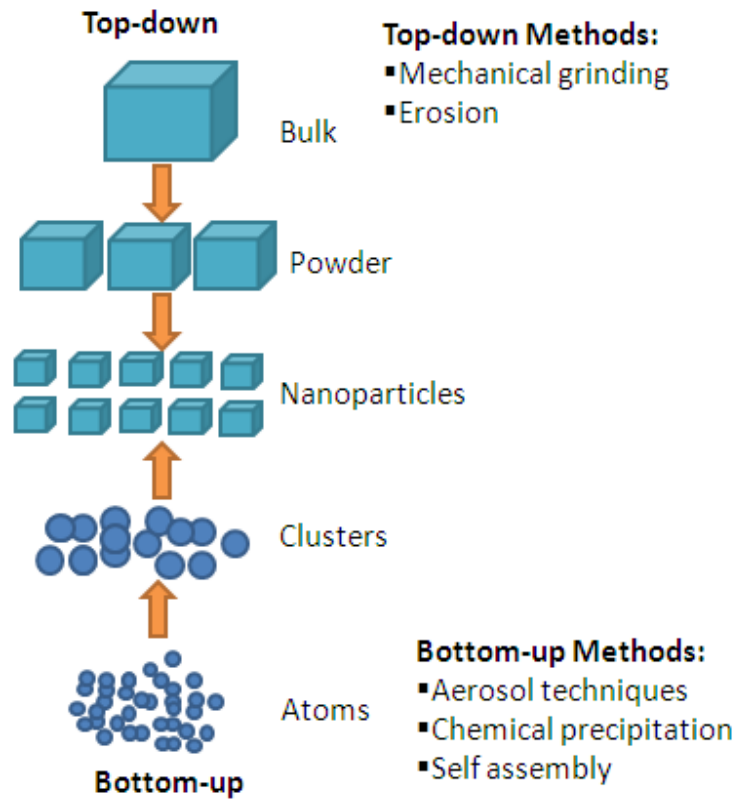


Figure 20. Illustrative example of top-down and bottom-up approaches.

### 5.3. Nanostructured 3D materials

As previously discussed, the bulk is considered to have a packing of atoms extending to the macroscopic scale. In other words the bulk has dimensions considerably larger than the nanoscale in all three orthogonal crystallographical directions. The periodicity, and extent of structural order defines the crystallinity, ie separates the crystalline, polycrystalline and the amorphous structures as mentioned in previous section. Polycrystalline bulk materials, if the grain sizes are in the nanoscale, can be classified as 3D nanostructures. In nanostructured materials a large volume fraction of the atoms are on the interfaces, mainly on grain boundaries due to very small grain sizes. Thus nanostructured materials have significantly different or improved properties than their polycrystalline counterparts, such as increased hardness, enhanced diffusivity, improved ductility, higher electrical resistivity<sup>115</sup>.

## 5.4. Nanofilms (2D)

A thin film is a layered structure of a material ranging from fractions of a nanometer to several micrometers in thickness in the direction normal to the layers, whereas having long range periodicity on other two dimensions. Electronic semiconductor devices and optical coatings are the main applications benefiting from thin film construction. The chemical, physical, mechanical, and electronic properties of thin films can be extremely different from those of the corresponding bulk materials. With the increase of the surface to volume ratio due to the reduction in size and dimensions, the low coordinated surface atoms play a dominant role in the thermodynamics and kinetics of these systems, resulting in complex phenomena such as surface reconstructions, island formation, nanostructure formation etc. The emergent films often contain nano or microscale morphological features that display novel size and morphology-dependent properties which can be exploited in a number of technological applications. Metal oxide thin films provide a rich platform for exploring novel device applications because they have a variety of functionalities. Many metal oxide thin film systems have traditionally been used as important device materials like dielectric insulators, temperature sensors, transparent conducting oxides, phosphors, etc.

Fabrication of 2D nanomaterials is usually accomplished on a substrate which is called epitaxial growth and over the past decades sophisticated techniques have been developed to achieve a controlled deposition down to single atomic layers. With the advances in microelectronic fabrication processes, several vapor-phase techniques were used to obtain controlled deposition of 2D nanomaterials<sup>116</sup>. Although vapor-phase techniques are energy intensive and usually require exceptionally clean environments, the technology is commercially viable by large scale production. Alternative methods to fabricate 2D nanomaterials are spin-coating of colloidal nanoparticles or layer by layer dip-coating processes into colloidal suspension of nanoparticles. Both these techniques require synthesis of nanoparticles in colloidal form by solution chemistry. The obtained 2D material is usually textured and non-epitaxial. Such strategies have potential applications in where cost efficiency is more important over high-quality and repeatable performance, for example qualitative sensors<sup>117</sup>. In recent years a single layer of

graphite sheet, which is called graphene, has been synthesized via solution based chemical techniques and without a supporting substrate<sup>118</sup>.

2D materials exhibit surfaces perpendicular to the growth direction. The stability of the exhibited surface is one of the main factor that determines the morphology of the 2D material and it can be defined by the surface energy ( $E_{sur}$ ):

$$E_{sur} = E_{slab} - n \times E_{bulk}$$

where  $n$  is the number of atoms,  $E_{slab}$  is the cohesive energy of finite crystal and the  $E_{bulk}$  is the cohesive energy per atom in infinite crystal. Thus the surface energy ( $E_{sur}$ ) becomes the excess energy associated with the surface. Surface energy plays an important role in growth and nucleation processes. For ionic materials, when there is a dipole moment perpendicular to the surface in the unit cell, the surface energy diverges and becomes infinite, which means such surfaces cannot exist<sup>119</sup>. The apparent occurrence of such polar surfaces has been attributed to some stabilization processes like adsorption of other atoms or surface roughening. Tasker categorized the surfaces of ionic or partly ionic crystals into three types as illustrated in Figure 21. Type 1 consists of stoichiometric proportions of cations and anions in each plane and thus exhibit neutral surfaces. Type 2 exhibit charged surfaces but has no dipole moment in the repeating units perpendicular to the surface due to the cancellation inside the unit cell. However the Type 3 surfaces exhibit charged surfaces with a dipole moment in the repeating unit perpendicular to the surface. Therefore these Type 3 surfaces have an infinite surface energy and an electric field throughout the crystal due to charged surface. Thus Type 3 surfaces cannot exist as a simple termination of the frozen bulk structure and can only be prepared as a reconstructed surface in such a way to compensate the polarity.

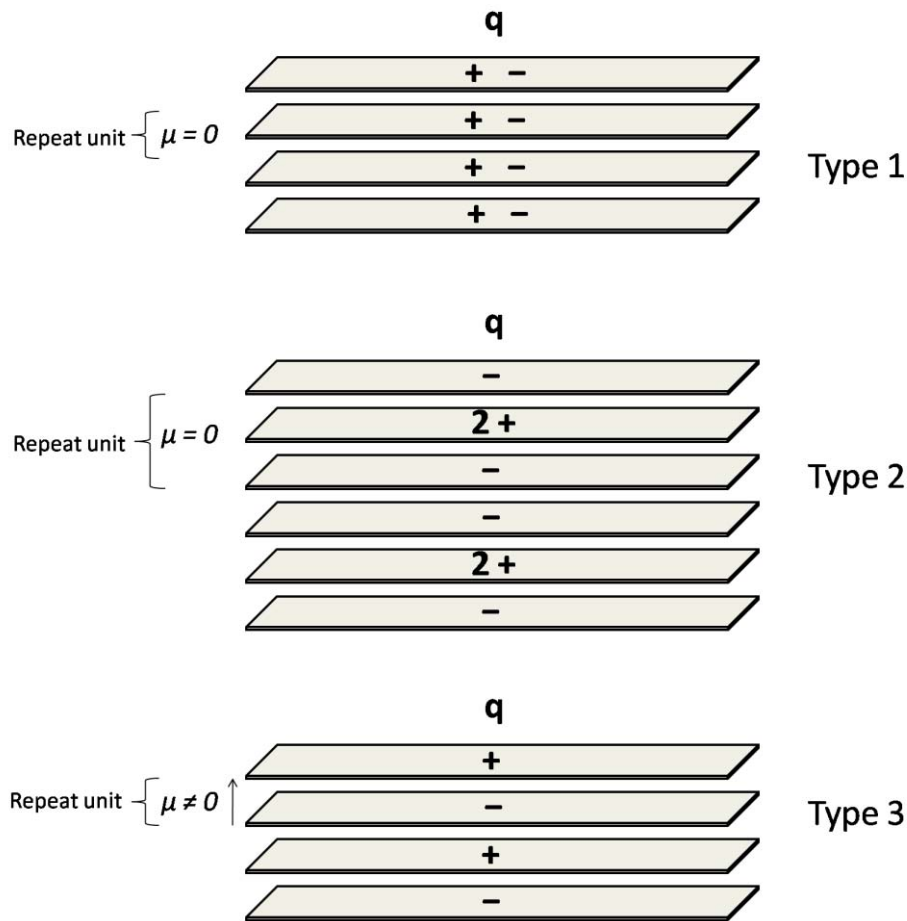


Figure 21. Distribution of charges  $q$  on planes for three stacking sequences parallel to surface.

ZnO thin films have been prepared by many methods like chemical vapor deposition<sup>120</sup>, sputtering<sup>121</sup>, sol-gel method<sup>122</sup>, pulsed layer deposition<sup>123</sup> and spray pyrolysis<sup>124</sup>. In Industry, for large-scale deposition sputtering is mainly used due to its high deposition rate and high uniformity. At room temperature, films grown by pulsed layer deposition technique tend to be amorphous, however at elevated substrate temperatures deposition can result in highly textured films with the c-axis oriented perpendicular to the substrate plane<sup>125</sup>. In other layer-by-layer growth techniques the prevalence of c-axis oriented material is also observed whereas it is considered to be a polar surface<sup>126</sup>.

For wurtzite ZnO, c-axis oriented [0001] Zn and [0001] O face terminations are both Tasker type 3 surfaces. These two surfaces can be seen as a stacking sequence of hexagonal Zn and O layers along the crystallographic c axis with alternating distances of  $R_1 = 0.61 \text{ \AA}$  and  $R_2 = 1.99 \text{ \AA}$  and thus a reconstruction of the surface layer charge by a factor of  $R_1 / (R_1 + R_2) \approx 1/4$  less positive for Zn terminated (or less negative for O

terminated) is needed for a charge compensation<sup>127</sup>. This charge compensation can be achieved by three suggested mechanisms<sup>128</sup>:

- Creation of surface states and transfer of negative charge from the O to the Zn face.
- Removal of surface atoms
- Oppositely charged foreign atom adsorption on the surfaces

Among them, which is the exact mechanism involving the stabilization of the [0001] surface of ZnO is still debated and a combination of different mechanisms can be also responsible such as surface reconstruction and hydrogen adsorption<sup>129</sup>. More recent work shows nanoisland reconstructions are responsible for stabilization process<sup>130,131</sup>. In terms of theoretical values of cleavage energies, non-polar surfaces [10 $\bar{1}$ 0] [11 $\bar{2}$ 0] are found to be more stable than the polar [0001]-Zn and [000 $\bar{1}$ ]-O surfaces<sup>132</sup>, whereas for thinner layers graphitic-like (layered)<sup>i</sup> layers, which can be seen as a flattening reconstruction of [0001] surfaces to get rid of the dipole moment, are found to be lower in energy up to the 36 layers<sup>133</sup>.

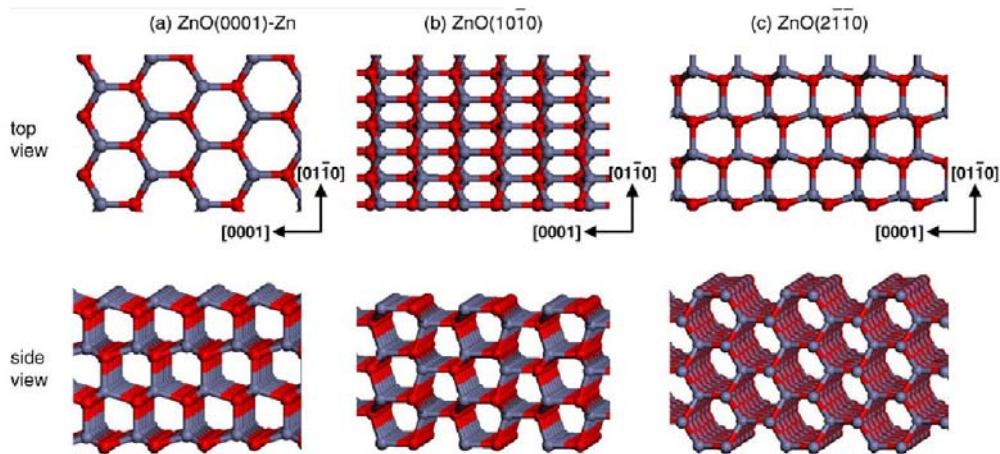


Figure 22. surfaces of wurtzite ZnO.

<sup>i</sup> In ref<sup>133</sup> the layer-ZnO structure is reported as being graphitic. Strictly speaking, the layer-ZnO phase has a different layer stacking to graphite, and is thus analogous to the layered hex-BN phase.

In a later theoretical work, Morgan suggested another promising nonpolar film structure (the Body Centred Tetragonal (BCT) structure), which is found energetically lower even than the layered phase up to 28 layers<sup>134</sup>. Experimentally, layered phase (see Figure 23) of ZnO for very thin layers are confirmed both on Ag(111)<sup>135</sup> and Pd(111)<sup>136</sup> surfaces. The BCT structure has still not been observed as a film structure itself possibly due to epitaxial symmetry issues, but has recently been observed as a surface reconstruction on the wurtzite ZnO (10 $\bar{1}$ 0) surface<sup>137</sup>.

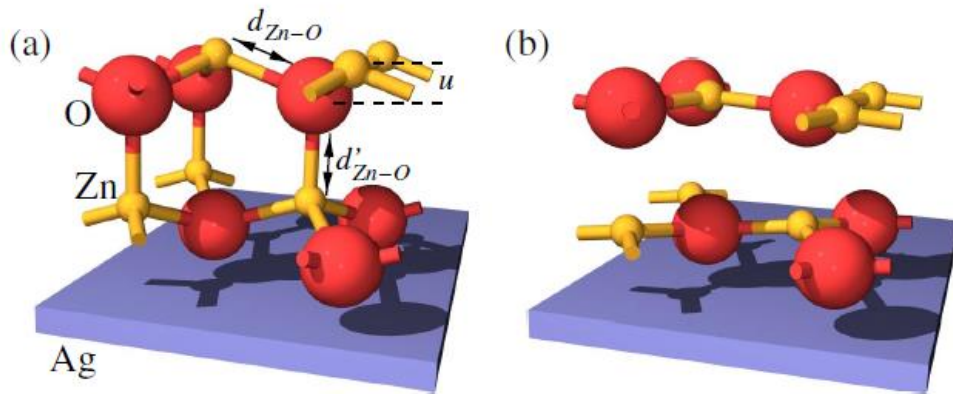


Figure 23. Illustrative model of (a) wz-ZnO and (b) layered-ZnO on Ag surface.

### 5.5. Nanowires (1D)

One dimensional nanomaterials have nanoscale sizes along two dimensions and they usually have a rod-like or wire-like appearance. Unlike films and particles, 1D nanomaterials have two possible axes of alignment with respect to a substrate. Deposition of nanowires parallel to a substrate can be achieved by various microelectronic fabrication technologies such as chemical etching<sup>138</sup>, electron or ion beam lithography<sup>139</sup> for semiconducting materials. Also electron or focused ion beam patterning/writing<sup>140</sup> X-ray or extreme UV photolithography can be used in combination with vapor-phase depositions to obtain nanowire patterns along the substrates which are compatible with the planar geometries of microelectronic devices<sup>141</sup>. These lithography based techniques belongs to ‘top-down’ approach. Besides, to obtain size and shape selective fabrication, ‘bottom-up’ approaches are used via crystallization of atoms or molecules in a controlled manner which usually results in vertical oriented nanowire-arrays to a substrate<sup>142</sup>. Several optoelectronic<sup>143</sup> and piezoelectric applications<sup>144</sup> make use of these vertically aligned nanowire arrays of semiconductors.

The interest in ZnO has increased with the discoveries of new nanostructured morphologies. It has been shown that ZnO can be grown in a wide variety of shapes and structures by using different growth techniques<sup>145</sup>. For example, as 1D nanostructures ZnO can take the shape of nanorods, nanotubes, nanocages, nanowires, nanotetrapods, nanoflowers and more<sup>146,147</sup>. 1D nanostructures of ZnO shows different novel properties to 3D and 2D structures due to their higher surface area to bulk ratios and single crystalline surface facets. The usually observed crystal faces on 1D nanostructures ZnO are the (0001), (10-10) and (2-1-10) facets of wurtzite.

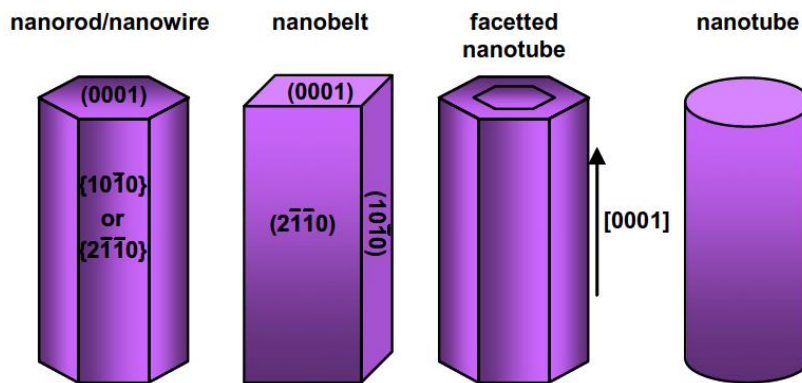


Figure 24. Schematic diagram of common 1D ZnO morphologies.

The most observed 1D nanostructures are nanorods and nanowires. The only difference of these two structure is that nanorods have a hexagonal cross section along the growth direction while nanowires have not. The growth direction is observed as [0001] while the nanorods show faces of (10 $\bar{1}$ 0) and (2 $\bar{1}$  $\bar{1}$ 0). Nanowires and nanorods can be grown with diameters as small as 4 nm<sup>148</sup> and 6.5 nm<sup>149</sup> respectively. Nanobelts are another observed 1D nanostructure which have rectangular cross-sections. Nanobelts can be grown with uniform width along their entire length with typical widths of 50-300 nm and thicknesses of 10-30 nm<sup>150</sup>. Hollow 1D nanotube nanostructures can also be grown with small wall thicknesses as small as 5 nm<sup>151</sup>. Another important nanostructure for ZnO is the nanotetrapod, which consist of a zinc blendestructured core connected with four wurtzite-structured arms. Nanotetrapods have the advantage that they may spontaneously orientate with one arm directed to the normal to the substrate, and have found immediate application in composite polymer/nanocrystal solar cells<sup>152</sup>.

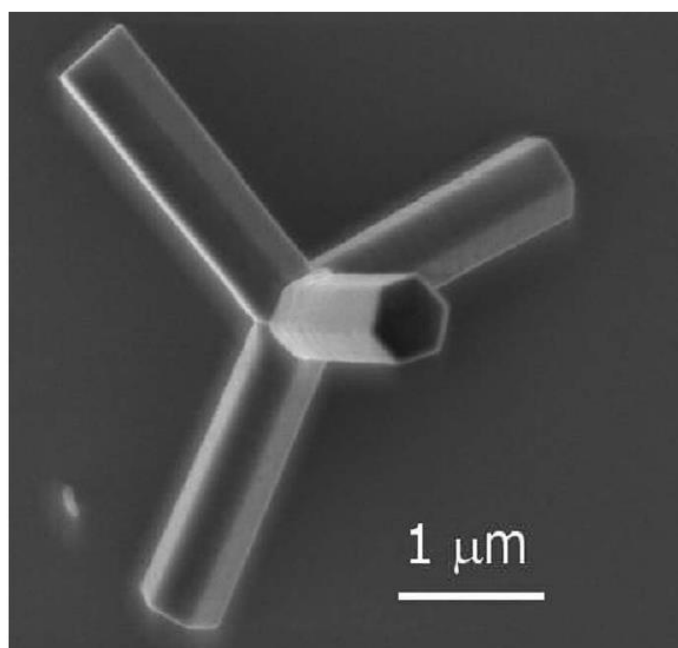


Figure 25. SEM image of a ZnO tetrapod.

## 5.6. Nanoclusters (0D)

Zero dimensional nanomaterials, or nanoparticles, have nanoscale sizes along all three dimensions. Zero dimensional nanoparticles can be single crystalline, polycrystalline or amorphous and may exhibit all possible morphologies. If the nanoparticles are single crystal, they are called nanocrystals. Nanoparticles with sufficiently small dimensions to observe quantum effects are called quantum dots. Nanoparticles are of great scientific interest because they form a bridge between atomic or molecular structures and bulk materials. First modern scientific experiments with nanomaterials were done by Michael Faraday in 19th century as the determination of the particulate nature of colloidal gold and size dependent optical properties<sup>153</sup>. 0D nanomaterials can be fabricated by physical processes like tribology<sup>154</sup> or vapor phase epitaxial depositions<sup>155</sup> as well as chemical synthesis techniques such as (co-)precipitation<sup>156</sup>, sol-gel processes<sup>157</sup> and thermal decomposition of organic complexes<sup>158</sup>.

The recent heavy interest on the synthesis and characterization of zero dimensional nanoparticles is mainly due to the wide range of applications of these materials in energy conversion, electronics and catalysis. The explanation of the structures and properties of nanoparticle materials is difficult because it is often highly problematic to

determine the structure from experiment. Although small angle scattering and X-ray absorption spectroscopy can provide useful information, they lack to give a detailed structural model. High resolution electron microscopy can provide detailed images of cluster structures, however they are often difficult to apply. A range of spectroscopic techniques that being employed usually give indirect and incomplete information. The difficulties are mainly related with the different behaviour of nanoparticles varying with size. Thus, the need to obtain atomic level models of crystal nucleation and the early stages of growth, which involves the formation and evolution of nano-clusters increases and stimulates the field further.

The structural and optical properties of ZnO nanoparticles are mainly determined by their size. Wood et al.<sup>159</sup> recognized three length scales, or regimes for ZnO nanoparticles which are macroscopic, quantum dots and clusters. Macroscopic particles maintain the crystal structure of the bulk and the optical band gap is practically constant while surfaces and point defects give rise to specific size-independent phenomena like UV, blue-green, yellow-orange and red luminescence. Quantum dots are nanoparticles with sizes of the order of the exciton radius, 15-30 Å at least in one dimension. In this regime even though the X-ray diffraction lines are broadened, the bulk crystal structure is preserved. The order of the stability between the phases change and the optical absorption bands shift and deform because of quantum size effects. The cluster regime is where the structures of the particles may differ significantly from that of the bulk phases. In this regime clear diffraction patterns are not obtainable and the optical properties cannot be directly correlated with those of the bulk. For ZnO and for many other materials experimental techniques are not capable of reliable characterization of the structure yet and thus is the least understood regime. The characteristic size separating the quantum dots and cluster regimes is not general and is found to be system dependent.

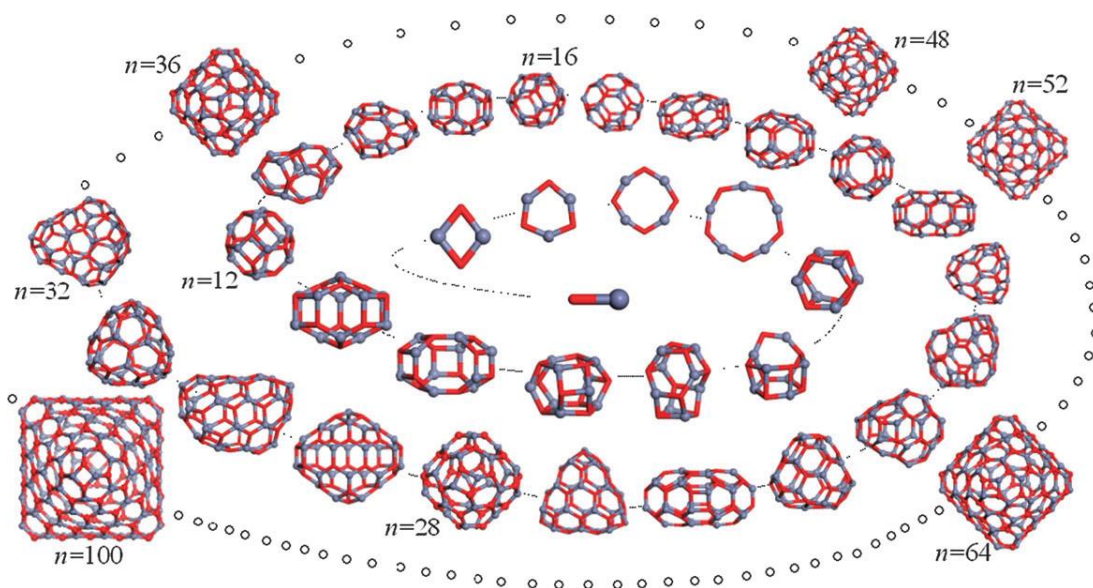


Figure 26. Global minimum structures of  $(\text{ZnO})_n$  nanoclusters.<sup>160</sup>

## **6. Nanoporous systems**

### **6.1. Introduction**

Low density crystalline bulk materials can possess periodic nanosized void spaces. This special class of materials, known as nanoporous materials, are abundant in nature, both in biological systems and in natural minerals. Some very well known examples of nanoporous systems are zeolites and metal organic frameworks (MOFs). Nanoporous materials are subdivided into three categories according to their pore radius:

- Microporous 0.2-2 nm
- Mesoporous 2-50 nm
- Macroporous >50 nm

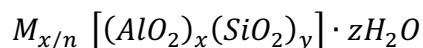
One of the main reason of the interest on porous solids is because their capability to interact with molecules, ions or atoms throughout the bulk of the material as well as their surfaces, which makes them very useful especially in catalysis or as membranes. In a porous structure, voids with molecular dimensions can manipulate, arrange, separate or activate molecules and the size and shape of voids determine these processes while the chemical identity of surfaces or reactive sites control selectivity and reactivity. Nanoporous materials are becoming increasingly important with the growing ability to

control their pore sizes, which in turn tailors their physical and chemical properties for particular applications.

## 6.2. Zeolites

Zeolites are a specific class of microporous oxide materials made up of silicon, aluminum and oxygen atoms. Zeolite minerals are broadly present in nature and have been known for more than 200 years. Primarily Swedish mineralogist Axel Fredrick Cronstedt discovered a natural occurring mineral which loses large amounts of steam upon heating. Thus, he named that material (which is nowadays known as stilbite) as 'zeolite'<sup>161</sup> which comes from the classical Greek, where 'zeo' means 'to boil' and 'litos' means 'stone' and later it became a general name for this type of material. Nowadays, zeolites are produced on a large scale and are available and used in a variety of applications such as ion exchangers in laundry detergents, where they replace calcium and magnesium ions in water with sodium ions present in the zeolite<sup>162</sup> or as adsorbents in gas stream purification to remove water and volatile organic molecules.<sup>163</sup>

Structurally, zeolites are based on fundamental building blocks of tetrahedral SiO<sub>4</sub> and AlO<sub>4</sub> units giving rise to a three dimensional network. It has a structural formula of



Where M is an exchangeable cation of valence n, z is the number of water molecules and x+y gives the number of tetrahedral building blocks present in the unit cell. Water and cations are found inside the pores. Si and Al atoms, which are called framework atoms, are coordinated tetrahedrally to four oxygen atoms bridging two framework atoms as shown in Figure 27.

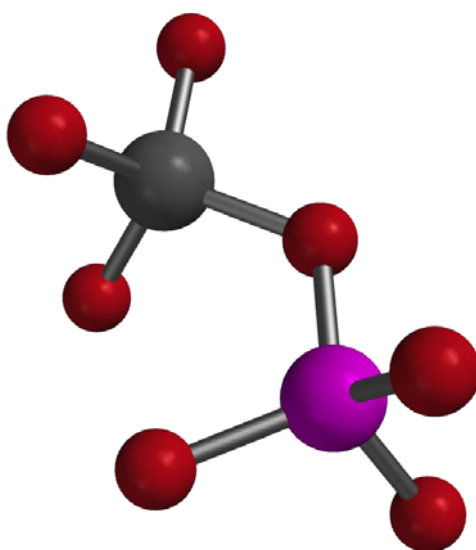


Figure 27. The building unit  $TO_4$  where T denotes for framework atoms.

This tetrahedral  $TO_4$  unit is called a called primary buiding unit (PBU). By further grouping PBUs one can also view zeolites in terms of an infinite lattice of identical building blocks called secondary building units (SBU). SBUs are chosen such a way that entire framework is described by one type of SBU only. Also it should be noted that SBU's are non-chiral and an integral number of SBU always exists in a unit cell. Some SBU structures are given in Figure 28.

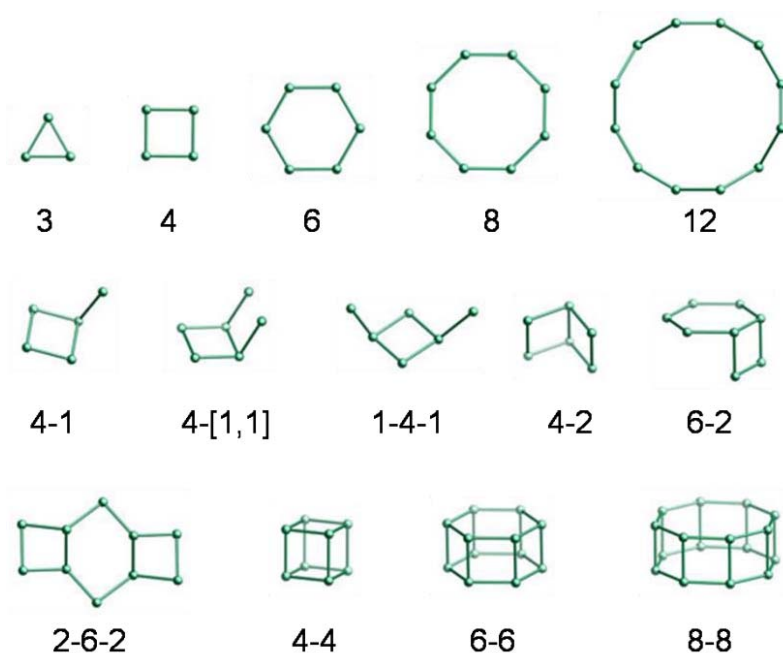


Figure 28. Examples of secondary building units (SBU) of zeolite frameworks. Each cyan ball represents one framework atom.

To understand the topology and identify the relations between framework types it is also useful to describe zeolite frameworks with composite building units (CBUs) and chains. The difference is that the latter cannot necessarily be used to build the entire framework and are not required to be non-chiral. Some examples of CBUs and chains are given in Figure 29. It should be noted that the three lower case letter codes of CBUs are related with the three capital letter codes of some zeolite structures.

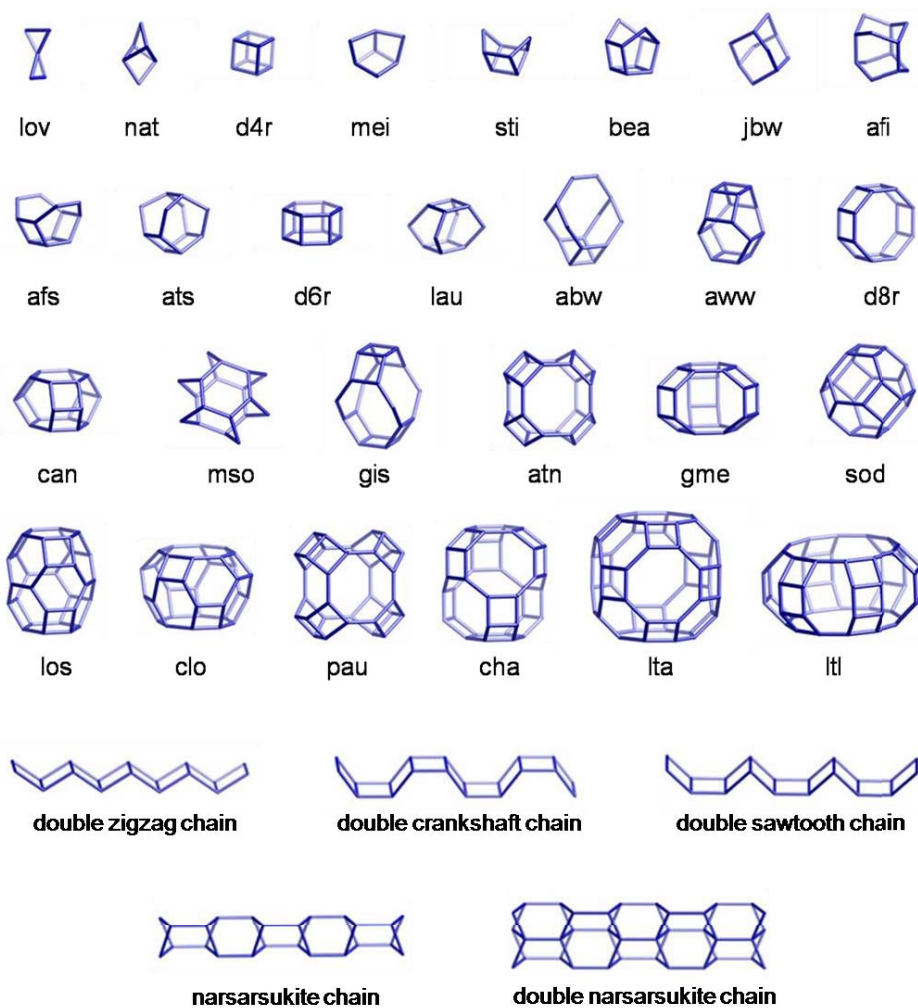


Figure 29. Examples of (a) composite building units (CBUs) and (b) chains for zeolite frameworks.

Zeolite frameworks are denoted with three capital letter codes assigned by the structural committee of International Zeolite Association (IZA). The three-letter codes are mainly derived from original mineral names and for interrupted frameworks three-letter

code is preceded by a hyphen. Some of the naturally found zeolite minerals and their three-letter codes are given in Table 5.

Table 5. Some natural zeolites and date of discoveries.

Stilbite	STI	1756	Edingtonite	EDI	1825
Natrolite	NAT	1758	Faujasite	FAU	1842
Chabazite	CHA	1772	Mordenite	MOR	1864
Analcime	ANA	1784	Offretite	OFF	1890
Laumontite	LAU	1785	Erionite	ERI	1890
Thomsonite	THO	1801	Dachiardite	DAC	1905
Heulandite	HEU	1801	Stellerite	STI	1909
Gmelinite	GME	1807	Ferrierite	FER	1918
Gismondine	GIS	1816	Yugawaralite	YUG	1952
Brewsterite	BRE	1822	Bikitaite	BIK	1957
Epistilbite	EPI	1823	Paulingite	PAU	1960
Phillipsite	PHI	1824	Mazzite	MAZ	1972
Levynite	LEV	1825	Merlionite	MER	1974

The porous structure of zeolites comes from the n-rings (where n is the number of tetrahedrally coordinated atoms in a ring) formed by these building units which form pore channels and inner cavities. A zeolite framework structure can have a pore system with infinite channels in one, two or three dimensions, corresponding to pore dimensionalities of 1, 2 and 3 respectively. The diameters of the cavities and pores for zeolite structures usually vary from 3 Å to 12 Å which coincides with the scale of many hydrocarbon molecules and thus make these materials attractive for applications as adsorbents and catalysts. Also zeolites can be used to fabricate nanostructures. For example, in the synthesis of ZnO nanostructures, zeolites<sup>164</sup> are also used as well as other mesoporous structures like porous carbons<sup>165</sup>, porous silicon<sup>166</sup> as nanoscale templates. The fabrication of ZnO inside a porous structure is a way to achieve extremely small nanostructures, which should improve the properties related with quantum size effect due to the immense size reduction. Control of the pore size, also restricts the maximum particle size, giving the opportunity to tune the properties of

nanostructures. Thus, zeolite structures with regularly distributed small pore sizes become promising.

### 6.3. Nanoporous ZnO

Although zeolite term is defined for aluminosilicates, it also encompasses for other microporous structures containing different elements such as gallium, germanium, boron, titanium<sup>167</sup>. While zeolite structures can be used in fabricating extremely small ZnO nanostructures, zeolite polymorphs of ZnO can also be imagined, knowing that zeolitically inspired ZnO-based structures can be synthesized with various techniques<sup>168,169,170</sup>. A structural analogy with aluminosilicate zeolites and ZnO can be made by assigning both Zn and O atoms as tetrahedral framework atoms since in ZnO both Zn and O atoms are tetrahedrally coordinated (O atoms bridge two framework atoms in aluminosilicate zeolites). The primary building units of such an analogy is given in Figure 30.

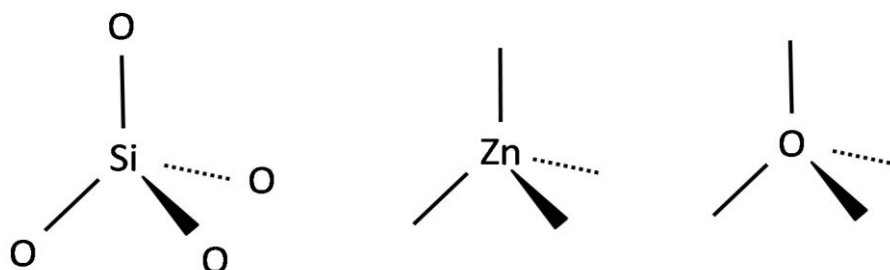


Figure 30. Primary building unit of Silicates (left) and the two analog primary buildings of ZnO (right).

Some zeolite frameworks, have been previously suggested as possible bulk polymorph structures for ZnO in theoretical calculations; (e.g. BCT<sup>171</sup> and SOD<sup>172</sup>). The BCT and SOD zeolite frameworks are shown in Figure 31.

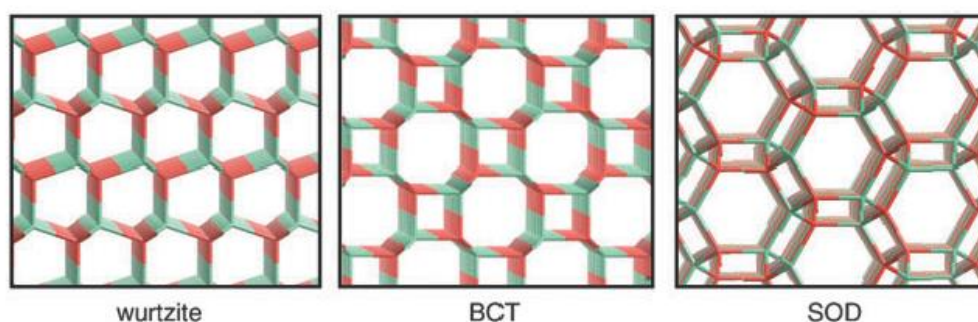


Figure 31. Structures of BCT and SOD zeolite frameworks.

The possibility of the BCT structure being a new ZnO polymorph follows theoretical results on similar materials such as ZnS and LiF. For ZnS nanocrystals, the BCT structure has been calculated to be more stable than the bulk phases<sup>173</sup>, and for bulk LiF, BCT structure is predicted as metastable<sup>174</sup>. Later for ZnO a wurtzite→BCT transition was observed for nanorods under uniaxial strain with molecular dynamics simulations<sup>175</sup>. For ZnO nanoclusters, the BCT structure has been also observed to form spontaneously in down-stroke pressure-driven transitions by molecular dynamics simulations<sup>176</sup>. Following these results, Morgan showed theoretically that for nanofilms of ZnO, the BCT structure is energetically more favorable than wurtzite structure up to 56 monolayers by density functional calculations<sup>171</sup>. With respect to the SOD framework, for (ZnO)<sub>12</sub> nanoclusters SOD cage structure has been found to be the ground state by means of density functional theory calculations and an extended SOD-ZnO phase was also suggested to be accessible via coalescence of nanocluster building blocks<sup>172</sup>. In a later theoretical study, the SOD structure has been found to be lower in energy than a previously suggested nested cage structures for (ZnO)<sub>60</sub> and the SOD motif was suggested as being very energetically competitive for larger (ZnO)<sub>n</sub> clusters due to smaller influence of surface reconstruction<sup>177</sup>. For bulk phases, the study of the energy versus volume equations of state for possible polymorphs revealed that SOD phase would be thermodynamically stable under suitable negative pressures<sup>178</sup>. It should be also noted that the energetical stabilities of SOD and BCT phases are closer to the ground state wurtzite structure than the experimentally obtained rocksalt phase as can be seen in Figure 32.

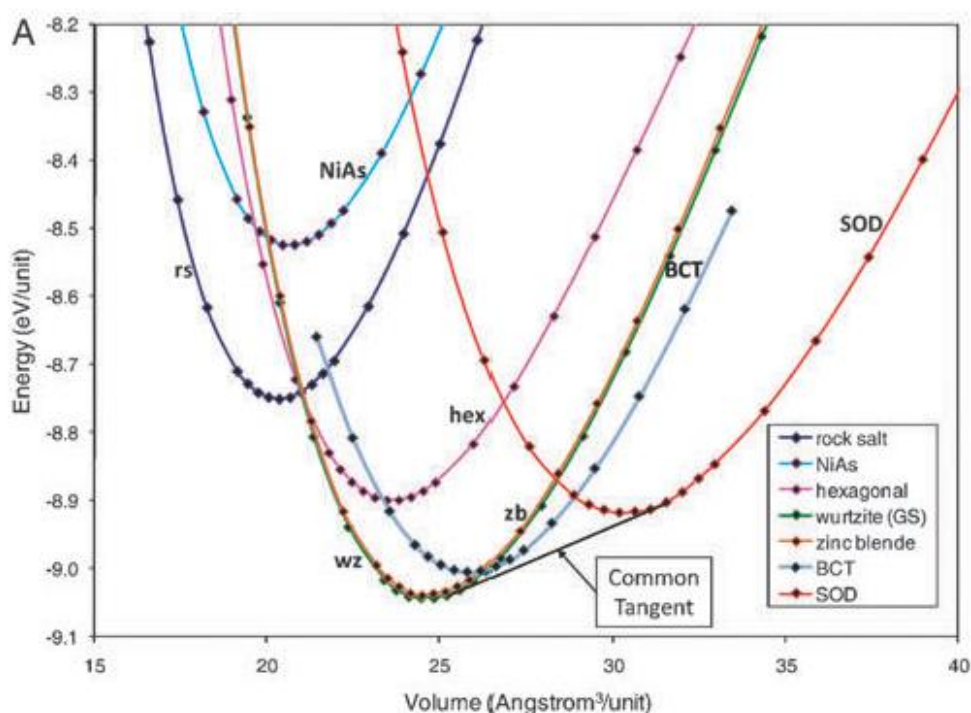


Figure 32. Energy versus volume plots for ZnO phases.<sup>178</sup>

As an alternative approach to the structural analogy in Figure 30, we can also follow an analogy with aluminosilicate zeolite structures. Starting from pure  $\text{SiO}_2$ , an aluminosilicate can be seen as a replacement of some fraction of  $\text{Si}^{+4}$  cations with cations having a similar ionic radius and a +3 charge (e.g.  $\text{Al}^{+3}$ ), and a larger cations (e.g.  $\text{K}^+$ ) to compensate the charge. The +3 cations incorporate into the 4-connected network and the charge-compensating larger cations reside in the void space, and determine the shape of framework together with the absorbed water. Such substitutions of silica are well-known to be energetically favorable from experimental calorimetry and theoretical calculations have showed that aluminosilicate zeolite frameworks are energetically the most likely products for large alkali metal cations ( $\text{K}^+$ ,  $\text{Rb}^+$ ,  $\text{Cs}^+$ )<sup>179</sup>. An analogy with ZnO can be made by substitution of a fraction of  $\text{Zn}^{+2}$  cations with similar sized cations such as  $\text{Li}^+$  and larger cations such as  $\text{K}^+$  to obtain a zeolitic framework. For ZnO such co-substitutions have reported in a small number of experimental studies<sup>180</sup>. For example  $|\text{K}|\text{[LiZn}_3\text{O}_4]$ , where 25% of  $\text{Zn}^{+2}$  cations were replaced by  $\text{K}^+$  and  $\text{Li}^+$  cations, was prepared experimentally and is found to have the ATN zeolite framework by means of single crystal X-ray techniques<sup>181</sup>. As can be seen in Figure 33 small  $\text{Li}^+$

cations incorporate into the 4-coordinated network as a  $Zn^{2+}$  cation while larger  $K^+$  cations open the structure and causes the porous ATN network. Theoretical results also supports that the co-substitution of  $Zn^{+2}$  cations in ZnO with  $Li^+/K^+$  or  $Li^+/Rb^+$  are energetically favored and that the thermodynamically stable dense polymorphic structure types found in the pure material are energetic destabilized, while open structures with large rings and cages are stabilized<sup>182</sup>.

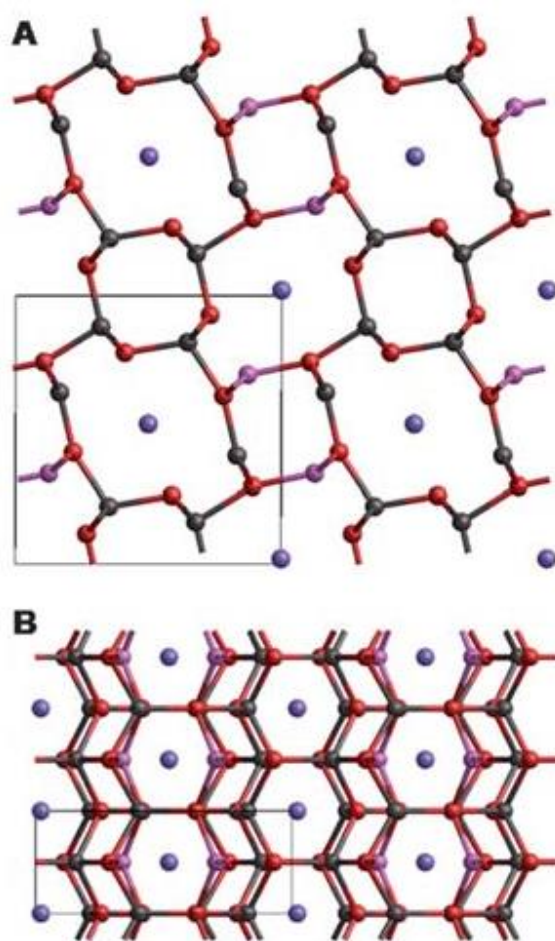


Figure 33. Top and side views of  $[K][LiZn_3O_4]$  structure in ATN zeolite framework.

## **CHAPTER 3. METHODOLOGY**

In order to understand the properties of the materials, their atomic configurations must be known. One of the simplest to describe but difficult to solve problem in computational chemistry is the determination of atomic configuration. Any computational approach to study a chemical system requires a mathematical model to calculate the energy of the system as a function of its configuration. The success of the approach will depend on the quality of the mathematical model used. For smaller chemical systems studied, quantum mechanical (QM) approaches are appropriate and feasible. Walter Kohn and John A. Pople jointly won the Nobel prize in chemistry in 1998 for the development of the density-functional theory and computational methods in quantum chemistry. However, QM methods are typically limited to system of approximately a few hundreds of atoms, although approaches to treat large systems are under development. Also some of the chemical or biological processes require higher time scales between microsecond to millisecond, while the individual time step of the methods commonly used today are of the order of femtosecond. Thus the energy function might be subjected to over  $10^8$  energy evaluations even in a single simulation. Large numbers of evaluations are also required for using global optimization techniques to search the configurational energy landscapes. Atomistic models can fulfil the demands required by computational studies of larger systems or larger evaluations. Atomistic models use force fields, in which atoms are the smallest particles in the system rather than the electrons and nuclei used in quantum mechanical descriptions. The mathematical equations in these energy functions include relatively simple terms to describe the physical interactions that dictate the structure and dynamical properties. These simplifications allow for the computational speed required to perform a large number of energy evaluations.

### **1. Energy Landscapes**

The investigation of the structural and dynamical behavior of complex chemical systems, such as large clusters, strongly correlates with the investigation of the

underlying potential energy surface (PES). The exact description is very complex, however, predictions can be made using knowledge of the stationary points of the PES. Stationary points of a PES are points with a vanishing gradient such as minima, maxima, or saddle points. Methods which investigate these points can be summarized as energy landscape methods. The concept of energy landscapes was first proposed by Bryngelson and Wolynes<sup>183</sup> in the context of free energy surfaces, and a detailed summary on energy landscapes is given in the textbook of David J. Wales.<sup>184</sup> The most important stationary points of a (potential) energy landscape are local minima and maxima, the global minimum and maximum, as well as transition states (first order saddle points). An illustration of a multi-dimensional PES is given in Figure 34

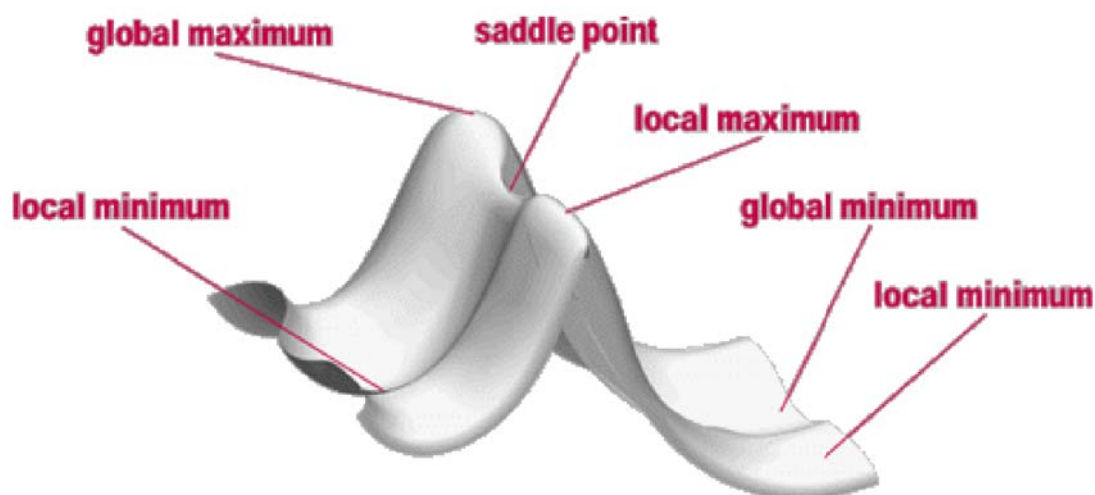


Figure 34. Illustration of a multi-dimensional potential energy surface with important stationary points.

The overall shape of the energy surface is determined by the energetic ordering of the local minima and their connectivity through transition states. One feature to describe the global topology of a PES is for instance the monotonic sequence introduced by Kunz and Berry.<sup>185186</sup> It is defined as a sequence of local minima connected by transition states for which the energy of the minima monotonically decreases. All monotonic sequences leading to the same local minimum therewith define a monotonic sequence basin or funnel (see Figure 35). Another common term is superbasin which emphasizes the analogy to a basin of attraction on the global scale of the PES. In contrast to the latter where every point of the configurational space with a non-vanishing gradient only belongs to one basin of attraction, a local minimum can belong to several monotonic

sequence basins. Systems with only one funnel converging to the global minimum are often referred to as single-funnel systems. A PES with such a topology is benign for global optimization as it can guide the system towards the global minimum. In contrast, multi-funnel systems contain multiple sequence basins. Once in a wrong funnel, the system then has to surmount several energy barriers to climb out of it and reach the global minimum, which makes global optimization in general more difficult.

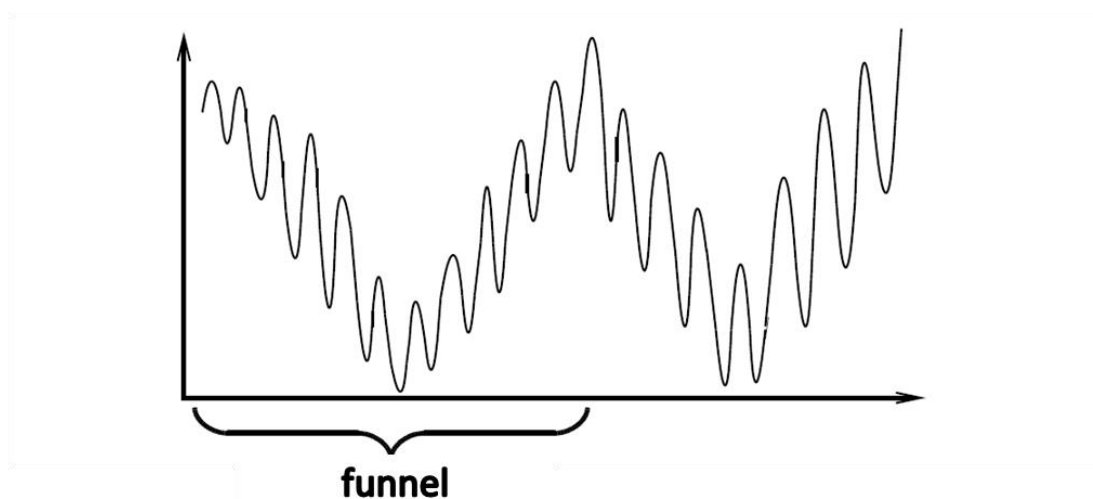


Figure 35. Schematic picture of a multi-funnel potential energy surface.

On the one hand, the behaviour of the energy landscape is defined by the system under investigation. On the other hand it depends on the underlying theoretical model for the energy calculations. More details on possible models are given in section 3.3. and 3.4. as Force Fields and Electronic Structure Methods. To identify the various points of the PES, different algorithms and approaches are required. Local extrema are located using local optimization algorithms, and the global extrema are investigated employing global optimization methods.

## **2. Exploring the Configurational Space**

Determining atomic configurations requires identifying the local minima of the PES, which is a high-dimensional function of the atomic coordinates. The main interest is the global minimum, which constitutes the most stable isomer at zero temperature. Energetically higher-lying and thus metastable isomers, however, might be observed in

experiment due to finite temperature or kinetic effects, thus additionally being of interest.

## 2.1. Local Optimization Methods

Energy minimisation, which is also called geometry optimisation, is simply used to find the local energy minimum of a system by iteratively adjusting the coordinates of the atoms in the system. Starting from a non-equilibrium configuration, energy minimisation employs the mathematical procedure of optimisation to move atoms so as to reduce the net forces (the gradients of potential energy) on the atoms until they become zero and the second derivatives are positive:

$$\frac{\partial U}{\partial r} = 0; \frac{\partial^2 U}{\partial r^2} > 0$$

where  $U$  is the internal energy of a system and  $r$  is the coordinate of the system (the Cartesian or internal coordinates). The term zero force is used since the first derivative of the internal energy with respect to distance is force. If the internal energy of a system with coordinates  $r$ , is  $U(r)$ , then the internal energy at a new set of coordinates  $r + dr$ , is:

$$U(r + dr) = U(r) + \frac{\partial U}{\partial r} dr + \frac{1}{2} \frac{\partial^2 U}{\partial r^2} dr^2 + \dots$$

The first derivative can be collectively written as the gradient vector  $g$  and the second derivative matrix is referred to as the Hessian matrix  $H$ .

Derivatives are useful in energy minimisation as they provide information about the shape of the PES and significantly enhance the efficiency in finding where a minimum is located. The direction of the gradient vector  $g$  indicates where the energy minimum lies and the magnitude indicates the steepness of the local slope. The second derivative indicates the curvature of the function, predicting where the function will change direction. The gradient-based algorithms are the most popular methods for energy minimisation, and they can be classified according to the highest-order derivative used. For example, first-order algorithms use the first derivative and second-order algorithms use both first and second derivatives.

### 2.1.1. Steepest Descent

The simplest approach to using gradient information within a local optimization is the Steepest Descent (SD) algorithm.<sup>187 188</sup> To find an energy minimum by first-order algorithms, the gradient vector  $g$  is used to determine the direction of movement and a line search is used to determine the magnitude of the step length. As the gradient vector  $g$  always points into the direction of the biggest function increase, the function value can be lowered by following the opposite direction. Once the steepest slope has been chosen, the energy can be searched along this direction by:

$$X_{n+1} = X_n - \lambda \cdot g$$

The step size  $\lambda$  is determined by a line minimization. The process continues until the gradient becomes flatter than a predefined cut-off value. A disadvantage of this method is that many small steps may be performed when proceeding down a long narrow valley. The SD method also often oscillates around the real minimum energy path because a subsequent step will be perpendicular to the previous step and the energy can be further lowered by following the gradient component along the previous search direction.

### 2.1.2. Conjugate Gradient

The Conjugate Gradient (CG) algorithm takes the gradient information of the current and the previous step to construct a search direction which is "conjugate" to the previous search direction. The search direction is given by:

$$d_i = -g_i + \beta_i d_{i-1}$$

For the determination of  $\beta$ , several possibilities are available such as the Fletcher-Reeves, the Polak-Ribiere or the Hestenes-Stiefel approaches.<sup>187</sup> For the first step,  $d_0 = -g_0$ . Each subsequent direction is a combination of the gradient at the current position and the previous search direction. The CG algorithm is more efficient than SD, where subsequent steps are made orthogonal to the previous search vectors. For a quadratic energy surface, this will converge to the minimum in a number of steps equal to the number of variables. However, in real world problems, the functions are not exactly quadratic and the algorithm takes more steps. The CG algorithm is very efficient at moderate to close distances from a minimum but has slow convergence when very close to an energy minimum.

### 2.1.3. Newton Raphson

The Newton Raphson (NR) method uses both the gradient and the second derivative ( $H$ ) of the potential energy surface.<sup>189</sup> In the NR method, the displacement vector  $\Delta r$  is given by:

$$\Delta r = -H^{-1}g$$

However, for a realistic potential energy surface, there is the possibility to reach other stationary points, such as transition state, when starting from a position not close to the minimum. Thus, the expression is modified to be:

$$\Delta r = -\lambda H^{-1}g$$

where  $\lambda$  is a scalar quantity determined by a line search along the search direction to find the one-dimensional minimum and the procedure becomes iterative like the CG method. The key step of the NR method is the inversion of the Hessian matrix  $H$ , which may vary slowly between consequent steps in large systems. It is therefore undesirable to invert the  $H$  at every step of the optimization. This is avoided by Quasi-Newton method, where Hessian matrix  $H$  does not need to be computed in every step and is updated by analyzing successive gradient vectors instead. One very widely used Quasi-Newton method is the BFGS method,<sup>190</sup> where the Hessian matrix  $H$  is initialized by performing an exact inversion of the second derivatives and is then subsequently updated for a number of cycles.

The most appropriate algorithm or combination of algorithms for a given problem depends on the size of the system, number of variables and the memory requirement. Most minimisation algorithms can go downhill or uphill on the PES and locate the minimum or maximum, respectively, that is near to the starting point, which is likely to be a local energy minimum, thus we require a means of generating different starting points to locate more than one local minimum. In this thesis, both Conjugate Gradient and Quasi-Newton algorithms are used during the energy minimisations.

## 2.2. Global Optimization Methods

The above described local optimization methods are deterministic schemes that approach the next local minimum from a starting point constructively, since the local

information obtained for a given configuration, like the energy and forces, uniquely guides the system to the next local minimum. In order to find all isomers and particularly the global minimum, a search algorithm is required that not only scans the local environment but samples the whole PES. Since local information is not enough to locate the global minimum of the system, stochastic methods are required that provide some recipe to systematically sample the huge configurational space. An ostensibly “simple” method that runs through all local minima quickly becomes unfeasible due to the computational cost associated with the huge number of possible structures. Due to the exponential growth of the number of local minima with system size global optimization is a difficult task and no known algorithm guarantees that one can locate the global minimum for anything but the most simple systems. One key feature of any search algorithm is the way new structures are generated, which can be called a trial move corresponding to a jump of the system in the configurational space. A simple trial move is to randomly displace the atomic positions. After such a jump, a criterion is required which decides whether this new structure is accepted and the search should continue from there, or if it should rather be discarded. Such an acceptance criterion is typically based upon the total energy since it is usually the quantity to optimize. As already stated in the Introduction chapter, several global optimization algorithms exist, such as simulated annealing or genetic algorithms. Here we discuss one other algorithm, the Monte Carlo Basin Hopping method, which we have used in this work.

### **2.2.1. Monte Carlo Basin-Hopping**

Basin Hopping algorithms<sup>191</sup> are one of the popular global optimization techniques based on the Monte Carlo method. With the basin-hopping scheme, Wales et al.<sup>192</sup> identified all known global minima of Lennard-Jones(LJ)-clusters containing up to 110 atoms and additionally new ones. The Monte Carlo algorithm is based on the idea of repeated random sampling in order to calculate results for a specific problem. Although it does not guarantee the correct result, statistically it should converge towards the right result. The basic idea of Basin hopping method is to generate a new structure and relax it at every step, where the existence of the relaxation is the main difference with respect to the pure Monte Carlo method. Each relaxation locates one of many local minima, of which the lowest energy one found correspond to a candidate for the global minimum. Like any other algorithm, the Basin Hopping algorithm does not guarantee to locate the

global minimum of the system since the number of possible configurations increases exponentially when the system size increases. However, The Basin Hopping effectively simplifies the PES so that the probability to find the global minimum increases. The energies of global and local minimum are unchanged, but the other points are transformed by:

$$\tilde{E}(X) = \min\{E(X)\}$$

where  $\tilde{E}$  is the transformed energy,  $X$  is the nuclear coordinates and the *min* indicates the local structural relaxation. The resulting steps are mapping any given configuration space to the nearest local minimum and thus the PES is converted into a set of interpenetrating staircases with steps corresponding basins of attraction (see Figure 36). The transformed done PES has no transition state regions, which accelerates the minimization by the (i) removal of the barriers to a lower energy minima and (ii) the increased possibility of the inter-basin hopping from and to any point on the PES.

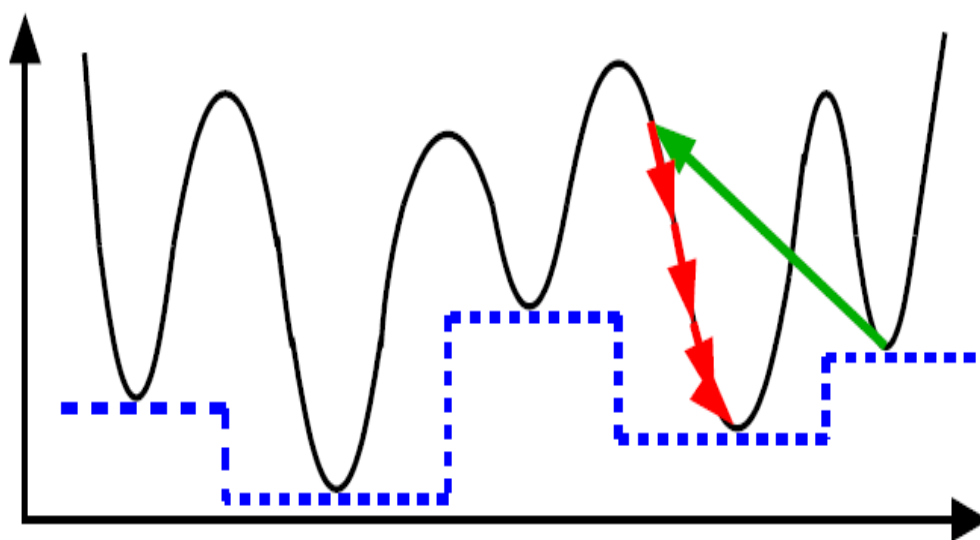


Figure 36. Schematic diagram of a one-dimensional PES, in which the original energy (solid line) is transformed onto the  $\tilde{E}$  (dashed line). The green arrow indicates a random move performed on a local minimum, which is followed by a local structural minimization (red arrows).

The simple Metropolis Monte Carlo<sup>193</sup> walk is the general method used for the random moves on the simplified PES with only the temperature as a variable. According to this method, a random move has applied to the system in each step, and accepted if a random number  $N$  is less than the metropolis criterion

$$N \leq e^{-\frac{\Delta E}{k_b T}}$$

where  $\Delta E$  is the energy difference between the structures,  $k_b$  is the Boltzmann constant, and  $T$  is the fictitious temperature variable that decides how high in energy structures will be accepted. Thus the probability of acceptance of a higher energy structure can be controlled with the  $T$  parameter, and a lower energy structure will be always accepted. A random move followed by a relaxation is called a step in Basin hopping and in order to search the global minima structures, these steps are repeated. Figure 37 shows a schematic diagram of a Basin Hopping run. To increase the probability to find the global minimum, multiple runs starting from different initial structures are often used.

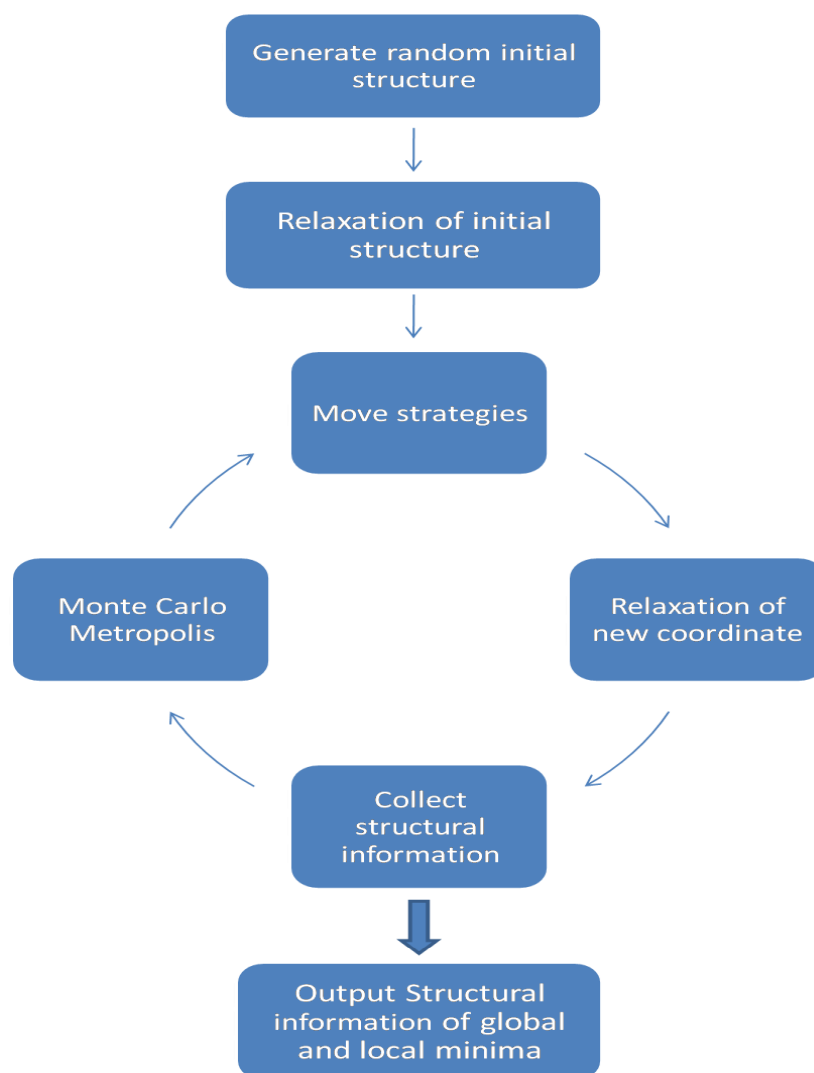


Figure 37. A schematic diagram of a Basin Hopping run.

### **3. Force Fields**

Over the last few decades atomistic simulation, in which we are only concerned with atoms, rather than electrons and sub-atomic particles, has developed significantly with the widespread use of computers. Correspondingly the field has evolved from one that was initially concerned with reproducing experimental numbers, to one where predictions are being made, and insight is being offered.

For ionic materials, these simulation methods are based on the use of Born Model employing force fields to describe the interaction between atoms. Such simulations are relatively less time consuming than calculations using quantum mechanical methods and allow modelling of large scale systems containing  $10^4 \sim 10^6$  atoms. As a result, they have been widely applied to identify the geometrical structures and properties for ionic materials.

The starting point for the majority simulation techniques is the calculation of the energy. In most formulations of the Born Model, the interaction energy of an N-body system can be written as an expansion of the coordinates ( $r_1, r_2, \dots, r_n$ ) in the following way:

$$\phi_{tot} = \sum_{i=1}^N \sum_{j>i}^N \phi_2(r_i, r_j) + \sum_{i=1}^N \sum_{j>i}^N \sum_{k>j}^N \phi_3(r_i, r_j, r_k) + \dots$$

For broad range of systems and applications there does not exist a universal set of analytical functions that manage to approximate  $\phi_{tot}$  well. Therefore the functional form of the force-field has to be chosen with care since it often has implications for the results. Consequently, even for one and the same class of systems more forms are in use in the literature. A few examples of popular potentials in use for the non-electrostatic part of pair interaction energies are the Lennard-Jones potential, the Buckingham potential, and the Morse potential.

In the simplest force-field models the total interaction ( $\phi_{tot}$ ) is approximated by neglecting higher order interactions ( $\phi_3 + \dots$ ), i.e. only the interactions between all pairs of atoms in the system are considered. For example, for a binary system consisting of Zn and O atoms described by a 2-body potential the total interaction would consist of a sum of Zn-Zn, Zn-O, and O-O types of interactions. These two-body terms can be

further decomposed into the long range electrostatic or Coulombic interactions, where the energy is calculated using the Ewald summation, and short range dispersive forces, i.e. non-Coulombic terms including overlap repulsion and van der Waals attraction between electron charge clouds.

### 3.1. Coulomb interaction

When considering ionic materials, the Coulomb interaction is by far the dominant term and can represent, typically, up to 90% of the total energy. It is given by Coulomb's law as:

$$U_{ij}^{coulomb} = \sum_{i < j} \frac{q_i q_j}{4\pi\epsilon_0 r_{ij}}$$

Where the  $q_i$  and  $q_j$  are the charges on atoms  $i$  and  $j$  respectively,  $r_{ij}$  is the distance between atoms  $i$  and  $j$ , and  $\epsilon_0$  is the permittivity of the free space. Despite having the simplest form, Coulomb interaction is in fact the most complicated potential to evaluate for periodic systems. For a finite system of charges, this expression can be evaluated directly, however for a periodic (infinite) system, the expression does not converge and numerical tricks must be applied to evaluate the energy because it has an infinite amount of charge and the energy of interaction is undefined. To overcome this problem Ewald summation method<sup>194</sup> is applied. In the method of Ewald summation, a Gaussian function is added to each point charge. The mean value of this Gaussian function is the value of the original point charge but with the opposite sign. The new system now can be evaluated in real space, which converges quickly since the overall amount of charge in the system are reduced by the addition of the Gaussian functions. To calculate the true energy a second set of the Gaussian functions of the opposite sign of the first ones are added, which cancels out the first set of Gaussian functions. The second set converges slowly in real space, however since they are Gaussian functions, they are evaluated easily in reciprocal space. Effectively, the Ewald method splits the conditionally convergent series into two convergent series, one in real space and the other in reciprocal space, each of which converges rapidly.

### 3.2. Electronic Polarizability

The Born model discussed above is formulated treating ions as point charges. However, for oxides, ions and defects will polarize other ions in the lattice. Polarizability relates to the tendency of the electron cloud of an atom to be distorted from its original shape by the presence of an electric field. One simple way to include the electronic polarizability of the atoms is to use the core-shell model<sup>195</sup>, which represents the polarisable ion as a massless shell connected to a core containing all the mass, where the total charge of the ion is the sum of the charges of both core and shell. The position of the core represents the location of the ion in the lattice and the position of the shell shows the electronic polarizability. The core and shell interact with each other by a harmonic spring where the equilibrium distance between them is set to 0, as shown in Figure 38, and the spring constant ( $K$ ) and the charge of the shell ( $Y$ ) determine the polarizability of the ion as:

$$\alpha_p = \frac{Y^2}{4\pi\epsilon_0 K}$$

Both  $K$  and  $Y$  can be obtained by fitting empirically to reproduce experimental properties. In shell model, the short range forces are assumed to act between the shells while the long range electrostatic forces act between all shells and cores, except between them for the same atom.

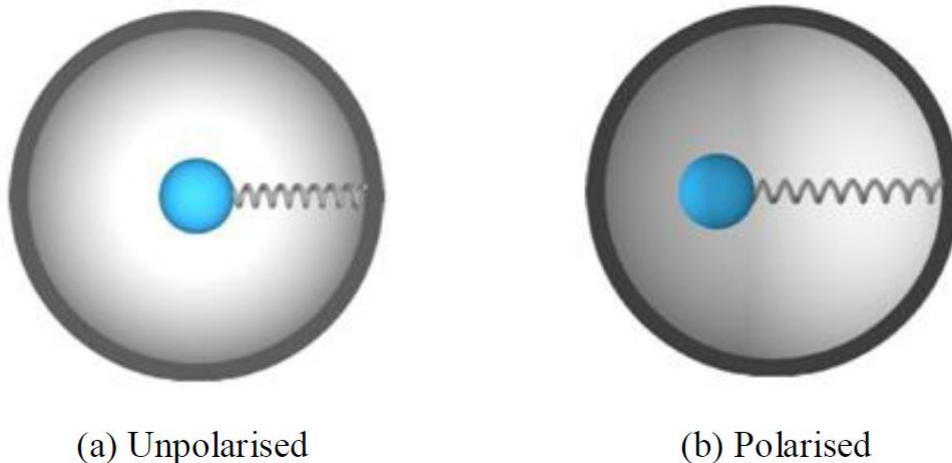


Figure 38. Schematic representation of the core-shell model. Blue sphere represents the core while the grey circle represents for the shell.

### 3.3. Interatomic Potential functions

The non-electrostatic short range interactions are usually expressed as:

$$U^{short-range}(r_1, \dots, r_N) = \sum_{A,B} U_{AB}(r_A, r_B) + \sum_{A,B,C} U_{ABC}(r_A, r_B, r_C) + \dots$$

where  $U_{AB}$  refers to the two-body interactions,  $U_{ABC}$  three-body interactions, and so on. This expression combines a number of interactions, containing covalent interaction, electronic polarizability, and non bonded interactions such as repulsion and van der Waals attraction. The two-body potential functions act between neighbouring charge clouds and gives the most contribution to the short-range interaction. Figure 39 displays a typical two-body short range interaction curve with interatomic distance. The short range potentials are usually handled by analytical functions which have both an attractive and a repulsive term. The repulsive term describes the Pauli repulsion due to the overlap of the closed shell electron configurations, while the attractive term arises at close interatomic separations due to an induced-dipole interaction and covalent effects. There exist a very wide range of different potential forms, in which the famous Lennard-Jones, Buckingham and Morse potentials are just a few examples. The choice of which potentials to be used depends on a number of factors, including the atomic species in the system, the computational capacity and the nature of the energy landscape.

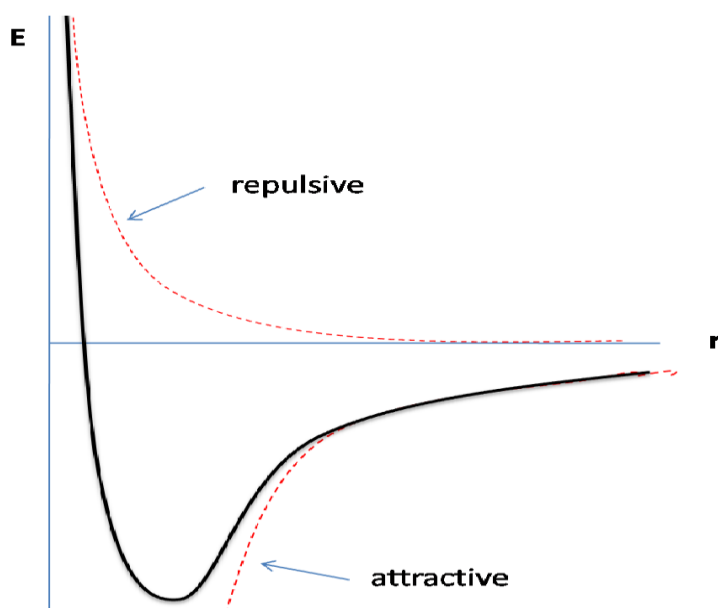


Figure 39. The non-Coulombic interaction including the attractive and repulsive components of ion separation.

### 3.3.1. Buckingham Potential

For ionic solids, the Buckingham potential<sup>196</sup> is one of the most widely used functional forms for the short range two-body potential.<sup>197</sup> It can be written as:

$$U_{ij}^{Buck} = A_{ij} \exp\left(-\frac{r_{ij}}{\rho_{ij}}\right) - \frac{C_{ij}}{r_{ij}^6}$$

Where  $A_{ij}$ ,  $\rho_{ij}$  and  $C_{ij}$  are constants and  $r_{ij}$  is the interatomic distance between the ions  $i$  and  $j$ .  $A_{ij}$  and  $\rho_{ij}$  are related to the number of electrons and the electron density respectively. The first term stand for the Pauli repulsion interaction and the second term stand for the van der Waals interactions.

### 3.3.1. Lennard-Jones Potential

The Lennard-Jones potential<sup>198</sup> is another very common potential with its simple form:

$$U_{ij}^{LJ} = \frac{A}{r_{ij}^{12}} - \frac{B}{r_{ij}^6}$$

with  $A = 4\varepsilon\sigma^{12}$  and  $B = 4\varepsilon\sigma^6$ , where  $\varepsilon$  is the depth of the potential well and  $\sigma$  is the finite distance where the inter-particle potential is 0. The repulsive first term is dependent on  $r^{-12}$  and thus acts at close range, while the attractive second term becomes dominant at longer range. Although there exist more accurate potentials, the Lennard-Jones potential is used extensively in computational simulations due to its computational simplicity.

## 4. Electronic Structure Calculations

### 4.1. Many-Body Schrodinger Equation

A theory for a stationary system of nuclei and interacting electrons is intrinsically quantum-mechanical, and is based on solving the time-independent Schrodinger equation of the form:

$$H\Psi(R; r) = E\Psi(R; r)$$

where  $H$  is the Hamiltonian of the system, containing the kinetic and potential energy operators;  $E$  is the energy of the system;  $\Psi$  is the wavefunction of the system;  $[R]$  are the positions of the nuclei, and  $[r]$  are the variables that describe the coordinates of the

electrons. The potential energy term arising from the repulsion from two electrons at  $r_i$ ,  $r_j$  is:

$$\frac{e^2}{|r_i - r_j|}$$

where  $e$  is the electronic charge. The potential term arising from the attraction of an electron at  $r$  and a nucleus at  $R$  can be written as:

$$\frac{Ze^2}{|R - r|}$$

where  $Z$  is the charge of the nucleus. The potential energy term for the repulsion of two nuclei can be written similarly:

$$\frac{Z_i Z_j e^2}{|R_i - R_j|}$$

For the kinetic energy of an electron the energy term will be:

$$\frac{\hbar^2}{2m_e} \nabla_r^2$$

Practically, it can be assumed that the nuclei move slower than the electrons, so that  $\varphi$  has only dependence on the electronic degrees of freedom. This is called the Born-Oppenheimer approximation.<sup>199</sup> Its validity comes from the huge mass difference between nuclei and electrons, making the former behave like classical particles. So the term for the kinetic energy of the nuclei can be omitted and taken into account as a classical contribution. In this case the Hamiltonian of the system becomes in atomic units:

$$H = - \sum_i -\frac{1}{2} \nabla_{r_i}^2 - \sum_{iI} \frac{Z_I}{|R_I - r_i|} + \frac{1}{2} \sum_{i \neq j} \frac{1}{|r_i - r_j|} + \frac{1}{2} \sum_{I \neq J} \frac{Z_I Z_J}{|R_I - R_J|}$$

The last term in the previous equation is a constant and the electronic Hamiltonian can be written as:

$$H_e = - \sum_i -\frac{1}{2} \nabla_{r_i}^2 - \sum_{iI} \frac{Z_I}{|R_I - r_i|} + \frac{1}{2} \sum_{i \neq j} \frac{1}{|r_i - r_j|}$$

Even with the proposed Born-Oppenheimer approximation, solving for  $\Psi(r)$  remains a difficult task, due to the many body nature of interactions. Each electron is affected by the motion of other electrons in the system, which is called correlation. Furthermore,

two electrons of the same spin can change their positions, in which case  $\Psi$  must change sign.

## 4.2. Density Functional Theory

The many-body Schrodinger equation is practically impossible to solve for many electron systems. Therefore one should apply approximate methods to solve the problem. Density Functional Theory (DFT) provides a general framework to deal with the ground-state energy of the electrons in many atom/electron systems. DFT is based upon two theorems, proved by Hohenberg and Kohn,<sup>200</sup> and a computational scheme proposed by Kohn and Sham.<sup>201</sup> The first theorem states that the electronic structure of the ground state of a system is uniquely determined by the ground state electronic density,  $\rho_0(r)$ . The second theorem states a variational criterion for the determination of  $\rho_0(r)$  and  $E_0$  starting from an arbitrary function  $\rho(r)$  constrained by the normalization condition:

$$\int dr \rho(r) = N$$

$$E[\rho] \geq E[\rho_0]$$

$$E[\rho_0] = E_0$$

where  $N$  is the total number of the electrons of the system.  $E_0$  can the functional therefore be found by minimizing with the method of Lagrange multipliers the functional  $E[\rho]$  with respect to arbitrary infinitesimal changes in the form of the function  $\rho(r)$ . Kohn and Sham<sup>201</sup> that the ground-state density of the original interacting system is equal to that of some chosen non-interacting system. This leads to independent-particle equations for the non-interacting system that can be soluble, if all the difficult many-body terms are incorporated into an exchange-correlation functional of the density. For such a system the kinetic energy is defined as:

$$T_S = -\frac{1}{2} \sum_i \nabla_i^2$$

This kinetic energy term forms part of the Hamiltonian operator that does not contain electron-electron interactions:

$$H_S = -\frac{1}{2} \sum_i \nabla_i^2 + \sum_i V_S(r_i)$$

where  $V_S(r)$  is an effective local potential. So the ground-state wavefunction associated with this Hamiltonian can be represented by a Slater determinant of the form:

$$\Psi_S = \frac{1}{\sqrt{N!}} \begin{vmatrix} \varphi_1(x_1) & \varphi_1(x_2) & \dots & \varphi_1(x_N) \\ \varphi_2(x_1) & \varphi_2(x_2) & \dots & \varphi_2(x_N) \\ \vdots & \vdots & \ddots & \vdots \\ \varphi_N(x_1) & \varphi_N(x_2) & \dots & \varphi_N(x_N) \end{vmatrix}$$

where the orbitals  $\varphi_i$  are termed Kohn-Sham orbitals. In this case the non-interacting kinetic energy is not equal to the interacting system's. Kohn and Sham accounted for that difference by defining the functional:

$$F[\rho(r)] = T_S[\rho(r)] + J[\rho(r)] + E_{XC}[\rho(r)]$$

where  $J[\rho(r)]$  stems for the classical Coulomb integral of the electron-electron term and  $E_{XC}[\rho(r)]$  is the exchange-correlation energy defined as:

$$E_{XC}[\rho] = (T[\rho] - T_S[\rho] + (E_{ee}[\rho] - J[\rho])) = T_C[\rho] + E_{ncl}[\rho]$$

The remaining part of the true kinetic energy,  $T_C$  is added to the non-classical electrostatic contributions,  $E_{ncl}$ . So everything that is unknown is contained in the exchange-correlation energy, which are the non-classical effects of self-interaction correction, exchange, correlation and a portion of the true kinetic energy. Thus, the total energy of the system can be expressed as:

$$E[\rho] = T_S[\rho] + J[\rho] + E_{XC}[\rho] + E_{Ne}[\rho]$$

In this expression, the only term for which no explicit form can be given is  $E_{XC}$ . If it were known, the exact ground-state energy could be found by solving the Kohn-Sham equations for independent particles. For an approximate form of  $E_{XC}$ , the Kohn-Sham method provides a practical approach to calculating ground-state properties.

### 4.3. Exchange-Correlation Functional

The important quantity in the Kohn-Sham method is the exchange-correlation energy, which is expressed as a functional of the density,  $E_{XC}[\rho]$ . In order for a DFT calculation to provide reasonable results an accurate approximation to exchange-correlation functional is necessary. The first approximation to be suggested was the Local Density Approximation (LDA).<sup>201</sup> The idea is to have an approximate the exchange-correlation of the system by using the properties of homogeneous electron gas:

$$E_{XC}^{LDA}[\rho] = \int dr \epsilon_{XC}(r, \rho(r))$$

where  $\epsilon_{XC}[\rho]$  is the exchange-correlation energy per particle of a uniform electron gas with the same density of the system.

Although LDA works surprisingly better than predicted since it is a crude approximation, it is insufficient for the systems having inhomogenous density. In this sense the next approximation was made by the extension of exchange correlation energy in terms of the density.<sup>202</sup> In this approach only the density and its first derivative is included and called Generalized Gradient Approximation (GGA):

$$E_{XC}^{GGA}[\rho] = \int dr f(\rho(r), \nabla\rho(r))$$

For choosing function  $f(\rho(r), \nabla\rho(r))$  there is no unique way so that there exists many of different GGA potentials. In general the GGA results are better than the LDA results, but it is not always the case. Thus it is necessary to compare the results to have a more accurate result. In this study, two of the widely used GGA potentials, PW91<sup>203</sup> and PBE<sup>204</sup> was used in addition to some LDA calculations.

#### 4.4. Plane Waves

Solving the Kohn-Sham equations in real space is a difficult job. Instead some different basis sets are used to expand Kohn-Sham orbitals, such as pseudoatomic orbitals, plane waves etc. Plane waves are a good choice for basis sets in periodic systems, due their convenient representaion and manipulation in reciprocal space with Fourier transformations. For periodic systems the reciprocal unit cell is called Brilliouin zone and the infinitely many vectors spanning this space are called k-vectors. Since observables should be calculated by integrating over the Brilliouin zone one should take as many k-vectors as necessary in a numeric calculation to get accurate results, which is called k-point sampling. According to Bloch' Theorem,<sup>205</sup> the wavefunction in a periodic system can be described by the product of a cell-periodic function,  $u(r, k)$ , and a plane wave:

$$\phi(r) = u(r, k)e^{ik \cdot r}$$

As any periodic function can be expanded in terms of plane waves,  $u(r, k)$  can be written as:

$$u(r, k) = \frac{1}{\sqrt{\Omega}} \sum_G c_i(k, G) e^{iG \cdot r}$$

where  $\Omega$  is the volume of the unit cell and  $c_i(k, G)$  are the expansion coefficients. So the wavefunction will become:

$$\phi(r) = \phi_i(r, k) = \frac{1}{\sqrt{\Omega}} \sum_G c_i(k, G) e^{i(k+G)\cdot r}$$

By this way the Kohn-Sham equations are transformed from a set of differential equations into a set of algebraic equations. The expansion requires infinitely many  $G$  vectors which is impossible to calculate. However this expansion can be truncated at some point, where for large  $G$  values, plane waves become negligible. This cut-off is called kinetic energy cut-off and denoted by  $E_{\text{cut}}$ .

#### 4.5. Projector Augmented Wave Method

Finite plane wave expansions are insufficient in describing the strong oscillations of the wave functions near the nucleus and needs huge number of plane waves for convergence and accuracy. Therefore some approximations are used. One of them is the pseudopotential method, which considers only the valence electrons and holds the core electrons to behave as in a free atom. In the pseudopotential approach, the Pauli repulsion of the core electrons is described by an effective potential that expels the valence electrons from the core region, causing the wave functions to be smooth. However, all the information about the charge density and wavefunctions near the nucleus is lost.<sup>206</sup> Another type of approximation is the augmented wave method. In this method basis functions are composed out of atom-like partial waves in the atomic regions and the bonding is appropriated by a set of functions. The space is divided by atom-centered spheres and an interstitial region for the bonds. The projector augmented wave (PAW) method is an extension of augmented wave methods and the pseudopotential approach, combining them into a unified electronic structure method. In PAW method, space is considered as two but linked regions; interstitial and augmented regions. There is a transformation operator defined to transform highly oscillating all-electron wavefunctions to numerically convenient pseudowavefunctions. The transformation operator is chosen in such a way that it only acts on the augmentation region. In the augmentation region, the wavefunction can be expanded in terms of the solutions for the isolated atom. These solutions are called all-electron partial waves. In the interstitial region the solutions can be found by simply pseudopotential methods. At

the end an all-electron wave function can be defined by combining these solutions by defined translation operator and projector operators.

#### **4.6. Self Consistent Cycle**

DFT calculations work within Kohn-Sham equations in a self-consistent manner. The calculations start with an initial guess for the charge density. By this density Kohn-Sham Hamiltonian is constructed and solved for Kohn-Sham eigenvalues and orbitals. By solved Kohn-Sham orbitals new charge density is constructed and compared with starting density. If they are not consistent the procedure repeats itself until the self consistency is achieved. This can be called electronic cycle and the tolerance for the convergence is given as a parameter in the calculations. For faster convergence in an electronic cycle, instead of using directly output density as an input in following step, some mixing schemes are used. For our calculations we used Broyden mixing scheme,<sup>207</sup> which mixes the output density with previous input density to get the subsequent input density. After the convergence for electronic cycles, quantum-mechanical forces can be calculated on the atoms by Hellmann-Feynman Theorem.<sup>208</sup> To get the equilibrium positions for the atoms in the system, atoms are moved along these forces (following one of the local optimisation methods detailed above) and then convergence of the electronic cycles is repeated to obtain new forces. This process is repeated until the forces drop below a threshold, at which point the optimization of the geometry is complete.

## **CHAPTER III Comparison of structures and stabilities of free space and surface-supported ZnO nanoclusters**

### **1. Introduction**

Nanostructured materials are highly topical due to unusual properties, which are tuneable to fit a wide range of different criteria required by different applications. Semiconducting clusters and nanoparticles are one of the simplest well known examples of such materials. With the development of nanoscience, device performance and efficiency can greatly benefit from utilising materials with nanoscale dimensions. Nanomaterials, by definition are nanosize and have an increase in surface area to volume ratio, show improved and/or novel properties due to quantum size and surface effects, which are attributed to the immense reduction in size. Furthermore, inevitably, clusters will agglomerate or settle on a surface. As the binding interaction between a cluster and a supporting system in equilibrium is typically quite strong (of the order 1 eV), a significant effect of the support should be included into a consideration of the cluster structure and properties. In this paper, we focus on one example of such an interaction, zinc oxide clusters of sub-nano size (i.e. <1-2 nm in diameter) supported on surfaces of a noble metal, silver.

Zinc oxide (ZnO) is an important and a heavily researched compound; a semiconducting oxide already widely used and with promising new device applications in areas such as gas sensors, optoelectronic devices, and photocatalysis due to its remarkable optical and electronic properties. In the extreme case, nanoclusters consist of only a few ZnO units. Experimentally, a large variety of low-dimensional structures of ZnO have been synthesized as ultrathin films, nanowires, nanotubes, nanocages, nanoparticles, *etc.* The atomic configurations of the smaller nanostructures, however, are not clear from experiment, especially for very small sizes, a few nanometers across, due to the limitations of the experimental techniques. Therefore, theoretical studies are expected to close the gap by searching configurational energy landscape and supplying reliable data based on electronic structure calculations. Although free space  $(\text{ZnO})_n$  nanoclusters

have been modelled,<sup>209,210,211,212,213</sup> for device applications it is important to understand how the properties of the nanoclusters change with the effect of a support.

This work follows our earlier investigation of an ultrathin ZnO film stabilisation on the metal surfaces,<sup>214</sup> where we have found that the degree of ZnO/Ag(111) commensurability controls the sheet-to-substrate adhesion energies. Silver surfaces have extensively been studied both experimentally and computationally.<sup>215, 216</sup> Silver crystallises exhibiting three important surfaces of differing morphology: (111), the most stable in the form of a triangular lattice (see Figure 40a), (100), having four-fold surface symmetry (Figure 40b), and (110), exhibiting a linear pattern of corrugation (Figure 40c). In general the possible adsorption locations on these surfaces are the symmetry unique sites: on-top, above a single metal atom, bridge site, between two metal atoms, and hollow site, where higher coordination is possible.

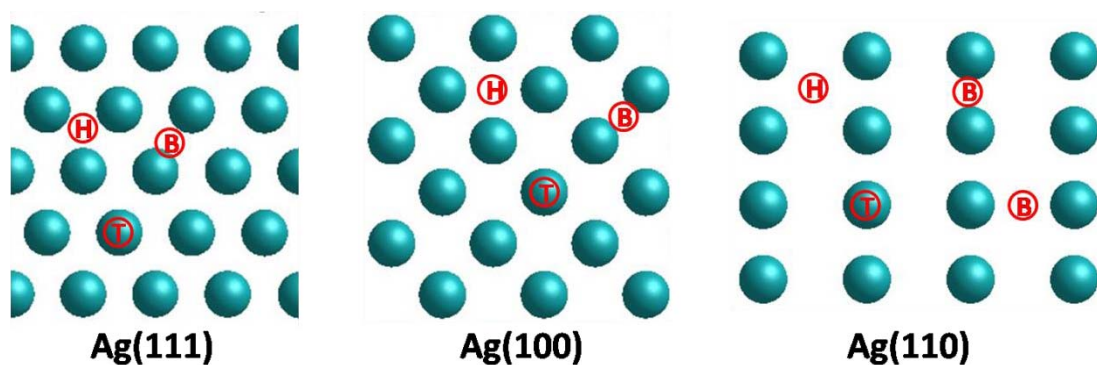


Figure 40. Top view of Ag(111), Ag(100) and Ag(110) surfaces. The symmetry unique sites hollow (H), bridge (B) and on-top (T) sites are indicated with letters.

Investigating how small nanoclusters adsorb on surfaces can provide valuable insight into the very initial stages of thin film growth. In contrast to abundant literature on straightforward oxidation processes at metal surfaces,<sup>217, 218</sup> there are only few theoretical studies of the very initial stages of growing a metal oxide on a surface of an alternative metal. This sparsity of reports, perhaps, arises from an additional complexity of the atom, monomer or cluster deposition, which would result in many possible adsorption geometries. Although the previous studies mainly focused on the opposite process, which is a metal nanocluster adsorption on an oxide surface,<sup>219,220,221,222</sup> there

are some examples where ZnO monomers were investigated on Ag(111)<sup>223</sup>, MgO(001)<sup>224</sup> and graphite<sup>225</sup> surfaces.

Like small sized nanoclusters, for 2D nanofilms and 1D nanowires there have been also theoretical arguments that wurtzite may not be the most stable phase when the crystal size goes down to nanometers. Firstly, Freeman et al.<sup>226</sup> found for free-standing thin films of ZnO that the layered phase is more stable than the wurtzite phase up to 36 layer thickness. Similarly Zhang et al.<sup>227</sup> showed that infinitely long ZnO nanowires can be transformed to a layered structure below a critical diameter and Kulkarni et al.<sup>228</sup> proposed that a uniaxial strain can also lead to a transformation from WZ to a layered phase. For thin films, layered phase were experimentally confirmed up to a few monolayers on Ag(111)<sup>229</sup> and Pd(111)<sup>230</sup> surfaces. To understand the effect of the surface, Bristowe et al. studied Ag/ZnO interfaces<sup>231</sup> and the initial growth of ZnO on Ag(111) surface<sup>223</sup> up to three units of ZnO by means of density functional theory. In their study they have found that ZnO dimers and trimers form linear chains of alternating Zn and O atoms parallel to the surface.

In this study, we have systematically searched for the global minimum structures of  $(\text{ZnO})_n$  nanoclusters on Ag(111) surface for the sizes  $n = 1-16, 20$  and  $24$ , first by Monte Carlo Basin Hopping method using interatomic potentials and then refined our results with the density functional theory calculations for the best candidate structures. In the next section we briefly explain the methods we used throughout this study. In the third section we start with a summary of what has been known for free space clusters, and after that we concentrate on the adhesion to Ag(111) surface modelled with interatomic potentials, followed by a comparison with adhesion to Ag surfaces of different morphologies. The last section focuses on the results refined by the *ab initio* DFT method.

## **2. Methodology**

Throughout this study we have modelled the ZnO nanocluster adhesion to the Ag surfaces with two complementary approaches to the definition of their energy, used in

exploration of their energy landscapes: the method of interatomic potentials (IPs) and density functional theory (DFT). Due to the high computational cost of the *ab-initio* DFT method, IPs have been employed as the energy definition during the search of the configurational energy landscape. Then a selection of the best candidate structures was refined by using DFT.

**Models** In both approaches, periodic boundary conditions have been imposed to model the Ag-supported ZnO nanoclusters. A more appropriate free space (or gas phase) IPs model was applied to bare ZnO nanoclusters, but periodic boundary conditions have still been necessary for the plane-wave DFT refinements because of the method limitations. To eliminate the interactions between the nanocluster and its periodic images in DFT calculations, large enough supercells were constructed in this case.

Silver surface models were built following bulk optimization with DFT. The lattice constant of the Ag bulk unit cell was found to be 4.15 Å, which is very close to a previous theoretical result<sup>232</sup> of 4.17 Å, and slightly higher than the experimental value<sup>233</sup> of 4.09 Å. Ag(111), Ag(100) and Ag(110) surfaces were cut from bulk as four-layer slabs; the three top layers have been relaxed while the bottom layer of silver slab was kept fixed. Similarly to bare clusters, large surface supercells of Ag support were chosen to keep clusters  $\geq 1$  nm apart, in particular,  $(8 \times 4\sqrt{3})$  for the cluster sizes  $n < 14$ , and  $(10 \times 6\sqrt{3})$  for larger sizes. During the search of the configurational energy landscape, which demands a large number of calculations to be performed for random positions of Zn and O atoms on the surface, a two-layer Ag slab was used and the Ag atoms kept fixed at their ZnO-free surface positions calculated from a four-layer slab calculation for simplicity. However, a three-layer Ag slab was used in the DFT calculations for nanoclusters on surface with only the bottom layer kept fixed.

**Global Optimisation Approach** In our study of the energy landscape of ZnO at nanoscale, we employ the Monte Carlo Basin Hopping (MCBH) method,<sup>234</sup> which is one of the most successful strategies of global optimisation that has previously been usefully applied to predict the structure of Lennard-Jones clusters containing up to 110 atoms.<sup>235</sup> A recent implementation of this approach in the Knowledge-Led Master

Controller (KLMC)<sup>236</sup> code utilizes local minimization routines of the General Utility Lattice Program (GULP),<sup>237</sup> which allowed us to use different methods, or analytical forms of interatomic potentials suitable for metals on one hand and for ionic semiconductors on the other. We have performed a search over energy landscapes of (ZnO)<sub>n</sub> nanoclusters for a range of sizes between  $n = 1$  and 16, and a larger sized clusters with  $n = 24$ . To find the global minimum (GM) and the low energy local minimum (LM) structures a two-stage procedure was used. First, the global optimization was applied separately to free-space and Ag-supported ZnO nanoclusters. As a second stage, an additional randomized scan is employed, in which multiple quenches are performed on the candidate cluster structures (found by the free space global optimization) placed initially at random positions and in random orientations above the Ag support, to find the best location for these structures on the surface. Next, randomized scan results were compared with the global optimization results for Ag-supported ZnO nanoclusters, to examine the effect of the support in the global optimization stage.

**Energy Definition** Classical interatomic potentials were used for the energy definition during the global optimization stage. The interatomic potential set included ZnO interatomic potentials employed by Whitmore *et al.*<sup>238</sup> to study ZnO surface structures and custom-parameterized interatomic potentials for the Ag–Zn and Ag–O interactions<sup>239</sup>. In the latter case, we fitted parameters of Buckingham interatomic potentials for Ag–O and Ag–Zn to reproduce the geometries and energies from a series of periodic DFT calculations on a (ZnO)<sub>6</sub> cluster interacting with a four-layer thick Ag(111) slab. In particular, the previously known drum structure of (ZnO)<sub>6</sub> was chosen and placed on the Ag(111) surface, and the best adsorption site was found to be on-top position (see Figure 41). Next, the adsorption energies were calculated by moving the cluster inward and outward of the surface by 0.1 Å displacements as shown in Figure 41. All of the parameters of the interatomic potentials are given in Table 6.

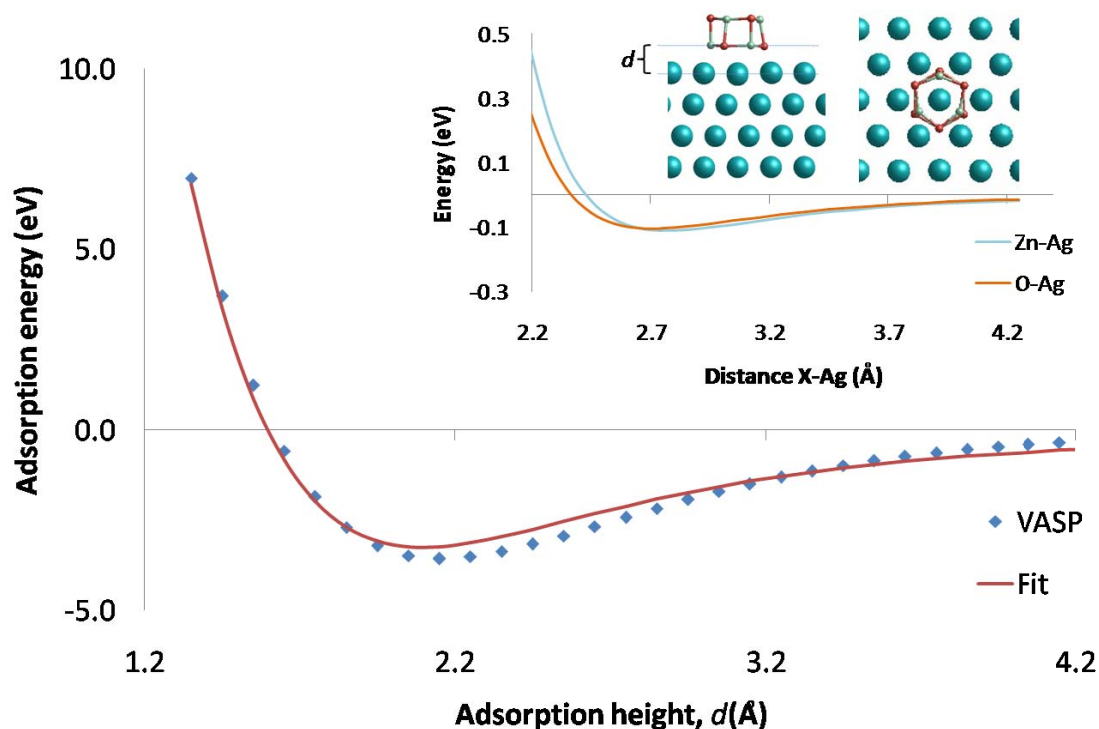


Figure 41. DFT calculated adsorption energy for  $(ZnO)_6$  nanocluster on Ag(111) surface as a function of the adsorption height. Inset shows the graphical forms of the fitted Ag-O and Ag-Zn Buckingham potentials.

Table 6. Parameters for interatomic potentials used in this study.

Buckingham potentials	Range (Å)	A (eV)	$\rho$ (Å)	C (eV Å <sup>6</sup> )
Zn core-O shell	0.0–2.2	592.342818	0.352159	12.896893
Zn core-O shell	3.1–3.3	157.297013	0.429673	5.815914
Zn core-O shell	3.6–12.0	912.517869	0.078935	11.723055
O shell-O shell	0.0–12.0	23674.698081	0.226404	33.476469
Ag core-O shell	0.0–12.0	13930	0.2301	83.4652
Ag core-Zn core	0.0–12.0	19068	0.2295	99.2348
Polynomial potentials	Range (Å)	$C_0$ (eV)	$C_1$ (eV Å)	$C_2$ (eV Å <sup>2</sup> )
Zn core-O shell	2.2–3.1	111.901725	-158.72704	89.657363
Zn core-O shell	3.3–3.6	64102.354057	-93216.170229	54188.8077
	Range (Å)	$C_3$ (eV Å <sup>3</sup> )	$C_4$ (eV Å <sup>4</sup> )	$C_5$ (eV Å <sup>5</sup> )
Zn core-O shell (cont.)	2.2–3.1	-24.98635	3.399631	-0.177932
Zn core-O shell (cont.)	3.3–3.6	-15741.070904	2284.873362	-132.581025

Spring potential	Range (Å)	$k^2$ (?)	$k^4$ (?)	
O core–O shell	0.0–0.6	55.518883	31506.808344	
L–J potential	Range (Å)	A (eV Å <sup>12</sup> )	C (eV Å <sup>6</sup> )	
Zn core–O shell	0.0–2.2	316.435204	0.000000	
EAM potential	A (eV)	x (eV)	p	q
Ag core	0.1028	1.178	10.928	3.139
Ion charges	charge ( $-e$ )			
Zn core	2.000000			
O core	1.754415			
O shell	-3.754415			
Ag core	0.000000			

Key low-energy structures for each size found at the global optimization stage have been refined on an energy landscape defined at a DFT level of theory. The VASP code<sup>240</sup> employed implements a generalized gradient approximation in the form of PW91 exchange-correlation density functional<sup>241</sup>. The projector augmented wave (PAW) approach<sup>242243</sup> [9, 10] was used to describe the effect of core electrons on the valence states as a standard procedure. Valence states are taken as  $d^{10}s^2$ ,  $s^2p^4$  and  $d^{10}s^1$  for Zn, O and Ag atoms respectively. One-electron valence states were expanded in a plane wave basis up to a kinetic energy cutoff of 400 eV, where the total energy is converged to 0.03 eV. Due to the spatial extent of the system, calculations were done only at the  $\Gamma$  point in reciprocal space. As the bottom layer of the Ag slab was fixed, the remaining atomic positions were optimized until the forces on the atoms became less than 0.02 eV/Å. These criteria are somewhat loose and were necessitated by the large volume of calculations, carried out on a large unit cell, however, we have found them to satisfy a minimum requirement of conserving the cluster ranking and essential structural features.

In this study, we report binding energies of the nanoclusters calculated as  $E_b = (E_n - nE_1)/n$ , where  $E_n$  is the total energy of the size  $n$  nanocluster, and  $E_1$  is the

energy of a single ZnO unit. For the supported nanoclusters, we have subtracted the energy of the surface from  $E_n$  and the stabilization energy was defined for a nanocluster as  $E_{stabilization} = E_n^{on\ surface} - E_n^{free\ space}$ . It should also be noted that the clusters may have different orientations on the surface, which also changes their stabilization energies. Here, in all cases we have reported the lowest energy orientation found for each cluster, but we also have given examples of other orientations for some of the global minima structures.

**Nomenclature** Here the nomenclature used by Al-Sunaidi *et al.* is refined to cover new structures that become stable on the support. Al-Sunaidi *et al.* used a nomenclature for nanoclusters consisting of a number and a letter; na, nb, nc, ... etc., where “n” refers to the number of ZnO units in the nanocluster, and the small letter “a” refers to the structure found with the lowest energy of formation at that nanocluster size with the rigid ion potential model. This lower-case letter changes alphabetically with each next lowest-energy structure. The same ordering was also followed with capital letters, corresponding to where Al-Sunaidi *et al.* refined their results with a potential model using shells, which is an improvement to the rigid ion model as it can account for electronic polarization effects on the oxygen anion. Our addition to the nomenclature extends it to define newly found nanoclusters, which were mostly found by global optimization in the presence of an Ag-support. The newly found nanoclusters were denoted with three characters like np1, nq1, nc1. Here the additional letter “p” stands for planar 2D-type nanoclusters. These cluster isomers are not reported after n=7 nanoclusters in free-space, because their energies are much higher than the bubble-type clusters. The letter “q” is used for the clusters having structures containing both planar and bubble-like parts. In rare cases, the letter “c” was used to denote the newly found bubble-type clusters within the range of lowest energy structures for the corresponding size “n”.

### **3. Results and Discussion**

Our global optimization study yielded many possible low energy structures for  $(ZnO)_n$  nanoclusters both in free-space and on Ag support. On a comparison with the earlier study of local minimum (LM) ZnO nanoclusters by Al-Sunaidi *et al.*<sup>244</sup>, it is observed

that the low-energy LM free-space nanoclusters were readily reproduced by KLMC with high efficiency in their range/diversity and energy ordering. In this section we first discuss what is known so far generally about free-space ZnO nanoclusters. Then we move to our results on the ZnO nanoclusters in the presence of the Ag(111) surface for different size clusters between  $n = 1$  to 16, followed by the investigation of the effect of the surface morphology by introducing Ag(110) and Ag(100) surfaces for several cluster sizes. As the last part, we have continued our discussion with the corresponding results obtained at a higher level of theory, DFT.

### 3.1. Free Space Clusters

Wood *et al.*<sup>245</sup> recognized three length scales, or regimes for ZnO nanoparticles, which are: macroscopic, quantum dots and clusters. While macroscopic particles and quantum dots preserve the bulk crystal structure, quantum size effects become important in quantum dots, where the nanoparticles have sizes at least in one dimension of the order of the exciton radius, 15-30 Å. The cluster regime is where the structures of the ZnO particles differ significantly from that of its bulk phases. In this regime, clear diffraction patterns are not obtainable, and the optical properties cannot be directly correlated with those of the bulk. According to their common structural features, the ZnO nanoparticles can be divided into families: sticks, rings, tubes, rods, spheroids (or bubbles), multilayered spheroids, and bulk cuts. Sticks, or 1D chains, are composed of alternating Zn and O atoms, which can form rings by bending and connecting their ends. Multiple rings of different sizes, the basic 2D structure, can fuse and results in planar 2D patchworks. The bending of these 2D patchworks in the third dimension can result in the creation of 3D tubes, if the ends are left open, or spheroids/bubbles, if completely closed. Multilayer spheroids, or nested bubbles are often referred to as onions. The coordination number of atoms depend both on the dimensionality of the structure and the position of the constituent ion on the structure, whether it is at an internal or an external site. Typically, the coordination number is two for 1D, three for 2D and four for 3D structures for the internal ions, while it is decreased by 1 for the external ions. According to previous studies of ZnO nanoclusters in free space<sup>246</sup>, ring structures are stable up to  $(\text{ZnO})_7$  and a preferential switch to bubble clusters than occurs. Bulklike wurtzite or other polymorph structures related to zinc blende or rocksalt phases were not

found stable for small sized nanoclusters. However, it is estimated<sup>247</sup> that the crossover will take place at the size  $(\text{ZnO})_{120}$  between bulk-like and bubble structures.

## **3.2. Interatomic Potential Based Global Optimization Results for ZnO Nanoclusters on the Ag(111) Surface**

### **3.2.1 $(\text{ZnO})_{1-4}$**

Before moving larger nanoclusters, we have started our consideration with the smallest possible clusters to gain insight on the system. Due to the simplicity we could easily constructed models to look at patterns and matching with the surface. For a single unit of ZnO, the only non-fragmented structure is a simple Zn-O dimer. Upon adsorption, for this dimer to align parallel with the Ag(111) surface and with atoms located on hollow sites the interatomic distance between Zn and O would need to be reduced by 0.038 Å, which increases the internal energy of the dimer by ~0.05 eV. However, our simulation predicts that the dimer rotates, with the O atom 2.00 Å and the Zn atom 2.08 Å above the outer Ag plane and thus maintains its free space value of 1.701 Å for the Zn-O interatomic distance. Upon a closer inspection, the Zn atom is displaced 0.04 Å from the hollow axis away from the O atom, the O atom is displaced 0.08 Å from the hollow axis towards the Zn atom, whereas the shell of the O atom is polarized away from the Zn atom by 0.04 Å from the hollow axis. The energy of the dimer in free-space is -30.86 eV/ZnO, which, upon exothermic adsorption onto the support, is lowered by a further 1.01 eV/ZnO.

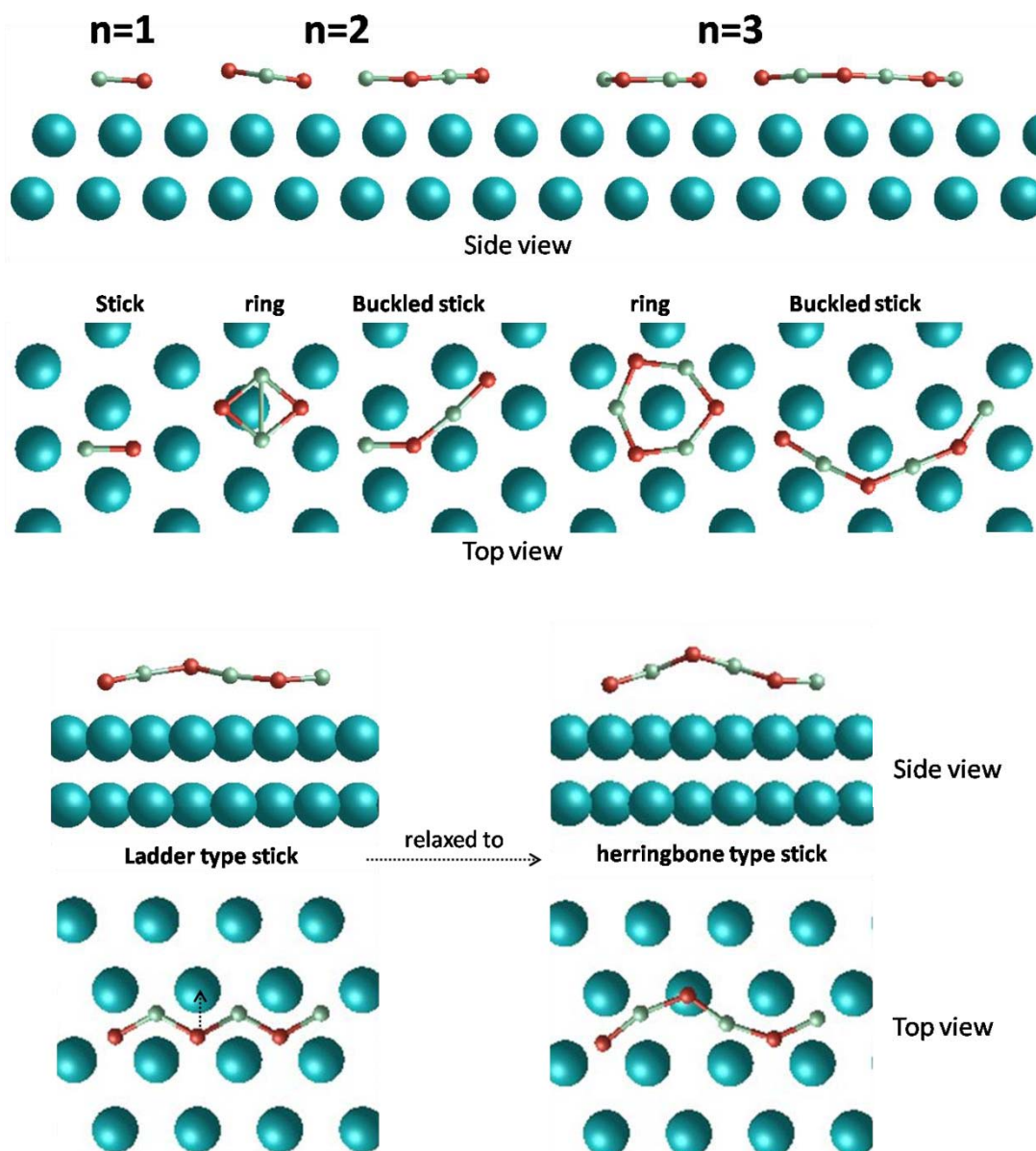


Figure 42. Nanocluster structures on the Ag(111) support for the sizes  $n = 1-3$ .

On adsorption, a second dimer, would adsorb onto an equivalent position, if the interaction between the two dimers is ignored. By construction, assuming now they do interact, this will be one of the nearest vacant hollow sites to where the first dimer is adsorbed. Note that a simple linear extension of the first dimer (as an alternating Zn-O-Zn-O stick) would result in the second dimer occupying an unfavorable top-site (directly above a silver atom). Even after careful construction on the surface (optimized  $n = 2$  sticks with atoms constrained to the hollow axes), the kink relaxes by 3.27 eV/ZnO and the semi-enclosed Ag relaxes by 1.95 eV/ZnO and they both become a

simple ring on the surface. The ring can be considered as two Zn-O-Zn triangles joint along their Zn-Zn sides as the interatomic distance between the Zn atoms is reduced by 0.1 Å, and this cluster when adsorbed has one of these triangles above an Ag top site and the adjacent O atom (from the second triangle) on or near the neighboring hollow axis. From the side view in Figure 42, it can also be seen that this ring is tilted: the adjacent O atom stabilizes at 2.05 Å above the Ag surface plane while the O atom within the triangle above the top site at 2.44 Å. The global search found not only the ring the structure butt alsoa buckled stick, which bends about the internal O atoms while the internal Zn atom retains its linear configuration. Note that the buckled stick is not stable in free space. On the support, the four-membered ring is more stable than the buckled stick by 2.10 eV/ZnO.

In principle, the number of possible configurations is expected to rise as the cluster size increases. Like the  $n = 2$  case,  $n = 1$  sticks can be brought together to form longer sticks and even a six-membered ring for  $(\text{ZnO})_3$ . Also the  $n = 1$  stick and  $n = 2$  ring can be combined to create a key-like structure. By careful consideration, only the ring was found to be stable and relaxed by 0.54 eV/ZnO while displacing slightly from the perfect hollow site, and the other structures relaxed by 3.3-5.3 eV/ZnO and became the ring, apart from the ladder type buckled stick, which relaxed by 1.17 eV/ZnO and become a herringbone type buckled stick. As shown in Figure 42, the middle oxygen atom moved from hollow site to the on-top site, while the Zn atoms tend to approach a linear configuration (the O-Zn-O angles widen to 161.1° and 163.3°). For the ring on surface, all of the Zn-O interatomic distances were found the same (1.804 Å), with the structure bending around O atoms considerably more than at the Zn atoms (O-Zn-O angles: 134.4°, Zn-O-Zn angles: 105.6°). Upon adsorption, Zn-O interatomic distances reduced only by 0.001 Å while the angles reduced by only 0.1°, which implies the internal interactions are much more decisive for the structure. Global optimization for  $n = 3$  has found both ring and herringbone stick on the surface, but also uncovered another buckled stick, which is slightly more favorable than the herringbone type buckled stick by 0.04 eV/ZnO. In the buckled stick, Zn atoms are in an almost linear configuration, with the bending angles around the middle Zn atom of 178.1° and of 173.1° around the other Zn atom, whereas at the oxygen atoms the bending is

pronounced ( $131.7^\circ$ ,  $148.8^\circ$ ). As for  $n=2$  stick, both  $(\text{ZnO})_3$  sticks are not stable in free space but are stabilized by the support. However, the  $(\text{ZnO})_3$  ring is more stable than the sticks by 2.4 eV/ZnO on the Ag(111) surface.

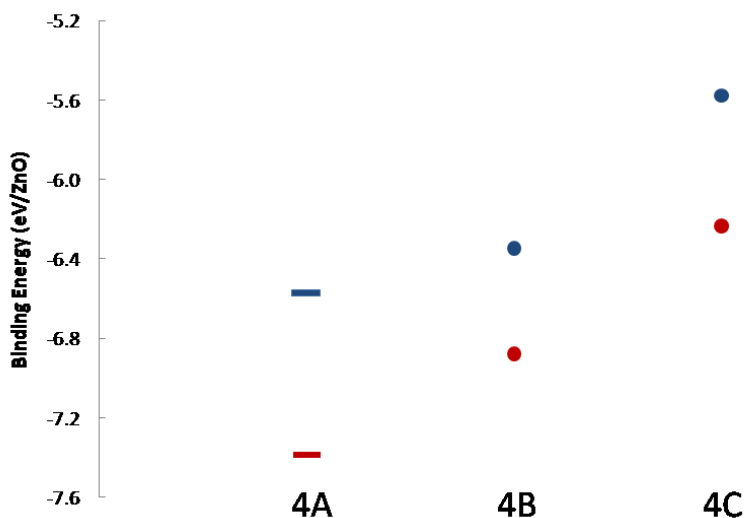


Figure 43. Energy ordering of  $(\text{ZnO})_4$  low-energy nanoclusters on the Ag(111) surface (red). Blue colored symbols are corresponding energies in free space. 2D planar structures are represented by sticks while 3D cluster structures are represented by filled circles.

For  $n = 4$ , three low-energy structures were found on the Ag(111) surface by global optimization, which correspond to the lowest energy structures 4A, 4B and 4C in free space (Figure 44). The energy ordering does not change in the supported case as can be seen in Figure 43, however the stabilization energies differ for each structure. The planar 4A structure is stabilized by 0.82 eV/ZnO, whereas this stabilization is significantly smaller for the 3D-cluster structures 4B and 4C, 0.53 and 0.66 eV/ZnO respectively. In Figure 44, it can be seen that the mid-point of the eight-membered ring (4A structure) is in the middle between a hollow and an on-top position. However, the centres of the four-membered ring and a distorted six-membered ring, the contacting parts to the support of the 4B and 4C structures respectively, are on an on-top position. We note that this ring-surface adsorption configuration was also found for  $n = 3$  six-membered ring (see Figure 42). The centre of the ring was on the on-top position where all atoms are located at all of the surrounding hollow sites with small displacements. The adsorption height (taken as the average distance of the first contacting atoms of the cluster from the surface plane) was found to be 2.11 Å for this configuration, which is very close to the

adsorption height of a single dimer, where both atoms are in hollow positions. However, the adsorption heights of the four-membered ring ( $n = 2$ ) and of the eight-membered ring ( $n = 4$ ) were found to be significantly greater, 2.25 and 2.30 Å, respectively. This difference is probably due to the poorer surface matching in  $n = 2$  and  $n = 4$  than the  $n = 1$  and  $n = 3$  cases, as the stabilization energies also follow the same ranking. For the eight-membered ring, two oxygen atoms are close to on-top positions, and the other two oxygen atoms are closer to the hollow sites, while the Zn atoms are further from symmetric positions on the surface. As we check the distances from the surface plane for all of the individual atoms of the ring and stick structures  $n = 2$  to  $n = 4$ , we observe that the hollow positioned atoms are always closest to the surface, and the distances are very similar for the closest atoms ( $\sim 2.05$  Å). However, the adsorption heights of the 3D-cluster structures 4B and 4C are found to be lower than that of 4A, 2.18 Å and 2.06 Å respectively, while their energies are considerably higher. This is possibly due to the effect of the internal structures of the clusters, *i.e.* the above atoms forcing the surface contacting atoms toward the surface. Furthermore, it should be also noted that the surface-contacting atoms of these 3D structures follows the same ranking of the distance from the surface plane in line with the above discussion.

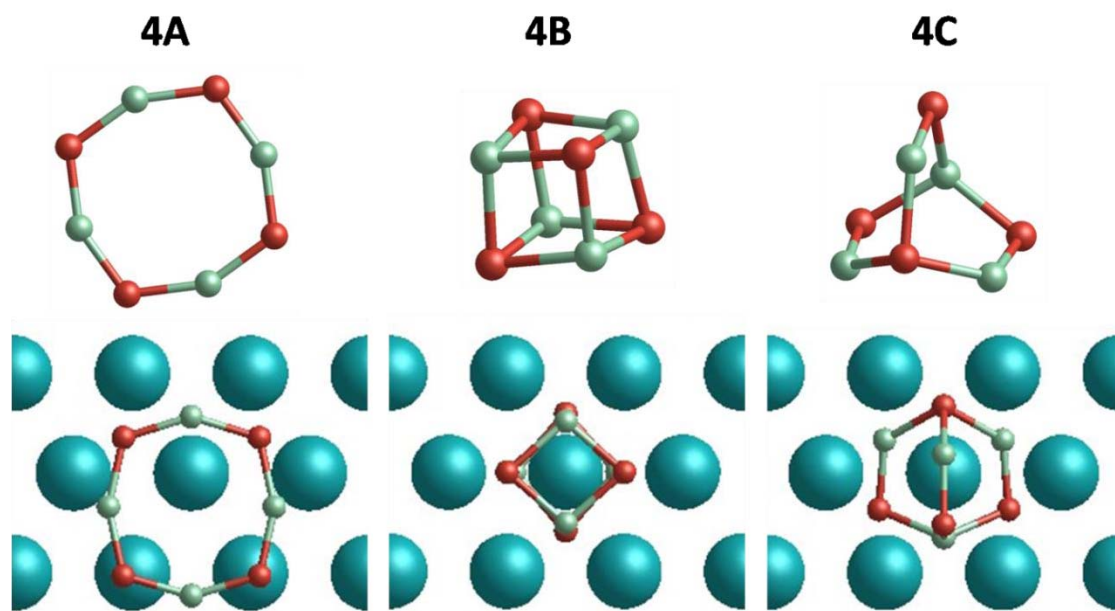


Figure 44. Nanoluster structures of  $(\text{ZnO})_4$  both in free space (above) and on the Ag(111) support (below).

### 3.2.2 (ZnO)<sub>5-6</sub>

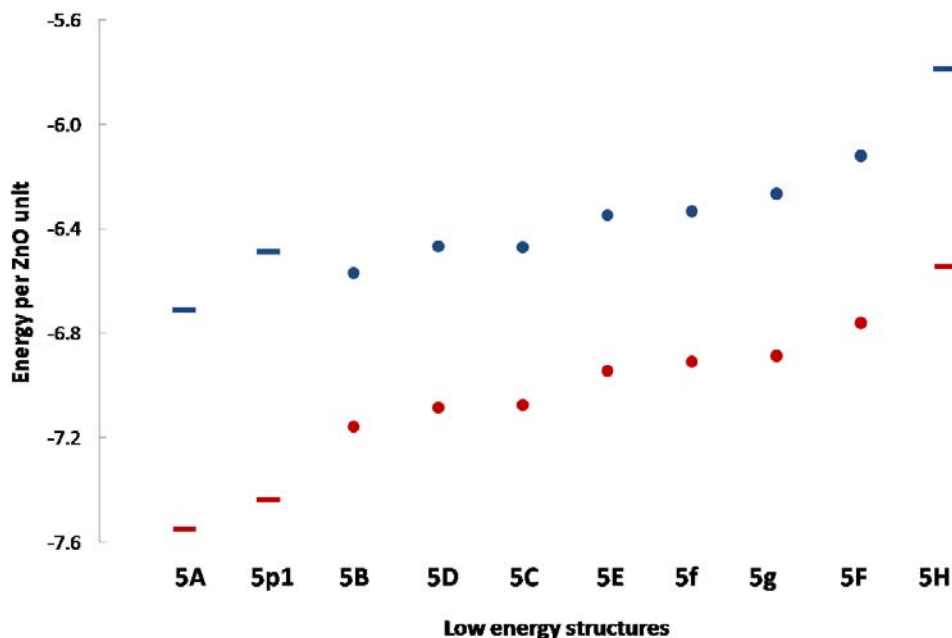


Figure 45. Energy ordering of (ZnO)<sub>5</sub> nanoclusters on the Ag(111) surface (red). Blue colored symbols are corresponding energies in free space. 2D planar structures are represented by bars while 3D cluster structures are represented by filled circles.

Ten clusters were found by global optimization on the Ag(111) support for the size  $n = 5$ . The energy ordering of these structures is given in Figure 45. The free space global minimum, 5A, which is a ten-membered planar ring structure, does not change ranking in the Ag-supported case. The stabilization energy of this cluster on the support is 0.84 eV/ZnO. The second lowest-energy Ag-supported structure is found to be 5p1, which is a distorted double ring (Figure 46). In free space, 5p1 is found to be the third lowest energy after the 3D cluster, 5B. The 5p1 structure is stabilized by the support by 0.95 eV/ZnO whereas 5B structure is only stabilized by 0.59 eV/ZnO. This higher stabilization can be probably attributed to the number of atoms contacting with the surface. Whereas for a planar structure all the atoms are close to the surface, 3D clusters only have a relatively small surface contact area. The next seven lowest energy structures on the Ag(111) surface are all 3D cluster structures and follow almost exactly the same ordering as in free space, with very similar surface stabilization energies of about 0.6 eV/ZnO. The only ranking change occurred between the 5C and 5D clusters, which

have the same structural configuration but with atom types exchanged (*i.e.* Zn  $\leftrightarrow$  O). They both have very similar energies both in free space (0.004 eV/ZnO difference) and on the Ag support (0.010 eV/ZnO difference) and they both make contact with the surface with their six-membered ring parts, where the ring is slightly distorted and positioned at an on-top surface site. This small stability switch can be attributed to these distorted rings where the oxygen and zinc distances to the surface differ slightly. The last structure found on the surface was another planar structure, which can be roughly described as a distorted 5H cluster, with a Zn-O tail. The stabilization energy for the 5H structure is found to be 0.75 eV/ZnO. For the size  $n = 5$ , the separation of the 2D and 3D cluster types becomes clearer, as the stabilization energies of 2D and 3D cluster types form two distinct groups (Figure 45).

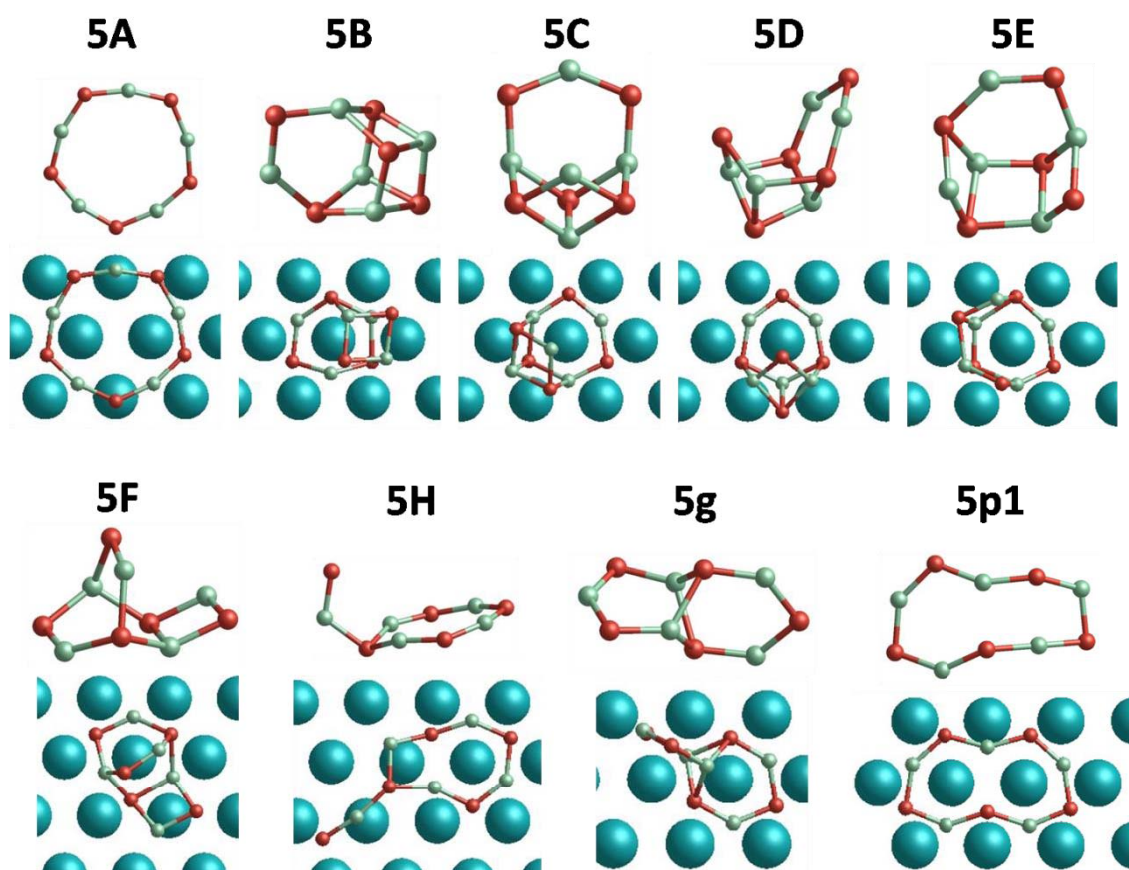


Figure 46. Structures of  $(\text{ZnO})_5$  clusters in free space and on support.

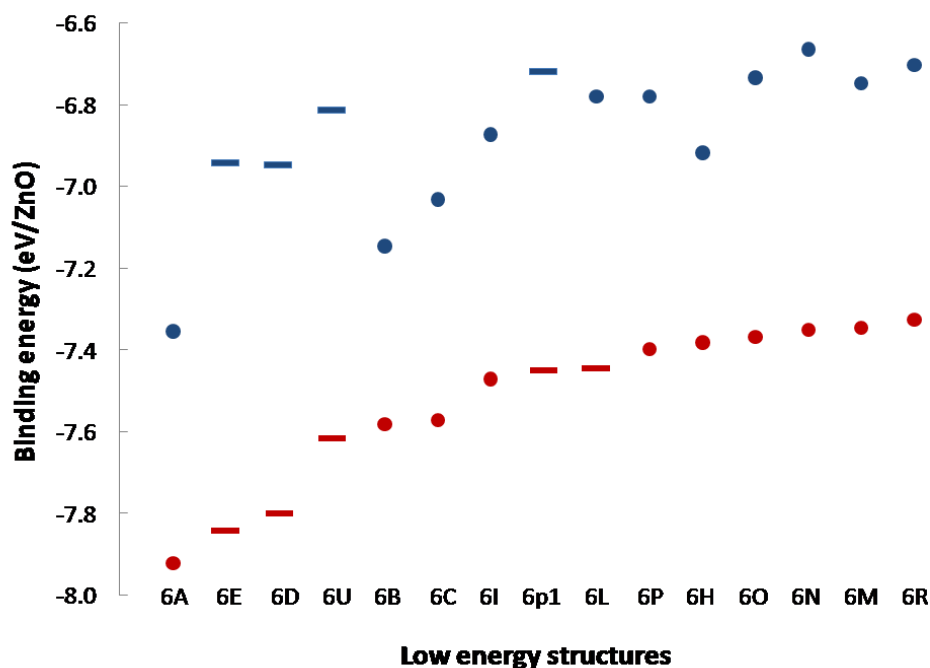


Figure 47. Energy ordering of  $(\text{ZnO})_6$  nanoclusters on Ag(111) surface (red). Blue colored symbols are corresponding energies at free-space. 2D planar structures are represented by bars while 3D cluster structures represented by filled circles.

For  $n = 6$ , the global minimum structure in free space, 6A, which is a drum-like hexagonal prism, retained its ranking on the addition of Ag support. It is adsorbed with one hexagonal face in an on-top position on the surface, and the stabilization energy was found to be 0.57 eV/ZnO. The next lowest energy cluster, 6B, was found to be ranked 5th when supported. The next lowest energy cluster, 6C, is ranked 6th. The 6C cluster binds to the surface by a six-membered ring, while the 6B by a part of a distorted six-membered ring, in which only four of the atoms make contact with the surface. The three planar structures, 6E, 6D and 6U, achieve a better rank when supported than either 6B or 6C. The stabilization energies for 6E, 6D and 6U are 0.90, 0.85 and 0.80 eV/ZnO whereas for 6B and 6C they are 0.44 and 0.54 eV/ZnO, respectively. 6D and 6E clusters also switch the ranking on the support. 6D structure is a ring, which is not the global minimum unlike smaller  $n = 2, 3, 4$  and 5 clusters. 6E structure can be seen as joint six-membered rings, which are connected with a four-membered ring. The four-membered ring of 6E is in an on-top position on the surface, while the six-membered rings adjust to match the neighboring on-top positions. The larger ring of 6D structure centers on a hollow site, with three oxygen atoms directly above Ag atoms. Thus the planarity of the

ring is distorted because the on-top oxygen atoms move 0.30 Å away from the surface, while oxygen atoms in the hollow position move 0.25 Å closer to the surface. Similar distortions can be also seen for the supported 6U structure, which consists of an eight- and a six-membered ring. These orientation differences due to the surface matching and the related distortions can explain the difference in the stabilization energy of these three planar clusters.

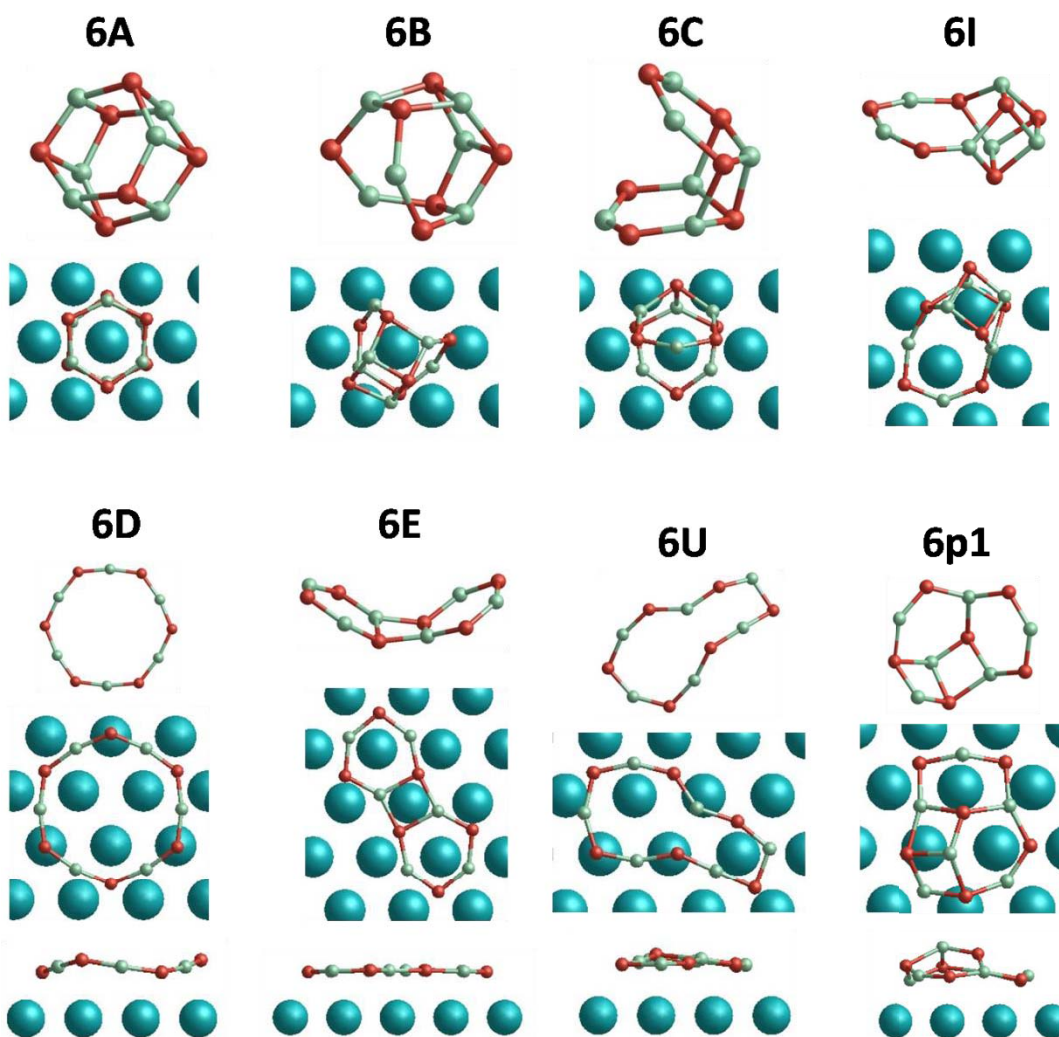


Figure 48. Structures of  $(\text{ZnO})_6$  in free space and on support. Side views of 2D clusters are also given beneath.

It should also be noted that for the 2D clusters, one single configuration on the support can correspond to different but closely related free-space clusters, which are also close in formation energies. In such cases, we have chosen the corresponding free-space cluster using a reverse process, i.e. relaxing the supported cluster again in free space.

First example emerges here at size  $n = 6$  (where 2D clusters start to form as multiple rings) as 6E cluster on the support, which also corresponds to 6F and 6G structures, i.e. all three structures converged to the same structure on the support. In free space, multiple rings do not stay planar, and the rings get tilted at their connection sites, where the atoms have coordination number of three instead of two, due to the polarization effects (when we switch off the shell model, the clusters all became planar again). However, planarity is improving on the support (The maximum difference on z-coordinate,  $\Delta_z = 0.07\text{\AA}$  for 6E on support). In a similar way, 6L structure becomes also more planar on the support, while the cluster unfolds from its ring part. However, the adjacent four-membered rings limit the planarity.

It should be noted that there is another low-energy orientation for the global minimum structure, 6A, in which the cluster binds to the surface via a four-membered ring in an on-top position instead of a six-membered ring. This orientation has a higher energy of 0.17 eV/ZnO than that of the lowest energy orientation of 6A, which would reduce its rank to 4<sup>th</sup> because the planar structures 6D and 6E are away from the global minimum only by 0.07 and 0.12 eV/ZnO, respectively.

In general, for sizes  $n = 5$  and 6, the lowest energy orientations for most of the structures were found to be those that minimize the on-top interactions of the contacting atoms as much as possible. The 3D type clusters tend to bind to the support by their six-membered ring faces, and the stabilization energy increases with a better matching. For the 2D clusters, it becomes more difficult for the adjacent rings to occupy better positions because of the lattice mismatch, and the structures which fit the surface better also stabilize more.

### 3.2.3 (ZnO)<sub>7-8</sub>

For the size  $n = 7$ , the global minimum structure in free space, 7A, was found to be the fifth lowest energy structure on the Ag support, while four planar structures which are not in the first ten lowest energy clusters in free space lower their energy significantly. The stabilization energies for these planar structures were found to be  $0.85 \pm 0.03$  eV/ZnO whereas the stabilization energy for the 3D cluster 7A is 0.50 eV/ZnO as the number of the contact atoms in 2D planar structures is higher. The large energy

difference of 7A relative to the planar structures result in this ranking change and the 7A is not global minimum anymore. The next lowest energy structure found on the surface is also another planar structure with the stabilization energy 0.79 eV/ZnO. The low energy metastable 3D cluster structures in free space align with a similar ordering on the surface with the stabilization energies of  $0.48 \pm 0.03$  eV/ZnO. Among these structures, 7E acquires the lowest energy on the surface, most probably because of a better orientation, where it binds to the surface via a six-membered ring again in a on-top position. In Figure 50, a clear separation of the stabilization energies of planar structures and the 3D clusters can be seen, starting from  $n = 7$  it holds for higher sizes. At size  $n = 7$ , clusters composed of both 2D and 3D parts form another class, which are distinguished in the energy graphs by the use of triangles. Not surprisingly, the stabilization energies of these quasi-planar structures lie between those of the 2D and 3D structures.

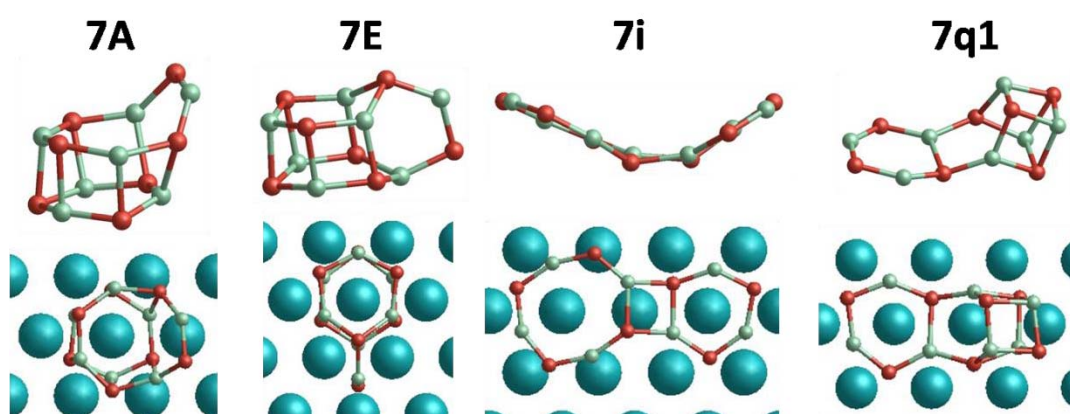


Figure 49. Structures of  $(\text{ZnO})_7$  clusters in free space and on support.

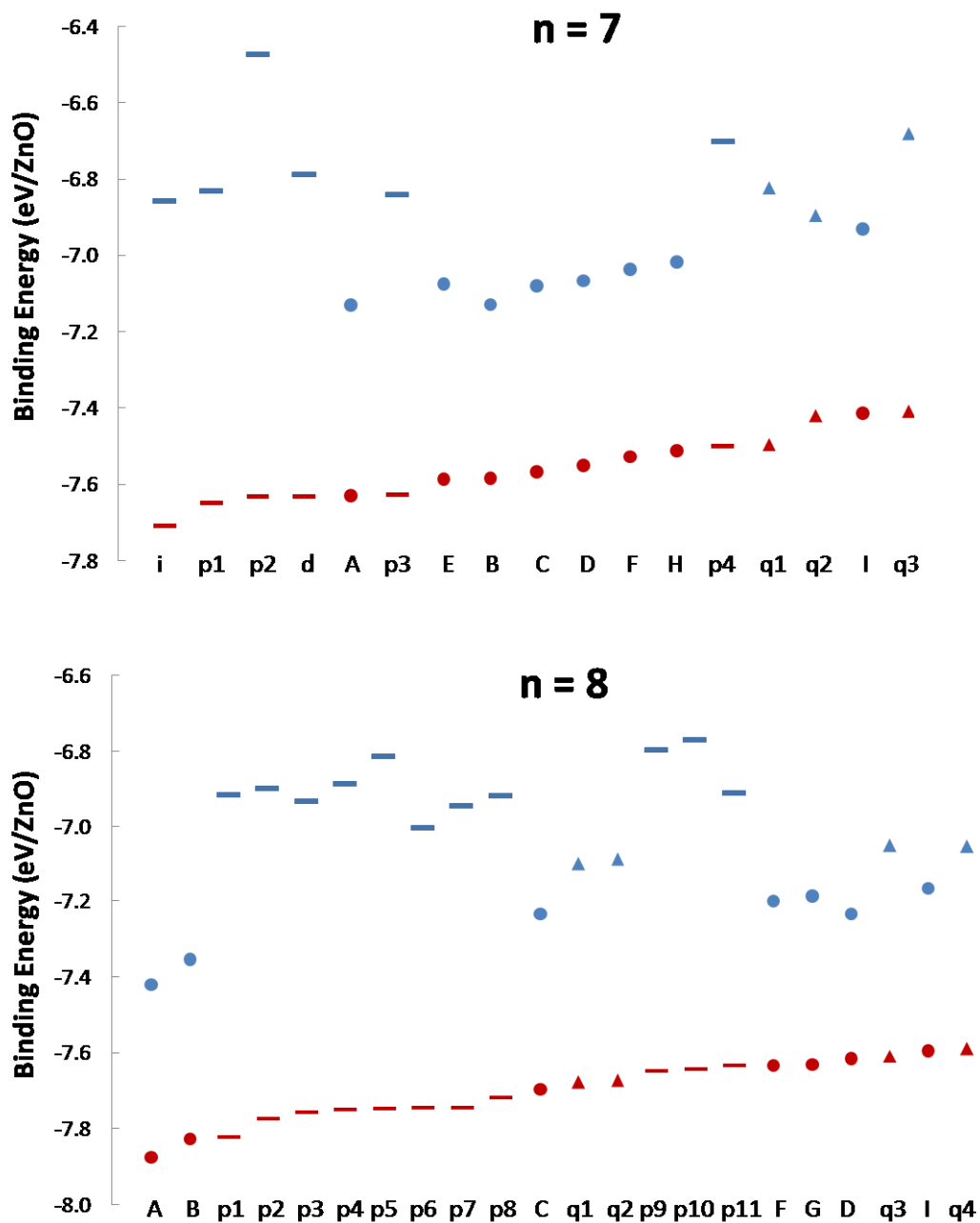


Figure 50. Energy ordering of  $(\text{ZnO})_7$  and  $(\text{ZnO})_8$  nanoclusters on Ag(111) surface (red). Blue colored symbols are corresponding energies of clusters in freespace. 2D planar structures are represented by bars while 3D cluster structures represented by filled circles. Triangles represent the clusters having both 3D and 2D parts.

For size  $n = 8$ , the global minimum and the second lowest energy structure retain their ranking in the supported case. The stabilization energies for these two structures, 8A and 8B, are 0.45 and 0.47 eV/ZnO, respectively. However, the third lowest energy structure

in free space found to be 11th on support, whereas eight new 2D structures fill the gap, which are even not found during global optimization in free space, at least among the fifty best solutions. The stabilization energy of 8C, 0.46 eV/ZnO, is almost the same as that of 8A or 8B, whereas the planar structures have stabilization energies of  $0.84 \pm 0.09$  eV/ZnO. The lowest energy 2D structure has almost the same energy as 8B with only a very small energy difference of 0.005 eV/ZnO, and all of the 2D structures are found to be lower in energy than the global minimum structure, 8A, with the other possible orientation, which has an energy difference of 0.16 eV/ZnO. The so-called quasi-planar class of clusters is also found in the first fifteen structures on support for size  $n = 8$ . Although these structures can be generated by free-space global optimization, there are still many more 3D clusters lower in energy, which are higher in energy on the surface. The average stabilization energies for these three types of clusters on the surface, planar, quasi-planar and 3D, are found to be 0.84, 0.57 and 0.45 eV/ZnO, respectively.

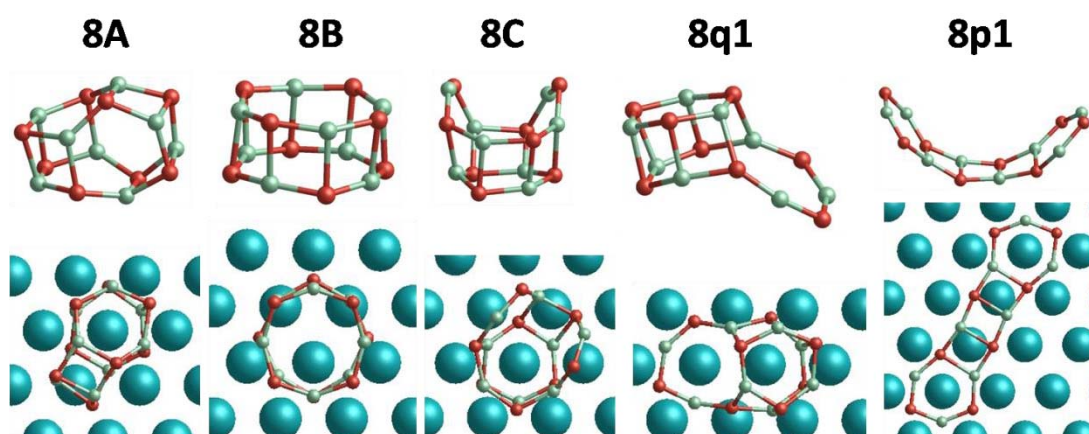


Figure 51. Structures of  $(\text{ZnO})_8$  in free space and on support.

### 3.2.4 $(\text{ZnO})_{9-10}$

For the size  $n = 9$ , again the two lowest energy clusters, 9A and 9B in free space found to be in the same ranking on the support with the stabilization energies of 0.42 and 0.39 eV/ZnO. The third lowest energy cluster was found to be 9G, with a higher stabilization energy of 0.53 eV/ZnO, which is the highest stabilization energy among all 3D clusters for  $n = 9$  size. This is probably due to the orientation of 9G clusters, which fits to the surface via two adjacent six-membered rings at on-top sites on the surface and has the

largest number of contact atoms among these 3D clusters. The planar structures were not found in a global optimization in freespace, which is also the case for cluster sizes higher than  $n = 9$ . However, global optimization in the presence of a support still results in low-energy planar structures, mixed with 3D cluster structures. For  $n = 9$ , rank 4 to 8 structures were found to be planar apart from the 7th, which is quasi-planar. The separation of stabilization energies can be seen clearly for  $n = 9$  size and the larger sizes up to the considered size  $n = 16$ . For  $n = 9$  size, the average stabilization energies are 0.45 and 0.85 eV/ZnO for 3D and planar structures, respectively.

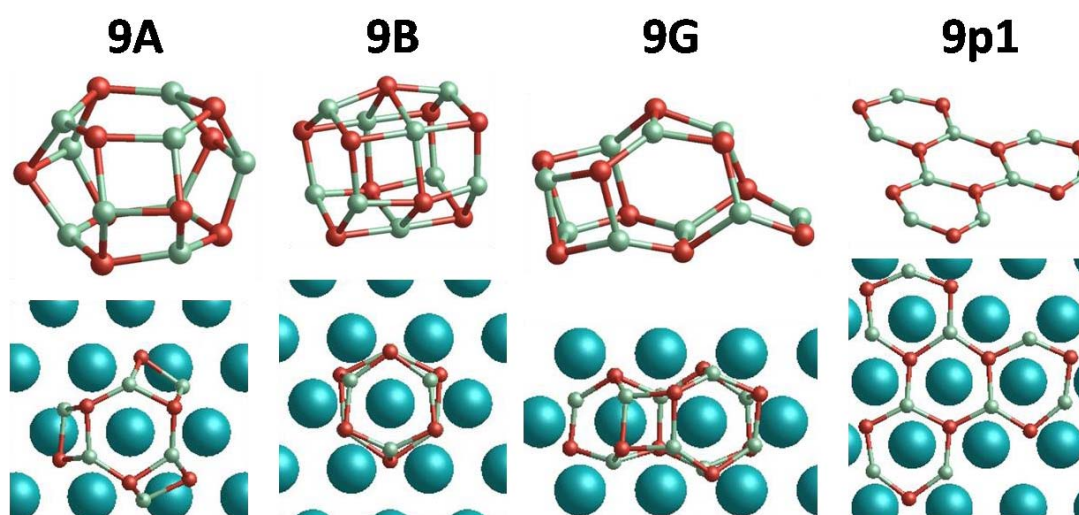


Figure 52 .Structures of  $(\text{ZnO})_9$ , both free space and on support.

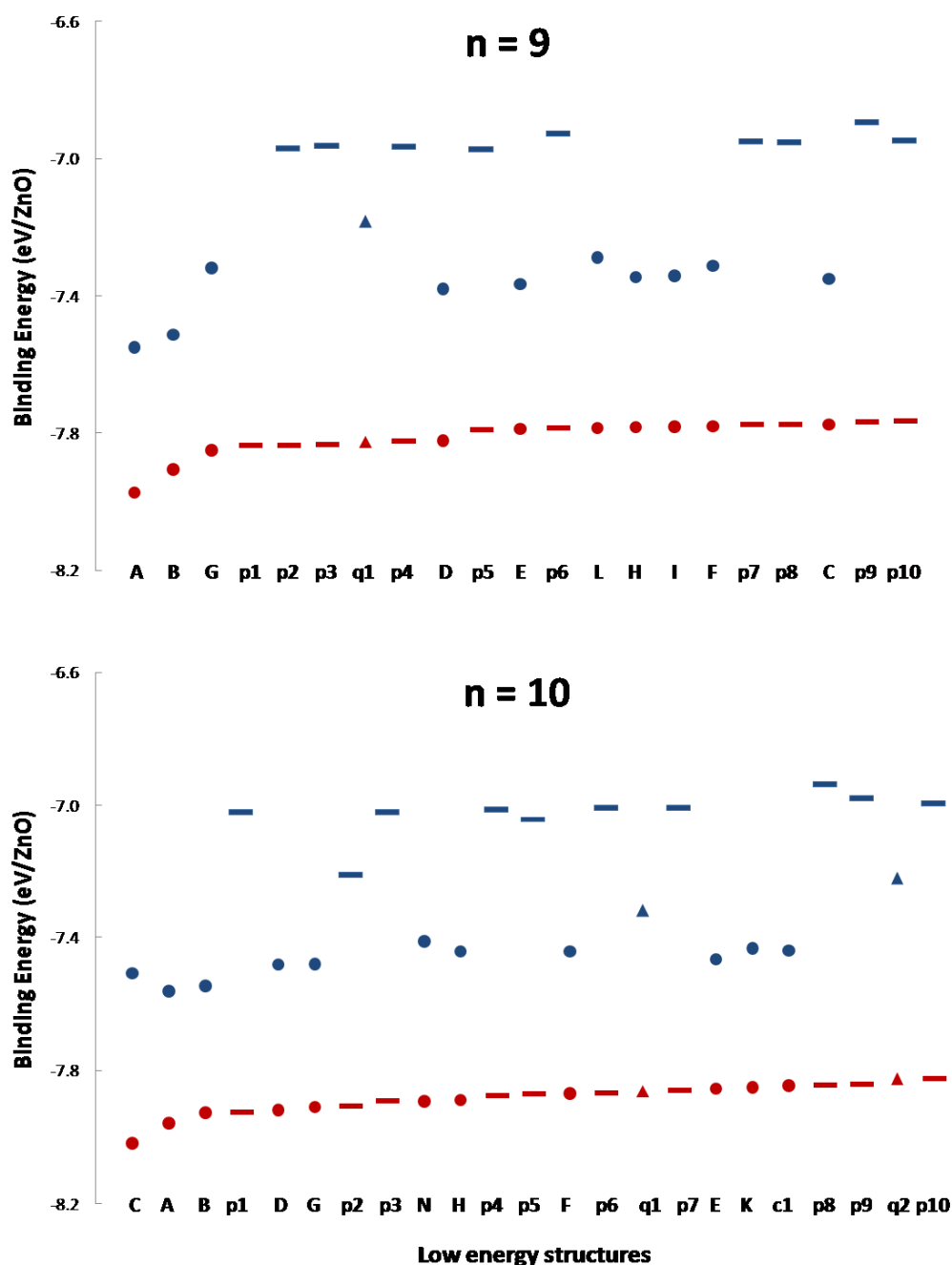


Figure 53. Energy ordering of  $(\text{ZnO})_9$  and  $(\text{ZnO})_{10}$  nanoclusters on Ag(111) surface (red). Blue colored symbols are corresponding energies in freespace. 2D planar structures are represented by bars whereas 3D cluster structures are represented by filled circles. Triangles represent the clusters having both 3D and 2D parts.

For size  $n = 10$ , the third lowest energy structure in free space, 10C, was found to be the global minimum on the support. Like the case 9G, 10C adsorbs by two adjacent six-membered rings enclosing two neighboring surface silver atoms, whereas the 10A and 10B structures interface via only one six-membered ring enclosing one surface silver

atom. The fourth ranking cluster on the surface was found to be a planar structure consisting of two four-membered, three six-membered and one eight-membered ring. Note that in the Figure 53 the free space energy of the 10p2 cluster is significantly lower than that of the other 2D structures and has the stabilization energy of 0.69 eV/ZnO. This is because in free space, this structure bends in such a way that results in a new bond between two rings. If we force the cluster to stay planar, its energy approximately equalizes with the energies of other planar structures. All of the planar structures are multiple rings from size  $n = 9$ , which usually consist of four-, six- and eight-membered rings, although rarely ten- or twelve-membered rings also occur. The orientation on the surface is mainly determined by the six-membered rings, where they fit on-top positions on the surface, followed by the same tendency for four-membered rings. The average stabilization energies found to be 0.85 and 0.43 eV/ZnO for 2D and 3D structures, respectively.

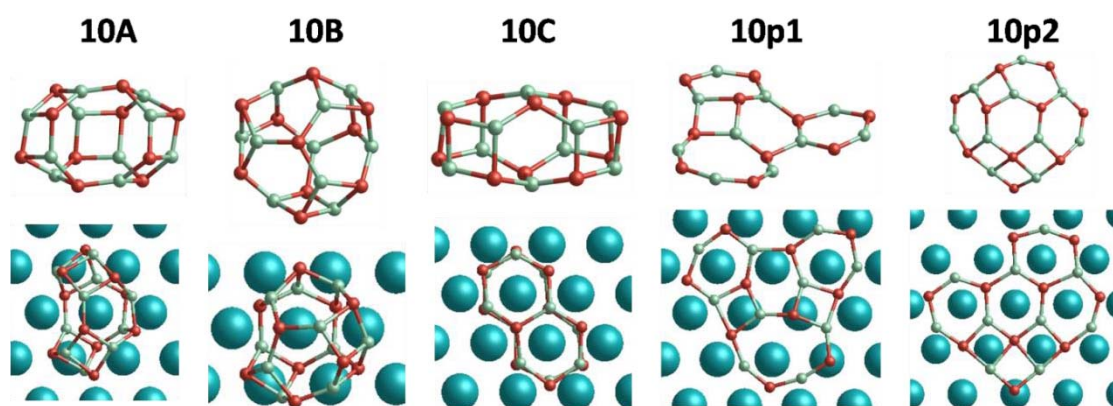


Figure 54. structures of  $(\text{ZnO})_{10}$  in free space and on support.

### 3.2.5 $(\text{ZnO})_{11-16}$

For sizes  $n = 11$  to 16, all the global minima structures  $nA$  were found to be the lowest energy structures again on the silver surface. The stabilization energies of 2D, quasi-planar and 3D structures follow the same trends as those of smaller sized clusters, in that they are much higher for 2D than 3D structures and the energies of quasi-planar structures are in the middle. The 2D structures, which are lowest-energy in free space, on the surface were found to be second for  $n = 11$  and 12, and fifth and fourth for  $n = 13$  and 14 respectively. For  $n = 13$  and 14 there is a mixture of low energy structures as 2D and 3D clusters, while there is a separation happening at size  $n = 15$ , where all the 2D

clusters are found to be higher in energy than almost all 3D cluster structures. The same situation also happens for  $n = 16$ . However, the energy differences between the lowest energy clusters of 2D and 3D (see Figure 55) do not increase as the cluster size increases from  $n = 11$  to  $n = 16$  and found to be 0.05, 0.12, 0.03, 0.09, 0.10, and 0.06 eV/ZnO respectively. Apart from the most stable 3D clusters  $nA$ , there are also ranking changes among 3D clusters on the surface, according to how they match the surface, following the trends seen above for smaller sizes. In general, the cluster adsorbing by two adjacent six-membered ring faces (11C, 11D, 12C, 13D, 13F, 14E, 15B, 16D) or other size adjacent rings (11F, 11c5, 12I, 13E, 13J) are stabilized more, while clusters adsorbed only by a single six-membered ring (11B, 11E, 13B, 13C, 14B, 15c4, 16B) or a single eight-membered ring (12B, 16C) are stabilized less. The higher stabilization of the six-membered rings can be also seen for the most stable 3D clusters shown in Figure 56. Similarly, 2D clusters match the surface as much as possible via hexagonal rings. However, there is a mismatch between a uniform hexagonal ZnO patchwork and the silver surface. Furthermore, the clusters consisting of only six-membered rings are not stable in free space and relax to alternative 2D structures, including four- and eight-membered rings, apart from size  $n = 9$ , which is also the most stable 2D cluster (9p1) on the surface and has  $D_{3h}$  symmetry. We have also considered chains of six-membered rings. For chains, all the rings collapsed into four-membered rings except from the ends, which is probably due to the polarity. In a chain of rings, all the corner atoms on one side are O atoms while on the other side are Zn atoms. Most of the 2D structures are found to be buckled in free space due to the polarization, while they become planar with the effect of support.

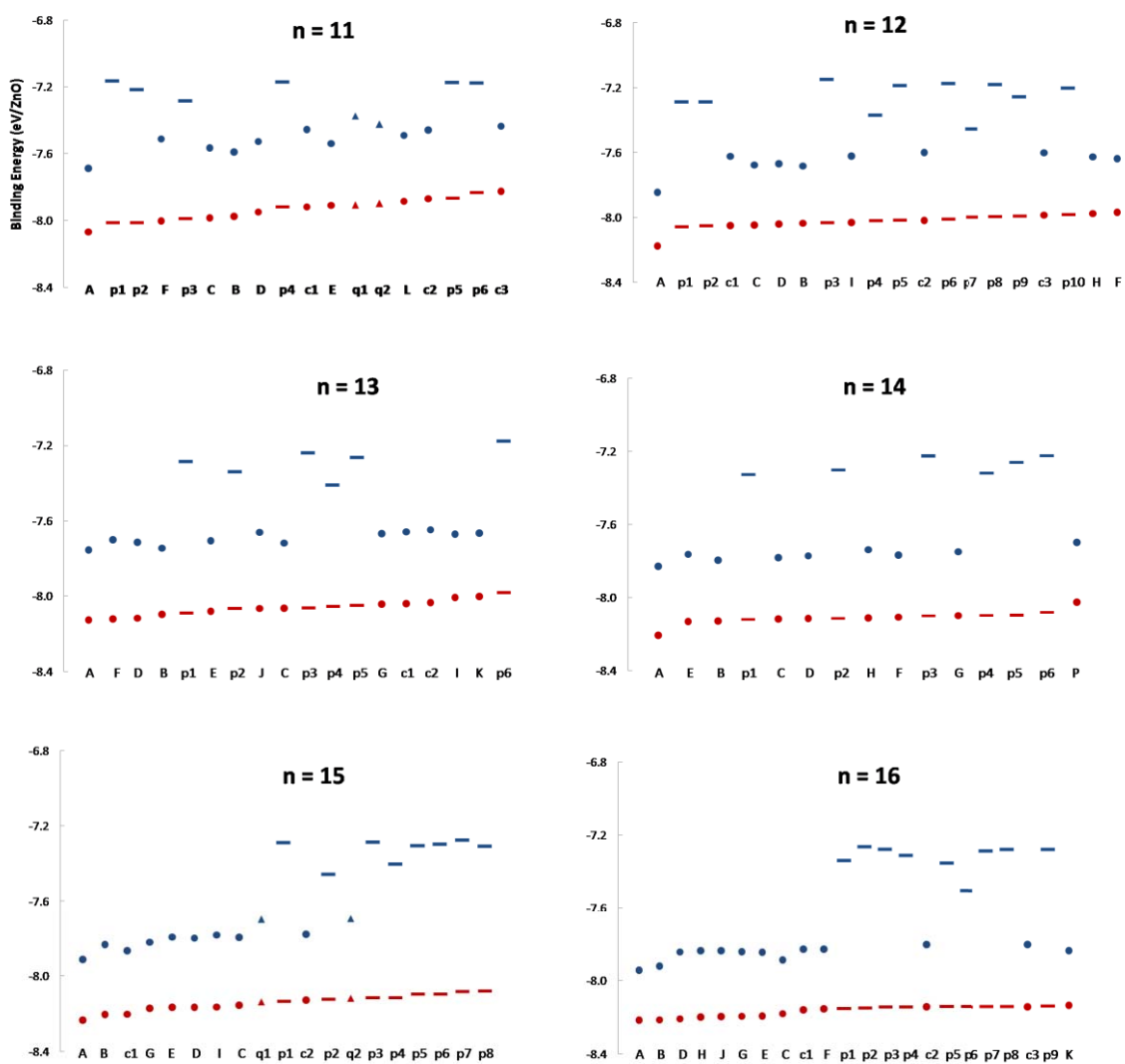


Figure 55. Energy ordering of  $(\text{ZnO})_{11}$  -  $(\text{ZnO})_{16}$  nanoclusters on Ag(111) surface (red). Blue colored symbols are corresponding energies infreespace. 2D planar structures are represented by bars whereas 3D cluster structures are represented by filled circles. Triangles represent the clusters having both 3D and 2D parts.

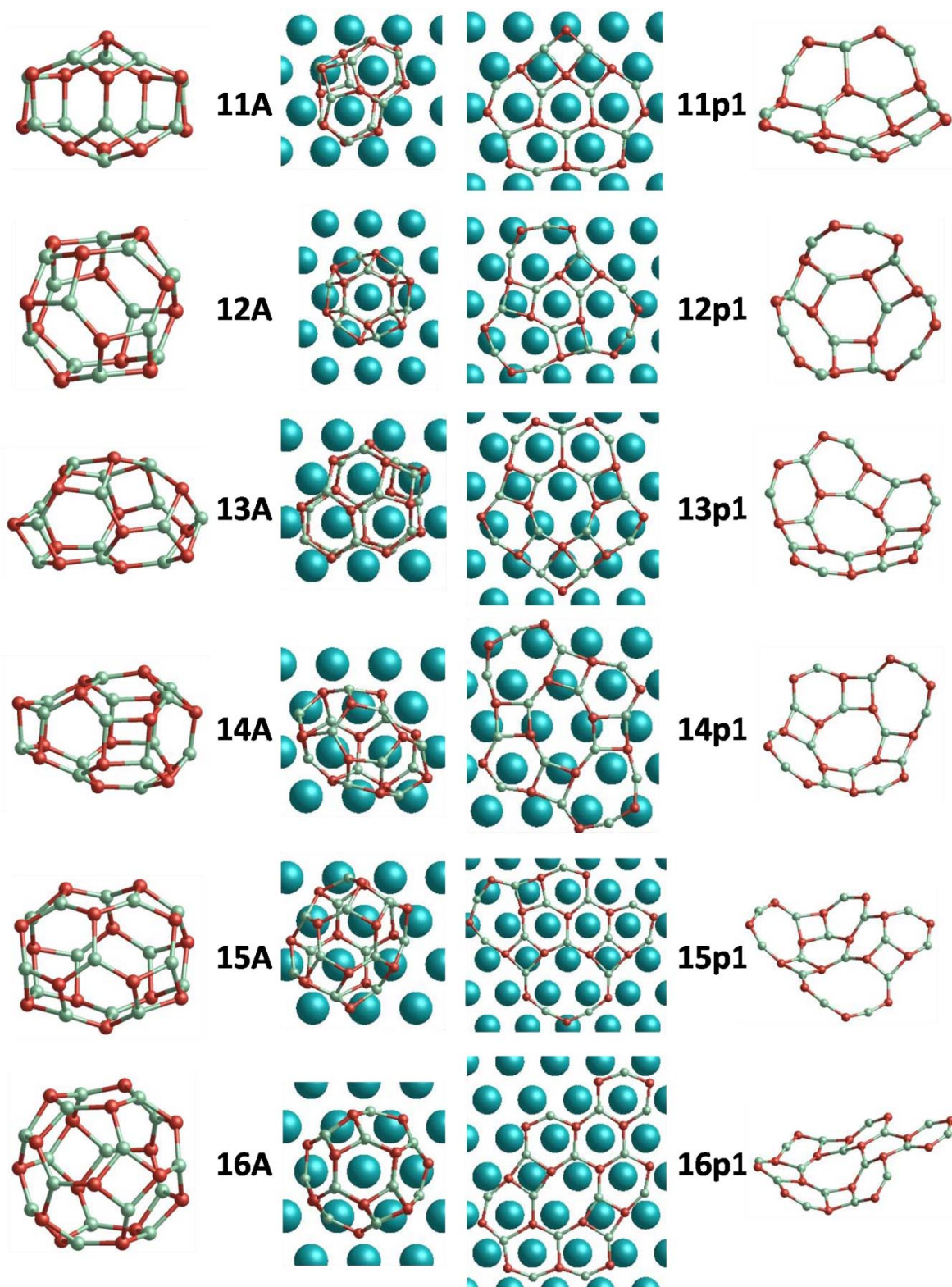


Figure 56. Structures of  $(\text{ZnO})_{11-16}$  in free space and on support.

### 3.2.6 (ZnO)<sub>20</sub>, (ZnO)<sub>24</sub>

As the size increases, a lower proportion of the outer surface of the low-energy free-space 3D clusters becomes available for a contact with the silver surface. Therefore the ranking changes between 3D and 2D clusters become more pronounced on the surface. For (ZnO)<sub>20</sub>, the free space GM structure, 20A, was found to be ranked 19<sup>th</sup> on the surface, as fifteen 3D and three 2D clusters surpassed it. Similarly, the 20C cluster, which also does not include a large adsorption face, decreased by fifteen ranks, whereas the 20D cluster, which adsorbs via a face consisting of five adjacent six-membered rings (see Figure 57), becomes the lowest energy structure on the surface. The 20D structure has stabilized by 0.37 eV/ZnO on the surface, whereas 20A and 20C stabilized by 0.25 and 0.29 eV/ZnO, respectively. The 20B and 20E clusters were found to be the second and the third lowest energy structures on the surface with 0.34 eV/ZnO stabilization energies. Among these structures, 20D can be seen as a double layered structure, where the bonds between internal atoms from the top view are cut and the cluster is ellipsoidal. 20B and 20E are also ellipsoidal clusters, whereas 20A and 20C are more spherical. Both cluster pairs are adsorbed via their adjacent six-membered rings, however, the 20B and 20E exhibit flatter faces. Global optimization generated new bubble clusters, which are mainly ellipsoidal, with stabilization energies about 0.33 eV/ZnO. The 2D clusters were found as 14<sup>th</sup>, 17<sup>th</sup> and 18<sup>th</sup> lowest energy structures, with the stabilization energies of about 0.87 eV/ZnO. The energy difference between the lowest energy 2D and 3D clusters (20p1 and 20D) on the surface was found to be 0.07 eV/ZnO. As shown in Figure 59, the 20p1, 20p2 and 20p3 structures mainly consist of six-membered rings.

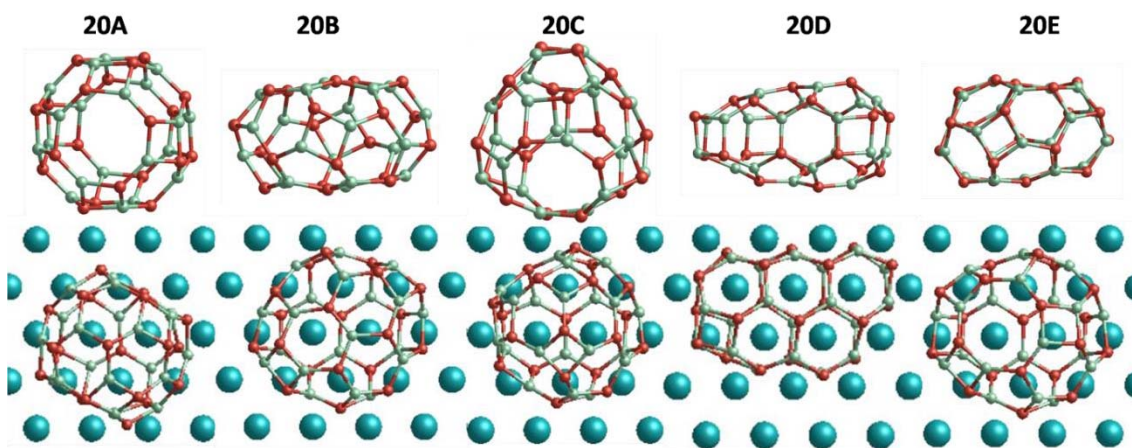


Figure 57. Structures of (ZnO)<sub>20</sub> in free space and on support.

One of the aims of this work was to check for the possibility of a ZnO monolayer formation. Therefore, a global optimization search was also performed for  $(\text{ZnO})_{20}$  using a considerably smaller unit cell, which allowed for periodical 2D structures to occur. Figure 59 shows the best two structures obtained from the search. Due to the additional bonds formed for the periodic structures, the 2D layers were found to be significantly lower in energy than the global minimum of the larger unit cell, 20D. The hexagonal layered structure, ML2, was found to be 0.39 eV/ZnO more stable than 20D, while ML1, a symmetric structure consisting of differently sized rings, was found to be 0.45 eV/ZnO more stable. Due to the rectangular periodicity of the surface and the lattice mismatch, the ML2 distorted significantly. When we cut the periodicity and place these structures within the large unit cell, ML1 and ML2 become 0.23 and 0.30 eV/ZnO higher in energy than the 20D, which are also higher than all of the considered structures. It should also be noted that ML1 is higher in energy than other planar structures in free space by about 0.1 eV/ZnO while ML2 is even higher by the same amount.

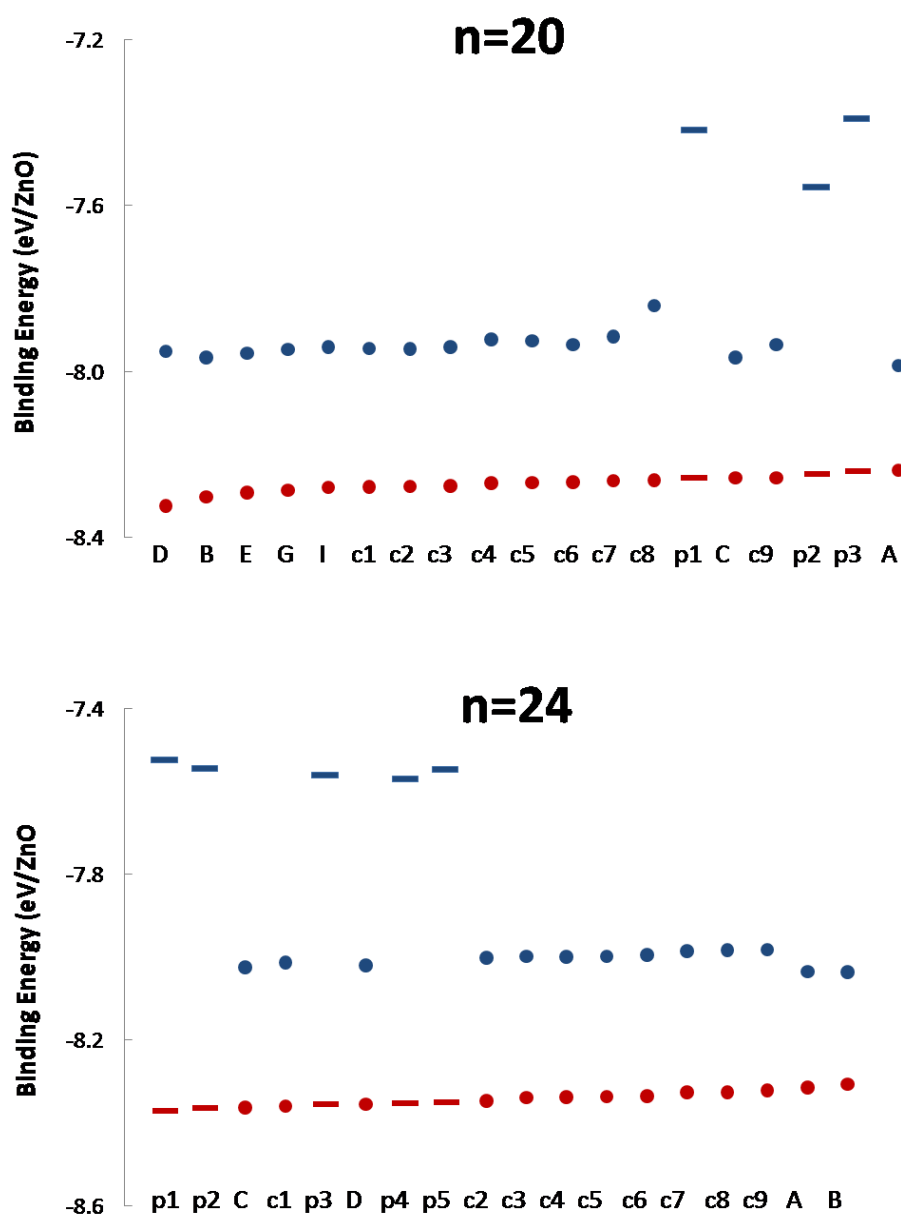


Figure 58. Energy ordering of  $(\text{ZnO})_{20}$  and  $(\text{ZnO})_{24}$  nanoclusters on Ag(111) surface (red). Blue colored symbols are corresponding energies in freespace. 2D planar structures are represented by bars whereas 3D cluster structures are represented by filled circles.

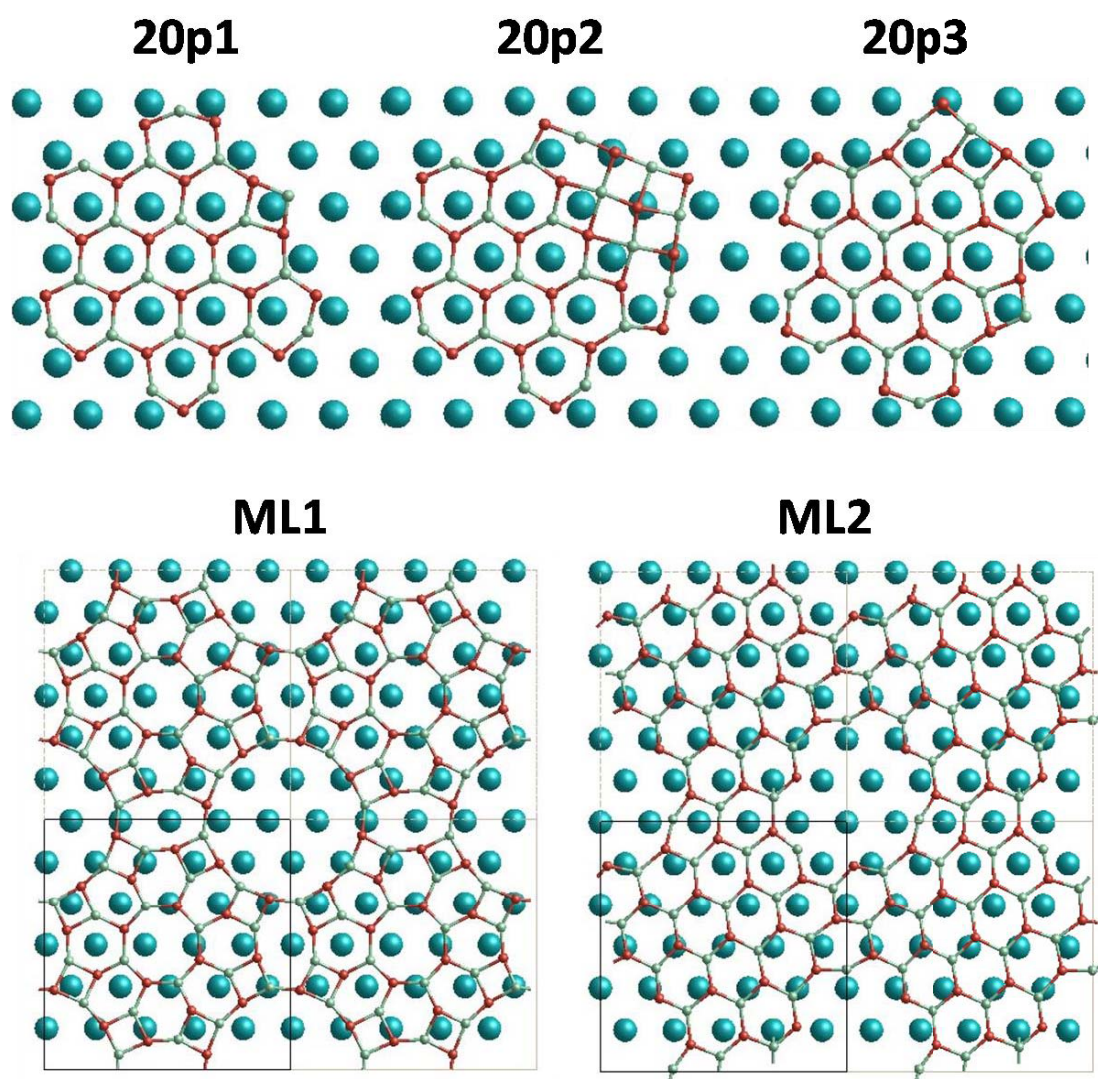


Figure 59. Top views of  $n = 20$  2D ZnO structures on Ag(111) surface.

For the size  $n = 24$ , again the ranks of the 2 lowest energy free space clusters deteriorated drastically on the surface, 24A becomes the 17<sup>th</sup> and 24B becomes 18<sup>th</sup> with the stabilization energies of 0.28 and 0.27 eV/ZnO, respectively, while all the other 3D clusters stabilized by 0.33-0.34 eV/ZnO. Like in the case of  $(\text{ZnO})_{20}$ , all the 3D clusters except 24A and 24B were found to adopt an ellipsoid bubble morphology, and the lowest energy 3D cluster, 24C, can be seen again as an inflated two layered structure, which has faces formed by adjacent hexagonal rings. For  $(\text{ZnO})_{24}$ , planar 2D structures closely surpassed the ellipsoidal bubbles in general, having 0.80-0.85 eV/ZnO stabilization energies. Planar 24p1 and 24p2 structures become 1<sup>st</sup> and 2<sup>nd</sup> lowest energy

structures on the surface, which are only 0.008 and 0.001 eV/ZnO more stable than the 3<sup>rd</sup> lowest energy structure on the surface, 24C, respectively. Global optimization generated three more planar structures, which are closely related. All the planar structures have a hexagonal core, which is surrounded by other sized rings as can be seen in Figure 60.

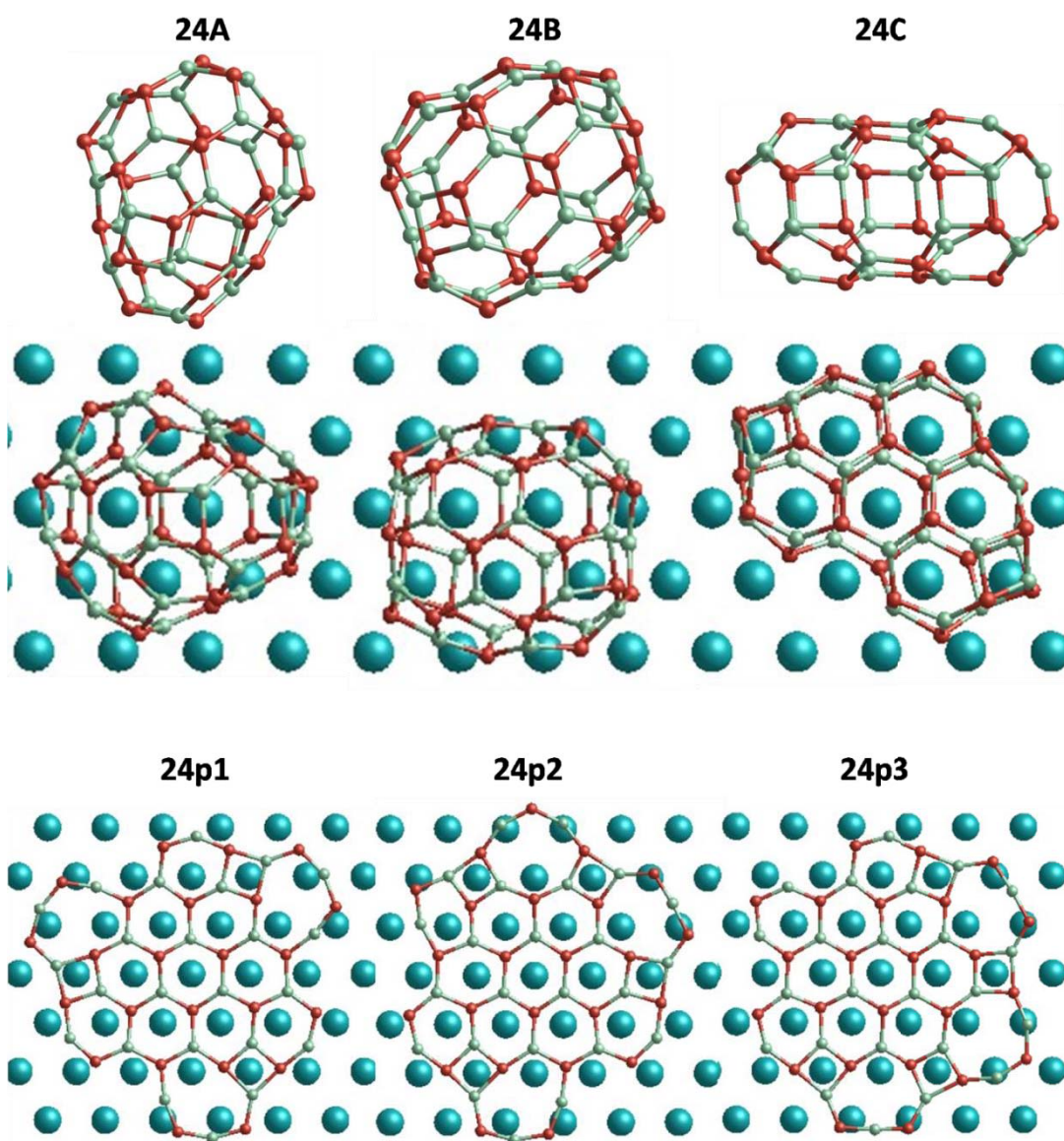


Figure 60.  $(\text{ZnO})_{24}$  structures: (a) 3D clusters in free space and on support, (b) 2D clusters on support.

### 3.2.7 General overview

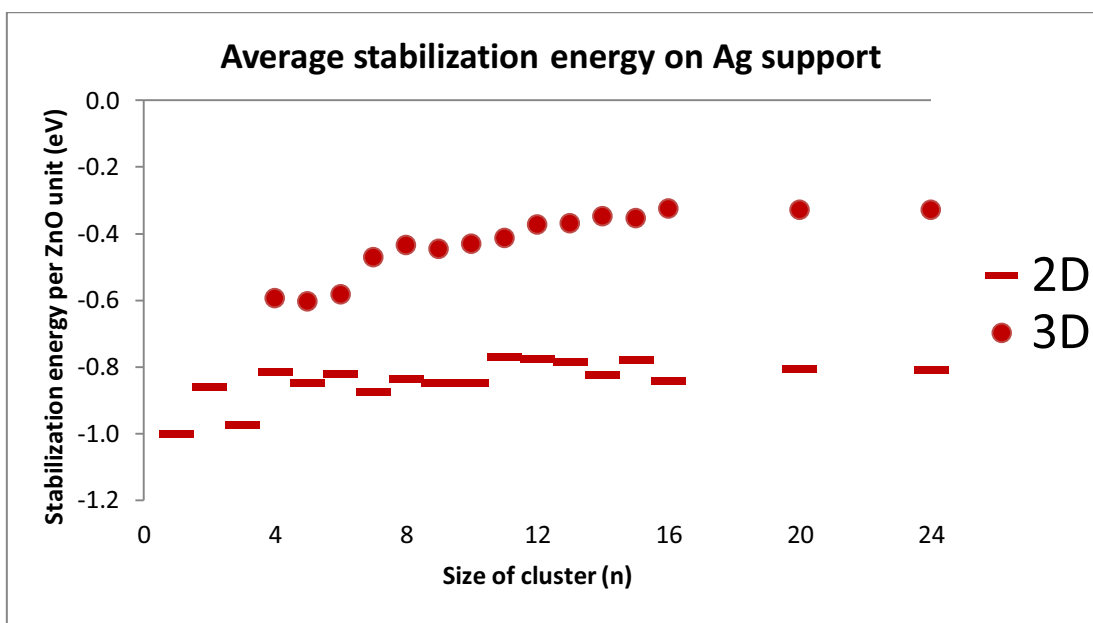


Figure 61. Average stabilization energies for 3D and planar structures on Ag support.

In Figure 61, the average stabilization energies for 3D and 2D structures on Ag support are given. For planar structures, the stabilization energy typically remains constant as the size increases, as all the atoms are binding to the surface, except for the single stick and the hexagonal ring. The single stick and the hexagonal ring are stabilized more because they match relatively well with the surface, however their extensions are not. For 3D clusters, since the fraction of atoms in contact with the surface decreases as the size increases, the stabilization energy decreases accordingly. However, as the bubbles grow with the increasing size, ellipsoidal bubbles become more stable on the surface, which preserve the fraction of atoms binding to the surface, and the stabilization energy becomes constant. Because average values are taken over all the clusters of each size, deviations are expected due to both some clusters matching the surface better than the others. Figure 62 shows the binding energies of the best 2D and 3D clusters both in free space and on the surface. In free space, after the size  $n = 5$ , 3D clusters become more stable than planar structures, and the energy difference is increasing as the size increases, so that planar structures cannot compete with the 3D type clusters. However, for supported case, planar structures compete with 3D clusters up to the considered size  $n = 24$ . Due to relatively lower energies of 2D structures in free space as can be seen in

Figure 62, most of the 2D structures are not found in global optimization runs in free space after the cluster size  $n = 8$ , however, they were produced by the reoptimization of the nanoclusters obtained from supported runs. It is also the case up to some extent for quasi-planar structures, which have both 2D and 3D parts, because they fill the energy region between 3D and 2D types in free space, and therefore have higher proportion to show up in the free space global optimization results.

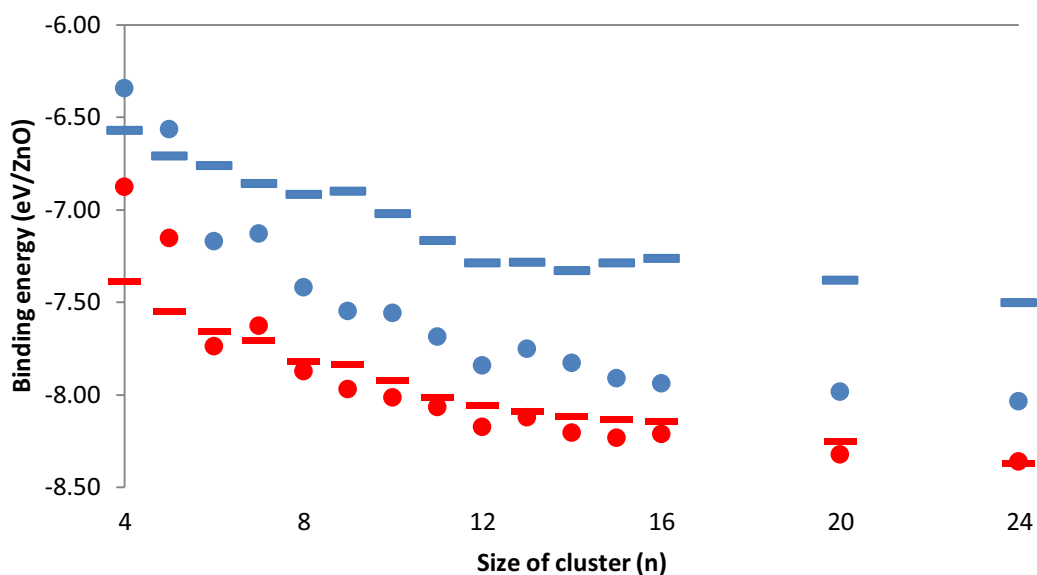


Figure 62. Energies of best 2D and 3D structures in free space and on support with size.

In Figure 63, the relative stabilities of clusters are given as  $E_{rel} = (2E_n - E_{n-1} - E_{n+1})/n$  and the nucleation energies are given as  $E_{nuc} = E_n - (E_{n-1} + E_1)$ . It can be seen from the figure that there is less variation in the relative stability on the surface, apart from size  $n = 3$ , a six-membered ring. The high stability of six-membered ring also leads to the tendency of 3D clusters to align with respect to the surface by a six-membered ring side whenever possible. The drum structure 6A and the sodalite (SOD) cage of 12A are the other relatively stable structures. The drum structure and the sodalite cage are the only structures that have the lower energy per formula unit than any cluster with one additional formula unit. The sodalite cage has also high energy difference of 0.12 eV/ZnO with the second lowest energy structure of the same size, indicating its special stability.

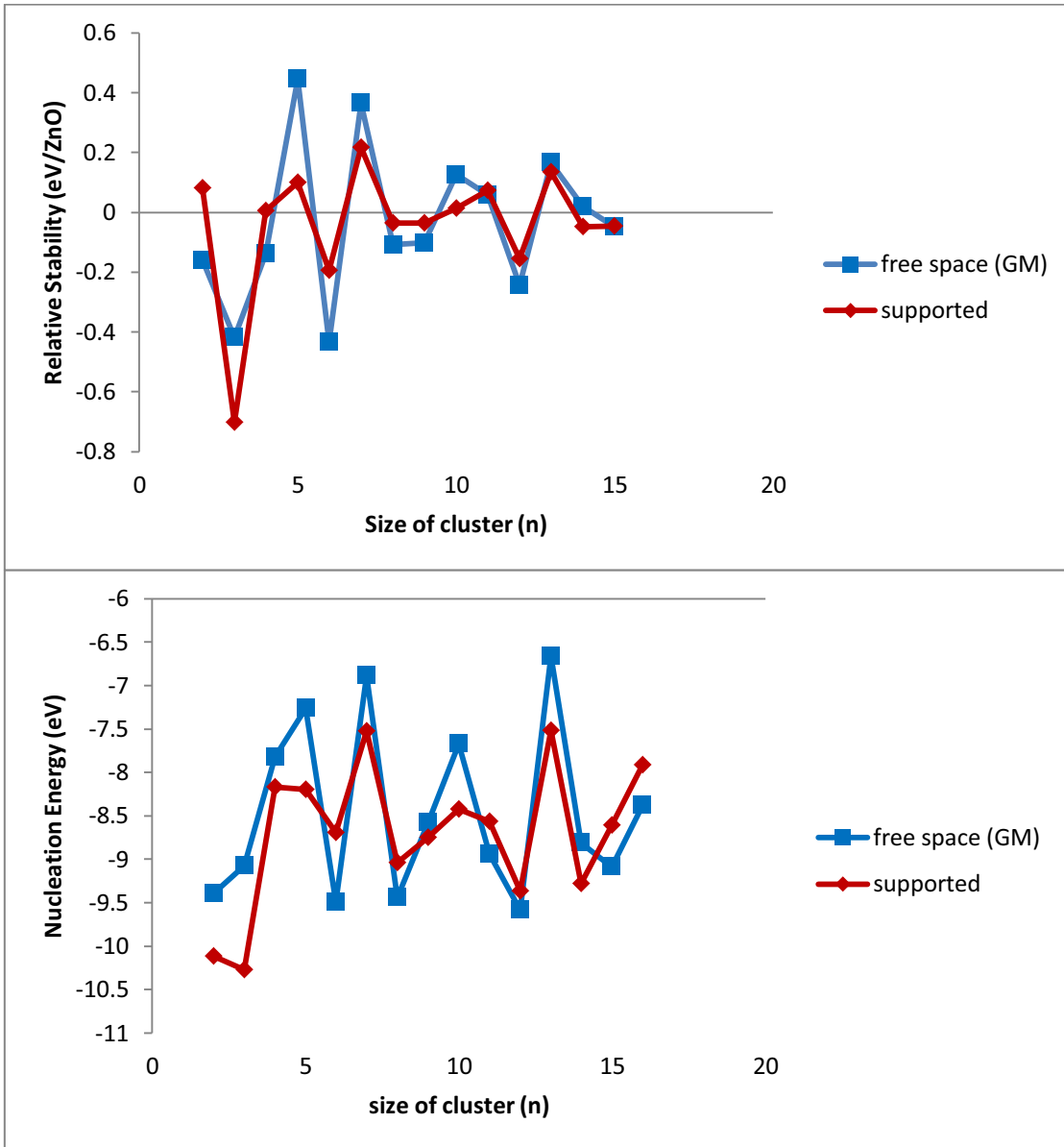


Figure 63. Relative stability and nucleation energy with respect to the cluster size.

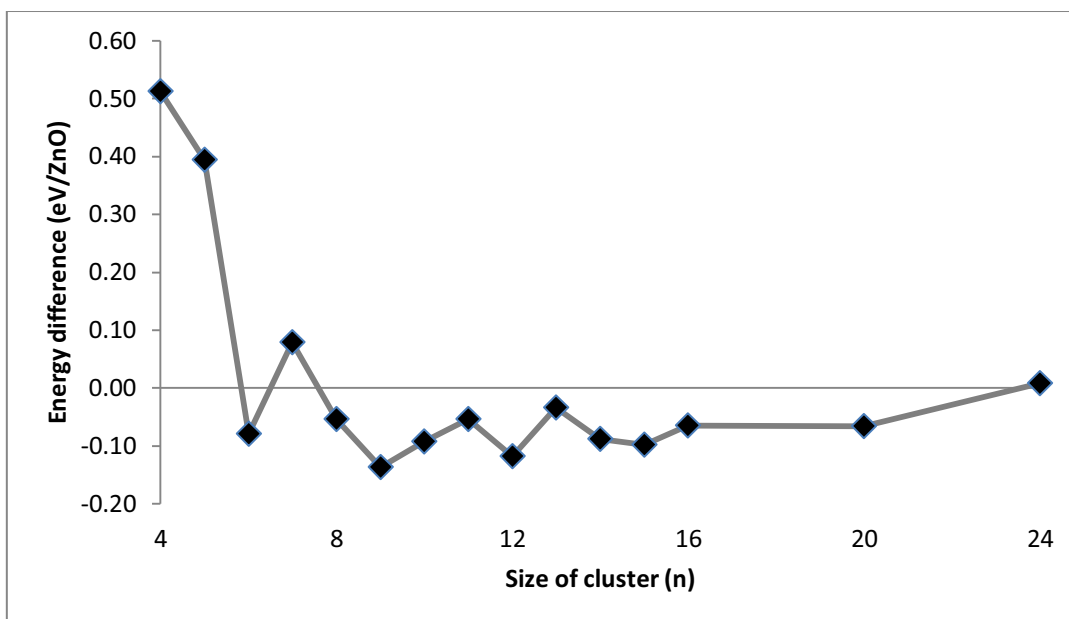


Figure 64. Energy difference of the best 2D and 3D clusters on support with respect to the cluster size. Positive values are where the 2D clusters are more stable than 3D clusters.

Figure 64 shows the energy differences of the best 3D and 2D clusters on support for each cluster size. According to the graph, for sizes  $n = 4, 5$  and  $7$  the 2D structures are preferred on support and the highest stability differences for the 3D structures are for the sizes  $n = 9, 12$  and  $15$ . After size  $n = 8$ , 3D clusters have higher stabilities, however the difference does slightly decrease as the size increases, and the 2D clusters stay within  $0.1 \text{ eV/ZnO}$  up to the considered size  $n = 24$ , where the 2D structures become more stable again. If we consider approaching a monolayer within periodic boundary conditions, where extra bonds will form for 2D structures, we may expect a complete monolayer growth. Indeed, our preliminary global optimization results for cluster sizes  $n = 12-16$  using a smaller unit cell, which allows the 2D structures to see their periodic image, showed that nanosheet structures, which are periodic in one dimension, become lower in energy than the global minimum clusters. These nanosheets mainly consist of four- and six-membered rings. The energy difference even increases in the  $(\text{ZnO})_{20}$  case, in which the periodicity was pronounced in two dimensions. Together with the relative stability of six-membered ring on support, it would be no surprise that a uniform monolayer formation of six-membered rings is possible on the surface of silver as the two are commensurate.

### 3.3. Effect of different surfaces; Ag(100) and Ag(110)

To study the effect of the surface morphology on the cluster adsorption, Ag(100) and Ag(110) surfaces were also studied for selected cluster sizes  $n = 6, 7, 8, 12, 13,$  and  $16$ . Ag(111) surface has a hexagonal surface periodicity, while Ag(100) surface has 4-fold symmetry and Ag(110) exhibit bumpy surface, where some extent of underlying second layer silver atoms are exposed at the surface.

$(\text{ZnO})_6, (\text{ZnO})_7, (\text{ZnO})_8$  The global minima were found to be the same on all three Ag surfaces for the small cluster sizes,  $n = 6, 7$  and  $8$ ; however, ranking varies for other low-energy clusters due to the surface morphology characterized by different stabilization energy trends. The global minimum of  $(\text{ZnO})_6$ , the drum structure (6A), stabilized slightly less on Ag(100) and Ag(110) surfaces, by  $0.48$  and  $0.50$  eV/ZnO respectively, than on Ag(111) surface where on adsorption the stabilization was  $0.57$  eV/ZnO. In general, 2D structures are affected more by the surface morphology. For example the second and third lowest energy structures on Ag(111), 6E and 6D, stabilize by  $0.10$  and  $0.02$  eV/ZnO less on Ag(100) and by  $0.16$  and  $0.12$  eV/ZnO less on Ag(110) surface, respectively. On Ag(100), 6D and 6E switch ranking and 6D becomes lower in energy, as the six-membered rings of the 6E structure do not match this surface periodicity as well as that of Ag(111), in which all the atoms on the rings find hollow positions (see Figure 65). In contrast, the stabilization of the 6D structure was found to be very similar on Ag(100) and Ag(111) surfaces. While the planarity is distorted on Ag(111) as half of the O atoms overlap the on-top positions, it is preserved on Ag(100), where only two Zn atoms match the hollow positions. On the rougher Ag (110) surface, the planarity of both 6D and 6E structures is distorted, and they are stabilized less than on the other surfaces, while another 3D cluster fitting the rough surface well, 6B, surpasses both and becomes the second lowest energy structure. Similarly 6H and 6I structures also fit the surface rows on Ag(110) and thus stabilizes more than in the Ag(111) case (see Figure 66). Also one 2D cluster, 6U, stabilizes more on the rough surface where the chains of atoms fit well to the surface rows.

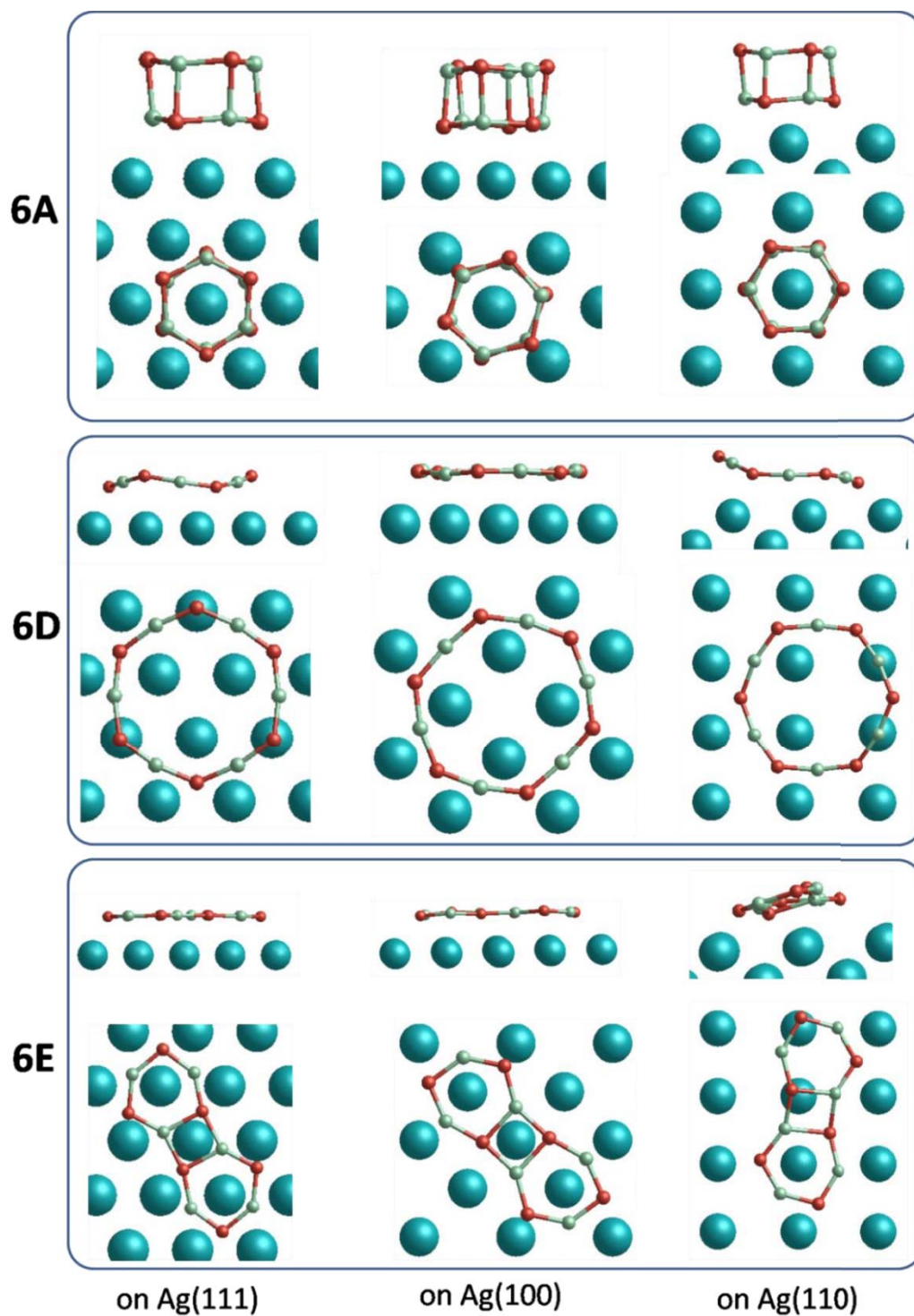


Figure 65. Top and side views of 6A, 6D and 6E clusters on Ag(111), Ag(100) and Ag(110) surfaces.

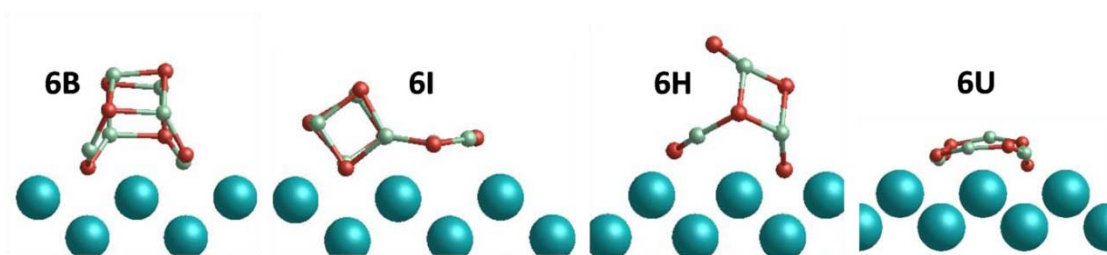


Figure 66. Side views of 6B, 6I, 6H, and 6U clusters on Ag(110) surface.

For size  $n = 7$ , planar 7i structure was found to be the global minimum on all three surfaces, however the stabilization energies on Ag(100) and Ag(110) was found to be 0.06 and 0.05 eV/ZnO less than on Ag(111). On the Ag(111) surface, five out of six lowest-energy structures found were 2D structures, however due to a weaker stabilization of 2D clusters, three/two remains in the six lowest energy structures on Ag(100)/Ag(110) surface. For 3D clusters, even more stabilization was observed on Ag(110) surface because of the open edges fitting the rough surface like in the  $(\text{ZnO})_6$  case. On Ag(100), 7B is the only 3D cluster, which is stabilized more than on Ag(111) surface. In the 7B case, two closest atoms to the surface are situated in hollow positions, while the six-membered ring at the interface between the cluster and the surface is stabilized around an on-top site.

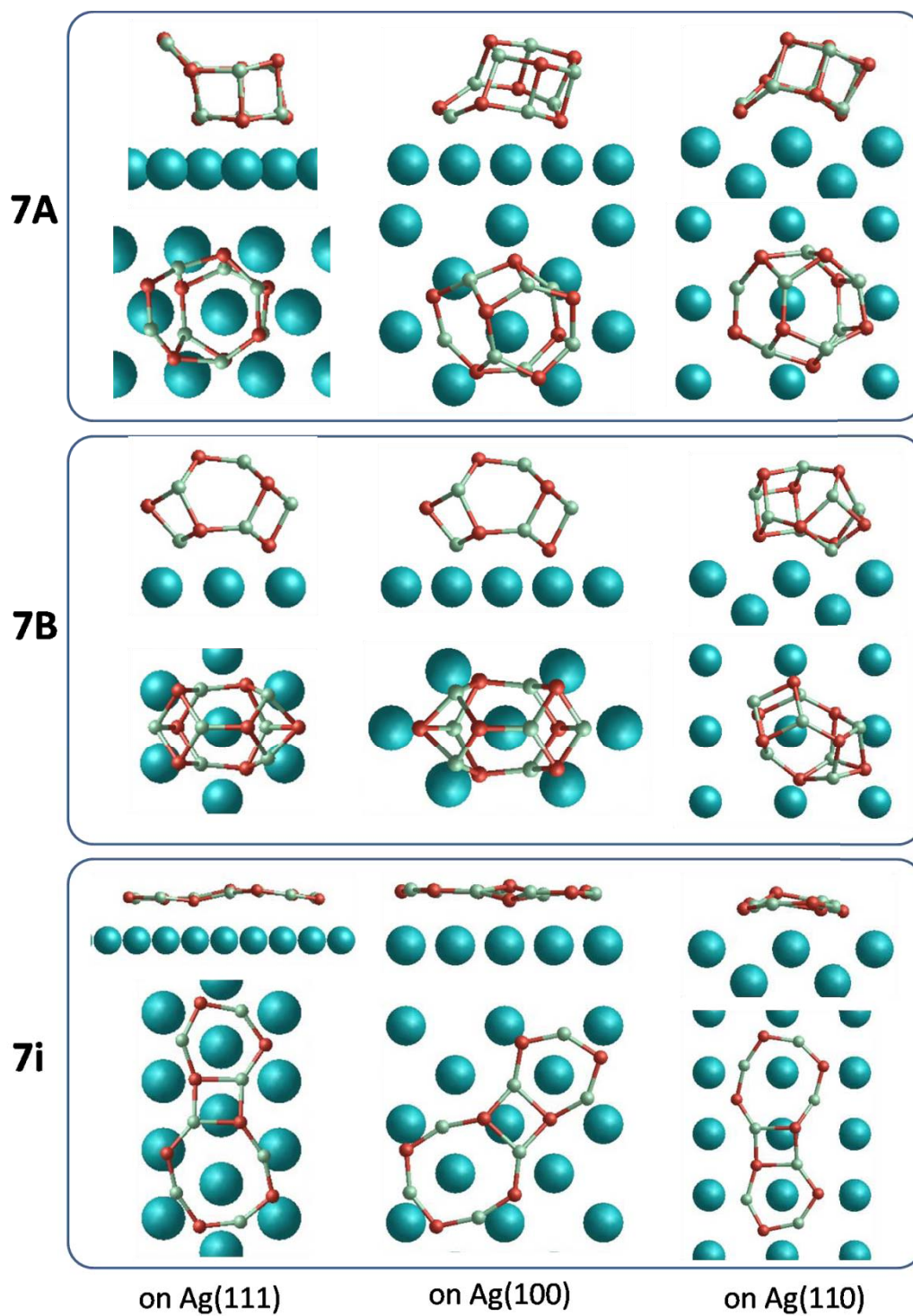


Figure 67. Top and side views of 7A, 7B and 7i clusters on Ag(111), Ag(100) and Ag(110) surfaces.

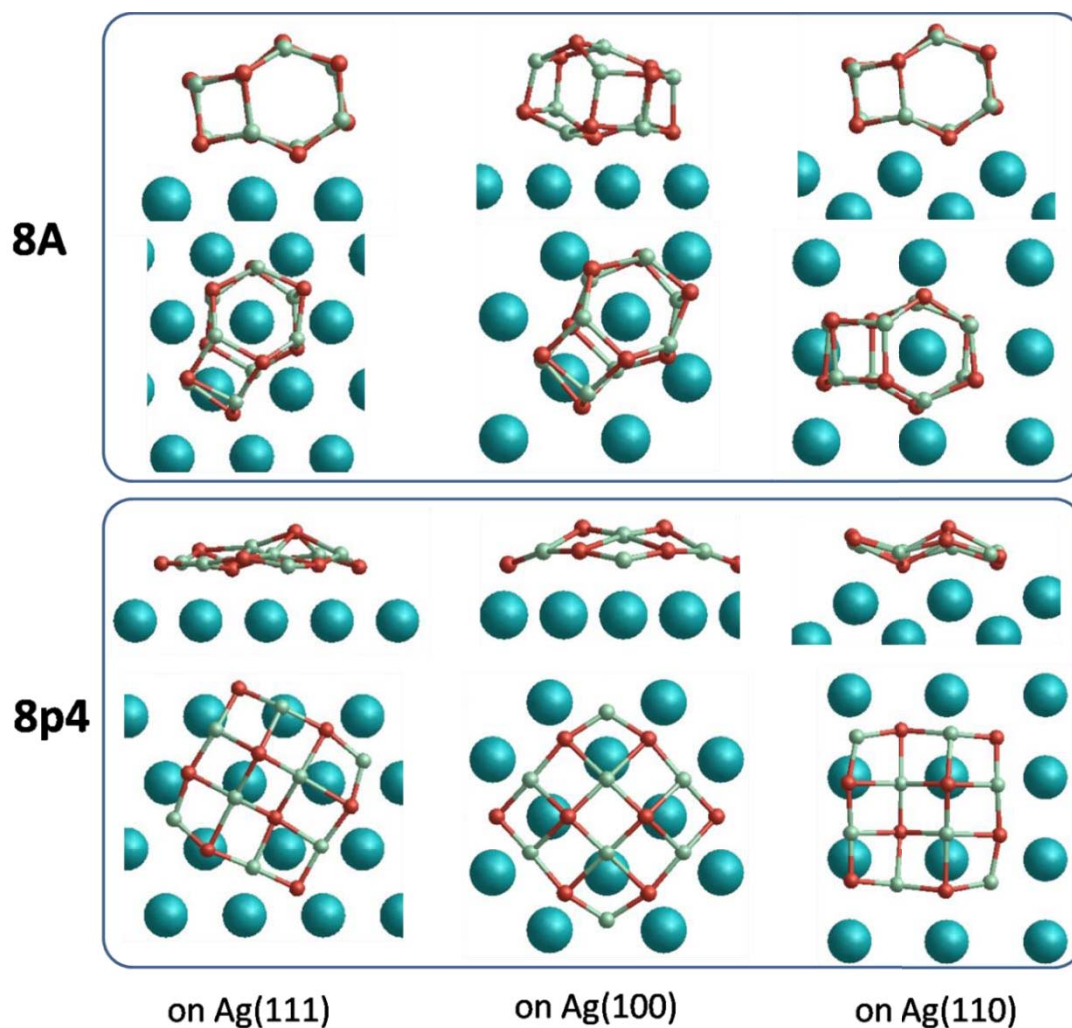


Figure 68. Top and side views of 8A and 8p4 clusters on Ag(111), Ag(100) and Ag(110) surfaces.

For  $(\text{ZnO})_8$ , all the different types of clusters except for 8p4 stabilized less on the Ag(100) surface. 2D clusters are being affected most and the 3D clusters affected least in general. As shown in Figure 68, 8p4 is a one-layered rocksalt template, which has a four-fold symmetry like Ag(100) surface, and its ranking was found to be increased from 16<sup>th</sup> to 9<sup>th</sup>. On Ag(100) surface, the edge atoms of 8p4 coincide with the hollow positions, and the planarity is distorted as the internal atoms move outward to the surface. 8p4 stabilizes even more on the Ag(110) surface, where the rows of the rocksalt template follow the rough surface by assuming a zigzag shape, however, its ranking increased only to 11<sup>th</sup>. On the Ag(110) surface, the 3D clusters, which fit the surface rows, are stabilized even more, and their rankings are changed drastically, while the rest are affected less and stabilized slightly less than on Ag(111).

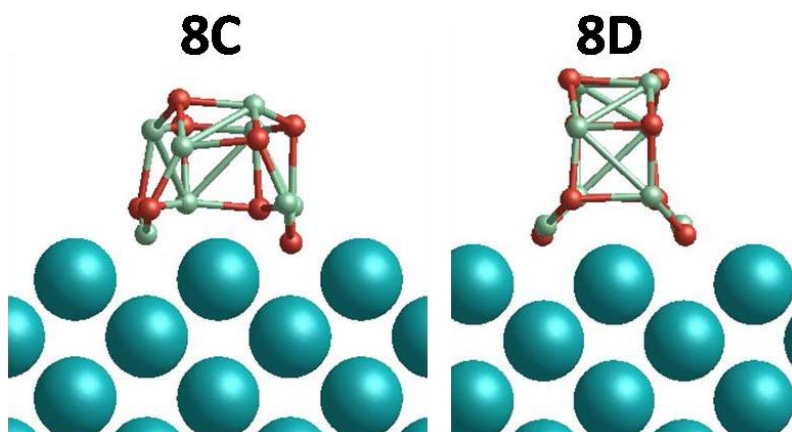


Figure 69. Side views of 8C and 8D clusters on Ag(110) surface.

For example 8C and 8D clusters have 0.10 and 0.07 eV/ZnO higher stabilization energies than on the Ag(111) surface, and this extra stabilization changed their ranking drastically where 8C even becomes the second lowest energy, structure and 8D surpasses 10 structures on Ag(110).

$(\text{ZnO})_{12}$ ,  $(\text{ZnO})_{13}$ ,  $(\text{ZnO})_{16}$  As the size increases, the difference in the stabilization energies on different surfaces of Ag does not change significantly both for 3D and 2D cluster types (see Figure 70). However, the ranking of 2D clusters drops drastically on Ag(100) and on Ag(110) surfaces for the larger sizes,  $(\text{ZnO})_{12}$  and  $(\text{ZnO})_{13}$ , because of the relative stabilities of 3D clusters to 2D ones in free space increases with the size. Thus, for the largest size we considered,  $(\text{ZnO})_{16}$ , all of the 2D clusters are higher in energy than the 3D clusters on Ag(100) and on Ag(110) surfaces.

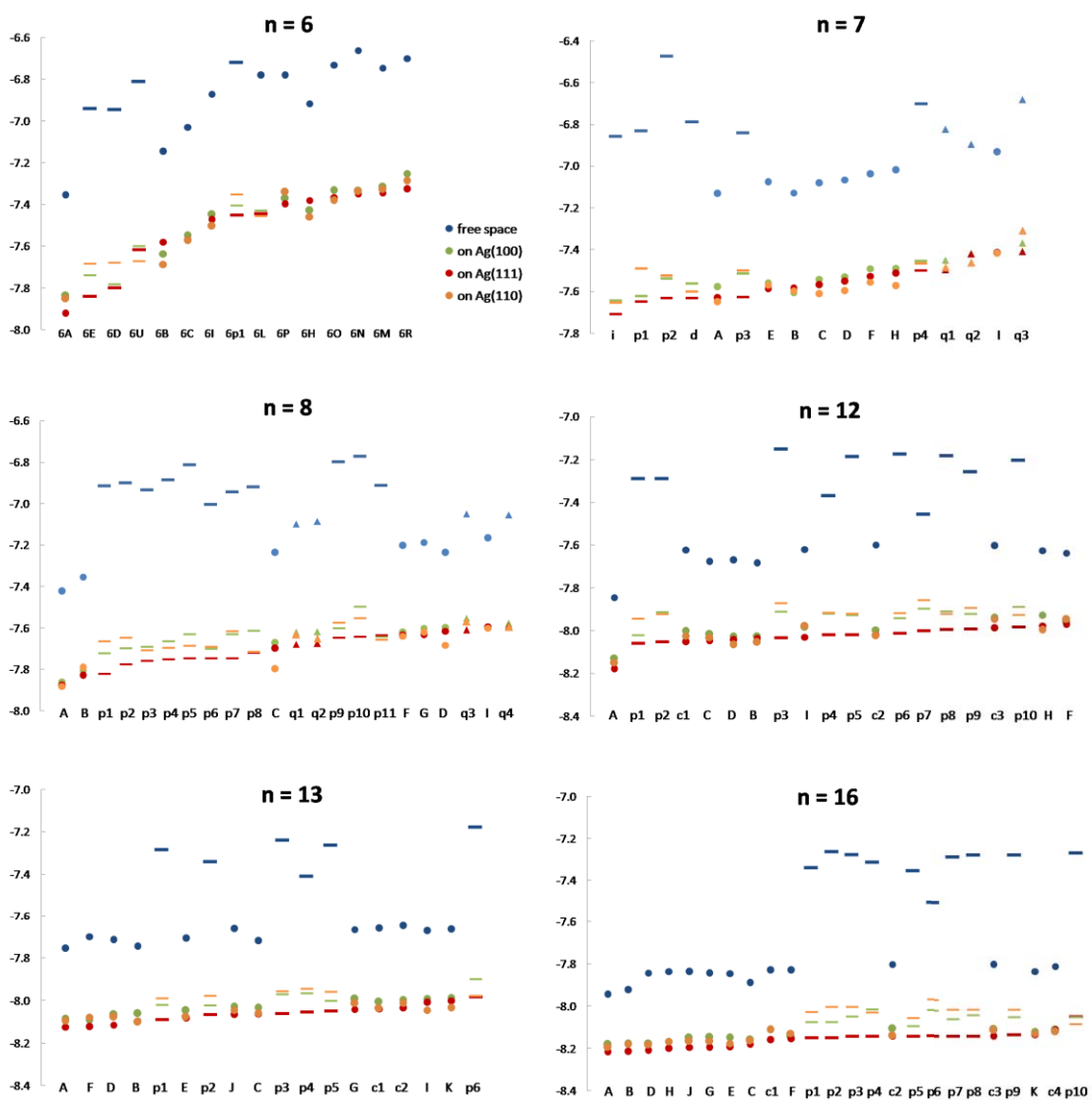


Figure 70. Binding energies of low-energy clusters for the selected sizes both in free space and on different Ag surfaces.

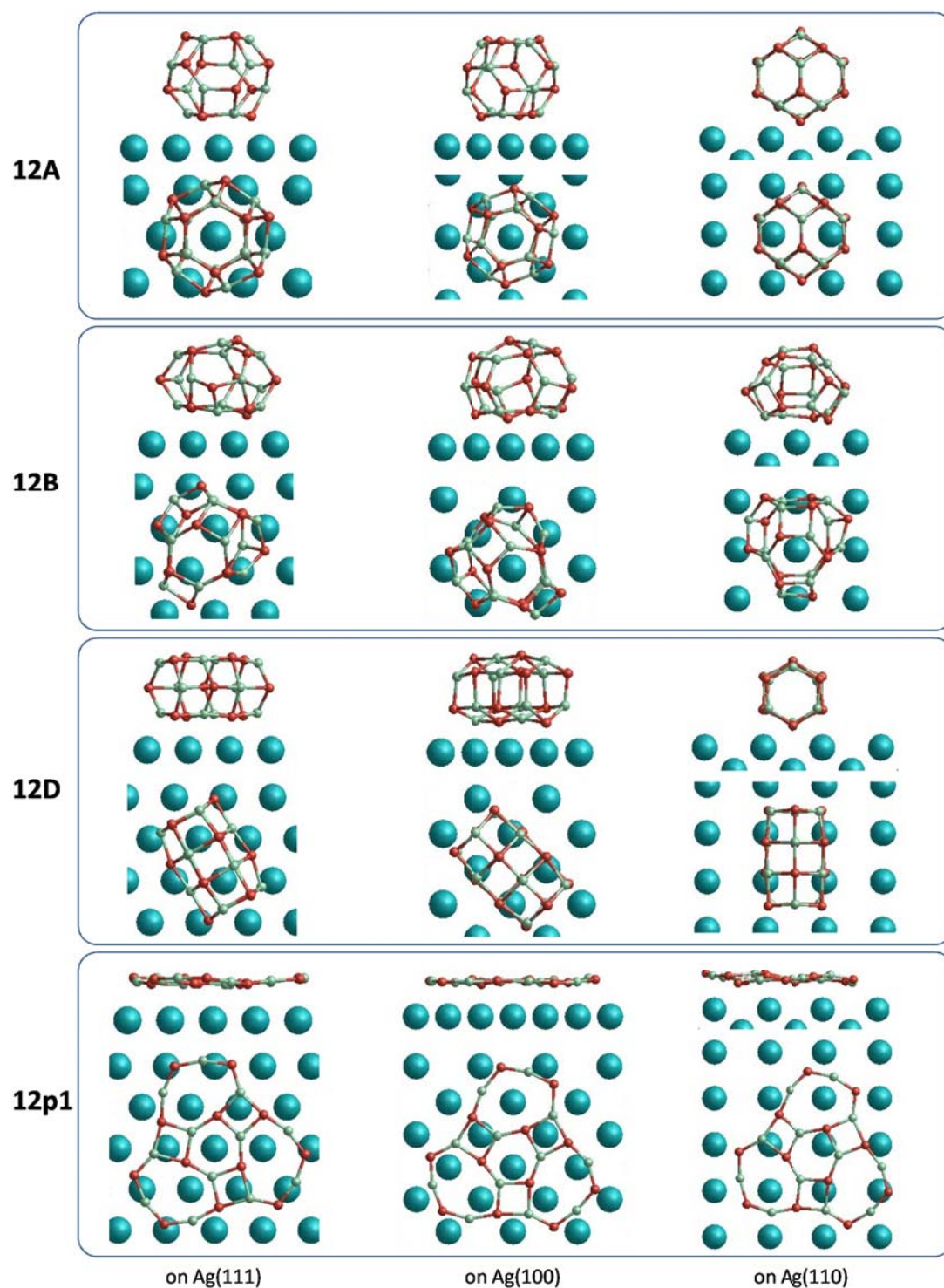


Figure 71. Top and side views of 12A, 12B, 12D, and 12p1 clusters on Ag(111), Ag(100) and Ag(110) surfaces.

For  $(\text{ZnO})_{12}$ , the highlighted sodalite cage, 12A, remained the global minimum by far for all surfaces due to its pronounced high stability in free space. 12A was stabilized more on Ag(111) surface, on which it is adsorbed via a six-membered ring matching the

hexagonal surface periodicity, and stabilized least (+0.05 eV/ZnO) on Ag(100), where the contact atoms of the hexagonal face of 12A do not match the hollow positions anymore. On Ag(110) surface, 12A cluster falls into the surface row from one edge and the stabilization energy decreases by 0.03 eV/ZnO. The lowest energy 2D cluster on Ag(111), 12p1, deteriorates to the 4<sup>th</sup> rank on Ag(100) and 11<sup>th</sup> on Ag(110), whereas the 3D clusters 12D and 12B become 2<sup>nd</sup> and 3<sup>rd</sup>, respectively, on both surfaces. 12D is a barrel, which can be seen as a folded 2D rock-salt sheet, and it fits well on the surface rows on the Ag(110) surface.

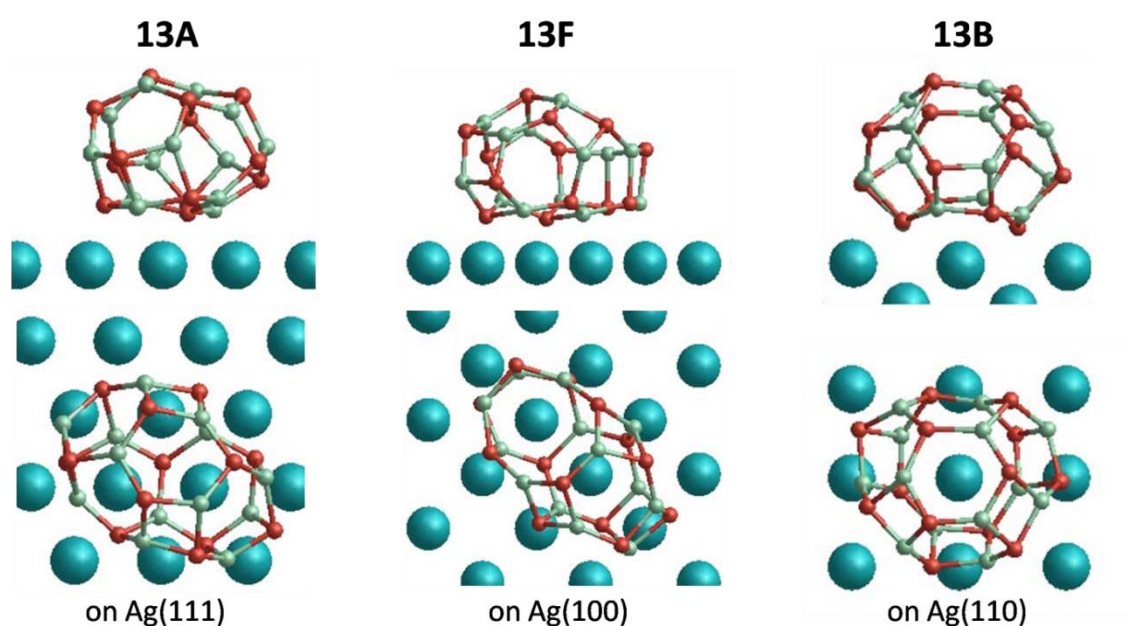


Figure 72. Top and side views of 13A on Ag(111), 13F on Ag(100) and, 13B on Ag(110) surfaces.

For  $(\text{ZnO})_{13}$ , 13p1, which is the lowest energy 2D cluster on Ag(111) surface, decreases its rank by 4 and 8 rungs and becomes 9<sup>th</sup> and 13<sup>th</sup> on Ag(100) and Ag(110) surfaces, respectively. The best four 3D clusters on the Ag(111) surface, 13A, 13F, 13D, and 13B, retained the first four rankings on both surfaces while the global minimum changes and becomes 13F on Ag(100) and 13B on Ag(110). The 13F fits well to the Ag(100) surface morphology where two adjacent six-membered rings match the surface Ag atoms, and the 13B matches the corrugated Ag(110) surface well by enclosing a Ag surface row.

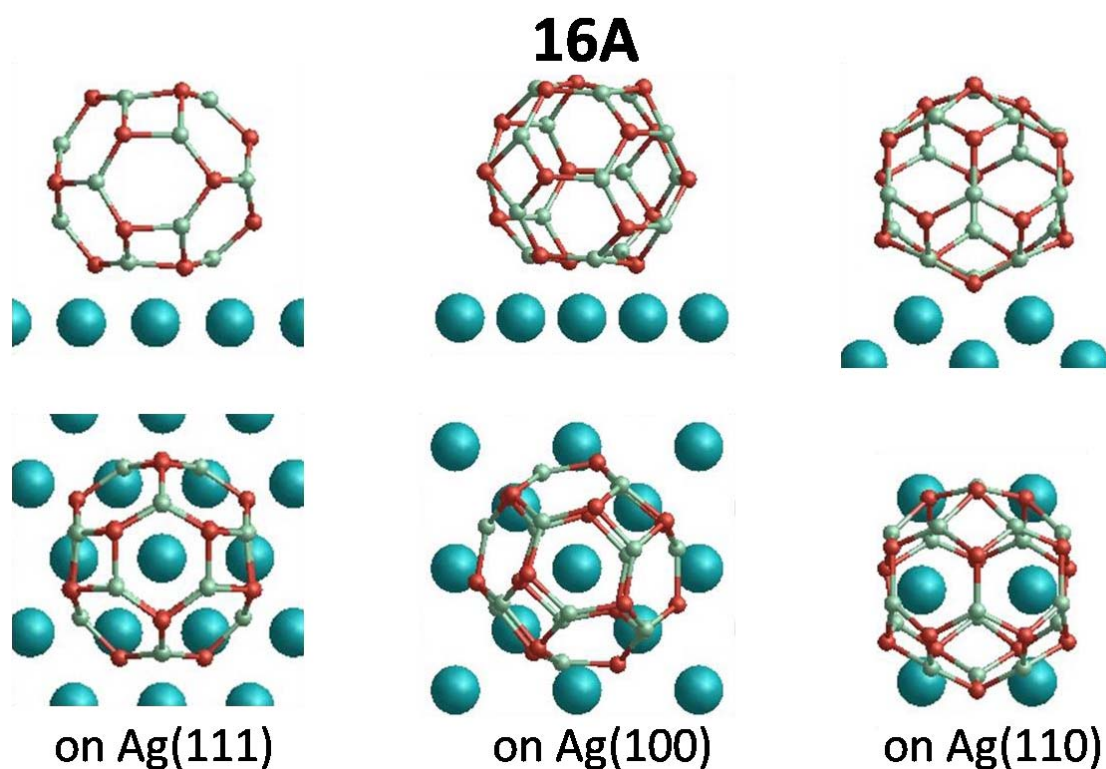


Figure 73. Top and side views of 16A cluster on Ag(111), Ag(100) and Ag(110) surfaces.

For size  $n = 16$ , 16A was found to be the global minimum on all surfaces, which is another symmetrical cage like 12A following the same stabilization trends. As the cluster size increased, 3D clusters show fewer handles and edges to fit to the Ag(110) surface, thus like on Ag(100) all the clusters on Ag(110) are found less stabilized than on Ag(111). Similarly, as the size increases, 2D islands stabilize less on both surfaces than on Ag(111). The only case where we observed more stabilization for 2D clusters on Ag(100) or Ag(110) surfaces were for the rock-salt sheets like 8p4, which are structures 13p6 and 16p10, and the difference is especially large for the Ag(110) surface, where these clusters assume a zigzag shape matching the surface corrugation of the Ag(110) surface. Nevertheless, the rock-salt sheets do not compete with 3D clusters as they were already not in the range of best twenty clusters on Ag(111) surface being 0.15 eV/ZnO higher in energy because they do not match the hexagonal symmetry of the surface.

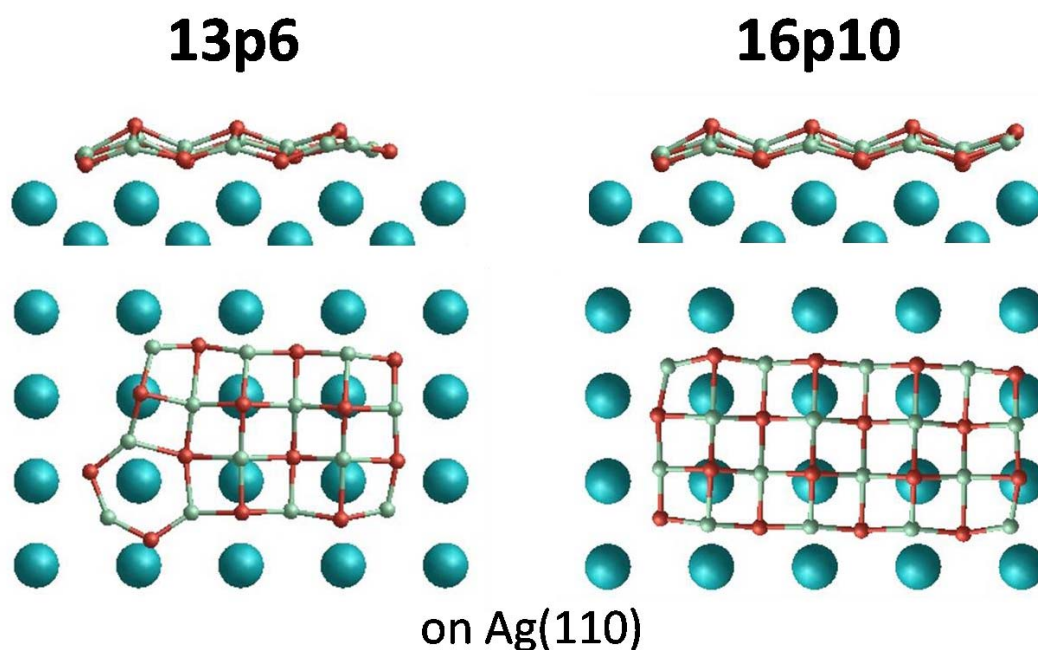


Figure 74. Top and side views of 13p6 and 16p10 clusters on Ag(110) surface.

Although being stabilized much more than the 3D clusters, all 2D clusters now decreased ranks significantly, and more 3D clusters become more stable than most of the 2D structures like 16c2, 16K, 16c3, and 16c4. Note that also for larger sizes, the relatively higher energy 2D clusters on corresponding surfaces were not generated during global optimization runs, but they are produced by the scan algorithms, and thus more 3D clusters are expected and indeed observed which are not characterized if not in the first twelve lowest energy clusters on any of the three different Ag surfaces.

Table 7. The average change of stabilization energy for 2D and 3D clusters from on Ag(111) surface to on Ag(100) and Ag(110) surfaces.

cluster size	on Ag(100)		on Ag(110)	
	2D clusters	3D clusters	2D clusters	3D clusters
n = 6	0.04 eV/ZnO	0.02 eV/ZnO	0.06 eV/ZnO	0.00 eV/ZnO
n = 7	0.05 eV/ZnO	0.02 eV/ZnO	0.03 eV/ZnO	-0.02 eV/ZnO
n = 8	0.06 eV/ZnO	0.02 eV/ZnO	0.05 eV/ZnO	0.02 eV/ZnO
n = 12	0.09 eV/ZnO	0.03 eV/ZnO	0.11 eV/ZnO	0.01 eV/ZnO
n = 13	0.07 eV/ZnO	0.03 eV/ZnO	0.08 eV/ZnO	0.01 eV/ZnO
n = 16	0.07 eV/ZnO	0.03 eV/ZnO	0.10 eV/ZnO	0.02 eV/ZnO

In conclusion, our investigation of cluster adhesion to surfaces of different morphologies using selected cluster sizes showed that the Ag(111) support exhibits more stabilization than Ag(100) and Ag(110) surfaces. In general, 2D clusters are stabilized significantly more than the 3D ones on all different surface morphologies, because they have larger contact areas with the surface. However, to compete with the 3D clusters on the surface, 2D clusters need to overcome the high energy differences in free space, which increase with the cluster size. Although 2D clusters are stabilized significantly more than 3D clusters on Ag(100) and on Ag(110) like on Ag(111), the stabilization differences for these two cluster families become lower on Ag(100) and on Ag(110) surfaces. According to Table 7, 3D clusters are less distorted on the corrugated Ag(110) surface than on Ag(111) in general. Especially clusters with handles, which fit the surface morphology better, become more stabilized compared to Ag(111). On the other hand, the difference with the stabilization energies on Ag(111) is less on the flat Ag(100) surface for 2D clusters, although they are still more affected than 3D clusters and become less favorable.

### 3.4. DFT results

For each cluster size between  $n = 1$  to 16, the best possible clusters were further investigated by means of DFT. The low-energy structures locally optimized with interatomic potentials have been used as starting points in DFT geometry optimization. For the size  $n = 1$  there was only one structure, and for  $n = 2$  and 3 there were ring and stick configurations.

For the simple Zn-O stick, both atoms remained about their hollow site positions., The O atom moved towards the support 0.39 Å with the height of the O atom over the surface plane decreasing to 1.61 Å. The Zn atom moved slightly in the same direction, and the height of the Zn atom is lowered to 2.00 Å from the value of 2.08 Å obtained with interatomic potentials. For sizes  $n = 2$  and 3, while the interatomic potentials gave the ring structure as global minimum both for free space and on the surface, DFT results showed a crossover due to the support. In free space, the linear stick structures are less stable with energy differences of 0.35 and 0.92 eV/ZnO respectively for  $n = 2$  and 3. However on the support the linear stick becomes more

stable with an energy difference of 0.35 eV/ZnO for  $n = 2$  and 0.11 eV/ZnO for  $n = 3$ . These results are also in line with the previous work of Bristowe *et al*<sup>223</sup> where they studied ZnO adsorption on Ag(111) surface for up to three units of ZnO. The four-membered ring becomes more parallel to the surface in the DFT case, where the centre of the ring moves to the on-top position and the O atoms point at the neighboring Ag surface atoms. While the corresponding neighboring Ag atoms move 0.26 Å outwards and the middle Ag surface atom moves 0.36 Å inwards, the other surface atoms displace maximum 0.05 Å. The heights of the ring atoms from the surface plane decreased to 1.92 and 1.95 Å for Zn atoms and 1.97 and 2.04 Å for O atoms. Similar surface distortions have been also observed in the six-membered ring case, where the middle surface atoms moved 0.22 Å inwards while two neighboring Ag surface atoms corresponding to the closing O atoms (see Figure 75) moved 0.09 Å outwards. The remaining Ag surface atoms displaced maximum 0.03 Å from the surface plane. As for stick structures, the clusters retain linear configuration around Zn atoms and bend around O atoms. At the same time, the O atoms overlapping on-top sites of the Ag surface move outwards from the surface.

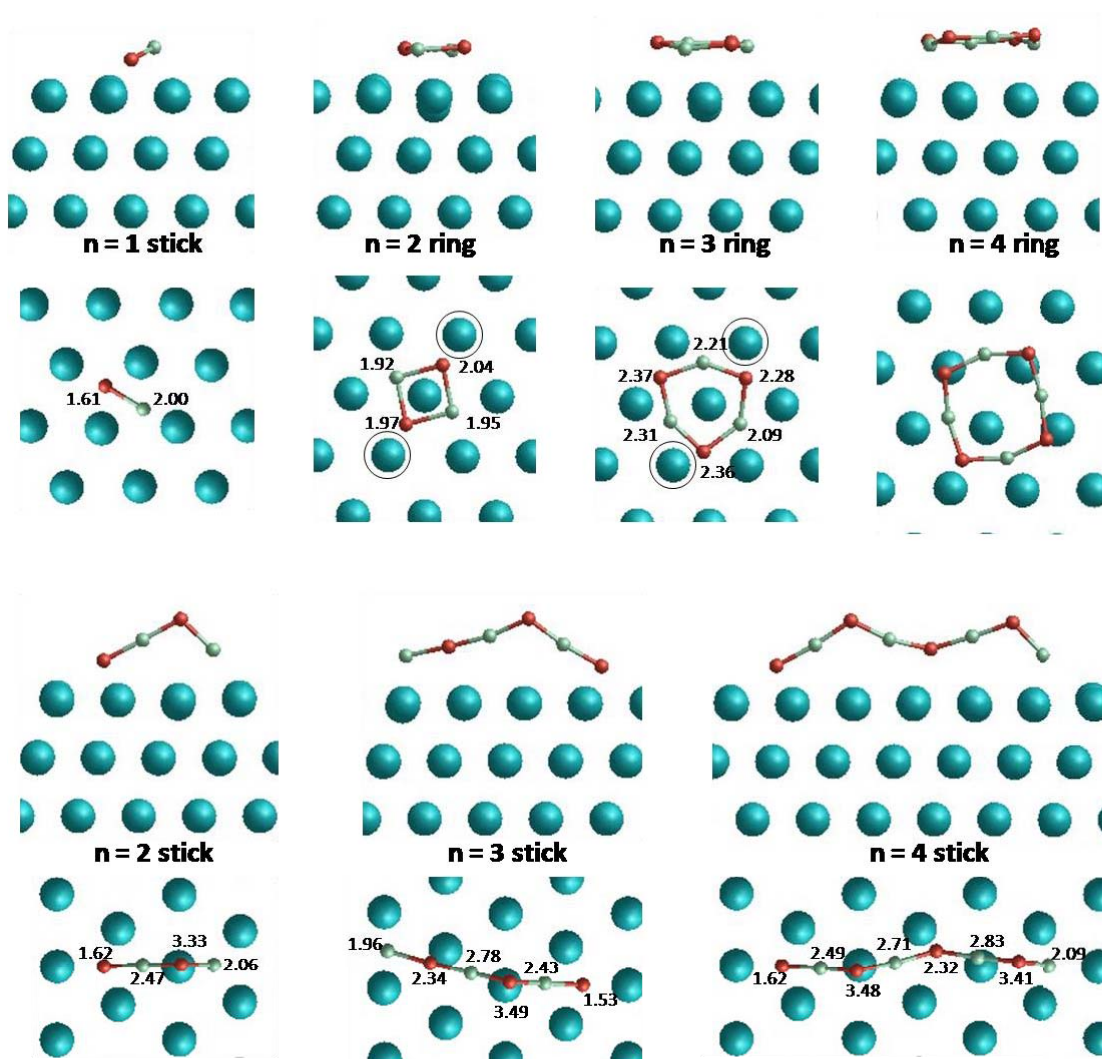


Figure 75. Side and top views of ring and stick structures of sizes  $n = 1$  to  $4$  on Ag(111) surface. Numbers represent the heights from the surface plane for each of the individual Zn and O atoms. Black circles indicate the silver surface atoms, which displaced outwards from the surface plane.

For  $n = 4$  and  $n = 5$ , the ring structures were found to be the global minimum on the surface, like the interatomic potential results. We have also constructed one stick configuration for size  $n = 4$  to compare, which ended up  $0.01$  eV/ZnO higher in energy than the eight-membered ring structure, 4A. Although being close in energy, considering the trend from  $n = 2$ , that the ring structures become more stable while the sticks become less stable as the size increases, no stick structure is expected to be global minimum from this size on. It should be noted that the higher energy candidate clusters of sizes  $n = 4$  to  $n = 9$  were found to undergo a strong reconstruction on the surface, which is mainly attributed to their relative instabilities in free space with respect to the

global minima of the corresponding size. For  $n = 6$ , the ring structure has been found to be the global minimum in free space, surpassing the drum structure, which was the global minimum both in free space and on support using the interatomic potentials. However in supported cluster case, another planar structure, consisting of fused rings, becomes energetically more favorable than the ring structure. Moreover, two other structures also surpass these structures, which are reconstructed structures of higher energy starting clusters selected from interatomic potential results. One of these structures is a distorted planar structure consisting of three joint rings, two six- and one four-membered rings, with an open end Zn atom, which fits the hollow position on the surface. The global minimum structure can be seen as a half bubble, which is the surprisingly stable sodalite cage of size  $n = 12$ . Similarly, for size  $n = 7$ , the global minimum structure on support was found to be one of the reconstructed planar structures, which can be also considered as a nucleated half sodalite cage of  $n = 6$  size from one four-membered ring side. However in free space, the ring structure was found again to be the global minimum, like all the smaller sizes down to  $n = 2$ .

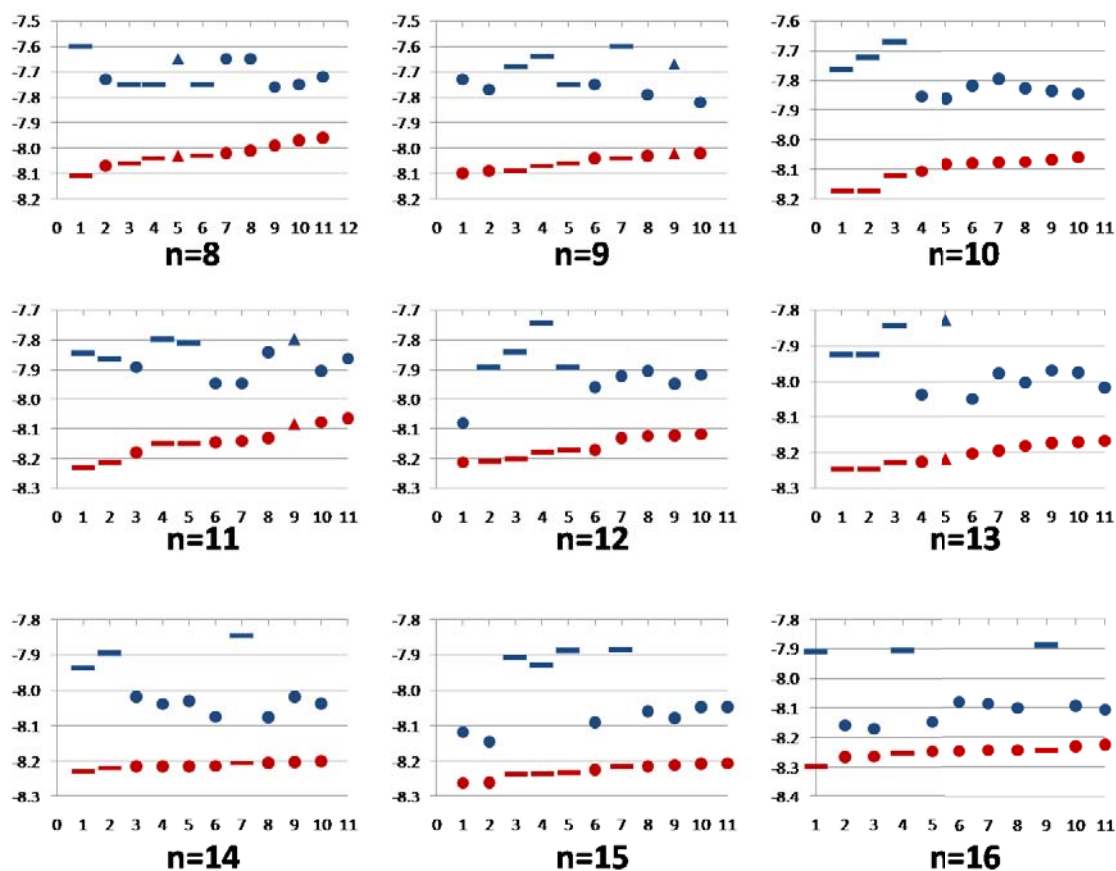


Figure 76. Binding energies of low-energy clusters calculated with DFT for the selected sizes both in free space and on Ag(111) surface.

For the size  $n = 8$ , the global minimum in free space was found to be the same as with the interatomic potentials, which is the first bubble cluster that becomes the global minimum in free space with density functional theory. Considering cluster size increase, from this size on the bubble structures become global minima in free space up to the largest considered size  $n = 16$  considered. For this size interval of  $n = 8$  to 16, clusters 9A, 10A, 10A, 12A, 15A and 16A were the global minima structures using both interatomic potentials and density functional theory. For sizes  $n = 8$  and 14, the second lowest energy structures at the interatomic potential level, 8B and 14B, become global minima, while for size  $n = 13$ , the global minimum is the third lowest energy structure from interatomic potentials.

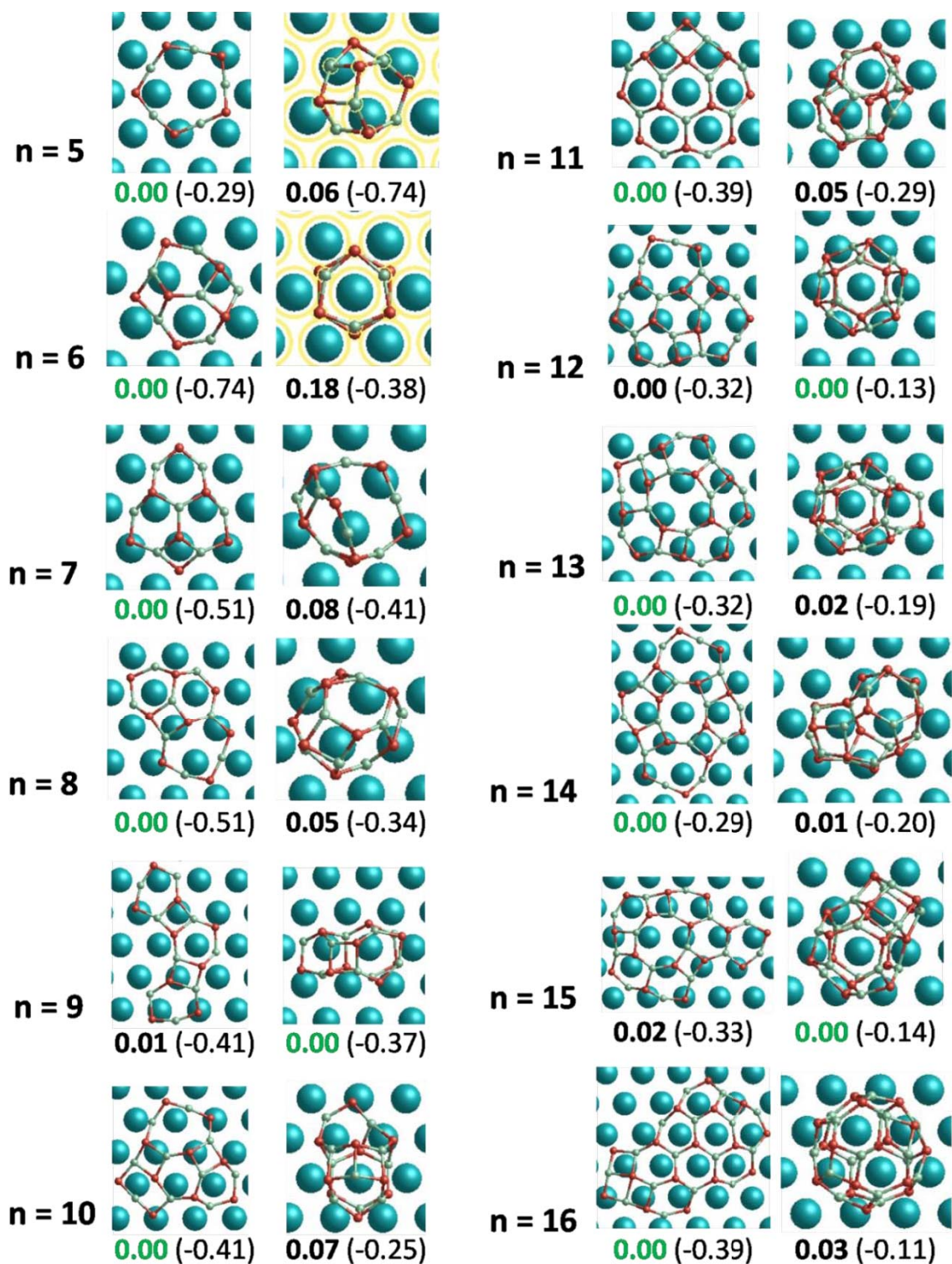


Figure 77. Structures and energetics of the lowest energy 2D and 3D  $(\text{ZnO})_n$  nanoclusters on Ag(111) support. Relative energies are given under the structures and the stabilization energies due to support are given in paranthesis.

Following our conclusions from the work using interatomic potentials, that the 2D structures stabilize and come into the range of stable clusters with the presence of

support, we have also calculated for each size the best three 2D structures with DFT. The same effect holds in density functional theory, as higher stabilization energies were observed for 2D structures on the surface than for the 3D structures. However, a clear separation of the stabilization energies between 2D and 3D clusters could be observed after size  $n = 10$ . It also concurs with the stabilities up to higher sizes of the 2D structures in free space from the DFT results, where the global minima are ring structures up to size  $n = 7$  and the energy difference of the best 2D and 3D clusters lies within 0.1 eV/ZnO up to size  $n = 12$ . Considering the DFT results for the supported nanoclusters, the competition between 2D and 3D clusters is found to be in favor of 2D clusters for most of the sizes, unlike the interatomic potential results. For sizes  $n = 9$ , 12 and 15, the 3D clusters are found to be global minima, from which the only size that has the same global minimum structure for both in free space and on support is the  $n = 12$  with the well-known sodalite cage structure. Recall also that with the interatomic potentials these three sizes had the largest energy difference between the best 3D and 2D clusters. In Figure 78 it can be seen that for the free space case, the sodalite cage is exceptionally stable, where it has a lower energy per formula unit than the global minima of the one and two ZnO unit bigger clusters. The lowest energy 2D cluster at this size has 0.19 eV/ZnO energy difference with the sodalite cage in free space, however the energy difference drops below 0.01 eV/ZnO in the supported case. Similarly, the closest lowest energy 3D cluster has also 0.13 eV/ZnO energy difference, however the stabilization on support is similar to and the energy difference remains as “high” as 0.09 eV/ZnO with the sodalite cage. In Figure 80 it can be seen both from relative stabilities and nucleation energy graphs that  $n = 9$  and  $n = 12$  sizes have higher stability in free space with respect to other sizes, however the situation changes in the supported case, where the other sizes have 2D global minima. For sizes  $n = 9$  and 15, supported global minima structures are different from those in free space and their energy differences are 0.09 and 0.03 eV/ZnO respectively in free space. The stabilization for size  $n = 9$  is stronger as the energy difference becomes again 0.08 eV/ZnO whereas for size  $n = 15$ , they stabilized about equally, and the energy difference is as small as 0.01 eV/ZnO on support. The 2D structures for sizes  $n = 9$  and 15 are again very high in energy with respect to the free space global minima, 0.14 and 0.24 eV/ZnO above 3D structures respectively, whereas they stabilize considerably

more on support and the energy differences decrease to 0.01 and 0.02 eV/ZnO, respectively. For other sizes, where 2D structures are global minima on silver support, the same conclusion holds that the 2D structures stabilize considerably more, as given in Figure 70. In general, the 2D structures have a distorted planarity, where the internal parts, which include three-coordinated atoms, stay higher above the surface than the external two-coordinated atoms.

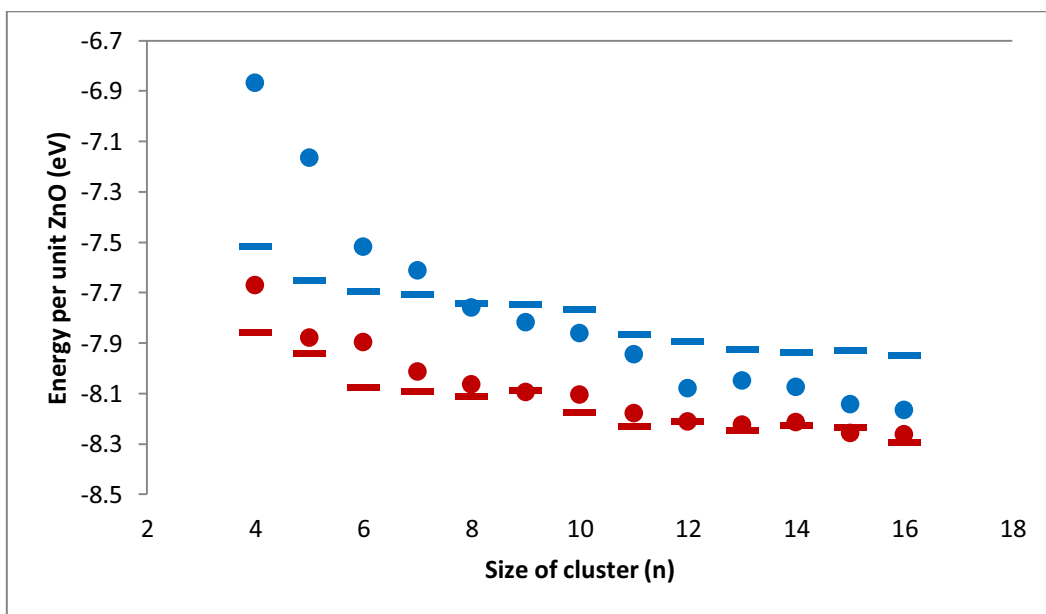


Figure 78. Energetical ordering of free space and supported nanoclusters with respect to cluster size

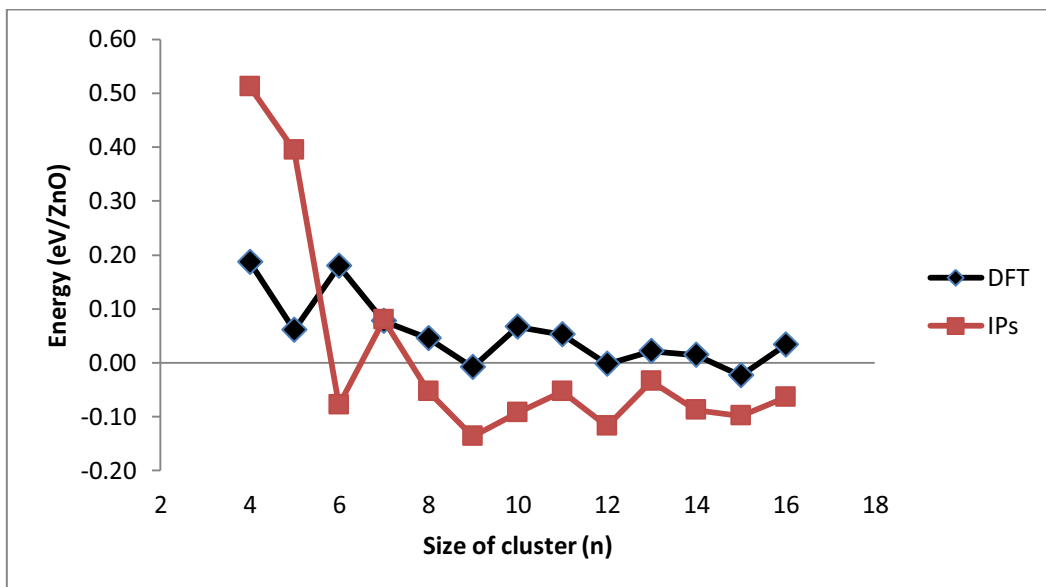


Figure 79. Energy difference of best 2D and 3D clusters with respect to the cluster size. Positive values are where the 2D clusters are more stable than the 3D clusters.

The energy differences between the best 3D and 2D clusters on support are shown in Figure 79 for interatomic potentials and DFT. The curves look very similar after size  $n = 7$ . While 3D structures are more favored in interatomic potential results, the DFT calculations tend to support 2D structures.

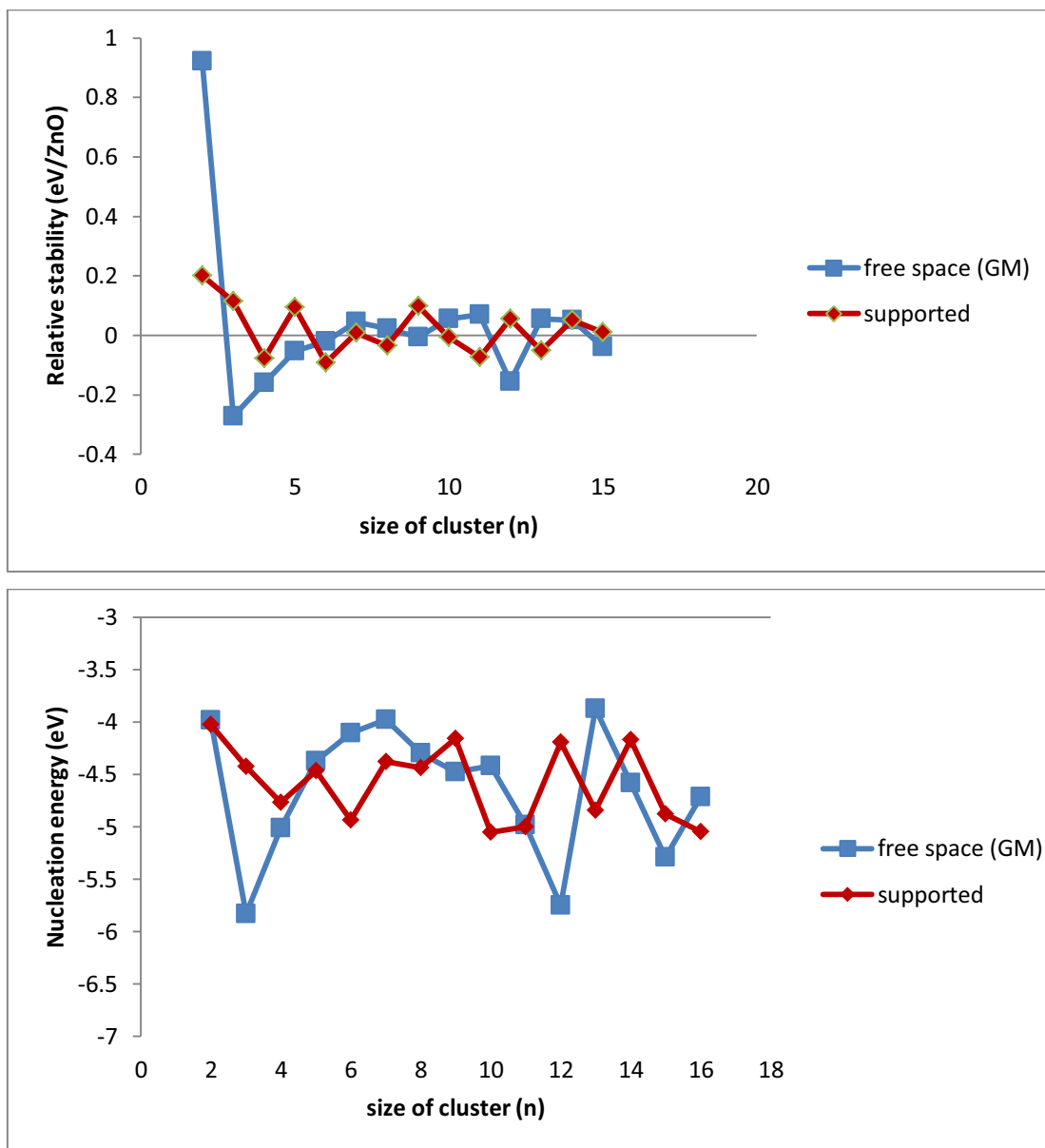


Figure 80. Relative stability and nucleation energy with respect to the cluster size.

The effect of support was also compared for different surfaces of silver at DFT level calculations. Like in the comparison on the Ag(111) support, DFT results show more stabilization for 2D structures as well as even a change in the global minimum on the

support. Heavy reconstructions also happened for some of the structures of the considered sizes of  $n = 6, 7$  and  $8$ . The global minima structures on the Ag(111), Ag(100) and Ag(110) surfaces at considered cluster sizes are given in Figure 81. For  $n = 6$ , Ag (111) and Ag(100) results are the same where a 2D structure is a distorted half sodalite cage, whereas on the corrugated Ag(110) surface the global minimum is another planar structure, which emerged from a dramatic reconstruction of the 6U structure. This structure, with two four-membered rings attached to an eight-membered ring, was not found on the interatomic potential global optimization, probably due to the relatively high energies of the four- and eight-membered rings compared to the six-membered ring. For sizes  $n = 7$  and  $8$ , the global minimum structures were all different on the Ag(111), Ag(100) and Ag(110) surfaces. It should also be noted that like the global minima of size  $n = 6$  case, the global minima of  $n = 7$  and  $8$  also emerged as reconstructed clusters. Thus, different surface symmetries may lead to distinctive reconstructions on cluster structures. For example on Ag(110) surface, two-coordinated Zn atoms has the tendency to fall into empty rows.

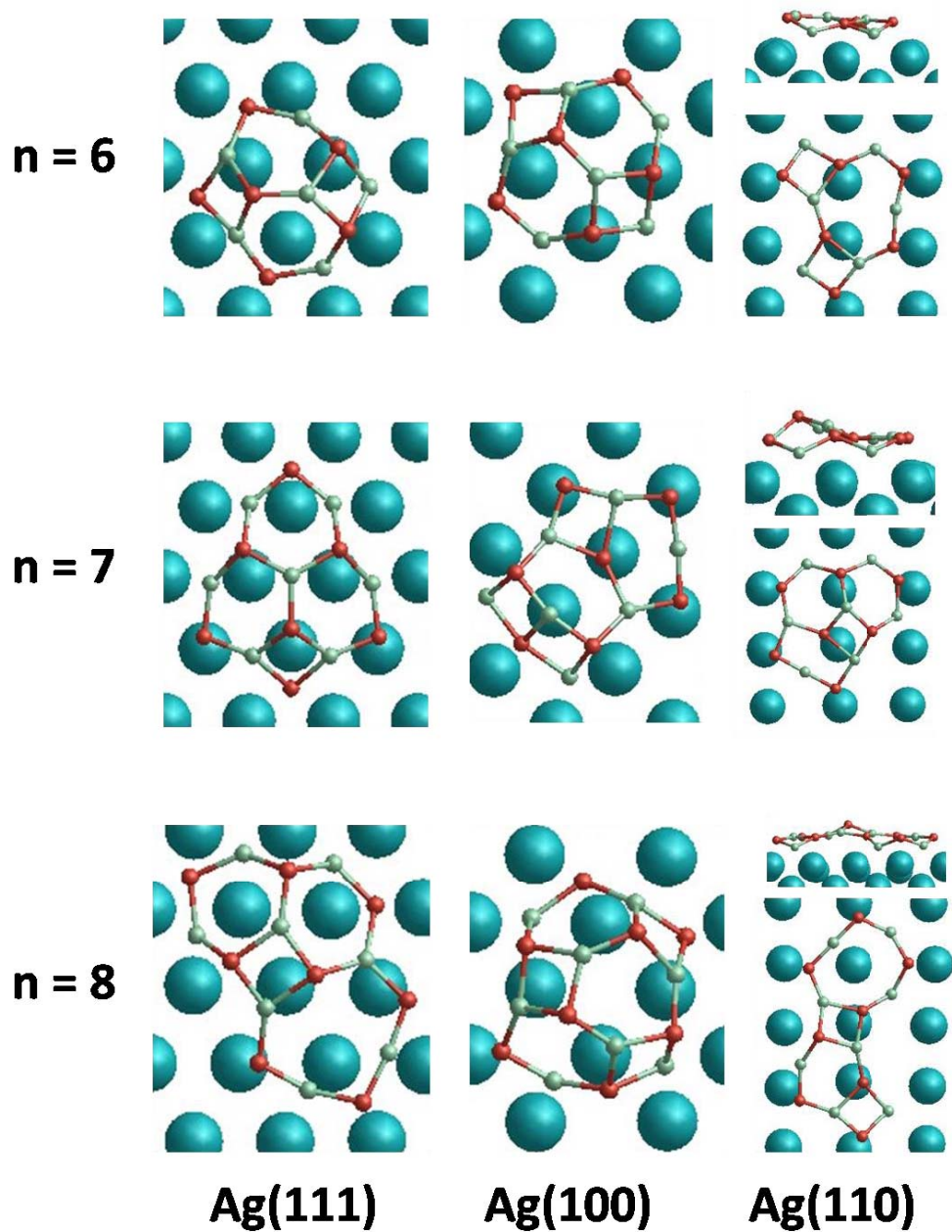


Figure 81. Global minima structures of  $(\text{ZnO})_n$  clusters on Ag(111), Ag(100) and Ag(110) surfaces.

## 5 Conclusions

In this study, we reported the low energy structures of  $(\text{ZnO})_n$  nanoclusters on the Ag supports for sizes  $n = 1-16, 20$  and  $24$ , and compared them with the corresponding free space nanoclusters. We observed that the presence of the support affects the ranking of the nanoclusters on the surface, but more drastically, it also stabilizes selectively 2D type structures, which are not stable in free space, with respect to the 3D clusters after a

certain size. According to our results with interatomic potentials, 2D clusters in free space become considerably higher in energy than the 3D configurations with the increasing size, because of which starting from size  $n = 8$  it is not likely to obtain 2D clusters in a free-space global optimization run. Thus, the presence of the support during the global optimization stage becomes crucial. Although the energy difference between 2D and 3D clusters are found to be lower in free space with DFT results, similar separation of binding energies of these two structural families emerges clearly at higher sizes, starting from  $n = 12$ . With the highlighted extra stabilization, 2D clusters come in the range of first few lowest-energy structures on the support by competing with 3D clusters, both for interatomic potentials and DFT level of theory. The extra stabilization is attributed mainly to the contact area, which is evidently greater for 2D clusters where all the atoms can interact with the surface. Moreover, the contact area determines the rankings of 3D clusters on support, which results in ellipsoid bubbles or inflated double layers being of lower energy on support whereas totally symmetric 3D clusters are more stable in free space. The other determining factor was found to be matching the cluster structure with the surface morphology. The six-membered ring, which is one of the main motifs for both 3D and 2D clusters, matches best the Ag(111) surface because it follows the same six-fold ( $C_6$ ) symmetry (or its subgroup trigonal  $C_3$ , with a three-fold axis, taking into account the distinction between Zn and O atoms). However because of the lattice difference, matching dies away for large extent. For 2D clusters the other flat surface Ag(100) is found to be a better match than the corrugated Ag(110) surface with interatomic potentials, while the 3D clusters can fit the corrugated surface better. To sum up, the preferential stabilities of the 2D structures of ZnO clusters can be seen as the initial stages of thin film growth and found in line with the experimentally observed layered-ZnO sheets on Ag(111) surface.

## **CHAPTER IV: One monolayer ZnO A theoretical study of a ZnO graphene analogue: adsorption on Ag(111) and hydrogen transport**

### **1. Introduction**

The possibility of a two-dimensional (2D) layered phase of zinc oxide (layer-ZnO) was first predicted theoretically by Freeman et al<sup>248</sup> where it was shown that free-standing thinfilms of wurtzite ZnO (wz-ZnO—the most stable ambient bulk phase of ZnO) are less stable than a phase based on 2D-ZnO sheets with a layer ordering analogous to that in hexagonal boron nitride. From these original densityfunctional theory (DFT) calculations thin isolated slabs of layer-ZnO of up to nine or more hexagonal sheets were reported to be energetically more stable than the corresponding c-oriented wz-ZnO slab. More recent DFT calculations by Morgan<sup>249</sup> have shown that the excess stability range of the layer-ZnO phase in isolated thin films is limited to a thickness of four hexagonal sheets, whereupon a bodycentred tetragonal (BCT-ZnO) phase is energetically preferred. For very thin films of one to four sheets, where both the above theoretical results agree upon the energetic preference for layer-ZnO, experiments have indeed prepared layer-ZnO supported on both Ag(111)<sup>250</sup> and Pd(111)<sup>251</sup>. For monolayer coverage, the layer-ZnO can be viewed structurally as a graphene analogue. Detailed calculations confirm that a single unsupported 2D-ZnO sheet has a planar structure<sup>252</sup>. Using DFT and interatomic potentials we investigate the strength of the interaction of a single planar 2D-ZnO sheet with the Ag(111) surface and how this affects the structural properties of the sheet. Building upon previous predictions of multi-centre bond (MCB) assisted hydrogen transport through Zn<sub>3</sub>O<sub>3</sub> hexagonal rings in the sodalite ZnO (SOD-ZnO) system<sup>253</sup>, we also investigate how H atoms interact with a 2D-ZnO sheet when passing through a Zn<sub>3</sub>O<sub>3</sub> aperture.

### **2. Methodology**

We employ three different methodological approaches in our study. Both periodic and cluster DFT calculations were used to calculate structures, energies and electronic states. In addition, we used classical interatomic potentials (IPs) to further study some structural

and energetic properties and trends. For the periodic DFT calculations we used the VASP code<sup>254</sup> employing the generalized gradient approximation (GGA)PW91 functional<sup>255</sup>, where the effect of core electrons on the valence states was described via the projector augmented wave (PAW) approach<sup>256,257</sup>. One-electron valence states were expanded in a plane wave basis up to an energy kinetic cutoff of 500 eV. For the cluster DFT calculations we used the GAMESS-UK<sup>258</sup> code with a combination of the B3LYP hybrid exchange–correlation functional<sup>259</sup> with the all-electron Ahlrichs pVDZ basis set<sup>260</sup>. The periodic classical calculations used the GULP code<sup>261</sup> and employed the ZnOIP by Whitmore et al<sup>262</sup>, an embedded-atom model IP for Ag due to Cleri and Rosato<sup>263</sup> and custom-parametrized IPs for the Ag–Zn and Ag–O interactions. In the latter case we fitted the geometries and energies of a series of periodic DFT calculations of a Zn<sub>6</sub>O<sub>6</sub> cluster interacting with a four-layer thick Ag(111) slab to Buckingham IPs for Ag–O and Ag–Zn. Although these metal–oxide IPs only have a two-body form and neglect an explicit account of polarization effects known to be important in metal–oxide interface interactions (e.g. image forces<sup>264</sup>), it is probable that such interactions (present in the DFT-modelled system) are, to some degree, subsumed in the IP parametrization. Furthermore, and importantly for the current study, due to the manner of their parametrization, they avoid any dependence on incommensurate mismatching between the Ag(111) surface and the 2D-ZnO layer.

In the DFT and IP periodic calculations both minimal 1:1 cell (i.e. with one unit cell of 2D-ZnO supported on one unit cell of Ag(111)) and a 7:8 supercell (i.e. 7 unit cells of 2D-ZnO and 8 unit cells of Ag) were used to describe the ZnO on-Ag(111) system. In the DFT calculations the unit cell case used a 5×5×1 Monkhorst–Pack<sup>265</sup> (MP) grid of *k*-points for the reciprocal space integration, whereas  $\Gamma$ -point integration was considered to be sufficient in the larger 7:8 system. In the case of the IP calculations additional 2D-ZnO:Ag(111) supercells of sizes 5:6, 6:7, 8:9 and 13:15 were also considered. In all Ag-containing calculations the Ag support was represented by a slab of four layers with the bottommost layer fixed to the atomic positions of bulk Ag (taken from a bulk Ag energy minimization at the corresponding level of theory). For the isolated 2D-ZnO sheet calculations the *a* and *b* lattice parameters were fully optimized with no constraints. The binding energies (BEs), calculated using the total energy difference between the combined and separated systems (i.e.  $E[2D\text{-ZnO-on-Ag}(111)] - E[\text{Ag}(111)\text{-slab}]$ )

$-E[2\text{D-ZnO}]$ ), are quoted using two ways of calculating  $E[2\text{D-ZnO}]$ : (i) via unconstrained optimizations of fully relaxed 2D-ZnO sheets and (ii) from optimizations where the 2D-ZnO sheet is constrained to have the same  $a$  and  $b$  lattice parameters as the corresponding Ag slab. Dispersion corrections to the binding energies in the DFT calculation were estimated using the DFT-D2 method due to Grimme<sup>266</sup>. Here the dispersive energy correction was applied to the total optimized ZnO-on-Ag(111) system using a single-point evaluation of parametrized two-body dispersive interaction terms. All periodic calculations used a vacuum separation in the  $c$  direction (i.e. perpendicular to the Ag(111) surface) of 12 Å, which was found to be sufficient to avoid the effects of spurious interactions between repeated images.

For studying the interaction of atomic hydrogen with a  $\text{Zn}_3\text{O}_3$  ring, a  $4\times 4\times 1$  supercell of a single unsupported planar 2D-ZnO sheet consisting of 32 atoms was used in the periodic DFT calculations. In order to obtain the projected density of states (PDOS) and projected charge densities of localized states calculations were done using a  $11\times 11\times 1$  MP mesh of  $k$ -points. In the cluster DFT calculations a finite system consisting of a  $\text{Zn}_3\text{O}_3$  ring with its six nearest-neighbour  $\text{Zn}_3\text{O}_3$  rings (24 atoms in total) was employed. All H transport barriers were computed via constrained energy minimizations (i.e. where the positions of the H atom and one or more 2D-ZnO atoms not in the  $\text{Zn}_3\text{O}_3$  ring were fixed) at points along a line through the centre of a  $\text{Zn}_3\text{O}_3$  ring and perpendicular to the plane of the 2D-ZnO sheet/cluster, until forces were lower than  $0.01\text{ eV \AA}^{-1}$ .

### **3. Results and discussion**

#### **3.1. Interaction of a 2D-ZnO single sheet with Ag(111)**

A summary of relevant distances and energies for the 2D-ZnO-on-Ag(111) system is given in Table 8. For the smallest 1:1 2D-ZnO-on-Ag(111) system the mismatch between the isolated optimized unit cell of the 2D-ZnO sheet and the Ag(111) slab in the  $a$ - $b$  direction is found to be between +12 (DFT) and +14 (IP) per cent. This means that, in order for the 2D-ZnO sheet to be accommodated in the fixed unit cell of the Ag(111) slab, it must be significantly compressed. For this reason the Ag-supported 2D-ZnO sheet in the 1:1 system is significantly buckled away from its energetically favoured planar free-space structure to have all Zn atoms bending inwards towards the Ag surface and the O atoms outwards, together with having relatively reduced Zn–O distances. Comparing this ZnO–Ag combined system with a similarly  $a$ - $b$  constrained system but with the buckled 2D-ZnO sheet far from the Ag(111) surface gives a binding energy of the distorted ZnO sheet with the Ag(111) surface of between 0.39 and 0.94 eV/ZnO, depending on the level of theory employed (see Table 8). Using the energy of the fully optimized 2D-ZnO unit cell (i.e. without the artificial  $a$ - $b$  constraint of the Ag(111) unit cell slab) and of the isolated Ag(111) unit cell slab as reference energies, however, shows that the 1:1 system is unstable to spontaneous ZnO–Ag separation.

Table 8. Energies and relevant distances for the 2D-ZnO-on-Ag(111) system. Column headings correspond to (i) level of theory: IP, DFT or DFT-D2, (ii) model: ratio of ZnO to Ag unit cells used, ((iii)–(iv))  $a_x$ : lattice parameter of isolated optimized subsystem (Å), (v) ratio of  $a$  parameters of the individually optimized ZnO sheet and the Ag(111) slab, ((vi)–(vii)) maximum and minimum distances in the 2D-ZnO-on-Ag(111) system (distances between ZnO and Ag(111) are in a direction normal to the surface and the ZnO sheet (Å)) and (viii)  $BE_{ZnO-Ag}$ : binding energy between ZnO sheet and Ag(111) surface (eV/ZnO). The first values correspond to BEs calculated using the energy of a relaxed isolated 2D-ZnO sheet, whereas the second values use the energy of a 2D-ZnO sheet constrained to have the corresponding Ag(111) supercell lattice parameters.

Level of theory	Model ZnO:Ag	$a_{ZnO}$	$a_{Ag}$	$a_{ZnO}/a_{Ag}$	Zn–O range	Zn–Ag(111) range	O–Ag(111) range	$BE_{ZnO-Ag}$
IP	1:1	3.237	2.888	1.121	1.74	2.03	2.52	−0.62/0.94
IP	8:9	5.898	25.996	0.996	1.87–1.92	2.09–2.48	1.73–2.81	0.85/0.85
IP	7:8	2.661	23.107	0.981	1.89–1.93	2.10–2.46	1.94–2.53	0.80/0.83
IP	13:15	2.085	43.326	0.971	1.90–1.94	2.05–2.48	2.05–2.48	0.75/0.83
IP	6:7	9.424	20.219	0.961	1.92–1.96	2.09–2.47	2.05–2.47	0.62/0.83
IP	5:6	6.186	17.330	0.934	1.88–2.52	2.10–2.49	2.08–2.47	0.44/0.85
DFT	1:1	3.360	2.938	1.144	1.69	2.48	3.18	−0.94/0.39
DFT-D2	1:1	3.360	2.938	1.144	1.69	2.48	3.18	−0.56/0.77
DFT	7:8	3.536	23.504	1.001	1.94–1.96	2.68–2.79	2.81–2.87	0.17/0.17
DFT-D2	7:8	3.536	23.504	1.001	1.94–1.96	2.68–2.79	2.81–2.87	0.59/0.59

From the unconstrained IP-based optimization of the 2D-ZnO unit cell we find a flat sheet to be most energetically favoured in line with the fully optimized isolated 2D-ZnO sheet from unconstrained DFT optimizations. Multiples of this IP-optimized flat sheet were also used to calculate the  $a_{ZnO}$  values in IP explorations of a series of X:Y systems starting from  $a_{ZnO}/a_{Ag}$  mismatches less than 1 and gradually increasing to unity. We find that, although, as expected, the smaller the mismatch the larger the unconstrained 2D-ZnO-on-Ag(111) binding energy, only when the mismatch is less than 1% does the constrained ZnO-on-Ag(111) binding energy become very similar to the unconstrained case (i.e. showing that the corresponding X:Y model is not unduly constraining the relaxations of the separate ZnO and Ag subsystems). For the IP calculations the best model in this respect was found to be the 8:9 system where the 2D-ZnO sheet is stretched by 0.3%. For the DFT calculations the 7:8 system was found to require a compression of the 2D-ZnO sheet of only 0.1%. It is noteworthy that a 7:8 commensurate ZnO-on-Ag(111) ordering is also that which is observed in experiment

[3], tending to support the accuracy of the DFT calculations. The 7:8 2D-ZnO-on-Ag(111) system from the DFT optimizations is shown in Figure 82.

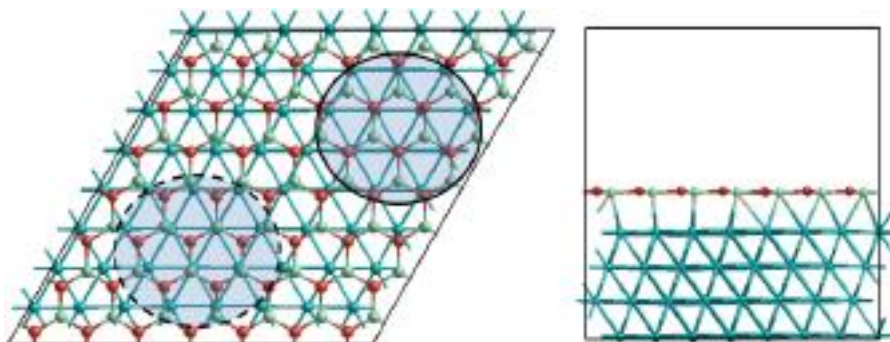


Figure 82. Top (left) and side (right) views of the 2D-ZnO-on-Ag(111) 7:8 system after optimization using DFT. The solid bounded region highlights where the oxygen atoms (red/dark grey balls) are near to being directly above the Ag atoms (blue/grey balls) in the underlying surface slab. The dashed bounded region highlights where the zinc atoms (light green/light grey balls) are near to being directly above the Ag atoms.

The 2D-ZnO-on-Ag(111) binding energy for these optimal systems ranges from 0.17 eV/ZnO for the bare 7:8 calculation to 0.85 eV/ZnO for the 8:9 IP calculation. The higher binding energy for the latter calculation is unlikely to be due to any improvement in the description over a pure GGA DFT treatment, especially considering that the Zn–Ag and O–Ag IPs are two-body fits to pure GGA DFT calculations. Nevertheless, it is likely that the 7:8 pure DFT-calculated 2D-ZnO-on-Ag(111) binding energy is a lower bound to the true binding energy due to the inherent omission of dispersive interactions in pure GGA DFT calculations. Applying a dispersion correction to the energy of the DFT optimized 7:8 system using the empirically parametrized two body DFT-D2 method gives a 2D-ZnO-on-Ag(111) binding energy of 0.59 eV/ZnO at the equilibrium DFT ZnO–Ag(111) separation. A recent investigation of organic molecules on Ag(111) has shown that this two-body corrective scheme tends to significantly overestimate the adsorption energies with respect to experiment<sup>267</sup>. Another experimental study of 2D-BN sheets on Ag(111)<sup>268</sup> has confirmed that the 2D-BN-on-Ag(111) binding energy is negligible, as predicted by pure DFT<sup>269</sup>, and thus that dispersive interactions do not play a significant role in this 2D-sheet-on-Ag(111) interaction. We also note that our calculations show no evidence of charge transfer or covalent bonding between the Ag(111) surface and the supported 2D-ZnO sheet, with both having indistinguishable

atomically partitioned charges in isolation and in the combined system. Considering the above we suggest that the actual 2D-ZnO-on-Ag(111) binding energy is likely to be in the energy range 0.15–0.5 eV/ZnO, and likely mainly due to non-bonding-induced polarization effects.

In both IP and DFT calculations (taking the 8:9 and 7:8 systems as examples, respectively) the Ag-supported ZnO sheet is found to slightly deviate from perfect planarity; the energetically preferred structure in isolation. In the DFT optimized system all the Zn atoms in the supported 2D-ZnO sheet are closer to the Ag(111) surface than their nearby O atoms (i.e. Zn atoms have generally smaller  $z$  coordinates—by  $\sim 0.1 \text{ \AA}$ —than nearby O atoms, where  $z$  is measured from the base of the Ag slab). Taking this sheet and re-optimizing in the absence of an Ag(111) substrate recovers the planar 2D-ZnO sheet. In the IP 8:9 2D-ZnO-on-Ag(111) system we find that the oxygen atoms oscillate both above and below nearby Zn atoms by approximately  $0.3 \text{ \AA}$ . We find that in this case these small local distortions are due to a real instability of the IP-treated isolated 2D-ZnO flat sheet which only emerges when one allows for more degrees of freedom than allowed for in the minimal unit cell case. This instability emerges for the 7:8 and 8:9 systems where the 2D-ZnO sheet is stretched by less than 2% and results in an increase in the range of O–Ag(111) distances observed (see Table 8).

In addition to these local structural oscillations, in both the DFT and IP calculations the deviations in the  $z$  coordinates of the Zn and O atoms follow a gradual rumpling or flexing, with amplitude  $\sim 0.1 \text{ \AA}$  (DFT) and  $\sim 0.15 \text{ \AA}$  (IP), which is mirrored by a similar out-of-phase rumpling of the atoms in the uppermost layers of the Ag slab, with amplitude  $\sim 0.2 \text{ \AA}$  (DFT) and  $\sim 0.35 \text{ \AA}$  (IP). The rumpling of both the Ag(111) surface and the 2D-ZnO sheet appears to be due to variations in the interaction between the two subsystems. We find that when O atoms are closest to being directly above an Ag atom (i.e. an on-top position) the interaction seems to be strongest, and vice versa. The  $z$  coordinates of the Zn atoms also follow the tendency of the O atoms where the Ag(111)-sheet separation is greatest, but are smallest for intermediate separations. In Figure 83 we show contour plots of the locally averaged  $z$  coordinates of the Zn and O atoms in the supported ZnO sheet and in the corresponding uppermost atoms in the supporting Ag(111) slab for the DFT-optimized 7:8 system. The upper right-hand part of each plot

is where the O atoms are lowest and the Ag atoms highest (i.e. indicating a stronger interaction). In Figure 82 we circle the corresponding region where O atoms are close to being perfectly at on-top positions. Conversely, the lower left-hand part of each plot is where the 2D-ZnO sheet and the Ag(111) surface are furthest apart and where the O atoms are furthest from on-top positions (shown by a dashed bounded region in Figure 82).

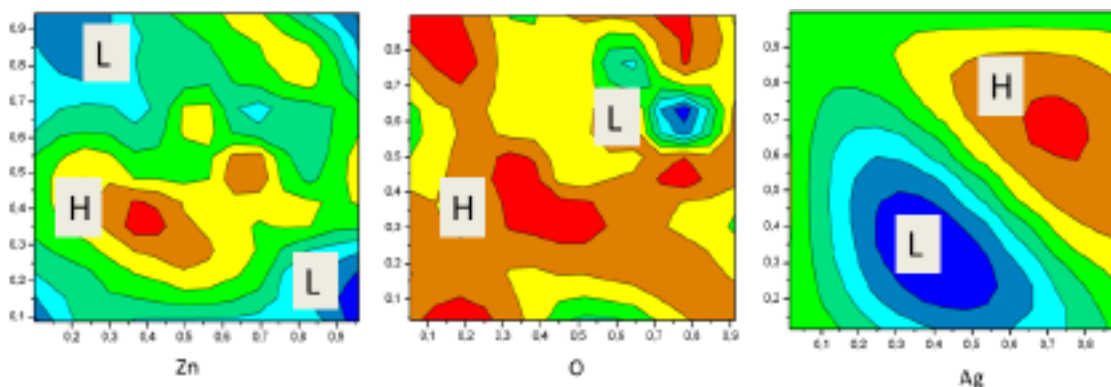


Figure 83. Contour plots of the locally averaged  $z$  coordinates of Zn, O and Ag atoms in the 7:8 system shown in Figure 82. The fractional  $x$ - $y$  coordinates in the square plots correspond to those in the oblique angled 7:8 supercell. The ‘L’ and ‘H’ labels correspond to relatively lower and higher regions (where the height is taken as the magnitude of the  $z$  coordinate measured from the bottom of the Ag slab).

### 3.2. Transport of hydrogen through a 2D-ZnO single sheet

The interaction of atomic hydrogen with the unsupported 2D-ZnO system was studied using both periodic and cluster DFT calculations. In particular, we focused on the interaction of H with a  $Zn_3O_3$  ring when passing through the sheet. When H is far from the sheet the electronic states of each are distinct and non-interacting. Taking first the periodic GGA DFT calculations, we see this non-interacting situation in the PDOS in Figure 84(a) where the narrow unperturbed H 1s state (solid line) is superimposed on top of the unperturbed 2D-ZnO states.

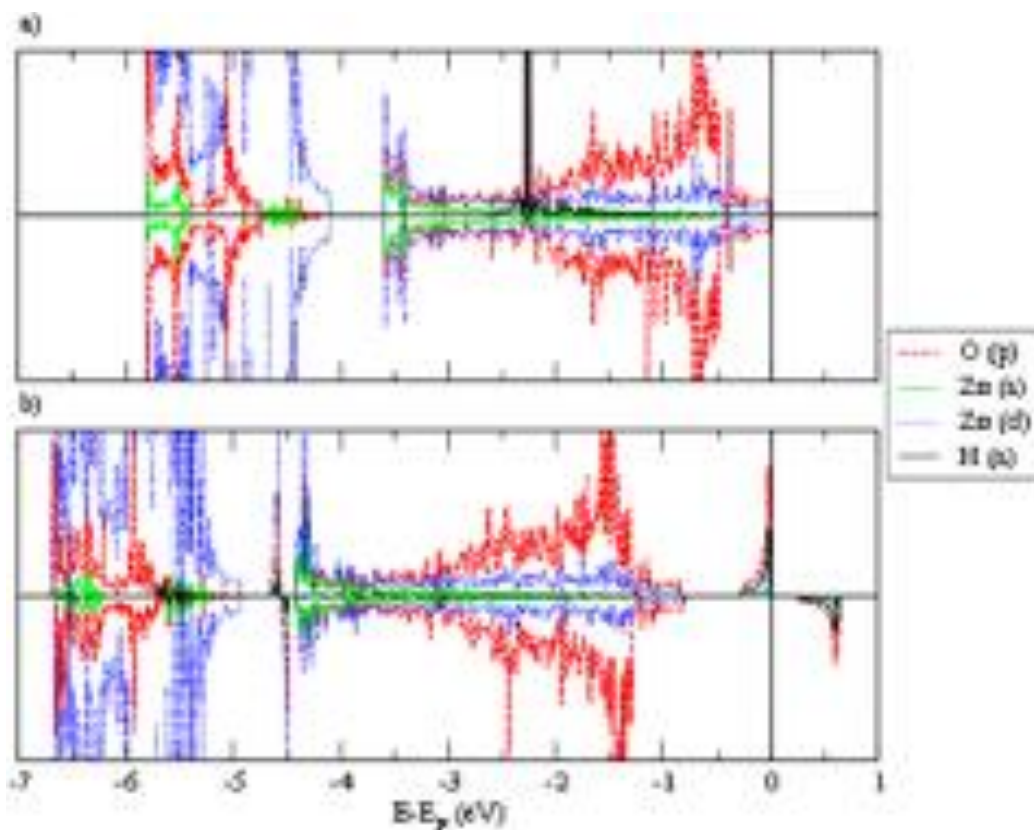


Figure 84. PDOS for the hydrogen and 2D-ZnO sheet where (a) the hydrogen atom is far from the sheet and (b) H is in the centre of a  $Zn_3O_3$  ring of the sheet ( $H@Zn_3O_3$ ).

H atoms are found to bind relatively weakly in an on-top manner to the Zn (0.32 eV) and O (0.04 eV) sites thus raising the possibility of transport through the 2D-ZnO sheet at suitably high temperatures. Upon approaching the centre of a  $Zn_3O_3$  hexagonal ring along a line perpendicular to the plane of the sheet, the H atom becomes firstly weakly adsorbed until a minimum energy position is reached at a distance of 1 Å from the 2D-ZnO sheet (-0.04 eV relative to the separate sheet and H atom). Subsequently entering the ring from this position incurs an increase in the relative system energy from this weak minimum to a maximum of +0.11 eV at the centre of the  $Zn_3O_3$  ring. The full calculated barrier is shown in Figure 85. The energy cost solely due to the H-induced structural distortion of the 2D-ZnO sheet is calculated to be 1.27 eV. Thus the interaction between H and the 2D-ZnO sheet, when H is in the centre of a  $Zn_3O_3$  ring ( $H@Zn_3O_3$ ), compensates for this effect by 1.16 eV. From our previous studies on H interacting with  $Zn_3O_3$  environments<sup>253-270</sup> and other results concerning interactions of atomic H with

undercoordinated centres in ZnO<sup>271</sup> we were led to look for evidence of possible MCBformation in the H@Zn<sub>3</sub>O<sub>3</sub>system.

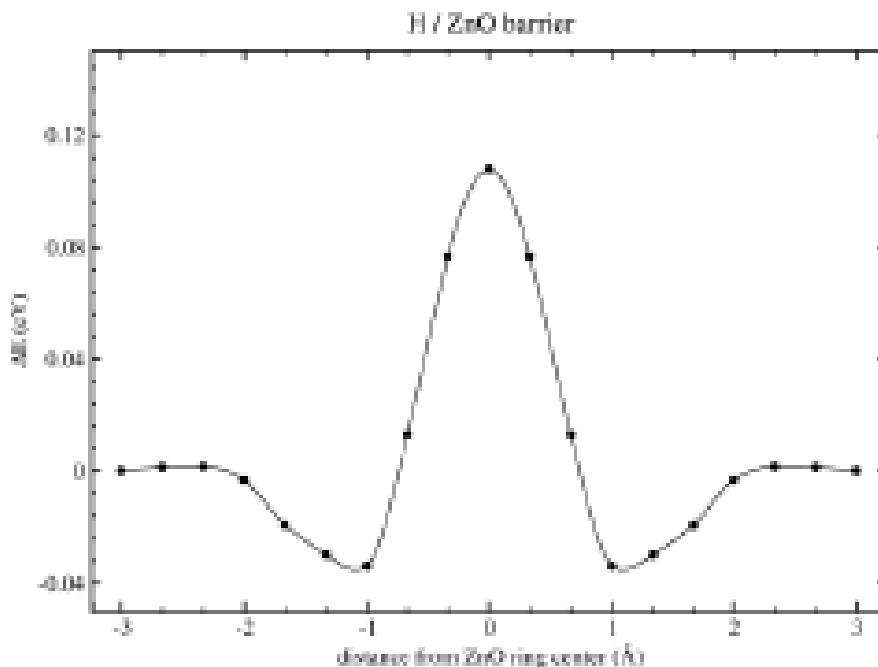


Figure 85. Transport barrier for a single H atom to pass through a Zn<sub>3</sub>O<sub>3</sub>ring of a 2D-ZnO sheet (GGA DFT calculation using a 4×4supercell).

The PDOS of the H@Zn<sub>3</sub>O<sub>3</sub>system (see Figure 84(b)) shows a number of distinct differences with respect to thenon-interacting case (Figure 84(a)). The first notable change is that the Fermi level is now located at an isolated  $\alpha$ -spin state, which is separated from the top of the O p-dominated 2D-ZnO conduction band by about 0.5 eV. This singly occupied state is easiest to visualize by the spin density of the system, which shows spin density on both the H atom and the three nearest O atoms in the surrounding Zn<sub>3</sub>O<sub>3</sub> ring (see Figure 86). In the cluster hybrid DFT calculations this state corresponds to an  $\alpha$ -spin highest occupied molecular orbital (HOMO). The spin density of this state (see Figure 86) is found to be very similar to that from the periodic GGA calculations, tending to confirm the general reliability of both methods. From analysing the charge distribution associated with this state, the spin on the O centres comes from charge deficiency (i.e. partially occupied O p-like states) and that on the H centre from a localized electron. From an orbital component analysis of the cluster DFT calculation, the electron on the H centre appears to be mainly localized in an H 2s-like state. The

corresponding unoccupied state (hole) can be found as a  $\beta$ -spin unoccupied peak at approximately +0.5 eV above the Fermi level in Figure 84(b).

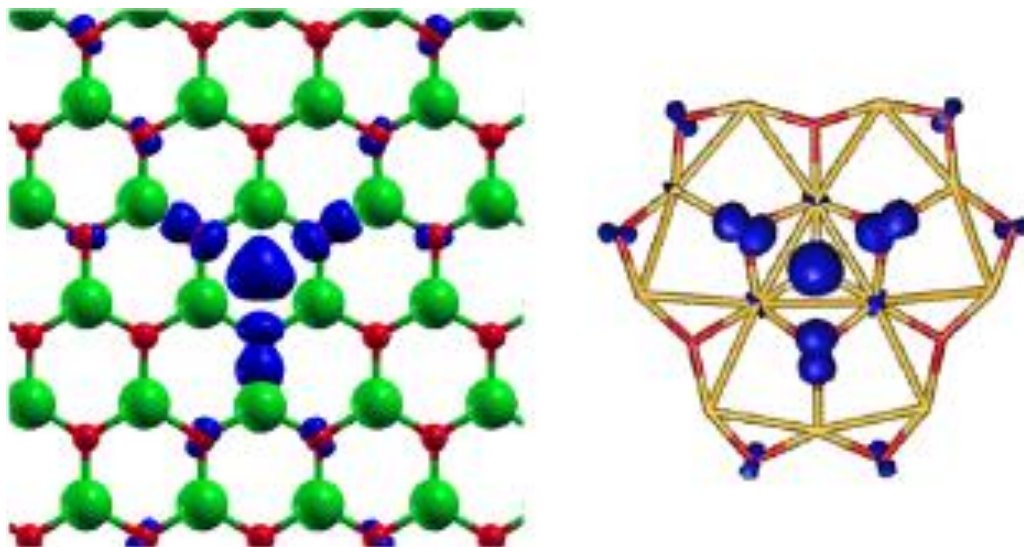


Figure 86. Spin density of the H@Zn<sub>3</sub>O<sub>3</sub> system for the 3×3 supercell GGA DFT calculation (left) and the B3LYP cluster calculation (right).

The  $\alpha$ -HOMO state is relatively high in energy, which thus further points towards the existence of a compensating low energy H@Zn<sub>3</sub>O<sub>3</sub> state to explain the low calculated transport barrier. In the periodic DFT calculations we find considerable disruption of the H@Zn<sub>3</sub>O<sub>3</sub> PDOS with respect to the noninteracting system, especially for energies >3.5 eV below the  $\alpha$ -HOMO. From inspection of the PDOS it was difficult to see any specific indication of MCB formation involving the H centre. In the hybrid cluster DFT calculations we were able to search the atomic orbital components of each discrete molecular orbital to find those which involved the H s-states and states of neighbouring atoms. From such a search the most probable candidate for an MCB bonded state is an  $\alpha$ -spin/ $\beta$ -spin pair of states found at -3.9 eV. This state involves both the Zn 4s states of the nearest three Zn atoms to the H centre, and the H 1s state (see Figure 87). This state is very similar in appearance and in its orbital constituents to that found for H atoms passing through the SOD-ZnO polymorph [6]. As in the H@SOD-ZnO case the present state requires charge donation to make a doubly occupied bonded state. The spin density plots in Figure 86 suggest that charge is depleted from the O p-states. Plotting the charge density difference of the periodic system (Figure 87) we confirm that charge is transferred from the O p-states to the region mainly between the H

centre and its three nearest Zn neighbours. We suggest that a consistent interpretation of these data is that (i) when the H atom is in the centre of a  $Zn_3O_3$  ring the considerable spatial confinement causes the H 1s electron to occupy a higher energy, more diffuse 2s-like state (the  $\alpha$ -HOMO state), (ii) to charge-compensate, the surrounding three O atoms donate charge to the charge-depleted region in the ring, and (iii) the donated charge (two electrons) lowers the energy of the system by filling a hybrid state formed by the combination of the empty H 1s orbital and the three surrounding empty Zn 4s orbitals (the MCB state).

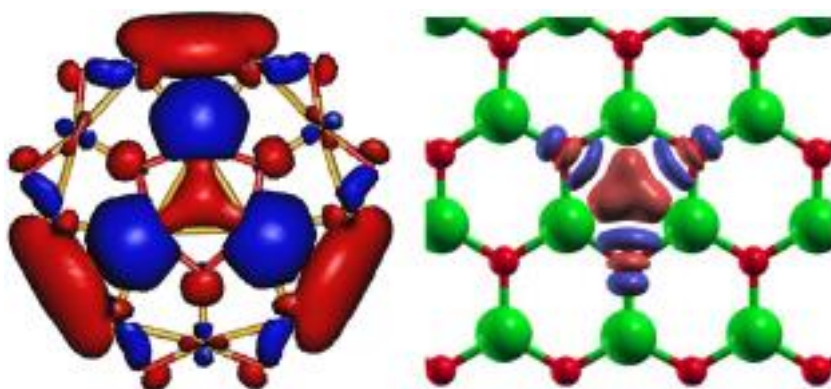


Figure 87. The proposed Zn 4s–H 1s MCB orbital from the B3LYP cluster calculation (left) with the charge density difference of the periodic DFT calculations (right). Relative charge increase is found in the centre of the ring and to a lesser extent on the oxygen sites (lighter grey) whereas charge is depleted (dark grey) from the p-like lobes of the oxygen sites.

#### **4. Conclusions**

We have employed a range of modelling methods to understand (i) the structure and interactions in the experimentally prepared 2D-ZnO-on-Ag(111) system and (ii) how H atoms interact with the 2D-ZnO sheet as they pass through a  $Zn_3O_3$  ring. The former calculations reveal subtle variations in the structure of both the supported 2D-ZnO sheet and the Ag(111) support itself which are not observed in the non-interacting system. The importance of the degree of 2D-ZnO/Ag(111) commensurability is also highlighted for calculating accurate sheet-on-substrate binding energies. The calculations of the unsupported 2D-ZnO sheet interacting with hydrogen provide strong evidence for H

forming a low energy Zn 4s–H 1s MCBstate when passing through a Zn<sub>3</sub>O<sub>3</sub> ring of the 2D-ZnO sheet, thus allowing for relatively facile H transport through the sheet. We note that 2D-ZnO has been prepared on Pd(111) [4] which is often employed in hydrogen membrane applications<sup>272</sup>. Palladium is fragile and expensive, however, which could potentially be addressed by using hybrid 2D-ZnO–Pd membranes or similar systems.

## **CHAPTER V: Effect of Finite Size on Epitaxial growth of ZnO on Ag(111)**

### **1. Introduction**

In general, there are three types of epitaxial growth of an adsorbate on a substrate: (i) Volmer-Weber (VW), (ii) Frank-van der Merwe (FM) and (iii) Stranski-Krastanov (SK).<sup>273</sup> In VW growth, internal adsorbate interactions are so dominant over the adsorbate-substrate interactions that 3D islands form on the substrate. Layer by layer growth is enhanced in FM growth, where the higher adsorbate-substrate interactions lead to adsorbates preferring surface sites and in which growth proceeds by fully formed layers. The SK growth mode lies between these two growth types, in which both 2D layers and 3D islands occur. In SK growth, a transition from the layer-by-layer growth to island based growth occurs at a critical layer thickness, which is dependent on several chemical and physical properties of the adsorbate and substrate (e.g. surface energies, lattice parameters). Figure 88 shows a schematic representation of these three main types of growth.

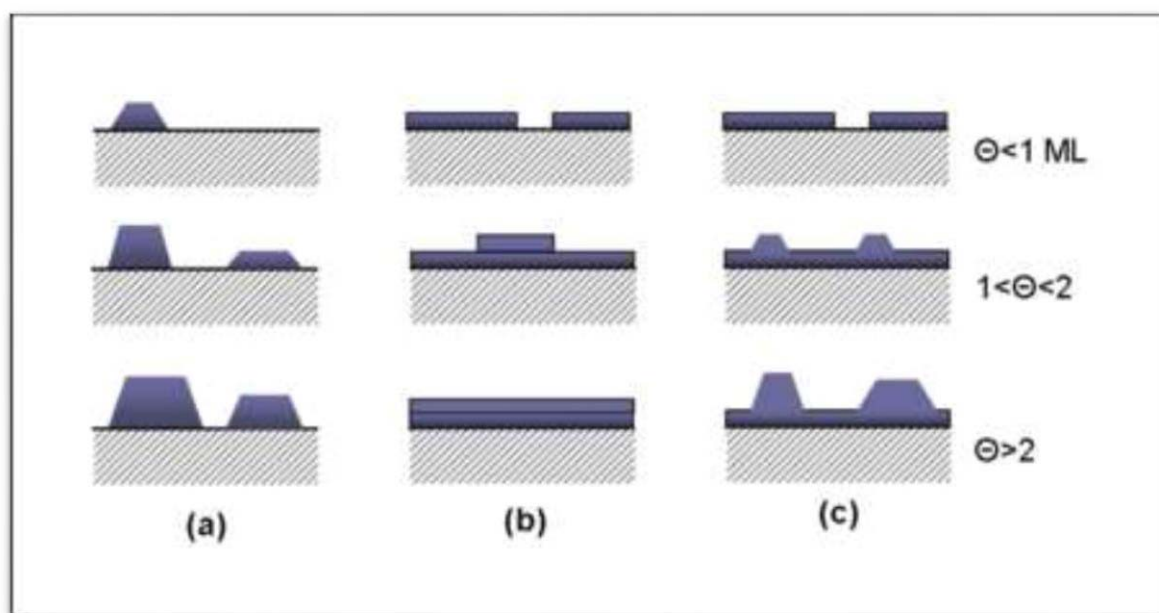


Figure 88. Main growth types in thin film formation; (a) Volmer-Weber, (b) Frank-van der Merwe, (c) Stranski-Krastanov. Here  $\Theta$  stands for the coverage.

As mentioned in the previous two chapters, ZnO nanofilms have been grown on Ag(111) metal substrates with 0-4.5 monolayer (ML) coverages.<sup>278</sup> With increasing coverage in this range a depolarized ZnO structure was observed for the first two full MLs followed by a phase transition to a new structural type starting from third layer. Figure 89 shows two STM images of 2.2 ML ZnO coverage from this work, from which the the triangular and truncated triangular forms of the islands can be observed for the incomplete third adlayers of ZnO, which was the basis of our model constructions To study the finite size effects of such islands on the the structure ZnO we modelled stoichiometric ZnO films with coverages between 2 ML and 2.7 ML. Where computationally feasible we also explicitly included the Ag(111) substrate. We note that the smallest coverage for which accurate experimental data was reported is for 2.7 ML ZnO films on Ag(111). We further note that the experiment data for the 2.7 ML film show that although the first 2 MLs are complete, the 3<sup>rd</sup> ML has 60% coverage with 10% of the 4<sup>th</sup> ML being already present. This feature of the observed films is also taken into account in our models.

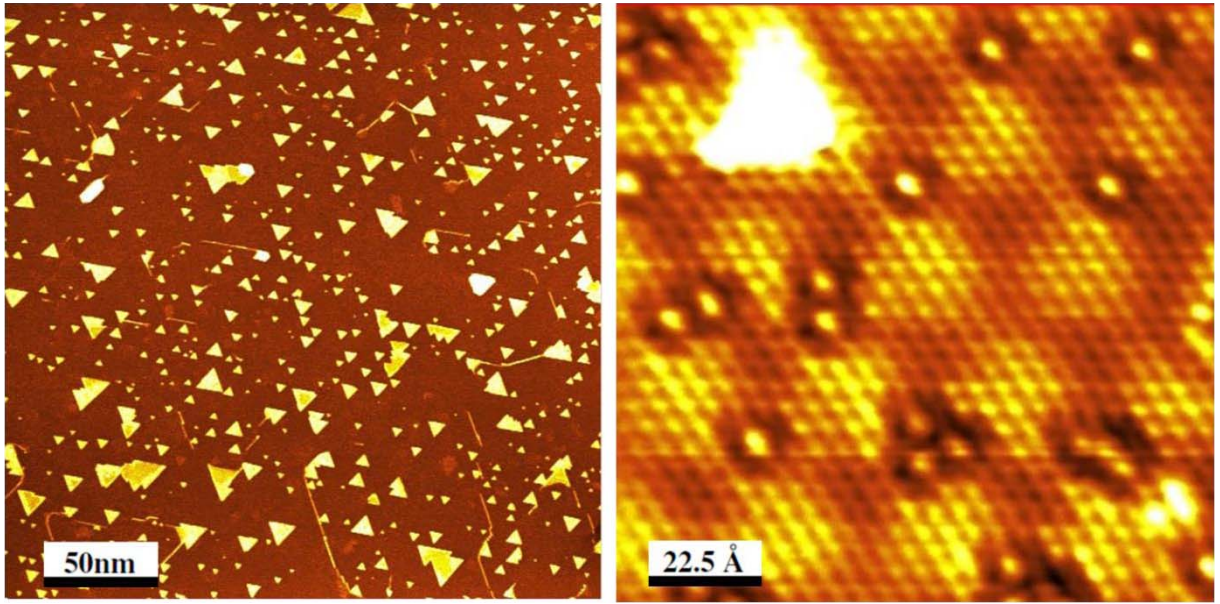


Figure 89. STM images of 2.2 ML ZnO on Ag(111)**Error! Bookmark not defined.**

## 2. Methodology

In this study we have used *ab-initio* density functional theory (DFT) as implemented in the VASP code<sup>189</sup> using the generalized gradient approximation PW91 exchange-correlation functional<sup>255</sup>. The projector augmented wave (PAW) approach<sup>205</sup> was used to describe the effect of core electrons on the valence states. One-electron valence states were expanded in a plane wave basis up to an energy kinetic cutoff of 400 eV. A 4 layer Ag slab with 8x8 surface periodicity was generated to simulate the Ag substrate which is experimentally known to be commensurate with a 7x7 supercell ZnO thin film grown on top. The lattice vector in the adsorption direction (*z*) was kept at 30 Å, which ensures 12 Å vacuum separations between periodic images for the highest coverage considered. Due to the spatial extent of the system, calculations were done only at  $\Gamma$  point in reciprocal space. All of the atomic positions were optimized until the forces on the atoms became less than 0.2 eV/nm. The binding energies (BE) were calculated by using the total energy differences between the combined and separated systems according to the formula:

$$BE = \frac{E[\text{ZnO on Ag}(111)] - E[\text{ZnO}] - E[\text{Ag}(111)]}{n}$$

where  $n$  is the number of ZnO unit in the system. All of the considered ZnO coverage models were prepared by initially placing Zn and O atoms according to their positions in a layered phase, while the Ag atoms are placed according their bulk positions.

### **3. Results and Discussion**

#### **3.1. ZnO coverages of 1 and 2 ML on Ag (111)**

The 1 ML single sheet of ZnO on Ag(111) surface is discussed in detail in chapter 4.3. Briefly, the Ag-supported ZnO sheet slightly deviates from perfect planarity, which is the preferred structure for an isolated single ZnO sheet. This deviations are characterized in two groups: (i) local structural oscillations, where the Zn atoms are slightly closer ( $\sim 0.1 \text{ \AA}$ ) to the surface than the O atoms, and (ii) a gradual rumpling of the ZnO sheet with a  $0.1 \text{ \AA}$  amplitude which is mirrored by an out-of-phase rumpling of the outermost atoms of the Ag surface. The Ag and ZnO sheets come closer according to this rumpling where the O atoms coincide with on-top positions on the surface. However, for 2 ML ZnO on Ag(111), in-phase rumpling is affected by the additional ZnO layer, with inter layer ZnO interactions in the z-direction being stronger than Ag-ZnO interactions. The binding energy of the 2 ML ZnO film on Ag(111) decreases to  $0.09 \text{ eV/ZnO}$  from the value of  $0.17 \text{ eV/ZnO}$  for 1ML ZnO coverage. As for local structural oscillations in the 2ML film, unlike for the 1 ML case, no Zn atoms were found to be closer to the Ag(111) surface, while small variations in local interlayer separations occurred throughout the unit cell for a 13 % of the bilayer connections. These minor interlayer structural distortions (see Figure 90c) do not follow the pattern of either a WZ or a BCT bond ordering but are appear to simply be substrate-induced perturbations to a perfect flat bilayer 2ML film. It should be also noted that for free standing 2ML ZnO nanofilms, both WZ and BCT structures directly relaxes to the a perfectly flat bilayer of the layered phase. For 3 layers in free space, the same spontaneous transformation to the layered phase happens for the WZ structure, whereas

the BCT phase can conserve its structure while being slightly compressed. Furthermore, the energetic stability of 3 layers of BCT-ZnO is found to be the almost exactly the same as that of a 3ML film of the layered phase. For 4 ML films while the BCT phase become the most stable polymorph in free space, there exists also a wide range of other energetically competing phases, which are lower in energy than the layered phase. The possible polymorphic structures of free-standing 4 ML ZnO films are discussed in detail in chapter 5.

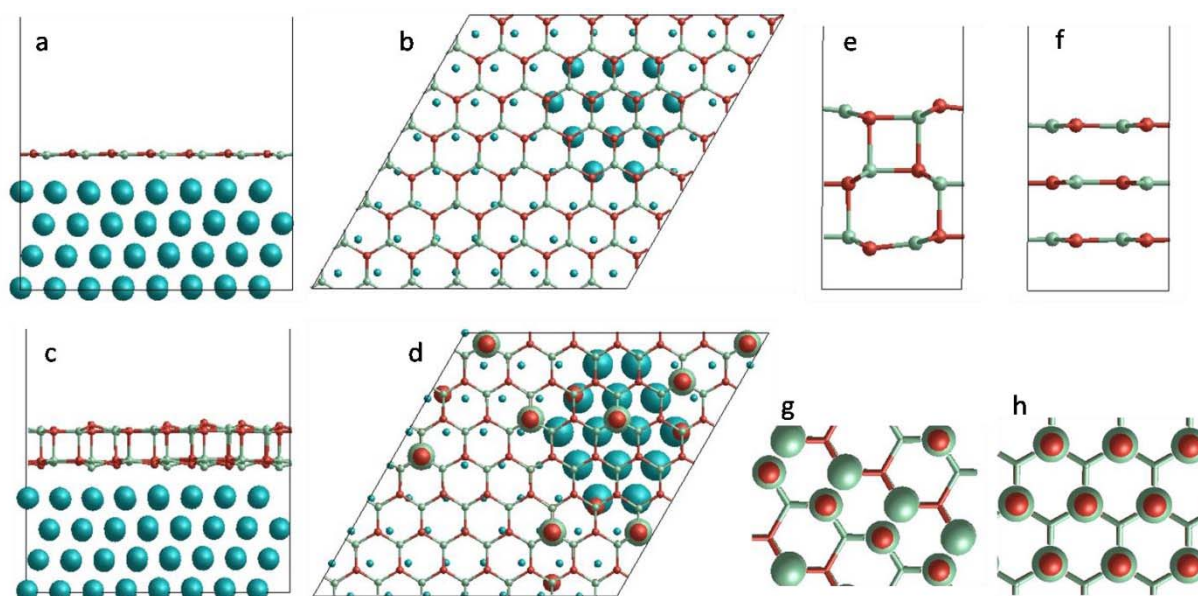


Figure 90. Optimized structures of 1 ML ZnO on Ag(111) surface (a-side view, b-top view), 2 ML ZnO on Ag(111) surface (c-side view, d-top view). e and f shows side views of the optimized geometries of 3 layer thick BCT-ZnO and layered-ZnO. g and h illustrate the interlayer spacings in the BCT and WZ ZnO structures. The larger balls for Zn and O atoms are used to indicate where the interlayer separations occur, while the bigger balls for Ag atoms in b and d are used for indicating the surface rumpling, i.e. where the surface atoms move outwards.

### 3.2. ZnO coverages of 2.2, 2.3 and 2.75 ML on Ag (111)

To study the effect of finite size, i.e. incomplete layers of ZnO on top of completed ones, found during growth, stoichiometric 2.2, 2.3 and 2.76 ML ZnO coverages on the Ag(111) surface were modelled. The 2.2 ML model contains 3 layers of ZnO, of which the incomplete top adlayer is a simple stoichiometric extension obtained from a hexagonal adlayer ZnO island.

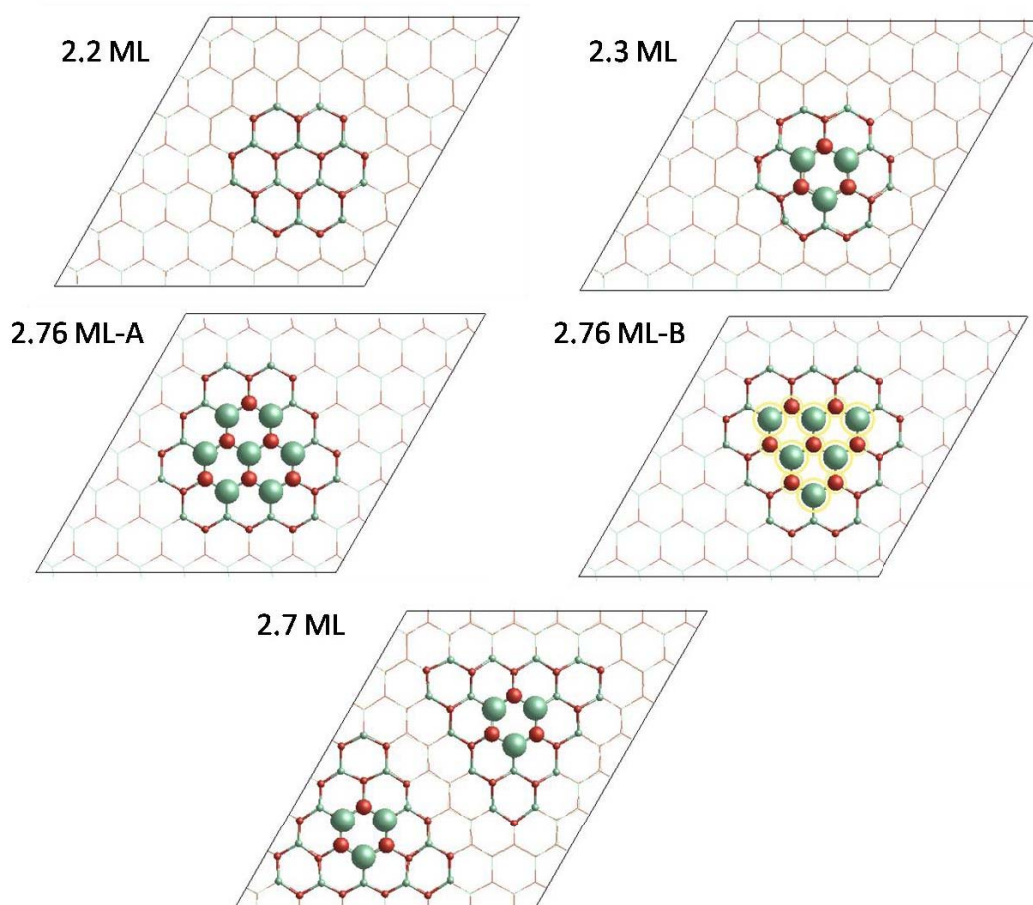


Figure 91. Initial structures of ZnO coverage models. Red and Green stands for O and Zn atoms, respectively. The first two complete MLs are shown with thin sticks while the third layer is shown with a larger ball and stick model and the top layer is differentiated by the largest balls.

The 2.3 ML model was obtained by adding a single hexagonal unit on top of the 2.2 ML hexagonal island, which helps us to compare the effect of a second adlayer, separately. The 2.2 ML hexagonal island model can be also extended in three directions to make a triangle, but which would result in a non-stoichiometric model in conflict with experiment. Although the small islands in the STM images appear triangular, atomic resolution has not been obtained and such images may result from hexagonal islands which can be also be regarded as truncated triangles. One possible strategy to construct stoichiometric films having triangular adlayers is to compensate the excess atoms of one kind in a triangular island with other islands having reduction of the same atom type. This can be done, for example, by constructing a small triangular island on top of a relatively larger truncated triangle such as in the case of our 2.76 ML models. In this type of construction, two possibilities emerge according to the choice of which type of

atom will be excess on which adlayer. In our study we constructed adlayer islands with both an excess of O atoms on the first adlayer (2.76 ML-A) and vice versa (2.76 ML-B) in order to compare their relative stabilities and structures. We note that adding a smaller island on top of the larger island is also in line with the experimentally observed pattern of growth for such films (see above).

It is more difficult to construct simple models with triangular islands in the first adlayer since stoichiometric compensation is not possible for a single triangular island. However, by constructing two types of triangular island on the first adlayer, they are able to stoichiometrically compensate each other. Due to the 7:8 ZnO-Ag commensuration, such a two island system was out of our computational limit while also taking into account Ag surface. Thus, we have considered only a free standing 2.70 ML ZnO system together. For comparison, we have calculated all other systems as free standing structures corresponding to same structures also modelled with the Ag(111) surface taken into account.

Figure 92 shows the optimized structure of the 2.2 ML coverage model. The binding energy with the Ag substrate was found to be 0.08 eV/ZnO, which is almost the same value as that for the 2 ML coverage case. A priori it would typically be expected that the binding energy per ZnO unit of the 2.2 ML with the surface would be decreased since the third adlayer of ZnO is further from the Ag surface. However, that the adsorption energy is higher than for the 2 ML case seems to be due to the structural reconstructions in the adlayer islands. After the optimization the edge Zn atoms of the 3<sup>rd</sup> layer move 0.42 Å towards the centre of the island while the rest of the Zn and O atoms does not displace more than 0.05 Å in x-y plane. As for distortions in z-direction, the local variations in interlayer separations observed in the 2ML case almost disappear, while ordered separations are found in the island. In Figure 92 it can be seen that the central hexagonal core of the island and the corresponding part of the first two ML under the this core converges to display the WZ structure which is, in turn, becomes encircled with smaller regions which display BCT-like structural motifs. The remaining bilayer part of the system not under the island preserves the layered ZnO structure. In the Ag(111) surface some minor rumpling of the Ag atoms in also observed, whereby the Ag atoms coinciding O positions of the film move slightly upwards towards the ZnO film.

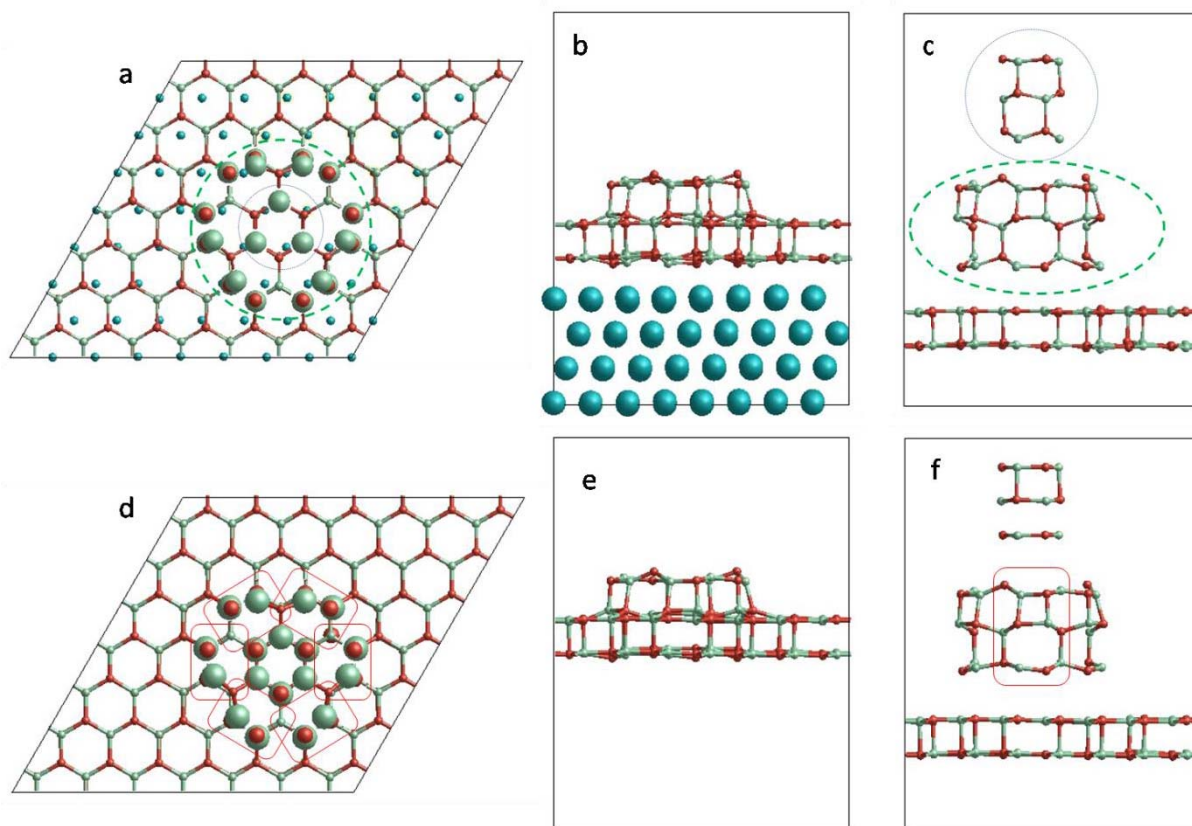


Figure 92. Optimized structures of both supported (a,b,c) and unsupported (d,e,f) 2.2 ML ZnO. Bigger balls are used to differentiate where the interlayer separations occur in top view figures (a and d). In c and f, cylindrical parts shown in a are separated from each other in side views. Red rectangles indicate the encircling BCT reconstructions which are not commensurate with each other.

If we compare the Ag(111)-supported 2.2 ML model with its free standing counterpart, the WZ phase does not form in the island, and the core of the island system remains in the layered phase. However, the BCT motifs are still found at the corners of the adlayer island, which is more compressed than in the Ag-supported case. Wen et al<sup>274</sup> studied theoretically free space nanostructures formed from 2 to 6 ML stackings of the hexagonal ZnO unit with the same size and stoichiometry as that which we employ as an adlayer island in our 2.2 ML model,. According to their results, the layered phase is more stable for 2 and 3 layered nanoclusters while the WZ phase becomes more stable for 4 and more layers. This result is also in line with our free standing 2.2 ML model, where the WZ-structured central hexagonal core found in the Ag(111)-supported case relaxes to the layered phase if unsupported. The emergence of the WZ phase is also affected by the addition of a hexagonal  $\text{Zn}_3\text{O}_3$  unit added as a 4<sup>th</sup> layer in our 2.3 ML

model on Ag(111). In this case, while first two layers under the core of the island have the WZ structure, the other two layers belonging to the incomplete adlayers converge to the layered phase. The BCT motifs form on the three edges of the hexagonal island and in the corresponding part of the first two layers immediately below the island. While the layered and WZ phases have trigonal symmetry the BCT structure does not and thus these three separate BCT-structured regions cannot extend and join each other to make an extended BCT phase commensurate with the WZ phase, the layered phase or even the Ag(111) surface. The overall mix of BCT and WZ structures in the the 2.2 ML and 2.3 ML models is also very similar to the structure of a hypothetical predicted ZnO polymorph which we named T1 in ref<sup>275</sup> (see also Figure 93). The only difference with respect to the pure T1 polymorph in the Ag-supported 2.2 ML case is that the core hexagon part displays a WZ structure, whereas T1 has a layered structure. With the addition of a 4<sup>th</sup> sublayer, as in the Ag-supported 2.3 ML model, the inner core becomes more of a mixture of WZ and layered structures and thus closer to the T1 structure. We note that the free standing 2.2 ML film displays the T1 structure exactly, as seen in Figure 93.

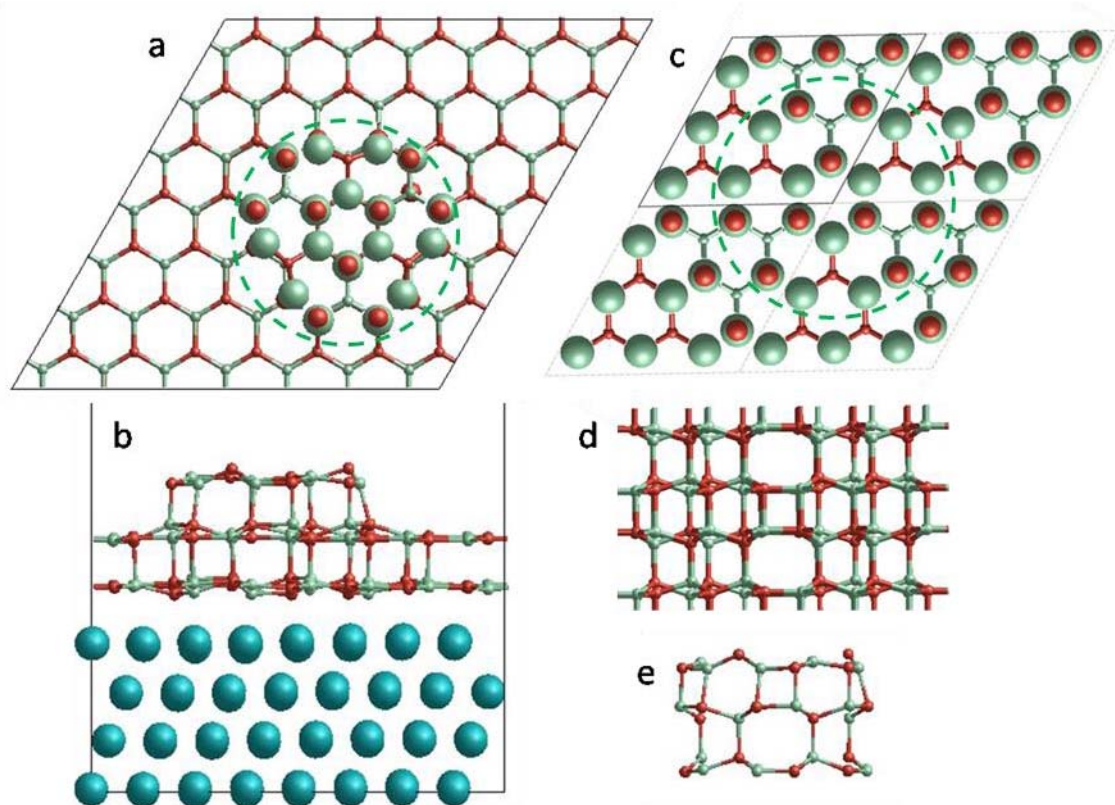


Figure 93. Comparison of 2.2 ML island with the T1-ZnO cut: a) Top view of unsupported 2.2 ML ZnO, b) side view of supported 2.2 ML ZnO, c) top view of T1-ZnO, d) side view of T1-ZnO, and e) cylindrical cut of the islands perimeter.

When we consider the 2.76 ML-A and 2.76 ML-B models, we observe similar structural reconstructions within and below the adlayer island as found in the 2.2 and 2.3 ML models. The inner core of the triangular island forms a WZ structure which is surrounded by edges having the BCT structure and corners with the T1 structure, as shown in Figure 94. The remaining part of the film around the island preserves the layered phase for the 2.76 ML-A model, while some local small interlayer distortions are observed in the 2.76 ML-B model. If we compare both models with their unsupported counterparts, the difference is found again only in the inner core of the island, where the WZ phase is more distorted and is mixed with the layered phase. The outer edge BCT reconstructions and corner reconstructions to the T1 structure are also observed in the islands the in free standing films. The same reconstructions are also observed for one size smaller island (2.65 ML) calculated without presence of the support, implying that the reconstructions are general of this type of island and hold for both adlayer islands having a Zn excess or a O excess.

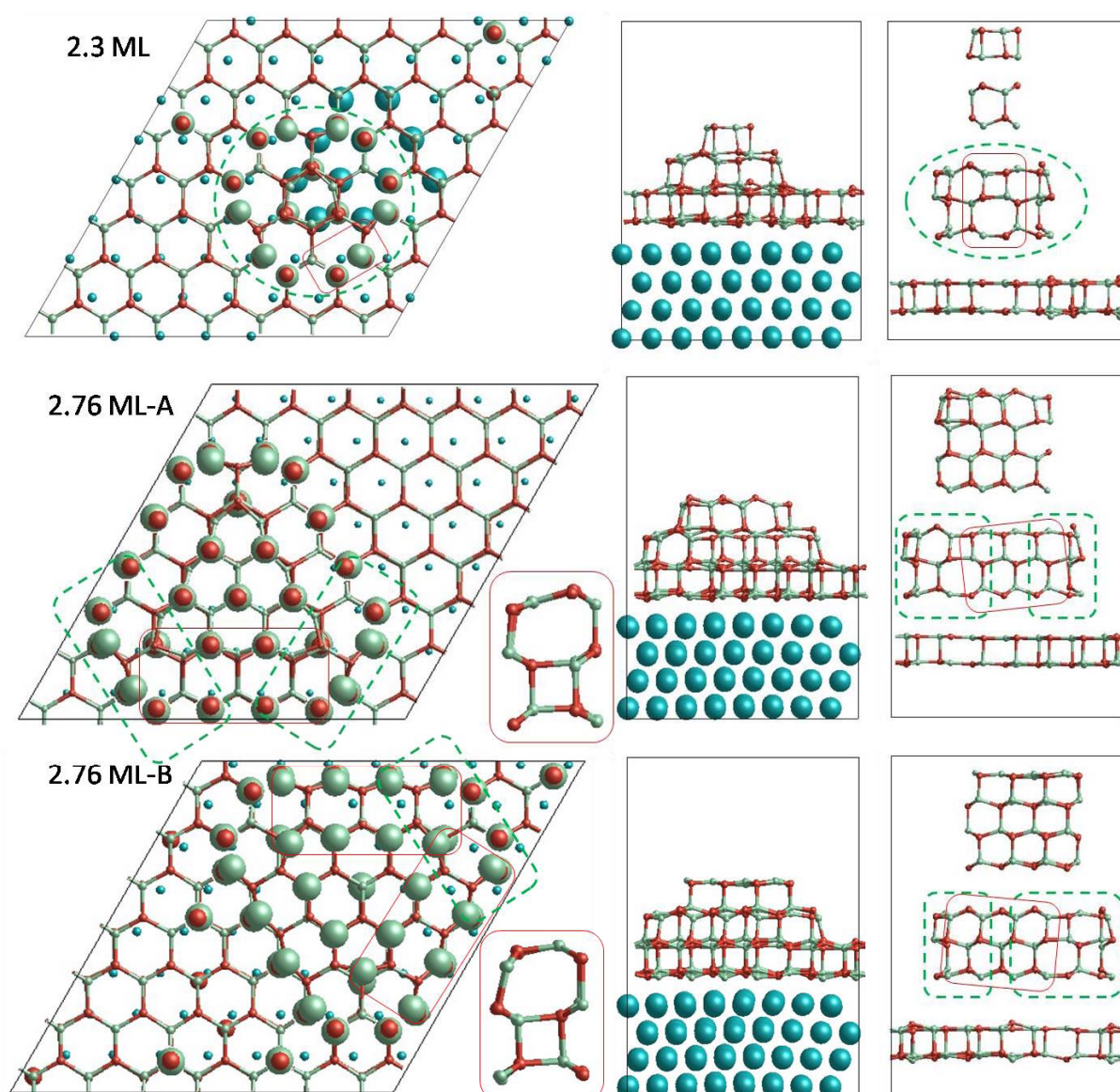


Figure 94. Top and side view structures of 2.3 ML, 2.76 ML-A and 2.76 ML-B models. Red circles indicate BCT reconstructions while green circles indicate T1 reconstructions.

Energetically, in the unsupported films, models having adlayer islands with a O excess case were found slightly more stable than the Zn excess case by 0.003 eV/ZnO. The 2.76 ML-A model film is also found to be energetically more preferred than the 2.76 ML-B model by 0.005 eV/ZnO. This result tends to support the fact that the islands with excess O in the first adlayer are more stable than those with excess Zn. Considering that the observed BCT and T1 reconstructions are not affected with the presence of the Ag surface, we constructed a 2.70 ML unsupported ZnO film model with fully triangular adlayer islands, instead of truncated triangular islands (Figure 95). In this case, two compensating triangles should be present in the model as it is not possible to

compensate excess atoms in the islands with a second smaller adlayer. We note that we have also added a small stoichiometric  $Zn_3O_3$  hexagonal unit on top of the triangular islands in this model in order to obtain the experimental 2.7 ML coverage and be more structurally compatible with the observed films, where a small amount of the 4<sup>th</sup> ML is observed to start before the 3<sup>rd</sup> ML is complete (see above).

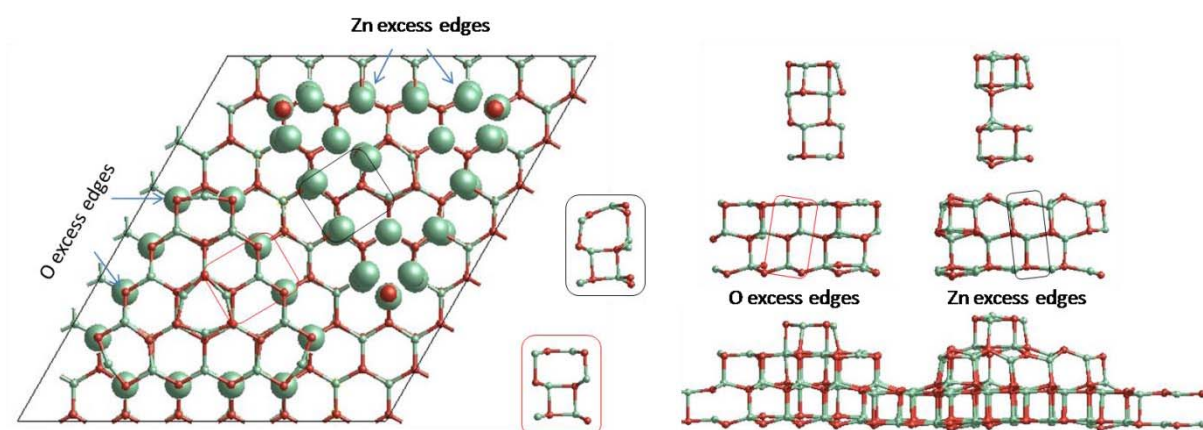


Figure 95. Top and side view structures of 2.70 ML free standing model. Black circle indicates the BCT reconstructed edge on Zn-excess island while Red circles indicates the BCT reconstructed edge on O-excess island.

In 2.70 ML case, the above-mentioned T1 reconstructions are not observed at the corners of the triangular islands and the edge BCT reconstructions are relatively more distorted and constrained to a smaller area, as shown in Figure 95. The considered 2.70 ML model was found to be approximately 0.04 eV/ZnO lower in energy than the other considered models formed mainly by truncated triangles. Table 9 summarizes the edge and corner proportions of these free standing ZnO films and their relative energies. These data imply that models with full triangles seem less favourable than the truncated ones, probably due to the higher percentage of corner atoms in the former.

Table 9 Relative energies (eV/ZnO) of considered free standing ZnO models and their corresponding corner and edge atom percentages.

coverage	Relative energy (eV/ZnO)	% corner atom	% edge atom	# of ZnO unit
2 ML	0.00	0.0	0.0	98
2.2 ML	0.03	0.0	5.5	110
2.3 ML	0.06	2.7	8.0	113
2.76 ML (A)	0.06	3.3	6.7	135
2.76 ML (B)	0.06	3.3	6.7	135
2.65 ML (A)	0.08	4.6	7.7	97

2.65 ML (B)	0.08	4.6	7.7	97
2.70 ML	0.12	9.9	4.0	151

As the smallest coverage considered in detail in experiment was a 2.7 ML ZnO film supported on Ag(111) we compare our calculated results with this case. We find that our Ag(111)-supported 2.3 ML, and in particular, our 2.76 ML-A model, agree reasonably well in terms of all observed structural parameters (see Table 10). Assumption of a WZ structure yields a poor match with nearly all experimental structural data. Although a pure layered phase model matches the observed interlayer spacing between layer 1 and 2 ( $d_{zn-zn}$ ) reasonably well, it fails to match the measured intralayer Zn-O z-coordinate separation values ( $u$ ) and interlayer Zn-O distances ( $d'_{zn-o}$ ) even for the first two layers in the 2.7 ML experimental film. Our Ag(111)-supported 2.3 ML and 2.76 ML-A island-containing models, however, improve the match with experiment with respect to intralayer z-coordinate Zn-O separation values, while maintaining (or even slightly improving) the reasonable agreement of the layered phase for the observed 1-2 interlayer spacing. The z-coordinate separation values ( $u$ ) our relatively small models tend to be generally lower those found in experiment. We note that several sizes of islands occur in experimental growth, and with island size increase the contribution of the WZ phase in the centre of island will increase which, in turn, is expected to result in an increase in the intralayer Zn-O separation values ( $u$ ). This tendency, seen for example in going from our 2.3 ML model to the 2.76 ML-A model, would tend to improve the agreement with experiment for larger models.

Table 10. Comparison of structural data for calculated model systems with experimental results **Error! Bookmark not defined.** in terms of interlayer Zn-Zn distances ( $d_{zn-zn}$ ), interlayer Zn-O ( $d'_{zn-o}$ ) distances and intralayer z-coordinate Zn-O spacings ( $u$ ).

Layer:	$d_{zn-zn}$ (Å)			$u$ (Å)				$d'_{zn-o}$ (Å)	
	1-2	2-3	3-4	1	2	3	4	1-2	2-3
2.7ML (exp) <b>Error! Bookmark not defined.</b>	2.3 6	2.5 0	2.5 0	0.2 0	0.2 6	0.2 8	0.5 7	2.1 0	2.2 2
2.2ML	2.4 4	2.3 6	x	0.1 0	0.0 8	0.1 6	x	2.0 8	2.2 8
2.3ML	2.4 4	2.4 4	2.6 0	0.1 2	0.0 9	0.1 4	0.0 8	2.0 8	2.1 9

2.76M-A	2.5 0	2.5 2	2.6 2	0.0 8	0.0 9	0.1 8	0.4 4	2.0 6	2.2 1
2.76ML-B	2.5 1	2.5 2	2.7 5	0.0 9	0.0 9	0.0 3	0.1 9	2.1 2	2.1 9
BCT-4L	2.6 2	2.7 1	2.6 2	0.1 0	0.0 1	0.0 1	0.1 0	2.0 8	2.1 1
WZ(bulk)	2.6 5	2.6 5	2.6 5	0.6 4	0.6 4	0.6 4	0.6 4	2.0 1	2.0 1
T1-4L	2.4 8	2.4 8	2.4 8	0.0 7	0.0 1	0.0 1	0.0 7	2.1 4	2.2 3
layered	2.3 0	2.3 8	2.3 0	0.0 5	0.0 2	0.0 2	0.0 5	2.3 3	2.3 7

Table 11 summarizes the calculated ZnO film-to-Ag substrate binding energies of the considered models and the relative energies of the corresponding free standing ZnO systems. According to Table 11, the binding energy with the Ag surface for 2ML ZnO is relatively less than the island models. This result is in line with the relatively high stability of the complete free standing bilayer structure. On the contrary the relatively unstable single ZnO sheet having the highest energy as free standing layer, binds most strongly with the Ag substrate. The addition of a 3<sup>rd</sup> layer in the case of the 2.2 ML model increases the binding energy very slightly, while being relatively destabilized as a free space system, which implies that Ag surface can interact with the partially covered films with reconstructed islands slightly more strongly than for a complete bilayer. However the addition of a 4<sup>th</sup> adlayer on top of 2.2 ML as in the case in 2.3 ML case leads to a slight decrease in the binding energy relative to the 2 and 2.2 ML models. This decrease is probably due to the 4<sup>th</sup> layer being relatively far from the Ag surface, and the fact that the addition of a small amount of the 4<sup>th</sup> layer does not cause such extensive reconstructions as in the case of 2.2 ML coverage. As the 3<sup>rd</sup> adlayer island size increases as, for example in the cases of the 2.76 ML models, although the internal ZnO structure is not energetically stabilized with respect to the lower coverage films, the binding energy slightly increases. We note that 2.76 ML-A model was found to be slightly (0.003 eV/ZnO) more stable than 2.76 ML-B model, where the main difference is that in the 2.76 ML-A model the edge atoms of the 3<sup>rd</sup> adlayer island are O instead of Zn.

Table 11. Energetic comparison of ZnO-Ag models.

coverage	ZnO-Ag binding energy (eV/ZnO)	Relative energies of free standing ZnO films (eV/ZnO)
1ML	0.17	0.21
2ML	0.08	0.00
2.2ML	0.08	0.03
2.3ML	0.07	0.06
2.76ML-A	0.09	0.06
2.76ML-B	0.09	0.06

In Figure 89, it can be seen that several sizes of triangular and/or truncated triangular islands are likely to form in a ZnO deposition ranging from 1 to 10 nm in size. Our models of 2.3 ML and 2.76 ML coverage on the Ag(111) surface give island sizes of 1.0 and 1.7 nm, respectively. Considering that our 2.65 ML and 2.76 ML models have different sized truncated triangular islands and exhibit the same edge and corner reconstructions, we believe that such reconstructions will be common for triangular types of island of larger sizes. The inner part of the island is likely to be formed by a mix of trigonally symmetric WZ and layered phases. We also suggest that truncated corners of islands will generally follow an atomic ordering based on the T1 structure and the edges to follow the BCT structure. We also note that BCT reconstructions have also been observed experimentally by He et al.<sup>137</sup> in ZnO(10  $\bar{1}$  0) surfaces. The T1 reconstruction gives the corner atoms, which are initially connected only to two atoms in the same layer, the possibility to also connect to the bottom layer. For the edges, similarly, the reconstructions of all two connected atoms with the layer below the island result in the BCT structured regions. Based on the above we suggest a general island structure as illustrated in Figure 96.

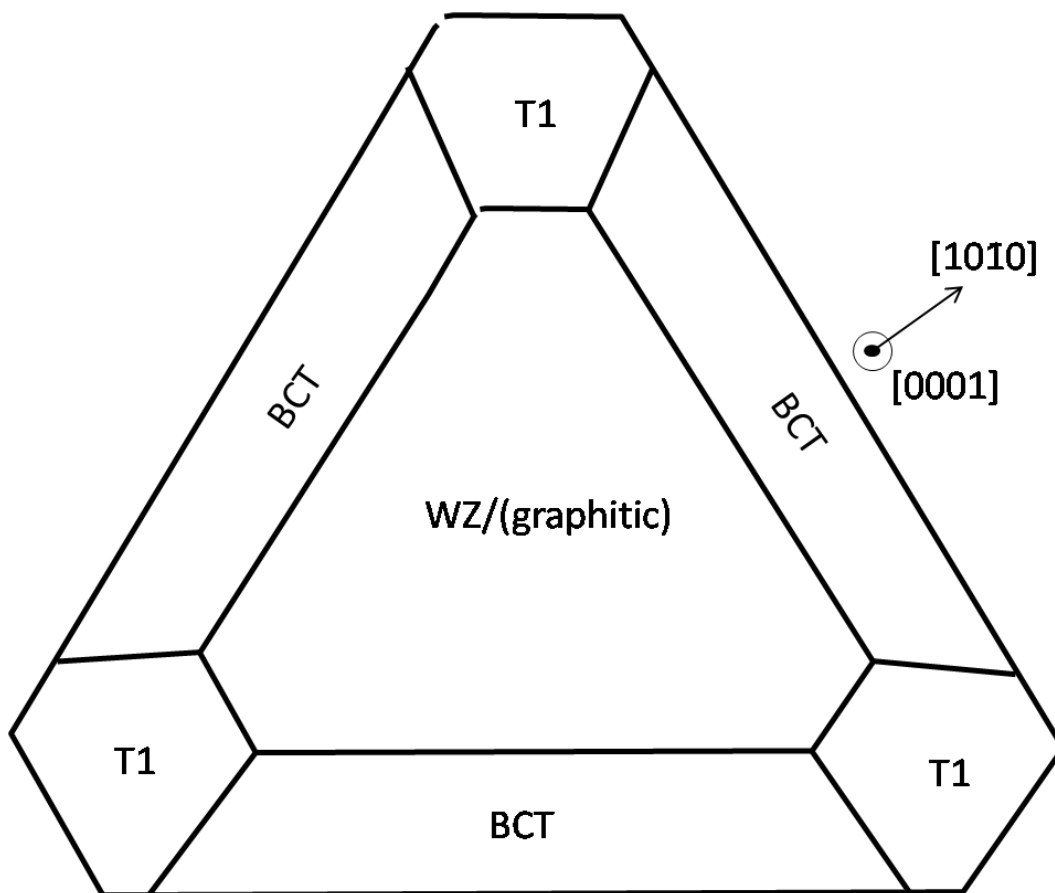


Figure 96. Illustrative model for a truncated triangular ZnO island.

According to our models and the experimental results **Error! Bookmark not defined.** the ZnO growth lies somewhere between FM and the SK growth modes. Although first two layers are said to exhibit only the layered ZnO phase, the influence of adlayers seem to induce structural changes in the layers underneath, namely first two complete MLs.

#### **4. Conclusions**

Following the experimental reports, and in particular measurements of a 2.7 ML Ag-supported ZnO film, we have theoretically creating models with 2 to 2.7 ML coverage by creating islands on a 3<sup>rd</sup> (and 4<sup>th</sup>) adlayer on top of a complete 2ML bilayer. The triangular adlayer islands are found to cause a structural transition to the WZ structure

in the island core and in local region in the two layers immediately below the island core. The islands are also found to have BCT structured reconstructions on their edges and T1 structured reconstructions on their corners. These models are found to better match the experimental structural data for the 2.7 ML film with respect to models assuming a purely layered or a purely WZ structure.

## **CHAPTER VI: Comparison of 3D-2D polymorphism of ZnO**

### **1. Introduction**

Size reduction of inorganic materials to the nanoscale often induces alternative atomic ordering, or polymorphism, relative to the most stable bulk crystal<sup>276</sup>. Nanoscale thin films are attractive well-defined systems to study this effect for theory and experiment. The (nano)technologically<sup>277</sup> important wide band gap wurtzite (wz) semiconductor ZnO, for example, exhibits polymorphism in [0001]-oriented nanofilms on Ag(111)<sup>278</sup> and Pd(111)<sup>279</sup>. For 3 monolayer (ML) thickness, these supported nanofilms have [0001]-stacked graphite like flat hexagonal layers with the stacking order of hexagonal BN. This layered form of ZnO (layered-ZnO) was first predicted to be more stable than wz-ZnO in density functional (DF) calculations for free-standing nanofilms  $\leq 9$  MLs.<sup>280</sup> The structure of layered-ZnO appears to be driven by the elimination of the energetic cost of the electric dipole due to ionic ordering in the stacking direction in nonreconstructed [0001]-oriented wz-ZnO films. Recent theoretical work has highlighted epitaxial strain as a possible means to stabilize supported layered-ZnO nanofilms for  $>9$  MLs.<sup>281</sup> Other DF studies of unsupported nanofilms have showed that the BCT-ZnO<sup>282</sup> structure is more stable than layered-ZnO and nonreconstructed wz-ZnO for [0001]-stacked nanofilms for 4–18 MLs.<sup>134</sup> The lack of (0001) basal plane trigonal symmetry in BCT-ZnO, however, is incompatible with epitaxial growth on (111) surfaces of fcc metals<sup>281</sup> and other substrates would be required.<sup>283</sup> Although BCT-ZnO is not a likely competing phase in experiments where layered-ZnO has thus far been observed, its relevance as a structural modification is highlighted by its observation at reconstructed ZnO (10 $\bar{1}$ 0) surfaces<sup>137</sup> and, as a predicted phase in

strained wz-ZnO nanorods.<sup>228</sup> Considerably expanding the handful of previously considered nanofilm polymorphs, we report over 20 ZnO polymorphs in both nanofilm and bulk form providing us with an unprecedented overview of the (nano)structural and energetic possibilities of this important material. We show that (i) the stability range of nanofilms and their energetic ordering are radically different than that of bulk polymorphs, (ii) there exist at least three nanofilm structures with trigonal basal plane symmetry compatible epitaxial growth on fcc metal (111) surfaces that are more stable than layered-ZnO, (iii) BCT-ZnO is one of many structurally related and near energetically degenerate polytypic phases, (iv) with increasing thickness atomically reconstructed wz-ZnO becomes more stable than BCT-ZnO for ~14 MLs, and is always more stable than nonreconstructed wz-ZnO, and (v) BCT-ZnO and layered-ZnO nanofilms are unstable to novel polymorphs under in-plane strain.

## **2. Methodology**

For all nanofilm and bulk structures, all unit cell parameters were optimized with all atoms optimized (forces  $< 0.01$  eV/Å<sup>-1</sup>) with periodic DF calculations employing the PW91 functional,<sup>241</sup> using the VASP code.<sup>240</sup> The projector augmented wave approach<sup>189,205</sup> was used to describe the effect of core electrons on valence states, with the latter represented by a plane wave basis with a 500 eV cutoff. Nanofilms were separated by over 10 Å in the c-stacking direction to avoid spurious periodic interactions. Reciprocal space  $k$ -point sampling was achieved through appropriate Monkhorst-Pack grids.<sup>265</sup> All nanofilms have between 32 and 128 atoms per cell, with supercell tests (up to 3×3) showing that all energies were converged to  $< 0.0005$  eV/ZnO. We generate 24 polymorphic structures using a bottom-up methodology based on nets first used to enumerate and classify bulk silicates having structures based on perpendicular linkages between two-dimensional hexagonal sheets.<sup>94</sup> Following the connectivity of the ten such nets in Ref. 94 with Zn-O bonding, we could generate nine distinct relaxed bulk ZnO polymorphs (including layered-ZnO, wz-ZnO, and BCT-ZnO). Such polymorphs have been predicted to be relatively stable bulk phases for

wurzite materials<sup>284</sup> and silicon.<sup>179</sup> For our remaining 15 polymorphs, we created new nets based on mixing together the “primary” nets which generated the nine stabilized polymorphs. New mixed nets were biased to those containing primary nets which previously generated more stable polymorphs. Using this method to search for stable nanofilm polymorphs has specific considerations: (i) a net which generates one bulk polymorph can often generate two [0001]-oriented nanofilms depending on the bulk cut, (ii) energetically detrimental polar surfaces can be avoided by consideration of the connectivity of the generating net.

### **3. Results and Discussion**

We first focus on 4 ML ZnO nanofilms, where experiments have not yet discerned a definite preferred atomic structure. Although nonreconstructed wz-ZnO is structurally unstable at this thickness (spontaneously converting into layered-ZnO) all other polymorphs either preserved their structure or converged to structures other than layered-ZnO. Unlike unreconstructed wz-ZnO, all other considered polymorphs have no dipole in the [0001] stacking direction. In a fully ionic picture the dipole in wz-ZnO can be quenched by atomically reconstructing the polar surfaces such that 25% of the charge on both terminating surfaces is compensated.<sup>119</sup> Structural relaxation and/or internal charge transfer may also assist dipole reduction<sup>129</sup> as in DF calculations of nonreconstructed wz-ZnO nanofilms.<sup>280,285</sup> Attempting to stabilize the wz-ZnO structure in 4 ML nanofilms, we transferred 25% of the Zn (O) ions from the (0001)-Zn(O) surface to the (0001)-O(Zn) surface, both as separated ions, and following experimental reconstruction patterns for bulk surfaces.<sup>128,131</sup> In all cases atomically reconstructed wz-ZnO 4 ML nanofilms were found to be  $>0.08$  eV/ZnO less stable than other 4 ML nanofilms considered.

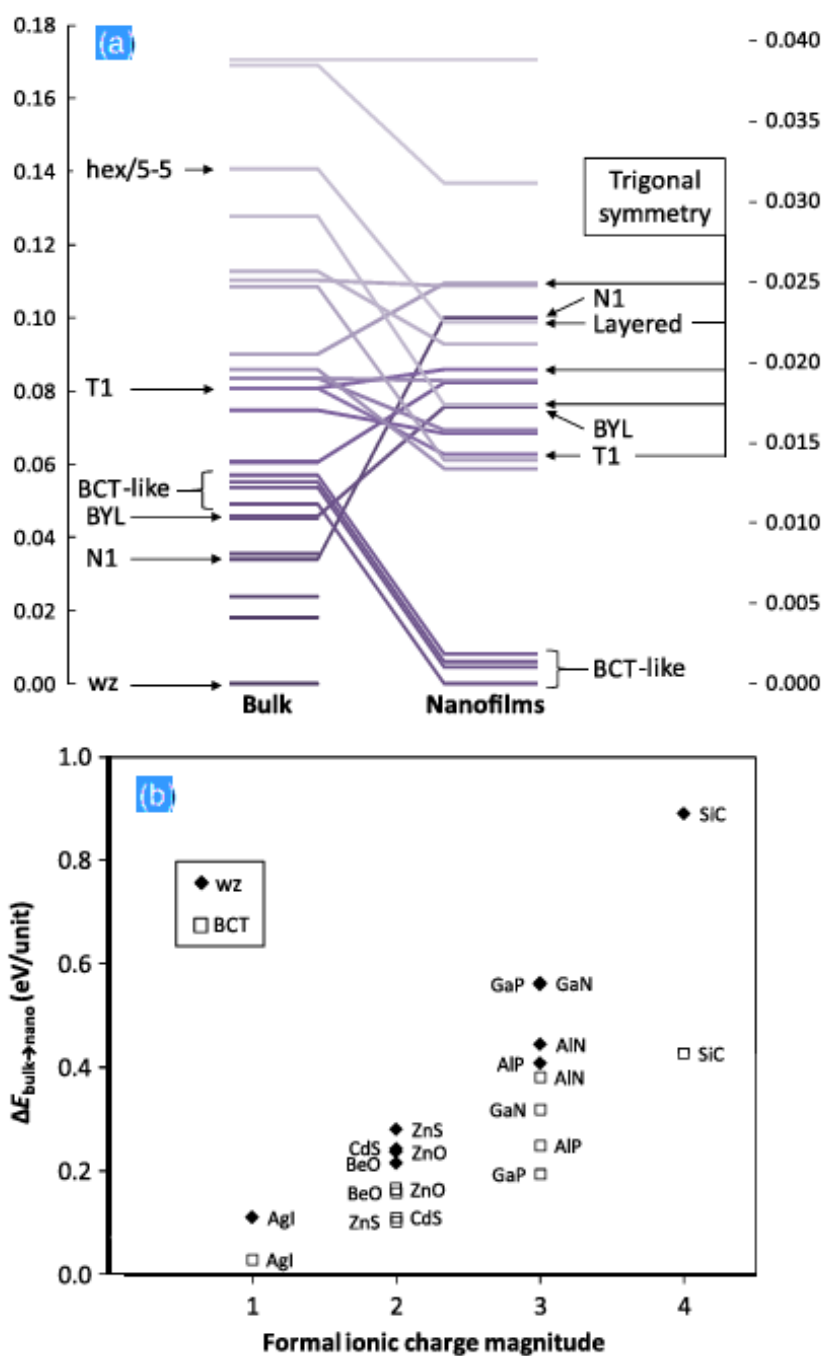


Figure 97. (a) Comparison of relative energies(eV/ZnO) of ZnO polymorphs as bulk and 4 ML nanofilms. Right and left energy y axes relate to bulk and nanofilm energies,respectively. (b)  $\Delta E_{\text{bulk} \rightarrow \text{nano}}$ (eV/unit) for wz and BCT for ten wurtzite materials.

In Figure 97 (a) we compare the energetic stabilities of 4 MLnanofilms and the corresponding bulk phase for a widerange of polymorphic structures, relative to the most stablenanofilm or bulk phase, respectively. For any single polymorphthe nanofilm stability is typically lower than in the bulk by  $\sim 0.1$  eV/ZnO. We highlight two important

general features: (i) the energy scale spanned by 4 ML nanofilms (0.04 eV/ZnO) is over four times smaller than that of the corresponding bulk structures (0.17 eV/ZnO), (ii) a significant stability reordering of corresponding structures occurs between 4 ML nanofilms and the bulk. The former suggests that interchanges between different polymorphs should be easier in nanofilms than in the bulk. On the ZnO(0001) surface, competition between nearly energetically degenerate reconstructed structures is found to be strongly dependent on temperature and the oxygen environment.<sup>286</sup> Our stoichiometric 0K structures provide a good starting point to explore such effects in nanofilms. The latter feature implied by Fig. 1(a) is that thin nanofilms are more likely to exhibit non-wz-ZnO phases. The most dramatic bulk-to-nanofilm energetic reordering occurs in the wz-to-BCT stability crossover. Using these two polymorphs as indicators of bulk and nanofilm stability, respectively, we can predict whether the energetic reordering in ZnO is general to other materials. The wz-to-BCT stability crossover can be quantified via the bulk-to-4ML-nanofilm destabilisation energy difference ( $\Delta E_{\text{bulk} \rightarrow \text{nano}}$ , i.e.,  $E_{\text{nanofilm}} - E_{\text{bulk}}$ , in eV/ZnO), being considerably lower for BCT-ZnO than for wz-ZnO. In Fig. 1(b) we plot the  $\Delta E_{\text{bulk} \rightarrow \text{nano}}$  for BCT and wz for ten materials showing that BCT is always less destabilized than wz such that a bulk-to-nanofilm stability crossover always occurs. The extent of the crossover is material specific, with  $\Delta E_{\text{bulk} \rightarrow \text{nano}}$  linearly increasing relative to a material's formal ionic charge [with  $\Delta E_{\text{bulk} \rightarrow \text{nano}}(\text{wz}) > \Delta E_{\text{bulk} \rightarrow \text{nano}}(\text{BCT})$  for all materials]. This strongly indicates that our findings for ZnO are applicable to many other materials. In the remainder we explore various physical implications suggested by the unique overview provided by Fig. 1(a).

Consistent with previous studies the most energetically stable 4 ML nanofilm has the BCT-ZnO structure. Within a very small energy range above BCT-ZnO for both bulk phases (0.01 eV/ZnO) and nanofilms (0.0025 eV/ZnO), we find three other structures. We call these structures BCT-like as they can be regarded as polytypes (i.e., different stacking sequences of structurally similar infinite two-dimensional layers<sup>287</sup>) with the constituent layers being parallel to the  $c$  axis. Polytypism also occurs in the stacking of the  $a - b$  aligned hexagonal layers with wurtzite (aligned stacking) and zinc blende (antialigned stacking) being the end members. For BCT-like structures, BCT is one end member with aligned layer stacking, with an antialigned layer stacked

structure (which we name BCT- $\omega$ , see Fig. 2) forming the other end member. Stacking variations allow potentially infinite possibilities, each giving rise to a distinct BCT-like polytype. Although close in energy, no structural changes in BCT- $\omega$  occurred in classical NPT molecular dynamics calculations (1 atm and 300–500 K for 100 ps), using dedicated potentials<sup>238</sup> and the GULP code.<sup>288</sup> The dynamical stability of BCT like polytypes (and *c*-stacked polytypes) may be due to the energetically expensive requirement of wholesale changes in bonding between all aligned layers for interconversions.

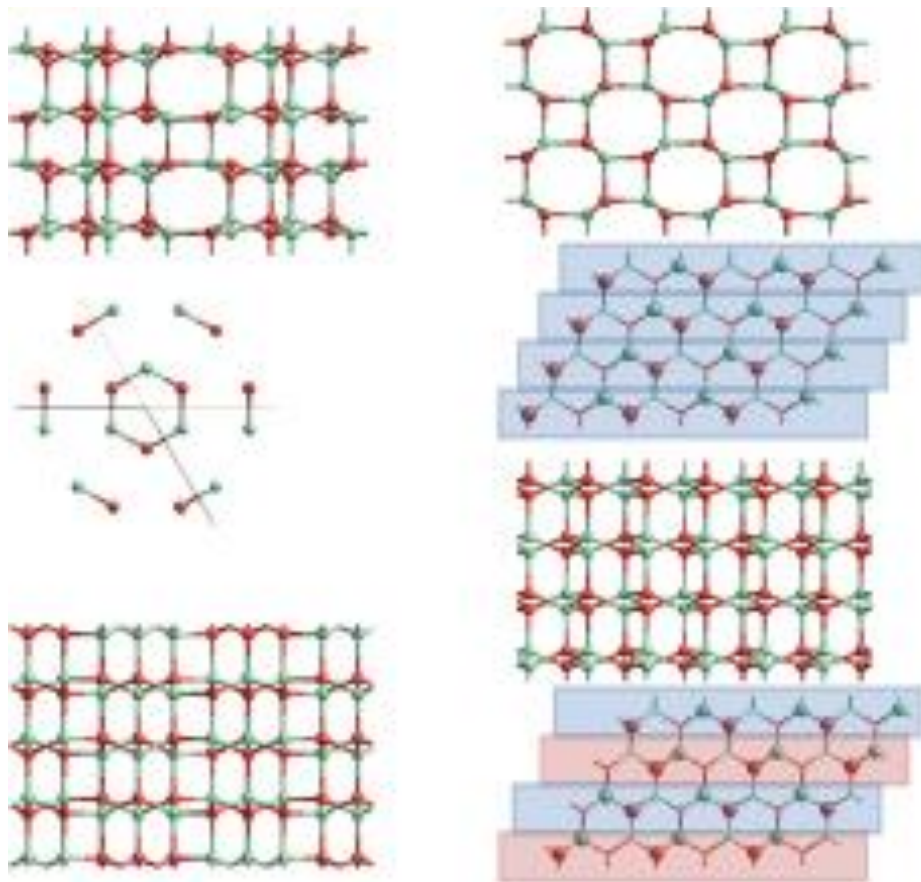


Figure 98. Selected polymorphs. Top left: T1 with its trigonal basal plane, bottom left: BYL, right: BCT (upper) and BCT- $\omega$  (lower) with respective *c*-aligned stacking sequences.

Although having high stabilities, due to their lack of trigonal (0001) basal plane symmetry, the BCT-like ZnO nanofilms are unlikely to explain the experimental observation that the fcc metal-supported layered-ZnO phase disappears for 3 ML.<sup>278,279</sup> Unlike the observed Zn deficiency on bulk-terminated polar (0001)-Zn surfaces,<sup>128</sup> in

Ref. 278, the 1:1 ZnO stoichiometry was kept fixed within all layers indicating that any dipole reduction is via another mechanism. The good structural agreement between experiment and theoretical calculations for freestanding layered-ZnO nanofilms<sup>280</sup> for the very thin 1–3 ML regime, indicates that metal support has a minor effect on nanofilm structure. Calculations on 1 ML layered-ZnO supported on Ag(111)<sup>214</sup> also show no indication of metal-ZnO charge transfer, confirming the rather passive role of the Ag support. The experimentally prepared 3.5 ML ZnO Ag(111)-supported nanofilm has a 55% 4 ML coverage (the third ML coverage being 5% undercomplete), and thus is formed by 50% of stoichiometric 4 ML ZnO.

Considering our set of stoichiometric nonpolar 4 ML nanofilms, we find three which have trigonal (0001) basal plane symmetry and are more energetically stable than layered-ZnO. The most stable of these (T1) is labeled in Figure 97 (see also Figure 98). In Table 12 we compare the calculated structures of T1-ZnO and layered-ZnO 4 ML nanofilms and bulk wz-ZnO with the experimental interlayer structural data for the 3.5 and 4.5 ML samples from Ref. 277. For interatomic distances between layers 1 and 2 in both 3.5 and 4.5 ML experimental samples, the best match with the calculated data is mainly for 4 ML layered-ZnO.

Table 12. Comparison of differences in calculated structural data [interlayer Zn-Zn ( $d_{\text{Zn-Zn}}$ ) and Zn-O ( $d_{\text{Zn-O}}$ ) distances] for layered-ZnO and T1-ZnO 4 ML nanofilms and bulk wz-ZnO with experimental data for 3.5 and 4.5 ML.<sup>278</sup> Best matches are underlined.

	3.5 ML			4.5 ML		
	Layer 1-2	Layer 2-3	Layer 3-4	Layer 1-2	Layer 2-3	Layer 3-4
$d_{\text{Zn-Zn}}(\text{Å})$						
Exp.	2.30	2.53	2.66	2.25	2.54	2.62
Layered	<u>0.00</u>	-0.15	-0.36	<u>0.05</u>	-0.16	-0.32
T1	0.18	<u>-0.05</u>	-0.18	0.23	<u>-0.06</u>	-0.14
wz (bulk)	0.35	0.12	<u>-0.01</u>	0.40	0.11	<u>-0.03</u>
$d'_{\text{Zn-O}}(\text{Å})$						
Exp.	2.27	2.40		2.10	2.26	
Layered	<u>0.06</u>	<u>-0.03</u>		0.23	0.11	
T1	-0.13	-0.18		<u>0.04</u>	<u>-0.03</u>	
wz (bulk)	-0.26	-0.39		-0.09	-0.25	

Following Ref. 278 this strongly indicates that this polymorph dominates the first two MLs. For layers 3 and 4 the interatomic Zn-O and Zn-Zn distances strongly point to an alternative structure in both samples, with the calculated bulk wz-ZnO interlayer distances matching well with experiment. Although free-standing 4 ML wz-ZnO nanofilms are inherently structurally unstable, it is perhaps possible in experiment that epitaxial effects and/or charge transfer from the support may help to stabilize more bulklike 4 ML nanofilm structures. Alternatively, the experimental data may point to another polymorphic structure for the 3.5 and/or 4.5 ML nanofilms. In Table 12, the calculated interlayer data for the T1-ZnO 4 ML nanofilm shows good agreement with the experimental data for the interatomic distances between layers 2 and 3, particularly for the 4.5 ML sample. Allowing for the estimated experimental error ( $\pm 0.1 \text{ \AA}$ ) an interpretation of the experimental data for layers 2 and 3 by layered-ZnO or wz-ZnO may also be possible. However, that there is at least one other candidate nanofilm structure that is fully compatible with the experimental interlayer data opens the possibility that such polymorphs could play a role in the observed structural instability of metal-supported ZnO for  $>2 \text{ ML}$ .<sup>278,279</sup>

Relative nanofilm structural stability can also be influenced by thickness. A previous study showed that BCT-ZnO is more energetically stable than layered-ZnO and unreconstructed wz-ZnO from 4–18 ML.<sup>134</sup> From Figure 97 we can choose a structure having an energetic stability between BCT-ZnO and layered-ZnO for 4 ML, and between wz-ZnO and BCT-ZnO in the bulk phase (e.g., N1 or BYL<sup>289</sup> in Figure 97). We can then predict that at some nanofilm thickness  $>4 \text{ ML}$  this phase will be more energetically favored than ZnO BCT. In Figure 99(a) we plot the energetic stability of BYL-ZnO (see also Figure 98) and that of BCT-ZnO relative to nanofilm thickness. Extrapolating from the calculated data points for 8, 12, 16, and 20 ML, we predict a crossover at a thickness of approximately 26 ML at which BYL-ZnO [blue line, Figure 99(a)] will be more stable than BCT-ZnO [gray line, Figure 99(a)]. Following previous work,<sup>280,281,134</sup> we also include unreconstructed wz-ZnO films (structurally stable for  $>9 \text{ ML}$  only) for comparison [green line, Figure 99(a)]. We find that the BCT-to-BYL

crossover occurs slightly before the thickness at which it is estimated that unreconstructed wz-ZnO becomes more stable than BCT-ZnO ( $\sim 28 \text{ ML}^{134}$ ). We also consider reconstructed wz-ZnO nanofilms. Although for 4 ML we could not stabilize the wz-ZnO structure, for  $\geq 8 \text{ ML}$  nanofilms atomic reconstruction can stabilize the wz-ZnO structure. Here we employ a simple individual ion transfer approach to quench the dipole in the 8–20 ML wz-ZnO nanofilms. As expected from our attempts with 4 ML nanofilms, 8 ML free-standing atomically reconstructed wz-ZnO nanofilms are considerably less stable than most other nanofilms (e.g., BCT-ZnO or BYL-ZnO). For increasing thickness, however, the stability of such nanofilms rapidly increases such that atomically reconstructed wz-ZnO becomes the most energetically stable ZnO phase for  $>16 \text{ ML}$  [red line, Figure 99(a)], well before either BYL-ZnO or unreconstructed wz-ZnO nanofilms start to energetically compete with BCT-ZnO. For all thicknesses considered, and by extrapolation, for all thicknesses  $\geq 9 \text{ ML}$ , our results imply that atomically reconstructed wz-ZnO should be always more stable than unreconstructed wz-ZnO. We note that the individual ion transfer method has been estimated to be 0.3 eV less efficient per transferred ion than more sophisticated atomic reconstructions.<sup>128</sup> In Figure 99(a) a dashed line shows the estimated downward shift due to such an improved model that has the main effect of causing the crossover with BCT-ZnO to occur at  $>14 \text{ ML}$  rather than  $>16 \text{ ML}$ .

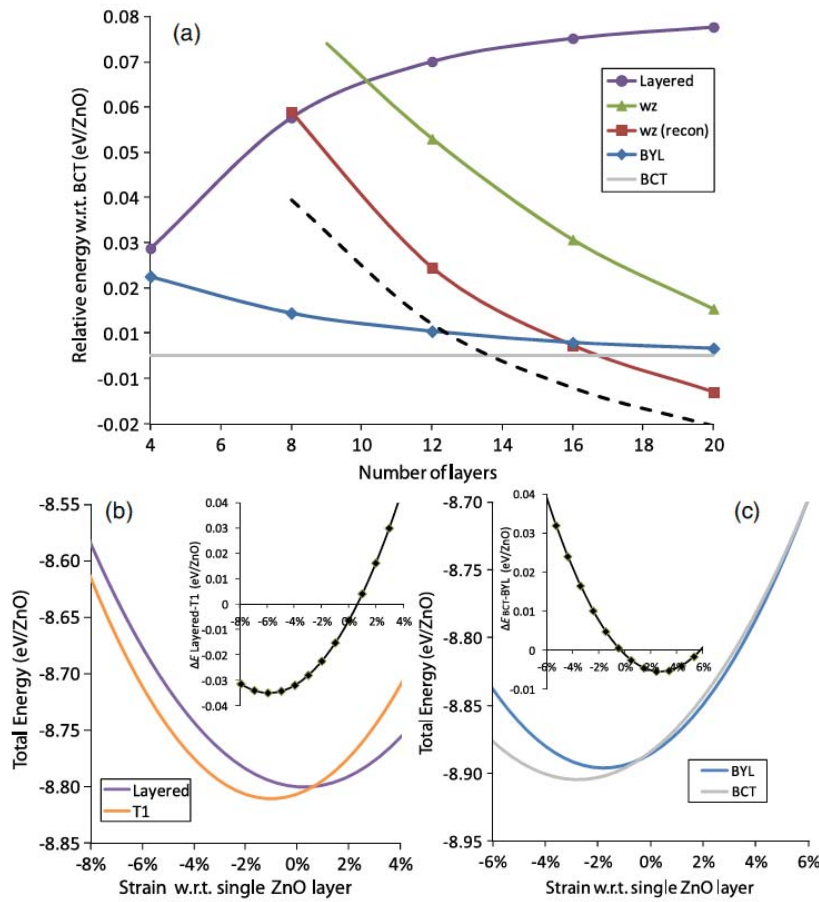


Figure 99. (a) Selected nanofilm energetic stability variation with thickness, (b) energy variation with in-plane strain for 4 ML layered-ZnO versus T1-ZnO, (c) energy variation with in-plane strain for 8 ML BCT-ZnO versus BYL-ZnO. Strains are relative to 1 ML layered-ZnO. Insets show polymorph energy differences.

Finally, we consider the effect of uniform in-plane  $a - b$  strain on relative nanofilm polymorphic stability. We examine two systems: (i) T1-ZnO versus layered-ZnO in 4 ML nanofilms, and (ii) BYL-ZnO versus BCT-ZnO in 8 ML nanofilms. In the first case, as the two polymorphs are compatible with growth on metal (111) substrates, our calculations indirectly investigate the possible effect of epitaxy on nanofilm polymorphism. In a similar study in Ref. 280 only unreconstructed 4 ML wz-ZnO was used as a comparison with 4 ML layered-ZnO and thus the latter was proposed to be the most stable nanofilm structure for all strains. In Figure 99(b) it can be seen that, although layered-ZnO is favored for larger positive strains, for small positive strains through to moderately compressive strains T1-ZnO is favored energetically. Our results imply that substrates with in-plane lattice mismatches that induce small compressive

epitaxial strains could help to stabilize T1-ZnO. In the second case we investigate the role of strain in potentially altering the energetic ordering of low energy free-standing BYL-ZnO 8 ML nanofilms relative to BCT-ZnO. For 8 ML nanofilms reconstructed w-ZnO is not energetically competitive with BCT-ZnO or BYL-ZnO but the latter two phases are close in energy. Under small positive strains we find that there is a small window of excess stability for the BYL-ZnO phase where energetic stability of the two nanofilms is inverted [see Figure 99(c)]. These results further confirm other theoretical studies which suggest that mechanical forces applied to ZnO nanosystems may be a fertile route to access new polymorphs.<sup>281228</sup>

#### **4. Conclusions**

In summary, we have developed a method to generate a wide range of new low energy nanofilm and bulk polymorphs using nets as a basis. Consideration of the energetic of these structures permits an unprecedented overview of nanoscale polymorphism in ZnO and its evolution with size and strain. Our results provide convincing evidence that low energy polymorphism in nanofilms of wurtzite materials should be very rich, and significantly beyond the handful of polymorphs previously considered in the literature. Our results strongly suggest that many new nanofilm polymorphs should be experimentally accessible, and in some cases (e.g., T1-ZnO), may have even already been observed.

# **CHAPTER VII: 3D polymorphism and effect of pore system (dimensionality): “Bandgap Engineering through Nanoporosity in ZnO”**

## **1. Introduction**

The tremendous success of solid-state device technologies is underpinned by our understanding of semiconductor physics and driven by our ever increasing ability to adapt and optimize the properties of such materials. This interplay between fundamental and applied approaches to materials research is well illustrated by the ongoing rapid development of the wide band gap ( $E_{\text{gap}}$ ) semiconductor zinc oxide (ZnO) for a variety of applications such as ultraviolet (UV) optoelectronics, solar cells and (bio)chemical sensors.<sup>8147290291</sup> For the first of these, efforts have focused on  $E_{\text{gap}}$  engineering through forming pseudo binary alloys of wurtzite ZnO (wz-ZnO,  $E_{\text{gap}} = 3.44 \text{ eV}$ <sup>292</sup>) with rocksalt MgO (rs-MgO,  $E_{\text{gap}} = 7.8 \text{ eV}$ ) to push the wz-ZnO  $E_{\text{gap}}$  further into the UV spectral range.<sup>48</sup> Due to metastable solid solubility constraints wz-Mg<sub>x</sub>Zn<sub>x-1</sub>O alloys can give maximum  $\Delta E_{\text{gap}}$  increases of  $\sim 0.55 \text{ eV}$  (for  $x=0.33$ ) before rs-MgO segregation. For sensor and solar cell applications increasing the surface area to volume ratio is paramount for enhancing device efficiency. One way to achieve this goal is to create nanoporous ZnO, as achieved by several experimental groups.<sup>293294295</sup> In recent years *ab initio* calculations based on Density Functional theory (DFT) have greatly assisted in our fundamental understanding of ZnO. In particular, such calculations have been used to investigate both  $E_{\text{gap}}$  engineering<sup>296</sup> and molecular sensing.<sup>297298</sup>

Herein, we use DFT calculations to compute the energetic stability ( $E_{\text{rel}}$ ) and  $\Delta E_{\text{gap}}$  shifts relative to wz-ZnO of 105 distinct ZnO polymorphs with varying degrees and types of nanoporosity. We find that nanoporosity (i.e. void volume proportion,  $V_{\text{pore}}$ ) is inextricably linked with both  $E_{\text{rel}}$  and  $\Delta E_{\text{gap}}$ . Generally, increasing  $V_{\text{pore}}$  tends to increase both  $E_{\text{rel}}$  and  $\Delta E_{\text{gap}}$ . Within this broad pattern, however, we find significant variations in  $\Delta E_{\text{gap}}$  ( $\sim 0.5 \text{ eV}$ ) for ZnO structures which can have almost exactly the same  $V_{\text{pore}}$  or  $E_{\text{rel}}$  values but different pore system dimensionality ( $D_{\text{pore}}$ ). Taking an upper limit to the range of  $E_{\text{rel}}$  as that of the experimentally prepared dense rs-ZnO polymorph<sup>18</sup>, we

estimate that altering  $V_{\text{pore}}$  and/or  $D_{\text{pore}}$  of a structure could lead to tailored  $\Delta E_{\text{gap}}$  shifts up to  $\sim 1.5$  eV. Our study strongly suggests that  $V_{\text{pore}}$  and/or  $D_{\text{pore}}$  could be employed in an effective morphological approach to  $E_{\text{gap}}$  engineering thus opening the door to optoelectronically tunable sensors, solar cells and other devices which could take advantage of this versatile combination.

## **2. Methodology**

Following previous studies,<sup>172 299</sup> we mined databases containing 4-connected nets (4CNs)<sup>94300301302303</sup> to obtain the underlying bonding topologies to produce a large range of ZnO structures. In addition to the 26 previously reported low density ZnO polymorphs<sup>304</sup>, we include 60 new 4CN-based structures, and 19 more structures based on manually creating nanoporous [001]-directed one dimensional ( $D_{\text{pore}} = 1$ ) linear nanopores with different shapes, diameters and patterns of inter-pore spacing in bulk wz-ZnO (wz-ZnO-NP structures). These wz-ZnO-NP structures were deliberately designed to avoid metastable internal (0001) polar surfaces. We note that none of the 4CN-based polymorphs appear to have internal polar surfaces. Other computational approaches to studying novel nanoporous ZnO materials based on using cage-like nanoclusters as building blocks have also been reported.<sup>305</sup> This approach tends to give rise to structures with relatively high porosities and high metastabilities with respect to most of the structures reported herein and only a few such structures are included in our study. All structures were optimised and checked to be energy minima by phonon calculations using the GULP<sup>288</sup> code with an empirical potential<sup>238</sup>. Subsequent DFT structure optimisations combined the gradient corrected PBE<sup>204</sup> functional and a projector augmented wave<sup>205</sup> description of atomic cores as implemented in the VASP 5.2 code.<sup>189240306</sup> To minimize spurious dependency of basis-set quality on unit-cell size, all reported energies and structures correspond to two sequential optimizations of both atomic positions and cell parameters (until forces were  $< 0.01$  eV/Å<sup>-1</sup>) and a final single point calculation. Calculations used a 500 eV plane-wave cut-off, with  $\Gamma$ -centred Monkhorst-Pack  $k$ -point grids<sup>265</sup> chosen so that the energy differences between polymorphs were converged to  $< 0.01$  eV. The optimised cell parameters, fractional coordinates, energetic stabilities and PBE  $E_{\text{gap}}$  values of all 105 nanoporous ZnO

polymorphs is provided in the Supporting Information. *Ab initio* molecular dynamics (using the above set-up) was used on a small representative set of structures to further verify thermal stability.  $V_{\text{pore}}$  and  $D_{\text{pore}}$  values were obtained using the Zeo++ code.<sup>307</sup> A probe size of 0.55 Å radius was chosen as the smallest size for which wz-ZnO was still reported as being nonporous (i.e.  $V_{\text{pore}}=0$ ). Ionic radii of 0.74 Å and 1.40 Å were used for Zn and O ions respectively. The reliability of the PBE functional for predicting  $\Delta E_{\text{gap}}$  shifts was tested using many body GW calculations to calculate  $E_{\text{gap}}$  for 13 selected ZnO structures with a varied range of  $V_{\text{pore}}$  and  $E_{\text{rel}}$ . The optimal GW setup was derived using a wz-ZnO unit cell for which we concluded that a manifold of virtual bands close to ten times the number of electrons in the cell was necessary to ensure convergence. This procedure was used for all other structures. The initial optimized structures and eigenvalue and eigenvector guesses were generated with a PBE pre-run. We then used the partially self-consistent GW scheme, as implemented in VASP 5.2, to update the eigenvalues up to convergence with a threshold of 0.01 eV. A plot of  $E_{\text{gap}}(\text{GW})$  versus  $E_{\text{gap}}(\text{PBE})$  could be fitted well with straight line ( $R^2=0.93$ ) confirming a good linear correspondence between both data sets, see Figure 100. A similar linear systematic underestimation of  $E_{\text{gap}}(\text{GW})$  data by  $E_{\text{gap}}(\text{PBE})$  data has been reported for a wide range of materials.<sup>308</sup> GW recalculates the eigenvalues taking into account the electron-electron screened potential, but the orbitals are still PBE orbitals. It is therefore reasonable to assume that some sort of linear trend is preserved, i.e. larger PBE gap implies larger GW gap. As the wz-ZnO  $E_{\text{gap}}(\text{GW})$  value slightly underestimates the experimental  $E_{\text{gap}}$  of 3.44 eV<sup>292</sup> by 0.36 eV, we report  $\Delta E_{\text{gap}}(\text{PBE}_{\text{GW-fit}})$  values (i.e.  $\Delta E_{\text{gap}}(\text{PBE})$  values corrected by the linear scaling of the  $E_{\text{gap}}(\text{PBE})$  data with respect to the  $E_{\text{gap}}(\text{GW})$  data in Figure 100) the as estimated predictions of  $\Delta E_{\text{gap}}$  values throughout.

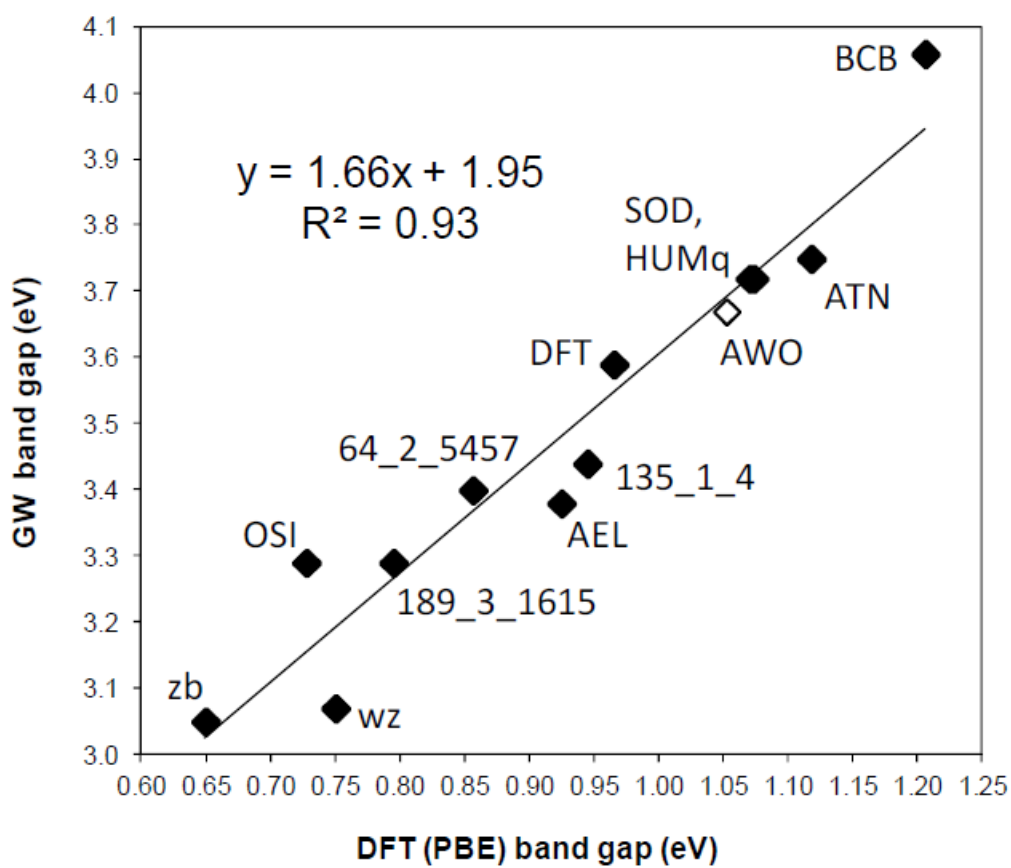


Figure 100.  $E_{\text{gap}}(\text{GW})$  versus  $E_{\text{gap}}(\text{PBE})$  for 13 structures showing the linear fit. The open point relates to a structure with an indirect  $E_{\text{gap}}$ . Structures and properties of the labelled polymorphs can be found in the full list also in the SI.

### 3. Results and Discussion

We first estimate the synthetic viability of our 105 ZnO polymorphs through their calculated  $E_{\text{rel}}$  (i.e. energy relative to wz-ZnO) values by taking an upper bound of +0.3 eV/ZnO, corresponding to the  $E_{\text{rel}}$  of the experimentally synthesized rs-ZnO polymorph.<sup>18172</sup> In Figure 101a we plot  $E_{\text{rel}}$  versus  $V_{\text{pore}}$  for all ZnO polymorphs, showing that the majority (88%) of structures are within the delimited  $E_{\text{rel}}$  viability range together with a tendency for  $E_{\text{rel}}$  to increase with increasing  $V_{\text{pore}}$ . This type of relation has been reported previously for smaller calculated data sets of purely 4CN-based materials<sup>172304</sup> and experimentally found for a variety of porous materials.<sup>309</sup> Unlike the 4CN-based polymorphs, the wz-ZnO-NP structures exhibit three-coordinated

atoms on their nanopore walls, but their  $E_{\text{rel}}$  values (open data points in Figure 101a) follow the same general stability pattern relative to  $V_{\text{pore}}$ . In fact, a number of wZ-ZnO-NP structures in our set are found to be the most stable polymorphs relative to their  $V_{\text{pore}}$  values. Within the studied range of structures, as  $V_{\text{pore}}$  increases, the range of  $E_{\text{rel}}$  values corresponding to a given  $V_{\text{pore}}$  also tends to increase indicating that, there are more relatively stable (i.e. with respect to  $E_{\text{rel}}$  of rs-ZnO) ways to make structures with higher  $V_{\text{pore}}$  values than with smaller  $V_{\text{pore}}$  values. Of course, this increase in the range of  $E_{\text{rel}}$  with increasing  $V_{\text{pore}}$ , if it continues, implies that polymorphs with relatively large  $V_{\text{pore}}$  values (i.e. approximately  $V_{\text{pore}} > 0.5$ ) will be metastable relative to rs-ZnO and thus few, relatively stable polymorphs will be found.<sup>305</sup>

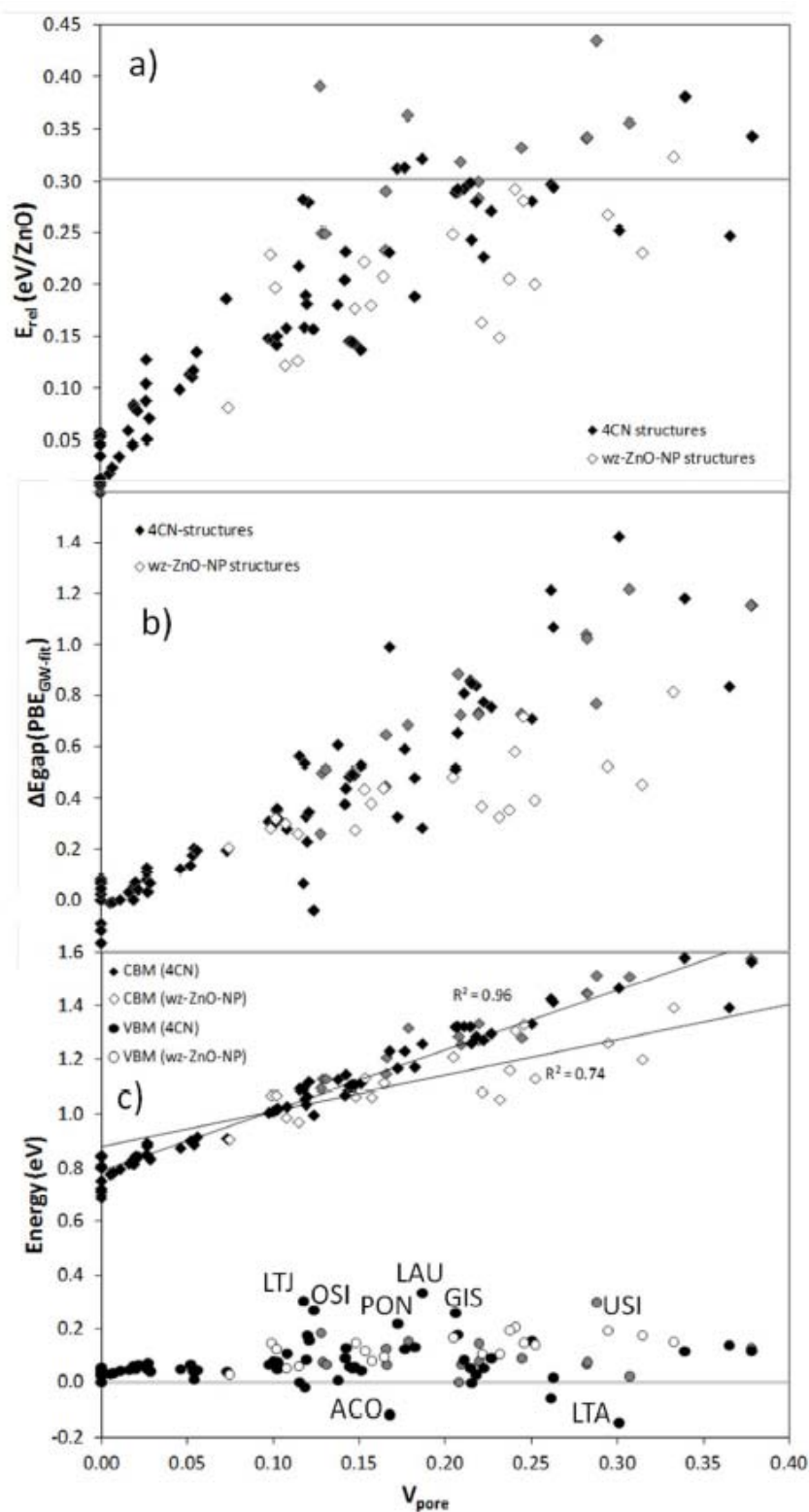


Figure 101. Variation relative to  $V_{\text{pore}}$  of: a)  $E_{\text{rel}}$  (grey line indicates  $E_{\text{rel}}$  of rs-ZnO), b)  $\Delta E_{\text{gap}}$ (PBE<sub>GW-fit</sub>), c) VBM and CBM values of all structures where some structures with outlying VBM values are labelled.

For electronic structure we find that the  $\Delta E_{\text{gap}}(\text{PBE}_{\text{GW-fit}})$  shifts also generally increase with increasing  $V_{\text{pore}}$  (see Figure 101b). Only considering polymorphs in the defined viable energy range (i.e. below the grey line in Figure 101a), nanoporosity can induce  $\Delta E_{\text{gap}}(\text{PBE}_{\text{GW-fit}})$  shifts up to  $\sim 1.5$  eV. Although our polymorphs have relatively low densities, this is primarily due to increased void spaces in the structures and not increased average bond lengths, which would reduce  $E_{\text{gap}}$  values (see effect of strain on  $\Delta E_{\text{gap}}$  in wz-ZnO in Figure 102).

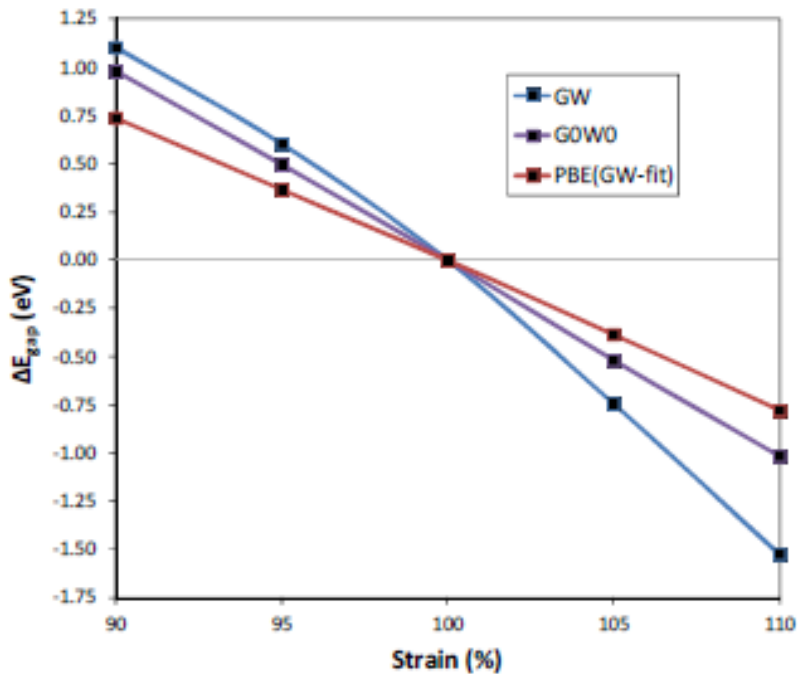


Figure 102.  $\Delta E_{\text{gap}}$  versus strain for wz-ZnO calculated at various levels of theory. The linear fit to the GW data for porous non-strained structures has been applied to the DFT PBE data.

As with  $E_{\text{rel}}$ , the range of possible  $\Delta E_{\text{gap}}(\text{PBE}_{\text{GW-fit}})$  shifts for a given  $V_{\text{pore}}$  value also tends to increase with increasing  $V_{\text{pore}}$ . Although  $E_{\text{rel}}$  and  $\Delta E_{\text{gap}}$  are not generally strongly correlated, we note that the minority (14%) of structures with indirect bandgaps (grey points in Figure 101 and Figure 105) have relatively higher  $E_{\text{rel}}$  values. In Figure 103 we show three selected pairs of structures where each pair has similar  $V_{\text{pore}}$  values, but significant differences in  $\Delta E_{\text{gap}}(\text{PBE}_{\text{GW-fit}})$ . For the pair of structures with the highest

$V_{\text{pore}}$  values, both are also found to have very similar  $E_{\text{rel}}$  values. In the case of the 19 wz-ZnO-NP structures, unlike the wide scatter observed in the  $E_{\text{rel}}$  values, their  $\Delta E_{\text{gap}}(\text{PBE}_{\text{GW-fit}})$  values tend to lie in a narrower range (0.61 eV) and often have the smallest  $\Delta E_{\text{gap}}(\text{PBE}_{\text{GW-fit}})$  values relative to their  $V_{\text{pore}}$  value. Although the nanoporous channels in the wz-ZnO-NP polymorphs are not large enough to exhibit extended bulk terminated surfaces, by virtue of their [001] orientation they tend to display infinite one dimensional “nano-facets” of both the stable  $(10\bar{1}0)$  and  $(11\bar{2}0)$  surfaces of wz-ZnO33. These surfaces, and thus the interior channel walls of the wz-ZnO-NP structures, possess 3-coordinated atoms, with associated relatively higher local structural distortions. Due to these features, the  $(11\bar{2}0)$  surface, in particular, is predicted to induce a  $\Delta E_{\text{gap}}$  shift of -0.24 eV<sup>34</sup>, tending to modulate positive  $\Delta E_{\text{gap}}$  shifts due to nanoporosity.

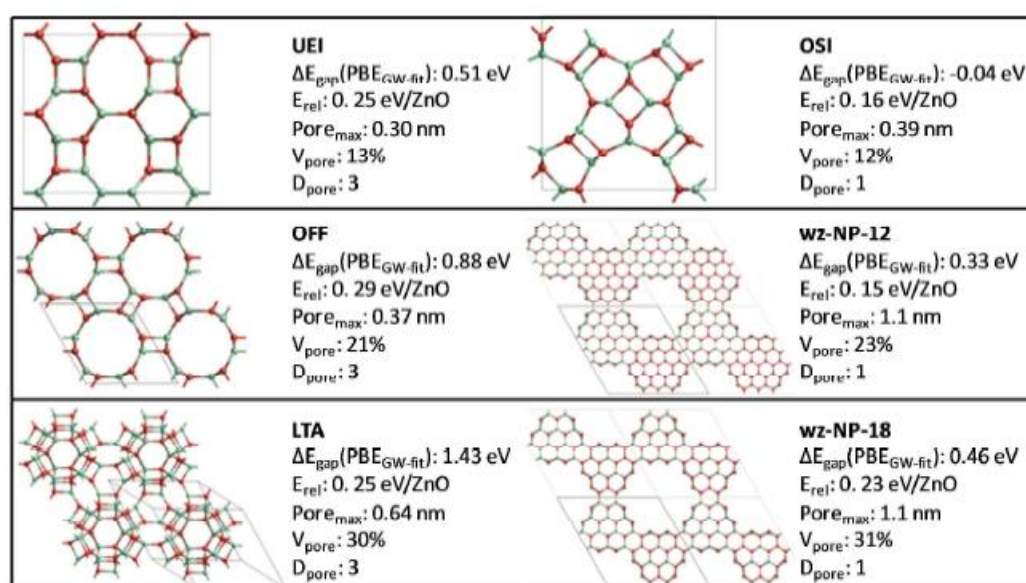


Figure 103. Comparison of a range of properties for three pairs of polymorphs having similar  $V_{\text{pore}}$  values. Key: green-zinc, red-oxygen, grey line-unit cell.

For our set of polymorphs, each having the same composition with very small variance in local atomic charge ( $\bullet \pm 0.05$  e according to Bader partitioned charges<sup>310</sup>), and the majority having 4-coordinated ions having similar local structural environments (e.g. Zn-O bonds between 1.95-2.05 Å, and average deviation of the Zn-O-Zn and O-Zn-O bond angles relative to the tetrahedral value of 109.47° of  $\leq 15^\circ$ ), we expect the highly

localized deeply shielded core level energies to be very similar in all structures. Taking the average energy of the Zn 1s core states as a common reference value for comparing band energies, in Figure 101c we plot the valence band maximum (VBM) and the conduction band minimum (CBM) for all structures (relative to wz-ZnO) versus  $V_{\text{pore}}$ . The plot reveals a number of insights into the physical basis underlying the results in Figure 101b. First, the VBM levels for most structures lie within  $\pm 0.2$  eV that of wz-ZnO with a no strong general increasing or decreasing tendency relative to  $V_{\text{pore}}$ . Second, VBM energies which differ most relative to that of wz-ZnO tend to correspond to structures having larger local structural distortions. In Figure 101c we label a few of the points corresponding to structures with outlying VBM values. For example, structures OSI and PON have some particularly long bonds ( $\sim 2.2$  Å), structures ACO and LTA have some very short bonds ( $\sim 1.9$  Å) and all apart from OSI have highly distorted bond angles ( $> 17.5^\circ$  average tetrahedral deviation). These specific structural features seem to be mainly responsible for the scatter of  $\Delta E_{\text{gap}}$  shifts (i.e. through VBM variability) for similar  $V_{\text{pore}}$  values. Third, the CBM shows a linear increase with increasing  $V_{\text{pore}}$ , providing further insight into the overall increase in  $\Delta E_{\text{gap}}$  with increasing  $V_{\text{pore}}$  in Figure 101b. The 4CN-based polymorphs have CBM values lying in a narrow ( $\sim 0.2$  eV) increasing band of energy with respect to  $V_{\text{pore}}$ . The wz-ZnO-NP structures seem to follow a similar but slightly shallower trend, in line with their relatively smaller  $\Delta E_{\text{gap}}$  shifts with increasing  $V_{\text{pore}}$ . Further, evidence supporting the generality of this phenomenon is also provided by our calculated data for other important semiconductor materials. In Figure 104 we show the VBM and CBM values for a selection of nine polymorphs of CdS and CdSe with a range of  $V_{\text{pore}}$  values. As with the case of the full set of 105 structures realised as ZnO we see the same average stability of the VBM and a clearly linearly increasing CBM with increasing  $V_{\text{pore}}$ .

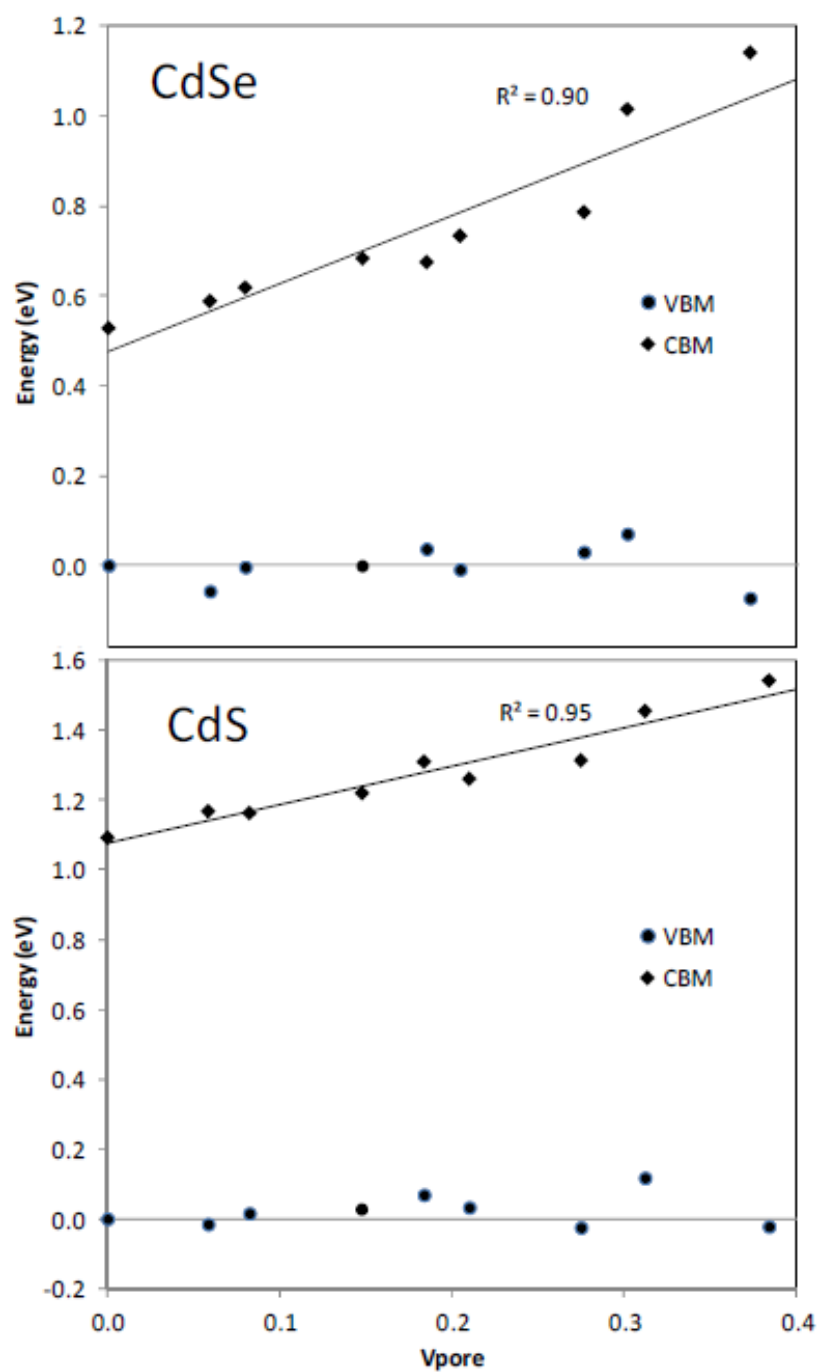


Figure 104. VBM and CBM dependence on  $V_{pore}$  for a selection of 4CN-based structures realised as CdSe (upper) and CdS (lower) polymorphs.

From an electronic band structure perspective we can see how increasing nanoporosity could produce a general trend for increasingly positive  $\Delta E_{gap}$  shifts as we find in the CBM data. Starting with an infinite dense material, bands are produced through the

accumulation of periodic orbital overlaps from atomic bonding in the crystal. Band dispersion results from overlap variation in such sums with respect to different crystal directions. Introducing regularly repeated void spaces in a dense crystal periodically removes atoms and thus their band-forming capacity, tending to resulting in proportionally smaller band widths. Assuming that such void formation does not introduce new mid-gap states through defects and that the remaining atomic/electronic structure of the material is relatively unperturbed, the band positions will remain fairly constant and their bandwidths will be reduced. Specifically considering this effect with respect to the VB and CB we would expect a tendency of increasing  $\Delta E_{\text{gap}}$  with increasing  $V_{\text{pore}}$ . This effect will tend to be more pronounced for: (i) higher  $V_{\text{pore}}$  values, and (ii) more dispersive bands. Although the descriptive periodic-atom removal model described above does not strictly apply to the full set of nanoporous structures we consider (e.g. the atomic structures of the zeolitic polymorphs are quite distinct from wz-ZnO) we propose that the general tendency for  $\Delta E_{\text{gap}}$  increase with increasing  $V_{\text{pore}}$  follows from the essential physics underlying our interpretation. To examine this link more explicitly, in Figure 105 we plot the bandwidth of the CB and VB of every nanoporous polymorph with respect to  $\Delta E_{\text{gap}}(\text{PBE}_{\text{GW-fit}})$  (Figure 105a) and  $V_{\text{pore}}$  (Figure 105b). Clearly, the plots show a general tendency for an decrease in the bandwidth of both the CB and VB with both increasing  $\Delta E_{\text{gap}}(\text{PBE}_{\text{GW-fit}})$  and  $V_{\text{pore}}$  strongly supporting our interpretation. In particular, we note that the CB is generally significantly more dispersive than the VB, which as suggested above, would account for the larger effect of porosity-induced dispersion reduction in the position of the CBM relative to the VBM, as we observe.

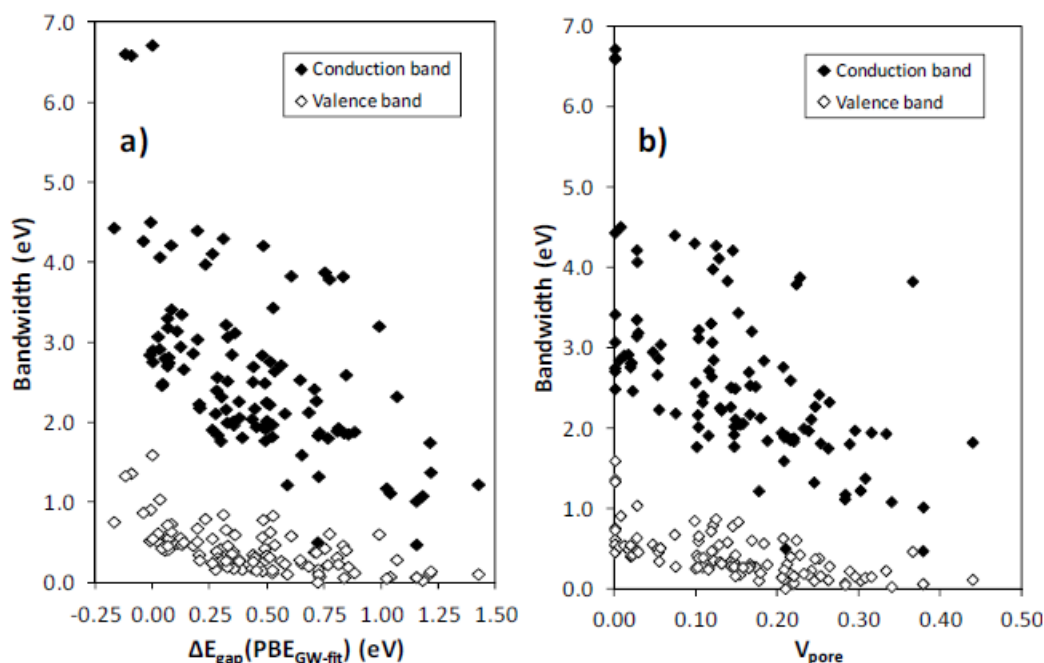


Figure 105. Plots of conduction band and valence band bandwidths versus: a)  $\Delta E_{\text{gap}}(\text{PBE}_{\text{GW-fit}})$  and b)  $V_{\text{pore}}$ .

Considering the  $\Gamma$  point, where the VBM and CBM are located for 86% of all our structures, band energies are determined by in-phase orbital overlap in all directions equally. For a given  $V_{\text{pore}}$ , we would expect the most effective way to increase  $\Delta E_{\text{gap}}$  would be to have internal void space which restricts overlap in most directions throughout the crystal. In this way we can imagine that  $\Delta E_{\text{gap}}$  should tend to also increase with increasing  $D_{\text{pore}}$ . Conversely, low dimensional  $D_{\text{pore}}$  systems which leave directions where little or no void space is encountered, would result in less dispersion reduction. As a further test of our proposal, in Figure 106a we investigate the correlation of  $\Delta E_{\text{gap}}$  with  $D_{\text{pore}}$  by binning our  $\Delta E_{\text{gap}}(\text{PBE}_{\text{GW-fit}})$  data with respect to the  $D_{\text{pore}}$  value of each respective structure. Consistent with our suggested physical mechanism, with increasing  $D_{\text{pore}}$  from 0-3, we see a striking monotonic increase in the average and highest  $\Delta E_{\text{gap}}(\text{PBE}_{\text{GW-fit}})$  shift. For each  $D_{\text{pore}}$  value we observe a range of  $\Delta E_{\text{gap}}(\text{PBE}_{\text{GW-fit}})$  shifts which reflect specific differences in structure and  $V_{\text{pore}}$ . Following our results Figure 101b and Figure 101c, the variance in  $\Delta E_{\text{gap}}(\text{PBE}_{\text{GW-fit}})$  for each  $D_{\text{pore}}$  value is also reasonably well correlated to  $V_{\text{pore}}$  and  $E_{\text{rel}}$ , as is shown by the incremental shading of data bars in Figure 106a. As our  $D_{\text{pore}}$  values depend somewhat on the probe radius

and ionic radii chosen in the Zeo++ code<sup>307</sup> we take average data as most physically meaningful for each  $D_{\text{pore}}$ . The dependence of both the average  $\Delta E_{\text{gap}}(\text{PBE}_{\text{GW-fit}})$  shift and the average  $E_{\text{rel}}$  magnitude on  $D_{\text{pore}}$  in our wide-ranging set of structures suggests that there may be a fundamental restriction on the obtainable  $\Delta E_{\text{gap}}$  and  $E_{\text{rel}}$  ranges for any particular  $D_{\text{pore}}$ , in line with the interpretation given above.

An additional factor, of importance for any practical application of nanoporosity for  $E_{\text{gap}}$ -engineering of materials, is the effect of pore size distribution on the size of the obtainable  $\Delta E_{\text{gap}}$  shift for any given  $V_{\text{pore}}$ . Based on the above arguments, we may expect that many smaller pores may be a more effective way to introduce voids that are encountered in more directions throughout a crystal, and thus produce higher  $\Delta E_{\text{gap}}$  shifts, than fewer large pores. In Figure 106b we plot  $\Delta E_{\text{gap}}(\text{PBE}_{\text{GW-fit}})$  against the ratio of the largest pore diameter ( $\text{Pore}_{\text{max}}$ , as measured by a spherical probe) to  $V_{\text{pore}}$  for all structures with  $V_{\text{pore}} > 0$ , where we subtract the effect of only  $1/V_{\text{pore}}$ . The  $(\text{Pore}_{\text{max}} - 1)/V_{\text{pore}}$  ratio is highest for structures with large  $V_{\text{pore}}$  values accomplished with relatively small pores and vice versa. Overall, the data confirm a sharp increase in the maximum range of obtainable  $\Delta E_{\text{gap}}(\text{PBE}_{\text{GW-fit}})$  values for decreasing  $(\text{Pore}_{\text{max}} - 1)/V_{\text{pore}}$  values. Specific to wz-ZnO-NP structures, in the inset in Figure 106b we show the  $\Delta E_{\text{gap}}(\text{PBE}_{\text{GW-fit}})$  values of six structures with similar  $V_{\text{pore}}$  values but different pore size distributions. Four of these structures are closely grouped with  $\Delta E_{\text{gap}}(\text{PBE}_{\text{GW-fit}})$  shifts between 0.33-0.39 eV and have respective  $\text{Pore}_{\text{max}}$  values between 0.94-1.1 nm. The structure with the largest  $\text{Pore}_{\text{max}}$  value only has one pore size, but the others in this subset also have additional smaller diameter ( $< 0.6$  nm) pores. The two remaining structures have only smaller pore sizes ( $\text{Pore}_{\text{max}}$ : 0.57 nm and 0.55 nm) and show the highest corresponding  $\Delta E_{\text{gap}}(\text{PBE}_{\text{GW-fit}})$  shifts (0.58 eV and 0.72 eV). This confirms the importance of smaller  $\text{Pore}_{\text{max}}$  values for obtaining higher  $\Delta E_{\text{gap}}$  shifts.

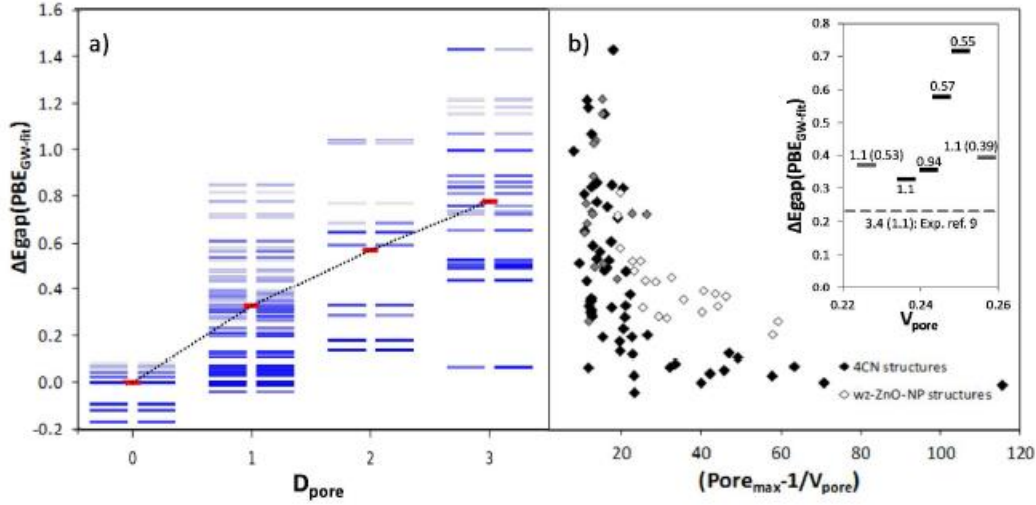


Figure 106. Dependence of  $\Delta E_{\text{gap}}(\text{PBE}_{\text{GW-fit}})$  on: a)  $D_{\text{pore}}$ , where shaded bars show  $\Delta E_{\text{gap}}(\text{PBE}_{\text{GW-fit}})$  values ordered by increasing magnitude (dark to light) relative to  $V_{\text{pore}}$  (right) and  $E_{\text{rel}}$  (left) for each  $D_{\text{pore}}$  (dashed line indicates average trend), b)  $(\text{Pore}_{\text{max}}-1)/V_{\text{pore}}$  (inset shows  $\Delta E_{\text{gap}}$  values of wz-ZnO-NP structures with similar  $V_{\text{pore}}$  values but different labelled  $\text{Pore}_{\text{max}}$  values – smaller pore sizes are in parentheses).

We have found one experimental report of a measured  $\Delta E_{\text{gap}}$  shift of +0.23 eV in nanoporous ZnO.<sup>295</sup> The reported sample has nanopore diameters ranging from 1 nm to 3.1-3.4 nm and intervening highly crystalline pore walls of similar or larger thicknesses. Although we do not know the  $V_{\text{pore}}$  of this sample, taking into account only  $\text{Pore}_{\text{max}}$  (i.e. 3.4 nm) we can compare it with our calculated wz-ZnO-NP data (dashed line in Figure 106b inset). Considering the many potential differences between our structures and this specific experimentally prepared sample (e.g.  $V_{\text{pore}}$ ,  $D_{\text{pore}}$ , surface states, defects, impurities, etc) the order of magnitude of the  $\Delta E_{\text{gap}}$  shift is very consistent with our predictions. We note that the experimentally observed  $\Delta E_{\text{gap}}$  shift in ref 295 was ascribed to quantum confinement by the authors. This would entail a more symmetric opening of the  $E_{\text{gap}}$  through band position shifts w.r.t wz-ZnO, which we do not observe in for our structures. We see no fundamental reason why further experimental efforts should not be able to reduce the  $\text{Pore}_{\text{max}}$  in such wz-ZnO-NP samples to achieve greater  $E_{\text{gap}}$  control.

#### **4. Conclusions**

Nanoporosity-induced bandwidth reduction is predicted to be a general means to controllably increase the band gap in semi-conducting materials. We also note that experimental progress has also been made in the fabrication of (cosubstituted) 4CN-based nanoporous ZnO polymorphs. The ATN zeolitic ZnO framework has, for example, been synthesised with 25% Zn atoms substituted by Li and K<sup>181</sup>. A theoretical study of such materials<sup>182</sup> has shown that they have significantly larger band gaps than wz-ZnO which appears to be due to their nanoporous ZnO framework and the “alloying” effect of the Li and K cations (viewing such materials as alloys of Li<sub>2</sub>O, K<sub>2</sub>O and ZnO). Due to the generality of the physical arguments put forward, we expect that the  $V_{\text{pore}}$  and, moreover,  $D_{\text{pore}}$  and  $\text{Pore}_{\text{max}}$ , could similarly affect  $E_{\text{gap}}$  values in a wide range of materials. The ability to use  $V_{\text{pore}}$ ,  $D_{\text{pore}}$  and  $\text{Pore}_{\text{max}}$  to tailor  $\Delta E_{\text{gap}}$  values potentially provides a new route to producing  $E_{\text{gap}}$ -engineered materials and devices with the added functionality of nanoporosity. We hope that our work provides inspiration for increased experimental work in this area.

## **Summary**

Throughout this thesis, we have studied ZnO and its properties in a bottom-up manner through a dimensionality range starting from 0D nanoparticles to 3D bulk phases. For the 0D clusters and the 2D nanofilms studied we also considered the effect of a support in models designed to study ZnO thin film growth on the Ag(111) surface.

In chapter 3, we have studied ZnO nanoclusters on a Ag support and compared their properties with free space ZnO nanoclusters. In this chapter we highlighted the importance of the presence of the support during the global optimization of the clusters (i.e. as opposed to global optimization of the clusters in free space and then introducing a support). Our results show that the presence of the support strongly affects the energetic stability ranking of the nanocluster isomers. More drastically, after a certain cluster size, the support also stabilizes selectively 2D type structures, which are not stable in free space, with respect to the 3D clusters. The extra stabilization of supported 2D clusters is attributed mainly to the contact area, which is evidently greater for 2D clusters where all the atoms can interact with the surface. The importance of the contact area is also observed for 3D clusters, as ellipsoid bubbles or inflated double layer clusters being of lower energy than more spherical clusters on the support whereas the latter, more symmetric 3D clusters are more stable in free space. Matching of the cluster structure with the surface morphology was found to be another factor determining cluster stability. The  $Zn_3O_3$  six-membered ring, which is one of the main motifs for both 3D and 2D clusters, matches best with the Ag(111) surface because it follows the same six-fold ( $C_6$ ) symmetry (or its trigonal  $C_3$  subgroup with a three-fold axis, taking into account the distinction between Zn and O atoms). However because of the lattice size differences, such matching dies away for larger ZnO clusters. The preferential stabilities of the 2D structures of ZnO clusters can be seen as the initial stages of thin film growth and is found to be in line with the experimentally observed layered ZnO sheets on the Ag(111) surface.

In Chapter 4, we have considered a full 2D-ZnO sheet on Ag(111) surface and also investigated also how H atoms interact with it. Following our results for ZnO

nanoclusters on the Ag surface, we highlighted the importance of the degree of 2D-ZnO:Ag(111) unit cell commensurability for calculating accurate sheet-on-substrate binding energies. We have found a 8:9 commensurate monolayer to be more favored with interatomic potentials and a 7:8 commensurate monolayer with DFT calculations, where the latter is found in experiment. Our calculations showed no evidence of charge transfer or covalent bonding between the Ag(111) surface and the 2D-ZnO sheet, but did show that the ZnO sheet and the Ag(111) surface exhibit small structural distortions in order to maximize their mutual interaction. Calculations of the unsupported 2D-ZnO sheet interacting with hydrogen provided strong evidence for H forming a low energy Zn 4s-H 1s multi center bonding state when passing through a Zn<sub>3</sub>O<sub>3</sub> ring of the 2D-ZnO sheet, thus allowing for relatively facile H transport through the sheet.

In chapter 5, we have extended our study of supported 2D ZnO nanofilms with higher coverage models, including triangular islands on top of two full monolayers, prepared to model the experimental system. Our results showed that the triangular adlayer islands induce a transition to the WZ structure in the island core and in local region in the two layers immediately below the island core. The islands are also found to have BCT-structured reconstructions on their edges and T1-structured reconstructions on their corners. These models are found to better match the experimental structural data for the experimental 2.7 ML Ag-supported ZnO film with respect to models assuming a purely layered or a purely WZ structure.

In chapter 6, we focused on 4ML nanofilms and compared bulk and the 4 ML nanofilm polymorphism of ZnO. Our results revealed that the stability range of nanofilms and their energetic ordering are radically different than that of bulk polymorphs. We have developed a method to generate a wide range of new low energy nanofilm and bulk polymorphs using nets as a basis, and showed that there exist at least three nanofilm structures with trigonal basal plane symmetry compatible epitaxial growth on fcc metal (111) surfaces that are more stable than layered-ZnO. While confirming the previous theoretical studies predicting the BCT-ZnO phase as being the lowest energy free-standing nanofilm for small thicknesses, we obtained a range of structurally related and near energetically degenerate phases, indicating there exists BCT polytypism. With

increasing thickness we found that atomically reconstructed wz-ZnO becomes more stable than BCT-ZnO for  $\sim 14$  MLs, and is always more stable than non-reconstructed wz-ZnO. We have also stressed the influence of strain on polymorphism by showing that BCT-ZnO and layered-ZnO nanofilms are unstable to novel polymorphs under in-plane strain. Together with the T1 structures and BCT structures which were also predicted as reconstructions on island corners in the previous chapter, our results strongly suggest that many new nanofilm polymorphs should be experimentally accessible, and in some cases, may have even already been observed.

In chapter 7, we focused on bulk polymorphism and, specifically, investigated the effect of nanoporosity. Our results showed that both energetic instability and band gap increase with nanoporosity and we predicted that nanoporosity could induce band gap increases of up to  $\sim 1.5$  eV relative to wurtzite ZnO. We showed that the band gap increase is related with bandwidth changes in the conduction band and the valence band. We suggested that the underlying physical mechanism for this effect is that introducing nanoporosity, and thus periodic internal void space, restricts extended orbital overlaps and thus decreases bandwidths. Due to the generality of this argument, we expect that nanoporosity could similarly affect bandgap values in a wide range of materials and could be employed as a band gap engineering method.

## **Summary in Catalan**

# **Efecte de la dimensionalitat i del polimorfisme en les propietats de l'òxid de zinc (ZnO)**

Nom del Programa de Doctorat:

**QUIMICA TEORICA I COMPUTACIONAL DELS MATERIALS**

Nom I cognom del doctorand:

**ILKER DEMIROGLU**

Nom i cognom i filiació dels directors de la Tesi:

**STEFAN THOMAS BROMLEY**

**QUIMICA FISICA**

**FACULTAT DE QUIMICA**

**FRANCESC ILLAS RIERA**

**QUIMICA FISICA**

**FACULTAT DE QUIMICA**

### **Resum:**

Els elements metàl·lics de la taula periòdica poden donar lloc a una varietat d'òxids que tenen una gran importància en la física, la química i la ciència dels materials. Entre els varis materials inorgànics que presenten a la actualitat interès tecnològic, els òxids metàl·lics tenen un paper preponderant. Degut a l'ampli ventall d'estructures i propietats, aquests compostos tenen també un gran nombre d'aplicacions. En la química industrial una gran part dels catalitzadors són òxids metàl·lics o empren òxids metàl·lics com a suports. En geologia, una gran part dels minerals esta constituïda per òxids metàl·lics. Els òxids metàl·lics apareixen també quan es parla de moltes propietats o fenòmens en física d'estat sòlid com son el ferromagnetisme i l'antiferromagnetisme, la

ferroelectricitat d'alta temperatura, la conductivitat d'ions ràpids, i la superconductivitat d'alta temperatura crítica. La rica varietat de propietats dels òxids metàl·lics, que va des dels sistemes metàl·lics fins a la superconductivitat, és una font constant de noves perspectives per l'aplicació d'aquests materials en les indústries de l'electrònica i de l'optoelectrònica.

La possibilitat de que un compost determinat es trobi en més d'una forma cristal·lina, o fase sòlida ordenada, representa un fenomen prou conegut anomenat polimorfisme. Aquest té una importància crucial en moltes branques de la ciència i de la tecnologia ja que els polimorfs sovint presenten diferències en les seves propietats físiques i químiques. L'avanç continu en el desenvolupament de dispositius que requereixen nanomaterials de baixa dimensionalitat com les nanopartícules, els nanofilis i les nanocapes, que tenen dimensionalitat 0, 1, i 2, respectivament, fa que assolir un coneixement profund i més general sobre les relacions entre l'estabilitat relativa de fases cristal·lines (polimorfs) amb diferent grandària i/o dimensionalitat que competeixen en estabilitat s'hagi convertit gairebé en una necessitat. El polimorfisme que exhibeix un determinat material es molt sensible a l'escala en grandària i a la dimensionalitat. Aquest fenomen es troba particularment amplificat quan es comparen polimorfs del material tridimensional (3D o *bulk*) amb el sistema corresponent a la nanoescala i per tant de dimensions reduïdes.

El treball de recerca desenvolupat en aquesta tesi es centra en ZnO, un dels semiconductors de tipus II-VI amb un ampli ventall d'aplicacions. El ZnO és un component clau en molts processos de manufactura en pintures, cosmètics, fàrmacs, plàstics, bateries, equipament elèctric, gomes, sabons, tèxtil, recobriments de sols i molt més. Apart de la seva aplicació en moltes indústries amb el consegüent impacte social, el desenvolupament de tecnologies de creixement de monocristalls d'alta qualitat i de capes epitaxials, ha crescut considerablement l'interès purament científic. Els estudis en aquest tipus de mostres de ZnO ben caracteritzades i ben definides són prometedors en quan el potencial per a moltes aplicacions en nanotecnologia com poden ser la spintrònica o com a font de recolliment d'energia. En aquest sentit, el ZnO es pot

considerar com un material amb futur, el que explica l'interès creixent que té el ZnO en la comunitat científica (veure Figure 1)

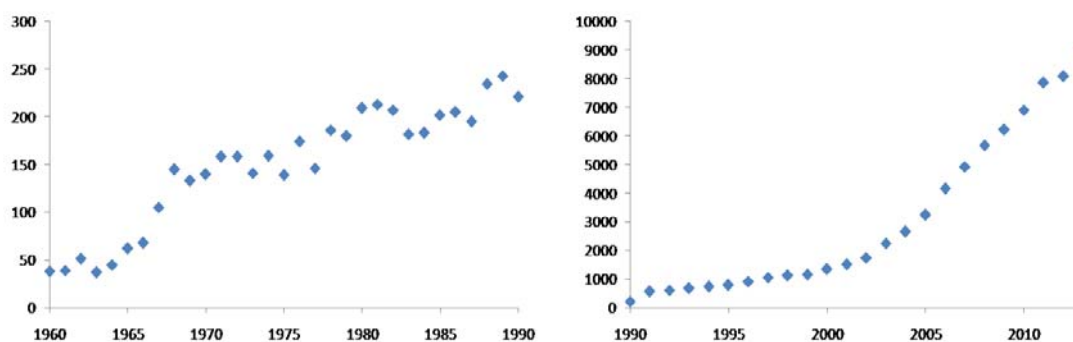


Figura 1 Nombre de vegades en les que “ZnO” apareix cada any desde 1960 fins 2013 (dades extretes de *web of science*).

En el capítol 1 es dona una introducció detallada dels conceptes més importants relacionats amb el present treball com són l'estructura cristal·logràfica, propietats semiconductor, polimorfisme i nanoescala. Tanmateix, es descriuen en detall les propietats més importants d'aquest material. Les propietats dels materials es troben íntimament lligades a la seva estructura a nivell atòmic. Totes les substàncies. Excepte l'heli, formen una o més fases sòlides si se les refreda suficientment. Així, la majoria de compostos químics exhibeixen fases sòlides, normalment, cristal·lines, on els àtoms, molècules i ions es troben empaquetats de manera regular amb un ordre a llarg abast. Si, però, hi ha només ordre a curt abast, el sòlid en qüestió es diu que és amorf (Figura 2)

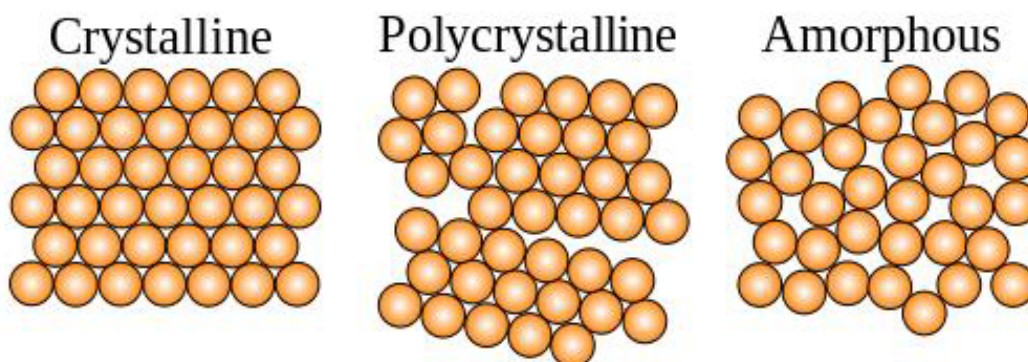


Figura 2. Exemples il·lustratius de sòlids cristal·lins i amorfs.

Per entendre les propietats d'un material cal conèixer la seva estructura a nivell atòmic. Un dels problemes més simples de descriure i alhora més difícils de resoldre en química computacional és precisament la determinació de l'estructura atòmica. L'aplicació de qualsevol mètode computacional per estudiar un sistema químic requereix un model matemàtic a través del qual es pugui calcular l'energia del sistema en funció de la seva configuració atòmica, i.e. en funció de la posició dels àtoms que el defineixen. Òbviament, l'èxit del camí escollit dependrà de la qualitat del model matemàtic que s'empri. Per a sistemes petits, constituïts per un nombre limitat d'àtoms, és possible emprar mètodes basat en la mecànica quàntica (QM). Walther Kohn i John Ople varen guanyar el premi Noble de Química el 1988 pel desenvolupament de la teoria del funcional de la densitat (DFT) i dels mètodes computacionals de la química quàntica. Malauradament, l'aplicació dels mètodes del tipus QM, precisos i computacionalment costosos, estan limitats a sistemes que continguin com a màxim uns pocs centenars d'àtoms, si bé hi ha desenvolupaments en curs que pretenen superar aquesta barrera. D'altra banda, cal considerar també l'escala temporal. Alguns processos químics i molts processos biològics es desenvolupen en una escala temporal que va del microsegon al milisegon però els mètodes computacionals actuals permeten anar en petites etapes de l'ordre del femtosegon. Així, és possible que fins i tot una única simulació requereixi avaluar l'energia del sistema de l'ordre de  $10^8$  vegades. Un gran nombre d'avaluacions de l'energia del sistema és també necessari quan hom pretén emprar mètodes d'optimització global per explorar els espais configuracionals amb un cert detall. Clarament els mètodes de tipus QM no són adequats per aquest tipus d'estudis, els temps de càlcul serien massa llargs, inclús pels superordinadors moderns. Els models anomenats "atomístics" són adequats per estudis que requereixen un gran nombre d'avaluacions de l'energia del sistema o simulacions molt llargues. Els models atomístics empenyen camps de força en els que els àtoms, i no els electrons o els nuclis que són els ingredients necessaris quan s'empren mètodes QM, constitueixen les partícules més petites del sistema. Les equacions matemàtiques que lliguen els camps de força amb l'energia del sistema, inclouen termes relativament senzills per a descriure les interaccions físiques que determinen l'estructura i governen les propietats dinàmiques. Aquestes simplificacions són les que permeten accelerar enormement el càlcul de l'energia, de manera que se'n poden fer moltíssimes amb un cost computacional

raonable. Al llarg d'aquest treball s'han emprat tant mètodes atomístics basats en camps de força clàssics com mètodes mecanoquàntics basats en la teoria del funcional de la densitat. El capítol 2 inclou una descripció prou detallada d'aquests dos tipus de tècniques computacionals.

En el capítol 3 es comencen a descriure els resultats de la recerca que s'ha duta terme i que s'inicia amb l'estudi dels sistemes amb dimensionalitat zero (0D) ja que els nanoclusters i les nanopartícules constitueixen un dels millors exemples de materials nanoestructurats que mostren propietats inusuals i que, a més, poden ser variades per ajustar-les als valors necessaris per algunes aplicacions. Encara que hi ha alguns estudis previs sobre nanoclusters de ZnO aïllats, en fase gas, és important entendre com canvien les seves propietats quan es troben suportat. Tanmateix, l'adsorció de nanoclusters de ZnO en superfícies metàl·liques constitueix una de les etapes inicial del creixement de capes de ZnO suportades en metalls pel que el seu estudi pot donar també informació important.

En aquesta part de l'estudi s'ha dut a terme una cerca sistemàtica de estructures corresponents als mínims globals per a nanoclusters  $(\text{ZnO})_n$  sobre la superfície Ag(111) amb  $n= 1-16, 20$  i  $24$ . En una primera etapa s'ha emprat el mètode anomenat "*Monte Carlo Basin Hopping*" avaluant l'energia amb potencials interatòmics (camps de força) i, posteriorment, s'han refinat els resultats emprant càlculs de tipus DFT aplicats a les estructures candidates a ser mínims globals. Aquest estudi ha predit varies estructures de baixa energies pels nanoclusters  $(\text{ZnO})_n$ , tant en fase gas com sobre el suport metàl·lic de plata. A través d'una comparació amb un estudi previ corresponents mínims locals de nanoclusters de ZnO s'observa que els mínims locals de mínima energia es troben ràpidament emprant el codi d'optimització KLMC. A més el codi es mostra altament eficient en l'ordre de les estructures tant en rang com en diversitat.

En les estructures  $(\text{ZnO})_n$  suportes, s'observa que la presència del suport afecta l'ordre d'estabilitats dels mateixos però de manera molt més dràstica afecta selectivament les estructures bidimensionals (2D) que, a partir d'una certa grandària, en fase gas són menys estables que les tridimensionals (3D). Per tant, tenir en compte la presència del suport durant la optimització de la nanoestructura resulta crucial.

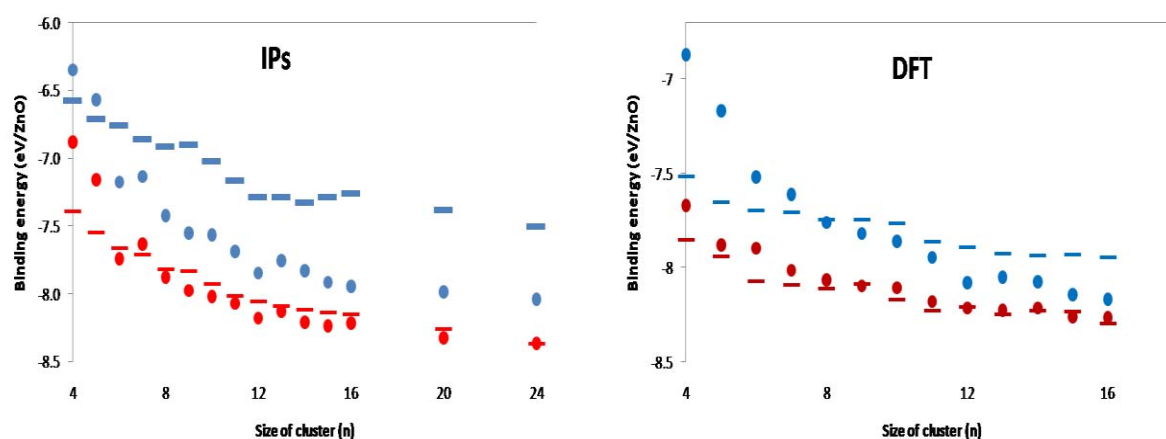


Figura 3 Energia relativaper a les estructures 2D i 3D en funció de la grandària i tant en fase gas com sobre el suport.

D'acord amb el nostres resultats, obtinguts amb els potencial interatòmics, els clústers 2D aïllats i en fase gas són menys estables que els clústers 3D, especialment quan més gran es la grandària del sistema (Figura 3). Conseqüentment, per a valors de  $n$  superiors a 8 no es trobaran estructures 2D es fase gas indicant, de nou, la gran importància del suport en la determinació de l'estructura final. La separació energètica entre les estructures 2D i 3D esdevé més petita quan l'energia s'obté de càlculs mecanoquàntics DFT però apareix clarament si bé per a valors de  $n$  superiors a 12.

La figura 4 mostra les diferències energètiques dels millors clústers, 3D i 2D, suportats per a cada tamany de cluster, ambdós potencials interatòmics i el DFT. D'acord amb els potencials interatòmics, per tamany  $n = 4, 5$  i  $7$  les estructures bidimensionals son preferides, i les majors diferències en estabilitat son per a les de mida  $n = 9, 12$  i  $15$ . A partir de la mida  $n = 8$  els clústers 3D presenten estabilitats mes elevades, per tant, la diferència disminueix lleugerament a mida que la grandària augmenta. Els clústers bidimensionals resten en  $0,1 \text{ eV/ZnO}$  fins els clústers considerats de mida  $n = 24$  on les estructures 2D de nou tornen a ser més estables. Els resultats del DFT semblen qualitativament similars als resultats dels potencials interatòmics a partir de la mida  $n=7$ , mentre que les estructures tridimensionals estan més afavorides en IPs, els calculs DFT tendeixen a afavorir les estructures 2D. La figura 5 resumeix les estructures amb energia més baixa obtingudes amb DFT de per ambdós tipus de clústers, 2D i 3D.

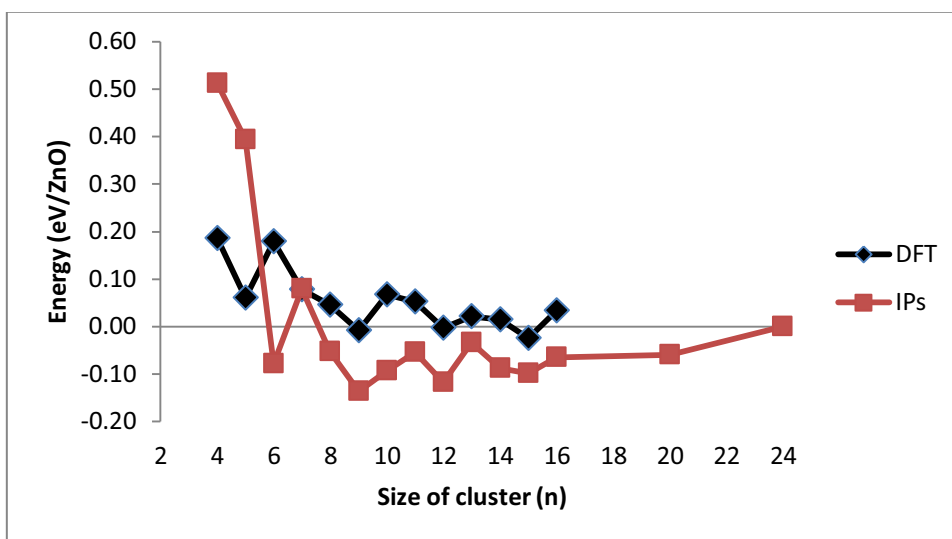


Figura 4. Diferència d'energies relatives entre clústers 2D i 3D de més baixa energia respecte la mida dels clústers.

Amb l'estabilització extra destacada, els clústers bidimensionals resten en el rang de les primeres estructures amb la energia més baixa competint amb els clústers 3D, en ambdós casos emprant potencials interatòmics i a nivell de càlcul DFT. Principalment l'estabilització extra s'atribueix principalment a l'àrea de contacte, que és evidentment més gran per clústers de dues dimensions on tots els àtoms poden interactuar amb la superfície. A més, l'àrea de contacte determina el rànquing dels clústers 3D suportats, el que resulta en que les bombolles el·lipsoides o bicapes inflades son suportades preferentment, mentre que clústers tridimensionals totalment simètrics són més estables en el buit. L'altre factor determinant es va trobar en l'encaix amb la morfologia de la superfície. L'anell de sis que és un dels patrons principals per tots dos tipus de clústers, 3D i 2D, encaixa millor amb la superfície Ag(111) ja que presenta la mateixa simetria radial d'ordre 6. Tanmateix, deguda la diferència de la cel·la, l'encaix no es vàlid cel·les grans. Mitjançant els potencials interatòmics, per a clústers 2D l'altre superfície plana Ag(100) s'ha trobat que és més adequada que no pas la superfície rugosa Ag(110); mentre els clústers tridimensionals poden encaixar millor en la superfície rugosa.

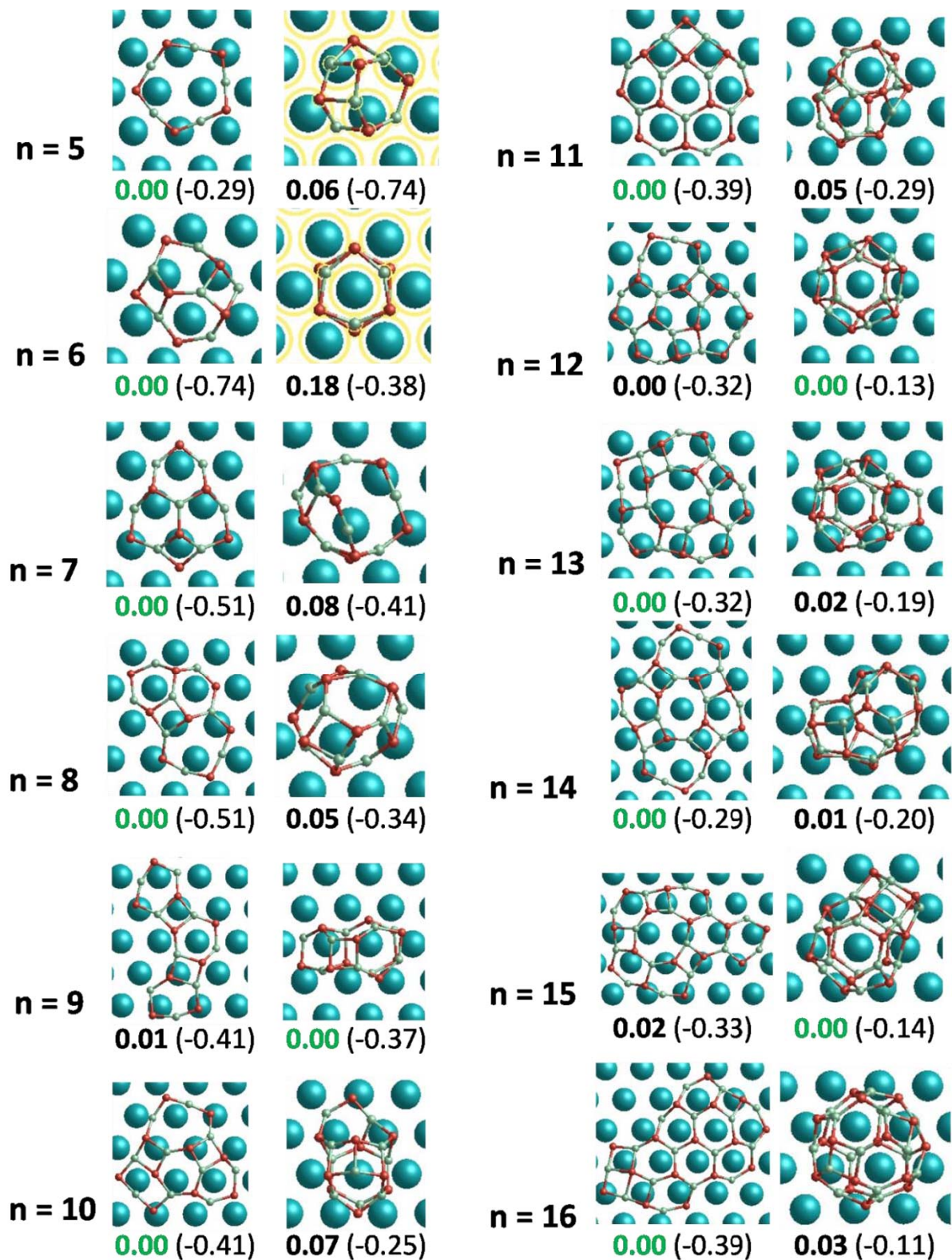


Figura 5. Estructures i energies dels nanoclusters 2D i 3D de menor energia  $(\text{ZnO})_n$  suportats en  $\text{Ag}(111)$ . Les energies relatives estan sota les estructures i les energies d'estabilització degudes al suport es troben entre parèntesis.

Si considerem l'aproximació d'una monocapa dins d'unes condicions de contorn periòdiques, on els enllaços extra formen una estructura 2D, podem esperar el creixement d'una monocapa completa. De fet, els nostres resultats preliminars obtinguts de l'optimització global per clústers de mides  $n = 12-16$  utilitzant una cel·la unitària més petita, els quals permeten a les estructures bidimensionals sentir l'efecte de la seva imatge periòdica, mostrant que les estructures nanolaminars, que són periòdiques en una dimensió, esdevenen de més baixa energia que els clústers obtinguts amb la optimització global. Aquestes nanolàmines principalment consisteixen en anells de 4 i 6 membres. La diferència d'energia augmenta inclús en el cas del  $(\text{ZnO})_{20}$ , on la periodicitat es destacable en dues dimensions. Juntament amb la estabilitat relativa dels anells de 6 membres suportats, no seria sorprenent que la formació d'una monocapa uniforme de anells de sis membres fos possible a la superfície de plata ja que ambdós són proporcionals. En conclusió, les estabilitats preferents de les estructures 2D de clústers ZnO es poden veure com les etapes inicials del creixement de la capa fina i concorda amb els resultats experimentals observats de làmines grafitiques de ZnO en la superfície Ag(111).

En el capítol 4 hem continuat amb les nostres consideracions per a una sola làmina d'òxid de zinc (ZnO) basades en el mateix pla bidimensional (2D) de topologia hexagonal com el grafé, però alternant àtoms veïns de Zn o O enlloc d'àtoms de carboni. Emprant DFT i els potencials interatòmics hem investigat la força de la interacció d'un únic pla 2D-ZnO amb la superfície Ag(111) i com aquesta afecta a les propietats estructurals de la capa. Construint sobre les prediccions prèvies de l'enllaç multi-centre (MCB) assisteixen el transport d'hidrogen a traves d'anells hexagonals de  $\text{Zn}_3\text{O}_3$  en el sistema sodalita ZnO (SOD-ZnO), també hem investigat com els àtoms d'hidrogen interactuen amb una capa 2D-ZnO quan passen a traves d'una apertura  $\text{Zn}_3\text{O}_3$ .

Per al sistema més petit 1:1 2D-ZnO en Ag(111), les discrepàncies entre la cel·la unitat de la làmina de 2D-ZnO aïllada i la capa (111) de plata en la direcció A-B es troba que és entre +12 (DFT) i +14 (IP) per cent, el que ens diu que per poder acomodar la lamina 2D-ZnO en la cel·la unitat fixa de Ag(111), deu haver-hi una compressió significativa.

Per aquesta raó la làmina 2D-ZnO suportada en plata per al sistema 1:1 està significativament torçada respecte l'estructura energèticament afavorida quan aquesta està lliure, on els àtoms de zinc estan orientats cap a la capa de plata i els àtoms d'oxigen cap a fora, juntament amb això les distàncies d'enllaç Zn-O són relativament més curtes. Comparant aquest sistema combinat ZnO-Ag amb un model similar, però amb la làmina d'òxid de zinc torçada i lluny de la capa de plata (111), dona energies d'enllaç de la làmina d'entre 0.39 i 0.94 eV/ZnO, depenent del nivell de teoria emprat. No obstant això, fent servir l'energia de la cel·la unitat de la làmina 2D-ZnO completament optimitzada (és a dir, sense la restricció a-b de la capa Ag(111) de la cel·la unitat) i la cel·la unitat de la capa de plata (111) aïllada com a referències d'energies, es mostra que el sistema 1:1 és inestable respecte a la separació espontània de ZnO-Ag. Des de la optimització basada en IP sense aplicar-hi restriccions a la cel·la unitat de la làmina plana 2D-ZnO trobem que és energèticament més favorable en concordança amb la optimització completa de la làmina 2D-ZnO aïllada, en DFT sense restriccions. Diverses d'aquestes làmines planes optimitzades amb IP s'han fet servir per a calcular els valors de  $a_{ZnO}$  en exploracions IP per a una sèrie de sistemes X:Y partint des de  $a_{ZnO}/a_{Ag}$  amb diferències menors que 1 i incrementant-les gradualment fins a la unitat. Trobem que, tot i que, com s'esperava, a menors diferències les energies de lligadura de els sistemes 2D-ZnO sobre Ag(111) sense restriccions són més grans, només quan la diferència és menor a un 1% l'energia de lligadura del sistema ZnO-en-Ag(111) amb restriccions es tornen molt semblants als casos amb restricció (és a dir, mostrant que el corresponent model X:Y no es exageradament restrictiu per a la relaxació dels subsistemes ZnO i Ag separats). Per els càlculs IP el millor model respecte aquest fet es va trobar el sistema 8:9 on la làmina 2D-ZnO s'estira en un 0.3%. En els càlculs DFT es va trobar que per el sistema 7:8 es requereixen compressions de la làmina 2D-ZnO de tan sols un 0.1%.

Es va estudiar també la interacció d'hidrogen atòmic amb el sistema de 2D-ZnO no suportat fent servir tant models periòdics com models de clúster a nivell DFT. En particular, ens centrem en la interacció de l'hidrogen amb un anell de  $Zn_3O_3$  quan travessa la làmina. Es va trobar que els àtoms d'hidrogen s'uneixen d'una manera relativament feble a la part superior del Zn (0.32eV) i O (0.04eV) elevant així la

possibilitat de transport a través de la làmina 2D-ZnO a altes temperatures. En apropar-se al centre d'un anell hexagonal  $Zn_3O_3$  al llarg d'una línia perpendicular al pla de la làmina, l'àtom d'H esdevé primerament adsorbit de forma feble fins que assoleix una posició de mínima energia a una distància d'1 Å de la làmina 2D-ZnO (- 0.04 eV respecte la làmina i l'àtom d'hidrogen per separat). Posteriorment, l'entrada a l'anell des de aquesta posició provoca un augment de l'energia relativa del sistema des de aquest mínim feble fins a un màxim de +0.11 eV en el centre de l'anell de  $Zn_3O_3$ . El cost d'energia només es degut a la distorsió estructural de la lamina de 2D-ZnO induïda per l'hidrogen i és de 1.27 eV. Així, la interacció entre l'hidrogen i la làmina 2D-ZnO, on l'hidrogen es troba al centre de l'anell  $Zn_3O_3$  ( $H@Zn_3O_3$ ), es compensa per aquest efecte en 1.16 eV. Els càlculs per a la làmina 2D-ZnO aïllada interaccionant amb l'hidrogen proporcionen una forta evidència per a la formació d'un estat d'enllaços multi-centres de baixa energia (Zn 4s-H 1s) quan passa a través de l'anell de  $Zn_3O_3$  de la làmina 2D-ZnO, permetent així de forma relativament fàcil el transport d'hidrogen a través de la làmina.

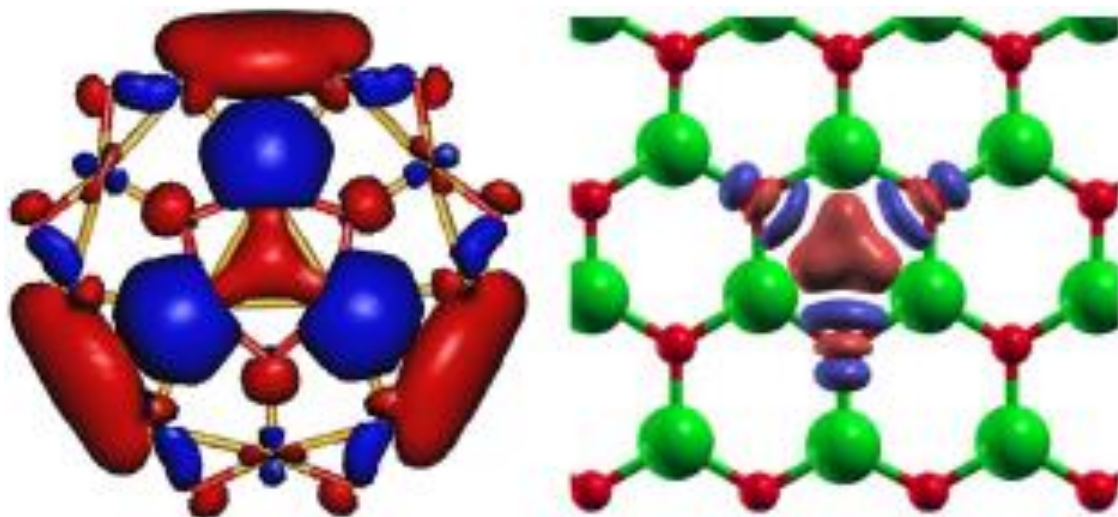


Figura 6. Orbital proposat per el Zn 4s-H 1s MCB obtingut amb el model de cluster utilitzant el funcional B3LYP (dret). Increment de carrega relatiu observat al centre de l'anell i amb menor abast als oxigens (gris clar) mentre la carrega disminueix (gris fosc) als lobuls dels orbitals p dels oxigens.

Després de considerar una sola làmina de ZnO sobre la superfície d' Ag(111) i el cas específic de les propietats de transport d'H, es va passar a l'estudi de multicapes de ZnO al Capítol 5. Un cop obtinguts els informes experimentals, i en particular mesures de 2.7 ML d'una lamina de ZnO suportada sobre plata, s'ha dissenyat models teòrics entre 2 i 2.7 ML de recobriment a partir de la creació d'illes amb una tercera ( i quarta ) capes incompletes a la part superior d'un sistema bicapa complet de 2ML, per estudiar els efectes de mida d'aquestes illes en l'estructura de ZnO. On computacionalment ha estat factible, s'ha inclòs explícitament la Ag (111) del substrat.

Per 2ML de ZnO sobre Ag (111), el desplaçament vertical d'una monocapa de ZnO es veu afectat per la capa de ZnO addicional, amb interaccions en la direcció de l'eix z més fortes que la interacció Ag-ZnO. També, a diferència del cas d'una monocapa, no es van trobar àtoms de Zn més propers a la superfície de plata en la pel·lícula de 2ML, mentre que les petites variacions en les separacions de capes intermèdies locals es van produir al llarg de tota la cel·la unitària per a un 13% de les connexions bicapa. Aquestes distorsions estructurals menors entre capes, no segueixen el patró d'una estructura tipus WZ o una ordenació BCT, però sembla ser que son perturbacions induïdes pel substrat a una lamina de 2ML perfecte.

A mesura que es treballava amb models d'illes de 2.2 ML, les variacions locals en la separació de les capes observades en el cas de 2ML quasi desapareixen, mentre que les separacions ordenades es troben a l'illa. A la Figura 7 es pot observar que el nucli hexagonal central de l'illa i la corresponent part dels dos primers ML sota aquest nucli convergeix per a mostrar l'estructura WZ, que a la vegada, queda rodejada de regions més petites que mostra una estructura similar al BCT. Si es compara el model de 2ML suportades sobre Ag (111) amb el seu homòleg lliure, la fase de WZ no es forma a l'illa i el nucli del sistema roman en fase de grafit. No obstant, els motius encara es troben a les cantonades de l'illa, que es més comprimit que en el cas amb plata suportada.

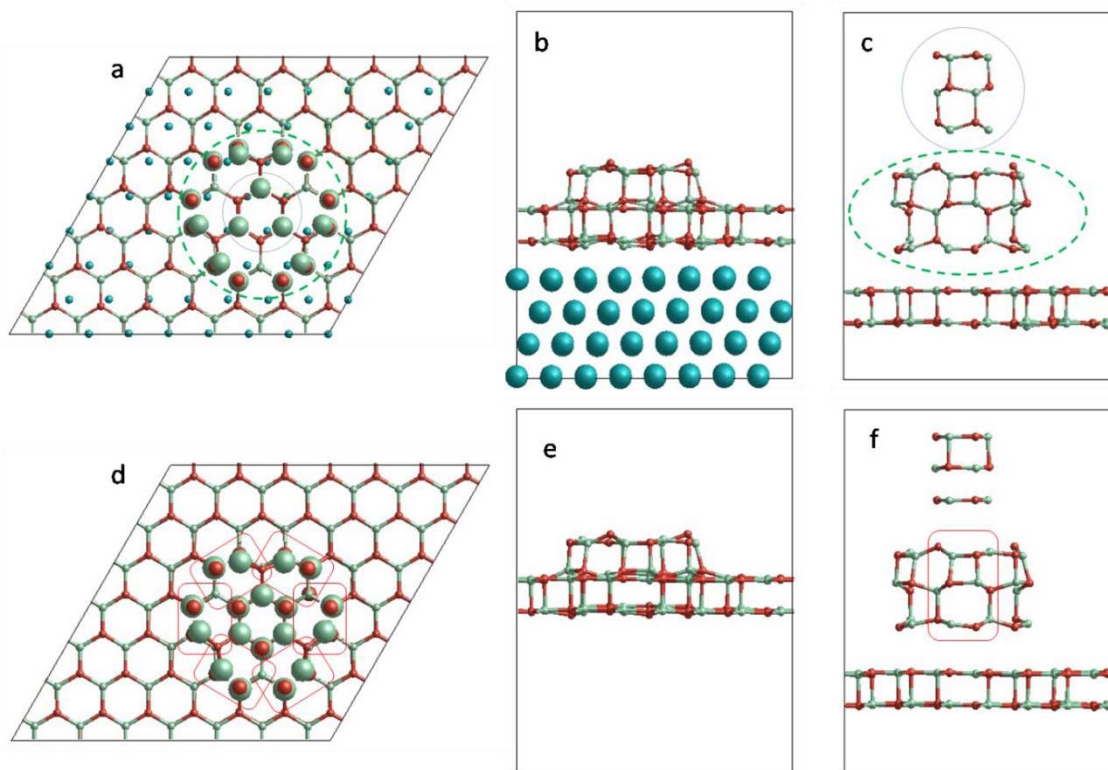


Figura 7: Estructures optimitzades de 2ML de ZnO amb suport (a,b,c) i sense suport (d,e,f). Les boles més grans s'utilitzen per a diferenciar la zona on es produeixen les separacions entre les capes en les principals figures de visualització (a i d). En c i f es mostren les parts cilíndriques separades entre sí, en vista lateral. El rectangle vermell indica les reconstruccions BCT que no estan en consonància amb la resta.

L'aparició de la fase de WZ també es veu afectada per l'addició d'una unitat hexagonal de  $Zn_3O_3$  com a una quarta capa del nostre model 2.3 ML sobre Ag (111). En aquest cas, mentre que dues primeres capes sota el nucli de l'illa tenen estructura WZ, les altres dues capes que pertanyen a les capes adsorbides incompletes convergeixen en fase grafit. Els motius BTC es formen a les tres cantonades de l'illa hexagonal i a la part corresponent de les dues primeres capes immediatament inferiors a l'illa. Mentre que les fases de grafit i WZ tenen simetria trigonal, la fase BTC no, i per tant, aquestes tres regions BTC separades no es poden expandir i unir-se entre si, per a fer una fase BCT expandida en concordança amb la fase WZ, la fase grafit o fins i tot la superfície de plata (111). La barreja global d'estructures WZ i BCT en els models 2.2 ML i 2.3ML es també molt similar a l'estructura d'un polimorf hipotètic predit de ZnO que hem anomenat T1.

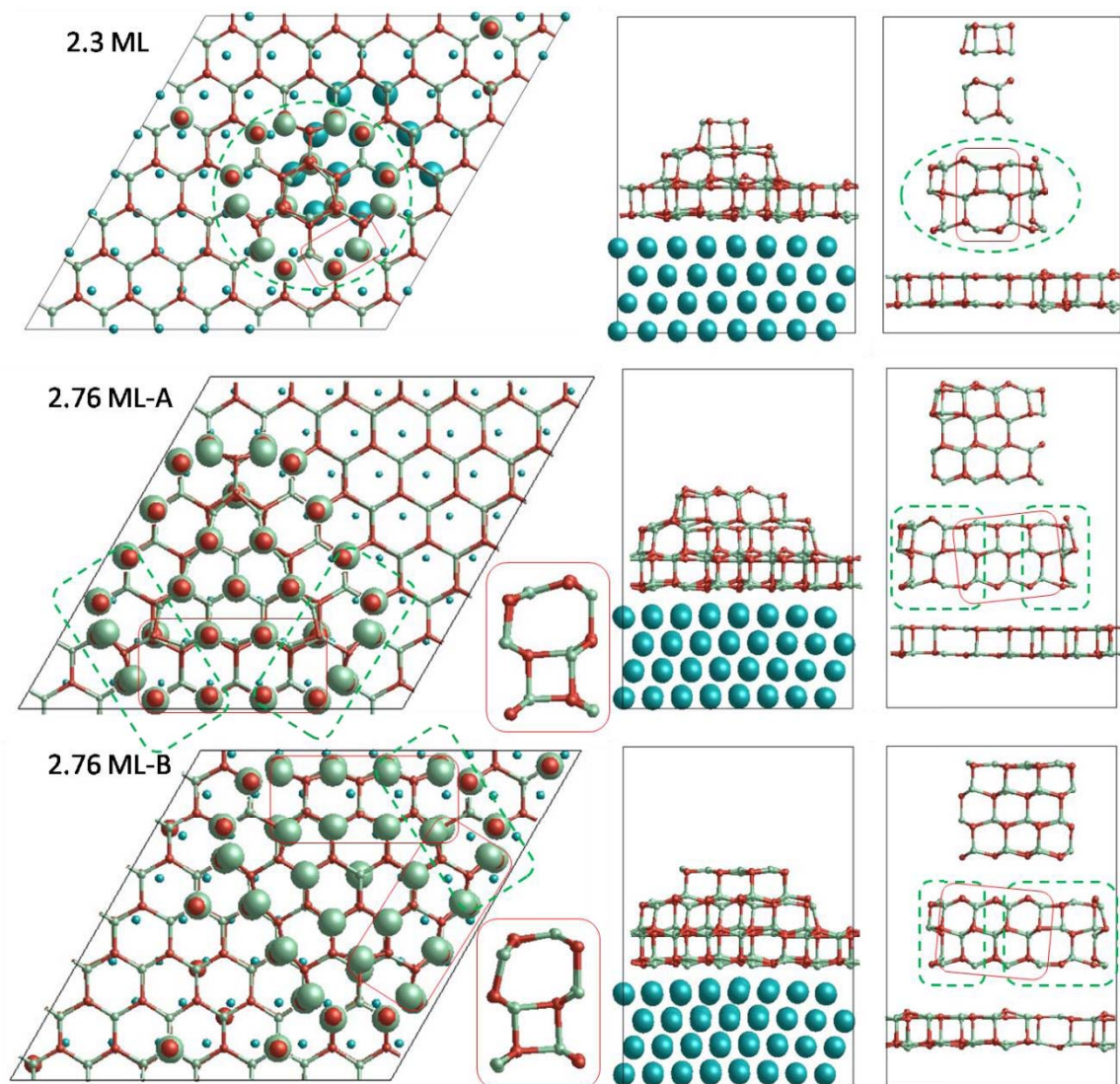


Figura 8: Vista superior i lateral de les estructures dels models 2.3ML, 2.76ML-A i 2.76ML-B. Els cercles vermells indiquen les reconstruccions BCT, mentre que els cercles verds indiquen les reconstruccions T1.

Quan canviem a models amb illes mes grans, observem reconstruccions estructurals similars a l'interior i sota l'illa formada per una nova capa incompleta com es veu als models 2.2 i 2.3. L'interior de les illes triangulars adopta estructura WZ i esta rodejada per vores amb estructures BCT i cantonades amb estructura T1, com es mostra a la Figura 8. S'ha observat que aquests models estan en un millor acord estructural amb les dades experimentals per el cas de les lamines formades per 2.7 ML que no pas respecte als models que assumeixen una estructura purament grafítica o purament WZ.

Per a les nano-lamines independents amb 2ML, totes dues estructures, WZ i BCT, es relaxen directament fins obtenir la doble capa perfectament plana de la fase laminada. Per al cas de 3 capes en el buit amb estructura WZ, succeeix la mateixa transformació espontània a una fase grafitica/laminada, mentre que la fase BCT pot conservar la seva estructura si comprimeix lleugerament. Es mes, es troba que l'estabilitat energètica de 3 capes de BCT-ZnO es gairebé la mateixa que per una lamina amb 3ML de la fase grafitica. Per el cas de lamines amb 4ML, mentre que la fase BCT esdevé en el polimorf mes estable al buit, tant mateix existeix un ampli rang de fases que competeixen energèticament, les quals tenen una energia inferior a la fase grafitica.

Al Capítol 6, hem continuat la nostra investigació comparant el polimorfisme de les nano-lamines de ZnO amb el sòlid bulk. Hem generat un ampli rang de polimorfs de ZnO basats en lamines hexagonals inspirades en l'enumeració de les seves xarxes subjacents característiques i evaluant l'estabilitat del sòlid "bulk" i les nano-lamines d'aquestes estructures mitjançant calculs ab initio. Hem observat un ampli polimorfisme d'estructures de baixa energia en les nano-lamines amb un ordre d'estabilitat totalment diferent al del sòlid "bulk". A partir d'aquestes bases generals hem pogut tenir un millor coneixement de les transicions estructurals observades durant el creixement epitaxial i les prediccions d'estabilitat de les nano-lamines en variar-ne el gruix la pressió exercida. Inicialment ens hem centrat en les nano-lamines de 4 ML, on els experimentals no han pogut discernir una estructura atòmica preferent definida. Tant mateix el wz-ZnO no reconstruït es estructuralment inestable per aquest gruix (es converteix espontàniament en ZnO laminat) tots els altres polimorfs o be mantenen la seva estructura o convergeixen a altres estructures diferents a les del ZnO laminat. A diferència del wz-ZnO sense reconstrucció, tots els altres polimorfs considerats no presenten dipol en la direcció d'empaquetament [0001]. Les nano-lamines de WZ-ZnO amb 4 ML que presenten reconstrucció atòmica s'ha observat que son  $> 0.08$  eV/ZnO menys estables que d'altres models de 4 ML considerats. Consistentment amb estudis previs s'ha observat que la nano-lamina amb 4 ML mes estable energèticament presenta una estructura BCT-ZnO. En un petit rang d'energies per sota el BCT-ZnO tant per la

fase “bulk” (0.01 eV/ZnO) i les nano-lamines (0.0025 eV/ZnO) hem trobat 3 estructures mes, les quals presenten un caràcter politipismic.

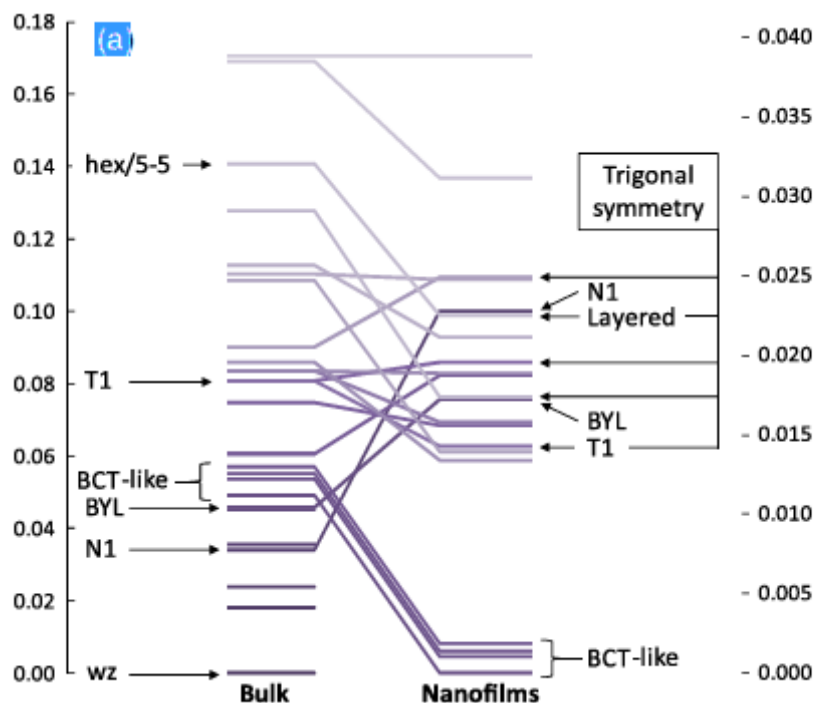


Figura 9 Comparació d’energies relatives (eV/ZnO) dels polimorfs de ZnO com a sòlid “bulk” i les nano-lamines amb 4 ML. Els eixos esquerre i dret fan referència a les energies del “bulk” i les nano-lamines, respectivament.

Per qualsevol polimorf l’estabilitat de les nano-lamines s’ha trobat típicament inferior a la del sòlid “bulk” amb diferències d’energia d’aproximadament 0.1 eV/ZnO. Hem destacat dos trets principals: (i) El rang d’energies que abasten les nano-lamines amb 4 ML (0.04 eV/ZnO) es mes de 4 vegades mes petit que el corresponent a les estructures del “bulk” (0.17 eV/ZnO), (ii) Te lloc un reordenament significatiu de les estructures corresponents entre les nano-lamines amb 4 ML i el sòlid “bulk”. Aquest fet suggereix que els intercanvis entre diferents polimorfs han de ser mes assequibles en les nano-lamines que no pas en el sòlid bulk i això implica que les nano-lamines fines presenten major tendència a no presentar fases wz-ZnO. El reordenament energetic entre “bulk” i nano-lamines mes dràstic ocorre en l’entrecreuament entre WZ a BCT. Fent us d’aquests dos polimorfs com a indicadors d’estabilitat del bulk i les nano-lamines, respectivament, hem predit que l’ordenament energetic del ZnO es general per altres

materials, representant  $\Delta E_{\text{bulk} \rightarrow \text{nano}}$  per a l'estructura BCT i wz per deu materials diferents. L'estructura BCT es troba sempre menys desestabilitzada que no pas l'estructura wz de tal manera que sempre succeeix una transició del “bulk” a nanolamines. L'abast de l'entrecruament s'ha vist que es específic per a cada material, amb un valor de  $\Delta E_{\text{bulk} \rightarrow \text{nano}}$  que creix linealment amb relació amb la càrrega iònica formal del material.

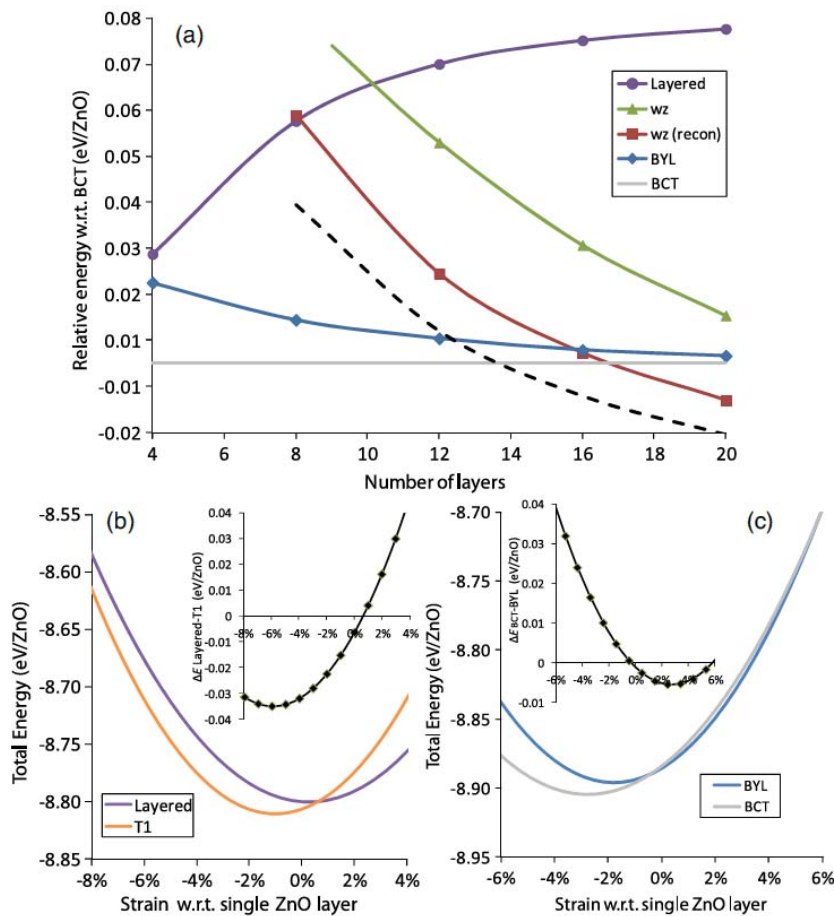


Figura 10 (a) Casos seleccionats de la variació d'estabilitat energètica de nanopel·lícules amb el gruix, (b) variació de l'energia amb la tensió dins el pla pel cas 4 ML layered-ZnO front T1-ZnO, (c) variació de l'energia amb la tensió dins el pla pel cas 8 ML BCT-ZnO front BYL-ZnO. Les tensions es mostren relatives al cas 1 ML layered-ZnO. Les imatges incrustades mostren les diferències d'energia entre polimorfs. Considerant el nostre conjunt de nanopel·lícules estequiomètriques apolars 4 ML, hem trobat que tres tenen una simetria trigonal en el pla basal (0001) i alhora són energèticament més estables que el layered-ZnO. Durant la comparació de les dades

estructurals d'aquests polimorfs amb les mostres experimentals 3.5 i 4.5 ML s'ha trobat que les dades del més estable (T1) estan molt d'acord, particularment amb la mostra de 4.5 ML. Tot i considerar el error experimental estimat ( $\pm 0.1 \text{ \AA}$ ) la interpretació de layered-ZnO o wz-ZnO és possible, i l'existència de que com a mínim una altra estructura de nanopel·lícula és completament compatible amb les dades experimentals obre la possibilitat a que aquests polimorfs juguin un paper important en la inestabilitat estructural observada en ZnO suportat en metalls per  $>2\text{ML}$ .

A més, hem estudiat la influència del gruix i tensió en la estabilitat estructural relativa de les nanopel·lícules. En augmentar el gruix, l'estabilitat del wz-ZnO amb reconstrucció atòmica creix ràpidament i esdevé la fase de ZnO més estable energèticament per  $>16 \text{ ML}$  [línia vermella, Figura 10(a)], molt abans que les nanopel·lícules BYL-ZnO o wz-ZnO sense reconstrucció comencen a ésser energèticament competitives vers la BCT-ZnO. Per tal de considerar l'efecte de la tensió en l'estabilitat estructural relativa de les nanopel·lícules hem examinat dos sistemes: (i) T1-ZnO front layered-ZnO amb nanopel·lícules de 4 ML, i (ii) BYL-ZnO front BCT-ZnO amb nanopel·lícules de 8 ML. En el primer cas, el layered-ZnO està afavorit per les tensions positives més grans, mentre que entre tensions positives petites i tensions compressives moderades el T1-ZnO és energèticament favorable, que implica que els substrats amb discordances de dimensions en el pla de la cel·la indueixen petites tensions epitaxials compressives que podrien ajudar a estabilitzar el T1-ZnO. En el segon cas hem trobat que hi ha un petit ventall de estabilitat d'excés sota petites tensions positives per a la fase BYL-ZnO on l'estabilitat energètica de les dues nanopel·lícules s'inverteix. Aquests resultats corroboren altres estudis teòrics que suggereixen que les forces mecàniques aplicades en nanosistemes ZnO poden ésser una ruta fèrtil per l'accés a nous polimorfs.

En aquest últim capítol ens centrem en el polimorfisme de bulki hem investigat l'efecte de la nanoporositat. En aquesta part de l'estudi hem explorat bases de dades que contenen 4 xarxes connectades (4CNs) per obtenir topologies d'enllaços que produeixin un gran nombre d'estructures de ZnO. A més dels 26 polimorfs de ZnO de baixa densitat que ja es varen proposar<sup>15</sup>, hem inclòs 60 noves estructures basades en 4CN, i

19 estructures més basades en crear nanopors linears monodimensionals ( $D_{\text{pore}} = 1$ ) orientats en la direcció [0001] amb diferents formes, diàmetres i disposició del espaiat entre pors en el bulkwz-ZnO (estructures wz-ZnO-NP).

Hem utilitzat càlculs DFT per estudiar l'estabilitat energètica ( $E_{\text{rel}}$ ) i el band gap ( $\Delta E_{\text{gap}}$ ) relatiu al wz-ZnO d'aquests 105 polimorfs amb diferents graus i tipus de nanoporositat. Primer vam estimar la viabilitat sintètica dels nostres 105 polimorfs de ZnO a partir dels valors calculats de  $E_{\text{rel}}$  (energia relativa al wz-ZnO) agafant un límit superior de +0.3 eV/ZnO, corresponent a la  $E_{\text{rel}}$  del polimorf sintetitzat experimentalment rs-ZnO. A la Figura 11a es pot veure com la majoria (88%) de les estructures es troben al rang delimitat de  $E_{\text{rel}}$  viables juntament amb la tendència que presenta la  $E_{\text{rel}}$  a augmentar amb l'increment de la nanoporositat (proporció de volum buit,  $V_{\text{pore}}$ ). A diferència dels polimorfs basats en 4CN, les estructures wz-ZnO-NP exhibeixen àtoms tricoordinats en les parets nanoporoses, però els seus valors de  $E_{\text{rel}}$  (punts oberts de la Figura 11a) segueixen el mateix patró general d'estabilitat relativa amb  $eV_{\text{pore}}$ . De fet, un nombre d'estructures de wz-ZnO-NP del nostre conjunt han estat trobades com els polimorfs més estables relatius als seus valors de  $V_{\text{pore}}$ .

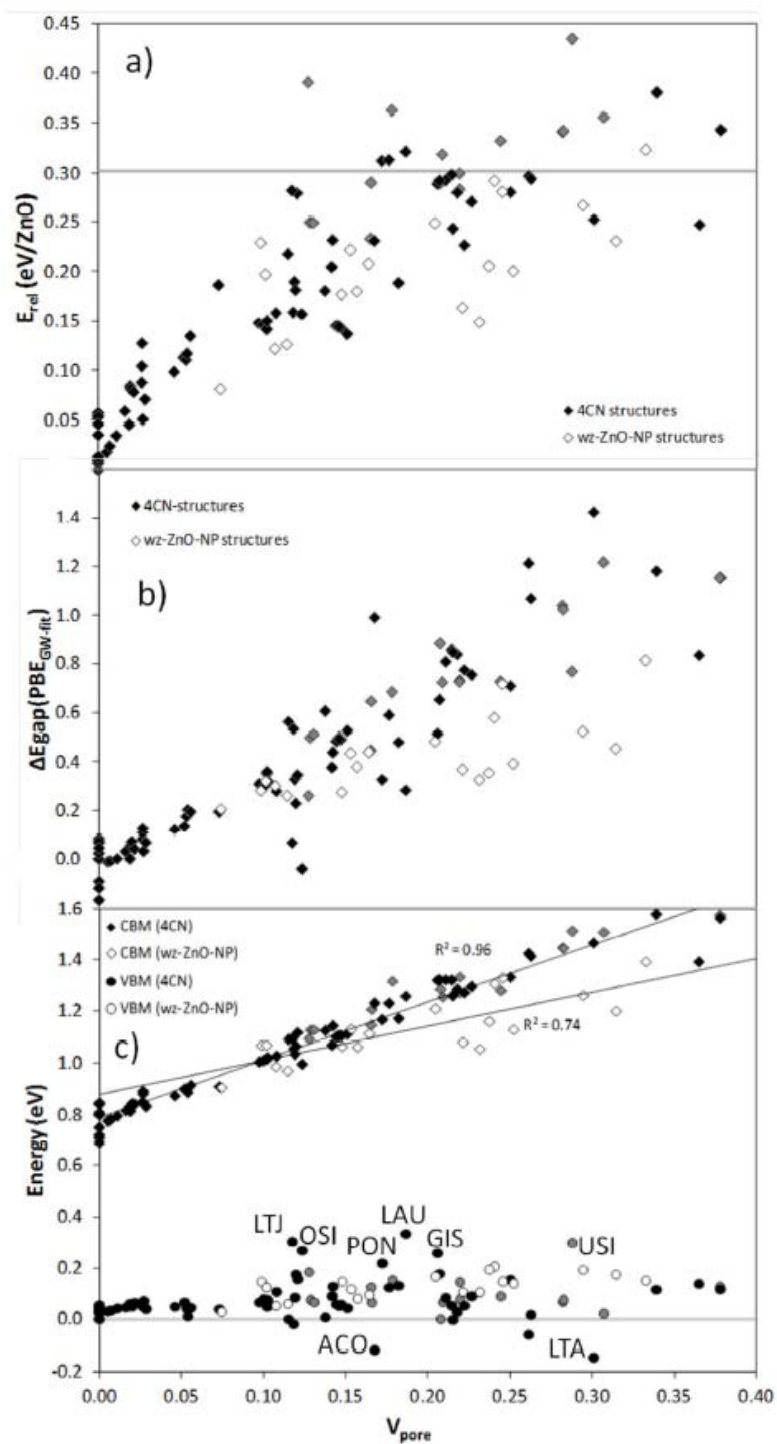


Figura 11. Variació relativa a  $V_{\text{pore}}$  de: a)  $E_{\text{rel}}$  (la línia gris indica la  $E_{\text{rel}}$  dels  $\text{ZnO}$ ), b)  $\Delta E_{\text{gap}}(\text{PBE}_{\text{GW-fit}})$ , c) Valors de VBM i de CBM de totes les estructures on es marquen els valors de VMD perifèrics.

En quant a l'estructura electrònica hem trobat que el  $\Delta E_{\text{gap}}(\text{PBE}_{\text{GW-fit}})$  també augmenta generalment amb l'increment del  $V_{\text{pore}}$  (veure Figura 11b). Agafant l'energia mitjana

dels estats 1s core del Zn com a valor de referència comú hem comparat les energies de la banda de valència màxima (VBM) i de la banda de conducció mínima (CBM), per a totes les estructures (relatives a la wz-ZnO) en front de  $V_{\text{pore}}$  (veure la Figura 11c). Aquesta comparació a revelat un important nombre de coneixements sobre la base física subjacent als resultats de la Figura 11b. Primer, els nivells VBM per a la majoria d'estructures s'estenen entre  $\pm 0.2$  eV sense una marcada tendència a incrementar o disminuir amb el  $V_{\text{pore}}$ . Segon, les energies VBM que difereixen més relativament a aquelles de la wz-ZnO tendeixen a correspondre a estructures que presenten grans distorsions estructurals locals. Tercer, la CBM mostra un increment lineal amb l'increment del  $V_{\text{pore}}$ , proporcionant una major comprensió del increment total en el  $\Delta E_{\text{gap}}$  amb l'increment del  $V_{\text{pore}}$  de la Figura 11b. Els polimorfs basats en 4CN presenten valors de CBM compresos en una estreta ( $\sim 0.2$  eV) banda d'energia respecte al  $V_{\text{pore}}$ . Les estructures wz-ZnO-Np semblen seguir una tendència similar però lleugerament menys marcada, en línia amb el seu  $\Delta E_{\text{gap}}$  menor a l'incrementar el  $V_{\text{pore}}$ .

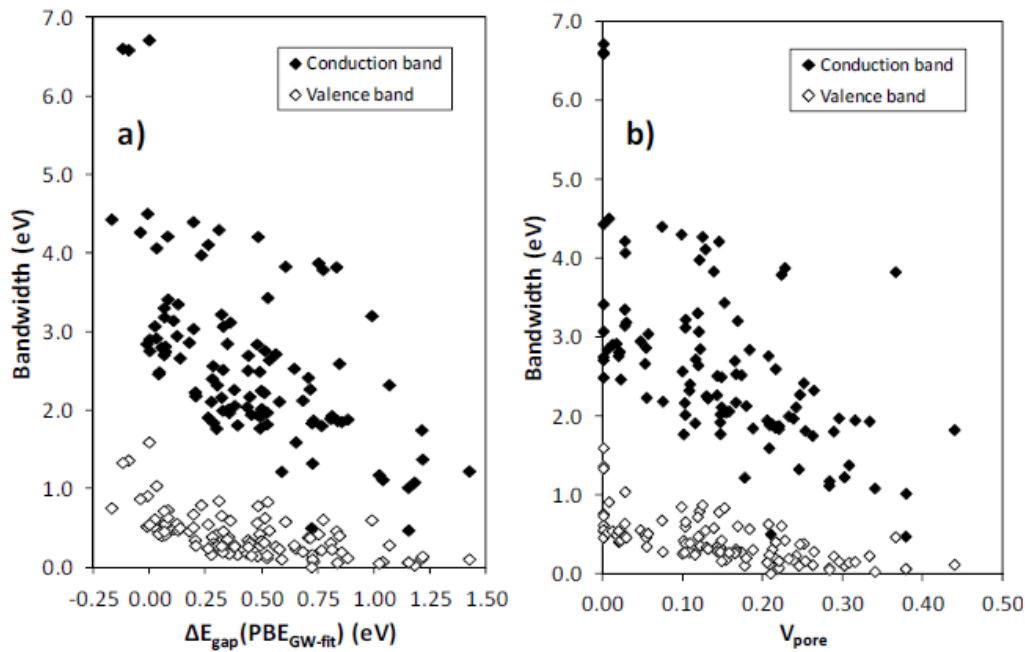


Figura 12. Gràfiques de les amplades de banda de les bandes de conducció i de valència en front de: a)  $\Delta E_{\text{gap}}(\text{PBE}_{\text{GW-fit}})$  i b)  $V_{\text{pore}}$

Hem investigat en detall les amplades de banda de la CB i de la VB per a cada polimorf nanoporós respecte al  $\Delta E_{\text{gap}}(\text{PBE}_{\text{GW-fit}})$  (Figura 12a) i a  $V_{\text{pore}}$  (Figura 12b), els quals

mostren una tendència general per reduir l'amplada de la banda tant en la CB com en la VB a l'incrementar el  $\Delta E_{\text{gap}}(\text{PBE}_{\text{GW-fit}})$  i el  $V_{\text{pore}}$ . Aquesta tendència confirma el mecanisme físic que hem suggerit referent a com canvia el  $\Delta E_{\text{gap}}$  amb la nanoporositat desde la perspectiva de l'estructura de bandes.

Hem conclòs els nostres resultats explicant que la nanoporositat està inextricablement connectada tant amb la  $E_{\text{rel}}$  com amb el  $\Delta E_{\text{gap}}$  i hem predit que la nanoporositat pot induir un increment en el band gap de fins a  $\sim 1.5$  eV relatiu a la wurtzita ZnO. Comprovant també la generalitat d'aquest fenomen, pel CdS i pel CdSe suggerim que la nanoporositat pot ser emprada com un mètode genèric d'enginyeria de band gapper materials funcionals morfològicament i electrònicament.

## **Publications:**

[1] IlkerDemiroglu, Daniele Stradi, FrancescIllas and Stefan T. Bromley, A theoretical study of a ZnO graphene analogue: adsorption on Ag(111) and hydrogen transport, *J. Phys. Conden. Matter*, 23 (2011) 334215.

[2] IlkerDemiroglu, Stefan T. Bromley, Nanofilm versus Bulk Polymorphism in Wurtzite Materials, *Phys. Rev. Lett.*, 110 (2013) 245501

[3] IlkerDemiroglu, Sergio Tosoni, FrancescIllas, Stefan T. Bromley, Bandgap engineering through nanoporosity, *Nanoscale*, 6 (2014) 1181

[4] Pentacene Multilayers on Ag(111), E. Mete, I. Demiroglu, M. F. Danisman and S. Ellialtioglu, *J. Phys. Chem C*, 114 (2010) 2724

[5] Influence of Steps on the Tilting and Adsorption Dynamics of Ordered Pentacene Films on Vicinal Ag(111) Surfaces, E. Mete, I. Demiroglu, E. Albayrak, G. Bracco, S. Ellialtioglu, M. F. Danisman, *J. Phys. Chem C*, 116 (2012) 19424

[6] Ilker Demiroglu, Stefan T. Bromley, Comparison of structures and stabilities of free space and surface-supported ZnO nanoclusters, Submitted to *Nanoscale*

## Appendix

Calculated properties, cell parameters and fractional coordinates of all 105 considered bulk structures. Structures 1-86 are 4CN-based structures. Structures 87-105 are wz-ZnO-NP structures. Both sets are ordered with respect to increasing  $V_{\text{pore}}$ . When  $V_{\text{pore}}$  is the same for two or more structures, they are ordered relative to increasing  $E_{\text{rel}}$ .

Str 1 (WZ)	$D_{\text{pore}}$ : 0
$\Delta E_{\text{gap}}(\text{PBE}_{\text{GW-fit}})$ : 0.00 eV	cell parameters
$E_{\text{rel}}$ : 0.00 eV/ZnO	3.271 3.271 15.970 90.00 90.00 120.00
Pore <sub>max</sub> : 0.18 nm	fractional coordinates
$V_{\text{pore}}$ : 0 %	Zn 0.000 0.000 1.000
$D_{\text{pore}}$ : 0	Zn 0.333 0.667 0.833
cell parameters	Zn 0.667 0.333 0.667
3.280 3.280 5.300 90.00 90.00 120.00	Zn 0.000 0.000 0.500
fractional coordinates	Zn 0.667 0.333 0.333
Zn 0.646 0.376 0.852	Zn 0.333 0.667 0.167
Zn 0.312 0.709 0.352	O 0.000 0.000 0.875
O 0.312 0.709 0.730	O 0.333 0.667 0.708
O 0.646 0.376 0.230	O 0.667 0.333 0.541
	O 0.000 0.000 0.375
	O 0.667 0.333 0.208
	O 0.333 0.667 0.041
Str 2 (4H)	Str 4 (ZB)
$\Delta E_{\text{gap}}(\text{PBE}_{\text{GW-fit}})$ : -0.09 eV	$\Delta E_{\text{gap}}(\text{PBE}_{\text{GW-fit}})$ : -0.17 eV
$E_{\text{rel}}$ : 0.01 eV/ZnO	$E_{\text{rel}}$ : 0.01 eV/ZnO
Pore <sub>max</sub> : 0.18 nm	Pore <sub>max</sub> : 0.18 nm
$V_{\text{pore}}$ : 0 %	$V_{\text{pore}}$ : 0 %
$D_{\text{pore}}$ : 0	$D_{\text{pore}}$ : 0
cell parameters	cell parameters
3.273 3.273 10.639 90.00 90.00 120.00	4.620 4.620 4.620 90.00 90.00 90.00
fractional coordinates	fractional coordinates
Zn 0.000 0.000 0.906	Zn 0.500 0.203 0.750
Zn 0.667 0.333 0.656	Zn 0.000 0.703 0.750
Zn 0.000 0.000 0.406	Zn 0.500 0.703 0.250
Zn 0.333 0.667 0.156	Zn 0.000 0.203 0.250
O 0.667 0.333 0.844	O 0.750 0.953 0.500
O 0.000 0.000 0.595	O 0.250 0.453 0.500
O 0.333 0.667 0.344	O 0.750 0.453 0.000
O 0.000 0.000 0.095	O 0.250 0.953 0.000
Str 3 (6H)	Str 5 (64_2_5204) <sup>18</sup>
$\Delta E_{\text{gap}}(\text{PBE}_{\text{GW-fit}})$ : -0.12 eV	$\Delta E_{\text{gap}}(\text{PBE}_{\text{GW-fit}})$ : 0.02 eV
$E_{\text{rel}}$ : 0.01 eV/ZnO	
Pore <sub>max</sub> : 0.18 nm	
$V_{\text{pore}}$ : 0 %	

$E_{\text{rel}}$ : 0.04 eV/ZnO	fractional coordinates
$\text{Pore}_{\text{max}}$ : 0.18 nm	Zn 0.845 0.653 0.840
$V_{\text{pore}}$ : 0 %	Zn 0.845 0.153 0.840
$D_{\text{pore}}$ : 0	Zn 0.169 0.653 0.839
cell parameters	Zn 0.169 0.153 0.839
5.377 13.149 5.699 89.99 89.98 90.02	Zn 0.507 0.589 0.836
fractional coordinates	Zn 0.507 0.089 0.836
Zn 0.670 0.190 0.920	Zn 0.007 0.905 0.666
Zn 0.798 0.690 0.920	Zn 0.007 0.405 0.666
Zn 0.674 0.435 0.917	Zn 0.669 0.841 0.663
Zn 0.794 0.935 0.917	Zn 0.669 0.341 0.663
Zn 0.294 0.935 0.591	Zn 0.346 0.841 0.662
Zn 0.174 0.435 0.591	Zn 0.346 0.341 0.662
Zn 0.298 0.690 0.589	Zn 0.346 0.591 0.339
Zn 0.170 0.190 0.588	Zn 0.346 0.091 0.339
Zn 0.670 0.314 0.420	Zn 0.669 0.591 0.339
Zn 0.798 0.814 0.420	Zn 0.669 0.091 0.339
Zn 0.674 0.068 0.417	Zn 0.007 0.655 0.336
Zn 0.794 0.568 0.417	Zn 0.007 0.155 0.336
Zn 0.174 0.069 0.091	Zn 0.507 0.839 0.166
Zn 0.294 0.569 0.091	Zn 0.507 0.339 0.166
Zn 0.298 0.814 0.089	Zn 0.169 0.903 0.163
Zn 0.170 0.314 0.088	Zn 0.169 0.403 0.163
O 0.172 0.690 0.919	Zn 0.845 0.903 0.163
O 0.296 0.190 0.919	Zn 0.845 0.403 0.163
O 0.176 0.936 0.918	O 0.845 0.843 0.837
O 0.292 0.436 0.918	O 0.845 0.343 0.837
O 0.792 0.436 0.591	O 0.170 0.843 0.837
O 0.676 0.936 0.591	O 0.169 0.343 0.837
O 0.672 0.690 0.589	O 0.507 0.903 0.837
O 0.796 0.190 0.589	O 0.507 0.403 0.837
O 0.172 0.814 0.419	O 0.007 0.591 0.665
O 0.296 0.314 0.419	O 0.007 0.091 0.665
O 0.292 0.068 0.418	O 0.669 0.651 0.664
O 0.176 0.568 0.418	O 0.669 0.151 0.664
O 0.792 0.068 0.091	O 0.345 0.651 0.664
O 0.676 0.568 0.091	O 0.345 0.151 0.664
O 0.796 0.314 0.089	O 0.669 0.901 0.338
O 0.672 0.814 0.089	O 0.669 0.401 0.338
	O 0.345 0.901 0.338
	O 0.345 0.401 0.338
Str 6 (BYL) <sup>19</sup>	O 0.007 0.341 0.337
$\Delta E_{\text{gap}}(\text{PBE}_{\text{GW}}\text{-fit})$ : 0.05 eV	O 0.007 0.841 0.337
$E_{\text{rel}}$ : 0.05 eV/ZnO	O 0.507 0.653 0.165
$\text{Pore}_{\text{max}}$ : 0.18 nm	O 0.507 0.153 0.165
$V_{\text{pore}}$ : 0 %	O 0.845 0.593 0.165
$D_{\text{pore}}$ : 0	O 0.845 0.093 0.165
cell parameters	O 0.169 0.593 0.165
9.858 10.831 5.707 90.00 90.02 90.00	

O 0.169 0.093 0.165

Str 7 (64\_2\_7625)<sup>18</sup>

$\Delta E_{\text{gap}}(\text{PBE}_{\text{GW}}\text{-fit}): 0.07 \text{ eV}$

$E_{\text{rel}}: 0.05 \text{ eV/ZnO}$

$\text{Pore}_{\text{max}}: 0.17 \text{ nm}$

$V_{\text{pore}}: 0 \%$

$D_{\text{pore}}: 0$

cell parameters

5.585 6.513 11.371 90.00 90.01 89.99

fractional coordinates

Zn 0.304 0.321 0.924

Zn 0.167 0.821 0.924

Zn 0.667 0.049 0.833

Zn 0.804 0.549 0.833

Zn 0.304 0.549 0.673

Zn 0.167 0.049 0.673

Zn 0.667 0.821 0.583

Zn 0.804 0.321 0.583

Zn 0.167 0.795 0.424

Zn 0.304 0.295 0.424

Zn 0.804 0.066 0.333

Zn 0.667 0.567 0.333

Zn 0.167 0.566 0.173

Zn 0.304 0.066 0.173

Zn 0.667 0.795 0.083

Zn 0.804 0.295 0.083

O 0.801 0.817 0.923

O 0.670 0.317 0.923

O 0.301 0.052 0.833

O 0.170 0.552 0.833

O 0.670 0.552 0.673

O 0.801 0.052 0.673

O 0.301 0.818 0.583

O 0.170 0.318 0.583

O 0.802 0.798 0.423

O 0.670 0.298 0.423

O 0.301 0.564 0.333

O 0.170 0.064 0.333

O 0.801 0.564 0.173

O 0.670 0.064 0.173

O 0.301 0.798 0.083

O 0.170 0.298 0.083

Str 8

$\Delta E_{\text{gap}}(\text{PBE}_{\text{GW}}\text{-fit}): 0.07 \text{ eV}$

$E_{\text{rel}}: 0.05 \text{ eV/ZnO}$

$\text{Pore}_{\text{max}}: 0.17 \text{ nm}$

$V_{\text{pore}}: 0 \%$

$D_{\text{pore}}: 0$

cell parameters

6.516 19.702 5.578 90.00 90.00 60.06

fractional coordinates

Zn 0.660 0.058 0.729

Zn 0.160 0.558 0.728

Zn 0.666 0.224 0.728

Zn 0.166 0.724 0.728

Zn 0.644 0.391 0.728

Zn 0.144 0.891 0.728

Zn 0.144 0.391 0.593

Zn 0.644 0.891 0.593

Zn 0.166 0.224 0.593

Zn 0.666 0.724 0.593

Zn 0.160 0.058 0.593

Zn 0.660 0.558 0.593

Zn 0.805 0.285 0.229

Zn 0.305 0.785 0.228

Zn 0.799 0.118 0.228

Zn 0.299 0.618 0.228

Zn 0.322 0.451 0.228

Zn 0.822 0.951 0.228

Zn 0.822 0.451 0.093

Zn 0.322 0.951 0.093

Zn 0.299 0.118 0.093

Zn 0.799 0.618 0.093

Zn 0.305 0.285 0.093

Zn 0.805 0.785 0.093

O 0.306 0.285 0.726

O 0.302 0.118 0.726

O 0.802 0.618 0.726

O 0.806 0.785 0.726

O 0.820 0.451 0.726

O 0.320 0.951 0.726

O 0.320 0.452 0.595

O 0.820 0.951 0.595

O 0.806 0.285 0.595

O 0.802 0.118 0.595

O 0.302 0.618 0.594

O 0.306 0.785 0.594

O 0.164 0.224 0.227

O 0.664 0.724 0.227

O 0.159 0.058 0.226

O 0.659 0.558 0.226

O 0.146 0.391 0.226

O 0.646 0.891 0.226

O 0.646 0.391 0.095

O 0.659 0.058 0.095	Zn 0.085 0.805 0.754
O 0.146 0.891 0.095	Zn 0.793 0.177 0.504
O 0.159 0.558 0.095	Zn 0.957 0.680 0.504
O 0.663 0.225 0.094	Zn 0.710 0.677 0.504
O 0.163 0.725 0.094	Zn 0.457 0.801 0.504
	Zn 0.046 0.301 0.504
Str 9 (64_1_1) <sup>18</sup>	Zn 0.546 0.180 0.504
$\Delta E_{\text{gap}}(\text{PBE}_{\text{GW-fit}})$ : 0.08 eV	Zn 0.293 0.305 0.504
$E_{\text{rel}}$ : 0.06 eV/ZnO	Zn 0.210 0.805 0.504
Pore <sub>max</sub> : 0.17 nm	Zn 0.669 0.175 0.254
V <sub>pore</sub> : 0 %	Zn 0.169 0.306 0.254
D <sub>pore</sub> : 0	Zn 0.918 0.177 0.254
cell parameters	Zn 0.834 0.675 0.254
5.706 6.513 5.566 90.00 90.00 90.00	Zn 0.334 0.806 0.254
fractional coordinates	Zn 0.585 0.677 0.254
Zn 0.555 0.813 0.715	Zn 0.418 0.305 0.254
Zn 0.055 0.045 0.715	Zn 0.085 0.805 0.254
Zn 0.555 0.313 0.582	Zn 0.957 0.680 0.004
Zn 0.055 0.545 0.582	Zn 0.793 0.177 0.004
Zn 0.875 0.813 0.215	Zn 0.710 0.677 0.004
Zn 0.375 0.045 0.215	Zn 0.457 0.801 0.004
Zn 0.875 0.313 0.082	Zn 0.046 0.301 0.004
Zn 0.375 0.545 0.082	Zn 0.293 0.305 0.004
O 0.874 0.312 0.714	Zn 0.210 0.805 0.004
O 0.374 0.546 0.714	Zn 0.546 0.180 0.004
O 0.874 0.812 0.582	O 0.586 0.299 0.754
O 0.374 0.046 0.582	O 0.335 0.183 0.754
O 0.055 0.546 0.214	O 0.169 0.683 0.754
O 0.555 0.312 0.214	O 0.917 0.799 0.754
O 0.055 0.046 0.082	O 0.835 0.299 0.754
O 0.555 0.812 0.082	O 0.669 0.799 0.754
	O 0.417 0.682 0.754
Str 10 (59_4_253337) <sup>18</sup>	O 0.086 0.182 0.754
$\Delta E_{\text{gap}}(\text{PBE}_{\text{GW-fit}})$ : -0.01 eV	O 0.545 0.795 0.504
$E_{\text{rel}}$ : 0.02 eV/ZnO	O 0.710 0.299 0.504
Pore <sub>max</sub> : 0.18 nm	O 0.458 0.187 0.504
V <sub>pore</sub> : 1 %	O 0.293 0.683 0.504
D <sub>pore</sub> : 1	O 0.210 0.182 0.504
cell parameters	O 0.793 0.799 0.504
22.770 5.328 6.577 90.00 90.00 90.00	O 0.958 0.294 0.504
fractional coordinates	O 0.045 0.687 0.504
Zn 0.669 0.175 0.754	O 0.586 0.299 0.254
Zn 0.834 0.675 0.754	O 0.335 0.183 0.254
Zn 0.334 0.806 0.754	O 0.169 0.683 0.254
Zn 0.169 0.306 0.754	O 0.917 0.799 0.254
Zn 0.918 0.177 0.754	O 0.835 0.299 0.254
Zn 0.585 0.677 0.754	O 0.669 0.799 0.254
Zn 0.418 0.305 0.754	O 0.417 0.682 0.254

O 0.086 0.182 0.254  
O 0.545 0.795 0.004  
O 0.710 0.299 0.004  
O 0.458 0.187 0.004  
O 0.293 0.683 0.004  
O 0.210 0.182 0.004  
O 0.793 0.799 0.004  
O 0.958 0.294 0.004  
O 0.045 0.687 0.004

Str 11 (59\_3\_250)<sup>18</sup>

$\Delta E_{\text{gap}}(\text{PBE}_{\text{GW-fit}})$ : -0.01 eV

$E_{\text{rel}}$ : 0.02 eV/ZnO

Pore<sub>max</sub>: 0.18 nm

V<sub>pore</sub>: 1 %

D<sub>pore</sub>: 1

cell parameters

17.069 5.342 3.288 90.00 90.00 90.00

fractional coordinates

Zn 0.443 0.793 0.771

Zn 0.114 0.797 0.770

Zn 0.226 0.300 0.770

Zn 0.891 0.167 0.770

Zn 0.779 0.665 0.770

Zn 0.561 0.172 0.770

Zn 0.279 0.800 0.271

Zn 0.391 0.298 0.271

Zn 0.943 0.672 0.270

Zn 0.061 0.292 0.270

Zn 0.614 0.668 0.270

Zn 0.725 0.165 0.270

O 0.225 0.676 0.771

O 0.444 0.178 0.771

O 0.890 0.791 0.770

O 0.114 0.173 0.770

O 0.561 0.787 0.770

O 0.780 0.289 0.770

O 0.390 0.674 0.271

O 0.061 0.677 0.270

O 0.280 0.176 0.270

O 0.944 0.287 0.270

O 0.725 0.789 0.270

O 0.614 0.291 0.270

Str 12 (59\_4\_280312)<sup>18</sup>

$\Delta E_{\text{gap}}(\text{PBE}_{\text{GW-fit}})$ : 0.00 eV

$E_{\text{rel}}$ : 0.03 eV/ZnO

Pore<sub>max</sub>: 0.18 nm

V<sub>pore</sub>: 1 %

D<sub>pore</sub>: 1

cell parameters

11.372 5.375 6.586 90.00 90.00 90.00

fractional coordinates

Zn 0.835 0.322 0.750

Zn 0.665 0.822 0.750

Zn 0.335 0.189 0.750

Zn 0.165 0.689 0.750

Zn 0.911 0.818 0.500

Zn 0.589 0.318 0.500

Zn 0.411 0.694 0.500

Zn 0.089 0.194 0.500

Zn 0.835 0.322 0.250

Zn 0.665 0.822 0.250

Zn 0.335 0.189 0.250

Zn 0.165 0.689 0.250

Zn 0.911 0.818 0.000

Zn 0.589 0.318 0.000

Zn 0.411 0.694 0.000

Zn 0.089 0.194 0.000

O 0.833 0.696 0.750

O 0.668 0.196 0.750

O 0.333 0.815 0.750

O 0.168 0.315 0.750

O 0.913 0.200 0.500

O 0.587 0.700 0.500

O 0.413 0.311 0.500

O 0.087 0.811 0.500

O 0.833 0.696 0.250

O 0.668 0.196 0.250

O 0.333 0.815 0.250

O 0.168 0.315 0.250

O 0.913 0.200 0.000

O 0.587 0.700 0.000

O 0.413 0.311 0.000

O 0.087 0.811 0.000

Str 13 ()

$\Delta E_{\text{gap}}(\text{PBE}_{\text{GW-fit}})$ : 0.03 eV

$E_{\text{rel}}$ : 0.06 eV/ZnO

Pore<sub>max</sub>: 0.19 nm

V<sub>pore</sub>: 2 %

D<sub>pore</sub>: 1

cell parameters

6.601 13.178 5.389 89.86 90.00 59.94

fractional coordinates

Zn 0.149 0.591 0.726

Zn 0.148 0.841 0.725	Zn 0.827 0.684 0.752
Zn 0.649 0.841 0.725	Zn 0.452 0.682 0.502
Zn 0.653 0.586 0.606	Zn 0.042 0.182 0.502
Zn 0.644 0.096 0.599	Zn 0.290 0.313 0.502
Zn 0.145 0.338 0.599	Zn 0.952 0.813 0.502
Zn 0.659 0.338 0.599	Zn 0.790 0.182 0.502
Zn 0.146 0.094 0.598	Zn 0.705 0.682 0.502
Zn 0.819 0.920 0.223	Zn 0.205 0.813 0.502
Zn 0.306 0.676 0.222	Zn 0.543 0.313 0.502
Zn 0.820 0.677 0.222	Zn 0.078 0.683 0.252
Zn 0.322 0.918 0.222	Zn 0.417 0.183 0.252
Zn 0.312 0.428 0.215	Zn 0.917 0.312 0.252
Zn 0.316 0.173 0.096	Zn 0.578 0.812 0.252
Zn 0.817 0.173 0.096	Zn 0.668 0.185 0.252
Zn 0.816 0.424 0.095	Zn 0.327 0.811 0.252
O 0.316 0.173 0.721	Zn 0.168 0.311 0.252
O 0.818 0.173 0.721	Zn 0.827 0.684 0.252
O 0.817 0.422 0.721	Zn 0.452 0.682 0.002
O 0.313 0.427 0.614	Zn 0.042 0.182 0.002
O 0.820 0.676 0.605	Zn 0.290 0.313 0.002
O 0.307 0.676 0.605	Zn 0.205 0.813 0.002
O 0.819 0.921 0.605	Zn 0.952 0.813 0.002
O 0.321 0.919 0.604	Zn 0.790 0.182 0.002
O 0.644 0.096 0.217	Zn 0.705 0.682 0.002
O 0.146 0.093 0.216	Zn 0.543 0.313 0.002
O 0.145 0.338 0.216	O 0.416 0.809 0.752
O 0.658 0.338 0.216	O 0.079 0.308 0.752
O 0.652 0.587 0.208	O 0.667 0.810 0.752
O 0.148 0.592 0.100	O 0.828 0.309 0.752
O 0.650 0.841 0.100	O 0.916 0.687 0.752
O 0.148 0.841 0.100	O 0.328 0.186 0.752
	O 0.167 0.686 0.752
	O 0.579 0.187 0.752
Str 14 (59_4_253313) <sup>18</sup>	O 0.042 0.808 0.502
$\Delta E_{\text{gap}}(\text{PBE}_{\text{GW}}\text{-fit}): 0.00 \text{ eV}$	O 0.453 0.309 0.502
$E_{\text{rel}}: 0.05 \text{ eV/ZnO}$	O 0.542 0.687 0.502
Pore <sub>max</sub> : 0.18 nm	O 0.953 0.186 0.502
V <sub>pore</sub> : 2 %	O 0.706 0.313 0.502
D <sub>pore</sub> : 1	O 0.289 0.682 0.502
cell parameters	O 0.789 0.813 0.502
22.669 5.462 6.584 90.02 89.99 89.99	O 0.206 0.182 0.502
fractional coordinates	O 0.416 0.809 0.252
Zn 0.078 0.683 0.752	O 0.079 0.308 0.252
Zn 0.417 0.183 0.752	O 0.828 0.309 0.252
Zn 0.578 0.812 0.752	O 0.667 0.810 0.252
Zn 0.917 0.312 0.752	O 0.916 0.687 0.252
Zn 0.668 0.185 0.752	O 0.328 0.186 0.252
Zn 0.327 0.811 0.752	O 0.167 0.686 0.252
Zn 0.168 0.311 0.752	

O 0.579 0.187 0.252  
O 0.042 0.808 0.002  
O 0.453 0.309 0.002  
O 0.542 0.687 0.002  
O 0.953 0.186 0.002  
O 0.706 0.313 0.002  
O 0.289 0.682 0.002  
O 0.789 0.813 0.002  
O 0.206 0.182 0.002

Str 15 ()

$\Delta E_{\text{gap}}(\text{PBE}_{\text{GW-fit}})$ : 0.06 eV

$E_{\text{rel}}$ : 0.08 eV/ZnO

$\text{Pore}_{\text{max}}$ : 0.19 nm

$V_{\text{pore}}$ : 2 %

$D_{\text{pore}}$ : 1

cell parameters

9.962 9.921 5.371 89.63 90.00 120.14

fractional coordinates

Zn 0.895 0.441 0.817

Zn 0.561 0.441 0.817

Zn 0.228 0.441 0.817

Zn 0.558 0.101 0.703

Zn 0.891 0.101 0.702

Zn 0.224 0.101 0.702

Zn 0.896 0.778 0.690

Zn 0.563 0.778 0.690

Zn 0.230 0.778 0.690

Zn 0.780 0.545 0.315

Zn 0.446 0.545 0.315

Zn 0.113 0.545 0.315

Zn 0.785 0.222 0.302

Zn 0.452 0.222 0.302

Zn 0.118 0.222 0.302

Zn 0.782 0.882 0.188

Zn 0.115 0.882 0.188

Zn 0.448 0.882 0.188

O 0.781 0.881 0.811

O 0.114 0.881 0.811

O 0.448 0.881 0.811

O 0.785 0.221 0.709

O 0.451 0.221 0.709

O 0.118 0.222 0.709

O 0.780 0.545 0.698

O 0.447 0.545 0.698

O 0.113 0.545 0.698

O 0.896 0.778 0.307

O 0.563 0.778 0.307

O 0.230 0.778 0.307

O 0.558 0.101 0.297

O 0.891 0.102 0.296

O 0.225 0.102 0.296

O 0.895 0.442 0.194

O 0.562 0.442 0.194

O 0.228 0.442 0.193

Str 16 (189\_3\_1615)<sup>18</sup>

$\Delta E_{\text{gap}}(\text{PBE}_{\text{GW-fit}})$ : 0.07 eV

$E_{\text{rel}}$ : 0.08 eV/ZnO

$\text{Pore}_{\text{max}}$ : 0.23 nm

$V_{\text{pore}}$ : 2 %

$D_{\text{pore}}$ : 1

cell parameters

9.924 9.925 5.395 90.00 90.00 120.00

fractional coordinates

Zn 0.888 0.437 0.817

Zn 0.563 0.437 0.817

Zn 0.563 0.111 0.817

Zn 0.890 0.766 0.805

Zn 0.890 0.109 0.805

Zn 0.233 0.109 0.805

Zn 0.558 0.771 0.689

Zn 0.228 0.771 0.689

Zn 0.228 0.442 0.689

Zn 0.781 0.548 0.319

Zn 0.781 0.218 0.319

Zn 0.452 0.218 0.319

Zn 0.776 0.881 0.203

Zn 0.119 0.881 0.203

Zn 0.119 0.223 0.203

Zn 0.446 0.878 0.192

Zn 0.446 0.553 0.192

Zn 0.121 0.553 0.192

O 0.447 0.879 0.811

O 0.447 0.553 0.811

O 0.121 0.553 0.811

O 0.119 0.881 0.800

O 0.119 0.223 0.800

O 0.776 0.881 0.800

O 0.781 0.548 0.694

O 0.781 0.218 0.694

O 0.452 0.218 0.694

O 0.558 0.771 0.315

O 0.228 0.771 0.315

O 0.228 0.442 0.315

O 0.890 0.766 0.208

O 0.890 0.109 0.208  
O 0.233 0.109 0.208  
O 0.563 0.437 0.198  
O 0.889 0.437 0.198  
O 0.563 0.111 0.198

Str 17 ()

$\Delta E_{\text{gap}}(\text{PBE}_{\text{GW-fit}})$ : 0.04 eV

$E_{\text{rel}}$ : 0.08 eV/ZnO

$\text{Pore}_{\text{max}}$ : 0.19 nm

$V_{\text{pore}}$ : 2 %

$D_{\text{pore}}$ : 1

cell parameters

22.823 5.416 6.631 90.02 89.99 90.33

fractional coordinates

Zn 0.422 0.303 0.754

Zn 0.582 0.679 0.754

Zn 0.837 0.696 0.754

Zn 0.332 0.674 0.754

Zn 0.919 0.181 0.754

Zn 0.084 0.814 0.754

Zn 0.671 0.311 0.754

Zn 0.167 0.297 0.754

Zn 0.547 0.176 0.505

Zn 0.294 0.177 0.504

Zn 0.212 0.694 0.504

Zn 0.791 0.297 0.504

Zn 0.958 0.683 0.504

Zn 0.046 0.312 0.504

Zn 0.709 0.811 0.504

Zn 0.457 0.805 0.504

Zn 0.422 0.303 0.255

Zn 0.582 0.679 0.254

Zn 0.837 0.696 0.254

Zn 0.332 0.674 0.254

Zn 0.919 0.181 0.254

Zn 0.084 0.814 0.254

Zn 0.671 0.311 0.254

Zn 0.167 0.297 0.254

Zn 0.547 0.176 0.005

Zn 0.294 0.177 0.004

Zn 0.212 0.694 0.004

Zn 0.958 0.683 0.004

Zn 0.791 0.297 0.004

Zn 0.046 0.312 0.004

Zn 0.709 0.811 0.004

Zn 0.457 0.805 0.004

O 0.583 0.300 0.755

O 0.333 0.297 0.754

O 0.167 0.701 0.754

O 0.919 0.807 0.754

O 0.837 0.292 0.754

O 0.084 0.187 0.754

O 0.421 0.682 0.754

O 0.670 0.688 0.754

O 0.545 0.799 0.505

O 0.458 0.183 0.504

O 0.791 0.701 0.504

O 0.295 0.802 0.504

O 0.958 0.304 0.504

O 0.045 0.692 0.504

O 0.709 0.185 0.504

O 0.212 0.291 0.504

O 0.583 0.300 0.255

O 0.333 0.297 0.254

O 0.167 0.701 0.254

O 0.919 0.807 0.254

O 0.837 0.292 0.254

O 0.084 0.187 0.254

O 0.421 0.682 0.254

O 0.670 0.688 0.254

O 0.545 0.799 0.005

O 0.458 0.183 0.004

O 0.791 0.701 0.004

O 0.295 0.802 0.004

O 0.958 0.304 0.004

O 0.045 0.692 0.004

O 0.709 0.185 0.004

O 0.212 0.291 0.004

Str 18 (SSCCCC)<sup>16</sup>

$\Delta E_{\text{gap}}(\text{PBE}_{\text{GW-fit}})$ : 0.08 eV

$E_{\text{rel}}$ : 0.09 eV/ZnO

$\text{Pore}_{\text{max}}$ : 0.19 nm

$V_{\text{pore}}$ : 3 %

$D_{\text{pore}}$ : 0

cell parameters

11.462 5.320 3.331 89.99 90.00 90.00

fractional coordinates

Zn 0.278 0.187 0.920

Zn 0.615 0.804 0.919

Zn 0.778 0.285 0.919

Zn 0.115 0.667 0.919

Zn 0.370 0.785 0.420

Zn 0.533 0.304 0.420

Zn 0.033 0.168 0.419

Zn 0.870 0.687 0.419  
O 0.279 0.778 0.920  
O 0.613 0.183 0.919  
O 0.114 0.289 0.919  
O 0.779 0.694 0.919  
O 0.369 0.193 0.419  
O 0.535 0.683 0.419  
O 0.869 0.278 0.419  
O 0.035 0.789 0.419

Str 19 ()

$\Delta E_{\text{gap}}(\text{PBE}_{\text{GW-fit}})$ : 0.11 eV

$E_{\text{rel}}$ : 0.10 eV/ZnO

$\text{Pore}_{\text{max}}$ : 0.23 nm

$V_{\text{pore}}$ : 3 %

$D_{\text{pore}}$ : 1

cell parameters

8.769 6.624 5.461 89.98 90.03 79.20

fractional coordinates

Zn 0.556 0.617 0.996

Zn 0.889 0.294 0.994

Zn 0.560 0.116 0.873

Zn 0.217 0.943 0.873

Zn 0.218 0.457 0.872

Zn 0.889 0.792 0.861

Zn 0.773 0.553 0.495

Zn 0.444 0.887 0.482

Zn 0.102 0.228 0.481

Zn 0.445 0.401 0.481

Zn 0.773 0.050 0.361

Zn 0.106 0.727 0.359

O 0.106 0.727 0.988

O 0.775 0.055 0.986

O 0.445 0.401 0.879

O 0.445 0.887 0.878

O 0.103 0.229 0.878

O 0.773 0.557 0.870

O 0.889 0.787 0.486

O 0.559 0.116 0.476

O 0.217 0.457 0.475

O 0.217 0.943 0.475

O 0.887 0.290 0.369

O 0.556 0.617 0.366

Str 20 ()

$\Delta E_{\text{gap}}(\text{PBE}_{\text{GW-fit}})$ : 0.13 eV

$E_{\text{rel}}$ : 0.13 eV/ZnO

$\text{Pore}_{\text{max}}$ : 0.22 nm

$V_{\text{pore}}$ : 3 %

$D_{\text{pore}}$ : 1

cell parameters

6.671 6.671 5.373 90.00 90.00 120.00

fractional coordinates

Zn 0.825 0.648 0.961

Zn 0.825 0.158 0.961

Zn 0.335 0.158 0.961

Zn 0.655 0.818 0.562

Zn 0.165 0.818 0.562

Zn 0.165 0.328 0.562

Zn 0.662 0.321 0.446

Zn 0.329 0.655 0.077

O 0.655 0.818 0.967

O 0.166 0.818 0.967

O 0.166 0.329 0.967

O 0.825 0.647 0.555

O 0.825 0.158 0.555

O 0.336 0.158 0.555

O 0.329 0.655 0.454

O 0.662 0.321 0.068

Str 21 (BCT)<sup>17</sup>

$\Delta E_{\text{gap}}(\text{PBE}_{\text{GW-fit}})$ : 0.03 eV

$E_{\text{rel}}$ : 0.05 eV/ZnO

$\text{Pore}_{\text{max}}$ : 0.16 nm

$V_{\text{pore}}$ : 3 %

$D_{\text{pore}}$ : 1

cell parameters

7.925 7.925 3.287 90.00 90.00 90.00

fractional coordinates

Zn 0.503 0.818 0.500

Zn 0.503 0.182 0.500

Zn 0.003 0.682 0.500

Zn 0.003 0.318 0.500

Zn 0.821 0.000 0.000

Zn 0.685 0.500 0.000

Zn 0.321 0.500 0.000

Zn 0.185 0.000 0.000

O 0.821 0.500 0.500

O 0.685 0.000 0.500

O 0.321 0.000 0.500

O 0.185 0.500 0.500

O 0.503 0.682 0.000

O 0.503 0.318 0.000

O 0.003 0.818 0.000

O 0.003 0.182 0.000

Str 22 ()  
 $\Delta E_{\text{gap}}(\text{PBE}_{\text{GW-fit}})$ : 0.07 eV  
 $E_{\text{rel}}$ : 0.07 eV/ZnO  
Pore<sub>max</sub>: 0.19 nm  
V<sub>pore</sub>: 3 %  
D<sub>pore</sub>: 1  
cell parameters  
8.711 6.587 5.484 90.16 90.17 79.25  
fractional coordinates  
Zn 0.780 0.034 0.874  
Zn 0.780 0.534 0.874  
Zn 0.458 0.856 0.874  
Zn 0.340 0.154 0.507  
Zn 0.017 0.976 0.507  
Zn 0.018 0.475 0.506  
Zn 0.347 0.654 0.380  
Zn 0.686 0.307 0.378  
Zn 0.678 0.810 0.371  
Zn 0.119 0.199 0.009  
Zn 0.112 0.702 0.003  
Zn 0.451 0.357 0.001  
O 0.345 0.649 0.993  
O 0.339 0.149 0.881  
O 0.015 0.474 0.881  
O 0.015 0.977 0.881  
O 0.782 0.032 0.500  
O 0.459 0.862 0.500  
O 0.783 0.536 0.500  
O 0.453 0.361 0.388  
O 0.114 0.702 0.380  
O 0.120 0.199 0.377  
O 0.678 0.810 0.003  
O 0.684 0.308 0.001

Str 23 (-LIT)<sup>17</sup>  
 $\Delta E_{\text{gap}}(\text{PBE}_{\text{GW-fit}})$ : 0.12 eV  
 $E_{\text{rel}}$ : 0.10 eV/ZnO  
Pore<sub>max</sub>: 0.20 nm  
V<sub>pore</sub>: 5 %  
D<sub>pore</sub>: 1  
cell parameters  
9.891 5.586 5.716 90.00 90.00 90.00  
fractional coordinates  
Zn 0.994 0.935 0.840  
Zn 0.670 0.933 0.831  
Zn 0.332 0.065 0.817  
Zn 0.832 0.435 0.683  
Zn 0.170 0.567 0.669

Zn 0.494 0.565 0.660  
Zn 0.506 0.065 0.340  
Zn 0.830 0.067 0.331  
Zn 0.168 0.935 0.317  
Zn 0.668 0.565 0.183  
Zn 0.330 0.433 0.169  
Zn 0.006 0.435 0.160  
O 0.995 0.563 0.838  
O 0.668 0.558 0.834  
O 0.332 0.436 0.818  
O 0.832 0.064 0.682  
O 0.168 0.942 0.666  
O 0.495 0.937 0.662  
O 0.505 0.437 0.338  
O 0.832 0.442 0.334  
O 0.168 0.564 0.318  
O 0.668 0.936 0.182  
O 0.332 0.058 0.166  
O 0.005 0.063 0.162

Str 24 (64\_2\_7619)<sup>18</sup>  
 $\Delta E_{\text{gap}}(\text{PBE}_{\text{GW-fit}})$ : 0.14 eV  
 $E_{\text{rel}}$ : 0.11 eV/ZnO  
Pore<sub>max</sub>: 0.20 nm  
V<sub>pore</sub>: 5 %  
D<sub>pore</sub>: 2  
cell parameters  
5.630 6.563 11.501 90.00 90.00 90.00  
fractional coordinates  
Zn 0.803 0.003 0.914  
Zn 0.673 0.503 0.914  
Zn 0.307 0.231 0.830  
Zn 0.169 0.731 0.830  
Zn 0.807 0.231 0.669  
Zn 0.669 0.731 0.669  
Zn 0.303 0.003 0.586  
Zn 0.173 0.503 0.586  
Zn 0.803 0.489 0.414  
Zn 0.673 0.989 0.414  
Zn 0.307 0.260 0.330  
Zn 0.169 0.760 0.330  
Zn 0.807 0.260 0.169  
Zn 0.669 0.760 0.169  
Zn 0.303 0.489 0.086  
Zn 0.173 0.989 0.086  
O 0.296 0.497 0.915  
O 0.180 0.997 0.915  
O 0.803 0.735 0.829

O 0.674 0.235 0.829  
 O 0.303 0.735 0.671  
 O 0.174 0.235 0.671  
 O 0.796 0.497 0.585  
 O 0.680 0.997 0.585  
 O 0.296 0.994 0.415  
 O 0.180 0.494 0.415  
 O 0.803 0.757 0.329  
 O 0.674 0.257 0.329  
 O 0.303 0.757 0.171  
 O 0.174 0.257 0.171  
 O 0.796 0.994 0.085  
 O 0.680 0.494 0.085

Str 25 (64\_2\_5457)<sup>18</sup>  
 $\Delta E_{\text{gap}}(\text{PBE}_{\text{GW-fit}})$ : 0.18 eV  
 $E_{\text{rel}}$ : 0.11 eV/ZnO  
 Pore<sub>max</sub>: 0.20 nm  
 V<sub>pore</sub>: 5 %  
 D<sub>pore</sub>: 2  
 cell parameters  
 5.647 13.252 5.680 90.00 90.00 90.00  
 fractional coordinates  
 Zn 0.305 0.691 0.907  
 Zn 0.173 0.191 0.907  
 Zn 0.170 0.935 0.902  
 Zn 0.308 0.435 0.902  
 Zn 0.808 0.435 0.595  
 Zn 0.670 0.935 0.595  
 Zn 0.673 0.191 0.591  
 Zn 0.805 0.692 0.591  
 Zn 0.305 0.806 0.407  
 Zn 0.173 0.306 0.407  
 Zn 0.308 0.062 0.402  
 Zn 0.171 0.562 0.402  
 Zn 0.807 0.062 0.095  
 Zn 0.671 0.562 0.095  
 Zn 0.673 0.306 0.091  
 Zn 0.805 0.806 0.091  
 O 0.807 0.191 0.911  
 O 0.671 0.691 0.910  
 O 0.797 0.935 0.910  
 O 0.681 0.435 0.910  
 O 0.297 0.935 0.587  
 O 0.181 0.435 0.587  
 O 0.307 0.191 0.587  
 O 0.171 0.691 0.587  
 O 0.807 0.306 0.411

O 0.671 0.806 0.411  
 O 0.798 0.562 0.410  
 O 0.680 0.062 0.410  
 O 0.180 0.062 0.087  
 O 0.297 0.562 0.087  
 O 0.171 0.806 0.087  
 O 0.307 0.306 0.087

Str 26 (AEN)<sup>17</sup>  
 $\Delta E_{\text{gap}}(\text{PBE}_{\text{GW-fit}})$ : 0.21 eV  
 $E_{\text{rel}}$ : 0.12 eV/ZnO  
 Pore<sub>max</sub>: 0.24 nm  
 V<sub>pore</sub>: 5 %  
 D<sub>pore</sub>: 1  
 cell parameters  
 6.690 8.692 10.869 90.00 90.01 90.00  
 fractional coordinates  
 Zn 0.872 0.509 0.938  
 Zn 0.372 0.509 0.938  
 Zn 0.622 0.821 0.836  
 Zn 0.122 0.821 0.836  
 Zn 0.622 0.197 0.836  
 Zn 0.122 0.197 0.836  
 Zn 0.872 0.697 0.645  
 Zn 0.372 0.697 0.645  
 Zn 0.872 0.321 0.645  
 Zn 0.372 0.321 0.645  
 Zn 0.622 0.009 0.544  
 Zn 0.122 0.009 0.544  
 Zn 0.622 0.509 0.438  
 Zn 0.122 0.509 0.438  
 Zn 0.872 0.197 0.336  
 Zn 0.372 0.197 0.336  
 Zn 0.872 0.821 0.336  
 Zn 0.372 0.821 0.336  
 Zn 0.622 0.321 0.145  
 Zn 0.122 0.321 0.145  
 Zn 0.622 0.697 0.145  
 Zn 0.122 0.697 0.145  
 Zn 0.872 0.009 0.044  
 Zn 0.372 0.009 0.044  
 O 0.622 0.009 0.936  
 O 0.122 0.009 0.936  
 O 0.872 0.697 0.837  
 O 0.872 0.321 0.837  
 O 0.372 0.697 0.837  
 O 0.372 0.321 0.837  
 O 0.122 0.821 0.644

O 0.622 0.821 0.644  
O 0.622 0.197 0.644  
O 0.122 0.197 0.644  
O 0.872 0.509 0.545  
O 0.372 0.509 0.545  
O 0.872 0.009 0.436  
O 0.372 0.009 0.436  
O 0.622 0.321 0.337  
O 0.122 0.321 0.337  
O 0.622 0.697 0.337  
O 0.122 0.697 0.337  
O 0.872 0.197 0.144  
O 0.372 0.197 0.144  
O 0.872 0.821 0.144  
O 0.372 0.821 0.144  
O 0.622 0.509 0.045  
O 0.122 0.509 0.045

Str 27 (ATV)<sup>17</sup>

$\Delta E_{\text{gap}}(\text{PBE}_{\text{GW-fit}})$ : 0.20 eV

$E_{\text{rel}}$ : 0.13 eV/ZnO

Pore<sub>max</sub>: 0.23 nm

$V_{\text{pore}}$ : 6 %

$D_{\text{pore}}$ : 1

cell parameters

5.280 10.095 5.895 90.00 90.00 90.00

fractional coordinates

Zn 0.811 0.250 0.840

Zn 0.311 0.750 0.840

Zn 0.811 0.906 0.666

Zn 0.811 0.594 0.666

Zn 0.311 0.406 0.666

Zn 0.311 0.094 0.666

Zn 0.811 0.406 0.334

Zn 0.811 0.094 0.334

Zn 0.311 0.906 0.334

Zn 0.311 0.594 0.334

Zn 0.811 0.750 0.160

Zn 0.311 0.250 0.160

O 0.692 0.750 0.837

O 0.192 0.250 0.837

O 0.688 0.406 0.671

O 0.688 0.094 0.671

O 0.188 0.906 0.671

O 0.188 0.594 0.671

O 0.688 0.906 0.329

O 0.688 0.594 0.329

O 0.188 0.406 0.329

O 0.188 0.094 0.329

O 0.692 0.250 0.163

O 0.192 0.750 0.163

Str 28 (JBW)<sup>17</sup>

$\Delta E_{\text{gap}}(\text{PBE}_{\text{GW-fit}})$ : 0.20 eV

$E_{\text{rel}}$ : 0.19 eV/ZnO

Pore<sub>max</sub>: 0.21 nm

$V_{\text{pore}}$ : 7 %

$D_{\text{pore}}$ : 1

cell parameters

3.353 10.166 4.751 90.00 90.00 90.00

fractional coordinates

Zn 0.750 0.608 0.893

Zn 0.750 0.904 0.893

Zn 0.750 0.256 0.610

Zn 0.250 0.756 0.389

Zn 0.250 0.405 0.106

Zn 0.250 0.108 0.106

O 0.750 0.408 0.871

O 0.750 0.104 0.871

O 0.750 0.756 0.626

O 0.250 0.256 0.374

O 0.250 0.604 0.128

O 0.250 0.908 0.128

Str 29 (SSCSSC)<sup>16</sup>

$\Delta E_{\text{gap}}(\text{PBE}_{\text{GW-fit}})$ : 0.31 eV

$E_{\text{rel}}$ : 0.15 eV/ZnO

Pore<sub>max</sub>: 0.22 nm

$V_{\text{pore}}$ : 10 %

$D_{\text{pore}}$ : 1

cell parameters

5.534 3.365 6.051 90.00 89.99 89.99

fractional coordinates

Zn 0.062 0.108 0.727

Zn 0.562 0.608 0.573

Zn 0.363 0.108 0.227

Zn 0.863 0.608 0.073

O 0.869 0.608 0.725

O 0.369 0.108 0.576

O 0.557 0.608 0.225

O 0.056 0.108 0.076

Str 30 (ABW)<sup>17</sup>

$\Delta E_{\text{gap}}(\text{PBE}_{\text{GW-fit}})$ : 0.30 eV

$E_{\text{rel}}$ : 0.15 eV/ZnO

Pore<sub>max</sub>: 0.22 nm

V <sub>pore</sub> : 10 %	O 0.162 0.250 0.747
D <sub>pore</sub> : 1	O 0.835 0.500 0.650
cell parameters	O 0.835 0.000 0.650
12.188 6.707 11.061 90.00 90.00 90.00	O 0.335 0.500 0.650
fractional coordinates	O 0.335 0.000 0.650
Zn 0.912 0.500 0.998	O 0.585 0.500 0.497
Zn 0.912 0.000 0.998	O 0.585 0.000 0.497
Zn 0.412 0.500 0.998	O 0.085 0.500 0.497
Zn 0.412 0.000 0.998	O 0.085 0.000 0.497
Zn 0.585 0.750 0.899	O 0.912 0.750 0.400
Zn 0.585 0.250 0.899	O 0.912 0.250 0.400
Zn 0.085 0.750 0.899	O 0.412 0.750 0.400
Zn 0.085 0.250 0.899	O 0.412 0.250 0.400
Zn 0.835 0.750 0.748	O 0.662 0.750 0.247
Zn 0.835 0.250 0.748	O 0.662 0.250 0.247
Zn 0.335 0.750 0.748	O 0.162 0.750 0.247
Zn 0.335 0.250 0.748	O 0.162 0.250 0.247
Zn 0.662 0.500 0.649	O 0.835 0.500 0.150
Zn 0.662 0.000 0.649	O 0.835 0.000 0.150
Zn 0.162 0.500 0.649	O 0.335 0.500 0.150
Zn 0.162 0.000 0.649	O 0.335 0.000 0.150
Zn 0.912 0.500 0.498	
Zn 0.912 0.000 0.498	Str 31 (DFT) <sup>17</sup>
Zn 0.412 0.500 0.498	$\Delta E_{\text{gap}}(\text{PBE}_{\text{GW}}\text{-fit}): 0.35 \text{ eV}$
Zn 0.412 0.000 0.498	E <sub>rel</sub> : 0.14 eV/ZnO
Zn 0.585 0.750 0.399	Pore <sub>max</sub> : 0.23 nm
Zn 0.585 0.250 0.399	V <sub>pore</sub> : 10 %
Zn 0.085 0.750 0.399	D <sub>pore</sub> : 1
Zn 0.085 0.250 0.399	cell parameters
Zn 0.835 0.750 0.248	8.631 8.631 8.907 57.08 122.92 96.99
Zn 0.835 0.250 0.248	fractional coordinates
Zn 0.335 0.750 0.248	Zn 0.710 0.449 0.862
Zn 0.335 0.250 0.248	Zn 0.210 0.949 0.862
Zn 0.662 0.500 0.149	Zn 0.818 0.840 0.862
Zn 0.662 0.000 0.149	Zn 0.318 0.340 0.862
Zn 0.162 0.500 0.149	Zn 0.715 0.795 0.521
Zn 0.162 0.000 0.149	Zn 0.323 0.686 0.521
O 0.585 0.500 0.997	Zn 0.823 0.186 0.521
O 0.585 0.000 0.997	Zn 0.215 0.295 0.521
O 0.085 0.500 0.997	Zn 0.494 0.516 0.362
O 0.085 0.000 0.997	Zn 0.994 0.016 0.362
O 0.912 0.750 0.900	Zn 0.885 0.624 0.362
O 0.912 0.250 0.900	Zn 0.385 0.124 0.362
O 0.412 0.750 0.900	Zn 0.539 0.619 0.021
O 0.412 0.250 0.900	Zn 0.039 0.119 0.021
O 0.662 0.750 0.747	Zn 0.648 0.011 0.021
O 0.662 0.250 0.747	Zn 0.148 0.511 0.021
O 0.162 0.750 0.747	O 0.883 0.624 0.865

O 0.383 0.124 0.865  
O 0.997 0.011 0.865  
O 0.496 0.511 0.865  
O 0.536 0.624 0.519  
O 0.036 0.124 0.519  
O 0.649 0.011 0.519  
O 0.149 0.511 0.519  
O 0.823 0.837 0.365  
O 0.323 0.337 0.365  
O 0.709 0.450 0.365  
O 0.209 0.951 0.365  
O 0.824 0.184 0.019  
O 0.324 0.684 0.019  
O 0.710 0.797 0.019  
O 0.210 0.297 0.019

Str 32 (SSSCSC)<sup>16</sup>

$\Delta E_{\text{gap}}(\text{PBE}_{\text{GW}}\text{-fit}): 0.36 \text{ eV}$

$E_{\text{rel}}: 0.14 \text{ eV/ZnO}$

Pore<sub>max</sub>: 0.23 nm

V<sub>pore</sub>: 10 %

D<sub>pore</sub>: 1

cell parameters

5.714 6.466 6.134 90.02 90.02 89.96

fractional coordinates

Zn 0.037 0.071 0.727

Zn 0.537 0.787 0.727

Zn 0.537 0.287 0.568

Zn 0.037 0.571 0.568

Zn 0.887 0.287 0.227

Zn 0.387 0.570 0.227

Zn 0.387 0.070 0.068

Zn 0.887 0.787 0.068

O 0.386 0.066 0.725

O 0.886 0.792 0.725

O 0.886 0.292 0.570

O 0.386 0.566 0.570

O 0.538 0.292 0.225

O 0.037 0.565 0.224

O 0.037 0.065 0.070

O 0.537 0.792 0.070

Str 33 (135\_1\_4)<sup>18</sup>

$\Delta E_{\text{gap}}(\text{PBE}_{\text{GW}}\text{-fit}): 0.32 \text{ eV}$

$E_{\text{rel}}: 0.15 \text{ eV/ZnO}$

Pore<sub>max</sub>: 0.28 nm

V<sub>pore</sub>: 10 %

D<sub>pore</sub>: 1

cell parameters

6.471 6.471 5.285 90.00 90.00 90.00

fractional coordinates

Zn 0.832 0.148 0.700

Zn 0.633 0.648 0.700

Zn 0.332 0.347 0.700

Zn 0.133 0.847 0.700

Zn 0.832 0.847 0.200

Zn 0.633 0.347 0.200

Zn 0.332 0.648 0.200

Zn 0.133 0.148 0.200

O 0.633 0.347 0.821

O 0.833 0.847 0.821

O 0.333 0.648 0.821

O 0.133 0.148 0.821

O 0.133 0.848 0.321

O 0.332 0.348 0.321

O 0.832 0.148 0.321

O 0.633 0.648 0.321

Str 34 (AEL)<sup>17</sup>

$\Delta E_{\text{gap}}(\text{PBE}_{\text{GW}}\text{-fit}): 0.28 \text{ eV}$

$E_{\text{rel}}: 0.16 \text{ eV/ZnO}$

Pore<sub>max</sub>: 0.32 nm

V<sub>pore</sub>: 11 %

D<sub>pore</sub>: 1

cell parameters

8.832 11.915 5.285 90.01 90.02 89.99

fractional coordinates

Zn 0.526 0.115 0.810

Zn 0.438 0.615 0.810

Zn 0.526 0.393 0.810

Zn 0.438 0.893 0.810

Zn 0.119 0.754 0.810

Zn 0.844 0.254 0.810

Zn 0.835 0.966 0.808

Zn 0.835 0.542 0.808

Zn 0.128 0.466 0.808

Zn 0.128 0.042 0.808

Zn 0.938 0.115 0.310

Zn 0.026 0.615 0.310

Zn 0.026 0.893 0.310

Zn 0.938 0.393 0.310

Zn 0.619 0.254 0.310

Zn 0.344 0.754 0.310

Zn 0.335 0.466 0.308

Zn 0.335 0.042 0.308

Zn 0.628 0.966 0.308

Zn 0.628 0.542 0.308  
 O 0.341 0.754 0.691  
 O 0.622 0.254 0.691  
 O 0.939 0.116 0.687  
 O 0.939 0.392 0.687  
 O 0.024 0.892 0.687  
 O 0.024 0.616 0.687  
 O 0.628 0.542 0.686  
 O 0.334 0.466 0.686  
 O 0.334 0.042 0.686  
 O 0.628 0.966 0.686  
 O 0.841 0.254 0.191  
 O 0.122 0.754 0.191  
 O 0.439 0.616 0.187  
 O 0.524 0.392 0.187  
 O 0.439 0.892 0.187  
 O 0.524 0.116 0.187  
 O 0.128 0.042 0.186  
 O 0.834 0.966 0.186  
 O 0.835 0.542 0.186  
 O 0.128 0.466 0.186

Str 35 (APD)<sup>17</sup>

$\Delta E_{\text{gap}}(\text{PBE}_{\text{GW-fit}})$ : 0.56 eV  
 $E_{\text{rel}}$ : 0.22 eV/ZnO  
 Pore<sub>max</sub>: 0.27 nm  
 $V_{\text{pore}}$ : 12 %  
 $D_{\text{pore}}$ : 1  
 cell parameters  
 5.281 13.064 6.545 90.00 90.00 90.00  
 fractional coordinates  
 Zn 0.312 0.202 0.902  
 Zn 0.188 0.702 0.902  
 Zn 0.801 0.052 0.897  
 Zn 0.699 0.552 0.897  
 Zn 0.301 0.052 0.603  
 Zn 0.199 0.552 0.603  
 Zn 0.812 0.202 0.598  
 Zn 0.688 0.702 0.598  
 Zn 0.312 0.298 0.402  
 Zn 0.188 0.798 0.402  
 Zn 0.801 0.448 0.397  
 Zn 0.699 0.948 0.397  
 Zn 0.301 0.448 0.103  
 Zn 0.199 0.948 0.103  
 Zn 0.812 0.298 0.098  
 Zn 0.688 0.798 0.098  
 O 0.809 0.701 0.899

O 0.691 0.201 0.899  
 O 0.301 0.553 0.898  
 O 0.199 0.053 0.898  
 O 0.801 0.553 0.602  
 O 0.699 0.053 0.602  
 O 0.309 0.701 0.601  
 O 0.191 0.201 0.601  
 O 0.809 0.799 0.399  
 O 0.691 0.299 0.399  
 O 0.301 0.947 0.398  
 O 0.199 0.447 0.398  
 O 0.801 0.947 0.102  
 O 0.699 0.447 0.102  
 O 0.309 0.799 0.101  
 O 0.191 0.299 0.101

Str 36 (LTJ)<sup>17</sup>

$\Delta E_{\text{gap}}(\text{PBE}_{\text{GW-fit}})$ : 0.07 eV  
 $E_{\text{rel}}$ : 0.28 eV/ZnO  
 Pore<sub>max</sub>: 0.24 nm  
 $V_{\text{pore}}$ : 12 %  
 $D_{\text{pore}}$ : 3  
 cell parameters  
 5.798 5.817 6.785 90.00 90.00 90.00  
 fractional coordinates  
 Zn 0.580 0.089 0.902  
 Zn 0.080 0.411 0.848  
 Zn 0.597 0.563 0.648  
 Zn 0.903 0.063 0.602  
 Zn 0.420 0.911 0.402  
 Zn 0.920 0.589 0.348  
 Zn 0.403 0.437 0.148  
 Zn 0.097 0.937 0.102  
 O 0.931 0.099 0.903  
 O 0.431 0.401 0.847  
 O 0.589 0.914 0.652  
 O 0.911 0.414 0.598  
 O 0.069 0.901 0.403  
 O 0.569 0.599 0.347  
 O 0.411 0.086 0.152  
 O 0.089 0.586 0.098

Str 37 (hUMQ)<sup>20</sup>

$\Delta E_{\text{gap}}(\text{PBE}_{\text{GW-fit}})$ : 0.54 eV  
 $E_{\text{rel}}$ : 0.16 eV/ZnO  
 Pore<sub>max</sub>: 0.26 nm  
 $V_{\text{pore}}$ : 12 %  
 $D_{\text{pore}}$ : 1

cell parameters  
 9.024 9.021 5.652 90.00 89.97 90.01  
 fractional coordinates  
 Zn 0.246 0.905 0.816  
 Zn 0.100 0.242 0.816  
 Zn 0.763 0.096 0.816  
 Zn 0.909 0.759 0.815  
 Zn 0.600 0.742 0.670  
 Zn 0.409 0.259 0.670  
 Zn 0.263 0.596 0.670  
 Zn 0.746 0.405 0.670  
 Zn 0.246 0.096 0.316  
 Zn 0.100 0.759 0.316  
 Zn 0.763 0.905 0.316  
 Zn 0.909 0.241 0.316  
 Zn 0.409 0.742 0.170  
 Zn 0.600 0.259 0.170  
 Zn 0.263 0.405 0.170  
 Zn 0.746 0.596 0.170  
 O 0.407 0.742 0.814  
 O 0.602 0.258 0.814  
 O 0.262 0.403 0.814  
 O 0.747 0.598 0.814  
 O 0.102 0.758 0.672  
 O 0.907 0.242 0.672  
 O 0.247 0.098 0.672  
 O 0.762 0.903 0.672  
 O 0.407 0.258 0.314  
 O 0.262 0.598 0.314  
 O 0.602 0.742 0.314  
 O 0.747 0.403 0.314  
 O 0.102 0.242 0.172  
 O 0.247 0.903 0.172  
 O 0.907 0.758 0.172  
 O 0.762 0.098 0.172

Str 38 (AFO)<sup>17</sup>  
 $\Delta E_{\text{gap}}(\text{PBE}_{\text{GW-fit}})$ : 0.33 eV  
 $E_{\text{rel}}$ : 0.19 eV/ZnO  
 $\text{Pore}_{\text{max}}$ : 0.35 nm  
 $V_{\text{pore}}$ : 12 %  
 $D_{\text{pore}}$ : 1  
 cell parameters  
 6.268 9.045 5.264 90.00 90.00 110.27  
 fractional coordinates  
 Zn 0.559 0.118 0.599  
 Zn 0.588 0.739 0.598  
 Zn 0.151 0.739 0.598

Zn 0.177 0.355 0.592  
 Zn 0.721 0.442 0.591  
 Zn 0.452 0.905 0.099  
 Zn 0.860 0.284 0.098  
 Zn 0.424 0.284 0.098  
 Zn 0.834 0.668 0.092  
 Zn 0.291 0.582 0.091  
 O 0.560 0.121 0.980  
 O 0.593 0.745 0.976  
 O 0.178 0.356 0.976  
 O 0.152 0.745 0.976  
 O 0.722 0.445 0.970  
 O 0.451 0.902 0.480  
 O 0.418 0.278 0.476  
 O 0.833 0.667 0.476  
 O 0.860 0.278 0.476  
 O 0.289 0.578 0.470

Str 39 (ATO)<sup>17</sup>  
 $\Delta E_{\text{gap}}(\text{PBE}_{\text{GW-fit}})$ : 0.23 eV  
 $E_{\text{rel}}$ : 0.18 eV/ZnO  
 $\text{Pore}_{\text{max}}$ : 0.34 nm  
 $V_{\text{pore}}$ : 12 %  
 $D_{\text{pore}}$ : 1  
 cell parameters  
 13.460 13.460 3.213 90.00 90.00  
 120.00  
 fractional coordinates  
 Zn 0.529 0.619 0.925  
 Zn 0.381 0.910 0.925  
 Zn 0.090 0.471 0.925  
 Zn 0.952 0.757 0.742  
 Zn 0.804 0.048 0.742  
 Zn 0.243 0.196 0.742  
 Zn 0.862 0.286 0.591  
 Zn 0.714 0.577 0.591  
 Zn 0.423 0.138 0.591  
 Zn 0.577 0.862 0.408  
 Zn 0.286 0.423 0.408  
 Zn 0.138 0.714 0.408  
 Zn 0.757 0.804 0.258  
 Zn 0.196 0.952 0.258  
 Zn 0.048 0.243 0.258  
 Zn 0.910 0.529 0.075  
 Zn 0.619 0.090 0.075  
 Zn 0.471 0.381 0.075  
 O 0.528 0.911 0.910  
 O 0.383 0.472 0.910

O 0.089 0.617 0.910  
 O 0.950 0.194 0.757  
 O 0.806 0.756 0.757  
 O 0.244 0.050 0.757  
 O 0.861 0.578 0.577  
 O 0.717 0.139 0.577  
 O 0.422 0.283 0.577  
 O 0.578 0.717 0.423  
 O 0.283 0.861 0.423  
 O 0.139 0.422 0.423  
 O 0.756 0.950 0.243  
 O 0.194 0.244 0.243  
 O 0.050 0.806 0.243  
 O 0.911 0.383 0.090  
 O 0.617 0.528 0.090  
 O 0.472 0.089 0.090

Str 40 (JRY)<sup>17</sup>

$\Delta E_{\text{gap}}(\text{PBE}_{\text{GW-fit}})$ : 0.35 eV  
 $E_{\text{rel}}$ : 0.28 eV/ZnO  
 Pore<sub>max</sub>: 0.25 nm  
 $V_{\text{pore}}$ : 12 %  
 $D_{\text{pore}}$ : 1  
 cell parameters  
 5.328 5.868 10.876 90.00 90.00 90.00  
 fractional coordinates  
 Zn 0.583 0.595 0.981  
 Zn 0.133 0.374 0.922  
 Zn 0.581 0.091 0.824  
 Zn 0.419 0.591 0.676  
 Zn 0.867 0.874 0.578  
 Zn 0.417 0.095 0.519  
 Zn 0.917 0.405 0.481  
 Zn 0.367 0.626 0.422  
 Zn 0.919 0.909 0.324  
 Zn 0.081 0.409 0.176  
 Zn 0.633 0.126 0.078  
 Zn 0.083 0.905 0.019  
 O 0.439 0.904 0.975  
 O 0.896 0.127 0.916  
 O 0.441 0.416 0.826  
 O 0.559 0.916 0.674  
 O 0.104 0.627 0.584  
 O 0.561 0.404 0.525  
 O 0.061 0.096 0.475  
 O 0.604 0.873 0.416  
 O 0.059 0.584 0.326  
 O 0.941 0.084 0.174

O 0.396 0.373 0.084  
 O 0.939 0.596 0.025

Str 41 (OSI)<sup>17</sup>

$\Delta E_{\text{gap}}(\text{PBE}_{\text{GW-fit}})$ : -0.04 eV  
 $E_{\text{rel}}$ : 0.16 eV/ZnO  
 Pore<sub>max</sub>: 0.39 nm  
 $V_{\text{pore}}$ : 12 %  
 $D_{\text{pore}}$ : 1  
 cell parameters  
 11.732 11.602 3.376 90.00 90.00 90.00  
 fractional coordinates  
 Zn 0.715 0.848 0.500  
 Zn 0.715 0.157 0.500  
 Zn 0.619 0.502 0.500  
 Zn 0.381 0.502 0.500  
 Zn 0.285 0.848 0.500  
 Zn 0.285 0.157 0.500  
 Zn 0.000 0.786 0.500  
 Zn 0.000 0.219 0.500  
 Zn 0.881 0.002 0.000  
 Zn 0.785 0.657 0.000  
 Zn 0.785 0.348 0.000  
 Zn 0.500 0.719 0.000  
 Zn 0.500 0.286 0.000  
 Zn 0.215 0.657 0.000  
 Zn 0.215 0.348 0.000  
 Zn 0.119 0.002 0.000  
 O 0.847 0.714 0.500  
 O 0.847 0.291 0.500  
 O 0.788 0.002 0.500  
 O 0.500 0.626 0.500  
 O 0.500 0.379 0.500  
 O 0.212 0.002 0.500  
 O 0.153 0.714 0.500  
 O 0.153 0.291 0.500  
 O 0.712 0.502 0.000  
 O 0.653 0.791 0.000  
 O 0.653 0.214 0.000  
 O 0.347 0.791 0.000  
 O 0.347 0.214 0.000  
 O 0.288 0.502 0.000  
 O 0.000 0.879 0.000  
 O 0.000 0.126 0.000

Str 42 (MVY)<sup>17</sup>

$\Delta E_{\text{gap}}(\text{PBE}_{\text{GW-fit}})$ : 0.26 eV  
 $E_{\text{rel}}$ : 0.39 eV/ZnO

Pore<sub>max</sub>: 0.25 nm  
 V<sub>pore</sub>: 13 %  
 D<sub>pore</sub>: 1  
 cell parameters  
 3.190 5.734 9.195 90.00 90.00 90.00  
 fractional coordinates  
 Zn 0.603 0.678 0.796  
 Zn 0.897 0.178 0.704  
 Zn 0.233 0.894 0.500  
 Zn 0.897 0.178 0.296  
 Zn 0.603 0.678 0.204  
 Zn 0.267 0.394 0.000  
 O 0.392 0.317 0.795  
 O 0.108 0.817 0.705  
 O 0.718 0.118 0.500  
 O 0.108 0.817 0.295  
 O 0.392 0.317 0.205  
 O 0.782 0.618 0.000

Str 43 AWO)<sup>17</sup>  
 ΔE<sub>gap</sub>(PBE<sub>GW</sub>-fit): 0.50 eV  
 E<sub>rel</sub>: 0.25 eV/ZnO  
 Pore<sub>max</sub>: 0.27 nm  
 V<sub>pore</sub>: 13 %  
 D<sub>pore</sub>: 3  
 cell parameters  
 5.832 10.117 11.881 90.00 90.00 90.20  
 fractional coordinates  
 Zn 0.690 0.506 0.919  
 Zn 0.190 0.006 0.919  
 Zn 0.674 0.141 0.829  
 Zn 0.174 0.641 0.829  
 Zn 0.835 0.844 0.820  
 Zn 0.335 0.344 0.820  
 Zn 0.835 0.344 0.680  
 Zn 0.335 0.844 0.680  
 Zn 0.674 0.641 0.671  
 Zn 0.174 0.141 0.671  
 Zn 0.690 0.006 0.581  
 Zn 0.190 0.506 0.581  
 Zn 0.810 0.494 0.419  
 Zn 0.310 0.994 0.419  
 Zn 0.826 0.859 0.329  
 Zn 0.326 0.359 0.329  
 Zn 0.665 0.156 0.320  
 Zn 0.165 0.656 0.320  
 Zn 0.665 0.656 0.180  
 Zn 0.165 0.156 0.180

Zn 0.826 0.359 0.171  
 Zn 0.326 0.859 0.171  
 Zn 0.810 0.994 0.081  
 Zn 0.310 0.494 0.081  
 O 0.815 0.002 0.917  
 O 0.315 0.502 0.917  
 O 0.688 0.341 0.829  
 O 0.188 0.841 0.829  
 O 0.827 0.643 0.828  
 O 0.327 0.143 0.828  
 O 0.827 0.143 0.672  
 O 0.327 0.643 0.672  
 O 0.688 0.841 0.671  
 O 0.188 0.341 0.671  
 O 0.815 0.502 0.583  
 O 0.315 0.002 0.583  
 O 0.685 0.998 0.417  
 O 0.185 0.498 0.417  
 O 0.812 0.659 0.329  
 O 0.312 0.159 0.329  
 O 0.673 0.357 0.328  
 O 0.173 0.857 0.328  
 O 0.673 0.857 0.172  
 O 0.173 0.357 0.172  
 O 0.812 0.159 0.171  
 O 0.312 0.659 0.171  
 O 0.685 0.498 0.083  
 O 0.185 0.998 0.083

Str 44 (UEI)<sup>17</sup>  
 ΔE<sub>gap</sub>(PBE<sub>GW</sub>-fit): 0.51 eV  
 E<sub>rel</sub>: 0.25 eV/ZnO  
 Pore<sub>max</sub>: 0.30 nm  
 V<sub>pore</sub>: 13 %  
 D<sub>pore</sub>: 3  
 cell parameters  
 11.887 5.859 10.095 90.00 90.00 90.00  
 fractional coordinates  
 Zn 0.821 0.333 0.840  
 Zn 0.679 0.833 0.840  
 Zn 0.321 0.167 0.840  
 Zn 0.179 0.667 0.840  
 Zn 0.828 0.672 0.636  
 Zn 0.672 0.172 0.636  
 Zn 0.328 0.828 0.636  
 Zn 0.172 0.328 0.636  
 Zn 0.919 0.189 0.501  
 Zn 0.581 0.689 0.501

Zn 0.419 0.311 0.501  
 Zn 0.081 0.811 0.501  
 Zn 0.821 0.833 0.340  
 Zn 0.679 0.333 0.340  
 Zn 0.321 0.667 0.340  
 Zn 0.179 0.167 0.340  
 Zn 0.828 0.172 0.136  
 Zn 0.672 0.672 0.136  
 Zn 0.328 0.328 0.136  
 Zn 0.172 0.828 0.136  
 Zn 0.919 0.689 0.001  
 Zn 0.581 0.189 0.001  
 Zn 0.419 0.811 0.001  
 Zn 0.081 0.311 0.001  
 O 0.917 0.315 0.999  
 O 0.583 0.815 0.999  
 O 0.417 0.185 0.999  
 O 0.083 0.685 0.999  
 O 0.828 0.684 0.837  
 O 0.672 0.184 0.837  
 O 0.328 0.816 0.837  
 O 0.172 0.316 0.837  
 O 0.828 0.327 0.639  
 O 0.672 0.827 0.639  
 O 0.328 0.173 0.639  
 O 0.172 0.673 0.639  
 O 0.917 0.815 0.499  
 O 0.583 0.315 0.499  
 O 0.417 0.685 0.499  
 O 0.083 0.185 0.499  
 O 0.828 0.184 0.337  
 O 0.672 0.684 0.337  
 O 0.328 0.316 0.337  
 O 0.172 0.816 0.337  
 O 0.828 0.827 0.139  
 O 0.672 0.327 0.139  
 O 0.328 0.673 0.139  
 O 0.172 0.173 0.139

Str 45 (ATN)<sup>17</sup>  
 $\Delta E_{\text{gap}}(\text{PBE}_{\text{GW-fit}})$ : 0.61 eV  
 $E_{\text{rel}}$ : 0.18 eV/ZnO  
 $\text{Pore}_{\text{max}}$ : 0.34 nm  
 $V_{\text{pore}}$ : 14 %  
 $D_{\text{pore}}$ : 1  
 cell parameters  
 8.312 8.312 3.392 90.00 90.00 90.00  
 fractional coordinates

Zn 0.902 0.731 0.500  
 Zn 0.727 0.137 0.500  
 Zn 0.309 0.906 0.500  
 Zn 0.133 0.313 0.500  
 Zn 0.809 0.406 0.000  
 Zn 0.633 0.813 0.000  
 Zn 0.402 0.231 0.000  
 Zn 0.227 0.637 0.000  
 O 0.902 0.310 0.500  
 O 0.729 0.905 0.500  
 O 0.306 0.138 0.500  
 O 0.134 0.733 0.500  
 O 0.806 0.638 0.000  
 O 0.634 0.233 0.000  
 O 0.402 0.810 0.000  
 O 0.229 0.405 0.000

Str 46 (SAF)<sup>17</sup>  
 $\Delta E_{\text{gap}}(\text{PBE}_{\text{GW-fit}})$ : 0.38 eV  
 $E_{\text{rel}}$ : 0.20 eV/ZnO  
 $\text{Pore}_{\text{max}}$ : 0.41 nm  
 $V_{\text{pore}}$ : 14 %  
 $D_{\text{pore}}$ : 1  
 cell parameters  
 9.513 18.309 5.260 90.00 90.00 90.00  
 fractional coordinates  
 Zn 0.902 0.777 0.695  
 Zn 0.598 0.277 0.695  
 Zn 0.402 0.723 0.695  
 Zn 0.098 0.223 0.695  
 Zn 0.786 0.136 0.692  
 Zn 0.714 0.636 0.692  
 Zn 0.286 0.364 0.692  
 Zn 0.214 0.864 0.692  
 Zn 0.895 0.948 0.688  
 Zn 0.605 0.448 0.688  
 Zn 0.395 0.552 0.688  
 Zn 0.105 0.052 0.688  
 Zn 0.899 0.330 0.686  
 Zn 0.601 0.830 0.686  
 Zn 0.399 0.170 0.686  
 Zn 0.101 0.670 0.686  
 Zn 0.902 0.223 0.195  
 Zn 0.598 0.723 0.195  
 Zn 0.402 0.277 0.195  
 Zn 0.098 0.777 0.195  
 Zn 0.786 0.864 0.192  
 Zn 0.714 0.364 0.192

Zn 0.286 0.636 0.192  
 Zn 0.214 0.136 0.192  
 Zn 0.895 0.052 0.188  
 Zn 0.605 0.552 0.188  
 Zn 0.395 0.448 0.188  
 Zn 0.105 0.948 0.188  
 Zn 0.899 0.670 0.186  
 Zn 0.601 0.170 0.186  
 Zn 0.399 0.830 0.186  
 Zn 0.101 0.330 0.186  
 O 0.897 0.222 0.815  
 O 0.603 0.722 0.815  
 O 0.397 0.278 0.815  
 O 0.103 0.778 0.815  
 O 0.893 0.051 0.808  
 O 0.606 0.551 0.808  
 O 0.394 0.449 0.808  
 O 0.106 0.949 0.808  
 O 0.787 0.863 0.808  
 O 0.713 0.363 0.808  
 O 0.287 0.637 0.808  
 O 0.213 0.137 0.808  
 O 0.902 0.667 0.808  
 O 0.598 0.167 0.808  
 O 0.402 0.833 0.808  
 O 0.098 0.333 0.808  
 O 0.897 0.778 0.315  
 O 0.603 0.278 0.315  
 O 0.397 0.722 0.315  
 O 0.103 0.222 0.315  
 O 0.893 0.949 0.308  
 O 0.606 0.449 0.308  
 O 0.394 0.551 0.308  
 O 0.106 0.051 0.308  
 O 0.787 0.137 0.308  
 O 0.713 0.637 0.308  
 O 0.287 0.363 0.308  
 O 0.213 0.863 0.308  
 O 0.902 0.333 0.308  
 O 0.598 0.833 0.308  
 O 0.402 0.167 0.308  
 O 0.098 0.667 0.308

Str 47 (APC)<sup>17</sup>

$\Delta E_{\text{gap}}(\text{PBE}_{\text{GW-fit}})$ : 0.44 eV

$E_{\text{rel}}$ : 0.23 eV/ZnO

Pore<sub>max</sub>: 0.26 nm

V<sub>pore</sub>: 14 %

D<sub>pore</sub>: 3

cell parameters

5.788 12.765 6.464 90.00 90.00 90.00

fractional coordinates

Zn 0.328 0.711 0.895

Zn 0.172 0.211 0.895

Zn 0.824 0.048 0.881

Zn 0.676 0.548 0.881

Zn 0.324 0.048 0.619

Zn 0.176 0.548 0.619

Zn 0.828 0.711 0.605

Zn 0.672 0.211 0.605

Zn 0.328 0.789 0.395

Zn 0.172 0.289 0.395

Zn 0.824 0.452 0.381

Zn 0.676 0.952 0.381

Zn 0.324 0.452 0.119

Zn 0.176 0.952 0.119

Zn 0.828 0.789 0.105

Zn 0.672 0.289 0.105

O 0.317 0.549 0.890

O 0.183 0.049 0.890

O 0.822 0.211 0.888

O 0.678 0.711 0.888

O 0.322 0.211 0.612

O 0.178 0.711 0.612

O 0.817 0.549 0.610

O 0.683 0.049 0.610

O 0.317 0.951 0.390

O 0.183 0.451 0.390

O 0.822 0.289 0.388

O 0.678 0.789 0.388

O 0.322 0.289 0.112

O 0.178 0.789 0.112

O 0.817 0.951 0.110

O 0.683 0.451 0.110

Str 48 (CAN)<sup>17</sup>

$\Delta E_{\text{gap}}(\text{PBE}_{\text{GW-fit}})$ : 0.48 eV

$E_{\text{rel}}$ : 0.15 eV/ZnO

Pore<sub>max</sub>: 0.33 nm

V<sub>pore</sub>: 14 %

D<sub>pore</sub>: 1

cell parameters

7.817 7.817 3.368 90.00 90.00 120.00

fractional coordinates

Zn 0.611 0.686 0.750

Zn 0.340 0.933 0.750

Zn 0.094 0.416 0.750  
Zn 0.936 0.607 0.250  
Zn 0.690 0.090 0.250  
Zn 0.419 0.337 0.250  
O 0.610 0.932 0.750  
O 0.341 0.417 0.750  
O 0.094 0.686 0.750  
O 0.936 0.337 0.250  
O 0.689 0.606 0.250  
O 0.420 0.091 0.250

Str 49 (AFG)<sup>17</sup>

$\Delta E_{\text{gap}}(\text{PBE}_{\text{GW-fit}})$ : 0.50 eV

$E_{\text{rel}}$ : 0.14 eV/ZnO

Pore<sub>max</sub>: 0.33 nm

V<sub>pore</sub>: 15 %

D<sub>pore</sub>: 3

cell parameters

7.848 7.849 13.415 90.00 90.00 120.00

fractional coordinates

Zn 0.844 0.426 0.875

Zn 0.573 0.670 0.875

Zn 0.328 0.155 0.875

Zn 0.654 0.076 0.750

Zn 0.168 0.345 0.750

Zn 0.923 0.831 0.750

Zn 0.838 0.417 0.625

Zn 0.582 0.673 0.625

Zn 0.326 0.161 0.625

Zn 0.241 0.489 0.500

Zn 0.995 0.758 0.500

Zn 0.509 0.003 0.500

Zn 0.835 0.408 0.375

Zn 0.590 0.679 0.375

Zn 0.320 0.164 0.375

Zn 0.995 0.758 0.251

Zn 0.509 0.003 0.251

Zn 0.241 0.489 0.250

Zn 0.838 0.417 0.125

Zn 0.582 0.673 0.125

Zn 0.326 0.161 0.125

Zn 0.923 0.831 0.000

Zn 0.654 0.076 0.000

Zn 0.168 0.345 0.000

O 0.842 0.670 0.875

O 0.575 0.157 0.875

O 0.328 0.424 0.875

O 0.923 0.345 0.751

O 0.654 0.831 0.751

O 0.168 0.075 0.751

O 0.836 0.672 0.625

O 0.582 0.162 0.625

O 0.327 0.417 0.625

O 0.510 0.759 0.500

O 0.240 0.003 0.500

O 0.995 0.489 0.500

O 0.835 0.677 0.375

O 0.589 0.164 0.375

O 0.321 0.410 0.375

O 0.995 0.489 0.251

O 0.240 0.003 0.251

O 0.510 0.759 0.251

O 0.836 0.672 0.125

O 0.582 0.162 0.125

O 0.327 0.417 0.125

O 0.168 0.075 0.000

O 0.654 0.831 0.000

O 0.923 0.345 0.000

Str 50 (TOL)<sup>17</sup>

$\Delta E_{\text{gap}}(\text{PBE}_{\text{GW-fit}})$ : 0.49 eV

$E_{\text{rel}}$ : 0.14 eV/ZnO

Pore<sub>max</sub>: 0.33 nm

V<sub>pore</sub>: 15 %

D<sub>pore</sub>: 3

cell parameters

7.863 7.863 20.073 90.00 90.00 120.00

fractional coordinates

Zn 0.748 0.746 1.000

Zn 0.258 0.002 1.000

Zn 0.003 0.257 1.000

Zn 0.588 0.928 0.917

Zn 0.344 0.416 0.917

Zn 0.077 0.661 0.917

Zn 0.748 0.747 0.833

Zn 0.258 0.002 0.833

Zn 0.003 0.257 0.833

Zn 0.930 0.587 0.750

Zn 0.662 0.075 0.750

Zn 0.418 0.343 0.750

Zn 0.748 0.747 0.666

Zn 0.258 0.002 0.666

Zn 0.003 0.257 0.666

Zn 0.344 0.416 0.583

Zn 0.589 0.929 0.583

Zn 0.076 0.661 0.583

Zn 0.750 0.740 0.500	O 0.743 0.995 0.167
Zn 0.995 0.255 0.500	O 0.010 0.749 0.167
Zn 0.265 0.010 0.500	O 0.256 0.262 0.167
Zn 0.589 0.929 0.417	O 0.930 0.343 0.083
Zn 0.344 0.416 0.417	O 0.417 0.074 0.083
Zn 0.076 0.661 0.417	O 0.662 0.587 0.083
Zn 0.748 0.746 0.333	
Zn 0.259 0.002 0.333	Str 51 (LIO) <sup>17</sup>
Zn 0.003 0.257 0.333	$\Delta E_{\text{gap}}(\text{PBE}_{\text{GW-fit}}): 0.50 \text{ eV}$
Zn 0.930 0.588 0.250	$E_{\text{rel}}: 0.14 \text{ eV/ZnO}$
Zn 0.662 0.075 0.250	Pore <sub>max</sub> : 0.33 nm
Zn 0.417 0.343 0.250	V <sub>pore</sub> : 15 %
Zn 0.742 0.749 0.167	D <sub>pore</sub> : 3
Zn 0.256 0.993 0.167	cell parameters
Zn 0.011 0.263 0.167	7.857 7.857 10.050 90.00 90.00 120.01
Zn 0.662 0.074 0.083	fractional coordinates
Zn 0.930 0.588 0.083	Zn 0.080 0.411 0.833
Zn 0.417 0.343 0.083	Zn 0.336 0.921 0.833
O 0.257 0.256 1.000	Zn 0.590 0.666 0.833
O 0.749 0.002 1.000	Zn 0.921 0.593 0.667
O 0.003 0.748 1.000	Zn 0.677 0.080 0.667
O 0.589 0.660 0.917	Zn 0.408 0.324 0.667
O 0.345 0.930 0.917	Zn 0.597 0.674 0.500
O 0.075 0.416 0.917	Zn 0.327 0.919 0.500
O 0.257 0.256 0.833	Zn 0.082 0.404 0.500
O 0.749 0.002 0.833	Zn 0.677 0.080 0.334
O 0.003 0.747 0.833	Zn 0.408 0.324 0.334
O 0.661 0.587 0.750	Zn 0.921 0.593 0.334
O 0.417 0.074 0.750	Zn 0.590 0.666 0.167
O 0.931 0.344 0.750	Zn 0.336 0.921 0.167
O 0.257 0.256 0.666	Zn 0.080 0.411 0.167
O 0.749 0.002 0.666	Zn 0.994 0.740 0.000
O 0.003 0.747 0.666	Zn 0.750 0.007 0.000
O 0.589 0.660 0.583	Zn 0.262 0.251 0.000
O 0.345 0.929 0.583	O 0.081 0.666 0.834
O 0.076 0.416 0.583	O 0.590 0.920 0.833
O 0.750 0.009 0.500	O 0.335 0.411 0.833
O 0.263 0.254 0.500	O 0.922 0.325 0.666
O 0.996 0.742 0.500	O 0.677 0.593 0.666
O 0.589 0.660 0.417	O 0.408 0.080 0.666
O 0.345 0.929 0.417	O 0.596 0.919 0.500
O 0.076 0.416 0.417	O 0.082 0.673 0.500
O 0.257 0.256 0.333	O 0.328 0.405 0.500
O 0.003 0.748 0.333	O 0.677 0.593 0.334
O 0.749 0.002 0.333	O 0.408 0.080 0.334
O 0.662 0.587 0.250	O 0.922 0.325 0.334
O 0.930 0.343 0.250	O 0.335 0.411 0.167
O 0.417 0.074 0.250	O 0.590 0.920 0.167

O 0.081 0.666 0.167  
O 0.994 0.252 0.000  
O 0.264 0.008 0.000  
O 0.749 0.738 0.000

Str 52 (LOS)<sup>17</sup>

$\Delta E_{\text{gap}}(\text{PBE}_{\text{GW-fit}})$ : 0.49 eV

$E_{\text{rel}}$ : 0.14 eV/ZnO

$\text{Pore}_{\text{max}}$ : 0.34 nm

$V_{\text{pore}}$ : 15 %

$D_{\text{pore}}$ : 3

cell parameters

7.887 7.887 6.670 90.00 90.00 120.00

fractional coordinates

Zn 0.587 0.935 0.750

Zn 0.344 0.424 0.750

Zn 0.076 0.667 0.750

Zn 0.748 0.755 0.500

Zn 0.256 0.009 0.500

Zn 0.002 0.263 0.500

Zn 0.928 0.594 0.250

Zn 0.660 0.083 0.250

Zn 0.417 0.350 0.250

Zn 0.748 0.755 0.000

Zn 0.256 0.009 0.000

Zn 0.002 0.263 0.000

O 0.587 0.667 0.750

O 0.344 0.936 0.750

O 0.075 0.424 0.750

O 0.748 0.009 0.500

O 0.256 0.263 0.500

O 0.002 0.755 0.500

O 0.929 0.351 0.250

O 0.660 0.594 0.250

O 0.417 0.082 0.250

O 0.748 0.009 0.000

O 0.256 0.263 0.000

O 0.002 0.755 0.000

Str 53 (SOD)<sup>17</sup>

$\Delta E_{\text{gap}}(\text{PBE}_{\text{GW-fit}})$ : 0.53 eV

$E_{\text{rel}}$ : 0.14 eV/ZnO

$\text{Pore}_{\text{max}}$ : 0.35 nm

$V_{\text{pore}}$ : 15 %

$D_{\text{pore}}$ : 3

cell parameters

5.663 5.663 5.663 90.00 90.00 90.00

fractional coordinates

Zn 0.000 0.500 0.750

Zn 0.750 0.000 0.500

Zn 0.250 0.000 0.500

Zn 0.000 0.500 0.250

Zn 0.500 0.750 0.000

Zn 0.500 0.250 0.000

O 0.500 0.000 0.750

O 0.000 0.750 0.500

O 0.000 0.250 0.500

O 0.500 0.000 0.250

O 0.750 0.500 0.000

O 0.250 0.500 0.000

Str 54 (AET)<sup>17</sup>

$\Delta E_{\text{gap}}(\text{PBE}_{\text{GW-fit}})$ : 0.45 eV

$E_{\text{rel}}$ : 0.23 eV/ZnO

$\text{Pore}_{\text{max}}$ : 0.41 nm

$V_{\text{pore}}$ : 17 %

$D_{\text{pore}}$ : 1

cell parameters

21.516 9.431 5.296 90.00 90.00 90.00

fractional coordinates

Zn 0.500 0.352 0.583

Zn 0.000 0.852 0.583

Zn 0.819 0.399 0.563

Zn 0.681 0.899 0.563

Zn 0.319 0.899 0.563

Zn 0.181 0.399 0.563

Zn 0.921 0.111 0.563

Zn 0.579 0.611 0.563

Zn 0.421 0.611 0.563

Zn 0.079 0.111 0.563

Zn 0.846 0.790 0.560

Zn 0.654 0.290 0.560

Zn 0.346 0.290 0.560

Zn 0.154 0.790 0.560

Zn 0.772 0.099 0.554

Zn 0.728 0.599 0.554

Zn 0.272 0.599 0.554

Zn 0.228 0.099 0.554

Zn 0.500 0.648 0.083

Zn 0.000 0.148 0.083

Zn 0.819 0.601 0.063

Zn 0.681 0.101 0.063

Zn 0.319 0.101 0.063

Zn 0.181 0.601 0.063

Zn 0.921 0.889 0.063

Zn 0.579 0.389 0.063

Zn 0.421 0.389 0.063	$\Delta E_{\text{gap}}(\text{PBE}_{\text{GW-fit}})$ : 0.65 eV
Zn 0.079 0.889 0.063	$E_{\text{rel}}$ : 0.29 eV/ZnO
Zn 0.846 0.210 0.060	Pore <sub>max</sub> : 0.28 nm
Zn 0.654 0.710 0.060	V <sub>pore</sub> : 17 %
Zn 0.346 0.710 0.060	D <sub>pore</sub> : 2
Zn 0.154 0.210 0.060	cell parameters
Zn 0.772 0.901 0.054	6.223 10.376 5.707 90.00 90.00 90.00
Zn 0.728 0.401 0.054	fractional coordinates
Zn 0.272 0.401 0.054	Zn 0.926 0.750 0.858
Zn 0.228 0.901 0.054	Zn 0.574 0.250 0.858
O 0.920 0.102 0.940	Zn 0.910 0.401 0.641
O 0.580 0.602 0.940	Zn 0.910 0.099 0.641
O 0.420 0.602 0.940	Zn 0.590 0.901 0.641
O 0.080 0.102 0.940	Zn 0.590 0.599 0.641
O 0.845 0.790 0.939	Zn 0.410 0.401 0.359
O 0.655 0.290 0.939	Zn 0.410 0.099 0.359
O 0.345 0.290 0.939	Zn 0.090 0.901 0.359
O 0.155 0.790 0.939	Zn 0.090 0.599 0.359
O 0.822 0.401 0.939	Zn 0.426 0.750 0.142
O 0.678 0.901 0.939	Zn 0.074 0.250 0.142
O 0.322 0.901 0.939	O 0.920 0.250 0.851
O 0.178 0.401 0.939	O 0.580 0.750 0.851
O 0.500 0.320 0.937	O 0.923 0.904 0.653
O 0.000 0.820 0.937	O 0.923 0.596 0.653
O 0.772 0.103 0.931	O 0.577 0.404 0.653
O 0.728 0.603 0.931	O 0.577 0.096 0.653
O 0.272 0.603 0.931	O 0.423 0.904 0.347
O 0.228 0.103 0.931	O 0.423 0.596 0.347
O 0.920 0.898 0.440	O 0.077 0.404 0.347
O 0.580 0.398 0.440	O 0.077 0.096 0.347
O 0.420 0.398 0.440	O 0.420 0.250 0.149
O 0.080 0.898 0.440	O 0.080 0.750 0.149
O 0.845 0.210 0.439	
O 0.655 0.710 0.439	Str 56 (ACO) <sup>17</sup>
O 0.345 0.710 0.439	$\Delta E_{\text{gap}}(\text{PBE}_{\text{GW-fit}})$ : 0.99 eV
O 0.155 0.210 0.439	$E_{\text{rel}}$ : 0.23 eV/ZnO
O 0.822 0.599 0.439	Pore <sub>max</sub> : 0.23 nm
O 0.678 0.099 0.439	V <sub>pore</sub> : 17 %
O 0.322 0.099 0.439	D <sub>pore</sub> : 3
O 0.178 0.599 0.439	cell parameters
O 0.500 0.680 0.437	6.278 6.278 6.278 90.00 90.00 90.00
O 0.000 0.180 0.437	fractional coordinates
O 0.772 0.897 0.431	Zn 0.835 0.165 0.835
O 0.728 0.397 0.431	Zn 0.165 0.835 0.835
O 0.272 0.397 0.431	Zn 0.665 0.665 0.665
O 0.228 0.897 0.431	Zn 0.335 0.335 0.665
	Zn 0.665 0.335 0.335
	Zn 0.335 0.665 0.335
Str 55 (ATT) <sup>17</sup>	

Zn 0.835 0.835 0.165  
Zn 0.165 0.165 0.165  
O 0.838 0.838 0.838  
O 0.162 0.162 0.838  
O 0.662 0.338 0.662  
O 0.338 0.662 0.662  
O 0.662 0.662 0.338  
O 0.338 0.338 0.338  
O 0.838 0.162 0.162  
O 0.162 0.838 0.162

Str 57 (PON)<sup>17</sup>

$\Delta E_{\text{gap}}(\text{PBE}_{\text{GW-fit}})$ : 0.33 eV

$E_{\text{rel}}$ : 0.31 eV/ZnO

Pore<sub>max</sub>: 0.30 nm

V<sub>pore</sub>: 17 %

D<sub>pore</sub>: 2

cell parameters

5.881 5.945 10.455 90.00 90.00 90.00

fractional coordinates

Zn 0.838 0.142 0.894  
Zn 0.338 0.858 0.894  
Zn 0.812 0.605 0.836  
Zn 0.312 0.395 0.836  
Zn 0.971 0.358 0.578  
Zn 0.471 0.642 0.578  
Zn 0.662 0.142 0.394  
Zn 0.162 0.858 0.394  
Zn 0.688 0.605 0.336  
Zn 0.188 0.395 0.336  
Zn 0.529 0.358 0.078  
Zn 0.029 0.642 0.078  
O 0.990 0.858 0.910  
O 0.490 0.142 0.910  
O 0.507 0.654 0.761  
O 0.007 0.346 0.761  
O 0.675 0.417 0.503  
O 0.175 0.583 0.503  
O 0.510 0.858 0.410  
O 0.010 0.142 0.410  
O 0.993 0.654 0.261  
O 0.493 0.346 0.261  
O 0.825 0.417 0.003  
O 0.325 0.583 0.003

Str 58 (ZON)<sup>17</sup>

$\Delta E_{\text{gap}}(\text{PBE}_{\text{GW-fit}})$ : 0.59 eV

$E_{\text{rel}}$ : 0.31 eV/ZnO

Pore<sub>max</sub>: 0.32 nm

V<sub>pore</sub>: 18 %

D<sub>pore</sub>: 2

cell parameters

9.108 9.988 10.863 90.00 90.00 90.00

fractional coordinates

Zn 0.769 0.341 0.965  
Zn 0.731 0.841 0.965  
Zn 0.927 0.098 0.929  
Zn 0.573 0.598 0.929  
Zn 0.425 0.901 0.924  
Zn 0.075 0.401 0.924  
Zn 0.433 0.273 0.834  
Zn 0.067 0.773 0.834  
Zn 0.933 0.273 0.666  
Zn 0.567 0.773 0.666  
Zn 0.925 0.901 0.576  
Zn 0.575 0.401 0.576  
Zn 0.427 0.098 0.571  
Zn 0.073 0.598 0.571  
Zn 0.270 0.341 0.535  
Zn 0.231 0.841 0.535  
Zn 0.769 0.159 0.465  
Zn 0.731 0.659 0.465  
Zn 0.927 0.402 0.429  
Zn 0.573 0.902 0.429  
Zn 0.425 0.599 0.424  
Zn 0.075 0.099 0.424  
Zn 0.433 0.227 0.334  
Zn 0.067 0.727 0.334  
Zn 0.933 0.227 0.166  
Zn 0.567 0.727 0.166  
Zn 0.925 0.599 0.076  
Zn 0.575 0.099 0.076  
Zn 0.427 0.402 0.071  
Zn 0.073 0.902 0.071  
Zn 0.270 0.159 0.035  
Zn 0.231 0.659 0.035  
O 0.272 0.339 0.949  
O 0.228 0.839 0.949  
O 0.434 0.098 0.924  
O 0.066 0.598 0.924  
O 0.921 0.904 0.918  
O 0.579 0.404 0.918  
O 0.935 0.271 0.842  
O 0.565 0.771 0.842  
O 0.435 0.271 0.658  
O 0.065 0.771 0.658

O 0.421 0.904 0.582  
 O 0.079 0.404 0.582  
 O 0.934 0.098 0.576  
 O 0.566 0.598 0.576  
 O 0.772 0.339 0.551  
 O 0.728 0.839 0.551  
 O 0.272 0.161 0.449  
 O 0.228 0.661 0.449  
 O 0.434 0.402 0.424  
 O 0.066 0.902 0.424  
 O 0.921 0.596 0.418  
 O 0.579 0.096 0.418  
 O 0.935 0.229 0.342  
 O 0.565 0.729 0.342  
 O 0.435 0.229 0.158  
 O 0.065 0.729 0.158  
 O 0.421 0.596 0.082  
 O 0.079 0.096 0.082  
 O 0.934 0.402 0.076  
 O 0.566 0.902 0.076  
 O 0.772 0.161 0.051  
 O 0.728 0.661 0.051

Str 59 (OWE)<sup>17</sup>

$\Delta E_{\text{gap}}(\text{PBE}_{\text{GW-fit}})$ : 0.68 eV  
 $E_{\text{rel}}$ : 0.36 eV/ZnO  
 $\text{Pore}_{\text{max}}$ : 0.30 nm  
 $V_{\text{pore}}$ : 18 %  
 $D_{\text{pore}}$ : 2  
 cell parameters  
 9.477 9.404 5.534 90.00 90.00 90.00  
 fractional coordinates  
 Zn 0.981 0.250 0.833  
 Zn 0.519 0.750 0.833  
 Zn 0.861 0.899 0.645  
 Zn 0.861 0.601 0.645  
 Zn 0.639 0.399 0.645  
 Zn 0.639 0.101 0.645  
 Zn 0.355 0.250 0.620  
 Zn 0.145 0.750 0.620  
 Zn 0.855 0.250 0.380  
 Zn 0.645 0.750 0.380  
 Zn 0.361 0.899 0.355  
 Zn 0.361 0.601 0.355  
 Zn 0.139 0.399 0.355  
 Zn 0.139 0.101 0.355  
 Zn 0.481 0.250 0.167  
 Zn 0.019 0.750 0.167

O 0.979 0.750 0.824  
 O 0.521 0.250 0.824  
 O 0.863 0.398 0.661  
 O 0.863 0.102 0.661  
 O 0.637 0.898 0.661  
 O 0.637 0.602 0.661  
 O 0.349 0.750 0.625  
 O 0.151 0.250 0.625  
 O 0.849 0.750 0.375  
 O 0.651 0.250 0.375  
 O 0.363 0.398 0.339  
 O 0.363 0.102 0.339  
 O 0.137 0.898 0.339  
 O 0.137 0.602 0.339  
 O 0.479 0.750 0.176  
 O 0.021 0.250 0.176

Str 60 (AFI)<sup>17</sup>

$\Delta E_{\text{gap}}(\text{PBE}_{\text{GW-fit}})$ : 0.48 eV  
 $E_{\text{rel}}$ : 0.19 eV/ZnO  
 $\text{Pore}_{\text{max}}$ : 0.48 nm  
 $V_{\text{pore}}$ : 18 %  
 $D_{\text{pore}}$ : 1  
 cell parameters  
 8.925 8.925 5.298 90.00 90.00 120.00  
 fractional coordinates  
 Zn 0.877 0.326 0.688  
 Zn 0.674 0.551 0.688  
 Zn 0.551 0.877 0.688  
 Zn 0.449 0.123 0.688  
 Zn 0.326 0.449 0.688  
 Zn 0.123 0.674 0.688  
 Zn 0.877 0.551 0.188  
 Zn 0.674 0.123 0.188  
 Zn 0.551 0.674 0.188  
 Zn 0.449 0.326 0.188  
 Zn 0.326 0.877 0.188  
 Zn 0.123 0.449 0.188  
 O 0.878 0.552 0.812  
 O 0.674 0.122 0.812  
 O 0.552 0.674 0.812  
 O 0.448 0.326 0.812  
 O 0.326 0.878 0.812  
 O 0.122 0.448 0.812  
 O 0.878 0.326 0.312  
 O 0.674 0.552 0.312  
 O 0.552 0.878 0.312  
 O 0.448 0.122 0.312

O 0.326 0.448 0.312  
 O 0.122 0.674 0.312  
  
 Str 61 (LAU)<sup>17</sup>  
 $\Delta E_{\text{gap}}(\text{PBE}_{\text{GW-fit}})$ : 0.29 eV  
 $E_{\text{rel}}$ : 0.32 eV/ZnO  
 Pore<sub>max</sub>: 0.33 nm  
 $V_{\text{pore}}$ : 19 %  
 $D_{\text{pore}}$ : 2  
 cell parameters  
 9.018 8.426 10.503 90.00 112.56 90.00  
 fractional coordinates  
 Zn 0.614 0.377 0.944  
 Zn 0.114 0.877 0.944  
 Zn 0.881 0.185 0.869  
 Zn 0.381 0.685 0.869  
 Zn 0.742 0.618 0.826  
 Zn 0.242 0.118 0.826  
 Zn 0.758 0.882 0.674  
 Zn 0.258 0.382 0.674  
 Zn 0.619 0.315 0.631  
 Zn 0.119 0.815 0.631  
 Zn 0.886 0.123 0.556  
 Zn 0.386 0.623 0.556  
 Zn 0.614 0.623 0.444  
 Zn 0.114 0.123 0.444  
 Zn 0.881 0.815 0.369  
 Zn 0.381 0.315 0.369  
 Zn 0.742 0.382 0.326  
 Zn 0.242 0.882 0.326  
 Zn 0.758 0.118 0.174  
 Zn 0.258 0.618 0.174  
 Zn 0.619 0.685 0.131  
 Zn 0.119 0.185 0.131  
 Zn 0.886 0.877 0.056  
 Zn 0.386 0.377 0.056  
 O 0.612 0.622 0.943  
 O 0.112 0.122 0.943  
 O 0.879 0.809 0.870  
 O 0.379 0.309 0.870  
 O 0.742 0.381 0.828  
 O 0.242 0.881 0.828  
 O 0.758 0.119 0.672  
 O 0.258 0.619 0.672  
 O 0.621 0.691 0.630  
 O 0.121 0.191 0.630  
 O 0.888 0.878 0.557  
 O 0.388 0.378 0.557

O 0.612 0.378 0.443  
 O 0.112 0.878 0.443  
 O 0.879 0.191 0.370  
 O 0.379 0.691 0.370  
 O 0.742 0.619 0.328  
 O 0.242 0.119 0.328  
 O 0.758 0.881 0.172  
 O 0.258 0.381 0.172  
 O 0.621 0.309 0.130  
 O 0.121 0.809 0.130  
 O 0.888 0.122 0.057  
 O 0.388 0.622 0.057  
  
 Str 62 (GIS)<sup>17</sup>  
 $\Delta E_{\text{gap}}(\text{PBE}_{\text{GW-fit}})$ : 0.52 eV  
 $E_{\text{rel}}$ : 0.29 eV/ZnO  
 Pore<sub>max</sub>: 0.29 nm  
 $V_{\text{pore}}$ : 21 %  
 $D_{\text{pore}}$ : 3  
 cell parameters  
 6.409 6.409 6.327 90.00 90.00 88.87  
 fractional coordinates  
 Zn 0.837 0.413 0.875  
 Zn 0.163 0.087 0.875  
 Zn 0.663 0.087 0.625  
 Zn 0.337 0.413 0.625  
 Zn 0.663 0.587 0.375  
 Zn 0.337 0.913 0.375  
 Zn 0.837 0.913 0.125  
 Zn 0.163 0.587 0.125  
 O 0.838 0.088 0.875  
 O 0.162 0.412 0.875  
 O 0.662 0.412 0.625  
 O 0.338 0.088 0.625  
 O 0.662 0.912 0.375  
 O 0.338 0.588 0.375  
 O 0.838 0.588 0.125  
 O 0.162 0.912 0.125  
  
 Str 63 (SIV)<sup>17</sup>  
 $\Delta E_{\text{gap}}(\text{PBE}_{\text{GW-fit}})$ : 0.65 eV  
 $E_{\text{rel}}$ : 0.29 eV/ZnO  
 Pore<sub>max</sub>: 0.32 nm  
 $V_{\text{pore}}$ : 21 %  
 $D_{\text{pore}}$ : 3  
 cell parameters  
 6.403 9.010 18.048 90.00 90.65 90.00  
 fractional coordinates

Zn 0.663 0.520 0.947	O 0.837 0.981 0.447
Zn 0.163 0.020 0.947	O 0.337 0.481 0.447
Zn 0.664 0.144 0.884	O 0.837 0.357 0.384
Zn 0.164 0.644 0.884	O 0.337 0.857 0.384
Zn 0.838 0.856 0.866	O 0.662 0.644 0.367
Zn 0.338 0.356 0.866	O 0.162 0.144 0.367
Zn 0.840 0.478 0.804	O 0.664 0.019 0.303
Zn 0.340 0.978 0.804	O 0.164 0.519 0.303
Zn 0.660 0.978 0.696	O 0.836 0.519 0.197
Zn 0.160 0.478 0.696	O 0.336 0.019 0.197
Zn 0.662 0.356 0.634	O 0.838 0.144 0.133
Zn 0.162 0.856 0.634	O 0.338 0.644 0.133
Zn 0.836 0.644 0.616	O 0.663 0.857 0.116
Zn 0.336 0.144 0.616	O 0.163 0.357 0.116
Zn 0.837 0.020 0.553	O 0.663 0.481 0.053
Zn 0.337 0.520 0.553	O 0.163 0.981 0.053
Zn 0.663 0.480 0.447	
Zn 0.163 0.980 0.447	Str 64 (OFF) <sup>17</sup>
Zn 0.664 0.856 0.384	$\Delta E_{\text{gap}}(\text{PBE}_{\text{GW-fit}}): 0.88 \text{ eV}$
Zn 0.164 0.356 0.384	$E_{\text{rel}}: 0.29 \text{ eV/ZnO}$
Zn 0.838 0.144 0.366	Pore <sub>max</sub> : 0.37 nm
Zn 0.338 0.644 0.366	V <sub>pore</sub> : 21 %
Zn 0.840 0.522 0.304	D <sub>pore</sub> : 3
Zn 0.340 0.022 0.304	cell parameters
Zn 0.660 0.022 0.196	8.036 8.036 10.395 90.00 90.00 120.00
Zn 0.160 0.522 0.196	fractional coordinates
Zn 0.662 0.644 0.134	Zn 0.998 0.249 0.902
Zn 0.162 0.144 0.134	Zn 0.751 0.749 0.902
Zn 0.836 0.356 0.116	Zn 0.251 0.002 0.902
Zn 0.336 0.856 0.116	Zn 0.582 0.931 0.750
Zn 0.837 0.980 0.053	Zn 0.348 0.418 0.750
Zn 0.337 0.480 0.053	Zn 0.069 0.652 0.750
O 0.837 0.019 0.947	Zn 0.998 0.249 0.598
O 0.337 0.519 0.947	Zn 0.751 0.749 0.598
O 0.837 0.643 0.884	Zn 0.251 0.002 0.598
O 0.337 0.143 0.884	Zn 0.998 0.749 0.402
O 0.662 0.356 0.867	Zn 0.751 0.002 0.402
O 0.162 0.856 0.867	Zn 0.251 0.249 0.402
O 0.664 0.981 0.803	Zn 0.582 0.652 0.250
O 0.164 0.481 0.803	Zn 0.348 0.931 0.250
O 0.836 0.481 0.697	Zn 0.069 0.418 0.250
O 0.336 0.981 0.697	Zn 0.998 0.749 0.098
O 0.838 0.856 0.633	Zn 0.751 0.002 0.098
O 0.338 0.356 0.633	Zn 0.251 0.249 0.098
O 0.663 0.143 0.616	O 0.993 0.741 0.904
O 0.163 0.643 0.616	O 0.748 0.007 0.904
O 0.663 0.519 0.553	O 0.259 0.252 0.904
O 0.163 0.019 0.553	O 0.582 0.660 0.750

O 0.340 0.922 0.750  
O 0.078 0.418 0.750  
O 0.993 0.741 0.596  
O 0.748 0.007 0.596  
O 0.259 0.252 0.596  
O 0.993 0.252 0.404  
O 0.748 0.741 0.404  
O 0.259 0.007 0.404  
O 0.582 0.922 0.250  
O 0.340 0.418 0.250  
O 0.078 0.660 0.250  
O 0.993 0.252 0.096  
O 0.748 0.741 0.096  
O 0.259 0.007 0.096

Str 65 (MOZ)<sup>17</sup>

$\Delta E_{\text{gap}}(\text{PBE}_{\text{GW-fit}})$ : 0.72 eV

$E_{\text{rel}}$ : 0.32 eV/ZnO

Pore<sub>max</sub>: 0.65 nm

V<sub>pore</sub>: 21 %

D<sub>pore</sub>: 3

cell parameters

19.478 19.478 10.531 90.00 90.00

120.00

fractional coordinates

Zn 0.908 0.711 0.903

Zn 0.803 0.092 0.903

Zn 0.711 0.803 0.903

Zn 0.289 0.197 0.903

Zn 0.197 0.908 0.903

Zn 0.092 0.289 0.903

Zn 0.802 0.503 0.903

Zn 0.701 0.198 0.903

Zn 0.503 0.701 0.903

Zn 0.497 0.299 0.903

Zn 0.299 0.802 0.903

Zn 0.198 0.497 0.903

Zn 0.906 0.298 0.902

Zn 0.702 0.608 0.902

Zn 0.608 0.906 0.902

Zn 0.392 0.094 0.902

Zn 0.298 0.392 0.902

Zn 0.094 0.702 0.902

Zn 0.945 0.165 0.750

Zn 0.944 0.579 0.750

Zn 0.835 0.779 0.750

Zn 0.834 0.369 0.750

Zn 0.779 0.945 0.750

Zn 0.635 0.056 0.750

Zn 0.631 0.465 0.750

Zn 0.579 0.635 0.750

Zn 0.535 0.166 0.750

Zn 0.465 0.834 0.750

Zn 0.421 0.365 0.750

Zn 0.369 0.535 0.750

Zn 0.365 0.944 0.750

Zn 0.221 0.055 0.750

Zn 0.166 0.631 0.750

Zn 0.165 0.221 0.750

Zn 0.056 0.421 0.750

Zn 0.055 0.835 0.750

Zn 0.906 0.298 0.598

Zn 0.702 0.608 0.598

Zn 0.608 0.906 0.598

Zn 0.392 0.094 0.598

Zn 0.298 0.392 0.598

Zn 0.094 0.702 0.598

Zn 0.802 0.503 0.597

Zn 0.701 0.198 0.597

Zn 0.503 0.701 0.597

Zn 0.497 0.299 0.597

Zn 0.299 0.802 0.597

Zn 0.198 0.497 0.597

Zn 0.908 0.711 0.597

Zn 0.803 0.092 0.597

Zn 0.711 0.803 0.597

Zn 0.289 0.197 0.597

Zn 0.197 0.908 0.597

Zn 0.092 0.289 0.597

Zn 0.908 0.197 0.403

Zn 0.803 0.711 0.403

Zn 0.711 0.908 0.403

Zn 0.289 0.092 0.403

Zn 0.197 0.289 0.403

Zn 0.092 0.803 0.403

Zn 0.802 0.299 0.403

Zn 0.701 0.503 0.403

Zn 0.503 0.802 0.403

Zn 0.497 0.198 0.403

Zn 0.299 0.497 0.403

Zn 0.198 0.701 0.403

Zn 0.906 0.608 0.402

Zn 0.702 0.094 0.402

Zn 0.608 0.702 0.402

Zn 0.392 0.298 0.402

Zn 0.298 0.906 0.402

Zn 0.094 0.392 0.402	O 0.089 0.801 0.905
Zn 0.945 0.779 0.250	O 0.800 0.302 0.904
Zn 0.944 0.365 0.250	O 0.698 0.499 0.904
Zn 0.835 0.055 0.250	O 0.501 0.200 0.904
Zn 0.834 0.465 0.250	O 0.499 0.800 0.904
Zn 0.779 0.835 0.250	O 0.302 0.501 0.904
Zn 0.635 0.579 0.250	O 0.200 0.698 0.904
Zn 0.631 0.166 0.250	O 0.942 0.367 0.750
Zn 0.579 0.944 0.250	O 0.941 0.781 0.750
Zn 0.535 0.369 0.250	O 0.841 0.059 0.750
Zn 0.465 0.631 0.250	O 0.838 0.470 0.750
Zn 0.421 0.056 0.250	O 0.781 0.841 0.750
Zn 0.369 0.834 0.250	O 0.633 0.574 0.750
Zn 0.365 0.421 0.250	O 0.632 0.162 0.750
Zn 0.221 0.165 0.250	O 0.574 0.942 0.750
Zn 0.166 0.535 0.250	O 0.530 0.368 0.750
Zn 0.165 0.945 0.250	O 0.470 0.632 0.750
Zn 0.056 0.635 0.250	O 0.426 0.058 0.750
Zn 0.055 0.221 0.250	O 0.368 0.838 0.750
Zn 0.906 0.608 0.098	O 0.367 0.426 0.750
Zn 0.702 0.094 0.098	O 0.219 0.159 0.750
Zn 0.608 0.702 0.098	O 0.162 0.530 0.750
Zn 0.392 0.298 0.098	O 0.159 0.941 0.750
Zn 0.298 0.906 0.098	O 0.059 0.219 0.750
Zn 0.094 0.392 0.098	O 0.058 0.633 0.750
Zn 0.802 0.299 0.097	O 0.800 0.302 0.596
Zn 0.701 0.503 0.097	O 0.698 0.499 0.596
Zn 0.503 0.802 0.097	O 0.501 0.200 0.596
Zn 0.497 0.198 0.097	O 0.499 0.800 0.596
Zn 0.299 0.497 0.097	O 0.302 0.501 0.596
Zn 0.198 0.701 0.097	O 0.200 0.698 0.596
Zn 0.908 0.197 0.097	O 0.911 0.199 0.595
Zn 0.803 0.711 0.097	O 0.801 0.712 0.595
Zn 0.711 0.908 0.097	O 0.712 0.911 0.595
Zn 0.289 0.092 0.097	O 0.288 0.089 0.595
Zn 0.197 0.289 0.097	O 0.199 0.288 0.595
Zn 0.092 0.803 0.097	O 0.089 0.801 0.595
O 0.908 0.610 0.906	O 0.908 0.610 0.594
O 0.702 0.092 0.906	O 0.702 0.092 0.594
O 0.610 0.702 0.906	O 0.610 0.702 0.594
O 0.390 0.298 0.906	O 0.390 0.298 0.594
O 0.298 0.908 0.906	O 0.298 0.908 0.594
O 0.092 0.390 0.906	O 0.092 0.390 0.594
O 0.911 0.199 0.905	O 0.908 0.298 0.406
O 0.801 0.712 0.905	O 0.702 0.610 0.406
O 0.712 0.911 0.905	O 0.610 0.908 0.406
O 0.288 0.089 0.905	O 0.390 0.092 0.406
O 0.199 0.288 0.905	O 0.298 0.390 0.406

O 0.092 0.702 0.406  
 O 0.911 0.712 0.405  
 O 0.801 0.089 0.405  
 O 0.712 0.801 0.405  
 O 0.288 0.199 0.405  
 O 0.199 0.911 0.405  
 O 0.089 0.288 0.405  
 O 0.800 0.499 0.404  
 O 0.698 0.200 0.404  
 O 0.501 0.302 0.404  
 O 0.499 0.698 0.404  
 O 0.302 0.800 0.404  
 O 0.200 0.501 0.404  
 O 0.942 0.574 0.250  
 O 0.941 0.159 0.250  
 O 0.841 0.781 0.250  
 O 0.838 0.368 0.250  
 O 0.781 0.941 0.250  
 O 0.633 0.058 0.250  
 O 0.632 0.470 0.250  
 O 0.574 0.633 0.250  
 O 0.530 0.162 0.250  
 O 0.470 0.838 0.250  
 O 0.426 0.367 0.250  
 O 0.368 0.530 0.250  
 O 0.367 0.942 0.250  
 O 0.219 0.059 0.250  
 O 0.162 0.632 0.250  
 O 0.159 0.219 0.250  
 O 0.059 0.841 0.250  
 O 0.058 0.426 0.250  
 O 0.800 0.499 0.096  
 O 0.698 0.200 0.096  
 O 0.501 0.302 0.096  
 O 0.499 0.698 0.096  
 O 0.302 0.800 0.096  
 O 0.200 0.501 0.096  
 O 0.911 0.712 0.095  
 O 0.801 0.089 0.095  
 O 0.712 0.801 0.095  
 O 0.288 0.199 0.095  
 O 0.199 0.911 0.095  
 O 0.089 0.288 0.095  
 O 0.908 0.298 0.094  
 O 0.702 0.610 0.094  
 O 0.610 0.908 0.094  
 O 0.390 0.092 0.094  
 O 0.298 0.390 0.094

O 0.092 0.702 0.094

Str 66 (PHI)<sup>17</sup>

$\Delta E_{\text{gap}}(\text{PBE}_{\text{GW-fit}})$ : 0.81 eV

$E_{\text{rel}}$ : 0.29 eV/ZnO

Pore<sub>max</sub>: 0.32 nm

V<sub>pore</sub>: 21 %

D<sub>pore</sub>: 3

cell parameters

6.418 9.026 9.030 90.00 90.59 90.00

fractional coordinates

Zn 0.837 0.106 0.983

Zn 0.337 0.606 0.983

Zn 0.340 0.227 0.858

Zn 0.840 0.727 0.858

Zn 0.660 0.227 0.642

Zn 0.160 0.727 0.642

Zn 0.663 0.606 0.517

Zn 0.163 0.106 0.517

Zn 0.837 0.894 0.483

Zn 0.337 0.394 0.483

Zn 0.840 0.273 0.358

Zn 0.340 0.773 0.358

Zn 0.660 0.773 0.142

Zn 0.160 0.273 0.142

Zn 0.663 0.394 0.017

Zn 0.163 0.894 0.017

O 0.663 0.607 0.986

O 0.163 0.107 0.986

O 0.664 0.230 0.857

O 0.165 0.730 0.857

O 0.835 0.730 0.643

O 0.336 0.230 0.643

O 0.837 0.107 0.514

O 0.337 0.607 0.514

O 0.663 0.393 0.486

O 0.163 0.893 0.486

O 0.664 0.770 0.357

O 0.165 0.270 0.357

O 0.835 0.270 0.143

O 0.336 0.770 0.143

O 0.837 0.893 0.014

O 0.337 0.393 0.014

Str 67 (MER)<sup>17</sup>

$\Delta E_{\text{gap}}(\text{PBE}_{\text{GW-fit}})$ : 0.86 eV

$E_{\text{rel}}$ : 0.30 eV/ZnO

Pore<sub>max</sub>: 0.39 nm

$V_{\text{pore}}$ : 21 %  
 $D_{\text{pore}}$ : 3  
 cell parameters  
 9.046 9.046 6.425 90.00 90.00 90.00  
 fractional coordinates  
 Zn 0.893 0.731 0.839  
 Zn 0.731 0.107 0.839  
 Zn 0.269 0.893 0.839  
 Zn 0.107 0.269 0.839  
 Zn 0.769 0.393 0.661  
 Zn 0.607 0.769 0.661  
 Zn 0.393 0.231 0.661  
 Zn 0.231 0.607 0.661  
 Zn 0.769 0.607 0.339  
 Zn 0.607 0.231 0.339  
 Zn 0.393 0.769 0.339  
 Zn 0.231 0.393 0.339  
 Zn 0.893 0.269 0.161  
 Zn 0.731 0.893 0.161  
 Zn 0.269 0.107 0.161  
 Zn 0.107 0.731 0.161  
 O 0.893 0.266 0.836  
 O 0.734 0.893 0.836  
 O 0.266 0.107 0.836  
 O 0.107 0.734 0.836  
 O 0.766 0.607 0.664  
 O 0.607 0.234 0.664  
 O 0.393 0.766 0.664  
 O 0.234 0.393 0.664  
 O 0.766 0.393 0.336  
 O 0.607 0.766 0.336  
 O 0.393 0.234 0.336  
 O 0.234 0.607 0.336  
 O 0.893 0.734 0.164  
 O 0.734 0.107 0.164  
 O 0.266 0.893 0.164  
 O 0.107 0.266 0.164

Str 68 (UMK)<sup>19</sup>  
 $\Delta E_{\text{gap}}(\text{PBE}_{\text{GW-fit}})$ : 0.85 eV  
 $E_{\text{rel}}$ : 0.24 eV/ZnO  
 $\text{Pore}_{\text{max}}$ : 0.48 nm  
 $V_{\text{pore}}$ : 22 %  
 $D_{\text{pore}}$ : 1  
 cell parameters  
 8.947 8.948 5.559 90.00 90.00 120.00  
 fractional coordinates  
 Zn 0.321 0.451 0.934

Zn 0.127 0.668 0.934  
 Zn 0.538 0.862 0.934  
 Zn 0.864 0.536 0.570  
 Zn 0.669 0.125 0.570  
 Zn 0.453 0.320 0.570  
 Zn 0.127 0.451 0.434  
 Zn 0.538 0.668 0.434  
 Zn 0.321 0.862 0.434  
 Zn 0.864 0.320 0.070  
 Zn 0.669 0.536 0.070  
 Zn 0.453 0.125 0.070  
 O 0.867 0.538 0.936  
 O 0.667 0.122 0.935  
 O 0.451 0.322 0.935  
 O 0.323 0.450 0.569  
 O 0.123 0.666 0.569  
 O 0.539 0.866 0.569  
 O 0.867 0.322 0.436  
 O 0.667 0.538 0.436  
 O 0.451 0.122 0.435  
 O 0.123 0.450 0.069  
 O 0.323 0.866 0.069  
 O 0.539 0.666 0.069

Str 69 (LEV)<sup>17</sup>  
 $\Delta E_{\text{gap}}(\text{PBE}_{\text{GW-fit}})$ : 0.84 eV  
 $E_{\text{rel}}$ : 0.28 eV/ZnO  
 $\text{Pore}_{\text{max}}$ : 0.37 nm  
 $V_{\text{pore}}$ : 22 %  
 $D_{\text{pore}}$ : 3  
 cell parameters  
 8.203 8.203 30.509 90.00 90.00 120.00  
 fractional coordinates  
 Zn 0.755 0.758 0.966  
 Zn 0.242 0.997 0.966  
 Zn 0.003 0.245 0.966  
 Zn 0.915 0.582 0.917  
 Zn 0.667 0.085 0.917  
 Zn 0.418 0.333 0.917  
 Zn 0.578 0.669 0.867  
 Zn 0.331 0.909 0.867  
 Zn 0.091 0.422 0.867  
 Zn 0.575 0.912 0.800  
 Zn 0.336 0.425 0.800  
 Zn 0.088 0.664 0.800  
 Zn 0.752 0.752 0.750  
 Zn 0.248 0.000 0.750  
 Zn 0.000 0.248 0.750

Zn	0.912	0.575	0.700	O	0.579	0.659	0.800
Zn	0.664	0.088	0.700	O	0.341	0.920	0.800
Zn	0.425	0.336	0.700	O	0.080	0.421	0.800
Zn	0.909	0.331	0.633	O	0.755	0.000	0.750
Zn	0.669	0.578	0.633	O	0.245	0.245	0.750
Zn	0.422	0.091	0.633	O	0.000	0.755	0.750
Zn	0.582	0.915	0.583	O	0.920	0.341	0.700
Zn	0.333	0.418	0.583	O	0.659	0.579	0.700
Zn	0.085	0.667	0.583	O	0.421	0.080	0.700
Zn	0.997	0.242	0.534	O	0.912	0.587	0.634
Zn	0.758	0.755	0.534	O	0.674	0.088	0.634
Zn	0.245	0.003	0.534	O	0.413	0.326	0.634
Zn	0.755	0.997	0.466	O	0.578	0.667	0.583
Zn	0.242	0.245	0.466	O	0.333	0.912	0.583
Zn	0.003	0.758	0.466	O	0.088	0.422	0.583
Zn	0.915	0.333	0.417	O	0.992	0.747	0.533
Zn	0.667	0.582	0.417	O	0.754	0.008	0.533
Zn	0.418	0.085	0.417	O	0.253	0.246	0.533
Zn	0.578	0.909	0.367	O	0.747	0.754	0.467
Zn	0.331	0.422	0.367	O	0.246	0.992	0.467
Zn	0.091	0.669	0.367	O	0.008	0.253	0.467
Zn	0.575	0.664	0.300	O	0.912	0.578	0.417
Zn	0.336	0.912	0.300	O	0.667	0.088	0.417
Zn	0.088	0.425	0.300	O	0.422	0.333	0.417
Zn	0.752	0.000	0.250	O	0.587	0.674	0.366
Zn	0.248	0.248	0.250	O	0.326	0.912	0.366
Zn	0.000	0.752	0.250	O	0.088	0.413	0.366
Zn	0.912	0.336	0.200	O	0.579	0.920	0.300
Zn	0.664	0.575	0.200	O	0.341	0.421	0.300
Zn	0.425	0.088	0.200	O	0.080	0.659	0.300
Zn	0.909	0.578	0.133	O	0.755	0.755	0.250
Zn	0.669	0.091	0.133	O	0.245	0.000	0.250
Zn	0.422	0.331	0.133	O	0.000	0.245	0.250
Zn	0.582	0.667	0.083	O	0.920	0.579	0.200
Zn	0.333	0.915	0.083	O	0.659	0.080	0.200
Zn	0.085	0.418	0.083	O	0.421	0.341	0.200
Zn	0.997	0.755	0.034	O	0.912	0.326	0.134
Zn	0.758	0.003	0.034	O	0.674	0.587	0.134
Zn	0.245	0.242	0.034	O	0.413	0.088	0.134
O	0.747	0.992	0.967	O	0.578	0.912	0.083
O	0.246	0.253	0.967	O	0.333	0.422	0.083
O	0.008	0.754	0.967	O	0.088	0.667	0.083
O	0.912	0.333	0.917	O	0.992	0.246	0.033
O	0.667	0.578	0.917	O	0.754	0.747	0.033
O	0.422	0.088	0.917	O	0.253	0.008	0.033
O	0.587	0.912	0.866				
O	0.326	0.413	0.866				
O	0.088	0.674	0.866				

Str 70 (EZT)<sup>17</sup>  
 $\Delta E_{\text{gap}}(\text{PBE}_{\text{GW-fit}})$ : 0.73 eV

$E_{\text{rel}}$ : 0.30 eV/ZnO  
 $\text{Pore}_{\text{max}}$ : 0.38 nm  
 $V_{\text{pore}}$ : 22 %  
 $D_{\text{pore}}$ : 3  
 cell parameters  
 6.893 8.088 13.962 89.45 90.00 90.00  
 fractional coordinates  
 Zn 0.500 0.133 0.926  
 Zn 0.759 0.875 0.884  
 Zn 0.241 0.875 0.884  
 Zn 0.500 0.540 0.823  
 Zn 0.000 0.616 0.807  
 Zn 0.500 0.884 0.693  
 Zn 0.000 0.960 0.677  
 Zn 0.741 0.625 0.616  
 Zn 0.259 0.625 0.616  
 Zn 0.000 0.367 0.574  
 Zn 0.793 0.000 0.500  
 Zn 0.207 0.000 0.500  
 Zn 0.000 0.633 0.426  
 Zn 0.741 0.375 0.384  
 Zn 0.259 0.375 0.384  
 Zn 0.000 0.040 0.323  
 Zn 0.500 0.116 0.307  
 Zn 0.000 0.384 0.193  
 Zn 0.500 0.460 0.177  
 Zn 0.759 0.125 0.116  
 Zn 0.241 0.125 0.116  
 Zn 0.500 0.867 0.074  
 Zn 0.707 0.500 0.000  
 Zn 0.293 0.500 0.000  
 O 0.500 0.366 0.923  
 O 0.760 0.625 0.885  
 O 0.240 0.625 0.885  
 O 0.500 0.954 0.824  
 O 0.000 0.888 0.808  
 O 0.500 0.612 0.692  
 O 0.000 0.546 0.676  
 O 0.740 0.875 0.615  
 O 0.260 0.875 0.615  
 O 0.000 0.134 0.577  
 O 0.792 0.500 0.500  
 O 0.208 0.500 0.500  
 O 0.000 0.866 0.423  
 O 0.740 0.125 0.385  
 O 0.260 0.125 0.385  
 O 0.000 0.454 0.324  
 O 0.500 0.388 0.308  
 O 0.000 0.112 0.192  
 O 0.500 0.046 0.176  
 O 0.760 0.375 0.115  
 O 0.240 0.375 0.115  
 O 0.500 0.634 0.077  
 O 0.708 1.000 0.000  
 O 0.292 1.000 0.000  
  
 Str 71 (EAB)<sup>17</sup>  
 $\Delta E_{\text{gap}}(\text{PBE}_{\text{GW-fit}})$ : 0.73 eV  
 $E_{\text{rel}}$ : 0.28 eV/ZnO  
 $\text{Pore}_{\text{max}}$ : 0.37 nm  
 $V_{\text{pore}}$ : 22 %  
 $D_{\text{pore}}$ : 3  
 cell parameters  
 8.196 8.196 10.188 90.00 90.00 120.00  
 fractional coordinates  
 Zn 0.575 0.912 0.851  
 Zn 0.337 0.425 0.851  
 Zn 0.088 0.663 0.851  
 Zn 0.575 0.663 0.649  
 Zn 0.337 0.912 0.649  
 Zn 0.088 0.425 0.649  
 Zn 0.752 0.000 0.500  
 Zn 0.248 0.248 0.500  
 Zn 0.000 0.752 0.500  
 Zn 0.912 0.337 0.351  
 Zn 0.663 0.575 0.351  
 Zn 0.425 0.088 0.351  
 Zn 0.912 0.575 0.149  
 Zn 0.663 0.088 0.149  
 Zn 0.425 0.337 0.149  
 Zn 0.752 0.752 0.000  
 Zn 0.248 0.000 0.000  
 Zn 0.000 0.248 0.000  
 O 0.580 0.661 0.848  
 O 0.339 0.919 0.848  
 O 0.081 0.420 0.848  
 O 0.580 0.919 0.652  
 O 0.339 0.420 0.652  
 O 0.081 0.661 0.652  
 O 0.754 0.754 0.500  
 O 0.246 0.000 0.500  
 O 0.000 0.246 0.500  
 O 0.919 0.580 0.348  
 O 0.661 0.081 0.348  
 O 0.420 0.339 0.348  
 O 0.919 0.339 0.152

O 0.661 0.580 0.152  
O 0.420 0.081 0.152  
O 0.754 0.000 0.000  
O 0.246 0.246 0.000  
O 0.000 0.754 0.000

Str 72 (ATS)<sup>17</sup>

$\Delta E_{\text{gap}}(\text{PBE}_{\text{GW-fit}})$ : 0.78 eV

$E_{\text{rel}}$ : 0.23 eV/ZnO

Pore<sub>max</sub>: 0.40 nm

V<sub>pore</sub>: 22 %

D<sub>pore</sub>: 1

cell parameters

8.430 13.663 3.391 90.00 90.00 89.72

fractional coordinates

Zn 0.872 0.527 0.750

Zn 0.689 0.164 0.750

Zn 0.616 0.750 0.750

Zn 0.372 0.027 0.750

Zn 0.189 0.664 0.750

Zn 0.116 0.250 0.750

Zn 0.889 0.731 0.250

Zn 0.815 0.317 0.250

Zn 0.633 0.954 0.250

Zn 0.389 0.231 0.250

Zn 0.315 0.817 0.250

Zn 0.133 0.454 0.250

O 0.888 0.248 0.750

O 0.810 0.663 0.750

O 0.634 0.028 0.750

O 0.388 0.748 0.750

O 0.310 0.163 0.750

O 0.134 0.528 0.750

O 0.695 0.818 0.250

O 0.616 0.233 0.250

O 0.370 0.954 0.250

O 0.195 0.318 0.250

O 0.116 0.733 0.250

O 0.870 0.454 0.250

Str 73 (BCB)<sup>19</sup>

$\Delta E_{\text{gap}}(\text{PBE}_{\text{GW-fit}})$ : 0.75 eV

$E_{\text{rel}}$ : 0.27 eV/ZnO

Pore<sub>max</sub>: 0.47 nm

V<sub>pore</sub>: 23 %

D<sub>pore</sub>: 3

cell parameters

8.825 8.827 3.400 90.00 90.00 90.03

fractional coordinates

Zn 0.787 0.656 0.574

Zn 0.636 0.245 0.574

Zn 0.376 0.806 0.574

Zn 0.226 0.396 0.574

Zn 0.894 0.410 0.074

Zn 0.622 0.913 0.074

Zn 0.391 0.139 0.074

Zn 0.119 0.641 0.074

O 0.779 0.414 0.574

O 0.619 0.798 0.574

O 0.394 0.253 0.574

O 0.234 0.638 0.574

O 0.900 0.662 0.074

O 0.642 0.132 0.074

O 0.371 0.920 0.074

O 0.113 0.390 0.074

Str 74 (LTL)<sup>17</sup>

$\Delta E_{\text{gap}}(\text{PBE}_{\text{GW-fit}})$ : 0.73 eV

$E_{\text{rel}}$ : 0.33 eV/ZnO

Pore<sub>max</sub>: 0.65 nm

V<sub>pore</sub>: 24 %

D<sub>pore</sub>: 3

cell parameters

11.418 11.418 10.623 90.00 90.00

120.00

fractional coordinates

Zn 0.844 0.335 0.903

Zn 0.665 0.509 0.903

Zn 0.509 0.844 0.903

Zn 0.491 0.156 0.903

Zn 0.335 0.491 0.903

Zn 0.156 0.665 0.903

Zn 0.905 0.624 0.750

Zn 0.718 0.095 0.750

Zn 0.624 0.718 0.750

Zn 0.376 0.282 0.750

Zn 0.282 0.905 0.750

Zn 0.095 0.376 0.750

Zn 0.844 0.335 0.597

Zn 0.665 0.509 0.597

Zn 0.509 0.844 0.597

Zn 0.491 0.156 0.597

Zn 0.335 0.491 0.597

Zn 0.156 0.665 0.597

Zn 0.844 0.509 0.403

Zn 0.665 0.156 0.403

Zn 0.509 0.665 0.403  
 Zn 0.491 0.335 0.403  
 Zn 0.335 0.844 0.403  
 Zn 0.156 0.491 0.403  
 Zn 0.905 0.282 0.250  
 Zn 0.718 0.624 0.250  
 Zn 0.624 0.905 0.250  
 Zn 0.376 0.095 0.250  
 Zn 0.282 0.376 0.250  
 Zn 0.095 0.718 0.250  
 Zn 0.844 0.509 0.097  
 Zn 0.665 0.156 0.097  
 Zn 0.509 0.665 0.097  
 Zn 0.491 0.335 0.097  
 Zn 0.335 0.844 0.097  
 Zn 0.156 0.491 0.097  
 O 0.849 0.511 0.906  
 O 0.662 0.151 0.906  
 O 0.511 0.662 0.906  
 O 0.489 0.338 0.906  
 O 0.338 0.849 0.906  
 O 0.151 0.489 0.906  
 O 0.899 0.272 0.750  
 O 0.728 0.627 0.750  
 O 0.627 0.899 0.750  
 O 0.373 0.101 0.750  
 O 0.272 0.373 0.750  
 O 0.101 0.728 0.750  
 O 0.849 0.511 0.594  
 O 0.662 0.151 0.594  
 O 0.511 0.662 0.594  
 O 0.489 0.338 0.594  
 O 0.338 0.849 0.594  
 O 0.151 0.489 0.594  
 O 0.849 0.338 0.406  
 O 0.662 0.511 0.406  
 O 0.511 0.849 0.406  
 O 0.489 0.151 0.406  
 O 0.338 0.489 0.406  
 O 0.151 0.662 0.406  
 O 0.899 0.627 0.250  
 O 0.728 0.101 0.250  
 O 0.627 0.728 0.250  
 O 0.373 0.272 0.250  
 O 0.272 0.899 0.250  
 O 0.101 0.373 0.250  
 O 0.849 0.338 0.094  
 O 0.662 0.511 0.094

O 0.511 0.849 0.094  
 O 0.489 0.151 0.094  
 O 0.338 0.489 0.094  
 O 0.151 0.662 0.094

Str 75 (VFI)<sup>17</sup>

$\Delta E_{\text{gap}}(\text{PBE}_{\text{GW-fit}})$ : 0.71 eV

$E_{\text{rel}}$ : 0.28 eV/ZnO

Pore<sub>max</sub>: 0.57 nm

V<sub>pore</sub>: 25 %

D<sub>pore</sub>: 1

cell parameters

11.552 11.552 5.372 90.00 90.00  
120.01

fractional coordinates

Zn 1.000 0.377 0.583

Zn 0.377 1.000 0.583

Zn 0.623 0.623 0.583

Zn 0.674 0.168 0.560

Zn 0.168 0.674 0.560

Zn 0.506 0.832 0.560

Zn 0.494 0.326 0.560

Zn 0.326 0.494 0.560

Zn 0.832 0.506 0.560

Zn 0.623 0.000 0.083

Zn 0.000 0.623 0.083

Zn 0.377 0.377 0.083

Zn 0.832 0.326 0.060

Zn 0.494 0.168 0.060

Zn 0.326 0.832 0.060

Zn 0.168 0.494 0.060

Zn 0.674 0.506 0.060

Zn 0.506 0.674 0.060

O 0.666 0.170 0.933

O 0.504 0.334 0.933

O 0.496 0.830 0.933

O 0.334 0.504 0.933

O 0.170 0.666 0.933

O 0.830 0.496 0.933

O 1.000 0.351 0.930

O 0.351 1.000 0.930

O 0.649 0.649 0.930

O 0.830 0.334 0.433

O 0.504 0.170 0.433

O 0.334 0.830 0.433

O 0.170 0.504 0.433

O 0.666 0.496 0.433

O 0.496 0.666 0.433

O 0.649 0.000 0.430  
O 0.000 0.649 0.430  
O 0.351 0.351 0.430

Str 76 (CHA)<sup>17</sup>

$\Delta E_{\text{gap}}(\text{PBE}_{\text{GW-fit}})$ : 1.21 eV

$E_{\text{rel}}$ : 0.30 eV/ZnO

Pore<sub>max</sub>: 0.39 nm

V<sub>pore</sub>: 26 %

D<sub>pore</sub>: 3

cell parameters

8.575 8.577 9.857 90.00 90.00 120.00

fractional coordinates

Zn 0.566 0.919 0.962

Zn 0.092 0.672 0.962

Zn 0.340 0.446 0.962

Zn 0.326 0.912 0.752

Zn 0.573 0.686 0.752

Zn 0.099 0.439 0.752

Zn 0.899 0.586 0.629

Zn 0.673 0.112 0.629

Zn 0.426 0.339 0.629

Zn 0.907 0.353 0.419

Zn 0.659 0.579 0.419

Zn 0.433 0.105 0.419

Zn 0.007 0.779 0.296

Zn 0.759 0.005 0.295

Zn 0.233 0.253 0.295

Zn 0.992 0.246 0.086

Zn 0.240 0.019 0.086

Zn 0.766 0.772 0.086

O 0.093 0.446 0.961

O 0.566 0.673 0.961

O 0.339 0.919 0.961

O 0.100 0.685 0.753

O 0.573 0.912 0.753

O 0.326 0.439 0.753

O 0.899 0.339 0.628

O 0.426 0.112 0.628

O 0.672 0.585 0.627

O 0.906 0.579 0.420

O 0.660 0.106 0.420

O 0.433 0.352 0.420

O 0.233 0.006 0.294

O 0.006 0.252 0.294

O 0.760 0.779 0.294

O 0.993 0.773 0.087

O 0.766 0.019 0.087

O 0.239 0.246 0.087

Str 77 (GME)<sup>17</sup>

$\Delta E_{\text{gap}}(\text{PBE}_{\text{GW-fit}})$ : 1.07 eV

$E_{\text{rel}}$ : 0.29 eV/ZnO

Pore<sub>max</sub>: 0.43 nm

V<sub>pore</sub>: 26 %

D<sub>pore</sub>: 3

cell parameters

8.670 8.670 6.440 90.00 90.00 120.00

fractional coordinates

Zn 0.571 0.673 0.910

Zn 0.327 0.898 0.910

Zn 0.102 0.429 0.910

Zn 0.571 0.898 0.590

Zn 0.327 0.429 0.590

Zn 0.102 0.673 0.590

Zn 0.898 0.327 0.410

Zn 0.673 0.571 0.410

Zn 0.429 0.102 0.410

Zn 0.898 0.571 0.090

Zn 0.673 0.102 0.090

Zn 0.429 0.327 0.090

O 0.569 0.896 0.910

O 0.327 0.431 0.910

O 0.104 0.673 0.910

O 0.569 0.673 0.590

O 0.327 0.896 0.590

O 0.104 0.431 0.590

O 0.896 0.569 0.410

O 0.673 0.104 0.410

O 0.431 0.327 0.410

O 0.896 0.327 0.090

O 0.673 0.569 0.090

O 0.431 0.104 0.090

Str 78 (AFR)<sup>17</sup>

$\Delta E_{\text{gap}}(\text{PBE}_{\text{GW-fit}})$ : 1.04 eV

$E_{\text{rel}}$ : 0.34 eV/ZnO

Pore<sub>max</sub>: 0.48 nm

V<sub>pore</sub>: 28 %

D<sub>pore</sub>: 2

cell parameters

14.284 8.771 9.083 90.00 90.00 90.00

fractional coordinates

Zn 0.816 0.622 0.938

Zn 0.684 0.878 0.938

Zn 0.483 0.860 0.923

Zn 0.017 0.640 0.923	O 0.014 0.642 0.429
Zn 0.412 0.454 0.922	O 0.412 0.452 0.420
Zn 0.088 0.046 0.922	O 0.088 0.048 0.420
Zn 0.909 0.862 0.773	O 0.907 0.870 0.274
Zn 0.591 0.638 0.773	O 0.592 0.630 0.274
Zn 0.409 0.138 0.727	O 0.407 0.130 0.226
Zn 0.091 0.362 0.727	O 0.092 0.370 0.226
Zn 0.912 0.546 0.578	O 0.912 0.548 0.080
Zn 0.588 0.954 0.578	O 0.588 0.952 0.080
Zn 0.983 0.140 0.577	O 0.986 0.142 0.071
Zn 0.517 0.360 0.577	O 0.514 0.358 0.071
Zn 0.316 0.378 0.562	O 0.317 0.379 0.060
Zn 0.184 0.122 0.562	O 0.183 0.121 0.060
Zn 0.816 0.878 0.438	
Zn 0.684 0.622 0.438	Str 79 (SFO) <sup>17</sup>
Zn 0.483 0.640 0.423	$\Delta E_{\text{gap}}(\text{PBE}_{\text{GW-fit}})$ : 1.03 eV
Zn 0.017 0.860 0.423	$E_{\text{rel}}$ : 0.34 eV/ZnO
Zn 0.412 0.046 0.422	Pore <sub>max</sub> : 0.47 nm
Zn 0.088 0.454 0.422	V <sub>pore</sub> : 28 %
Zn 0.909 0.638 0.273	D <sub>pore</sub> : 2
Zn 0.591 0.862 0.273	cell parameters
Zn 0.409 0.362 0.227	14.435 8.766 9.091 90.00 98.36 90.00
Zn 0.091 0.138 0.227	fractional coordinates
Zn 0.912 0.954 0.078	Zn 0.934 0.873 0.980
Zn 0.588 0.546 0.078	Zn 0.434 0.373 0.980
Zn 0.983 0.360 0.077	Zn 0.733 0.890 0.919
Zn 0.517 0.140 0.077	Zn 0.233 0.390 0.919
Zn 0.316 0.122 0.062	Zn 0.662 0.297 0.903
Zn 0.184 0.378 0.062	Zn 0.162 0.797 0.903
O 0.817 0.879 0.940	Zn 0.341 0.612 0.793
O 0.683 0.621 0.940	Zn 0.841 0.112 0.793
O 0.486 0.642 0.929	Zn 0.659 0.612 0.707
O 0.014 0.858 0.929	Zn 0.159 0.112 0.707
O 0.412 0.048 0.920	Zn 0.838 0.797 0.597
O 0.088 0.452 0.920	Zn 0.338 0.297 0.597
O 0.907 0.630 0.774	Zn 0.767 0.390 0.581
O 0.592 0.870 0.774	Zn 0.267 0.890 0.581
O 0.407 0.370 0.726	Zn 0.566 0.373 0.520
O 0.092 0.130 0.726	Zn 0.066 0.873 0.520
O 0.912 0.952 0.580	Zn 0.934 0.127 0.480
O 0.588 0.548 0.580	Zn 0.434 0.627 0.480
O 0.986 0.358 0.571	Zn 0.733 0.110 0.419
O 0.514 0.142 0.571	Zn 0.233 0.610 0.419
O 0.317 0.121 0.560	Zn 0.662 0.703 0.403
O 0.183 0.379 0.560	Zn 0.162 0.203 0.403
O 0.817 0.621 0.440	Zn 0.841 0.888 0.293
O 0.683 0.879 0.440	Zn 0.341 0.388 0.293
O 0.486 0.858 0.429	Zn 0.659 0.388 0.207

Zn 0.159 0.888 0.207  
 Zn 0.838 0.203 0.097  
 Zn 0.338 0.703 0.097  
 Zn 0.767 0.610 0.081  
 Zn 0.267 0.110 0.081  
 Zn 0.566 0.627 0.020  
 Zn 0.066 0.127 0.020  
 O 0.933 0.129 0.981  
 O 0.433 0.629 0.981  
 O 0.736 0.108 0.925  
 O 0.236 0.608 0.925  
 O 0.663 0.702 0.900  
 O 0.163 0.202 0.900  
 O 0.843 0.880 0.795  
 O 0.343 0.380 0.795  
 O 0.657 0.380 0.705  
 O 0.157 0.880 0.705  
 O 0.837 0.202 0.600  
 O 0.337 0.702 0.600  
 O 0.764 0.608 0.575  
 O 0.264 0.108 0.575  
 O 0.567 0.629 0.519  
 O 0.067 0.129 0.519  
 O 0.933 0.871 0.481  
 O 0.433 0.371 0.481  
 O 0.736 0.892 0.425  
 O 0.236 0.392 0.425  
 O 0.663 0.298 0.400  
 O 0.163 0.798 0.400  
 O 0.843 0.120 0.295  
 O 0.343 0.620 0.295  
 O 0.657 0.620 0.205  
 O 0.157 0.120 0.205  
 O 0.837 0.798 0.100  
 O 0.337 0.298 0.100  
 O 0.764 0.392 0.075  
 O 0.264 0.892 0.075  
 O 0.567 0.371 0.019  
 O 0.067 0.871 0.019

Str 80 (USI)<sup>17</sup>

$\Delta E_{\text{gap}}(\text{PBE}_{\text{GW-fit}})$ : 0.77 eV

$E_{\text{rel}}$ : 0.44 eV/ZnO

Pore<sub>max</sub>: 0.42 nm

$V_{\text{pore}}$ : 29 %

$D_{\text{pore}}$ : 2

cell parameters

13.825 8.406 6.433 90.00 108.75 90.15

fractional coordinates

Zn 0.286 0.118 0.896  
 Zn 0.786 0.618 0.896  
 Zn 0.689 0.177 0.801  
 Zn 0.189 0.677 0.801  
 Zn 0.841 0.329 0.653  
 Zn 0.341 0.829 0.653  
 Zn 0.785 0.886 0.635  
 Zn 0.285 0.386 0.635  
 Zn 0.072 0.368 0.535  
 Zn 0.572 0.868 0.535  
 Zn 0.928 0.632 0.465  
 Zn 0.428 0.132 0.465  
 Zn 0.715 0.614 0.365  
 Zn 0.215 0.114 0.365  
 Zn 0.659 0.171 0.347  
 Zn 0.159 0.671 0.347  
 Zn 0.811 0.323 0.199  
 Zn 0.311 0.823 0.199  
 Zn 0.214 0.382 0.104  
 Zn 0.714 0.882 0.104  
 O 0.785 0.382 0.892  
 O 0.285 0.882 0.892  
 O 0.183 0.306 0.800  
 O 0.683 0.806 0.800  
 O 0.847 0.678 0.663  
 O 0.347 0.178 0.663  
 O 0.785 0.108 0.633  
 O 0.285 0.608 0.633  
 O 0.573 0.129 0.531  
 O 0.073 0.629 0.531  
 O 0.927 0.371 0.469  
 O 0.427 0.871 0.469  
 O 0.715 0.392 0.367  
 O 0.215 0.892 0.367  
 O 0.153 0.322 0.337  
 O 0.653 0.822 0.337  
 O 0.817 0.694 0.200  
 O 0.317 0.194 0.200  
 O 0.715 0.118 0.108  
 O 0.215 0.618 0.108

Str 81 (LTA)<sup>17</sup>

$\Delta E_{\text{gap}}(\text{PBE}_{\text{GW-fit}})$ : 1.43 eV

$E_{\text{rel}}$ : 0.25 eV/ZnO

Pore<sub>max</sub>: 0.64 nm

$V_{\text{pore}}$ : 30 %

$D_{\text{pore}}$ : 3

cell parameters  
 10.759 10.759 10.759 60.00 60.00  
 60.00  
 fractional coordinates  
 Zn 0.719 0.281 0.914  
 Zn 0.281 0.086 0.914  
 Zn 0.086 0.719 0.914  
 Zn 0.586 0.219 0.781  
 Zn 0.414 0.586 0.781  
 Zn 0.219 0.414 0.781  
 Zn 0.914 0.086 0.719  
 Zn 0.281 0.914 0.719  
 Zn 0.086 0.281 0.719  
 Zn 0.781 0.414 0.586  
 Zn 0.414 0.219 0.586  
 Zn 0.219 0.781 0.586  
 Zn 0.781 0.219 0.414  
 Zn 0.586 0.781 0.414  
 Zn 0.219 0.586 0.414  
 Zn 0.914 0.719 0.281  
 Zn 0.719 0.086 0.281  
 Zn 0.086 0.914 0.281  
 Zn 0.781 0.586 0.219  
 Zn 0.586 0.414 0.219  
 Zn 0.414 0.781 0.219  
 Zn 0.914 0.281 0.086  
 Zn 0.719 0.914 0.086  
 Zn 0.281 0.719 0.086  
 O 0.720 0.089 0.911  
 O 0.280 0.720 0.911  
 O 0.089 0.280 0.911  
 O 0.589 0.411 0.780  
 O 0.411 0.220 0.780  
 O 0.220 0.589 0.780  
 O 0.911 0.280 0.720  
 O 0.280 0.089 0.720  
 O 0.089 0.911 0.720  
 O 0.780 0.220 0.589  
 O 0.411 0.780 0.589  
 O 0.220 0.411 0.589  
 O 0.780 0.589 0.411  
 O 0.589 0.220 0.411  
 O 0.220 0.780 0.411  
 O 0.911 0.089 0.280  
 O 0.720 0.911 0.280  
 O 0.089 0.720 0.280  
 O 0.780 0.411 0.220  
 O 0.589 0.780 0.220

O 0.411 0.589 0.220  
 O 0.911 0.720 0.089  
 O 0.720 0.280 0.089  
 O 0.280 0.911 0.089  
  
 Str 82 (AFS)<sup>17</sup>  
 $\Delta E_{\text{gap}}(\text{PBE}_{\text{GW-fit}})$ : 1.22 eV  
 $E_{\text{rel}}$ : 0.36 eV/ZnO  
 $\text{Pore}_{\text{max}}$ : 0.56 nm  
 $V_{\text{pore}}$ : 31 %  
 $D_{\text{pore}}$ : 3  
 cell parameters  
 8.526 8.526 16.493 90.00 90.00 120.00  
 fractional coordinates  
 Zn 0.667 0.333 0.945  
 Zn 0.517 0.645 0.868  
 Zn 0.355 0.872 0.868  
 Zn 0.128 0.483 0.868  
 Zn 0.864 0.574 0.811  
 Zn 0.710 0.136 0.811  
 Zn 0.426 0.290 0.811  
 Zn 0.574 0.864 0.689  
 Zn 0.290 0.426 0.689  
 Zn 0.136 0.710 0.689  
 Zn 0.872 0.355 0.632  
 Zn 0.645 0.517 0.632  
 Zn 0.483 0.128 0.632  
 Zn 0.333 0.667 0.555  
 Zn 0.667 0.333 0.445  
 Zn 0.517 0.872 0.368  
 Zn 0.355 0.483 0.368  
 Zn 0.128 0.645 0.368  
 Zn 0.864 0.290 0.311  
 Zn 0.710 0.574 0.311  
 Zn 0.426 0.136 0.311  
 Zn 0.574 0.710 0.189  
 Zn 0.290 0.864 0.189  
 Zn 0.136 0.426 0.189  
 Zn 0.872 0.517 0.132  
 Zn 0.645 0.128 0.132  
 Zn 0.483 0.355 0.132  
 Zn 0.333 0.667 0.055  
 O 0.333 0.667 0.940  
 O 0.869 0.349 0.873  
 O 0.651 0.520 0.873  
 O 0.480 0.131 0.873  
 O 0.576 0.867 0.810  
 O 0.291 0.424 0.810

O 0.133 0.709 0.810  
O 0.867 0.576 0.690  
O 0.709 0.133 0.690  
O 0.424 0.291 0.690  
O 0.520 0.651 0.627  
O 0.349 0.869 0.627  
O 0.131 0.480 0.627  
O 0.667 0.333 0.560  
O 0.333 0.667 0.440  
O 0.869 0.520 0.373  
O 0.651 0.131 0.373  
O 0.480 0.349 0.373  
O 0.576 0.709 0.310  
O 0.291 0.867 0.310  
O 0.133 0.424 0.310  
O 0.867 0.291 0.190  
O 0.709 0.576 0.190  
O 0.424 0.133 0.190  
O 0.520 0.869 0.127  
O 0.349 0.480 0.127  
O 0.131 0.651 0.127  
O 0.667 0.333 0.060

Str 83 (SAO)<sup>17</sup>

$\Delta E_{\text{gap}}(\text{PBE}_{\text{GW-fit}})$ : 1.18 eV

$E_{\text{rel}}$ : 0.38 eV/ZnO

$\text{Pore}_{\text{max}}$ : 0.49 nm

$V_{\text{pore}}$ : 34 %

$D_{\text{pore}}$ : 3

cell parameters

8.925 8.925 13.591 90.00 90.00 90.00

fractional coordinates

Zn 0.606 0.877 0.948  
Zn 0.394 0.123 0.948  
Zn 0.896 0.878 0.874  
Zn 0.104 0.122 0.874  
Zn 0.700 0.117 0.807  
Zn 0.300 0.883 0.807  
Zn 0.617 0.800 0.693  
Zn 0.383 0.200 0.693  
Zn 0.622 0.396 0.626  
Zn 0.378 0.604 0.626  
Zn 0.623 0.106 0.552  
Zn 0.377 0.894 0.552  
Zn 0.704 0.704 0.500  
Zn 0.296 0.296 0.500  
Zn 0.894 0.377 0.448  
Zn 0.106 0.623 0.448

Zn 0.604 0.378 0.374  
Zn 0.396 0.622 0.374  
Zn 0.800 0.617 0.307  
Zn 0.200 0.383 0.307  
Zn 0.883 0.300 0.193  
Zn 0.117 0.700 0.193  
Zn 0.878 0.896 0.126  
Zn 0.122 0.104 0.126  
Zn 0.877 0.606 0.052  
Zn 0.123 0.394 0.052  
Zn 0.796 0.204 0.000  
Zn 0.204 0.796 0.000  
O 0.607 0.121 0.947  
O 0.393 0.879 0.947  
O 0.894 0.127 0.876  
O 0.106 0.873 0.876  
O 0.703 0.885 0.807  
O 0.297 0.115 0.807  
O 0.615 0.203 0.693  
O 0.385 0.797 0.693  
O 0.627 0.606 0.624  
O 0.373 0.394 0.624  
O 0.621 0.893 0.553  
O 0.379 0.107 0.553  
O 0.704 0.296 0.500  
O 0.296 0.704 0.500  
O 0.893 0.621 0.447  
O 0.107 0.379 0.447  
O 0.606 0.627 0.376  
O 0.394 0.373 0.376  
O 0.797 0.385 0.307  
O 0.203 0.615 0.307  
O 0.885 0.703 0.193  
O 0.115 0.297 0.193  
O 0.873 0.106 0.124  
O 0.127 0.894 0.124  
O 0.879 0.393 0.053  
O 0.121 0.607 0.053  
O 0.796 0.796 0.000  
O 0.204 0.204 0.000

Str 84 (BBZ)<sup>19</sup>

$\Delta E_{\text{gap}}(\text{PBE}_{\text{GW-fit}})$ : 0.83 eV

$E_{\text{rel}}$ : 0.25 eV/ZnO

$\text{Pore}_{\text{max}}$ : 0.84 nm

$V_{\text{pore}}$ : 36 %

$D_{\text{pore}}$ : 3

cell parameters

12.902 12.901 3.370 90.00 90.00  
 120.01  
 fractional coordinates  
 Zn 0.822 0.334 0.500  
 Zn 0.673 0.512 0.500  
 Zn 0.498 0.836 0.500  
 Zn 0.495 0.185 0.500  
 Zn 0.320 0.509 0.500  
 Zn 0.172 0.687 0.500  
 Zn 0.909 0.548 0.000  
 Zn 0.622 0.099 0.000  
 Zn 0.534 0.636 0.000  
 Zn 0.460 0.386 0.000  
 Zn 0.372 0.923 0.000  
 Zn 0.085 0.474 0.000  
 O 0.819 0.503 0.500  
 O 0.667 0.189 0.500  
 O 0.504 0.340 0.500  
 O 0.489 0.681 0.500  
 O 0.326 0.832 0.500  
 O 0.175 0.518 0.500  
 O 0.912 0.375 0.000  
 O 0.632 0.561 0.000  
 O 0.547 0.926 0.000  
 O 0.447 0.096 0.000  
 O 0.362 0.461 0.000  
 O 0.082 0.646 0.000

Str 85 (FAU)<sup>17</sup>

$\Delta E_{\text{gap}}(\text{PBE}_{\text{GW-fit}})$ : 1.16 eV

$E_{\text{rel}}$ : 0.34 eV/ZnO

Pore<sub>max</sub>: 0.67 nm

$V_{\text{pore}}$ : 38 %

$D_{\text{pore}}$ : 3

cell parameters

15.834 15.834 15.834 90.00 90.00  
 90.00

fractional coordinates

Zn 0.880 0.196 0.965  
 Zn 0.870 0.554 0.965  
 Zn 0.380 0.696 0.965  
 Zn 0.370 0.054 0.965  
 Zn 0.715 0.120 0.946  
 Zn 0.535 0.130 0.946  
 Zn 0.215 0.620 0.946  
 Zn 0.035 0.630 0.946  
 Zn 0.696 0.465 0.880  
 Zn 0.554 0.785 0.880

Zn 0.196 0.965 0.880  
 Zn 0.054 0.285 0.880  
 Zn 0.696 0.285 0.870  
 Zn 0.554 0.965 0.870  
 Zn 0.196 0.785 0.870  
 Zn 0.054 0.465 0.870  
 Zn 0.715 0.630 0.804  
 Zn 0.535 0.620 0.804  
 Zn 0.215 0.130 0.804  
 Zn 0.035 0.120 0.804  
 Zn 0.880 0.554 0.785  
 Zn 0.870 0.196 0.785  
 Zn 0.380 0.054 0.785  
 Zn 0.370 0.696 0.785  
 Zn 0.630 0.804 0.715  
 Zn 0.620 0.446 0.715  
 Zn 0.130 0.304 0.715  
 Zn 0.120 0.946 0.715  
 Zn 0.965 0.380 0.696  
 Zn 0.785 0.370 0.696  
 Zn 0.465 0.880 0.696  
 Zn 0.285 0.870 0.696  
 Zn 0.946 0.035 0.630  
 Zn 0.804 0.715 0.630  
 Zn 0.446 0.535 0.630  
 Zn 0.304 0.215 0.630  
 Zn 0.946 0.215 0.620  
 Zn 0.804 0.535 0.620  
 Zn 0.446 0.715 0.620  
 Zn 0.304 0.035 0.620  
 Zn 0.965 0.870 0.554  
 Zn 0.785 0.880 0.554  
 Zn 0.465 0.370 0.554  
 Zn 0.285 0.380 0.554  
 Zn 0.630 0.446 0.535  
 Zn 0.620 0.804 0.535  
 Zn 0.130 0.946 0.535  
 Zn 0.120 0.304 0.535  
 Zn 0.880 0.696 0.465  
 Zn 0.870 0.054 0.465  
 Zn 0.380 0.196 0.465  
 Zn 0.370 0.554 0.465  
 Zn 0.715 0.620 0.446  
 Zn 0.535 0.630 0.446  
 Zn 0.215 0.120 0.446  
 Zn 0.035 0.130 0.446  
 Zn 0.696 0.965 0.380  
 Zn 0.554 0.285 0.380

Zn 0.196 0.465 0.380	O 0.466 0.695 0.880
Zn 0.054 0.785 0.380	O 0.284 0.055 0.880
Zn 0.696 0.785 0.370	O 0.966 0.555 0.870
Zn 0.554 0.465 0.370	O 0.784 0.195 0.870
Zn 0.196 0.285 0.370	O 0.466 0.055 0.870
Zn 0.054 0.965 0.370	O 0.284 0.695 0.870
Zn 0.715 0.130 0.304	O 0.630 0.716 0.805
Zn 0.535 0.120 0.304	O 0.620 0.534 0.805
Zn 0.215 0.630 0.304	O 0.130 0.216 0.805
Zn 0.035 0.620 0.304	O 0.120 0.034 0.805
Zn 0.880 0.054 0.285	O 0.695 0.370 0.784
Zn 0.870 0.696 0.285	O 0.555 0.880 0.784
Zn 0.380 0.554 0.285	O 0.195 0.870 0.784
Zn 0.370 0.196 0.285	O 0.055 0.380 0.784
Zn 0.630 0.304 0.215	O 0.945 0.120 0.716
Zn 0.620 0.946 0.215	O 0.805 0.630 0.716
Zn 0.130 0.804 0.215	O 0.445 0.620 0.716
Zn 0.120 0.446 0.215	O 0.305 0.130 0.716
Zn 0.965 0.880 0.196	O 0.880 0.466 0.695
Zn 0.785 0.870 0.196	O 0.870 0.284 0.695
Zn 0.465 0.380 0.196	O 0.380 0.966 0.695
Zn 0.285 0.370 0.196	O 0.370 0.784 0.695
Zn 0.946 0.535 0.130	O 0.716 0.805 0.630
Zn 0.804 0.215 0.130	O 0.534 0.445 0.630
Zn 0.446 0.035 0.130	O 0.216 0.305 0.630
Zn 0.304 0.715 0.130	O 0.034 0.945 0.630
Zn 0.946 0.715 0.120	O 0.716 0.445 0.620
Zn 0.804 0.035 0.120	O 0.534 0.805 0.620
Zn 0.446 0.215 0.120	O 0.216 0.945 0.620
Zn 0.304 0.535 0.120	O 0.034 0.305 0.620
Zn 0.965 0.370 0.054	O 0.880 0.784 0.555
Zn 0.785 0.380 0.054	O 0.870 0.966 0.555
Zn 0.465 0.870 0.054	O 0.380 0.284 0.555
Zn 0.285 0.880 0.054	O 0.370 0.466 0.555
Zn 0.630 0.946 0.035	O 0.945 0.130 0.534
Zn 0.620 0.304 0.035	O 0.805 0.620 0.534
Zn 0.130 0.446 0.035	O 0.445 0.630 0.534
Zn 0.120 0.804 0.035	O 0.305 0.120 0.534
O 0.695 0.380 0.966	O 0.695 0.880 0.466
O 0.555 0.870 0.966	O 0.555 0.370 0.466
O 0.195 0.880 0.966	O 0.195 0.380 0.466
O 0.055 0.370 0.966	O 0.055 0.870 0.466
O 0.630 0.034 0.945	O 0.630 0.534 0.445
O 0.620 0.216 0.945	O 0.620 0.716 0.445
O 0.130 0.534 0.945	O 0.130 0.034 0.445
O 0.120 0.716 0.945	O 0.120 0.216 0.445
O 0.966 0.195 0.880	O 0.966 0.695 0.380
O 0.784 0.555 0.880	O 0.784 0.055 0.380

O 0.466 0.195 0.380  
 O 0.284 0.555 0.380  
 O 0.966 0.055 0.370  
 O 0.784 0.695 0.370  
 O 0.466 0.555 0.370  
 O 0.284 0.195 0.370  
 O 0.630 0.216 0.305  
 O 0.620 0.034 0.305  
 O 0.130 0.716 0.305  
 O 0.120 0.534 0.305  
 O 0.695 0.870 0.284  
 O 0.555 0.380 0.284  
 O 0.195 0.370 0.284  
 O 0.055 0.880 0.284  
 O 0.945 0.620 0.216  
 O 0.805 0.130 0.216  
 O 0.445 0.120 0.216  
 O 0.305 0.630 0.216  
 O 0.880 0.966 0.195  
 O 0.870 0.784 0.195  
 O 0.380 0.466 0.195  
 O 0.370 0.284 0.195  
 O 0.716 0.305 0.130  
 O 0.534 0.945 0.130  
 O 0.216 0.805 0.130  
 O 0.034 0.445 0.130  
 O 0.716 0.945 0.120  
 O 0.534 0.305 0.120  
 O 0.216 0.445 0.120  
 O 0.034 0.805 0.120  
 O 0.880 0.284 0.055  
 O 0.870 0.466 0.055  
 O 0.380 0.784 0.055  
 O 0.370 0.966 0.055  
 O 0.945 0.630 0.034  
 O 0.805 0.120 0.034  
 O 0.445 0.130 0.034  
 O 0.305 0.620 0.034

Str 86 (EMT)<sup>17</sup>

$\Delta E_{\text{gap}}(\text{PBE}_{\text{GW-fit}})$ : 1.16 eV

$E_{\text{rel}}$ : 0.34 eV/ZnO

Pore<sub>max</sub>: 0.69 nm

$V_{\text{pore}}$ : 38 %

$D_{\text{pore}}$ : 3

cell parameters

11.201 11.201 18.270 89.99 90.00

120.00

fractional coordinates

Zn 0.261 0.213 0.945

Zn 0.799 0.561 0.945

Zn 0.451 0.751 0.945

Zn 0.345 0.015 0.911

Zn 0.168 0.667 0.911

Zn 0.998 0.844 0.911

Zn 0.569 0.272 0.857

Zn 0.202 0.443 0.857

Zn 0.740 0.810 0.857

Zn 0.105 0.078 0.816

Zn 0.472 0.907 0.816

Zn 0.934 0.540 0.816

Zn 0.329 0.335 0.762

Zn 0.677 0.506 0.762

Zn 0.506 0.683 0.762

Zn 0.413 0.137 0.727

Zn 0.223 0.599 0.727

Zn 0.875 0.789 0.727

Zn 0.167 0.023 0.642

Zn 0.355 0.845 0.642

Zn 0.989 0.657 0.642

Zn 0.355 0.023 0.531

Zn 0.168 0.657 0.531

Zn 0.989 0.845 0.531

Zn 0.224 0.138 0.445

Zn 0.414 0.789 0.445

Zn 0.875 0.599 0.445

Zn 0.329 0.507 0.410

Zn 0.506 0.336 0.410

Zn 0.677 0.684 0.410

Zn 0.472 0.078 0.357

Zn 0.106 0.541 0.357

Zn 0.934 0.907 0.357

Zn 0.202 0.272 0.316

Zn 0.741 0.443 0.316

Zn 0.570 0.811 0.316

Zn 0.169 0.015 0.262

Zn 0.998 0.667 0.262

Zn 0.346 0.844 0.262

Zn 0.451 0.213 0.227

Zn 0.261 0.561 0.227

Zn 0.800 0.751 0.227

Zn 0.319 0.327 0.142

Zn 0.507 0.693 0.142

Zn 0.686 0.505 0.142

Zn 0.507 0.327 0.031

Zn 0.319 0.505 0.031

Zn 0.685 0.693 0.031  
 O 0.451 0.211 0.946  
 O 0.259 0.561 0.945  
 O 0.801 0.753 0.945  
 O 0.169 0.016 0.912  
 O 0.346 0.843 0.912  
 O 0.996 0.666 0.912  
 O 0.200 0.269 0.857  
 O 0.743 0.443 0.857  
 O 0.569 0.813 0.857  
 O 0.474 0.080 0.816  
 O 0.105 0.538 0.816  
 O 0.932 0.907 0.816  
 O 0.329 0.507 0.761  
 O 0.505 0.334 0.761  
 O 0.678 0.683 0.761  
 O 0.223 0.139 0.727  
 O 0.415 0.789 0.727  
 O 0.873 0.597 0.727  
 O 0.357 0.023 0.641  
 O 0.165 0.655 0.641  
 O 0.989 0.847 0.641  
 O 0.165 0.023 0.532  
 O 0.357 0.847 0.532  
 O 0.990 0.655 0.532  
 O 0.416 0.140 0.445  
 O 0.224 0.597 0.445  
 O 0.873 0.789 0.445  
 O 0.329 0.335 0.412  
 O 0.505 0.684 0.412  
 O 0.678 0.508 0.411  
 O 0.105 0.081 0.357  
 O 0.475 0.908 0.357  
 O 0.933 0.538 0.357  
 O 0.570 0.270 0.316  
 O 0.200 0.443 0.316  
 O 0.743 0.813 0.315  
 O 0.346 0.016 0.261  
 O 0.997 0.843 0.261  
 O 0.170 0.667 0.261  
 O 0.259 0.211 0.227  
 O 0.452 0.754 0.227  
 O 0.802 0.561 0.227  
 O 0.318 0.503 0.141  
 O 0.509 0.327 0.141  
 O 0.685 0.695 0.141  
 O 0.317 0.327 0.032  
 O 0.509 0.695 0.032

O 0.685 0.503 0.032  
 Str 87 (WZ-ZnO-NP-1)  
 $\Delta E_{\text{gap}}(\text{PBE}_{\text{GW-fit}})$ : 0.21 eV  
 $E_{\text{rel}}$ : 0.08 eV/ZnO  
 $\text{Pore}_{\text{max}}$ : 0.53 nm  
 $V_{\text{pore}}$ : 7 %  
 $D_{\text{pore}}$ : 1  
 cell parameters  
 19.702 19.702 5.309 90.00 90.00  
 120.00  
 fractional coordinates  
 Zn 0.889 0.111 0.999  
 Zn 0.722 0.945 0.999  
 Zn 0.889 0.444 0.999  
 Zn 0.722 0.444 0.999  
 Zn 0.389 0.945 0.999  
 Zn 0.389 0.111 0.999  
 Zn 0.890 0.278 0.999  
 Zn 0.555 0.943 0.999  
 Zn 0.555 0.278 0.999  
 Zn 0.553 0.775 0.998  
 Zn 0.553 0.444 0.998  
 Zn 0.389 0.775 0.998  
 Zn 0.389 0.281 0.998  
 Zn 0.058 0.444 0.998  
 Zn 0.058 0.281 0.998  
 Zn 0.455 0.743 0.526  
 Zn 0.455 0.379 0.526  
 Zn 0.091 0.379 0.526  
 Zn 0.778 0.222 0.501  
 Zn 0.611 0.222 0.501  
 Zn 0.611 0.055 0.501  
 Zn 0.778 0.389 0.501  
 Zn 0.778 0.056 0.501  
 Zn 0.445 0.056 0.501  
 Zn 0.945 0.889 0.501  
 Zn 0.945 0.722 0.501  
 Zn 0.111 0.889 0.501  
 Zn 0.943 0.389 0.501  
 Zn 0.943 0.220 0.501  
 Zn 0.613 0.891 0.501  
 Zn 0.613 0.389 0.501  
 Zn 0.444 0.891 0.501  
 Zn 0.444 0.220 0.501  
 Zn 0.945 0.556 0.499  
 Zn 0.945 0.055 0.499  
 Zn 0.778 0.556 0.499

Zn 0.778 0.889 0.499	O 0.944 0.555 0.878
Zn 0.277 0.889 0.499	O 0.944 0.055 0.878
Zn 0.277 0.055 0.499	O 0.778 0.890 0.878
Zn 0.777 0.722 0.499	O 0.778 0.555 0.878
Zn 0.112 0.722 0.499	O 0.278 0.890 0.878
Zn 0.112 0.057 0.499	O 0.278 0.055 0.878
Zn 0.609 0.719 0.498	O 0.445 0.388 0.875
Zn 0.609 0.556 0.498	O 0.445 0.724 0.875
Zn 0.277 0.719 0.498	O 0.109 0.388 0.875
Zn 0.277 0.225 0.498	O 0.612 0.724 0.875
Zn 0.114 0.556 0.498	O 0.612 0.555 0.875
Zn 0.114 0.225 0.498	O 0.278 0.724 0.875
Zn 0.212 0.621 0.026	O 0.278 0.221 0.875
Zn 0.212 0.257 0.026	O 0.110 0.555 0.875
Zn 0.576 0.621 0.026	O 0.110 0.221 0.875
Zn 0.889 0.778 0.001	O 0.889 0.778 0.380
Zn 0.056 0.945 0.001	O 0.056 0.945 0.380
Zn 0.056 0.778 0.001	O 0.056 0.778 0.380
Zn 0.889 0.944 0.001	O 0.722 0.278 0.380
Zn 0.889 0.611 0.001	O 0.722 0.111 0.380
Zn 0.222 0.944 0.001	O 0.556 0.111 0.380
Zn 0.722 0.278 0.001	O 0.889 0.944 0.379
Zn 0.722 0.111 0.001	O 0.889 0.611 0.379
Zn 0.556 0.111 0.001	O 0.222 0.944 0.379
Zn 0.724 0.780 0.001	O 0.889 0.278 0.379
Zn 0.724 0.611 0.001	O 0.555 0.944 0.379
Zn 0.223 0.780 0.001	O 0.555 0.278 0.379
Zn 0.223 0.109 0.001	O 0.722 0.778 0.379
Zn 0.053 0.611 0.001	O 0.722 0.611 0.379
Zn 0.053 0.109 0.001	O 0.223 0.778 0.379
O 0.778 0.222 0.880	O 0.223 0.111 0.379
O 0.611 0.222 0.880	O 0.055 0.611 0.379
O 0.611 0.055 0.880	O 0.055 0.111 0.379
O 0.945 0.889 0.880	O 0.888 0.445 0.378
O 0.945 0.722 0.880	O 0.888 0.110 0.378
O 0.111 0.889 0.880	O 0.723 0.945 0.378
O 0.778 0.389 0.879	O 0.723 0.445 0.378
O 0.778 0.056 0.879	O 0.389 0.945 0.378
O 0.445 0.056 0.879	O 0.389 0.110 0.378
O 0.777 0.722 0.879	O 0.557 0.612 0.375
O 0.111 0.722 0.879	O 0.221 0.612 0.375
O 0.111 0.056 0.879	O 0.221 0.276 0.375
O 0.945 0.389 0.879	O 0.557 0.779 0.375
O 0.945 0.222 0.879	O 0.557 0.445 0.375
O 0.611 0.889 0.879	O 0.389 0.779 0.375
O 0.611 0.389 0.879	O 0.389 0.276 0.375
O 0.444 0.889 0.879	O 0.055 0.445 0.375
O 0.444 0.222 0.879	O 0.055 0.276 0.375

Str 88 (WZ-ZnO-NP-2)	$D_{\text{pore}}$ : 1
$\Delta E_{\text{gap}}(\text{PBE}_{\text{GW}}\text{-fit})$ : 0.28 eV	cell parameters
$E_{\text{rel}}$ : 0.23 eV/ZnO	21.778 8.781 5.340 90.01 89.98 87.71
$\text{Pore}_{\text{max}}$ : 0.39 nm	fractional coordinates
$V_{\text{pore}}$ : 10 %	Zn 0.419 0.605 0.942
$D_{\text{pore}}$ : 1	Zn 0.919 0.105 0.942
cell parameters	Zn 0.368 0.242 0.941
9.935 9.877 5.348 90.00 90.00 120.19	Zn 0.868 0.742 0.941
fractional coordinates	Zn 0.821 0.392 0.941
Zn 0.780 0.226 1.000	Zn 0.321 0.892 0.941
Zn 0.774 0.555 0.999	Zn 0.723 0.680 0.940
Zn 0.114 0.555 0.999	Zn 0.572 0.640 0.940
Zn 0.443 0.231 0.998	Zn 0.224 0.180 0.940
Zn 0.121 0.231 0.998	Zn 0.072 0.140 0.940
Zn 0.578 0.420 0.526	Zn 0.773 0.043 0.939
Zn 0.176 0.420 0.526	Zn 0.273 0.543 0.939
Zn 0.890 0.446 0.503	Zn 0.669 0.334 0.939
Zn 0.220 0.107 0.500	Zn 0.169 0.834 0.939
Zn 0.886 0.779 0.499	Zn 0.513 0.347 0.920
Zn 0.226 0.779 0.499	Zn 0.013 0.846 0.920
Zn 0.879 0.103 0.498	Zn 0.641 0.964 0.914
Zn 0.557 0.103 0.498	Zn 0.141 0.464 0.914
Zn 0.422 0.913 0.026	Zn 0.638 0.769 0.442
Zn 0.824 0.913 0.026	Zn 0.138 0.269 0.442
Zn 0.110 0.887 0.003	Zn 0.686 0.119 0.442
O 0.890 0.448 0.877	Zn 0.587 0.406 0.442
O 0.221 0.109 0.877	Zn 0.186 0.619 0.442
O 0.890 0.777 0.874	Zn 0.087 0.906 0.442
O 0.220 0.777 0.874	Zn 0.783 0.832 0.440
O 0.889 0.114 0.873	Zn 0.283 0.332 0.440
O 0.558 0.114 0.873	Zn 0.434 0.371 0.440
O 0.563 0.442 0.872	Zn 0.934 0.871 0.440
O 0.213 0.442 0.872	Zn 0.734 0.469 0.439
O 0.110 0.886 0.377	Zn 0.234 0.969 0.439
O 0.779 0.225 0.377	Zn 0.837 0.177 0.439
O 0.780 0.556 0.374	Zn 0.337 0.677 0.439
O 0.110 0.556 0.374	Zn 0.494 0.664 0.421
O 0.111 0.219 0.373	Zn 0.994 0.165 0.421
O 0.442 0.219 0.373	Zn 0.365 0.048 0.413
O 0.437 0.891 0.372	Zn 0.865 0.548 0.413
O 0.787 0.891 0.372	O 0.514 0.313 0.570
	O 0.014 0.813 0.570
	O 0.627 0.976 0.567
Str 89 (WZ-ZnO-NP-3)	O 0.127 0.476 0.567
$\Delta E_{\text{gap}}(\text{PBE}_{\text{GW}}\text{-fit})$ : 0.32 eV	O 0.418 0.595 0.566
$E_{\text{rel}}$ : 0.20 eV/ZnO	O 0.918 0.095 0.566
$\text{Pore}_{\text{max}}$ : 0.36 nm	O 0.574 0.630 0.566
$V_{\text{pore}}$ : 10 %	O 0.074 0.130 0.566

O	0.366	0.248	0.566	Zn	0.466	0.933	0.998
O	0.866	0.748	0.566	Zn	0.466	0.534	0.998
O	0.818	0.390	0.565	Zn	0.067	0.534	0.998
O	0.318	0.890	0.565	Zn	0.709	0.854	0.527
O	0.722	0.683	0.563	Zn	0.146	0.854	0.527
O	0.271	0.545	0.563	Zn	0.146	0.291	0.527
O	0.771	0.045	0.563	Zn	0.531	0.867	0.501
O	0.222	0.183	0.563	Zn	0.531	0.665	0.501
O	0.669	0.333	0.563	Zn	0.335	0.867	0.501
O	0.169	0.833	0.563	Zn	0.335	0.469	0.501
O	0.492	0.697	0.071	Zn	0.133	0.469	0.501
O	0.992	0.197	0.071	Zn	0.133	0.665	0.501
O	0.140	0.263	0.066	Zn	0.333	0.667	0.501
O	0.640	0.764	0.066	Zn	0.933	0.669	0.499
O	0.432	0.380	0.066	Zn	0.933	0.263	0.499
O	0.932	0.880	0.066	Zn	0.737	0.669	0.499
O	0.588	0.416	0.066	Zn	0.737	0.067	0.499
O	0.379	0.035	0.066	Zn	0.331	0.263	0.499
O	0.879	0.535	0.066	Zn	0.331	0.067	0.499
O	0.088	0.916	0.066	Zn	0.734	0.467	0.499
O	0.689	0.122	0.065	Zn	0.734	0.266	0.499
O	0.189	0.622	0.065	Zn	0.533	0.266	0.499
O	0.284	0.328	0.063	Zn	0.933	0.466	0.498
O	0.784	0.828	0.063	Zn	0.534	0.466	0.498
O	0.736	0.467	0.063	Zn	0.534	0.067	0.498
O	0.236	0.967	0.063	Zn	0.854	0.709	0.027
O	0.337	0.678	0.063	Zn	0.854	0.146	0.027
O	0.837	0.178	0.063	Zn	0.291	0.146	0.027
				Zn	0.867	0.531	0.001
				Zn	0.867	0.335	0.001
				Zn	0.665	0.531	0.001
				Zn	0.665	0.133	0.001
				Zn	0.469	0.335	0.001
				Zn	0.469	0.133	0.001
				Zn	0.667	0.333	0.001
				O	0.333	0.667	0.879
				O	0.733	0.467	0.878
				O	0.733	0.267	0.878
				O	0.533	0.267	0.878
				O	0.534	0.867	0.878
				O	0.534	0.666	0.878
				O	0.334	0.867	0.878
				O	0.334	0.466	0.878
				O	0.133	0.666	0.878
				O	0.133	0.466	0.878
				O	0.731	0.865	0.876
				O	0.135	0.865	0.876
				O	0.135	0.269	0.876

Str 90 (WZ-ZnO-NP-4)  
 $\Delta E_{\text{gap}}(\text{PBE}_{\text{GW}}\text{-fit}): 0.30 \text{ eV}$   
 $E_{\text{rel}}: 0.12 \text{ eV/ZnO}$   
 $\text{Pore}_{\text{max}}: 0.53 \text{ nm}$   
 $V_{\text{pore}}: 11 \%$   
 $D_{\text{pore}}: 1$   
cell parameters  
16.415 16.415 5.322 90.00 90.00  
120.00  
fractional coordinates  
Zn 0.669 0.933 0.999  
Zn 0.669 0.737 0.999  
Zn 0.263 0.933 0.999  
Zn 0.263 0.331 0.999  
Zn 0.067 0.737 0.999  
Zn 0.067 0.331 0.999  
Zn 0.467 0.734 0.999  
Zn 0.266 0.734 0.999  
Zn 0.266 0.533 0.999

O	0.934	0.666	0.876	Zn	0.619	0.954	0.999
O	0.934	0.268	0.876	Zn	0.189	0.524	0.999
O	0.732	0.666	0.876	Zn	0.907	0.954	0.999
O	0.732	0.066	0.876	Zn	0.907	0.524	0.999
O	0.334	0.268	0.876	Zn	0.619	0.236	0.999
O	0.334	0.066	0.876	Zn	0.189	0.236	0.999
O	0.934	0.467	0.876	Zn	0.906	0.808	0.997
O	0.533	0.467	0.876	Zn	0.474	0.808	0.997
O	0.533	0.066	0.876	Zn	0.906	0.669	0.997
O	0.667	0.333	0.379	Zn	0.474	0.237	0.997
O	0.467	0.733	0.378	Zn	0.335	0.669	0.997
O	0.267	0.733	0.378	Zn	0.335	0.237	0.997
O	0.267	0.533	0.378	Zn	0.819	0.608	0.524
O	0.867	0.534	0.378	Zn	0.535	0.782	0.524
O	0.867	0.334	0.378	Zn	0.535	0.324	0.524
O	0.666	0.534	0.378	Zn	0.361	0.608	0.524
O	0.666	0.133	0.378	Zn	0.819	0.782	0.524
O	0.466	0.334	0.378	Zn	0.361	0.324	0.524
O	0.466	0.133	0.378	Zn	0.238	0.905	0.502
O	0.865	0.731	0.376	Zn	0.952	0.333	0.502
O	0.865	0.135	0.376	Zn	0.952	0.191	0.502
O	0.269	0.135	0.376	Zn	0.810	0.191	0.502
O	0.666	0.732	0.376	Zn	0.093	0.332	0.501
O	0.666	0.934	0.376	Zn	0.810	0.332	0.501
O	0.268	0.934	0.376	Zn	0.810	0.050	0.501
O	0.268	0.334	0.376	Zn	0.381	0.047	0.501
O	0.066	0.732	0.376	Zn	0.381	0.905	0.501
O	0.066	0.334	0.376	Zn	0.238	0.762	0.501
O	0.467	0.934	0.376	Zn	0.238	0.047	0.501
O	0.467	0.533	0.376	Zn	0.096	0.905	0.501
O	0.066	0.533	0.376	Zn	0.096	0.762	0.501
				Zn	0.095	0.048	0.501
				Zn	0.524	0.048	0.501
Str 91 (WZ-ZnO-NP-5)				Zn	0.095	0.619	0.501
$\Delta E_{\text{gap}}(\text{PBE}_{\text{GW}}\text{-fit}): 0.26 \text{ eV}$				Zn	0.380	0.189	0.500
$E_{\text{rel}}: 0.13 \text{ eV/ZnO}$				Zn	0.954	0.763	0.500
$\text{Pore}_{\text{max}}: 0.78 \text{ nm}$				Zn	0.380	0.763	0.500
$V_{\text{pore}}: 11 \%$				Zn	0.953	0.476	0.500
$D_{\text{pore}}: 1$				Zn	0.953	0.048	0.500
cell parameters				Zn	0.095	0.476	0.500
23.047 23.047 5.318 90.00 90.00				Zn	0.667	0.190	0.500
120.00				Zn	0.667	0.048	0.500
fractional coordinates				Zn	0.095	0.190	0.500
Zn 0.476 0.953 1.000				Zn	0.954	0.619	0.499
Zn 0.476 0.095 1.000				Zn	0.954	0.907	0.499
Zn 0.190 0.667 1.000				Zn	0.524	0.189	0.499
Zn 0.190 0.095 1.000				Zn	0.524	0.907	0.499
Zn 0.048 0.953 1.000				Zn	0.236	0.189	0.499
Zn 0.048 0.667 1.000							

Zn 0.236 0.619 0.499	O 0.953 0.049 0.878
Zn 0.808 0.906 0.497	O 0.953 0.476 0.878
Zn 0.808 0.474 0.497	O 0.094 0.476 0.878
Zn 0.669 0.906 0.497	O 0.094 0.190 0.878
Zn 0.237 0.474 0.497	O 0.667 0.190 0.878
Zn 0.669 0.335 0.497	O 0.667 0.049 0.878
Zn 0.237 0.335 0.497	O 0.953 0.906 0.877
Zn 0.324 0.535 0.024	O 0.953 0.619 0.877
Zn 0.782 0.535 0.024	O 0.524 0.190 0.877
Zn 0.608 0.819 0.024	O 0.524 0.906 0.877
Zn 0.608 0.361 0.024	O 0.237 0.619 0.877
Zn 0.782 0.819 0.024	O 0.237 0.190 0.877
Zn 0.324 0.361 0.024	O 0.955 0.763 0.876
Zn 0.905 0.238 0.002	O 0.379 0.763 0.876
Zn 0.333 0.952 0.002	O 0.379 0.187 0.876
Zn 0.191 0.952 0.002	O 0.236 0.475 0.875
Zn 0.191 0.810 0.002	O 0.810 0.475 0.875
Zn 0.332 0.810 0.001	O 0.810 0.907 0.875
Zn 0.332 0.093 0.001	O 0.668 0.907 0.875
Zn 0.050 0.810 0.001	O 0.668 0.332 0.875
Zn 0.905 0.381 0.001	O 0.236 0.332 0.875
Zn 0.905 0.096 0.001	O 0.813 0.765 0.872
Zn 0.762 0.238 0.001	O 0.813 0.620 0.872
Zn 0.047 0.381 0.001	O 0.523 0.765 0.872
Zn 0.047 0.238 0.001	O 0.523 0.329 0.872
Zn 0.762 0.096 0.001	O 0.378 0.620 0.872
Zn 0.048 0.095 0.001	O 0.378 0.329 0.872
Zn 0.619 0.095 0.001	O 0.905 0.238 0.380
Zn 0.048 0.524 0.001	O 0.333 0.952 0.380
Zn 0.763 0.954 0.000	O 0.191 0.952 0.380
Zn 0.189 0.380 0.000	O 0.191 0.810 0.380
Zn 0.763 0.380 0.000	O 0.905 0.381 0.379
O 0.238 0.905 0.880	O 0.905 0.096 0.379
O 0.952 0.333 0.880	O 0.047 0.381 0.379
O 0.952 0.191 0.880	O 0.047 0.238 0.379
O 0.810 0.191 0.880	O 0.762 0.238 0.379
O 0.381 0.047 0.879	O 0.762 0.096 0.379
O 0.381 0.905 0.879	O 0.048 0.095 0.379
O 0.238 0.762 0.879	O 0.619 0.095 0.379
O 0.238 0.047 0.879	O 0.048 0.524 0.379
O 0.096 0.905 0.879	O 0.333 0.810 0.379
O 0.096 0.762 0.879	O 0.333 0.094 0.379
O 0.095 0.048 0.879	O 0.049 0.810 0.379
O 0.524 0.048 0.879	O 0.476 0.953 0.378
O 0.095 0.619 0.879	O 0.049 0.953 0.378
O 0.094 0.333 0.879	O 0.476 0.094 0.378
O 0.810 0.333 0.879	O 0.190 0.094 0.378
O 0.810 0.049 0.879	O 0.190 0.667 0.378

O 0.049 0.667 0.378	Zn 0.932 0.468 0.502
O 0.906 0.953 0.377	Zn 0.736 0.468 0.502
O 0.619 0.953 0.377	Zn 0.131 0.063 0.502
O 0.190 0.524 0.377	Zn 0.730 0.667 0.502
O 0.906 0.524 0.377	Zn 0.137 0.667 0.502
O 0.190 0.237 0.377	Zn 0.734 0.269 0.501
O 0.619 0.237 0.377	Zn 0.929 0.266 0.500
O 0.763 0.955 0.376	Zn 0.537 0.266 0.500
O 0.763 0.379 0.376	Zn 0.933 0.667 0.500
O 0.187 0.379 0.376	Zn 0.931 0.864 0.498
O 0.907 0.810 0.375	Zn 0.133 0.864 0.498
O 0.475 0.810 0.375	Zn 0.732 0.067 0.497
O 0.907 0.668 0.375	Zn 0.535 0.067 0.497
O 0.475 0.236 0.375	Zn 0.927 0.060 0.496
O 0.332 0.668 0.375	Zn 0.333 0.060 0.496
O 0.332 0.236 0.375	Zn 0.724 0.861 0.496
O 0.765 0.523 0.372	Zn 0.337 0.861 0.496
O 0.620 0.378 0.372	Zn 0.691 0.745 0.031
O 0.329 0.523 0.372	Zn 0.254 0.745 0.031
O 0.765 0.813 0.372	Zn 0.698 0.951 0.027
O 0.620 0.813 0.372	Zn 0.453 0.951 0.027
O 0.329 0.378 0.372	Zn 0.868 0.732 0.002
	Zn 0.064 0.732 0.002
	Zn 0.669 0.137 0.002
Str 92 (WZ-ZnO-NP-6)	Zn 0.663 0.533 0.002
$\Delta E_{\text{gap}}(\text{PBE}_{\text{GW}}\text{-fit}): 0.28 \text{ eV}$	Zn 0.070 0.533 0.002
$E_{\text{rel}}: 0.18 \text{ eV/ZnO}$	Zn 0.066 0.931 0.001
Pore <sub>max</sub> : 0.56 nm	O 0.535 0.467 0.878
V <sub>pore</sub> : 15 %	O 0.132 0.467 0.878
D <sub>pore</sub> : 1	O 0.131 0.063 0.878
cell parameters	O 0.735 0.269 0.878
16.402 16.483 5.335 90.00 90.00	O 0.934 0.469 0.878
119.84	O 0.734 0.469 0.878
fractional coordinates	O 0.734 0.666 0.877
Zn 0.871 0.934 1.000	O 0.132 0.666 0.877
Zn 0.263 0.934 1.000	O 0.932 0.864 0.876
Zn 0.867 0.533 1.000	O 0.131 0.864 0.876
Zn 0.869 0.336 0.998	O 0.933 0.665 0.876
Zn 0.667 0.336 0.998	O 0.935 0.270 0.874
Zn 0.265 0.133 0.997	O 0.535 0.270 0.874
Zn 0.068 0.133 0.997	O 0.736 0.072 0.874
Zn 0.873 0.140 0.996	O 0.535 0.072 0.874
Zn 0.467 0.140 0.996	O 0.931 0.064 0.874
Zn 0.463 0.339 0.996	O 0.333 0.064 0.874
Zn 0.076 0.339 0.996	O 0.336 0.260 0.874
Zn 0.546 0.455 0.531	O 0.124 0.260 0.874
Zn 0.109 0.455 0.531	O 0.733 0.866 0.872
Zn 0.347 0.249 0.527	O 0.333 0.866 0.872
Zn 0.102 0.249 0.527	

O 0.668 0.733 0.378	Zn 0.573 0.842 0.849
O 0.265 0.733 0.378	Zn 0.156 0.510 0.849
O 0.669 0.137 0.378	Zn 0.409 0.006 0.849
O 0.065 0.931 0.378	Zn 0.173 0.641 0.379
O 0.866 0.731 0.378	Zn 0.809 0.005 0.379
O 0.066 0.731 0.378	Zn 0.388 0.172 0.378
O 0.668 0.534 0.377	Zn 0.594 0.966 0.377
O 0.066 0.534 0.377	Zn 0.991 0.374 0.375
O 0.868 0.336 0.376	Zn 0.491 0.837 0.355
O 0.669 0.336 0.376	Zn 0.744 0.831 0.352
O 0.867 0.535 0.376	Zn 0.074 0.510 0.352
O 0.865 0.930 0.374	Zn 0.908 0.675 0.352
O 0.265 0.930 0.374	Zn 0.238 0.336 0.352
O 0.265 0.129 0.374	Zn 0.655 0.174 0.351
O 0.064 0.129 0.374	Zn 0.328 0.501 0.351
O 0.869 0.136 0.374	Zn 0.825 0.498 0.349
O 0.467 0.136 0.374	Zn 0.157 0.166 0.349
O 0.676 0.940 0.374	Zn 0.240 0.837 0.349
O 0.464 0.940 0.374	Zn 0.323 1.000 0.349
O 0.467 0.334 0.372	Zn 0.659 0.664 0.349
O 0.067 0.334 0.372	Zn 0.742 0.336 0.349
	Zn 0.573 0.502 0.348
	Zn 0.410 0.664 0.348
Str 93 (WZ-ZnO-NP-7)	O 0.491 0.836 0.730
$\Delta E_{\text{gap}}(\text{PBE}_{\text{GW}}\text{-fit}): 0.44 \text{ eV}$	O 0.744 0.837 0.726
$E_{\text{rel}}: 0.22 \text{ eV/ZnO}$	O 0.239 0.341 0.726
$\text{Pore}_{\text{max}}: 0.54 \text{ nm}$	O 0.658 0.670 0.726
$V_{\text{pore}}: 15 \%$	O 0.325 0.003 0.726
$D_{\text{pore}}: 1$	O 0.244 0.833 0.725
cell parameters	O 0.906 0.669 0.725
22.855 11.416 5.349 90.01 90.01 60.02	O 0.739 0.338 0.725
fractional coordinates	O 0.823 0.506 0.725
Zn 0.806 0.371 0.878	O 0.157 0.669 0.725
Zn 0.176 0.001 0.878	O 0.076 0.499 0.725
Zn 0.594 0.334 0.877	O 0.573 0.506 0.725
Zn 0.389 0.539 0.877	O 0.409 0.670 0.725
Zn 0.991 0.632 0.875	O 0.160 0.170 0.725
Zn 0.491 0.671 0.855	O 0.401 0.173 0.725
Zn 0.235 0.676 0.852	O 0.825 0.002 0.725
Zn 0.748 0.164 0.851	O 0.581 0.993 0.724
Zn 0.327 0.838 0.851	O 0.321 0.507 0.724
Zn 0.075 0.329 0.851	O 0.661 0.168 0.724
Zn 0.907 0.496 0.851	O 0.991 0.346 0.723
Zn 0.656 0.509 0.851	O 0.491 0.672 0.229
Zn 0.658 0.004 0.849	O 0.326 0.834 0.226
Zn 0.324 0.338 0.849	O 0.741 0.671 0.226
Zn 0.827 0.840 0.849	O 0.242 0.170 0.226
Zn 0.243 0.173 0.849	O 0.574 0.835 0.226
Zn 0.739 0.677 0.849	

O	0.657	0.504	0.226	Zn	0.779	0.221	0.502
O	0.408	0.001	0.226	Zn	0.779	0.057	0.502
O	0.906	0.506	0.225	Zn	0.277	0.889	0.501
O	0.077	0.335	0.225	Zn	0.111	0.889	0.501
O	0.661	0.001	0.225	Zn	0.111	0.723	0.501
O	0.321	0.341	0.225	Zn	0.946	0.723	0.501
O	0.820	0.343	0.225	Zn	0.277	0.723	0.501
O	0.162	0.001	0.225	Zn	0.277	0.054	0.501
O	0.241	0.670	0.225	Zn	0.946	0.891	0.498
O	0.741	0.171	0.224	Zn	0.946	0.555	0.498
O	0.825	0.837	0.224	Zn	0.445	0.891	0.498
O	0.157	0.505	0.224	Zn	0.445	0.054	0.498
O	0.579	0.337	0.223	Zn	0.109	0.555	0.498
O	0.991	0.660	0.223	Zn	0.109	0.054	0.498
O	0.404	0.510	0.223	Zn	0.944	0.389	0.498
				Zn	0.944	0.056	0.498
				Zn	0.611	0.056	0.498
Str 94 (WZ-ZnO-NP-8)				Zn	0.776	0.890	0.498
$\Delta E_{\text{gap}}(\text{PBE}_{\text{GW}}\text{-fit}): 0.38 \text{ eV}$				Zn	0.776	0.386	0.498
$E_{\text{rel}}: 0.18 \text{ eV/ZnO}$				Zn	0.614	0.890	0.498
Pore <sub>max</sub> : 0.78 nm				Zn	0.614	0.224	0.498
V <sub>pore</sub> : 16 %				Zn	0.110	0.386	0.498
D <sub>pore</sub> : 1				Zn	0.110	0.224	0.498
cell parameters				Zn	0.746	0.789	0.025
19.795 19.795 5.331 90.00 90.00				Zn	0.746	0.458	0.025
120.00				Zn	0.542	0.789	0.025
fractional coordinates				Zn	0.542	0.254	0.025
Zn 0.891 0.946 0.998				Zn	0.211	0.458	0.025
Zn 0.891 0.445 0.998				Zn	0.211	0.254	0.025
Zn 0.555 0.946 0.998				Zn	0.221	0.943	0.002
Zn 0.555 0.109 0.998				Zn	0.221	0.779	0.002
Zn 0.054 0.445 0.998				Zn	0.057	0.779	0.002
Zn 0.054 0.109 0.998				Zn	0.889	0.277	0.001
Zn 0.389 0.944 0.998				Zn	0.889	0.111	0.001
Zn 0.056 0.944 0.998				Zn	0.723	0.111	0.001
Zn 0.056 0.611 0.998				Zn	0.723	0.946	0.001
Zn 0.890 0.776 0.998				Zn	0.723	0.277	0.001
Zn 0.890 0.614 0.998				Zn	0.054	0.277	0.001
Zn 0.386 0.776 0.998				O	0.943	0.222	0.879
Zn 0.386 0.110 0.998				O	0.778	0.222	0.879
Zn 0.224 0.614 0.998				O	0.778	0.057	0.879
Zn 0.224 0.110 0.998				O	0.278	0.889	0.879
Zn 0.789 0.746 0.525				O	0.111	0.889	0.879
Zn 0.789 0.542 0.525				O	0.111	0.722	0.879
Zn 0.458 0.746 0.525				O	0.948	0.724	0.877
Zn 0.458 0.211 0.525				O	0.276	0.724	0.877
Zn 0.254 0.542 0.525				O	0.276	0.052	0.877
Zn 0.254 0.211 0.525				O	0.945	0.890	0.876
Zn 0.943 0.221 0.502							

O 0.945 0.556 0.876  
 O 0.444 0.890 0.876  
 O 0.444 0.055 0.876  
 O 0.110 0.556 0.876  
 O 0.110 0.055 0.876  
 O 0.944 0.388 0.876  
 O 0.944 0.056 0.876  
 O 0.612 0.056 0.876  
 O 0.779 0.892 0.875  
 O 0.779 0.387 0.875  
 O 0.613 0.892 0.875  
 O 0.613 0.221 0.875  
 O 0.108 0.387 0.875  
 O 0.108 0.221 0.875  
 O 0.783 0.727 0.872  
 O 0.783 0.556 0.872  
 O 0.444 0.727 0.872  
 O 0.444 0.217 0.872  
 O 0.273 0.556 0.872  
 O 0.273 0.217 0.872  
 O 0.222 0.943 0.379  
 O 0.222 0.778 0.379  
 O 0.057 0.778 0.379  
 O 0.889 0.278 0.379  
 O 0.889 0.111 0.379  
 O 0.722 0.111 0.379  
 O 0.724 0.948 0.377  
 O 0.724 0.276 0.377  
 O 0.052 0.276 0.377  
 O 0.890 0.945 0.376  
 O 0.890 0.444 0.376  
 O 0.556 0.945 0.376  
 O 0.556 0.110 0.376  
 O 0.055 0.444 0.376  
 O 0.055 0.110 0.376  
 O 0.388 0.944 0.376  
 O 0.056 0.944 0.376  
 O 0.056 0.612 0.376  
 O 0.892 0.779 0.375  
 O 0.892 0.613 0.375  
 O 0.387 0.779 0.375  
 O 0.387 0.108 0.375  
 O 0.221 0.613 0.375  
 O 0.221 0.108 0.375  
 O 0.727 0.783 0.372  
 O 0.727 0.444 0.372  
 O 0.556 0.783 0.372  
 O 0.556 0.273 0.372

O 0.217 0.444 0.372  
 O 0.217 0.273 0.372

Str 95 (WZ-ZnO-NP-9)

$\Delta E_{\text{gap}}(\text{PBE}_{\text{GW-fit}})$ : 0.44 eV

$E_{\text{rel}}$ : 0.21 eV/ZnO

Pore<sub>max</sub>: 0.52 nm

$V_{\text{pore}}$ : 16 %

$D_{\text{pore}}$ : 1

cell parameters

13.109 13.109 5.345 90.00 90.00

120.00

fractional coordinates

Zn 0.587 0.671 0.998

Zn 0.329 0.915 0.998

Zn 0.586 0.915 0.998

Zn 0.329 0.413 0.998

Zn 0.085 0.671 0.998

Zn 0.085 0.414 0.998

Zn 0.333 0.667 0.996

Zn 0.180 0.820 0.528

Zn 0.639 0.820 0.528

Zn 0.180 0.361 0.528

Zn 0.417 0.583 0.501

Zn 0.417 0.834 0.501

Zn 0.166 0.583 0.501

Zn 0.414 0.085 0.498

Zn 0.413 0.329 0.498

Zn 0.915 0.586 0.498

Zn 0.671 0.587 0.498

Zn 0.671 0.085 0.498

Zn 0.915 0.329 0.498

Zn 0.667 0.333 0.496

Zn 0.361 0.180 0.028

Zn 0.820 0.639 0.028

Zn 0.820 0.180 0.028

Zn 0.583 0.417 0.001

Zn 0.583 0.166 0.001

Zn 0.834 0.417 0.001

O 0.417 0.583 0.876

O 0.165 0.583 0.876

O 0.417 0.835 0.876

O 0.667 0.333 0.876

O 0.167 0.833 0.875

O 0.666 0.833 0.875

O 0.167 0.334 0.875

O 0.917 0.584 0.874

O 0.416 0.083 0.874

O 0.416 0.334 0.874  
 O 0.666 0.584 0.874  
 O 0.666 0.083 0.874  
 O 0.917 0.334 0.874  
 O 0.835 0.417 0.376  
 O 0.583 0.417 0.376  
 O 0.583 0.165 0.376  
 O 0.333 0.667 0.376  
 O 0.334 0.167 0.375  
 O 0.833 0.666 0.375  
 O 0.833 0.167 0.375  
 O 0.334 0.917 0.374  
 O 0.083 0.666 0.374  
 O 0.584 0.666 0.374  
 O 0.584 0.917 0.374  
 O 0.334 0.416 0.374  
 O 0.083 0.416 0.374

Str 96 (WZ-ZnO-NP-10)

$\Delta E_{\text{gap}}(\text{PBE}_{\text{GW-fit}})$ : 0.48 eV

$E_{\text{rel}}$ : 0.25 eV/ZnO

Pore<sub>max</sub>: 0.57 nm

V<sub>pore</sub>: 20 %

D<sub>pore</sub>: 1

cell parameters

13.172 26.428 5.356 90.00 90.01

119.92

fractional coordinates

Zn 0.181 0.690 0.882

Zn 0.928 0.690 0.881

Zn 0.923 0.411 0.879

Zn 0.633 0.915 0.879

Zn 0.176 0.914 0.878

Zn 0.183 0.193 0.869

Zn 0.187 0.535 0.866

Zn 0.165 0.799 0.853

Zn 0.907 0.292 0.852

Zn 0.912 0.802 0.852

Zn 0.415 0.798 0.852

Zn 0.664 0.674 0.851

Zn 0.412 0.923 0.851

Zn 0.659 0.296 0.851

Zn 0.415 0.674 0.851

Zn 0.159 0.298 0.851

Zn 0.668 0.800 0.851

Zn 0.908 0.167 0.849

Zn 0.164 0.419 0.849

Zn 0.664 0.046 0.849

Zn 0.407 0.047 0.849

Zn 0.422 0.304 0.848

Zn 0.658 0.169 0.847

Zn 0.410 0.170 0.847

Zn 0.426 0.547 0.847

Zn 0.563 0.321 0.382

Zn 0.566 0.600 0.380

Zn 0.810 0.095 0.379

Zn 0.359 0.096 0.378

Zn 0.815 0.824 0.378

Zn 0.304 0.316 0.375

Zn 0.302 0.476 0.367

Zn 0.578 0.717 0.354

Zn 0.582 0.212 0.353

Zn 0.831 0.712 0.353

Zn 0.827 0.339 0.353

Zn 0.575 0.086 0.352

Zn 0.826 0.213 0.352

Zn 0.074 0.338 0.351

Zn 0.322 0.208 0.351

Zn 0.071 0.209 0.350

Zn 0.584 0.842 0.350

Zn 0.328 0.715 0.349

Zn 0.324 0.593 0.349

Zn 0.580 0.962 0.349

Zn 0.323 0.962 0.349

Zn 0.080 0.840 0.347

Zn 0.075 0.710 0.347

Zn 0.064 0.464 0.347

Zn 0.329 0.839 0.345

O 0.581 0.717 0.728

O 0.579 0.212 0.727

O 0.580 0.337 0.727

O 0.072 0.337 0.727

O 0.825 0.211 0.727

O 0.575 0.086 0.726

O 0.826 0.335 0.726

O 0.831 0.717 0.726

O 0.584 0.594 0.725

O 0.824 0.088 0.725

O 0.333 0.090 0.725

O 0.332 0.715 0.725

O 0.330 0.839 0.725

O 0.580 0.840 0.724

O 0.078 0.838 0.724

O 0.828 0.839 0.724

O 0.328 0.964 0.724

O 0.079 0.714 0.724

O	0.577	0.963	0.724	Zn	0.464	0.663	0.879
O	0.073	0.213	0.724	Zn	0.189	0.663	0.879
O	0.317	0.330	0.723	Zn	0.215	0.914	0.877
O	0.333	0.214	0.721	Zn	0.688	0.914	0.877
O	0.334	0.592	0.720	Zn	0.078	0.670	0.853
O	0.072	0.462	0.719	Zn	0.581	0.670	0.852
O	0.317	0.471	0.717	Zn	0.955	0.673	0.852
O	0.908	0.295	0.228	Zn	0.707	0.673	0.852
O	0.168	0.677	0.227	Zn	0.330	0.296	0.852
O	0.665	0.676	0.227	Zn	0.955	0.296	0.852
O	0.415	0.799	0.226	Zn	0.208	0.795	0.852
O	0.661	0.294	0.226	Zn	0.576	0.795	0.852
O	0.162	0.797	0.226	Zn	0.079	0.545	0.851
O	0.414	0.674	0.226	Zn	0.455	0.545	0.851
O	0.659	0.169	0.226	Zn	0.333	0.423	0.851
O	0.412	0.922	0.226	Zn	0.207	0.425	0.851
O	0.915	0.675	0.226	Zn	0.080	0.423	0.851
O	0.660	0.922	0.225	Zn	0.329	0.048	0.851
O	0.162	0.920	0.225	Zn	0.333	0.921	0.851
O	0.663	0.799	0.225	Zn	0.708	0.048	0.851
O	0.913	0.797	0.225	Zn	0.578	0.921	0.851
O	0.154	0.295	0.225	Zn	0.583	0.049	0.850
O	0.906	0.418	0.225	Zn	0.456	0.049	0.850
O	0.907	0.170	0.224	Zn	0.330	0.548	0.850
O	0.409	0.045	0.224	Zn	0.207	0.548	0.850
O	0.414	0.172	0.224	Zn	0.706	0.422	0.850
O	0.659	0.045	0.224	Zn	0.581	0.297	0.850
O	0.413	0.297	0.221	Zn	0.706	0.297	0.850
O	0.155	0.419	0.221	Zn	0.581	0.422	0.850
O	0.417	0.550	0.219	Zn	0.581	0.172	0.849
O	0.167	0.178	0.217	Zn	0.830	0.422	0.849
O	0.172	0.540	0.215	Zn	0.456	0.422	0.849
				Zn	0.955	0.422	0.849
Str 97 (WZ-ZnO-NP-11)				Zn	0.955	0.546	0.849
$\Delta E_{\text{gap}}(\text{PBE}_{\text{GW}}\text{-fit}): 0.37 \text{ eV}$				Zn	0.581	0.546	0.849
$E_{\text{rel}}: 0.16 \text{ eV/ZnO}$				Zn	0.326	0.170	0.849
Pore <sub>max</sub> : 1.12 nm				Zn	0.833	0.677	0.849
V <sub>pore</sub> : 22 %				Zn	0.834	0.170	0.848
D <sub>pore</sub> : 1				Zn	0.831	0.548	0.848
cell parameters				Zn	0.706	0.548	0.848
26.269 26.317 5.335 90.01 90.00				Zn	0.831	0.296	0.848
119.94				Zn	0.455	0.172	0.848
fractional coordinates				Zn	0.455	0.296	0.848
Zn 0.088 0.313 0.882				Zn	0.707	0.172	0.848
Zn 0.215 0.313 0.882				Zn	0.305	0.097	0.383
Zn 0.087 0.788 0.881				Zn	0.781	0.097	0.383
Zn 0.691 0.788 0.881				Zn	0.305	0.223	0.383
Zn 0.464 0.938 0.880				Zn	0.907	0.223	0.383

Zn 0.907 0.697 0.382	O 0.914 0.216 0.729
Zn 0.780 0.697 0.382	O 0.914 0.712 0.729
Zn 0.280 0.571 0.377	O 0.787 0.712 0.729
Zn 0.560 0.848 0.372	O 0.664 0.339 0.728
Zn 0.278 0.848 0.372	O 0.789 0.464 0.728
Zn 0.788 0.586 0.352	O 0.789 0.339 0.728
Zn 0.288 0.966 0.352	O 0.664 0.464 0.728
Zn 0.668 0.966 0.352	O 0.664 0.214 0.728
Zn 0.288 0.337 0.352	O 0.539 0.339 0.728
Zn 0.039 0.337 0.352	O 0.539 0.214 0.728
Zn 0.417 0.215 0.352	O 0.914 0.588 0.727
Zn 0.788 0.215 0.352	O 0.789 0.589 0.727
Zn 0.416 0.341 0.352	O 0.663 0.588 0.727
Zn 0.914 0.586 0.352	O 0.914 0.339 0.727
Zn 0.914 0.341 0.352	O 0.414 0.339 0.727
Zn 0.662 0.586 0.352	O 0.290 0.340 0.727
Zn 0.416 0.089 0.351	O 0.039 0.340 0.727
Zn 0.662 0.089 0.351	O 0.414 0.214 0.727
Zn 0.039 0.715 0.351	O 0.790 0.214 0.727
Zn 0.665 0.715 0.351	O 0.539 0.089 0.727
Zn 0.789 0.463 0.351	O 0.163 0.463 0.727
Zn 0.664 0.463 0.351	O 0.290 0.463 0.727
Zn 0.664 0.339 0.350	O 0.414 0.089 0.727
Zn 0.789 0.339 0.350	O 0.291 0.965 0.726
Zn 0.540 0.339 0.350	O 0.665 0.089 0.726
Zn 0.539 0.214 0.350	O 0.539 0.463 0.726
Zn 0.664 0.214 0.350	O 0.664 0.965 0.726
Zn 0.539 0.463 0.350	O 0.913 0.463 0.726
Zn 0.913 0.464 0.350	O 0.038 0.712 0.726
Zn 0.414 0.590 0.350	O 0.664 0.712 0.726
Zn 0.165 0.590 0.349	O 0.039 0.588 0.726
Zn 0.537 0.962 0.349	O 0.538 0.588 0.726
Zn 0.414 0.962 0.349	O 0.414 0.587 0.726
Zn 0.539 0.088 0.349	O 0.163 0.587 0.726
Zn 0.289 0.460 0.349	O 0.540 0.713 0.725
Zn 0.161 0.460 0.349	O 0.162 0.713 0.725
Zn 0.158 0.841 0.348	O 0.287 0.585 0.725
Zn 0.162 0.334 0.348	O 0.415 0.463 0.725
Zn 0.673 0.841 0.348	O 0.164 0.339 0.725
Zn 0.415 0.464 0.348	O 0.038 0.463 0.725
Zn 0.039 0.464 0.348	O 0.540 0.965 0.725
Zn 0.040 0.589 0.348	O 0.415 0.965 0.725
Zn 0.538 0.589 0.348	O 0.162 0.838 0.723
Zn 0.538 0.713 0.348	O 0.665 0.838 0.723
Zn 0.165 0.713 0.348	O 0.286 0.842 0.720
O 0.291 0.216 0.729	O 0.545 0.842 0.720
O 0.291 0.090 0.729	O 0.081 0.299 0.229
O 0.788 0.090 0.729	O 0.208 0.299 0.229

O 0.706 0.422 0.228  
 O 0.706 0.297 0.228  
 O 0.581 0.297 0.228  
 O 0.079 0.671 0.228  
 O 0.581 0.671 0.227  
 O 0.581 0.172 0.227  
 O 0.206 0.422 0.227  
 O 0.457 0.671 0.227  
 O 0.203 0.671 0.227  
 O 0.581 0.422 0.227  
 O 0.956 0.299 0.227  
 O 0.078 0.795 0.227  
 O 0.332 0.299 0.227  
 O 0.830 0.422 0.227  
 O 0.706 0.795 0.227  
 O 0.831 0.547 0.227  
 O 0.705 0.547 0.227  
 O 0.079 0.421 0.227  
 O 0.704 0.670 0.227  
 O 0.332 0.421 0.227  
 O 0.955 0.670 0.227  
 O 0.081 0.546 0.227  
 O 0.455 0.546 0.227  
 O 0.456 0.924 0.226  
 O 0.831 0.298 0.226  
 O 0.456 0.172 0.226  
 O 0.705 0.172 0.226  
 O 0.456 0.047 0.226  
 O 0.332 0.048 0.226  
 O 0.706 0.048 0.226  
 O 0.456 0.298 0.226  
 O 0.580 0.047 0.226  
 O 0.956 0.546 0.226  
 O 0.331 0.545 0.226  
 O 0.204 0.545 0.226  
 O 0.580 0.546 0.226  
 O 0.457 0.423 0.226  
 O 0.955 0.423 0.225  
 O 0.208 0.921 0.225  
 O 0.702 0.920 0.225  
 O 0.830 0.671 0.225  
 O 0.331 0.924 0.225  
 O 0.582 0.924 0.225  
 O 0.331 0.173 0.225  
 O 0.831 0.173 0.225  
 O 0.583 0.796 0.224  
 O 0.202 0.796 0.224

Str 98 (WZ-ZnO-NP-12)  
 $\Delta E_{\text{gap}}(\text{PBE}_{\text{GW-fit}})$ : 0.33 eV  
 $E_{\text{rel}}$ : 0.15 eV/ZnO  
 $\text{Pore}_{\text{max}}$ : 1.12 nm  
 $V_{\text{pore}}$ : 23 %  
 $D_{\text{pore}}$ : 1  
 cell parameters  
 22.980 22.980 5.327 90.00 90.00  
 120.00  
 fractional coordinates  
 Zn 0.905 0.238 0.998  
 Zn 0.620 0.096 0.997  
 Zn 0.047 0.523 0.997  
 Zn 0.047 0.096 0.997  
 Zn 0.904 0.381 0.997  
 Zn 0.904 0.094 0.997  
 Zn 0.762 0.239 0.997  
 Zn 0.762 0.094 0.997  
 Zn 0.049 0.381 0.997  
 Zn 0.049 0.239 0.997  
 Zn 0.759 0.946 0.996  
 Zn 0.759 0.384 0.996  
 Zn 0.197 0.384 0.996  
 Zn 0.819 0.922 0.530  
 Zn 0.819 0.468 0.530  
 Zn 0.675 0.922 0.530  
 Zn 0.675 0.324 0.530  
 Zn 0.221 0.468 0.530  
 Zn 0.221 0.324 0.530  
 Zn 0.811 0.332 0.501  
 Zn 0.811 0.050 0.501  
 Zn 0.093 0.332 0.501  
 Zn 0.954 0.476 0.501  
 Zn 0.954 0.049 0.501  
 Zn 0.666 0.189 0.501  
 Zn 0.666 0.049 0.501  
 Zn 0.094 0.476 0.501  
 Zn 0.094 0.189 0.501  
 Zn 0.951 0.903 0.500  
 Zn 0.951 0.620 0.500  
 Zn 0.523 0.903 0.500  
 Zn 0.523 0.192 0.500  
 Zn 0.240 0.620 0.500  
 Zn 0.240 0.192 0.500  
 Zn 0.952 0.333 0.500  
 Zn 0.952 0.191 0.500  
 Zn 0.810 0.191 0.500  
 Zn 0.238 0.905 0.498

Zn 0.523 0.047 0.497	O 0.666 0.190 0.876
Zn 0.096 0.620 0.497	O 0.666 0.048 0.876
Zn 0.096 0.047 0.497	O 0.095 0.476 0.876
Zn 0.381 0.904 0.497	O 0.095 0.190 0.876
Zn 0.381 0.049 0.497	O 0.809 0.334 0.876
Zn 0.239 0.762 0.497	O 0.809 0.046 0.876
Zn 0.239 0.049 0.497	O 0.096 0.334 0.876
Zn 0.094 0.904 0.497	O 0.381 0.905 0.876
Zn 0.094 0.762 0.497	O 0.381 0.048 0.876
Zn 0.946 0.759 0.496	O 0.238 0.762 0.876
Zn 0.384 0.759 0.496	O 0.238 0.048 0.876
Zn 0.384 0.197 0.496	O 0.095 0.905 0.876
Zn 0.922 0.819 0.030	O 0.095 0.762 0.876
Zn 0.922 0.675 0.030	O 0.953 0.906 0.876
Zn 0.468 0.819 0.030	O 0.953 0.619 0.876
Zn 0.468 0.221 0.030	O 0.524 0.906 0.876
Zn 0.324 0.675 0.030	O 0.524 0.189 0.876
Zn 0.324 0.221 0.030	O 0.237 0.619 0.876
Zn 0.332 0.811 0.001	O 0.237 0.189 0.876
Zn 0.332 0.093 0.001	O 0.525 0.048 0.874
Zn 0.050 0.811 0.001	O 0.095 0.618 0.874
Zn 0.476 0.954 0.001	O 0.095 0.048 0.874
Zn 0.476 0.094 0.001	O 0.952 0.762 0.874
Zn 0.189 0.666 0.001	O 0.381 0.762 0.874
Zn 0.189 0.094 0.001	O 0.381 0.191 0.874
Zn 0.049 0.954 0.001	O 0.334 0.953 0.378
Zn 0.049 0.666 0.001	O 0.190 0.953 0.378
Zn 0.903 0.951 0.000	O 0.190 0.809 0.378
Zn 0.903 0.523 0.000	O 0.906 0.811 0.378
Zn 0.620 0.951 0.000	O 0.906 0.666 0.378
Zn 0.620 0.240 0.000	O 0.476 0.811 0.378
Zn 0.192 0.523 0.000	O 0.476 0.237 0.378
Zn 0.192 0.240 0.000	O 0.332 0.666 0.378
Zn 0.333 0.952 0.000	O 0.332 0.237 0.378
Zn 0.191 0.952 0.000	O 0.905 0.238 0.377
Zn 0.191 0.810 0.000	O 0.476 0.953 0.377
O 0.953 0.334 0.878	O 0.476 0.095 0.377
O 0.953 0.190 0.878	O 0.190 0.666 0.377
O 0.809 0.190 0.878	O 0.190 0.095 0.377
O 0.811 0.906 0.878	O 0.048 0.953 0.377
O 0.811 0.476 0.878	O 0.048 0.666 0.377
O 0.666 0.906 0.878	O 0.334 0.809 0.376
O 0.666 0.332 0.878	O 0.334 0.096 0.376
O 0.237 0.476 0.878	O 0.046 0.809 0.376
O 0.237 0.332 0.878	O 0.905 0.381 0.376
O 0.238 0.905 0.877	O 0.905 0.095 0.376
O 0.953 0.476 0.876	O 0.762 0.238 0.376
O 0.953 0.048 0.876	O 0.762 0.095 0.376

O	0.048	0.381	0.376	Zn	0.941	0.886	0.502
O	0.048	0.238	0.376	Zn	0.281	0.225	0.502
O	0.906	0.953	0.376	Zn	0.275	0.891	0.502
O	0.906	0.524	0.376	Zn	0.946	0.221	0.500
O	0.619	0.953	0.376	Zn	0.781	0.058	0.500
O	0.619	0.237	0.376	Zn	0.109	0.386	0.500
O	0.189	0.524	0.376	Zn	0.111	0.056	0.499
O	0.189	0.237	0.376	Zn	0.944	0.386	0.498
O	0.618	0.095	0.374	Zn	0.780	0.223	0.498
O	0.048	0.525	0.374	Zn	0.935	0.718	0.498
O	0.048	0.095	0.374	Zn	0.448	0.232	0.498
O	0.762	0.952	0.374	Zn	0.277	0.058	0.497
O	0.762	0.381	0.374	Zn	0.109	0.889	0.497
O	0.191	0.381	0.374	Zn	0.104	0.552	0.497
				Zn	0.615	0.063	0.497
				Zn	0.939	0.552	0.496
				Zn	0.614	0.228	0.496
				Zn	0.105	0.723	0.495
				Zn	0.444	0.062	0.495
				Zn	0.909	0.788	0.032
				Zn	0.379	0.258	0.032
				Zn	0.912	0.621	0.032
				Zn	0.545	0.255	0.032
				Zn	0.917	0.456	0.027
				Zn	0.711	0.250	0.027
				Zn	0.220	0.111	0.002
				Zn	0.056	0.947	0.002
				Zn	0.886	0.941	0.002
				Zn	0.225	0.281	0.002
				Zn	0.891	0.275	0.002
				Zn	0.221	0.946	0.000
				O	0.779	0.889	0.878
				O	0.277	0.388	0.878
				O	0.945	0.054	0.877
				O	0.113	0.221	0.877
				O	0.612	0.893	0.877
				O	0.274	0.555	0.877
				O	0.275	0.891	0.877
				O	0.944	0.889	0.877
				O	0.277	0.222	0.877
				O	0.946	0.221	0.877
				O	0.110	0.056	0.875
				O	0.276	0.057	0.875
				O	0.110	0.891	0.875
				O	0.779	0.052	0.874
				O	0.114	0.388	0.874
				O	0.947	0.386	0.874
				O	0.780	0.219	0.874

Str 99 (WZ-ZnO-NP-13)  
 $\Delta E_{\text{gap}}(\text{PBE}_{\text{GW-fit}})$ : 0.36 eV  
 $E_{\text{rel}}$ : 0.21 eV/ZnO  
Pore<sub>max</sub>: 0.94 nm  
V<sub>pore</sub>: 24 %  
D<sub>pore</sub>: 1  
cell parameters  
19.810 19.810 5.342 90.00 90.00  
120.51  
fractional coordinates  
Zn 0.386 0.109 1.000  
Zn 0.058 0.781 1.000  
Zn 0.056 0.111 0.999  
Zn 0.386 0.944 0.998  
Zn 0.223 0.780 0.998  
Zn 0.718 0.935 0.998  
Zn 0.232 0.448 0.998  
Zn 0.058 0.277 0.997  
Zn 0.889 0.109 0.997  
Zn 0.552 0.104 0.997  
Zn 0.063 0.615 0.997  
Zn 0.552 0.939 0.996  
Zn 0.228 0.614 0.996  
Zn 0.723 0.105 0.995  
Zn 0.062 0.444 0.995  
Zn 0.788 0.909 0.532  
Zn 0.258 0.379 0.532  
Zn 0.621 0.912 0.531  
Zn 0.255 0.545 0.531  
Zn 0.456 0.917 0.527  
Zn 0.250 0.711 0.527  
Zn 0.947 0.056 0.502  
Zn 0.111 0.220 0.502

O	0.943	0.722	0.874	Zn	0.827	0.409	1.000
O	0.445	0.224	0.874	Zn	0.591	0.173	1.000
O	0.447	0.899	0.873	Zn	0.336	0.664	0.999
O	0.268	0.720	0.873	Zn	0.598	0.919	0.997
O	0.442	0.058	0.873	Zn	0.081	0.402	0.997
O	0.109	0.724	0.873	Zn	0.184	0.364	0.530
O	0.110	0.554	0.872	Zn	0.636	0.816	0.530
O	0.613	0.057	0.872	Zn	0.939	0.382	0.518
O	0.947	0.556	0.872	Zn	0.618	0.061	0.518
O	0.611	0.220	0.872	Zn	0.419	0.581	0.505
O	0.889	0.779	0.378	Zn	0.669	0.586	0.502
O	0.388	0.277	0.378	Zn	0.414	0.331	0.502
O	0.221	0.112	0.377	Zn	0.409	0.827	0.500
O	0.054	0.945	0.377	Zn	0.173	0.591	0.500
O	0.893	0.612	0.377	Zn	0.664	0.336	0.499
O	0.555	0.274	0.377	Zn	0.402	0.081	0.497
O	0.891	0.275	0.377	Zn	0.919	0.598	0.497
O	0.889	0.944	0.377	Zn	0.364	0.184	0.030
O	0.222	0.277	0.377	Zn	0.816	0.636	0.030
O	0.221	0.946	0.377	Zn	0.382	0.939	0.018
O	0.056	0.110	0.375	Zn	0.061	0.618	0.018
O	0.057	0.276	0.375	Zn	0.581	0.419	0.005
O	0.891	0.110	0.375	Zn	0.586	0.669	0.002
O	0.388	0.114	0.374	Zn	0.331	0.414	0.002
O	0.052	0.779	0.374	O	0.419	0.581	0.878
O	0.386	0.947	0.374	O	0.665	0.582	0.876
O	0.219	0.780	0.374	O	0.418	0.335	0.876
O	0.722	0.943	0.374	O	0.664	0.336	0.875
O	0.224	0.445	0.374	O	0.172	0.336	0.875
O	0.899	0.447	0.373	O	0.664	0.828	0.875
O	0.720	0.268	0.373	O	0.418	0.828	0.870
O	0.058	0.442	0.373	O	0.172	0.582	0.870
O	0.724	0.109	0.373	O	0.415	0.086	0.869
O	0.554	0.110	0.372	O	0.914	0.585	0.869
O	0.057	0.613	0.372	O	0.928	0.357	0.866
O	0.556	0.947	0.372	O	0.643	0.072	0.866
O	0.220	0.611	0.372	O	0.581	0.419	0.378
				O	0.335	0.418	0.376
				O	0.582	0.665	0.376
				O	0.336	0.664	0.375
				O	0.828	0.664	0.375
				O	0.336	0.172	0.375
				O	0.828	0.418	0.370
				O	0.582	0.172	0.370
				O	0.086	0.415	0.369
				O	0.585	0.914	0.369
				O	0.357	0.928	0.366
				O	0.072	0.643	0.366
Str 100 (WZ-ZnO-NP-14)							
$\Delta E_{\text{gap}}(\text{PBE}_{\text{GW-fit}})$ : 0.58 eV							
$E_{\text{rel}}$ : 0.29 eV/ZnO							
Pore <sub>max</sub> : 0.57 nm							
V <sub>pore</sub> : 24 %							
D <sub>pore</sub> : 1							
cell parameters							
13.242 13.242 5.374 90.00 90.00							
119.71							
fractional coordinates							

Str 101 (WZ-ZnO-NP-15)  
 $\Delta E_{\text{gap}}(\text{PBE}_{\text{GW-fit}})$ : 0.72 eV  
 $E_{\text{rel}}$ : 0.28 eV/ZnO  
Pore<sub>max</sub>: 0.56 nm  
V<sub>pore</sub>: 25 %  
D<sub>pore</sub>: 1  
cell parameters  
11.516 11.520 5.365 89.99 90.03  
119.99  
fractional coordinates  
Zn 0.312 0.000 0.565  
Zn 0.937 0.376 0.564  
Zn 0.561 0.625 0.564  
Zn 0.430 0.326 0.540  
Zn 0.611 0.168 0.540  
Zn 0.104 0.674 0.540  
Zn 0.263 0.494 0.540  
Zn 0.769 0.506 0.540  
Zn 0.443 0.833 0.540  
Zn 0.561 1.000 0.064  
Zn 0.312 0.375 0.064  
Zn 0.936 0.625 0.064  
Zn 0.430 0.167 0.041  
Zn 0.263 0.833 0.040  
Zn 0.610 0.506 0.040  
Zn 0.104 0.494 0.040  
Zn 0.769 0.326 0.040  
Zn 0.443 0.674 0.040  
O 0.440 0.334 0.914  
O 0.106 0.666 0.914  
O 0.602 0.169 0.914  
O 0.270 0.504 0.913  
O 0.767 0.496 0.913  
O 0.433 0.831 0.913  
O 0.284 0.000 0.912  
O 0.936 0.348 0.912  
O 0.588 0.652 0.912  
O 0.440 0.169 0.414  
O 0.271 0.831 0.414  
O 0.602 0.496 0.413  
O 0.106 0.504 0.413  
O 0.767 0.334 0.413  
O 0.433 0.666 0.413  
O 0.589 0.000 0.412  
O 0.284 0.348 0.412  
O 0.936 0.652 0.411

Str 102 (WZ-ZnO-NP-16)  
 $\Delta E_{\text{gap}}(\text{PBE}_{\text{GW-fit}})$ : 0.39 eV  
 $E_{\text{rel}}$ : 0.20 eV/ZnO  
Pore<sub>max</sub>: 1.12 nm  
V<sub>pore</sub>: 25 %  
D<sub>pore</sub>: 1  
cell parameters  
23.039 23.062 5.342 89.99 90.00  
119.97  
fractional coordinates  
Zn 0.100 0.357 0.882  
Zn 0.244 0.357 0.882  
Zn 0.098 0.759 0.881  
Zn 0.648 0.758 0.881  
Zn 0.390 0.614 0.877  
Zn 0.212 0.614 0.877  
Zn 0.246 0.901 0.874  
Zn 0.643 0.901 0.874  
Zn 0.236 0.485 0.855  
Zn 0.087 0.623 0.853  
Zn 0.523 0.622 0.853  
Zn 0.089 0.481 0.852  
Zn 0.380 0.481 0.852  
Zn 0.948 0.337 0.852  
Zn 0.947 0.626 0.852  
Zn 0.666 0.626 0.851  
Zn 0.377 0.337 0.851  
Zn 0.235 0.766 0.851  
Zn 0.518 0.766 0.851  
Zn 0.666 0.055 0.851  
Zn 0.377 0.055 0.851  
Zn 0.521 0.055 0.850  
Zn 0.380 0.910 0.849  
Zn 0.518 0.910 0.849  
Zn 0.948 0.482 0.849  
Zn 0.521 0.482 0.849  
Zn 0.809 0.195 0.848  
Zn 0.664 0.340 0.848  
Zn 0.373 0.195 0.848  
Zn 0.809 0.630 0.848  
Zn 0.664 0.197 0.847  
Zn 0.807 0.339 0.847  
Zn 0.521 0.197 0.847  
Zn 0.520 0.339 0.847  
Zn 0.664 0.483 0.847  
Zn 0.806 0.483 0.847  
Zn 0.750 0.112 0.383  
Zn 0.350 0.112 0.383

Zn 0.893 0.254 0.382	O 0.473 0.245 0.727
Zn 0.349 0.254 0.382	O 0.473 0.387 0.727
Zn 0.749 0.654 0.382	O 0.902 0.529 0.727
Zn 0.893 0.654 0.381	O 0.616 0.529 0.727
Zn 0.315 0.828 0.369	O 0.759 0.530 0.726
Zn 0.501 0.828 0.369	O 0.042 0.672 0.726
Zn 0.476 0.102 0.352	O 0.331 0.386 0.726
Zn 0.614 0.102 0.352	O 0.617 0.671 0.726
Zn 0.757 0.247 0.352	O 0.044 0.386 0.726
Zn 0.477 0.247 0.352	O 0.617 0.961 0.726
Zn 0.473 0.958 0.352	O 0.332 0.961 0.726
Zn 0.329 0.962 0.352	O 0.044 0.529 0.725
Zn 0.621 0.962 0.352	O 0.187 0.387 0.725
Zn 0.757 0.526 0.352	O 0.473 0.529 0.725
Zn 0.902 0.389 0.351	O 0.186 0.528 0.724
Zn 0.902 0.528 0.351	O 0.183 0.672 0.724
Zn 0.475 0.389 0.351	O 0.476 0.672 0.724
Zn 0.614 0.528 0.351	O 0.330 0.528 0.724
Zn 0.043 0.674 0.351	O 0.184 0.816 0.722
Zn 0.619 0.674 0.351	O 0.620 0.815 0.721
Zn 0.616 0.245 0.350	O 0.324 0.821 0.718
Zn 0.328 0.385 0.350	O 0.484 0.821 0.718
Zn 0.045 0.385 0.350	O 0.236 0.341 0.228
Zn 0.616 0.387 0.350	O 0.092 0.341 0.228
Zn 0.759 0.387 0.350	O 0.234 0.481 0.228
Zn 0.184 0.381 0.348	O 0.089 0.624 0.227
Zn 0.179 0.819 0.348	O 0.523 0.624 0.227
Zn 0.628 0.819 0.348	O 0.088 0.766 0.227
Zn 0.045 0.530 0.347	O 0.521 0.053 0.227
Zn 0.186 0.672 0.347	O 0.665 0.766 0.227
Zn 0.474 0.672 0.347	O 0.091 0.481 0.227
Zn 0.472 0.530 0.347	O 0.664 0.340 0.227
Zn 0.188 0.530 0.345	O 0.378 0.481 0.227
Zn 0.330 0.530 0.345	O 0.663 0.197 0.226
O 0.758 0.103 0.729	O 0.663 0.056 0.226
O 0.333 0.103 0.729	O 0.521 0.197 0.226
O 0.901 0.246 0.728	O 0.380 0.056 0.226
O 0.333 0.246 0.728	O 0.949 0.341 0.226
O 0.616 0.102 0.727	O 0.807 0.340 0.226
O 0.474 0.102 0.727	O 0.379 0.341 0.226
O 0.757 0.670 0.727	O 0.521 0.340 0.226
O 0.901 0.670 0.727	O 0.663 0.482 0.226
O 0.616 0.245 0.727	O 0.948 0.623 0.226
O 0.474 0.960 0.727	O 0.663 0.623 0.226
O 0.759 0.387 0.727	O 0.807 0.482 0.226
O 0.616 0.387 0.727	O 0.950 0.482 0.225
O 0.902 0.387 0.727	O 0.521 0.482 0.225
O 0.759 0.245 0.727	O 0.382 0.622 0.225

O 0.227 0.622 0.225  
O 0.807 0.198 0.224  
O 0.379 0.198 0.224  
O 0.522 0.913 0.224  
O 0.379 0.913 0.224  
O 0.806 0.624 0.224  
O 0.239 0.909 0.223  
O 0.658 0.909 0.223  
O 0.229 0.767 0.223  
O 0.525 0.767 0.222

Str 103 (WZ-ZnO-NP-17)

$\Delta E_{\text{gap}}(\text{PBE}_{\text{GW-fit}})$ : 0.53 eV

$E_{\text{rel}}$ : 0.27 eV/ZnO

$\text{Pore}_{\text{max}}$ : 0.83 nm

$V_{\text{pore}}$ : 29 %

$D_{\text{pore}}$ : 1

cell parameters

16.447 16.447 5.358 90.00 90.00

120.78

fractional coordinates

Zn 0.862 0.929 0.999

Zn 0.070 0.138 0.999

Zn 0.867 0.331 0.996

Zn 0.669 0.133 0.996

Zn 0.661 0.922 0.995

Zn 0.078 0.339 0.995

Zn 0.868 0.132 0.992

Zn 0.743 0.887 0.530

Zn 0.113 0.257 0.530

Zn 0.542 0.890 0.528

Zn 0.110 0.458 0.528

Zn 0.747 0.253 0.527

Zn 0.935 0.065 0.501

Zn 0.935 0.265 0.501

Zn 0.735 0.065 0.501

Zn 0.928 0.467 0.500

Zn 0.533 0.072 0.500

Zn 0.929 0.862 0.499

Zn 0.138 0.070 0.499

Zn 0.331 0.867 0.496

Zn 0.133 0.669 0.496

Zn 0.922 0.661 0.495

Zn 0.339 0.078 0.495

Zn 0.132 0.868 0.492

Zn 0.887 0.743 0.030

Zn 0.257 0.113 0.030

Zn 0.890 0.542 0.028

Zn 0.458 0.110 0.028

Zn 0.253 0.747 0.027

Zn 0.065 0.935 0.001

Zn 0.265 0.935 0.001

Zn 0.065 0.735 0.001

Zn 0.467 0.928 0.000

Zn 0.072 0.533 0.000

O 0.733 0.865 0.876

O 0.135 0.267 0.876

O 0.935 0.065 0.875

O 0.938 0.267 0.874

O 0.733 0.062 0.874

O 0.737 0.263 0.874

O 0.931 0.866 0.873

O 0.134 0.069 0.873

O 0.531 0.866 0.873

O 0.134 0.469 0.873

O 0.935 0.466 0.873

O 0.534 0.065 0.873

O 0.132 0.868 0.872

O 0.333 0.871 0.872

O 0.129 0.667 0.872

O 0.928 0.664 0.871

O 0.336 0.072 0.871

O 0.865 0.733 0.376

O 0.267 0.135 0.376

O 0.065 0.935 0.375

O 0.267 0.938 0.374

O 0.062 0.733 0.374

O 0.263 0.737 0.374

O 0.866 0.931 0.373

O 0.069 0.134 0.373

O 0.866 0.531 0.373

O 0.469 0.134 0.373

O 0.466 0.935 0.373

O 0.065 0.534 0.373

O 0.868 0.132 0.372

O 0.871 0.333 0.372

O 0.667 0.129 0.372

O 0.664 0.928 0.371

O 0.072 0.336 0.371

Str 104 (WZ-ZnO-NP-18)

$\Delta E_{\text{gap}}(\text{PBE}_{\text{GW-fit}})$ : 0.46 eV

$E_{\text{rel}}$ : 0.23 eV/ZnO

$\text{Pore}_{\text{max}}$ : 1.12 nm

$V_{\text{pore}}$ : 31 %

$D_{\text{pore}}$ : 1

cell parameters	Zn 0.409 0.121 0.031
19.707 19.707 5.351 90.00 90.00	Zn 0.890 0.445 0.001
120.00	Zn 0.555 0.445 0.001
fractional coordinates	Zn 0.555 0.110 0.001
Zn 0.557 0.943 0.999	O 0.609 0.888 0.877
Zn 0.557 0.614 0.999	O 0.609 0.721 0.877
Zn 0.386 0.943 0.999	O 0.279 0.888 0.877
Zn 0.386 0.443 0.999	O 0.279 0.391 0.877
Zn 0.057 0.614 0.999	O 0.112 0.721 0.877
Zn 0.057 0.443 0.999	O 0.112 0.391 0.877
Zn 0.721 0.442 0.999	O 0.445 0.890 0.875
Zn 0.721 0.279 0.999	O 0.445 0.555 0.875
Zn 0.558 0.279 0.999	O 0.110 0.555 0.875
Zn 0.562 0.781 0.996	O 0.945 0.556 0.874
Zn 0.219 0.781 0.996	O 0.945 0.389 0.874
Zn 0.219 0.438 0.996	O 0.611 0.556 0.874
Zn 0.389 0.778 0.991	O 0.611 0.055 0.874
Zn 0.389 0.611 0.991	O 0.444 0.389 0.874
Zn 0.222 0.611 0.991	O 0.444 0.055 0.874
Zn 0.591 0.879 0.531	O 0.445 0.723 0.873
Zn 0.591 0.712 0.531	O 0.277 0.723 0.873
Zn 0.288 0.879 0.531	O 0.277 0.555 0.873
Zn 0.288 0.409 0.531	O 0.778 0.556 0.872
Zn 0.121 0.712 0.531	O 0.778 0.222 0.872
Zn 0.121 0.409 0.531	O 0.444 0.222 0.872
Zn 0.445 0.890 0.501	O 0.779 0.389 0.872
Zn 0.445 0.555 0.501	O 0.611 0.389 0.872
Zn 0.110 0.555 0.501	O 0.611 0.221 0.872
Zn 0.943 0.557 0.499	O 0.888 0.609 0.377
Zn 0.943 0.386 0.499	O 0.888 0.279 0.377
Zn 0.614 0.557 0.499	O 0.721 0.609 0.377
Zn 0.614 0.057 0.499	O 0.721 0.112 0.377
Zn 0.443 0.386 0.499	O 0.391 0.279 0.377
Zn 0.443 0.057 0.499	O 0.391 0.112 0.377
Zn 0.442 0.721 0.499	O 0.890 0.445 0.375
Zn 0.279 0.721 0.499	O 0.555 0.445 0.375
Zn 0.279 0.558 0.499	O 0.555 0.110 0.375
Zn 0.781 0.562 0.496	O 0.556 0.945 0.374
Zn 0.781 0.219 0.496	O 0.556 0.611 0.374
Zn 0.438 0.219 0.496	O 0.389 0.945 0.374
Zn 0.778 0.389 0.491	O 0.389 0.444 0.374
Zn 0.611 0.389 0.491	O 0.055 0.611 0.374
Zn 0.611 0.222 0.491	O 0.055 0.444 0.374
Zn 0.879 0.591 0.031	O 0.723 0.445 0.373
Zn 0.879 0.288 0.031	O 0.723 0.277 0.373
Zn 0.712 0.591 0.031	O 0.555 0.277 0.373
Zn 0.712 0.121 0.031	O 0.556 0.778 0.372
Zn 0.409 0.288 0.031	O 0.222 0.778 0.372

O 0.222 0.444 0.372	Zn 0.888 0.348 0.024
O 0.389 0.779 0.372	Zn 0.652 0.740 0.024
O 0.389 0.611 0.372	Zn 0.260 0.112 0.024
O 0.221 0.611 0.372	Zn 0.267 0.733 0.003
	Zn 0.464 0.723 0.001
Str 105 (WZ-ZnO-NP-19)	Zn 0.277 0.941 0.001
$\Delta E_{\text{gap}}(\text{PBE}_{\text{GW}}\text{-fit}): 0.81 \text{ eV}$	Zn 0.059 0.536 0.001
$E_{\text{rel}}: 0.32 \text{ eV/ZnO}$	O 0.933 0.067 0.875
$\text{Pore}_{\text{max}}: 0.75 \text{ nm}$	O 0.930 0.266 0.873
$V_{\text{pore}}: 33 \%$	O 0.734 0.864 0.873
$D_{\text{pore}}: 1$	O 0.136 0.070 0.873
cell parameters	O 0.534 0.861 0.872
16.419 16.419 5.373 90.00 90.00	O 0.139 0.872 0.872
120.00	O 0.128 0.466 0.872
fractional coordinates	O 0.334 0.866 0.872
Zn 0.667 0.935 0.998	O 0.332 0.666 0.872
Zn 0.068 0.333 0.998	O 0.134 0.668 0.872
Zn 0.065 0.932 0.998	O 0.938 0.872 0.871
Zn 0.868 0.931 0.996	O 0.734 0.062 0.871
Zn 0.863 0.132 0.996	O 0.128 0.266 0.871
Zn 0.069 0.137 0.996	O 0.931 0.467 0.869
Zn 0.951 0.895 0.526	O 0.533 0.664 0.869
Zn 0.744 0.049 0.526	O 0.336 0.069 0.869
Zn 0.105 0.256 0.526	O 0.267 0.733 0.375
Zn 0.940 0.452 0.524	O 0.466 0.730 0.373
Zn 0.548 0.688 0.524	O 0.270 0.936 0.373
Zn 0.312 0.060 0.524	O 0.064 0.534 0.373
Zn 0.933 0.067 0.502	O 0.666 0.928 0.372
Zn 0.923 0.264 0.501	O 0.072 0.939 0.372
Zn 0.736 0.859 0.501	O 0.061 0.334 0.372
Zn 0.141 0.077 0.501	O 0.868 0.934 0.372
Zn 0.533 0.868 0.498	O 0.866 0.132 0.372
Zn 0.135 0.467 0.498	O 0.066 0.134 0.372
Zn 0.132 0.865 0.498	O 0.466 0.928 0.371
Zn 0.337 0.869 0.496	O 0.262 0.534 0.371
Zn 0.332 0.663 0.496	O 0.072 0.738 0.371
Zn 0.131 0.668 0.496	O 0.864 0.333 0.369
Zn 0.456 0.905 0.026	O 0.667 0.731 0.369
Zn 0.249 0.544 0.026	O 0.269 0.136 0.369
Zn 0.095 0.751 0.026	

## References

---

- <sup>1</sup> J. L. G. Fierro, *Metal Oxides: Chemistry and Applications*, CRC Press, Florida, 2006.
- <sup>2</sup> Cheetham, A. K. *Science* 1994, 264, 794.
- <sup>3</sup> J. Gopalakrishnan, *J. Chem Mater.* 1995, 7, 1265
- <sup>4</sup> A. Navrotsky, *Proc. Natl. Acad. Sci.*, 2004, 101, 12096.
- <sup>5</sup> C. Jagadish and J. Pearton, *Zinc Oxide Bulk, Thin Films and Nanostructures Processing, Properties and Applications*, Elsevier, Oxford, UK, Amsterdam, Netherlands, (2006).
- <sup>6</sup> J. C. Phillips, *Reviews of Modern Physics* 42 (1970) 317.
- <sup>7</sup> D. C. Reynolds, D. C Look and B. Jogai, 1996, *Solid State Commun.* 99, 873
- <sup>8</sup> Ozgur, U.; Alivov, Y. I.; Liu, C.; Teke, A.; Reshchikov, M. A.; Dogan, S.; Avrutin, V.; Cho, S. J.; Morkoc, H. *Journal of Applied Physics* 2005, 98 (4) 041301
- <sup>9</sup> O. Dulub, L. A. Boatner, and U Diebold, *Surface Science* 519 (2002) 201.
- <sup>10</sup> Ozgur, U.; Alivov, Y. I.; Liu, C.; Teke, A.; Reshchikov, M. A.; Dogan, S.; Avrutin, V.; Cho, S. J.; Morkoc, H. *Journal of Applied Physics* 2005, 98 (4) 041301
- <sup>11</sup> A. D. Corso, M. Posternak, R. Resta, and A. Baldereschi, *Phys. Rev. B* 1994, 50, 10715.
- <sup>12</sup> C. S. Wei, Y. Y. Lin, Y. C. Hu, C. W. Wu, C. K. Shih, C. T. Huang, S. H. Chang, *Sens. Actuators A* 128 (1) (2006) 18.
- <sup>13</sup> B. Kumar, S. W. Kim, *Nano Energy* (2012) 1, 342-355.
- <sup>14</sup> Kogure, T. and Bando, Y. (1993) *Journal of Electron Microscopy*, 47, 7903.
- <sup>15</sup> Ashrafi, A.B.M.A., Ueta, A., Avramescu, A., Kumano, H., Suemune, I., Ok, Y.-W. and Seong, T.-Y. (2000) *Applied Physics Letters*, 76, 550.
- <sup>16</sup> Kim, S.-K., Jeong, S.-Y. and Cho, C.-R. (2003) *Applied Physics Letters*, 82, 562.
- <sup>17</sup> C. H. Bates, W. B. White, R. Roy, *Science* 137, 993 (1962)
- <sup>18</sup> Nanocrystallinity as a Route to Metastable Phases: Rock Salt ZnO Andrey N. Baranov, Petr S. Sokolov, Viktor A. Tafeenko, Christian Lathe, Yan V. Zubavichus Aleksey A. Veligzhanin, Mikhail V. Chukichev, and Vladimir L. Solozhenko
- <sup>19</sup> C. Jagadish, and S. J. Pearton (eds.), *Zinc Oxide Bulk, Thin Films, and Nanostructures* (Elsevier, Amsterdam, 2006), p. 1.
- <sup>20</sup> Ü. Özgür, Ya. L. Alivov, C. Liu, A. Teke, M. Reshchikov, S. Dogan, V. Avrutin, S.J. Cho, and H. Morkoc, *J. Appl. Phys* 2005, 98, 041301.
- <sup>21</sup> D. C. Look, *Mater. Sci. Eng* 2001, 80, 383.
- <sup>22</sup> T. Olorunyolemi, A. Birnoim, Y. Carmel, O. Wilson, I. Liloyd, S. Smith, and R. Campbell, *J. Am. Cera. Socie* 2002, 85, 1249.
- <sup>23</sup> D. I. Florescu, L. G. Mourokh, F. H. Pollak, D. C. Look, G. Cantwell, and X.Li, *J. Appl. Phys* 2002, 91, 890.

- 
- <sup>24</sup> D. P. Norton, M. Ivill, Y. Li, Y.W. Kwon, J. M. Erie, H. S. Kim, K. Ip, S. J. Pearton, Y. W. Heo, S. Kim, B. S. Kang, F. Ren, A. F. Hebard, and J. Kelly, Charge carrier and spin doping in ZnO thin films, *Thin Solid Films* 496 (2006), 160–168.
- <sup>25</sup> Mang A, Reimann K and Rübénacke St 1995 *Solid State Commun.* 94 251.
- <sup>26</sup> Reynolds D C, Look D C and Jogai B 1996 *Solid State Commun.* 99 873.
- <sup>27</sup> Janotti A and Van de Walle C.G. *Phys. Rev. B* (2007) 6, 44.
- <sup>28</sup> J. C. Fan, K. M. Sreekanth, Z. Xie, S. L. Chang, K. V. Rao, *Progress in Materials Science* 58 (2013) 874-985
- <sup>29</sup> E. Ohshima, H. Ogino, I. Niikura, K. Maeda, M. Sato, M. Ito, and *Journal of Crystal Growth* 260 (2004) 166.
- <sup>30</sup> J. M. Ntep, S. S. Hassani, A. Lusson, A. Tromson-Carli, D. Ballutaud, Didier, and R. Triboulet, *Journal of Crystal Growth* 207 (1999) 30.
- <sup>31</sup> D. C. Look, *Materials Science and Engineering B* 80 (2001) 383.
- <sup>32</sup> p-Type ZnO materials: Theory, growth, properties and devices J.C. Fan , K.M. Sreekanth , Z. Xie , S.L. Chang , K.V. Rao
- <sup>33</sup> Look, D. C., Hemsley, J. W. & Sizelove, J. R. Residual native shallow donor in ZnO. *Physical Review Letters* 82, 2552 (1999).
- <sup>34</sup> Kasai, P. H. Electron spin resonance studies of donors and acceptors in ZnO. *Physical Review* 130, 989 (1963).
- <sup>35</sup> Kohan, A. F., Ceder, G., Morgan, D. & de Walle, C. G. V. First-principles study of native point defects in ZnO. *Physical Review B* 61, 15019 (2000).
- <sup>36</sup> Ozgur, U.; Alivov, Y. I.; Liu, C.; Teke, A.; Reshchikov, M. A.; Dogan, S.; Avrutin, V.; Cho, S. J.; Morkoc, H. *Journal of Applied Physics* 2005, 98 (4) 041301
- <sup>37</sup> C. G. Van de Walle, *Phys. Rev. Lett.* (2000) 85, 1012.
- <sup>38</sup> Janotti A and Van de Walle C.G. *Phys. Rev. B* (2007) 6, 44.
- <sup>39</sup> Vines L. Et al. *Journal of Applied physics* 107, 103707 (2010).
- <sup>40</sup> McCluskey M., Jokela S. *Physica B: Condensed Matter* 401-402, 355-357 (2007).
- <sup>41</sup> A. K. Das, P. Misra, L. M. Kukreja, *Journal of Physics D: Applied Physics* 42, 165405 (2009).
- <sup>42</sup> Pankove J I and Johnson N M (ed) 1991 *Hydrogen in Semiconductors, Semiconductors and Semimetals* vol 34 (Boston: Academic)
- <sup>43</sup> Van de Walle C G and Johnson N M 1998 *Gallium Nitride (GaN) II (Semiconductors and Semimetals* vol 57) ed J I Pankove and T D Moustakas (Boston: Academic) p 157
- <sup>44</sup> Van de Walle C G and Neugebauer J 2006 *Annu. Rev. Mater. Res.* 36 179
- <sup>45</sup> A. Janetti, C. G. Van de Walle, *Rep. Prog. Phys.* 72 (2009) 126501
- <sup>46</sup> T. Gruber, C. Kirchner, R. Kling, F. Reuss, A. Waag, *Appl. Phys. Lett.* 2004,84, 5359.
- <sup>47</sup> Janotti A and Van de Walle C.G. *Phys. Rev. B* (2007) 6, 44.
- <sup>48</sup> A. Ohtomo, M. Kawasaki, T. Koida, K. Masubuchi, H. Koinuma, Y. Sakurai, Y. Yoshida, T. Yasuda, Y. Segawa, *Appl. Phys. Lett.* 1998, 71, 2466.

- 
- <sup>49</sup> T. Makino, Y. Segawa, A. Ohtomo, K. Tamura, H. Koinuma, *Appl. Phys. Lett.* 2001, 78, 1237.
- <sup>50</sup> Reynolds D C, Look D C and Jogai B 1996 *Solid State Commun.* 99 873
- <sup>51</sup> Bagnall D M, Chen Y F, Zhu Z, Yao T, Koyama S, Shen M Y and Goto T 1997 *Appl. Phys. Lett.* 70 2230
- <sup>52</sup> Madelung O (ed) 1996 *Semiconductors—Basic Data 2nd Revised Edn* (Berlin: Springer)
- <sup>53</sup> Shionoya S and Yen W H (ed) 1997 *Phosphor Handbook* By Phosphor Research Society (Boca Raton, FL: CRC Press)
- <sup>54</sup> Van de Walle *Rep. Prog. Phys.* 2009
- <sup>55</sup> Larciprete M C et al 2006 *Appl. Phys. B—Lasers Opt.* 82 431
- <sup>56</sup> Tuomisto F, Saarinen K, Look D C and Farlow G C 2005 *Phys. Rev. B* 72 085206
- <sup>57</sup> Look D C, Hemsley J W and Sizelove J R 1999 *Phys. Rev. Lett.* 82 2552
- <sup>58</sup> Rohit Khanna, K. Ip, K. Allums, K. Baik, C. Abernathy, S. Pearton, Y. Heo, D. Norton, F. Ren, S. Shojah-Ardalan, and R. Wilkins, Proton irradiation of ZnO Schottky diodes, *Journal of Electronic Materials* 34 (2005), no. 4, 395-398.
- <sup>59</sup> F. Patolsky, G. F. Zheng, and C. M. Lieber, *Anal. Chem.* 2006, 78, 4260.
- <sup>60</sup> Z. L. Wang, *Materials Today*, 2004, 7, 26.
- <sup>61</sup> J. Zhou, N. S. Xu, and Z. L. Wang, *Advanced Materials* 18 (2006) 2432.
- <sup>62</sup> A. R. Verma, P. Krishna, *Polymorphism and polytypism in crystals*, 1966, John Wiley & Sons, Inc. New York
- <sup>63</sup> W. D. Ross, *Aristotle's Metaphysics*, 1924, Oxford: Clarendon Press
- <sup>64</sup> *The New Dictionary of the History of Ideas*, 2004, Charles Scribner's Sons, New York
- <sup>65</sup> A. Arzruni *Physikalische Chemie der Krystalle*, 1893, Braunschweig, F. Vieweg und Sohn, 365
- <sup>66</sup> E. Mitscherlich, *Ann. Chim. Phys.* 1822, 19, 350
- <sup>67</sup> E. Mitscherlich, *Ann. Chim. Phys.* 1823, 24, 264
- <sup>68</sup> M. L. Frankenheim, *J. Prakt. Chem.* 1839, 16, 1
- <sup>69</sup> O. Lehmann, *Z. Krist.* 1877, 1, 97
- <sup>70</sup> W. B. Jensen, *J. Chem Educ.* 2006, 83, 838
- <sup>71</sup> W. C. McCrone, Polymorphism. In *Physics and chemistry of the organic solid state*, vol. 2, D. Fox, M. M. Labes, A Weissberger, Eds. Intercity publishers: New York, 1965
- <sup>72</sup> J. Dunitz, *Acta Crystallogr. B* 1995, 51, 619.
- <sup>73</sup> J. Bernstein, *Cryst. Growth Des.* 2011, 11, 632
- <sup>74</sup> C. N. Fenner, *Amer. J. Sci.* 1913, 36, 331
- <sup>75</sup> Klein and Hurlbut. *Manual of Mineralogy*, p. 527. John Wiley & Sons, 21st edition, 1962
- <sup>76</sup> K. J. Kingma, R. E. Cohen, R. J. Hemley, H. K. Mao, *Nature*, 1995, 374, 243
- <sup>77</sup> J. Heines, J. M. Leger, F. Gorelli, M. Hanfland, *Phys. Rev. Lett.* 2001, 87, 155503
- <sup>78</sup> R. J. Hemley, C. T. Prewitt, K. J. Kingma, *Rev. Miner.* 1996, 41, 81.

- 
- <sup>79</sup> L. S. Dubrovinsky, N. A. Dubrovinskaia, S. K. Saxena, F. Tutti, S. Rekhi, T. Le Bihan, G. Shen, J. Hu, *Chem. Phys. Lett.* 2001, 333, 264.
- <sup>80</sup> T. Sekine, M. Akaichi, N. Setaka, *Geochem. Cosmochem. Acta*, 1987, 51, 379.
- <sup>81</sup> L. Liu, W. A. Basset, J. Sharry, *J. Geophys. Res.* 1978, 83, 2301.
- <sup>82</sup> N. W. Jepps, T. F. Page, *Progr. Cryst. Growth Charact.* 1983, 7 259.
- <sup>83</sup> R. S. Ramsdell, *Amer. Mineralogist*, 1947, 32, 64.
- <sup>84</sup> T. Kusumori, *AIST Today*, 2004, 4, 14
- <sup>85</sup> P. Krishna, *Crystal Growth and Characterization of Polytype Structures*, Pergamon Press, 1983, Oxford.
- <sup>86</sup> F. Bechstedt, P. Käckell, A. Zywiets, K. Karch, B. Adolph, K. Tenelsen, J. Furthmüller, *Phys. Stat. Sol. B* 1997, 202, 35.
- <sup>87</sup> P. Pirouz, J. W. Yang, *Ultramicroscopy*, 1993, 51, 189.
- <sup>88</sup> W. J. Choyke, D. R. Hamilton, L. Patrick, *Phys. Rev.* 1964, 133, A 1163.
- <sup>89</sup> B. Wenzien, P. Käckell, F. Bechstedt, C. Cappellini, *Phys. Rev. B*, 1995, 52, 10897.
- <sup>90</sup> S. M. Woodley, R. Catlow, *Nature Mater.* 2008, 7, 937.
- <sup>91</sup> Hofmann, D. W. M. & Apostolakis, J. Crystal structure prediction by data mining. *J. Mol. Struct.* 647, 17–39.
- <sup>92</sup> Fischer, C. C., Tibbetts, K. J., Morgan, D. & Ceder, G. Predicting crystal structure by merging data mining with quantum mechanics. *Nature Mater.* 5, 641–646 (2006).
- <sup>93</sup> S. Curtarolo, D. Morgan, K. Persson, J. Rodgers, G. Ceder, *Phys. Rev. Lett.* 2003, 91, 135503.
- <sup>94</sup> J. V. Smith, *Am. Mineral.* 1977, 62, 703.
- <sup>95</sup> Wells, A. F. The geometrical basis of crystal chemistry. 1–4. *Acta Crystallogr.* 7, 535–554; 842–853 (1954).
- <sup>96</sup> O’Keefe, M. & Hyde, B. G. *Crystal Structures I. Patterns and Symmetry* (Mineral. Soc. Am., 1996).
- <sup>97</sup> Treacy, M. M. J., Rivin, I., Balkovsky, E., Randall, K. H. & Foster, M. D. Enumeration of periodic tetrahedral frameworks. II. Polynodal graphs. *Micropor. Mesopor. Mater.* 74, 121–132 (2004).
- <sup>98</sup> S. Kirkpatrick, J. C. D. Gellat, M. P. Vecchi, *Science*, 1983, 671.
- <sup>99</sup> Schon, J. C. & Jansen, M. First step towards planning of syntheses in solid-state chemistry: Determination of promising structure candidates by global optimization. *Angew. Chem. Int Ed. Engl.* 35, 1287–1304 (1996).
- <sup>100</sup> Schon, J. C. & Jansen, M. Determination, prediction, and understanding of structures, using the energy landscapes of chemical systems. *Z. Kristallogr.* 216, 307–325 (2001).
- <sup>101</sup> S. M. Woodley, A. A. Sokol, *Angewandte Chemie*, 2012, 51, 3752
- <sup>102</sup> D. A. Coley, *An Introduction to Genetic Algorithms for Scientists and Engineers*, 1999, World Scientific.
- <sup>103</sup> Johnston, R. L. Evolving better nanoparticles: Genetic algorithms for optimising cluster geometries. *Dalton Trans.* 22, 4193–4207 (2003).

- 
- <sup>104</sup> Woodley, S. M. Engineering microporous architectures: Combining an evolutionary algorithm with predefined exclusion zones. *Phys. Chem. Chem. Phys.* 9, 1070–1077 (2006).
- <sup>105</sup> Abraham, N. L. & Probert, M. I. J. A periodic genetic algorithm with real-space representation for crystal structure and polymorph prediction. *Phys. Rev. B* 73, 224104 (2006).
- <sup>106</sup> L. D. Lloyd, R. L. Johnston, S. Salhi, *J. Comp. Chem.* 2005, 26, 1069.
- <sup>107</sup> J. J. Wu, H. I. Wen, C. H. Tseng, S. C. Liu, *Adv. Funct. Mater.* 2004, 14, 806.
- <sup>108</sup> H.J.Ko, Y.Chen, S.K.Hong and T.Yao: *J. Cryst. Growth*, 2000, 209, 816.
- <sup>109</sup> T.Gruber, C.Kirchner, K.Thonke, R.Sauer and A.Waag: *Phys. Status Solidi A*, 2002, 192, 166.
- <sup>110</sup> I.Ozerov, D.Nelson, A.V.Bulgakov, W.Marine and M.Sentis: *Appl. Surf. Sci.*, 2003, 212-213, 349.
- <sup>111</sup> H.Usui, Y.Shimizu, T.Sasaki and N.Koshizaki: *J. Phys. Chem. B*, 2005, 109, 120.
- <sup>112</sup> L.Spanhel and M.A.Anderson: *J. Am. Chem. Soc.*, 1991, 113, 2826.
- <sup>113</sup> Y.Li, G.W.Meng, L.D.Zhang and F.Philipp: *Appl. Phys. Lett.*, 2000, 76, 2011.
- <sup>114</sup> Y.D.Wang, K.Y.Zang, S.J.Chua and C.G.Fonstad: *Appl. Phys. Lett.*, 2006, 89, 263116.
- <sup>115</sup> C. Suryanarayana, *Inter. Mater. Rev.* 40 (1995) 41.
- <sup>116</sup> B. A. Joyce, *Rep. Prog. Phys.* 48, 1637 (1985).
- <sup>117</sup> S. H. M. Jafri, J. Dutta, D. Sweatman, A. B. Sharma, *Appl. Phys. Lett.* 89, 133123 (2006).
- <sup>118</sup> A. K. Geim, K. S. Novoselov, *Nat. Mater.* 6, 183 (2007).
- <sup>119</sup> P. W. Tasker, *J. Phys. C.: Solid State Phys.* 12, 4977 (1979).
- <sup>120</sup> W. W. Wenas, A. Yamada, K. Takahashi, M. Yoshino, and M. Konagai: *J. Appl. Phys.* 70 (1991) 7119.
- <sup>121</sup> K. H. Kim, K. C. Park, and D. Y. Ma: *J. Appl. Phys.* 81 (1997) 7764.
- <sup>122</sup> Y. Natsume and H. Sakata: *Thin Solid Films* 372 (2000) 30.
- <sup>123</sup> S. Hayamizu, H. Tamaka, and T. Kawai: *J. Appl. Phys.* 80 (1996) 787.
- <sup>124</sup> A. T. Silver, J. C. Joubert, and M. Labeau: *J. Appl. Phys.* 76 (1994) 1992.
- <sup>125</sup> S. J. Henley, M. N. R. Ashfold, D. Cherns, *Surf. Coat. Tech.*, 177, 271 (2004).
- <sup>126</sup> L. Niinisto, J. Paivasaari, J. Niinisto, M. Putkomen, M. Nieminen, *Phys. Status Solidi A.*, 201, 1443 (2004).
- <sup>127</sup> C. Noguera, *J. Phys.: Condens. Matter* 12, R367 (2000).
- <sup>128</sup> O. Dulub, U. Diebold, G. Kresse, *Phys. Rev. Lett.* 90, 016102 (2003).
- <sup>129</sup> J. Goniakowski, F. Finocchi, C. Noguera, *Reports on Progress in Physics* 71, 016501 (2008).
- <sup>130</sup> O. Dulub, U. Diebold, and G. Kresse, *Phys. Rev. Lett.* 90, 016102 (2003).
- <sup>131</sup> J.V. Lauristen, S. Porrsgaard, M. K. Rasmussen, M. C. R. Jensen, R. Bechstein, K. Meinander, B. S. Clausen, S. Helveg, R. Wahl, G. Kresse, and F. Besenbacher, *ACS Nano* 5, 5987 (2011).
- <sup>132</sup> A. Wander, F. Schedin, P. Steadman, A. Norris, R. McGrath, T. S. Turner, G. Thornton, N. M. Harrison, *Phys. Rev. Lett.*, 86, 3811 (2001).

- 
- <sup>133</sup> C. L. Freeman, F. Claeysens, N. L. Allan, *Phys. Rev. Lett.*, 96, 066102 (2006)
- <sup>134</sup> B. J. Morgan, *Phys. Rev. B* 80, 174105 (2009).
- <sup>135</sup> C. Tusche, H. L. Meyerheim, J. Kirschner, *Phys. Rev. Lett.*, 99, 026102 (2007)
- <sup>136</sup> G. Weirum, G. Barcaro, A. Fortunelli, F. Weber, R. Schennach, S. Surnev, F. P. Netzer, J. *Phys. Chem. C.*, 114, 15432 (2010).
- <sup>137</sup> M. He, R. Yu, J. Zhu, *Angew. Chem.* 124, 7864 (2012).
- <sup>138</sup> R. Juhasz, K. Kylmänen, A. Galeckas, J. Linnros, *Mater. Sci. Eng. C* 25, 733 (2005).
- <sup>139</sup> V. Tuboltsev, J. Räisänen, *Nanotechnol.* 20, 335302 (2009).
- <sup>140</sup> V. Tuboltsev, J. Räisänen, *Nanotechnol.* 20, 335302 (2009).
- <sup>141</sup> Y. Xia, P. Yang, Y. Sun, Y. Wu, B. Mayers, B. Gates, Y. Yin, F. Kim, H. Yan, *Adv. Mater.* 15, 353 (2003).
- <sup>142</sup> Y. Xia, P. Yang, Y. Sun, Y. Wu, B. Mayers, B. Gates, Y. Yin, F. Kim, H. Yan, *Adv. Mater.* 15, 353 (2003).
- <sup>143</sup> M. H. Huang, S. Mao, H. Feick, H. Yan, Y. Wu, H. Kind, E. Weber, R. Russo, P. Yang, *Science* 292, 1897 (2001).
- <sup>144</sup> Z. L. Wang, J. Song, *Science* 312, 242 (2006).
- <sup>145</sup> M. J. S. Spencer, *Progress in Materials Science* 57, 437 (2012).
- <sup>146</sup> Z. L. Wang, *Mater. Today* 7, 26 (2004)
- <sup>147</sup> Z. L. Wang, *J. Phys.: Condens Matter* 16, R829 (2004).
- <sup>148</sup> D. Stichtenoth, C. Ronning, T. Niermann, L. Wischmeier, T. Voss, C. J. Chien, *Nanotechnology*, 18, 435701 (2007).
- <sup>149</sup> X. Cao, N. Wang, L. Wang, *Nanotechnology*, 21, 065603 (2010).
- <sup>150</sup> Z. W. Pan, Z. R. Dai, Z. L. Wang, *Science* 291, 1947 (2001).
- <sup>151</sup> X. Ren, C. H. Jiang, D. D. Li, L. He, *Mater Lett.* 62, 3114, (2008).
- <sup>152</sup> N. C. Greenham, X. G. Peng, A. P. Alivisatos, *Phys. Rev. B* 54, 17628 (1996)
- <sup>153</sup> M. Faraday, *Philos. Trans. R. Soc. London*, 147, 145 (1857).
- <sup>154</sup> B. Poudel, Q. Hao, Y. Ma, Y. Lan, A. Minnich, B. Yu, X. Yan, D. Wang, A. Muto, D. Vashaee, X. Chen, J. Liu, M. S. Dresselhaus, G. Chen, Z. Ren, *Science* 320, 634 (2008).
- <sup>155</sup> M. L. Lee, G. Dezsi, R. Venkatasubramanian, *Thin Solid Films* 518, s76 (2010).
- <sup>156</sup> L. A. Thomas, L. Dekker, M. Kallumadil, P. Southern, M. Wilson, S. P. Nair, Q. A. Pankhurst, I. P. Parkin, *J. Mater. Chem.* 19, 6529 (2009).
- <sup>157</sup> D. Grosso, P. A. Sermon, *J. Mater. Chem.* 10, 359 (2000).
- <sup>158</sup> R. Xie, U. Kolb, J. Li, T. Basche, A. Mews, *J. Am. Chem. Soc.* 127, 7480 (2005).
- <sup>159</sup> A. Wood, M. Giersig, M. Hilgendorff, A. Vilas-Campos, L. M. Liz-Marzan, P. Mulvaney, *Aust. J. Chem.* 2003, 56, 1051
- <sup>160</sup> M. A. Zwijnenburg, S. T. Bromley, *Phys. Chem. Chem. Phys.*, 2010, 12, 14579
- <sup>161</sup> H. Van Bekkum, E. M. Flanigen, P. A. Jacobs, J. C. Jansen, *Introduction to Zeolite Science and Practice*, 2nd edition, Elsevier Science, Amsterdam, (2001)

- 
- <sup>162</sup>E. M. Flanigen, Zeolites and molecular sieves an historical perspective. *Stud. Surf. Catal.*, 58, 13-34, 1991.
- <sup>163</sup>J. Weitkamp, *Solid State Ion.* 131 (2001) 175.
- <sup>164</sup>C. Bouvy, W. Marine, R. Sporken, B. L. Su, *Chem. Phys. Lett.*, 2006, 428, 312
- <sup>165</sup>T. Wagner, T. Waitz, J. Roggenbuck, M. Froba, C. D. Kohl, M. Tiemann, *Thin Solid Films*, 2007, 515, 8360
- <sup>166</sup>R. G. Singh, F. Singh, V. Agarwal, R. M. Mehra, *J. Phys. D:Appl. Phys.* 2007, 40, 3090
- <sup>167</sup>H. Van Bekkum, E. M. Flanigen, J. C. Jansen (Eds.), *Introduction to zeolite science and practise*, Elsevier, Amsterdam, (1991)
- <sup>168</sup>G. Ning, X. Zhao, J. Li, C Zhang, *Optical Materials*, 2006, 28, 385
- <sup>169</sup>F. Xu, P. Zhang, A. Navrotsky, Z. Yuan, T. Ren, M. Halasa, B. Su, *Chem. Mater.* 2007, 19, 5680
- <sup>170</sup>M. Fu, J. Zhou, Q. F. Xiao, B. Li, R. L. Zong, W. Chen, Zhang, *J. Adv. Mater.* 2006,18, 1001
- <sup>171</sup>B. J. Morgan, *Phys. Rev. B*, 2009, 80, 174105
- <sup>172</sup>J. Carrasco, F. Illas, S. T. Bromley, *Phys. Rev. Lett.* 2007, 99, 235502
- <sup>173</sup>S. Hamad, C. R. A. Catlow, *J. Cryst. Growth*, 2006, 294, 2
- <sup>174</sup>K. Doll, J. C. Schön, M. Jansen, *Phys. Chem. Chem. Phys.*, 2007, 9, 6128
- <sup>175</sup>J. Wang, A. J. Kulkarni, K. Sarasamak, S. Limpijumnong, F. J. Ke, M. Zhou, *Phys. Rev. B*, 2007,76, 172103
- <sup>176</sup>B. J. Morgan, *Phys. Rev. B*, 2008, 78, 024110
- <sup>177</sup>B. Wang, X. Wang, J. Zhao, *J. Phys. Chem. C*, 2010, 114, 5741
- <sup>178</sup>W. Sangthong, J. Limtrakul, F. Illas, S. T. Bromley, *Phys. Chem. Chem. Phys.*, 2010, 12,8513
- <sup>179</sup>M. A. Zwijnenburg, S. T. Bromley, *Phys. Chem. Chem. Phys.*, 2010, 12, 14579
- <sup>180</sup>H. Müller-Buschbaum, *Z. Anorg. Allg. Chem.*, 2010, 636, 275
- <sup>181</sup>R. Hoppe, E. Seipp, R. Baier, *J. Solid State Chem.*, 1988, 72, 52
- <sup>182</sup>M. A. Zwijnenburg, S. T. Bromley, *J. Mater. Chem.*, 2011, 21, 15255
- <sup>183</sup>J. D. Bryngelson, P. G. Wolynes, *P. Natl. Acad. Sci. USA* 1987, 84, 7524–7528.
- <sup>184</sup>J. D. Wales, *Energy Landscapes*; Cambridge University Press: United Kingdom, 2003.
- <sup>185</sup>R. E. Kunz and R. S. Berry, *J. Chem. Phys.* 103, 1904 (1995).
- <sup>186</sup>R. S. Berry and R. Breitengraser-Kunz, *Phys. Rev. Lett.* 74, 3951 (1995).
- <sup>187</sup>F. Jensen, *Introduction to Computational Chemistry*; John Wiley and Sons: second ed.; 2006.
- <sup>188</sup>W. H. Press, S. A. Teukolsky, W. T. Vetterling, B. P. Flannery, *Numerical Recipes*; Cambridge University Press: New York, 3rd ed.; 2007.
- <sup>189</sup>G. Kresse, D. Joubert, *Phys. Rev. B* 1999, 59, 1758.
- <sup>190</sup>W. K. Press, S. A. Teukolsky, W. T. Vetterlin, and B. T. Flannery, *Numerical Recipes*, 3rd edition ed. (Cambridge University Press, Cambridge, 2007).

- 
- <sup>191</sup> Z. Li and H. A. Scheraga, Proc. Natl. Acad. Sci. U.S.A. 84, 6611 (1987).
- <sup>192</sup> D.J. Wales, J.P.K Doye. J. Phys. Chem. A. 101, 5111, (1997)
- <sup>193</sup> N. Metropolis, A. W. Rosenbluth, M. N. Rosenbluth, A. H. Teller, E. Teller. J. Chem. Phys. 21, 1087, (1953)
- <sup>194</sup> Ewald, P. P. (1921). Annalen der Physik 64, 253-287.
- <sup>195</sup> Dick, B. G. & Overhauser, A. W. (1958). Physical Review 112, 90-103.
- <sup>196</sup> Buckingham A. (1938) *Mathematical and Physical Sciences* 168: 264-283.
- <sup>197</sup> J. D. Gale, J. Chem. Soc., Faraday Trans. 1997, 93 (4), 629
- <sup>198</sup> Lennard-Jones, J. E. (1924) *Proceedings of the Royal Society A* 106: 463-477.
- <sup>199</sup> Born, M. ; Oppenheimer, J. R. *Zur Quantentheorie der Molekeln. Ann. d. Physik* 1927, 84, 457.
- <sup>200</sup> Hohenberg, P.; Kohn, W., *Physical Review* 1964, 136 (3B), B864.
- <sup>201</sup> Kohn, W.; Sham, L. J., *Physical Review* 1965, 140 (4A), A1133.
- <sup>202</sup> Kokalj, A., *Comp. Mat. Sci.* 2003, 28, 155.
- <sup>203</sup> Perdew, J. P.; Chevary, J.A.; Vosko, S.H.; Jackson, K.A.; Pederson, M. R.; Singh, D. J.; and C. Fiolhais, *Phys. Rev. B* 1992, 46, 6671.
- <sup>204</sup> Perdew, J. P.; Burke, K.; Ernzerhof, M. *Phys. Rev. Lett.* 1996, 77, 3865.
- <sup>205</sup> Blöchl, P. E. *Phys. Rev. B* 1994, 50, 17953.
- <sup>206</sup> Blöchl, P. E., *Bull. Mater. Sci.* 2003, 26, 33.
- <sup>207</sup> Broyden, C. G., *Math. Comput.* 1965, 19, 547.
- <sup>208</sup> Feynman, R. P., *Phys. Rev.* 1939, 56, 340.
- <sup>209</sup> Behrman, E. C.; Foehrweiser, R. K.; Myers, J. R.; French, B. R.; Zandler, M. E. *Phys. Rev. A* 1994, 49, R1543.
- <sup>210</sup> Matxain, J. M.; Fowler, J. E.; Ugalde, J. M. *Phys. Rev. A* 2000, 62, 053201.
- <sup>211</sup> C. R. A. Catlow, S. T. Bromley, S. Hamad, M. Mora-Fonz, A. A. Sokol, S. M. Woodley, *Phys. Chem. Chem. Phys.*, 2010, 12, 786.
- <sup>212</sup> A. A. Al Sunaidi, A. A. Sokol, C. R. A. Catlow, S. M Woodley, *J. Phys. Chem. C*, 2008, 112, 18860.
- <sup>213</sup> G. Mallocci, L. Chiodo, A. Rubio, A. Mattoni, *J. Phys. Chem. C*, 2012, 116, 8741.
- <sup>214</sup> I. Demiroglu, D. Stradi, F. Illas, S. T. Bromley, *J. Phys.: Condens. Matter*, 2011, 23, 334215.
- <sup>215</sup> M. Chelvayohan, C. H. B. Mee, 1982, *J. Phys. C: Solid State Phys.* 15 2305
- <sup>216</sup> A. Goldman, V. Dose, G. Borstel, *Phys. Rev. B*, 1985, 32, 1971
- <sup>217</sup> A. Michaelides, K. Reuter, M. Scheffler, *J. Vac. Sci. Technol. A*, 2005, 23, 1487.
- <sup>218</sup> E. Lundgren, A. Mikkelsen, J. N. Andersen, M. Schmid, P. Varga, *J. Phys. Condens. Matter*, 2006, 18, R481.
- <sup>219</sup> Y. Zheng , L. Zheng , Y. Zhan , X. Lin , Q. Zheng ,K. Wei, *Inorg. Chem.*, 2007, 46, 6980.
- <sup>220</sup> C. R. A. Catlow, S. A. French, A. A. Sokol, M. Alfredsson, S. T. Bromley, *Faraday Discuss.*, 2003, 124, 185.

- 
- <sup>221</sup> A. M. Ferrari, G. Pacchioni, *J. Phys. Chem.*, 1996, 100, 9032.
- <sup>222</sup> J. C. Sharp, Y. X. Yao, C. T. Campbell, *J. Phys. Chem. C*, 2013, 117, 24932.
- <sup>223</sup> C. L. Phillips, P. D. Bristowe, *Surf. Sci*, 2011, 605, 450.
- <sup>224</sup> J. J. BelBruno, *Surf. Sci.* 2008, 602, 1837.
- <sup>225</sup> E. Sanville, J. J. BelBruno, *Phys. Rev. B*, 2007, 76, 085412.
- <sup>226</sup> C. L. Freeman, F. Claeysens, N. L. Allan, J. H. Harding, *Phys. Rev. Lett.* 2006, 96, 066102.
- <sup>227</sup> L. Zhang, H. Huang, *Appl. Phys. Lett.* 2007, 90, 023115.
- <sup>228</sup> A. J. Kulkarni, M. Zhou, K. Sarasamak, S. Limpijumnong, *Phys. Rev. Lett.* 2006, 97, 105502.
- <sup>229</sup> C. Tusche, H. L. Meyerheim, J. Kirschner, *Phys. Rev. Lett.* 2007, 99, 026102.
- <sup>230</sup> G. Weirum, G. Barcaro, A. Fortunelli, F. Weber, R. Schennach, S. Surnev, F. P. Netzer, *J. Phys. Chem. C*, 2010, 114, 15432.
- <sup>231</sup> Z. Lin, P. D. Bristowe, *Phys. Rev. B*, 2007, 75, 205423.
- <sup>232</sup> Y. Wang, W. Wang, K. Fan, J. Deng, *Surface Science*, 2001, 490, 125
- <sup>233</sup> M. E. Straumanis, S. M. Riad, *J. Mater. Sci.* 1988, 23, 757.
- <sup>234</sup> Z. Li and H. A. Scheraga, *Proc. Natl. Acad. Sci. U.S.A.* 84, 6611 (1987).
- <sup>235</sup> D.J. Wales, J.P.K Doye. *J. Phys. Chem. A.* 101, 5111, (1997)
- <sup>236</sup> S. M. Woodley, *J. Phys. Chem. C.* 2013, 117, 24003.
- <sup>237</sup> J. D. Gale, A. L. Rohl, *Mol. Simul.* 2003, 29, 291.
- <sup>238</sup> L. Whitmore, A. A. Sokol, C. R. A. Catlow, *Surf. Sci.* 2002, 498, 135.
- <sup>239</sup> I. Demiroglu, D. Stradi, F. Illas, S. T. Bromley, *J. Phys.: Condens. Matter*, 2011, 23, 334215.
- <sup>240</sup> G. Kresse, J. Hafner, *Phys. Rev. B*, 1993, 47, 558.
- <sup>241</sup> J. P. Perdew, Y. Wang, *Phys. Rev. B*, 1992, 45, 13244.
- <sup>242</sup> P. E. Blöchl, *Phys. Rev. B*, 1994, 50, 17953.
- <sup>243</sup> G. Kresse, D. Joubert, *Phys. Rev. B*, 1999, 59, 1758.
- <sup>244</sup> A. A. Al-Sunaidi, A. A. Sokol, C. R. A. Catlow, S. M. Woodley, *J. Phys. Chem. C*, 2008, 112, 18860.
- <sup>245</sup> A. Wood, M. Giersig, M. Hilgendorff, A. Vilas-Campos, L. M. Liz-Marzan, P. Mulvaney, *Aust. J. Chem.* 2003, 56, 1051
- <sup>246</sup> A. C. Reber, S. N. Khanna, J. S. Hunjan, M. R. Beltran, *Eur. Phys. J. D* 2007, 43, 221.
- <sup>247</sup> C. R. A. Catlow, S. A. French, A. A. Sokol, A. A. Al-Sunaidi, S. M. Woodley, *J. Comput. Chem.*, 2008, 29, 2234.
- <sup>248</sup> Freeman C L, Claeysens F, Allan N L and Harding J H 2006 *Phys. Rev. Lett.* 96 066102
- <sup>249</sup> Morgan B J 2009 *Phys. Rev. B* 80 174105
- <sup>250</sup> Tusche C, Mayerheim H L and Kirschner J 2007 *Phys. Rev. Lett.* 99 026102
- <sup>251</sup> Weirum G, Barcaro G, Fortunelli F, Weber F, Schennach R, Surnev S and Netzer F 2010 *J. Phys. Chem. C* 114 15432
-

- 
- <sup>252</sup>Topakal M, Cahangirov S, Bekaroglu E and Ciraci S 2009 *Phys. Rev. B* 80 235119
- <sup>253</sup>Stradi D, Illas F and Bromley S T 2010 *Phys. Rev. Lett.* 105 045901
- <sup>254</sup>Kresse G and Hafner J 1993 *Phys. Rev. B* 47 558
- <sup>255</sup>Perdew J P and Wang Y 1992 *Phys. Rev. B* 45 13244
- <sup>256</sup>Blöchl P E 1994 *Phys. Rev. B* 50 17953
- <sup>257</sup>Kresse G and Joubert D 1999 *Phys. Rev. B* 59 1758
- <sup>258</sup>Guest M F, Bush I J, van Dam H J J, Sherwood P, Thomas J M H, van Lenthe J H, Havenith R W A and Kendrick J 2005 *Mol. Phys.* 103 719
- <sup>259</sup>Stephens P J, Devlin F J, Chabalowski C F and Frisch M J 1994 *J. Phys. Chem.* 98 11623
- <sup>260</sup>Schafer A, Horn H and Ahlrichs R 1992 *J. Chem. Phys.* 97 2571
- <sup>261</sup>Gale J D and Rohl A L 2003 *Mol. Simul.* 29 291
- <sup>262</sup>Whitmore L, Sokol A A and Catlow C R A 2002 *Surf. Sci.* 498 135
- <sup>263</sup>Cleri F and Rosato V 1993 *Phys. Rev. B* 48 22
- <sup>264</sup>Duffy D M, Harding J H and Stoneham A M 1993 *Phil. Mag. A* 67 865
- <sup>265</sup>Monkhorst H J and Pack J D 1976 *Phys. Rev. B* 13 5188
- <sup>266</sup>Grimme S 2006 *J. Comput. Chem.* 27 1787
- <sup>267</sup>Mercurio G *et al* 2010 *Phys. Rev. Lett.* 104 036102
- <sup>268</sup>Müller F, Hüfner S, Sachdev H, Laskowski R, Blaha P and Schwarz K 2010 *Phys. Rev. B* 82 113406
- <sup>269</sup>Laskowski R, Blaha P and Schwarz K 2008 *Phys. Rev. B* 78 045409
- <sup>270</sup>French S A, Sokol A A, Bromley S T, Catlow C R A, Rogers S C and Sherwood P 2003 *J. Chem. Phys.* 118 317
- <sup>271</sup>Janotti A and Van deWalle C G 2007 *Nature Mater.* 6 44
- <sup>272</sup>Scholl D S and Ma Y H 2006 *MRS Bull.* 31 770
- <sup>273</sup>Locklin, J.; Roberts, M. E.; Mannsfeld, S. C.B.; Bao, Z. N. *Polymer Reviews* 2006, 46 (1), 79.
- <sup>274</sup>B. Wen, R. Molnik, *Chem. Phys. Lett.*, 2008, 466, 84.
- <sup>275</sup>4L ZnO - PRL
- <sup>276</sup>A. Navrotsky, *Proc. Natl. Acad. Sci. U.S.A.* 101, 12 096 (2004).
- <sup>277</sup>X. Wang, J. Song, and Z. L. Wang, *J. Mater. Chem.* 17, 711 (2007).
- <sup>278</sup>C. Tusche, H. L. Mayerheim, and J. Kirschner, *Phys. Rev. Lett.* 99, 026102 (2007).
- <sup>279</sup>G. Weirum, G. Barcaro, A. Fortunelli, F. Weber, R. Schennach, S. Surnev, and F. P. Netzer, *J. Phys. Chem. C* 114, 15 432 (2010).
- <sup>280</sup>C. L. Freeman, F. Claeysens, N. L. Allan, and J. H. Harding, *Phys. Rev. Lett.* 96, 066102 (2006).
- <sup>281</sup>D. Wu, M.G. Lagally, and F. Liu, *Phys. Rev. Lett.* 107, 236101 (2011).
- <sup>282</sup>BCT refers to the International Zeolite Association code for the Body Centered Tetragonal framework which has the underlying 4-connected topology of the silicate Mg-BCTT.

- 
- <sup>283</sup> B. J. Morgan, *Phys. Rev. B* 82, 153408 (2010).
- <sup>284</sup> M. A. Zwijnenburg, F. Illas, and S. T. Bromley, *Phys. Rev. Lett.* 104, 175503 (2010).
- <sup>285</sup> A. Wander and N. M. Harrison, *J. Chem. Phys.* 115, 2312 (2001).
- <sup>286</sup> M. Valtiner, M. Todorova, G. Grundmeier, and J. Neugebauer, *Phys. Rev. Lett.* 103, 065502 (2009).
- <sup>287</sup> G. S. Oleinik and N.V. Danilenko, *Russ. Chem. Rev.* 66, 553 (1997).
- <sup>288</sup> J. D. Gale, *Z. Kristallogr.* 220, 552 (2005).
- <sup>289</sup> The BYL-ZnO polymorph has the same underlying net as the mineral beryllonite: <http://rcsr.anu.edu/nets/byl>.
- <sup>290</sup> C. Klingshirn, *Phys. Stat. Sol. (b)* 244, 3027 (2007).
- <sup>291</sup> L. Schmidt-Mende, J. L. MacManus-Driscoll, *Mater. Today* 10, 40 (2007).
- <sup>292</sup> D. C. Reynolds, D. C. Look, B. Jogai, C. W. Litton, G. Cantwell, and W. C. Harsch, *Phys. Rev. B* 60, 2340 (1999).
- <sup>293</sup> W. C. T. Lee, C. E. Kendrick, R. P. Millane, Z. Liu, S. P. Ringer, K. Washburn, P. T. Callaghan and S. M. Durbin, *J. Phys. D: Appl. Phys.* 45, 135301 (2012).
- <sup>294</sup> B. Reesja-Jayan, E. De la Rosa, S. Sepulveda-Guzman, R. A. Rodriguez and M. Jose Yacaman, *J. Phys. Chem. C* 112, 240 (2008).
- <sup>295</sup> S. Bhattacharyya and A. Gedanken, *Micro. Meso. Mater.* 110, 533 (2008).
- <sup>296</sup> A. Schleife, C. Rodl, J. Furthmuller and F. Bechstedt, *New J. Phys.* 13, 085012 (2011).
- <sup>297</sup> B. Meyer, D. Marx, O. Dulub, U. Diebold, M. Kunat, D. Langenberg and C. Woll, *Angew. Chem. Int. Ed.* 43, 6642 (2004).
- <sup>298</sup> J. Prades, A. Cirera and J. R. Morante, *Sens. Actuators B* 142, 179 (2009).
- <sup>299</sup> M. A. Zwijnenburg, F. Illas and S. T. Bromley, *Phys. Rev. Lett.* 104, 175503 (2010).
- <sup>300</sup> Ch. Baerlocher and L. B. McCusker, Database of Zeolite Structures: <http://www.izastructure.org/databases/>
- <sup>301</sup> M. D. Foster and M. M. J. Treacy, A Database of Hypothetical Structures: <http://www.hypotheticalzeolites.net>
- <sup>302</sup> M. O'Keeffe, M. A. Peskov, S. J. Ramsden and O. M. Yaghi, *Accts. Chem. Res.* 41, 1782 (2008).
- <sup>303</sup> Y. Li, J. Yu, D. Liu, W. Yan, R. Xu and Y. Xu, *Chem. Mater.*, 15, 2780 (2003).
- <sup>304</sup> M. A. Zwijnenburg, F. Illas and S. T. Bromley, *Phys. Rev. Lett.* 104, 175503 (2010).
- <sup>305</sup> S. M. Woodley, M. B. Watkins, A. A. Sokol, S. A. Shevlin and C. R. A. Catlow, *Phys. Chem. Chem. Phys.*, 11, 3176 (2009).
- <sup>306</sup> G. Kresse and J. Furthmuller. *Phys. Rev. B*, 54, 11169 (1996).
- <sup>307</sup> T. F. Willems, C. H. Rycroft, M. Kazi, J. C. Meza and M. Haranczyk, *Micro. Meso. Mater.* 149, 134 (2012).
- <sup>308</sup> M. Shishkin and G. Kresse, *Phys. Rev. B*, 75, 235102 (2007).
- <sup>309</sup> J. Hughes and A. Navrotsky, *J. Amer. Chem. Soc.*, 133, 9184 (2011).

---

<sup>310</sup> R. F. Bader, *Atoms in Molecules: A Quantum Theory* (Oxford University Press, Oxford, 1990).